UDK 669+666+678+53

ISSN 1580-2949
MTAEC9, 48(5)607–800(2014)

MATER. TEHNOL.	LETNIK VOLUME 48	ŠTEV. NO. 5	STR. P. 607–800	LJUBLJANA SLOVENIJA	SEP.–OCT. 2014

VSEBINA – CONTENTS

PREGLEDNI ČLANEK – REVIEW ARTICLE

An overview of the influence of stainless-steel surface properties on bacterial adhesion
Vpliv lastnosti površine nerjavnega jekla na adhezijo bakterij
M. Hočevar, M. Jenko, M. Godec, D. Drobne . . . 609

IZVIRNI ZNANSTVENI ČLANKI – ORIGINAL SCIENTIFIC ARTICLES

Adsorption of hexavalent chromium from an aqueous solution of steel-making slag
Adsorpcija heksavalentnega kroma iz vodne raztopine jeklarske žlindre
A. Štrkalj, Z. Glavaš, G. Matijašić . . . 619

Structural, mechanical and cytotoxicity characterization of as-cast biodegradable Zn-xMg (x = 0.8–8.3 %) alloys
Strukturne, mehanske in citotoksične lastnosti biorazgradljive Zn-xMg (x = 0,8–8,3 %) zlitine v litem stanju
J. Kubásek, I. Pospíšilová, D. Vojtěch, E. Jablonská, T. Ruml . . . 623

Structural characterization of a bulk and nanostructured Al-Fe system
Karakterizacija strukture osnove in nanostrukture sistema Al-Fe
A. Fekrache, M. Yacine Debili, S. Lallouche . . . 631

Wear behavior of Al/SiC/graphite and Al/FeB/graphite hybrid composites
Vedenje hibridnih kompozitov Al/SiC/grafit in Al/FeB/grafit pri obrabi
S. Şahın, N. Yüksel, H. Durmuş, S. Gençalp İrızalp . . . 639

Mathematical model for an Al-coil temperature calculation during heat treatment
Matematični model za izračun temperature v Al-kolobarju med toplotno obdelavo
F. Vode, F. Tehovnik, J. Burja, B. Arh, B. Podgornik, D. Steiner Petrovič, M. Malenšek, L. Kočevar, M. Lažeta . . . 647

Investigating the effects of cutting parameters on the hole quality in drilling the Ti-6Al-4V alloy
Preiskava vpliva parametrov rezanja na kvaliteto izvrtine, izvrtane v zlitino Ti-6Al-4V
Y. Hışman Çelik . . . 653

Influence of graphite on the hardness and wear behavior of AA6061–B_4C composite
Vpliv grafita na trdoto in vedenje kompozita AA6061–B_4C pri obrabi
S. Prabagaran, Govindarajulu Chandramohan, P. Shanmughasundaram . . . 661

Tribology of CrAg7N coatings deposited on Vanadis 6 ledeburitic tool steel
Tribologija prevlek CrAg7N na ledeburitnem orodnem jeklu Vanadis 6
P. Bílek, P. Jurči, M. Hudáková, Ľ. Čaplovič, M. Novák . . . 669

Morphology and magnetic properties of Fe_3O_4-alginic acid nanocomposites
Morfologija in magnetne lastnosti nanokompozitov Fe_3O_4-alginska kislina
M. Kaźmierczak, K. Pogorzelec-Glaser, A. Hilczer, S. Jurga, Ł. Majchrzycki, M. Nowicki, R. Czajka, F. Matelski, R. Pankiewicz, B. Łęska, L. Kępiński, B. Andrzejewski . . . 675

Microstructural comparison of the thermomechanically treated and cold deformed Nb-microalloyed trip steel
Primerjava mikrostruktur termomehansko obdelanega in hladno deformiranega, z Nb-mikrolegiranega trip-jekla
A. Grajcar, K. Radwański . . . 679

Control of the metallurgical processing of ICDP cast irons
Kontrola metalurške obdelave litega železa ICDP
J. Hampl, T. Válek, P. Lichý, T. Elbel . . . 685

Synthesis comparison and characterization of chitosan-coated magnetic nanoparticles prepared with different methods
Primerjava postopkov in karakterizacija magnetnih nanodelcev, prevlečenih s hitozanom
G. Hojnik Podrepšek, Ž. Knez, M. Leitgeb . . . 689

Study of phase transformations in Cr-V tool steel
Študij faznih premen v orodnem jeklu Cr-V
M. Pašák, R. Čička, P. Bílek, P. Jurči, Ľ. Čaplovič . . . 693

Model antimicrobial polymer system based on poly(vinyl chloride) and crystal violet
Model protimikrobnega polimernega sistema na osnovi polivinilklorida in kristal violeta
J. Klofáč, I. Kuřitka, P. Bažant, K. Jedličková, J. Sedlák . . . 697

Effect of the tool geometry and welding parameters on the macrostructure, fracture mode and weld strength of friction-stir spot-welded polypropylene sheets
Vpliv geometrije orodja in parametrov varjenja na makrostrukturo, vrsto preloma in trdnost zvara pri torno-vrtilnem točkastem varjenju polipropilenskih plošč
M. Kemal Bilici, A. İrfan Yükler, A. Kastan 705

Microstructural analysis of CuAlNiMn shape-memory alloy before and after the tensile testing
Analiza mikrostrukture zlitine CuAlNiMn z oblikovnim spominom pred nateznim preizkusom in po njem
I. Ivanić, M. Gojić, S. Kožuh, B. Kosec 713

Effect of the initial microstructure on the properties of low-alloyed steel upon mini-thixoforming
Vpliv začetne mikrostrukture na lastnosti malolegiranega jekla po predelavi mini-thixoforming
B. Mašek, D. Aišman, H. Jirková 719

Experimental investigation of the surface properties obtained by cutting Brass-353 ($\alpha+\beta$) with an abrasive water jet and other cutting methods
Preiskava lastnosti površine medenine 353 ($\alpha+\beta$) po rezanju z abrazijskim vodnim curkom in drugimi metodami rezanja
A. Akkurt 725

Influence of the working technology on the development of alloys H13-w(Cu) 87.5 %
Vpliv tehnologije izdelave na razvoj zlitine H13-w(Cu) 87,5 %
U. Artiček, M. Bojinovič, M. Brunčko, I. Anžel 735

Microstructure characteristics of the Al-w(Cu) 4.5 % model alloy
Mikrostrukturne značilnosti modelne zlitine Al-w(Cu) 4,5 %
B. Šuštaršič, M. Jenko, B. Šarler 743

Chromite spinel formation in steelmaking slags
Nastanek kromitnih spinelov v jeklarskih žlindrah
J. Burja, F. Tehovnik, J. Medved, M. Godec, M. Knap 753

STROKOVNI ČLANKI – PROFESSIONAL ARTICLES

Recycling of jute wastes using pulpzyme enzyme
Recikliranje odpadkov jute z uporabo encima pulpzima
K. Mohajershojaei, F. Dadashian 757

Influences of the heat input on a 2205 duplex stainless steel weld
Vpliv vnosa toplote v zvar dupleksnega nerjavnega jekla 2205
B. Rajkumar Gnanasundaram, M. Natarajan. 761

Tribological behavior and characterization of borided cold-work tool steel
Tribološko vedenje in karakterizacija boriranega orodnega jekla za delo v hladnem
I. Gunes 765

Microstructures of the Al-Fe-Cu-X alloys prepared at various solidification rates
Mikrostruktura zlitin Al-Fe-Cu-X po različnih hitrostih strjevanja
M. Voděrová, P. Novák, F. Průša, D Vojtěch 771

Assessment of the post-impact damage propagation in a carbon-fibre composite under cyclic loading
Ocena napredovanja poškodbe po udarcu pri ponavljajočih se obremenitvah kompozita z ogljikovimi vlakni
D. Kytýř, T. Fíla, J. Šleichrt, T. Doktor, M. Šperl. 777

Possibilities for increasing the purity of steel in production using secondary-metallurgy equipment
Možnosti povečanja čistosti jekla pri proizvodnji z uporabo opreme za sekundarno metalurgijo
M. Korbáš, L. Čamek, M. Raclavský 781

Effect of different surface-heat-treatment methods on the surface properties of AISI 4140 steel
Vpliv različnih toplotnih obdelav površine na lastnosti površine jekla AISI 4140
A. Ayday, M. Durman 787

Preparation and application of polymer inclusion membranes (PIMs) including alamine 336 for the extraction of metals from an aqueous solution
Priprava in uporaba membrane iz polimera (PIM) in alamina 336 za ločenje kovin iz vodnih raztopin
Y. Yildiz, A. Manzak, B. Aydın, O. Tutkun 791

Accelerated carbide spheroidisation and refinement (ASR) of the C45 steel during controlled rolling
Pospešena sferoidizacija in udrobnjenje karbidov (ASR) pri kontroliranem valjanju jekla C45
D. Hauserova, J. Dlouhy, Z. Novy 797

UDK 669.14.018.8:620.179.11
Review article/Pregledni članek

ISSN 1580-2949
MTAEC9, 48(5)609(2014)

AN OVERVIEW OF THE INFLUENCE OF STAINLESS-STEEL SURFACE PROPERTIES ON BACTERIAL ADHESION

VPLIV LASTNOSTI POVRŠINE NERJAVNEGA JEKLA NA ADHEZIJO BAKTERIJ

Matej Hočevar[1,2], Monika Jenko[1], Matjaž Godec[1], Damjana Drobne[3]
[1]Institute of Metals and Technology, Lepi pot 11, 1000 Ljubljana, Slovenia
[2]Jožef Stefan International Postgraduate School, Jamova 39, 1000 Ljubljana, Slovenia
[3]Department of Biology, Biotechnical Faculty, University of Ljubljana, Večna pot 111, 1000 Ljubljana, Slovenia
matej.hocevar@imt.si

Prejem rokopisa – received: 2014-02-06; sprejem za objavo – accepted for publication: 2014-06-02

The adhesion and growth of bacteria on the surface of stainless steel promotes corrosion of the material, microbiological contamination, healthcare problems and results in economic losses. There are numerous factors influencing the adhesion of bacteria to stainless steel, and material properties are one of the most important ones. In particular, surface roughness, topography, chemistry and surface energy can promote or inhibit the adhesion and growth of bacteria. Surface roughness and topography are generally accepted as crucial parameters, especially when the surface features are comparable to the size of the bacteria. The roughening of the surface increases the area available for adhesion and protects the bacteria from environmental factors, like liquid shear stress, mechanical forces and disinfectants. The surface chemistry and surface energy of the material can also affect microbial attachment and survival. The surface chemistry of stainless steel is significantly affected by the formation of an ultra-thin passive chromium-rich oxide film on the surface in the presence of an oxidative environment. Surface energy is also an important factor in the initial adhesion and it is commonly known that the minimal relative adhesion to surfaces occurs at surface energies ranging between 20 mN/m and 30 mN/m (Baier curve). Materials with a high surface energy, such as stainless steel, are mainly hydrophilic, frequently negatively charged and susceptible to contamination, and thus are rarely clean. This paper presents an overview of the mechanism and theories of bacterial adhesion on surfaces in general, together with a comprehensive overview of stainless-steel surface properties that may influence the adhesion of bacteria. Here we give a literature review and discuss how to manage the stainless-steel surfaces in food processing, medicine and other industries in order to reduce the adhesion of bacteria.

Keywords: stainless steel, surface properties, adhesion, bacteria

Adhezija in rast bakterij na površini nerjavnega jekla pospešuje korozijo materiala, povzroča mikrobiološko kontaminacijo, zdravstvene težave in posledično gospodarsko škodo. Na adhezijo bakterij vplivajo številni dejavniki, med katerimi so lastnosti materiala med pomembnejšimi. Sem spadajo predvsem hrapavost, topografija, kemijska sestava in površinska energija. Hrapavost in topografija površine sta splošno sprejeta kot ključna dejavnika, ki vplivata na adhezijo bakterij na površino, predvsem kadar so topografske značilnosti na površini primerljive velikosti z bakterijo. Povečana hrapavost po eni strani pomeni večjo površino za pritrjevanje, po drugi strani pa ščiti bakterije pred okoljskimi dejavniki, kot so strižne napetosti v tekočih medijih, mehanske sile in razkužila. Kemijska sestava površine in površinska energija materiala lahko tudi vplivata na adhezijo in preživetje bakterij. Na kemijske lastnosti površine izrazito vpliva oksidna plast, ki se ustvari na površini nerjavnega jekla. Površinska energija je prav tako pomemben dejavnik pri začetni fazi adhezije. Splošno znano je razmerje med adhezijo in površinsko energijo, ki ga opisuje Baierjeva krivulja, kjer minimalno adhezijo na površini opazimo pri površinski energiji med 20 mN/m in 30 mN/m. Materiali z visoko površinsko energijo, kot je na primer nerjavno jeklo, so pogosto hidrofilni, negativno nabiti in dovzetni za kontaminacijo, tako da so te površine redko čiste. Članek daje splošen pregled mehanizmov in teorije adhezije bakterij na površine. Podrobno je podan pregled površinskih lastnosti nerjavnega jekla, ki lahko vplivajo na adhezijo bakterij. V članku razpravljamo o tem, kako zmanjšati adhezijo bakterij v živilskopredelovalni industriji ter pri medicinski uporabi. Za uspešno zmanjševanje neželene adhezije bakterij je potrebno poglobljeno znanje o dejavnikih, ki v največji meri vplivajo na adhezijo bakterij.

Ključne besede: nerjavno jeklo, lastnosti površine, adhezija, bakterije

1 INTRODUCTION

Bacteria generally exist freely or as a population attached to surfaces.[1] When available, bacteria prefer to grow on surfaces[2] forming aggregates known as biofilms. Bacterial adhesion and the subsequent biofilm formation is a complex physico-chemical process consisting of several stages, including the development of a surface-conditioning film, the approach of bacteria to the surface, adhesion (initial reversible and subsequent irreversible adhesion), the growth and division of organisms and finally detachment and dispersal of cells.[1,3–5]

The adhesion of bacteria to surfaces depends on the properties of the material (surface topography, roughness, surface chemistry and surface energy), the bacteria (surface charge, surface hydrophobicity and appendages) and the surrounding environment (type of medium, temperature, pH, period of exposure and bacterial concentration).[6,7] Among them, the material surface properties are one of the most important.

Stainless steels are commonly used in industrial, medical and food-processing applications,[8,9] and the adhesion of bacteria to stainless steel represents a chronic source of microbial contamination that leads to the deterioration of food, healthcare problems, the enhanced corrosion of stainless steel and reduces the performance of plants, pipelines, cooling towers and heat exchangers.[1,3,10–12]

Stainless steels can be produced in various grades and finishes, and additional surface treatments can affect surface physico-chemical properties.[13–15] The same type of stainless steel may have distinctly different surface properties, including topography, roughness, molecular composition, electrochemistry and physico-chemistry.[15] Additionally, an ultra-thin oxide film composed of chromium and iron oxides forms on the stainless-steel surface, which makes the steel resistant to corrosion.[14,15] The surface properties of stainless steel depend on the stainless-steel grade, the surface finish applied and the cleaning process used.[15] The passive oxide layer is also very susceptible to contamination from the environment (dissolve solutes and molecules from air)[16,17] and contamination can alter the surface properties and influence the adhesion.

The influence of stainless-steel surface properties on the adhesion and retention of bacteria has been extensively investigated. There have been numerous studies on different stainless steels, including AISI 302[18], AISI 304[8,13,19–32], AISI 316[13,23–26,32–37] and AISI 430[13,25] using different bacteria. However, it is still not clear as to which characteristics of stainless steels are favourable for bacterial adhesion as they are often interrelated.[15]

To reduce microbial adhesion and retention on stainless-steel surfaces it is necessary to understand the factors governing microbial adhesion through the systematic research of the various surface properties involved.

This review summarizes the influence of the surface properties of stainless steel, especially surface roughness, topography, chemistry and energy on the adhesion and retention behaviour of bacteria. The aim of this review is to summarize the available literature data on the material surface characteristics that are responsible for bacterial adhesion. We will emphasize the stainless-steel-bacterial adhesion in order to provide information about how to produce and maintain the surfaces in order to reduce bacterial contamination.

2 THEORY AND MECHANISM OF BACTERIAL ADHESION TO A SURFACE

The adhesion of bacteria to a substrate surface is governed by the physico-chemical properties of both the substrate and the bacterium, and also the environmental conditions.[6,7,38] Bacteria may adhere to the surface either directly to the bare material (nonspecific adhesion) or indirectly to the conditioning film (specific adhesion) on the surface. Usually, nonspecific adhesion is investigated and these results are the closest to the predictions of theoretical models.[39] However, in natural environments the first step of the adhesion process is the formation of a conditioning layer[4,5] of organic and inorganic molecules that may alter the physico-chemical properties of the surface, provide a nutrient source for bacteria or inhibit the adhesion of certain bacteria.[5]

2.1 Theoretical background of bacterial adhesion

2.1.1 Physico-chemical Models of Bacterial Adhesion

Concepts developed in colloidal research are a common approach to predicting bacterial adhesion to surfaces.[2,10] If bacteria are treated as colloids in suspension, it is possible to model the bacterial adhesion to surfaces as the sum of the chemical and physical properties of bacteria and the material surface.[39] Three colloidal models are commonly applied when studying bacterial adhesion to surfaces: the thermodynamic theory, the Deryaguin–Landau–Verwey–Overbeek (DLVO) theory and the extended-DLVO (XDLVO) theory.[10,39,40]

2.1.1.1 Thermodynamic theory

The thermodynamic approach is based on the total change in the potential Gibbs free energy (energy available in a closed system) when a bacterium attaches to a surface and is calculated from the Lifshitz-van der Waals forces and Lewis acid-base interactions[39]:

$$\Delta G_{\mathrm{ADH}} = \Delta G_{\mathrm{LW}} + \Delta G_{\mathrm{AB}} \tag{1}$$

ΔG_{ADH} is the total change of the Gibbs free energy of adhesion, ΔG_{LW} is the Gibbs free energy change of the Lifshitz-van der Waals forces and ΔG_{AB} is the Gibbs free energy change of the Lewis acid-base forces. Thermodynamic theory assumes that adhesion is always reversible and distance independent. The theory does not include the effects of surface charge and the electrolyte concentration of the surrounding media. This theory is the most accurate with uncharged surfaces or in the presence of large quantities of ions.[39]

2.1.1.2 DLVO theory

The DLVO theory like the thermodynamic approach also assumes that adhesion is the sum of interfacial energies. However, the DLVO theory considers electrostatic forces instead of acid-base interactions[39]:

$$U^{\mathrm{DLVO}} = U^{\mathrm{LW}} + U^{\mathrm{EL}} \tag{2}$$

U^{DLVO} is the total interaction energy, U^{LW} is the Lifshitz-van der Waals interactions energy and U^{EL} is the electrostatic interaction energy. DLVO theory assumes that adhesion can be reversible and distance dependent. The theory is most accurate when electrostatic forces are predominant; however, it is limited due to the disregarded effects of the polar interactions.[39]

2.1.1.3 XDLVO theory

In an attempt to more accurately model bacterial adhesion the XDLVO theory combined the features of the thermodynamic approach and DLVO theory. The XDLVO model assumes that adhesion is the sum of the Lifshitz-van der Waals, electrostatic and Lewis acid-base interactions[39]:

$$U^{DLVO} = U^{LW} + U^{EL} + U^{AB} \qquad (3)$$

U^{DLVO} is the total interaction energy, U^{LW} is the Lifshitz-van der Waals interaction energy, U^{EL} is the electrostatic interaction energy and U^{AB} is the Lewis acid-base interaction energy. Like with the DLVO, also XDLVO theory assumes that adhesion can be reversible and distance dependent.[39]

All three models favour bacterial adhesion when the product of the equations' theories is negative. An increase or decrease in bacterial adhesion for one set of parameters compared to a different set of parameters is calculated. These three theoretic models that predict the bacterial adhesion to surfaces were developed for ideal systems; however, the actual bacterial adhesion is complex and can behave completely differently from the prediction of the developed models.[39]

2.2 Mechanism of bacterial adhesion

Actual bacterial adhesion frequently deviates from the above-described adhesion models.[10] Solid materials exposed to various environments adsorb organic and inorganic material, thus forming a conditioning layer to which microorganisms attach.[10] The conditioning layer changes the physico-chemical properties of the surface and thus plays an important role in the bacterial attachment process.[5,10]

The adhesion of bacteria to solid surfaces is a two-phase process composed of an initial reversible (physical) followed by an irreversible (molecular and cellular) phase.[2,5,41] The adhesion of bacteria to the surface may be passive or active and this depends on the motility of the bacteria and the transportation of cells by gravity, the diffusion of bacteria and the fluid dynamic forces.[3,5] Initial adhesion also depends on the physico-chemical properties of bacteria cells, their growth phase and the availability of nutrients.[3]

The adhesion of bacteria to surfaces occurs rapidly, within seconds.[42,43] Planktonic microbial cells are transported from the suspension to the conditioned surface either by bacterial appendages or by physical forces, thus enabling an initial reversible adhesion.[1,3,41] The long-range physical forces, including van der Waals forces, steric and electrostatic interactions, influence the initial reversible adhesion. During this initial stage the bacteria still show Brownian motion and can be easily removed from the surface.[3,41]

After an initial reversible adhesion a number of cells adhere irreversibly. In this phase molecular reactions between bacterial surface structures and substrate surfaces become predominant. In contrast to reversible adhesion, various short-range forces such as dipole-dipole interactions, hydrogen, ionic and covalent bonding and hydrophobic interactions are involved.[1–3,41] Once the bacteria attach, irreversible strong physical or chemical forces are required to remove them from the surface.[3]

The irreversibly attached bacterial cells start to grow, divide and form microcolonies, the basic structural unit of the biofilm.[1,3,44] The production of additional extracellular polymeric substances (EPS) helps to strongly bind the cells to the surface and stabilize the microcolonies from the environmental fluctuations[1,3] and the presence of nutrients in the conditioning film and the surrounding environment determines the rapid growth and division of cells.[1] The biofilm not only enables the strong attachment of the cells to the surface, but also helps collect diffuse nutrients, acts as a protection against environmental stress, antibiotics and disinfectants and enables intercellular communications. As the biofilm ages the attached bacteria detach and disperse from the biofilm and colonize new niches.[1,3]

3 FACTORS AFFECTING BACTERIAL ADHESION TO SURFACES

Bacterial adhesion is a complex process affected by the characteristics of the bacteria, environmental properties and the physical and chemical properties of a material surface.[6,7,38] Environmental factors including the type of medium, temperature, pH, shear stress of the flowing medium, bacterial concentration, chemical treatment and the presence of antibiotics may influence bacterial adhesion by either changing the surface characteristics of the bacteria and material or influencing the interactions in a reversible phase of adhesion. Furthermore, different bacterial species and strains adhere differently for a given material. This is due to the differences in the physic-chemical characteristics of the bacteria, including surface hydrophobicity, surface charge, appendages and EPS production.[6,7] The physical and chemical properties of a material surface that can influence bacterial adhesion to the material surface include surface roughness, topography or physical configuration, chemical composition, surface energy and hydrophobicity.[6,7] However, the surface characteristics can be quickly altered by the adsorption of organic and inorganic compounds forming a conditioning layer.[3,5,10] This review will focus on the properties of stainless steel that can influence bacterial adhesion.

3.1 Stainless-steel surface properties affecting bacterial adhesion

Stainless steels are iron-based alloys containing at least 10.5 % Cr with numerous alloying elements that improve the mechanical and corrosion properties.[9] Stainless steel is the material of choice in the food-processing industry[14,15,45], mainly because it is inert, resistant to corrosion, stable at various temperatures and hygienic.[45,46]

Stainless steel can be produced in various grades (AISI 302, AISI 304, AISI 316, AISI 420) and finishes (2B, 2R, 2D, number 4 finish), thus having different surface properties (chemistry, topography, roughness, energy).[13,14] Furthermore, additional surface treatments such as mechanical or electro polishing can be applied to modify the surface topography and roughness and achieve functionally and aesthetically improved surfaces.[13,45] When the commonly used 2B surface finish is additionally grinded/polished with SiC papers and diamond paste, different surface patterns are obtained (**Figure 1**).[47] Stainless steel forms an ultra-thin oxide film on the surface composed of chromium and iron oxides that protects the steel from corrosion. The composition of the oxide film depends on the metal substrate, the surface finish and the surrounding environment.[15]

3.1.1 Effect of surface roughness and topography on bacterial adhesion

Stainless steel produced in different surface finishes is designated by a system of standardized numbers: No. 1, 2D, 2B, and 2BA for unpolished finishes; and No. 3, 4, 6, 7, and 8 for polished finishes.[9] The 2B pickling finish, the 2R bright annealed finish and finish 4 are the most often used.[14,15] During production, stainless steel goes through annealing and pickling processes where the stainless steel is softened and descaled. These processes clean the surface of the material prior to processing to a given finish.[14] After cold rolling, which reduces the thickness of the steel, final annealing (in oxidising atmosphere) and pickling follows and the surface finish obtained is designated as a 2D surface finish. When the 2D surface finish is finally light passed on polished rolls 2B or pickling finish is obtained.[9,15] To achieve a bright finish or a 2R finish, the stainless steel is annealed in a protective atmosphere and the final pickling process is avoided.[15] Finish 4 is achieved when 2D or 2R sheets are further polished with fine-grained polish belts.[9,15] The surface composition, topography and roughness for a given material may differ considerably according to the different surface finishes applied.[15]

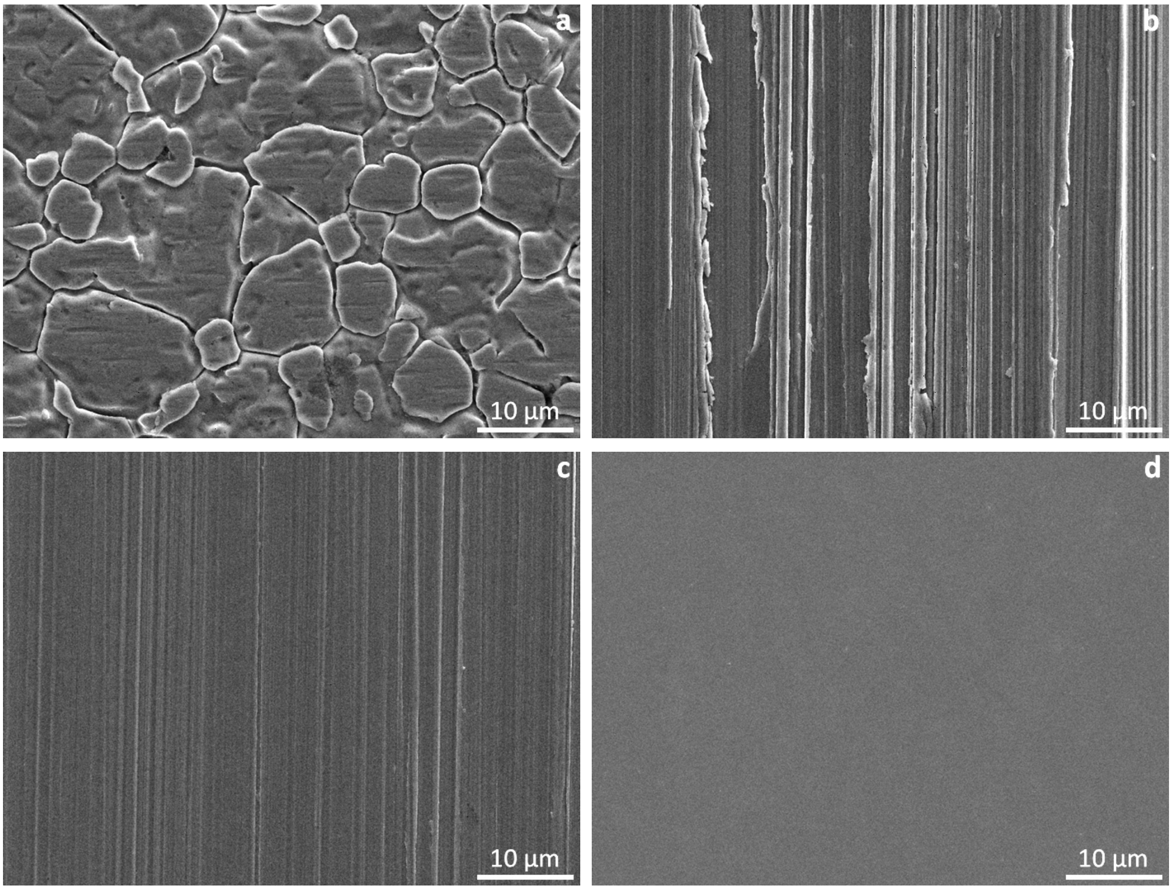

Figure 1: Secondary-electron (SE) images taken on scanning electron microscope illustrate the surface features of different surface finishes of AISI 316L stainless steel: a) 2B surface finish, b) 2B surface finish grinded with 100 SiC grit paper, c) 2B surface finish grinded with 800 SiC grit paper and d) 2B surface finish polished with diamond paste 3 µm and 1 µm to mirror finish. The 2B surface finish (a) has a network of subsurface crevices between the oxide grain boundaries; mechanically grinded surface finishes (b, c) exhibit scratch patterns with long linear alternating grooves and ridges; and the mirror surface finish (d) is the smoothest without pronounced topography features.[47]

Slika 1: Slike sekundarnih elektronov (SE), posnete z vrstičnim elektronskim mikroskopom, prikazujejo topografske karakteristike različno obdelanih površin nerjavnega jekla AISI 316L: a) 2B površina, b) 2B površina, brušena z granulacijo papirja 100 SiC, c) 2B površina, brušena z granulacijo papirja 800 SiC in d) 2B površina, polirana z diamantno pasto 3 µm in 1 µm. 2B površina (a) ima mrežo razpok med oksidnimi zrni na površini; na mehansko poliranih površinah (b, c) je opazen vzorec prask z dolgimi izmeničnimi dolinami; polirana površina (d) na drugi strani nima izrazite topografije.[47]

When studying bacterial adhesion to surfaces, a comprehensive characterization of the surface-roughness parameters and visualisation of the surface topography is very important.[38,48] Surface roughness is a two-dimensional parameter of a material surface and is usually described as the arithmetic average roughness (R_a) and the root mean square roughness (R_q)[6,38], whereas the topography is a-three dimensional parameter and describes the shape of the surface features.[6] The R_a and R_q, are commonly reported surface-roughness parameters when investigating bacterial adhesion; however, they are measures of the height variation without information about the topography (surface features).[38,48] Therefore, it is important to measure the spatial or amplitude parameters that give information about the spatial variation and to visualize and describe the morphological features of the surface.[38]

Stainless-steel grades AISI 302, AISI 304 and AISI 316 are most often used in adhesion studies due to their application in the food industry and medicine.[14,15,33,49] In the literature regarding adhesion and retention, bacteria genus Escherichia, Staphylococcus, Listeria, Pseudomonas, Streptococcus and Salmonella are the most often studied.[14] Although a number of studies have investigated the influence of the surface topography and roughness of different stainless steels on the adhesion of different bacteria the conclusions from these studies are not consistent.[38,48]

Several researchers including Jullien et al.[13], Ortega et al.[19], Whitehead and Verran[23], Flint et al.[26], Peterman et al.[27], Hilbert et al.[50] and observed no direct correlation between the surface roughness of the AISI 304/316 stainless R_a ranging between 0.01 μm and 3.3 μm and the adhesion of bacteria or spores. Arnold et al.[8,30] and Ortega et al.,[29] on the other hand, reported a positive correlation between the adhesion of bacteria and the surface roughness of the AISI 304 stainless steel. However, Goulter-Thorsen et al.[20] reported that *E. coli* attached in greater numbers to significantly smoother AISI 304 stainless steels. Also interesting are the findings of Medilanski et al.[51] who reported that minimal adhesion occurs at $R_a = 0.16$ μm and attachment to both rougher and smother surfaces was significantly higher. The increased adhesion of bacteria on rougher surfaces may be explained due to the increase in the surface area available for adhesion[6,7] and the roughening of the surface might also facilitate a firmer attachment by providing more contact points.[52] The opposing observations reported between the different studies are probably due to the various experimental conditions, different bacterial species tested, the material studied and methods used for bacteria detection.[26,42]

Besides surface roughness, also the topography of the surface or surface features such as pits, crevices, scratches, grooves and ridges, play an important part in the adhesion process.[15,38,43,45] Many researchers concluded that if the surface features are comparable to the size of the bacteria they can promote bacterial attachment and increase the subsequent microbial retention.[6,7,43,48]

The bacteria attach differently to surfaces with different surface topographies or special surface features and often the pattern of adhesion reflects the surface topography (**Figure 2**).[47] Medilanski et al.[51] studied the influence of an AISI 304 stainless-steel surface topography (three surface finishes with scratches and two without observable scratches) on the adhesion of four bacteria strains (*Desulfovibrio desulfuricans*, *Pseudomonas aeruginosa*, *Pseudomonas putida* and *Rhodococcus* sp.) and found that bacterial cells attach into scratches in the longitudinal orientation when the width of the scratches corresponds to the width of the bacterial cells. Rougher surfaces with wider scratches exhibit a higher fraction of bacteria adhered in other orientations and the smoothest surfaces exhibit a random cell orientation.[51] Flint et al.[26] observed that surface flaws (scrapes, scratches and pitting) on AISI 304 stainless steel did not always affect the number of adhered bacteria; however, bacteria often aligned with the lines created by the surface flaws. Similar observations were made by Whitehead and Verran[23] on AISI 304 and AISI 316 stainless steel. Barnes et al.[21] compared the 2B and 8 mirror finish of AISI 304 stainless steel and reported that *Staphylococcus aureus* attach in greater numbers to a rougher 2B surface finish, whereas little differences between the 2B and number 8 mirror finish were observed for *Listeria monocytogenes.* Furthermore, scanning electron microscopy revealed that bacteria cells did not orient exclusively along polishing lines.[21] Using microbial retention assays with a range of differently sized, unrelated microorganisms on engineered surfaces (silicon wafers) with controlled topographical features Whitehead et al.[53,54] and Verran et al.[55] demonstrated that the size of the surface features is important with respect to the size of the bacteria, and its subsequent retention.

The wear of the surfaces may change the adhesion and retention of bacteria[14,45] with the introduction of new random features (i.e., scratches) different dimensions[45], especially on smooth polished surfaces. Studies of simulated worn surfaces demonstrated that the hygienic status of stainless steel was not affected in terms of microbial retention; however, the cleanability was affected in terms of the reduced removal of organic soil.[45] Holah and Thorpe[46] observed the increased retention of bacterial cells on abraded sinks compared to unused ones, this is due to the fact that rougher surfaces have an increase in the number of attachment sites, a larger surface contact area and topographical features that reduce the cleaning shear forces. Verran et al.[32] simulated wear on AISI 304 and AISI 316 stainless steel and studied the retention of *Pseudomonas aeruginosa* and *Staphylococcus aureus*. The results showed that wear corresponding to $R_a < 0.8$ μm did not significantly affect the retention of microorganisms, but the pattern of

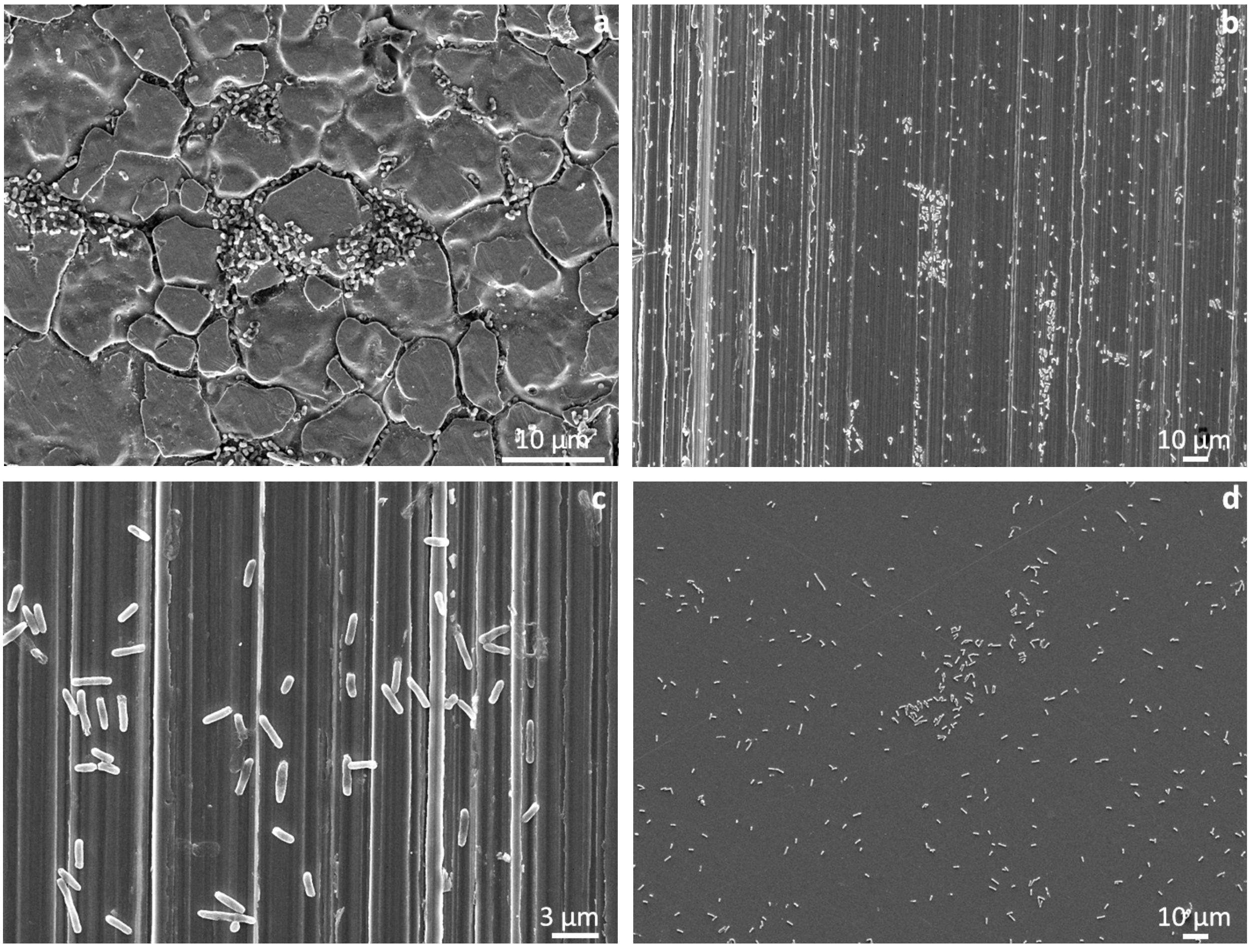

Figure 2: SE images of attachment patterns of *Escherichia coli* cells to surfaces with different surface finishes of AISI 316L stainless steel: a) 2B surface finish, b) 2B surface finish grinded with 100 SiC grit paper, c) 2B surface finish grinded with 800 SiC grit paper and d) 2B surface finish polished with diamond paste 3 µm and 1 µm to mirror finish. On 2B surface finish (a) microorganisms attach to the crevices between oxide grain boundaries, whereas on mechanically polished surface finishes (b, c) bacteria align often along longitudinal scratches (when comparable to the size of the bacteria). On the other hand, mirror finish (d) exhibited a less pronounced topography and microorganisms were observed to be distributed across the surfaces more randomly.[47]

Slika 2: SE-slike razporeditve celic bakterije *Escherichia coli* na različno obdelanih površinah nerjavnega AISI jekla 316L: a) 2B površina, b) 2B površina, brušena z granulacijo papirja 100 SiC, c) 2B površina, brušena z granulacijo papirja 800 SiC in d) 2B površina, polirana z diamantno pasto 3 µm in 1 µm. Na površini 2B (a) se bakterije pritrjujejo v razpoke med oksidnimi zrni na površini, medtem ko se na mehansko brušenih vzorcih (b, c) bakterije pogosto orientirajo vzdolž prask (kadar so primerljivih velikosti z bakterijami). Po drugi strani poliran vzorec nima izrazite topografije in razporeditev bakterij na površini je naključna.[47]

the attachment was highly affected by the surface topography.[32] Linear surface features will be more easily cleaned along rather than across the features and presumably also more easily than surfaces with random linear features across the surface. Furthermore, an increase in the surface roughness may cause the entrapment of microorganisms within the surface features and reduce the cleanability; however, if the surface features are significantly larger than the microbial cells, then they are relatively easily removed from the surface.[14] Therefore, it is important to visualise the surface features as well as measure the roughness parameters as the wear of food contact surfaces can affect the topography without any observable change in roughness.[45]

3.1.2 Effect of surface chemistry, hydrophobicity and energy

Stainless steels, produced in various grades and finishes, also vary in surface properties like chemistry, topography, roughness and surface energy.[14,15] Stainless steel forms an invisible oxide film (passivation) on the surface composed of chromium and iron oxides that protects the steel from corrosion.[14,15,45] The composition of the oxide film depends on the metal substrate, the surface finish and the surrounding medium.[15] When scratched from surface the oxide layer forms within seconds and due to the speed of re-passivation it is difficult to determine the exact chemical composition of the surface.[45] The passive film on a stainless steel is not static but it changes (grows, dissolves and may adsorb or incorporate anions) according to the environment.[56]

From a physico-chemical standpoint, the energy characteristics of stainless steel depend on the surface finish and on the cleaning process used[15] and a high- or low-energy surface can be obtained depending on the cleaning treatment.[15,28]

Surface energy is inversely proportional to the thickness of the contaminating carbon layer that is not eliminated by cleaning. The cleaning also affects the surface charge of the steel. For a given surface finish, and with a pH above the isoelectric point, a more or less negatively charged surface can be obtained.[15] In the food industry, the electrostatic interactions are repulsive because stainless-steel surfaces are generally negatively charged at neutral or alkaline pH and microorganisms are also negatively charged at these pH values in low-concentration aqueous solutions. In weakly charged liquids such as water, repulsive electrostatic interactions are significant, whereas in high electrolyte concentrations (milk, wine) the effect of surface charge is obscured.[15] Metals compared to polymers have a high surface energy, they are mainly hydrophilic, frequently negatively charged[6,15,17] and when exposed adsorb dissolved solutes or atmospheric contaminants, thus being rarely clean.[17] On the other hand, metal oxides provide positively-charged surfaces that can significantly increase the adhesion of negatively-charged bacteria to surfaces, primarily due to their positive charge and hydrophobicity.[40]

It is thought that hydrophobic materials are more susceptible to bacterial adhesion in contrast to hydrophilic.[6,7] The adhesion of vegetative cells, bacterial spores and freshwater bacteria has been shown to increase with increasing surface hydrophobicity. The cell attachment to hydrophobic plastic occurs very quickly compared to hydrophilic surfaces (metals oxides, metal and glass) where longer exposure times are needed.[43] Marine *Pseudomonas* sp. attach in large numbers to hydrophobic plastics with little or no surface charge, moderate to hydrophilic metals with a positive or neutral surface charge and few to hydrophilic, negatively charged materials such as glass and oxidized plastics.[6] Teixeira et al.[57] reported that hydrophobic and hydrophilic bacteria attach in greater numbers to relatively hydrophobic surfaces with a low surface energy like AISI 316 and AISI 304 stainless steel compared to polymethylmethacrylate (PMMA) and glass which are more hydrophilic. Sinde and Carballo[58] studied the adhesion of *Salmonella* spp. and *Listeria monocytogens* strains to AISI 304 stainless steel, rubber and polytetrafluorethylene (PTFE). The attachment results showed that in general *Salmonella* and *Listeria monocytogens* strains adhered in greater numbers to more hydrophobic material (rubber and PTFE), with stainless steel being the least hydrophobic.[58] Boulangé-Petermann et al.[28] studied the wettability of AISI 304 stainless steel with 2B and 2RB surface finishes with respect to the cleaning process. The cleaning process affected the wettability of a solid stainless steel surface; however, the results obtained regarding bacterial adhesion showed no direct correlation between the wettability or surface energy and the adhesion of *Streptococcus thermophiles*.[28] Flint et al.[26] studied the adhesion of thermoresistant streptococci (*Streptococcus thermophilus* and *Streptococcus waiu*) to different substrates (stainless steel, aluminium, zinc, cooper and glass) and different grades of stainless steel (AISI 304L and AISI 316L). The influence of substrate hydrophobicity, charge and a thin oxide film on stainless steel surfaces was also investigated with respect to the adhesion of thermo-resistant streptococci.[26] The results showed that bacteria preferentially attach to stainless steel and zinc compared to copper, aluminium and glass. Bacteria adhere in higher numbers to AISI 316L stainless steel with a 2B surface finish compared to AISI 304L stainless steel with the same surface finish, indicating the role of the chemical composition on the adhesion.[26] On the other hand, Percival et al.[59,60] reported a greater number of adhering viable cells on AISI 304 stainless steel compared to grade AISI 316 in a water piping system over a period of a few months. Flint et al.[26] also observed that negatively charged surfaces attracted more bacteria than positively charged surfaces and the unpassivated stainless-steel surface (without oxide layer) reduced the adhesion of thermo-resistant streptococci, thus suggesting that a stainless-steel surface oxide film enhances adhesion. However, when stainless steel is exposed to air repassivation occurs and the ability to attract bacteria is restored.[26]

The influence of surface energy on adhesion has been studied extensively and the surface energy of the material is an important factor influencing adhesion. The Baier curve demonstrates the relationship between the relative adhesion of organisms and the energy of the surface where minimal adhesion occurs between 20–30 mN/m.[61] The surface energy of the substrate also depends on the conditioning layer (defined by the surrounding environment) and surface structure with surface irregularities. In an aqueous environment a conditioning film forms immediately after exposure of the surface and changes the substrate properties and affects microbial retention.[43]

More comprehensive investigations on different stainless steels with well-known properties (roughness, topography and surface chemistry) are necessary in order to determine the effect of surface chemistry on bacterial adhesion. However, surface physico-chemical properties are interrelated, therefore, it is difficult to draw the conclusions of the effects on adhesion due solely to one of them.[15]

4 CONCLUSIONS

Bacterial adhesion is governed by properties of the material surface, bacterial surface characteristics and the surrounding environment, therefore a comprehensive and multidisciplinary approach is necessary in order to improve the understanding of factors contributing to the adhesion and retention of bacteria to surfaces.

The adhesion of bacteria to stainless steel and retention on surfaces can enhance the corrosion of steel, present the source of contamination in the food-processing industry, cause healthcare problems in medicine and decreases the performance of equipment in other industries, thus causing economic losses. Therefore, it is important to control and reduce the adhesion process.

Stainless-steel surface properties including roughness, topography, chemistry, surface energy and hydrophobicity affect the adhesion of bacteria. These factors are interdependent.

The surface topography and roughness play a crucial role, especially when they are comparable to the size of the bacteria and can promote the adhesion and retention while reducing the cleanability of the surface. On the other hand, hydrophobicity and surface energy also play an important role in the adhesion process as hydrophobic surfaces are more susceptible to adhesion in comparison to hydrophilic ones and a low surface energy is better than a high surface energy.

The physico-chemical properties of the substrate are important in initial cell adhesion; however, once a biofilm is formed the effect of surface properties on adhesion diminishes, but the effect on retention and cleanability is still observable.

In order to reduce or manage the adhesion to stainless-steel surfaces in food processing, medical application and other industries, knowledge of factors that govern bacterial adhesion is necessary for each material being used. It is important to take into account the grade of the steel, the surface finish applied, the surface roughness, the cleaning procedures used and the age of the steel.

A surface-modification approach should concentrate on a reduction of the initial bacterial adhesion process and, on the other hand, cleaning protocols used should be improved, to increase the removal of bacteria. With wear these protocols should be adjusted (intensified).

Stainless steel is hard, inert, hygienic and has good wear resistance compared to plastic and ceramics, and when using smooth surfaces with effective cleaning and disinfection procedures this is the best approach to reducing adhesion in food processing, medicine and industry.

However, we also have to take into account the properties of different bacteria and surrounding environment where stainless steel is exposed. Therefore, the adhesion of a particular group of bacteria that are expected to contaminate the surfaces should be tested.

Acknowledgment

The work was conducted at the Institute of Metals and Technology in the frame of research programme Surface physics and chemistry of metallic materials (P2-0132).

5 REFERENCES

[1] T. R. Garrett, M. Bhakoo, Z. B. Zhang, Progress in Natural Science, 18 (**2008**), 1049–1056

[2] Y. H. An, R. B. Dickinson, R. J. Doyle, Mechanisms of Bacterial Adhesion and Pathogenesis of Implant and Tissue Infections, In: Y. H. An, R. J. Friedman (Eds.), Handbook of Bacterial Adhesion, Humana Press, New Jersey 2000, 1–27

[3] C. G. Kumar, S. K. Anand, International Journal of Food Microbiology, 42 (**1998**), 9–27

[4] B. Gottenbos, H. C. van der Mei, H. J. Busscher, Models for studying initial adhesion and surface growth in biofilm formation on surfaces, In: J. D. Ron (Ed.), Methods in Enzymology, Academic Press, Massachusetts, 1999, 523–534

[5] S. L. Percival, S. Malic, H. Cruz, D. W. Williams, Introduction to Biofilms, In: S. Percival, D. Knottenbelt, C. Cochrane (Eds.), Biofilms and Veterinary Medicine, Springer-Verlag, Berlin Heidelberg 2011, 41–68

[6] K. Merritt, Y. H. An, Factors Influencing Bacterial Adhesion, In: Y. H. An, R. Friedman (Eds.), Handbook of Bacterial Adhesion, Humana Press, New Jersey 2000, 53–72

[7] Y. H. An, R. J. Friedman, Journal of Biomedical Materials Research, 43 (**1998**), 338–348

[8] J. W. Arnold, G. W. Bailey, Poultry Science, 79 (**2000**), 1839–1845

[9] S. D. Washko, G. Aggen, Wrought stainless steel, In: ASM International Handbook Committee (Eds.), Properties and selection: Irons, Steels, and High-Performance Alloys, ASM International, Ohio 1990, 2004–2195

[10] K. Hori, S. Matsumoto, Biochemical Engineering Journal, 48 (**2010**), 424–434

[11] Z. Lewandowski, H. Beyenal, Mechanisms of Microbially Influenced Corrosion, In: H. C. Flemming, P. S. Murthy, R. Venkatesan, K. Cooksey (Eds.), Marine and Industrial Biofouling, Springer-Verlag, Berlin Heidelberg, 2009, 35–64

[12] J. P. Marechal, C. Hellio, International Journal of Molecular Sciences, 10 (**2009**), 4623–4637

[13] C. Jullien, T. Benezech, B. Carpentier, V. Lebret, C. Faille, Journal of Food Engineering, 56 (**2003**), 77–87

[14] J. Verran, Testing surface cleanability in food processing, In: H. L. M. Lelieveld, A. Mostert, J. T. Holah (Eds.), Handbook of Hygiene Control in the Food Industry, CRC press, New York, 2005, 556–571

[15] L. Boulangé-Petermann, Biofouling, 10 (**1996**), 275–300

[16] O. Santos, T. Nylander, R. Rosmaninho, G. Rizzo, S. Yiantsios, N. Andritsos, A. Karabelas, H. Müller-Steinhagen, L. Melo, L. Boulangé-Petermann, C. Gabet, A. Braem, C. Tragardh, M. Paulsson, Journal of Food Engineering, 64 (**2004**), 63–79

[17] M. Fletcher, Methods for Studying Adhesion and Attachment to Surfaces, In: R. Grigorova, J. R. Norris (Eds.), Methods in Microbiology, Academic Press, Massachusetts 1990, 251–283

[18] L. Rivas, N. Fegan, G. A. Dykes, International Journal of Food Microbiology, 115 (**2007**), 89–94

[19] M. P. Ortega, T. Hagiwara, H. Watanabe, T. Sakiyama, Food Control, 21 (**2010**), 573–578

[20] R. M. Goulter-Thorsen, E. Taran, I. R. Gentle, K. S. Gobius, G. A. Dykes, Journal of Food Protection, 74 (**2011**), 1359–1363

[21] L. M. Barnes, M. F. Lo, M. R. Adams, A. H. L. Chamberlain, Applied and Environmental Microbiology, 65 (**1999**), 4543–4548

[22] J. H. Ryu, L. R. Beuchat, Applied and Environmental Microbiology, 71 (**2005**), 247–254

[23] K. A. Whitehead, J. Verran, International Biodeterioration & Biodegradation, 60 (**2007**), 74–80

[24] E. Vanhaecke, J. P. Remon, M. Moors, F. Raes, D. Derudder, A. Vanpeteghem, Applied and Environmental Microbiology, 56 (**1990**), 788–795

[25] C. Jullien, T. Benezech, C. Le Gentil, L. Boulangé-Petermann, P. E. Dubois, J. P. Tissier, M. Traisnel, C. Faille, Biofouling, 24 (**2008**), 163–172

[26] S. H. Flint, J. D. Brooks, P. J. Bremer, Journal of Food Engineering, 43 (**2000**), 235–242

[27] L. Boulangé-Petermann, J. Rault, M. N. Bellon-Fontaine, Biofouling, 11 (**1997**), 201–216

[28] L. Boulangé-Petermann, B. Baroux, M. N. Bellon-Fontaine, Journal of Adhesion Science and Technology, 7 (**1993**), 221–230

[29] M. P. Ortega, T. Hagiwara, H. Watanabe, T. Sakiyama, Japan Journal of Food Engineering, 9 (**2008**), 251–259

[30] J. W. Arnold, D. H. Boothe, G. W. Bailey, Transactions of the Asae, 44 (**2001**), 347–356

[31] A. Allion, J. P. Baron, L. Boulangé-Petermann, Biofouling, 22 (**2006**), 269–278

[32] J. Verran, D. L. Rowe, R. D. Boyd, Journal of Food Protection, 64 (**2001**), 1183–1187

[33] W. C. Chiang, I. S. Tseng, P. Moller, L. R. Hilbert, T. Tolker-Nielsen, J. K. Wu, Materials Chemistry and Physics, 119 (**2010**), 123–130

[34] J. A. Barish, J. M. Goddard, Food and Bioproducts Processing, 91 (**2013**), 352–361

[35] M. Hjelm, L. R. Hilbert, P. Møller, L. Gram, Journal of Applied Microbiology, 92 (**2002**), 903–911

[36] G. G. Geesey, R. J. Gillis, R. Avci, D. Daly, M. Hamilton, P. Shope, G. Harkin, Corrosion Science, 38 (**1996**), 73–95

[37] C. Faille, J. M. Membre, J. P. Ussier, M. N. Bellon-Fontaine, B. Carpentier, M. A. Laroche, T. Benezech, Biofouling, 15 (**2000**), 261–274

[38] R. J. Crawford, H. K. Webb, V. K. Truong, J. Hasan, E. P. Ivanova, Advances in Colloid and Interface Science, 179 (**2012**), 142–149

[39] T. F. Moriarty, A. H. C. Poulsson, E. T. J. Rochford, R. G. Richards, Bacterial Adhesion and Biomaterial Surfaces, In: P. Ducheyne (Ed.), Comprehensive Biomaterials, Elsevier Ltd., Oxford 2011, 75–100

[40] F. M. Al-Abbas, J. R. Spear, A. Kakpovbia, N. M. Balhareth, D. L. Olson, B. Mishra, The Journal of Pipeline Engineering, 11 (**2012**), 63–72

[41] J. Palmer, S. Flint, J. Brooks, Journal of Industrial Microbiology & Biotechnology, 34 (**2007**), 577–588

[42] F. Riedewald, PDA Journal of Pharmaceutical Science and Technology, 60 (**2006**), 164–171

[43] K. A. Whitehead, J. Verran, The Effect of Substratum Properties on the Survival of Attached Microorganisms on Inert Surfaces, In: H. C. Flemming, P. S. Murthy, R. Venkatesan, K. Cooksey (Eds.), Marine and Industrial Biofouling, Springer-Verlag, Berlin Heidelberg 2009, 13–33

[44] J. W. Costerton, International Journal of Antimicrobial Agents, 11 (**1999**), 217–221

[45] J. Verran, P. Airey, A. Packer, K. A. Whitehead, Microbial Retention on Open Food Contact Surfaces and Implications for Food Contamination, In: A. I. Laskin, S. Sariaslani, G. M. Gadd (Eds.), Advances in Applied Microbiology, Academic Press, Massachusetts 2008, 223–246

[46] J. T. Holah, R. H. Thorpe, Journal of Applied Bacteriology, 69 (**1990**), 599–608

[47] M. Hočevar, M. Godec, M. Jenko, D. Drobne, N. Gunde-Cimerman, S. Novak, The adhesion of bacteria to austenitic stainless steel with different surface roughness, Proc. of the MC 2013: Microscopy conference, Regensburg, Germany, 2013, 35–36

[48] K. A. Whitehead, J. Verran, Food and Bioproducts Processing, 84 (**2006**), 253–259

[49] J. A. Disegi, L. Eschbach, Injury, 31 (**2000**), S2–S6

[50] L. R. Hilbert, D. Bagge-Ravn, J. Kold, L. Gram, International Biodeterioration & Biodegradation, 52 (**2003**), 175–185

[51] E. Medilanski, K. Kaufmann, L. Y. Wick, O. Wanner, H. Harms, Biofouling, 18 (**2002**), 193–203

[52] J. Verran, R. D. Boyd, Biofouling, 17 (**2001**), 59–71

[53] K. A. Whitehead, J. Colligon, J. Verran, Colloids and Surfaces B-Biointerfaces, 41 (**2005**), 129–138

[54] K. A. Whitehead, D. Rogers, J. Colligon, C. Wright, J. Verran, Colloids and Surfaces B-Biointerfaces, 51 (**2006**), 44–53

[55] J. Verran, A. Packer, P. Kelly, K. A. Whitehead, Letters in Applied Microbiology, 50 (**2010**), 258–263

[56] C. O. A. Olsson, D. Landolt, Electrochimica Acta, 48 (**2003**), 1093–1104

[57] P. Teixeira, Z. Lopes, J. Azeredo, R. Oliveira, M. J. Vieira, Food Microbiology, 22 (**2005**), 247–251

[58] E. Sinde, J. Carballo, Food Microbiology, 17 (**2000**), 439–447

[59] S. L. Percival, J. S. Knapp, R. G. J. Edyvean, D. S. Wales, Water Research, 32 (**1998**), 2187–2201

[60] S. L. Percival, J. S. Knapp, R. G. J. Edyvean, D. S. Wales, Water Research, 32 (**1998**), 243–253

[61] T. Vladkova, Surface Modification Approach to Control Biofouling, In: H. C. Flemming, P. S. Murthy, R. Venkatesan, K. Cooksey (Eds.), Marine and Industrial Biofouling, Springer-Verlag, Berlin Heidelberg 2009, 135–163

UDK 544.726:544.3:544.4
Original scientific article/Izvirni znanstveni članek

ISSN 1580-2949
MTAEC9, 48(5)619(2014)

ADSORPTION OF HEXAVALENT CHROMIUM FROM AN AQUEOUS SOLUTION OF STEEL-MAKING SLAG

ADSORPCIJA HEKSAVALENTNEGA KROMA IZ VODNE RAZTOPINE JEKLARSKE ŽLINDRE

Anita Štrkalj[1], Zoran Glavaš[1], Gordana Matijašić[2]

[1]University of Zagreb, Faculty of Metallurgy, Aleja narodnih heroja 3, 44 000 Sisak, Croatia
[2]University of Zagreb, Faculty of Chemical Engineering and Technology, Marulićev trg 19, 10 000 Zagreb, Croatia
strkalj@simet.hr

Prejem rokopisa – received: 2013-01-15; sprejem za objavo – accepted for publication: 2013-11-18

A batch removal of Cr(VI) ions from an aqueous solution under different experimental conditions using steel-making slag as a low-cost adsorbent is presented in this paper. The obtained results showed that the steel-making slag is an effective adsorbent for the removal of Cr(VI) ions from aqueous solutions. The adsorption of Cr(VI) with the steel-making slag follows the Langmuir isotherm equation. Among the tested kinetics models in this study (pseudo-first-order, pseudo-second-order, Elovich and intraparticle-diffusion models), the pseudo-second-order equation successfully predicted the adsorption. The thermodynamic parameters for the adsorption process were determined and discussed.

Keywords: adsorption, Cr(VI) ions, steel-making slag, isotherms, kinetic, thermodynamic

V članku je predstavljena raziskava odstranjevanja ionov Cr(VI) iz vodne raztopine z jeklarsko žlindro kot poceni adsorbenta pri različnih eksperimentalnih razmerah. Dobljeni rezultati so pokazali, da je jeklarska žlindra učinkovit adsorbent za odstranjevanje Cr(VI) ionov iz vodnih raztopin. Adsorpcija ionov Cr(VI) z jeklarsko žlindro se sklada z Langmuirovo izotermno enačbo. V tej študiji je od preizkušenih kinetičnih modelov (psevdo prvega reda, psevdo drugega reda, Elovichev model in model difuzije med delci) enačba psevdo drugega reda uspešno napovedala adsorpcijo. Določeni in obravnavani so termodinamični parametri za proces adsorpcije.

Ključne besede: adsorpcija, ioni Cr(VI), jeklarska žlindra, izoterme, kinetika, termodinamika

1 INTRODUCTION

Over the last few decades, due to their increased use in the treatment of metals and ceramic, glass production, mining operations and the production of batteries, various heavy metals were released into terrestrial and aquatic ecosystems.[1] The increase in the environmental contamination with heavy metals is a big concern for ecological systems and human health due to their toxicity, accumulation in food and persistence in nature.[2]

The main focus in water and wastewater treatment is given to hexavalent chromium due to its carcinogenic properties.[3] Cr(VI) ions are considered as one of the top 16 toxic pollutants and due to their carcinogenic effect on humans, they have become a serious health problem.[4] Cr(VI) ions can be released into the environment from various industrial operations such as the treatment of metals, production of iron and steel and the production of inorganic chemicals.[5]

Heavy metals can be removed from aqueous solutions using various techniques such as ion exchange,[6] precipitation[7] and adsorption.[8] Adsorption has been successfully used to remove heavy metals.[9] For several decades, activated carbon has been used as an adsorbent for the purification of industrial wastewater.[10] Although it is a most appropriate adsorbent for removing heavy metals, its widespread use was limited due to its high cost. Steel-making slag as an alternative adsorbent has been used to remove heavy metals in the environmental field. Due to its unique properties, steel-making slag is used as an alternative adsorbent for removing heavy metals from aqueous solutions. Steel-making slag is a by-product of the steel production and a waste material that is widely used due to its useful properties.[11]

2 EXPERIMENTAL WORK

Adsorption experiments were performed using the batch-equilibration technique. The initial concentrations of Cr(VI) ions were prepared in the range of 50–300 mg/L of dissolving $K_2Cr_2O_7$ in distilled water. A series of Erlenmeyer flasks containing steel-making-slag samples 1 g and solutions 50 mL were sealed until equilibrium was obtained. Then the adsorbent was removed by filtration. The concentration of Cr(VI) ions was determined using an atomic absorption spectrometer with a graphite furnace, equipped with Zeeman background correction. A Cr hollow-cathode lamp operating at the current of 4 mA was used as a line source. The measurements were performed at 357.9 nm, with the slit fixed at 0.8 nm. The atomization was carried out with the following parameters: T = 2400 °C, the ramp rate of 1200 °C/s and the dwell time of 6 s.[12] Each analysis was performed in triplicate and the average value was taken as the result. The chemical composition of the steel-making slag was determined with the standard chemical analysis[13] and the result in mass fractions (w) is: CaO – 36 %, MgO –

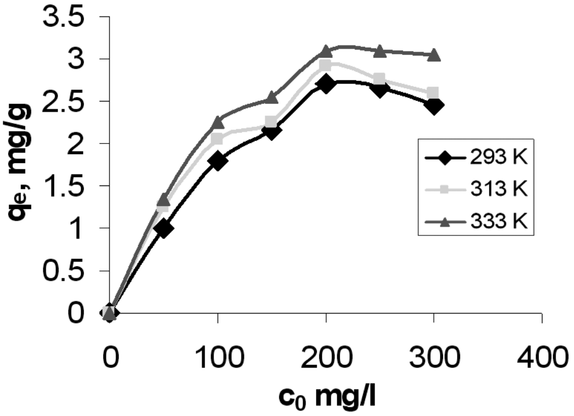

Figure 1: Adsorption isotherms of system steel-making slag – Cr(VI) ions

Slika 1: Adsorpcijske izoterme sistema jeklarska žlindra – ioni Cr(VI)

0.3 %, MnO – 18 %, SiO_2 – 17 %, Al_2O_3 – 1.4 %, FeO – 27 %.

3 RESULTS AND DISCUSSION

3.1 Adsorption isotherms

Figure 1 shows the adsorption isotherms of Cr(VI) ions on the steel-making slag. The adsorption of Cr(VI) ions on the steel-making slag increased with an increase in the ion concentration. This finding is similar to the other studies.[11,14]

The adsorption-equilibrium data were processed using two isotherms: the Freundlich and Langmuir isotherms. The Langmuir isotherm (Equation 1) and the Freundlich isotherm (Equation 2) can be expressed as:[7,8]

$$q_{\mathrm{e}} = \frac{q_{\max} K_{\mathrm{L}} c_{\mathrm{e}}}{1 + K_{\mathrm{L}} c_{\mathrm{e}}} \tag{1}$$

$$q_{\mathrm{e}} = K_{\mathrm{F}} c_{\mathrm{e}}^{1/n} \tag{2}$$

where c_e is the equilibrium concentration of Cr(VI) ions, q_{max} (mg/g) and q_e (mg/g) are the maximum adsorption capacity and the adsorbed amount of Cr(VI) ions. K_F (mg/g) and n are the Freundlich constants. K_F (L/mg) is the adsorption capacity of the adsorbent and n is the intensity of adsorption. K_L is the Langmuir constant related to the energy of adsorption. The parameters of the two isotherms calculated with Equations (1) and (2) are presented in **Table 1** and the fitting curves for the experimental data are shown in **Figures 2** and **3**.

Table 1: Parameters of the Langmuir and Freundlich adsorption-isotherm models

Tabela 1: Parametri Langmuirovega in Freundlichovega modela adsorpcijskih izoterm

	Langmuir			Freundlich		
T K	q_{max} mg/g	K_L L/mg	r^2	n	K_F mg/g	r^2
293	3.14	0.020	0.9580	2.24	0.251	0.8678
313	3.05	0.034	0.9765	2.51	0.366	0.9327
333	3.59	0.029	0.9912	2.80	0.930	0.9172

A comparison of the correlation coefficients and the fitting curves obtained using the two models shows that the Langmuir model was more suitable for the adsorption of Cr(VI) ions from aqueous solutions by the steel-making slag. The Langmuir theory considers the adsorption onto the materials with homogeneous specific surfaces. Therefore, the maximum adsorption capacity (q_{max}) can be obtained from the fittings of the adsorption isotherm.[9]

The main feature of the Langmuir adsorption isotherm is a dimensionless constant called the separation factor or equilibrium parameter (R_L), presented by the following equation:[15,16]

$$R_L = \frac{1}{1 + K_{\mathrm{L}} c_0} \tag{3}$$

where c_0 is the initial concentration of Cr(VI) ions (mg/L). The R_L value indicates the shape of the isotherm to be irreversible ($R_L = 0$), favorable ($0 < R_L < 1$), linear ($R_L = 1$) or unfavorable ($R_L > 1$).[17,18] The R_L value for the studied Cr(VI) ions/steel-making slag system varied from 0.17 to 0.63. It means that the steel-making slag is

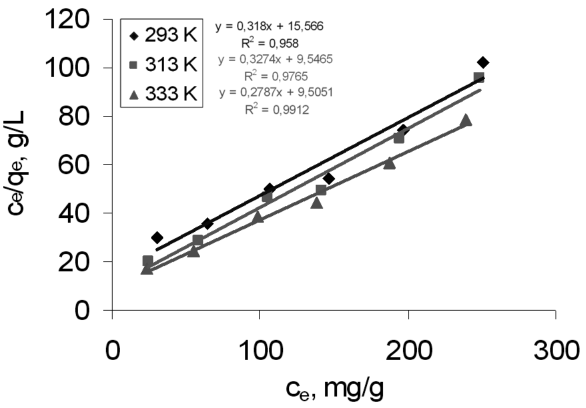

Figure 2: Langmuir isotherms for the adsorption of Cr(VI) ions by steel-making slag

Slika 2: Langmuirove izoterme adsorpcije ionov Cr(VI) na jeklarsko žlindro

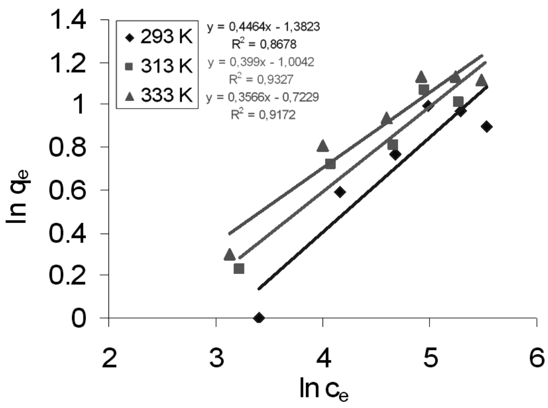

Figure 3: Freundlich isotherms for the adsorption of Cr(VI) ions by steel-making slag

Slika 3: Freundlichove izoterme za adsorpcijo ionov Cr(VI) na jeklarsko žlindro

Table 2: Constants of the adsorption kinetic models (system Cr(VI) ions – steel-making slag)
Tabela 2: Konstante kinetičnih modelov adsorpcije (sistem Cr(VI) ioni – jeklarska žlindra)

Pseudo first order		Pseudo second order		Elovich model			Intraparticle-diffusion model		
k_1 L/min	r^2	k_2 g/(mg min)	r^2	β g/mg	α mg/(g min)	r^2	k_{id} h^{-1}	a	r^2
0.121	0.9204	2.777	0.9999	1.560	2.615	0.9061	17.227	0.340	0.8200

favorable for the adsorption of Cr(VI) ions from aqueous solutions under the conditions used in this study.

For the Freundlich isotherm, as shown in **Table 1**, n is equal to 2.24. In many cases $n > 1$; this may be a result of the distribution of surface sites or another factor causing a decrease in the adsorbent/adsorbate interaction due to an increase in the surface density.[19] The values of n in the range from 2 to 10 indicate a good adsorption.[20]

3.2 Adsorption dynamics

The study of adsorption dynamics describes the rate of solute removal. This rate controls the residence time of the adsorbate uptake at the solid/solution interface. The kinetics of the Cr(VI) ion adsorption on steel-making slag was analyzed using pseudo-first-order, pseudo-second-order, Elovich and intraparticle-diffusion-kinetic models[21–24] (diagram not shown here). The correlation coefficient (r^2) indicates the fitting experimental data and the values predicted by the model. A high value of r^2 (close or equal to 1) indicates that the model successfully describes the kinetics of the adsorption of Cr(VI) ions.

The pseudo-first-order equation is generally expressed as follows:[15]

$$\frac{\mathrm{d}q_t}{\mathrm{d}t} = k_1 (q_e - q_t) \tag{4}$$

where q_e and q_t are the adsorption capacities at equilibrium and at time t, respectively (mg/g), and k_1 is the rate constant of the pseudo-first-order adsorption (L/min).

The pseudo-second-order adsorption-kinetic-rate equation is expressed as:[15]

$$\frac{\mathrm{d}q_t}{\mathrm{d}t} = k_2 (q_e - q_t)^2 \tag{5}$$

where k_2 is the rate constant of the pseudo-second-order adsorption (g/(mg min)).

The Elovich model equation is generally expressed as:[15]

$$\frac{\mathrm{d}q_t}{\mathrm{d}t} = \alpha \exp(-\beta q_t) \tag{6}$$

where α is the initial adsorption rate (mg/(g min)) and β is the desorption constant (g/mg) during the experiment.

The intraparticle-diffusion model is expressed as:[15]

$$R = k_{id} (t)^a \tag{7}$$

where R is the percent of the Cr(VI) ions adsorbed, a is the gradient of linear plots and k_{id} is the intraparticle-diffusion-rate constant (h^{-1}).

Figure 4 shows the results of the adsorption capacity of Cr(VI) ions on the steel-making slag versus time at 293 K. The parameters of adsorption-kinetic models are presented in **Table 2**.

The kinetic adsorption of Cr(VI) ions on the steel-making slag followed the pseudo-second-order model (the correlation coefficient (r^2) was the highest – 0.9999). The r^2 values indicate that the intraparticle-diffusion process is the rate-limiting step. Higher values of k_{id} indicate a better mechanism of adsorption and an increase in the adsorption rate, which is related to an improved bonding between Cr(VI) ions and the adsorbent particles.[24]

3.3 Thermodynamic studies

It is necessary to perform thermodynamic studies of the adsorption process to conclude whether the process is spontaneous or not. The Gibbs free energy change ($\Delta G°$) is an important parameter determining the spontaneity of the chemical reaction. In order to determine the Gibbs free energy of the process it is necessary to know the entropy and enthalpy. The reaction occurs spontaneously at a given temperature if $\Delta G°$ has a negative value. The Gibbs free energy change ($\Delta G°$), the enthalpy change ($\Delta H°$) and the entropy change ($\Delta S°$) were calculated from a variation of the thermodynamic equilibrium Langmuir constant, K_L. The thermodynamic parameters were calculated using the following equations:[25]

$$\Delta G° = -RT \ln K_L \tag{8}$$

$$\ln K_L = \frac{\Delta S°}{R} - \frac{\Delta H°}{RT} \tag{9}$$

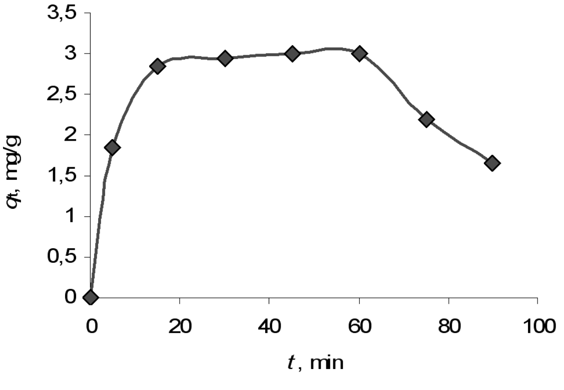

Figure 4: Adsorption capacity of Cr(VI) ions on steel-making slag versus time at 293 K

Slika 4: Časovna odvisnost kapacitete adsorpcije ionov Cr(VI) na jeklarsko žlindro pri 293 K where $\Delta H°$ and $\Delta S°$ were determined from the slope and the intercept of the plot of $\ln K_L$ versus $1/T$ (diagram not shown here). Thermodynamic parameters are given in **Table 3**.

Table 3: Thermodynamic parameters of the adsorption of Cr(VI) ions on steel-making slag
Tabela 3: Termodinamični parametri adsorpcije ionov Cr(VI) na jeklarsko žlindro

T K	$\Delta G°$, J mol^{-1}	$\Delta H°$, kJ mol^{-1}	$\Delta S°$, J mol^{-1} K^{-1}
293 313 333	–9.529	–3.397	–2.159

A negative value of $\Delta G°$ (**Table 3**) indicates that the adsorption is highly favorable and spontaneous. A negative value of $\Delta H°$ indicates that the adsorption is exothermic. The adsorption in the solid/liquid system consists of two processes: the adsorption of the adsorbate (solute) and desorption of the solvent (water) molecules that have been previously adsorbed. In an endothermic process, to be adsorbed, the adsorbate particles have to displace more than one water molecule. This results in the endothermic reaction of the adsorption process. On the order hand, in an exothermic process, the total energy consumed for bond breaking is lower than the total energy released during the formation of the bond between an adsorbate and an adsorbent. This results in the release of the extra energy in the form of heat. Therefore, $\Delta H°$ will be negative. The value of $\Delta H°$ also indicates the type of adsorption. The heat produced during the physical adsorption is the same as the heats of condensation, i.e., 2.1–20.9 kJ mol^{-1}.[26] On the order hand, the heat of chemisorption generally falls into the range of 80–200 kJ mol^{-1}.[26] Accordingly, the data in **Table 3** show that the adsorption of Cr(VI) ions can be attributed to the physical-adsorption process. A negative value of $\Delta S°$ indicates that the adsorption process is enthalpy driven. A negative value of the entropy change ($\Delta S°$) also indicates a decreased disorder at the solid/liquid interface during the adsorption process causing the adsorbate ions/molecules to escape from the solid phase to the liquid phase.[26] It this case, there is a decrease in the amount of the adsorbate that can be adsorbed.[27]

4 CONCLUSIONS

The present study shows that steel-making slag is an effective adsorbent for a Cr(VI) ion removal from an aqueous solution. The equilibrium studies confirmed that the Langmuir model was better in describing the adsorption of Cr(VI) ions on steel-making slag. The dimensionless-separation factor (R_L) showed that steel-making slag could be used for the removal of Cr(VI) ions from an aqueous solution. The amount of the adsorbed Cr(VI) ions increased with an increase in the temperature. The kinetics of the adsorption of Cr(VI) ions on steel-making slag followed a pseudo-second-order model. The r^2 values indicate that the intraparticle-diffusion process is the rate-limiting step. The negative value of $\Delta G°$ indicates that the adsorption is highly favorable and spontaneous. A negative value of $\Delta H°$ indicates that the adsorption is exothermic. A negative value of $\Delta S°$ indicates that the adsorption process is enthalpy driven.

5 REFERENCES

[1] B. Zhu, T. X. Fan, D. Zhang, Journal of Hazardous Materials, 153 (**2008**), 300

[2] S. Dahiya, R. M. Tripathi, A. G. Hegde, Journal of Hazardous Materials, 150 (**2008**), 376

[3] N. P. Chermisnoff, Handbook of Water and Wastewater Treatment Technologies, Butterworth-Heinemann, Boston 2002, 124

[4] G. F. Nordberg, B. A. Fowler, M. Nordberg, L. Friberg, Handbook of Toxicology of Metals, European Environment Agency, Copenhagen 2005, 491

[5] H. Gao, Y. Liu, G. Zeng, W. Xu, T. Li, W. Xia, Journal of Hazardous Materials, 150 (**2007**) 2, 446

[6] I. Lee, Y. Kuan, J. Chern, Journal of the Chinese Institute of Chemical Engineers, 38 (**2007**) 1, 71

[7] K. Kosińska, T. Miśkiewicz, Environment Protection Engineering, 38 (**2012**) 2, 51

[8] A. Štrkalj, A. Rađenović, J. Malina, Journal of Mining and Metallurgy, Section B: Metallurgy, 46 (**2010**) 1, 33

[9] N. C. Kothiyal, S. Sharma, The Holistic Approach to Environment, 3 (**2013**) 2, 63

[10] G. Zhao, X. Wu, X. Tan, X. Wang, The Open Colloid Science Journal, 4 (**2011**), 19

[11] L. Ćurković, M. Trgo, A. Rastovčan-Mioč, N. Vukojević-Medvidović, Indian Journal of Chemical Technology, 16 (**2009**), 84

[12] Manuel AAS ZEEnit 600/650, Analytik Jena AG, Germany, 2006

[13] Perkin-Elmer Corporation, Analitical Methods for Atomic Absorption Spectroscopy, Perkin-Elmer Corporation, USA, 1994, 261

[14] K. Do-Hyung, S. Min-Chul, C. Hyun-Doc, S. Chang-Il, B. Kitae, Desalination, 223 (**2008**), 283

[15] D. Do. Duond, Adsorption Analysis: Equilibria and Kinetics, Imperial College Press, London 1998, 244

[16] K. Hall, L. Eagleton, A. Acrivos, T. Vermeulen, Industrial and Engineering Chemistry Fundamentals, 5 (**1966**) 2, 212

[17] P. K. Malik, Journal of Hazardous Materials, 113 (**2004**) 1–3, 81

[18] P. Pandey, S. S. Sambi, S. K. Sharma, S. Singh, Batch Adsorption Studies for the Removal of Cu(II) Ions by ZeoliteNaX from Aqueous Stream, Proceedings of the World Congress on Engineering and Computer Science, San Francisco, USA, 2009, 20

[19] F. Rouquerol, J. Rouquerol, K. Sing, Adsorption by Powders and Porous Solids, Academic Press, London 1999, 281

[20] A. Ozer, H. B. Pirincci, Journal of Hazardous Materials, 137 (**2006**) 2, 849

[21] Y. S. Ho, D. A. J. Wase, C. F. Forster, Water Research, 29 (**1995**) 5, 1327

[22] C. Chang, C. Chang, K. Chen, W. Tsai, J. Shie, Y. Chen, Journal of Colloid and Interface Science, 277 (**2004**), 29

[23] A. Štrkalj, A. Rađenović, J. Malina, Archives of Metallurgy and Materials, 55 (**2010**) 2, 449

[24] A. Štrkalj, A. Rađenović, J. Malina, Canadian Metallurgical Quarterly, 50 (**2011**) 1, 3

[25] M. Suzuki, Adsorption Engineering, Elsevier Science Publisher, Amsterdam 1990, 300

[26] G. Rosa, H. E. Reynel-Avila, A. Bonilla-Petriciolet, I. Cano-Rodríguez, C. Velasco-Santos, A. L. Martínez-Hernández, International Journal of Chemical and Biological Engineering, 1 (**2008**) 4, 185

[27] D. M. Ruthven, Principles of Adsorption & Adsorption Processes, John Willey and Sons, Inc., Canada 1984, 114

UDK 669.55:620.17
Original scientific article/Izvirni znanstveni članek

ISSN 1580-2949
MTAEC9, 48(5)623(2014)

STRUCTURAL, MECHANICAL AND CYTOTOXICITY CHARACTERIZATION OF AS-CAST BIODEGRADABLE Zn-xMg (x = 0.8–8.3 %) ALLOYS

STRUKTURNE, MEHANSKE IN CITOTOKSIČNE LASTNOSTI BIORAZGRADLJIVE Zn-xMg (x = 0,8–8,3 %) ZLITINE V LITEM STANJU

Jiří Kubásek[1], **Iva Pospíšilová**[1], **Dalibor Vojtěch**[1], **Eva Jablonská**[2], **Tomáš Ruml**[2]
[1]Department of Metals and Corrosion Engineering, Institute of Chemical Technology, Prague, Technická 5, 166 28 Prague 6, Czech Republic
[2]Department of Microbiology, Institute of Chemical Technology, Prague, Technická 5, 166 28 Prague 6, Czech Republic
kubasek.jiri@gmail.com

Prejem rokopisa – received: 2013-04-05; sprejem za objavo – accepted for publication: 2013-11-04

In the present work, the structural, tensile, compressive and bending mechanical properties as well as the cytotoxicity of the Zn-Mg biodegradable alloys containing mass fractions from 0 % up to 8.3 % Mg were studied. It was found that the maximum tensile and compressive strengths of 170 MPa and 320 MPa, respectively, were obtained for the Zn-0.8Mg alloy. This alloy also showed the highest tensile elongation of 2 %. Mechanical properties were discussed in relation to the various structural features of the alloys. The structure of the strongest Zn-0.8Mg alloy was composed of a fine mixture of α-Zn dendrites and α-Zn + Mg_2Zn_{11} eutectics. The cytotoxicity was evaluated with an indirect contact assay using human osteosarcoma cells (U-2 OS). The cytotoxicity of the Zn-0.8Mg alloy extract was low and only slightly higher than in the case of the pure-Mg extract.

Keywords: biodegradable material, zinc, mechanical properties, structure, cytotoxicity

V tem delu so bile preučevane struktura, natezne, tlačne in upogibne mehanske lastnosti biorazgradljive zlitine Zn-Mg z masnim deležem od 0 % do 8,3 % Mg. Ugotovljeno je bilo, da sta bili pri zlitini Zn-0,8Mg doseženi največja natezna in tlačna trdnost 170 MPa oziroma 320 MPa. Ta zlitina je tudi pokazala največji raztezek 2 % pri natezni obremenitvi. Mehanske lastnosti so prikazane v odvisnosti od mikrostrukturnih značilnosti zlitin. Mikrostruktura najmočnejše zlitine Zn-0,8Mg je bila sestavljena iz α-Zn-dendritov in α-Zn + Mg_2Zn_{11}-evtektika. Citotoksičnost je bila ocenjena s posrednim preizkusom kontakta s celicami človeškega osteosarkoma (U-2 OS). Citotoksičnost ekstrakta zlitine Zn-0,8Mg je bila majhna in samo malo večja v primerjavi z ekstraktom čistega Mg.

Ključne besede: biorazgradljiv material, cink, mehanske lastnosti, struktura, citotoksičnost

1 INTRODUCTION

Biodegradable implant materials progressively degrade in the human body after the implantation, producing relatively non-toxic compounds and, simultaneously, they are being replaced by the growing tissue. Biodegradable polymeric materials have been known and used for a long time. However, polymeric materials are not suitable for the load-bearing applications such as screws or plates for fractured bones, due to their low mechanical strength.[1] Among biodegradable metallic materials, magnesium alloys have attracted the greatest interest since the beginning of the 20th century.[2] The reason for this is that magnesium is relatively non-toxic to the human body and excessive amounts of it can be readily excreted by the kidneys. Moreover, it is very important for many biological functions of the human body. The main disadvantage of most magnesium alloys explored so far is that they corrode too rapidly in physiological environments, producing excessive amounts of hydrogen and increasing the alkalinity close to the implant.[2–6] Both factors retard the healing process. Therefore, large efforts have been devoted to finding magnesium-based alloys degrading at acceptably low rates and many kinds of Mg-based alloys, like AZ, AM, LAE, WE, Mg-Zn, Mg-Zn-Ca, Mg-Zn-Mn-Ca, Mg-Zn-Y, Mg-Gd, Mg-Zn-Si and others, have been studied until now.[7–16]

In Mg-based biodegradable alloys, zinc is often one of the major constituents. Zinc is known to improve the strength and corrosion resistance of magnesium and, from the biological point of view, it is generally considered relatively non-toxic.[17] In the majority of the Mg biodegradable alloys given above, the concentrations of zinc do not exceed several mass fractions w/%. But a deep eutectic in the Mg-Zn binary-phase diagram[18] with about 51 % Zn supports the glass-forming ability (GFA) of Mg-Zn-based alloys with high concentrations of zinc. Amorphous ternary Mg-Zn-Ca alloys whose compositions are close to the eutectic point were already prepared[19,20] and shown to be promising candidates for biodegradable implants. Due to the unordered atomic structures and high Zn contents, amorphous alloys have an excellent strength, high corrosion resistance, low hydrogen evolution rate and a good biocompatibility in animals. Until now, bulk amorphous Mg-Zn-Ca samples of only a few millimeters in size have been prepared.

The fact that zinc is a biologically tolerable element, even when its content in Mg-based alloys approaches

w = 50 %,[21] indicates that Zn-based alloys may also be promising candidates for biodegradable implants. This has motivated our research of Zn-based biodegradable alloys. The main advantage of these materials over Mg-Zn metallic glasses is that they are much easier to prepare using the classical routes like gravity or die casting, hot rolling, hot extrusion, ECAP, etc. In our previous work[22] we provided information on the basic mechanical and corrosion properties of three binary Zn-Mg alloys containing w(Mg) = 1–3 %. We have shown that these alloys are significantly more corrosion resistant in a simulated body fluid (SBF) than Mg alloys. Possible zinc doses and toxicity were estimated and found to be negligible when compared to the tolerable biological daily limit of zinc. Magnesium was shown to strengthen the alloys and it is also known to support the healing process of the hard tissue.[22]

To properly design a load-bearing implant, the mechanical properties of an implant material are of a great importance. For this reason, this work is focused on the mechanical characterization including the hardness, tensile, compressive and bending properties of a series of the Zn-Mg binary alloys containing w(Mg) = 0–8 %. These limits were selected to be around the eutectic point in the Zn-Mg system (approximately w(Mg) = 3 %).[18] Moreover, the cytotoxicity of zinc was also assessed and compared with magnesium and other elements.

2 EXPERIMENTAL WORK

In this study, pure zinc and six binary Zn-Mg alloys containing w = 0.8–8.3 % of Mg were studied. The designations and chemical compositions of the studied alloys are given in **Table 1**.

Zn-based alloys were prepared by melting pure zinc (99.95 %) and magnesium (99.90 %) in a resistance furnace in air. To prevent an excessive evaporation of volatile zinc, the melting temperature did not exceed 500 °C, and the homogenization was ensured with an intense mechanical stirring using a graphite rod. After a sufficient homogenization, the melts were poured into a cast-iron mold to prepare cylindrical ingots of 20 mm in diameter and 130 mm in length. The chemical compositions were verified at both ends of the ingots with X-ray fluorescence spectrometry (XRF), as shown in **Table 1**.

The structures of the alloys were studied using light (LM) and scanning electron microscopy (SEM, Tescan Vega 3) with energy dispersive X-ray spectrometry (EDS, Oxford Instruments Inca 350). The phase composition was also confirmed with an X-ray diffraction analysis (XRD, X Pert Pro).

The mechanical properties of the as-cast alloys were characterized with hardness, tensile, compressive and bending tests. The samples for these tests were cut directly from the as-cast ingots. A loading of 5 kg was used for Vickers-hardness measurements. The rod samples for tensile tests had a diameter and length of 10 mm and 120 mm, respectively. Compressive tests were realized with rectangular samples of 10 mm × 10 mm × 15 mm in size. The compressive loading direction was parallel to the longest dimension. For three-point bending tests, rod samples of 4 mm in diameter and 40 mm in length were used. All the mechanical tests used a deformation rate of 1 mm/min. Fracture surfaces were examined after the tensile and bending tests using SEM.

The cytotoxicity of Zn-Mg alloys was assessed by using human osteosarcoma cells (U-2 OS). The investigated Zn-0.8Mg alloy and pure magnesium were used in these tests. Pure magnesium was used for comparison because it is generally considered to have a good biocompatibility and it is, thus, the basis of the most extensively studied metallic biomaterials. Before the extraction, cells were cultured in Dulbecco's modified Eagle's medium (DMEM) with a 10 % fetal bovine serum (FBS), 100 U/mL penicillin, 1 mg/mL streptomycin and 250 ng/mL amphotericin B at 37 °C in a humidified atmosphere of 5 % CO_2. The cytotoxicity was evaluated with an indirect-contact assay. Extracts were prepared by immersing the alloys in a DMEM medium containing a 5 % FBS and antibiotics at 37 °C for 7 d. The ratio of the surface area of the alloy samples to the extraction medium was 1 cm^2/mL. The extracts were then withdrawn and diluted twice. The concentrations of Zn and Mg released from Zn-0.8Mg and Mg, respectively, were determined using inductively coupled plasma mass spectrometry (ICP MS). The cells were seeded at a density of cells 2.5×10^4 mL^{-1} and incubated in 96-well cell culture plates for 24 h to allow attachment. The medium was then replaced with 100 µL of the extracts. The controls for a comparison of the cell viability involved both pure DMEM medium (100 % viability) and 0.64 % phenol in the DMEM medium as the toxic control. After the incubation of the cells in a humidified atmosphere of 5 % CO_2 at 37 °C for 1 d the extracts were removed. The cells were then washed twice using phosphate buffered saline (PBS) and overlaid with a phenol red-free DMEM medium containing 5 µL of the WST-1 reagent (Roche) per well. The plates were incubated with WST-1 for 4 h at 37 °C. The assay is based on the reduction of tetrazolium salt to soluble formazan due to mitochondrial enzymes of the viable

Table 1: Chemical compositions of the investigated alloys in mass fractions (w/%)
Tabela 1: Kemijske sestave preiskovanih zlitin v masnih deležih (w/%)

Alloy designation	Zn	Zn-0.8Mg	Zn-1.6Mg	Zn-2.5Mg	Zn-3.5Mg	Zn-5.4Mg	Zn-8.3Mg
Mg concentration	<0.01	0.79 ± 0.05	1.57 ± 0.04	2.51 ± 0.03	3.47 ± 0.03	5.36 ± 0.12	8.32 ± 0.04

cells. The absorbance of the samples characterizing the cell viability was measured using a microplate reader at 450 nm with a reference wavelength of 630 nm. The higher the absorbance, the higher is the viability of the cells.

3 RESULTS AND DISCUSSION

3.1 Structures

The light micrographs of the investigated alloys are shown in **Figure 1**. It is seen in **Figure 1a** that the pure zinc is composed of almost equi-axed grains of approximately 20 µm in size. The structures of the alloys from Zn-0.8Mg to Zn-2.5Mg (**Figures 1b** to **1d**) are hypoeutectic, i.e., they are composed of the primary α-Zn dendrites (light) and the α-Zn + Mg_2Zn_{11} eutectic mixture (dark) in interdendritic regions, dominated by the lamellar and rod morphologies of the eutectic phases (see also a detailed view inserted in **Figure 1d**). The presence of the two phases of α-Zn and Mg_2Zn_{11} in the alloys was also confirmed with XRD (not shown). The average thickness of the dendritic branches in these alloys is approximately 30 µm and the volume fraction of the eutectic mixture increases with the increasing Mg concentration. In all the hypoeutectic alloys the average eutectic interparticle spacing is approximately 2 µm (**Figure 1d**). The composition of the Zn-3.5Mg alloy is very close to the eutectic point in the binary Zn-Mg phase diagram.[18] Its structure (**Figure 1e**) is, thus, dominated by a very fine rod-and-lamellar α-Zn + Mg_2Zn_{11} eutectic mixture, in which the average eutectic interparticle spacing is close to that in the previous alloys (2 µm). The eutectic mixture creates the colonies of 50–200 µm in size that differ in the spatial orientation of the rods and lamellae. The Zn-5.4Mg and Zn-8.3Mg alloys (**Figures 1f** and **1g**, respectively) are hypereutectic, containing sharp-edged Mg_2Zn_{11} intermetallic phases (light) and the α-Zn+Mg_2Zn_{11} eutectic mixture (dark). Rod and lamellar eutectic particles are observed (**Figure 1g**). Like in the hypoeutectic and eutectic alloys, the average eutectic interparticle spacing is approximately 2 µm. The volume fraction and dimensions of the primary inter-

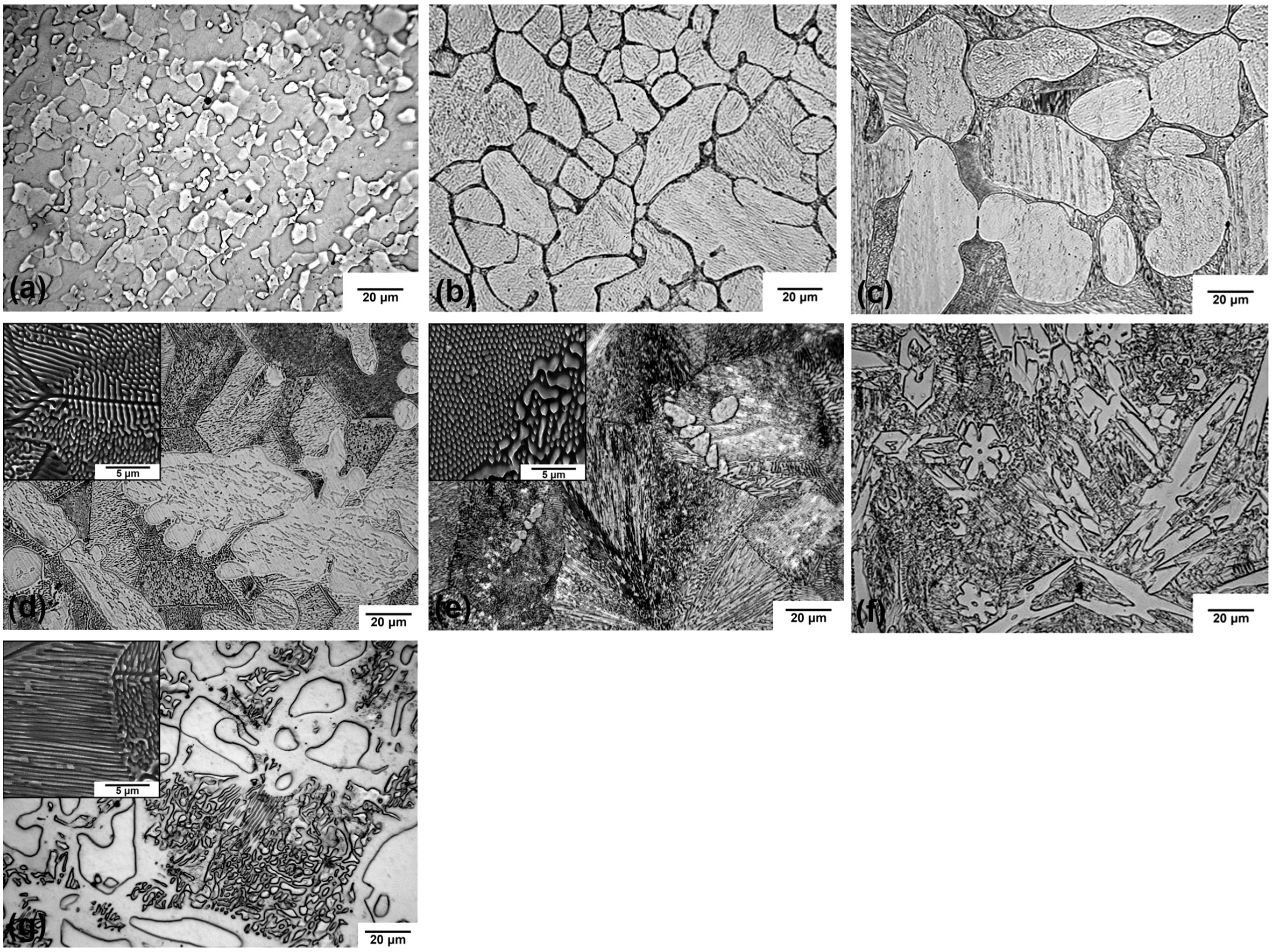

Figure 1: Light and detailed SEM micrographs of the alloys: a) Zn, b) Zn-0.8Mg, c) Zn-1.6Mg, d) Zn-2.5Mg, e) Zn-3.5Mg, f) Zn-5.4Mg, g) Zn-8.3Mg

Slika 1: Svetlobni in podrobni SEM-posnetki mikrostrukture zlitin: a) Zn, b) Zn-0,8Mg, c) Zn-1,6Mg, d) Zn-2,5Mg, e) Zn-3,5Mg, f) Zn-5,4Mg, g) Zn-8,3Mg metallic phases increase with the increasing Mg contents in the alloys. The nature of the Mg_2Zn_{11} intermetallic phases was verified with XRD (not shown) and EDS, determining mole fractions $x = 15.1$ % Mg and $x = 84.9$ % Zn in these particles. Due to enrichment in magnesium, the particles are often surrounded by a thin layer of the α-Zn phase.

3.2 Mechanical properties

Figure 2 shows various mechanical properties of the Zn-Mg alloys as functions of the Mg content. One can see that there is a direct relationship between the Mg content and mechanical properties. The hardness of the Zn-Mg alloys increases with the Mg concentration from approximately 37 HV5 for the pure zinc up to 226 HV5 for the Zn-8.3Mg alloy (**Figure 2a**). This behavior can be attributed to the increasing volume fraction of the hard Mg_2Zn_{11} intermetallic phase due to magnesium (**Figure 1**).

The compressive mechanical properties summarized in **Figure 2b** show a similar trend, i.e., the compressive yield strength increases with the Mg concentration from 80 MPa (the pure zinc) up to 625 MPa (the Zn-3.5Mg alloy). The ultimate compressive strength of the alloys containing 0–3.5 % Mg was not measured because they were not broken during the loading, suggesting a good compressive plasticity of hypoeutectic and eutectic alloys. In the case of hypoeutectic alloys this plasticity is attributable to a relatively large volume fraction of the soft α-Zn phase (**Figures 1a** to **1d**). The compressive plasticity of the eutectic Zn-3.5Mg alloy is a little surprising because this alloy contains approximately volume fraction $\varphi = 50$ % of the brittle Mg_2Zn_{11} eutectic phase (**Figure 1e**). A detailed insert in **Figure 1e** shows that the eutectic mixture is very fine and that the average diameter of eutectic rods and the thickness of eutectic lamellae do not significantly exceed 1 μm. During the compressive loading, hard eutectic particles act as stress concentrators. The larger are the particles, the higher is the local-stress increase around them. In the case of fine eutectic particles, the local-stress increase in their vicinity is probably small; therefore, the alloy shows an unlimited plastic deformation in compression. In contrast, at higher Mg concentrations the fracture took place before the onset of the plastic deformation, therefore, only the values of the ultimate compressive strength of the Zn-5.4Mg and Zn-8.3Mg alloys are shown in **Figure 2b**. Both these alloys contain sharp-edged primary Mg_2Zn_{11} intermetallic phases (**Figures 1f** to **1g**). Their sizes, shapes and brittle nature indicate that the stress concentration around them is high. Fracture cracks, thus, grow at a low nominal compressive stress of slightly above 200 MPa, i.e., significantly below the onset of the plastic deformation.

Bending mechanical properties are illustrated in **Figure 2c**. It is observed that a bending strength first

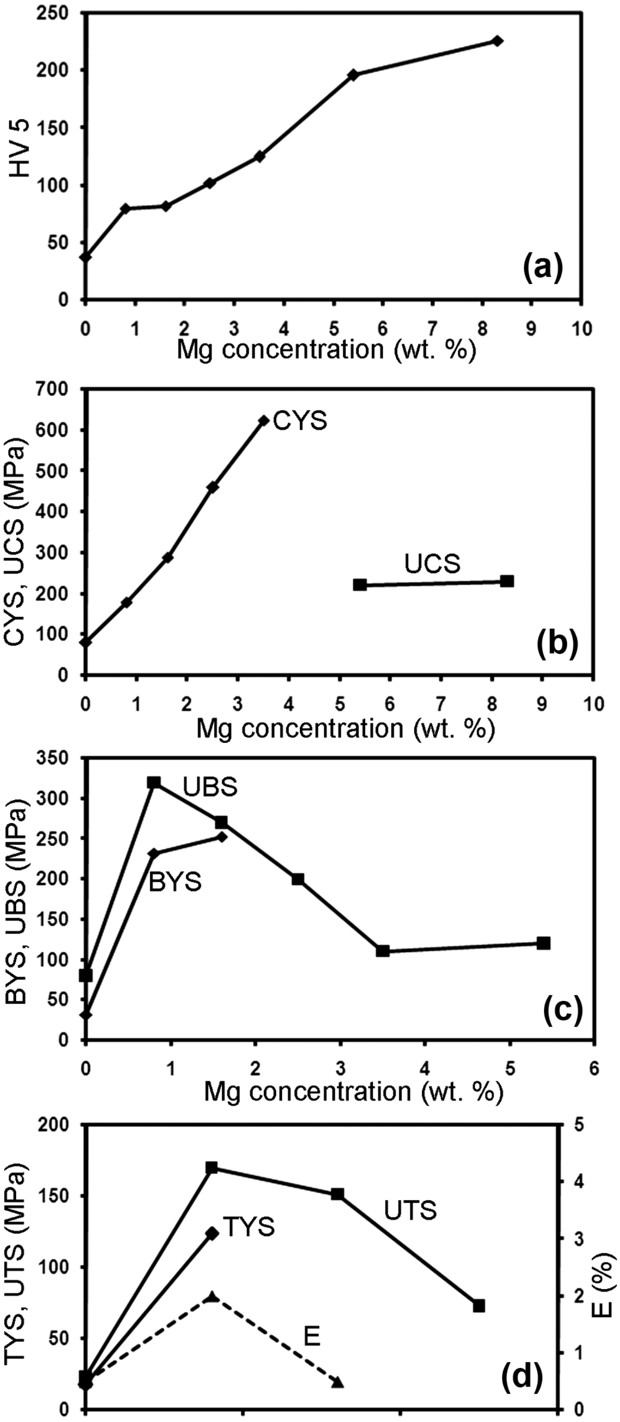

Figure 2: Mechanical properties of Zn-Mg alloys versus Mg concentration: a) Vickers hardness HV5, b) compressive tests (*UCS* – ultimate compressive strength, *CYS* – compressive yield strength), c) bending tests (*UBS* – ultimate bending strength, *BYS* – bending yield strength), d) tensile tests (*UTS* – ultimate tensile strength, *TYS* – tensile yield strength, *E* – elongation)

Slika 2: Mehanske lastnosti zlitin Zn-Mg glede na koncentracijo Mg: a) trdota po Vickersu HV5, b) tlačni preizkus (*UCS* – končna tlačna trdnost, *CYS* – meja plastičnosti pri tlačnem preizkusu), c) upogibni preizkus (*UBS* – končna upogibna trdnost, *BYS* – meja plastičnosti pri upogibnem preizkusu), d) natezni preizkus (*UTS* – končna natezna trdnost, *TYS* – meja plastičnosti pri nateznem preizkusu, *E* – raztezek)

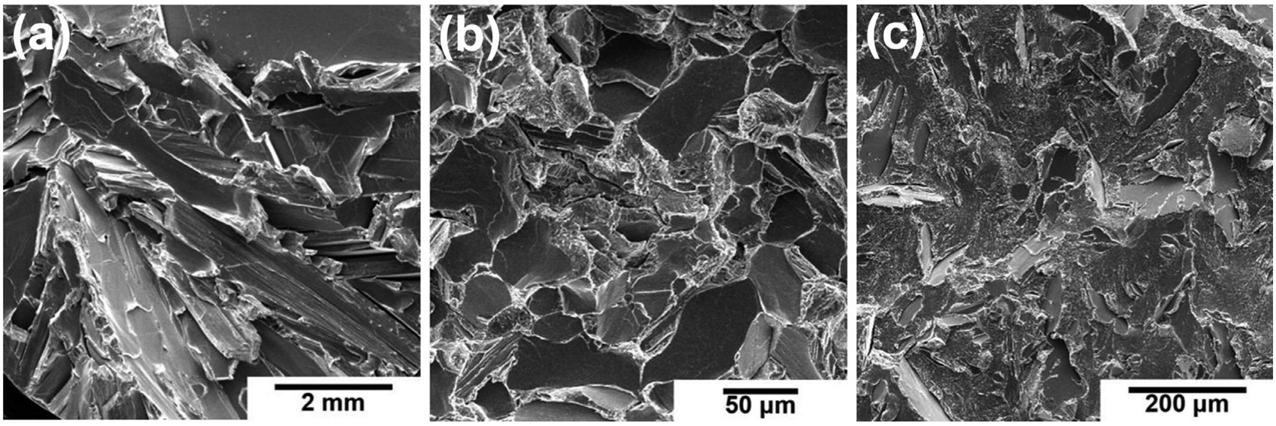

Figure 3: Fracture surfaces of Zn-Mg alloys after the tensile tests: a) Zn, b) Zn-0.8Mg, c) Zn-2.5Mg
Slika 3: Površina preloma zlitin Zn-Mg po nateznih preizkusih: a) Zn, b) Zn-0,8Mg, c) Zn-2,5 Mg

increases with the increasing Mg concentration and reaches the maximum of 320 MPa at 0.8 % Mg. At higher Mg concentrations, the bending strength progressively reduces to 110–120 MPa at 3.5–5.4 % Mg. The bending yield strength also increases with the increasing Mg concentration, i.e., with the increasing volume fraction of the eutectic mixture, and reaches 253 MPa at 1.6 % Mg. The alloys with higher Mg amounts fracture before the onset of the macroscopic plastic deformation. The results illustrated in **Figure 2c** also show that the plasticity of Zn-Mg alloys during bending is lower compared to that during compressive loading. In the compressive tests, the Zn-3.5Mg alloy can withstand a significant plastic deformation, whereas in the bending tests this alloy is macroscopically brittle. The reason for this difference is in the nature of the local stresses in the alloys during loading. During macroscopic compressive loading, the compressive component of the local stresses predominates. On the other hand, bending induces the local tensile stresses supporting the formation and growth of defects and macroscopic fracture cracks.

Tensile mechanical properties are summarized in **Figure 2d**. As in the previous case, the ultimate tensile strength increases up to 170 MPa at 0.8 % Mg. Higher Mg concentrations lead to a decrease in the ultimate tensile strength to 73 MPa for the Zn-2.5Mg alloy. The tensile yield strength reaches the maximum of 124 MPa at 0.8 % Mg. At this concentration an elongation of the alloy is 2 %. The alloys with the Mg concentrations above this limit fractured before the macroscopic plastic deformation due to an increased fraction of the brittle Mg_2Zn_{11} phase. These results confirm the above finding that the plasticity of Zn-Mg alloys decreases with the increasing tensile component during loading. In the tensile testing, the most detrimental tensile-stress component is the most pronounced supporting an easy nucleation and growth of fracture cracks.

The fracture surfaces of the selected alloys after tensile testing are shown in **Figure 3**. One can observe that zinc shows a brittle and intercrystalline fracture (**Figure 3a**) without any plastic deformation. Individual grains are clearly visible in this figure. **Figure 3b** shows the fracture surface of the Zn-0.8Mg alloy with the highest bending and tensile strengths. In contrast to the pure zinc, this surface has a significantly refined morphology, in which both the primary zinc and eutectic (**Figure 1b**) can be clearly distinguished. The primary zinc dendrites are characterized by an almost brittle fracture that corresponds to the flat facets on the fracture surface. The eutectic mixture that surrounds these facets exhibits a refined morphology and there is an indication of a plastic deformation in this area. The refined fracture morphology with a certain degree of plastic deformation is associated with improved bending and tensile strengths of this alloy because both the fine grains and the hard network represent barriers for the growing crack. It appears that the Zn-0.8Mg alloy provides the optimum volume fractions of both structural components. The fracture surface of the Zn-2.5Mg alloy in **Figure 3c** also includes the flat facets of the primary α-Zn and the regions of refined morphology corresponding to the α-Zn + Mg_2Zn_{11} eutectic mixture (**Figure 1d**). But a high portion of the brittle Mg_2Zn_{11} eutectic phase negatively affects both the bending and tensile strengths because this phase acts as a source of defects during mechanical loading at which fracture cracks nucleate.

Based on the results shown in **Figure 2**, it can be assumed that the Zn-0.8Mg alloy is the most promising material for load-bearing implants because it reaches the maximum bending and tensile strengths of 320 MPa and 168 MPa, respectively. The Zn-0.8Mg alloy also shows a good plasticity in all three loading modes. In compression this alloy is able to be deformed without a fracture. When considering an application of Zn-Mg alloys as, for example, the fixation screws or plates for fractured bones, the mechanical properties of the alloys should be compared to those of bones or other biomaterials. **Table 2** provides a summary of the tensile, compressive and bending mechanical properties of bones, the Zn-0.8Mg

Table 2: Basic mechanical properties of various biomaterials and natural bones (PLA-polylactic acid)[1,23–28]
Tabela 2: Osnovne mehanske lastnosti različnih biomaterialov in naravnih kosti (PLA-polimlečna kislina)[1,23–28]

Tissue/material	Density (g/cm^3)	Tensile strength (MPa)	Elastic modulus (GPa)	Compressive strength (MPa)	Bending strength (MPa)
Bone	≈ 2	30–280	5–20	160–240	2–150
Zn-0.8Mg	≈ 7	170	≈ 90	–	320
PLA	≈ 1	≈ 50	≈ 3	–	60–150
Hydroxyapatite	≈ 3	10–80	70–100	60–500	≈ 50
Wrought Ti-based alloy	≈ 4.5	700–1200	110	–	–
Wrought Co-based alloy	≈ 8.5	600–1000	220	–	–
Wrought stainless steels	≈ 8	800–1100	200	–	–

alloy, biodegradable polymers (polylactic acid, PLA), hydroxyapatite, inert Ti-, Co- and Fe-based alloys.[1,23–28] One can see that the Zn-0.8Mg alloy is characterized by significantly higher tensile and bending strengths as compared to the biodegradable PLA and hydroxyapatite. Moreover, the strength and elastic modulus of this alloy are much closer to those of the bone, as compared to the inert Ti-, Co- or Fe-based biomaterials.

3.3 Cytotoxicity

The Zn and Mg concentrations in the extracts prepared using the Zn-0.8Mg alloy and Mg are 4 µg/mL and 43 µg/mL, respectively. The significantly lower concentration of zinc results from a much better corrosion resistance of the zinc alloy as compared to magnesium, as shown in our previous work.[22] **Figure 4** illustrates the cytotoxic effects of the extracts on the U-2 OS cells, expressed as the percent absorbance of the DMEM control. It is observed that pure magnesium is tolerated well by U-2 OS cells because these cells are fully viable in the extract containing 43 µg/mL Mg (almost a 100 % absorbance). This measurement confirms the presumption stated in the experimental section that magnesium has a good biocompatibility. What is more important in this study is that the U-2 OS cells exposed to the extract from the Zn-0.8Mg alloy also show a good viability of 80 %, i.e., only slightly lower than in the case of the Mg extract. Due to a low corrosion rate of zinc,[22] its concentrations in the extracts are very low and, therefore, such extracts are not toxic for the cells. A similar situation can be expected in the case of Zn implants in the human body. The zinc present in the body fluids would probably not cause any toxic effects, despite the lower tolerable biological limits of zinc as compared to magnesium.

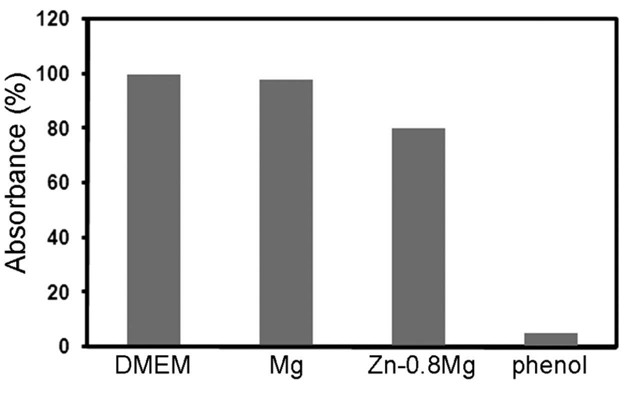

Figure 4: Cytotoxic effects of diluted extracts on the U-2 OS cells, expressed as the percent absorbance of the DMEM control
Slika 4: Citotoksičen vpliv raztopljenih ekstraktov na celice U-2 OS, izražen kot delež absorbance kontrolnega DMEM

4 CONCLUSIONS

Biodegradable Zn-Mg alloys containing from 0 % to more than 8 % Mg were investigated in this work. It was shown that only the alloys containing relatively low concentrations of Mg (approximately 1 %) are suitable for the load-bearing implants in the as-cast state, because they have high tensile and bending strengths and an acceptable elongation. The strength of such alloys is higher than those of biodegradable polymers and hydroxyapatite and comparable to that of the bones. Good mechanical properties result from a relatively fine structure composed of primary zinc and interdendritic eutectic. It is assumed that an additional improvement in the strength can be achieved with hot extrusion. At the Mg concentrations of above 1 %, Zn-Mg alloys become relatively brittle mainly during tensile loading.

Zn-Mg alloys can be considered as the alternatives to Mg-based biodegradable alloys. The main advantage of zinc alloys over magnesium alloys lies in their significantly better corrosion resistance in simulated body fluids. Therefore, the concentrations of the Zn ions extracted from alloys are low and they do not cause any significant toxic effects, as demonstrated with the cytotoxicity tests involving human osteosarcoma U-2 OS cells in this study.

Acknowledgements

The research of the biodegradable metallic materials was financially supported by the Czech Science Foundation (project no. P108/12/G043).

5 REFERENCES

[1] J. R. Davis, Handbook of materials for medical devices, ASM International, Materials Park 2003

[2] F. Witte, The history of biodegradable magnesium implants: a review, Acta Biomater, 6 (**2010**), 1680–92

[3] C. Y. Zhang, R. C. Zeng, C. L. Liu, J. C. Gao, Comparison of calcium phosphate coatings on Mg-Al and Mg-Ca alloys and their corrosion behavior in Hank's solution, Surface and Coatings Technology, 204 (**2010**), 3636–40

[4] M. D. Pereda, C. Alonso, L. Burgos-Asperilla, J. A. del Valle, O. A. Ruano, P. Perez et al., Corrosion inhibition of powder metallurgy Mg by fluoride treatments, Acta Biomater, 6 (**2010**), 1772–82

[5] J. E. Gray-Munro, C. Seguin, M. Strong, Influence of surface modification on the in vitro corrosion rate of magnesium alloy AZ31, J Biomed Mater Res A, 91 (**2009**), 221–30

[6] S. Hiromoto, T. Shishido, A. Yamamoto, N. Maruyama, H. Somekawa, T. Mukai, Precipitation control of calcium phosphate on pure magnesium by anodization, Corrosion Science, 50 (**2008**), 2906–13

[7] R. Erbel, C. Di Mario, J. Bartunek, J. Bonnier, B. de Bruyne, F. R. Eberli et al., Temporary scaffolding of coronary arteries with bioabsorbable magnesium stents: a prospective, non-randomised multicentre trial, Lancet, 369 (**2007**), 1869–75

[8] C. Di Mario, H. Griffiths, O. Goktekin, N. Peeters, J. Verbist, M. Bosiers et al., Drug-eluting bioabsorbable magnesium stent, J Interv Cardiol, 17 (**2004**), 391–5

[9] P. Peeters, M. Bosiers, J. Verbist, K. Deloose, B. Heublein, Preliminary results after application of absorbable metal stents in patients with critical limb ischemia, Journal of endovascular therapy: an official journal of the International Society of Endovascular Specialists, 12 (**2005**), 1–5

[10] S. Zhang, X. Zhang, C. Zhao, J. Li, Y. Song, C. Xie et al., Research on an Mg-Zn alloy as a degradable biomaterial, Acta Biomater, 6 (**2010**), 626–40

[11] Z. Li, X. Gu, S. Lou, Y. Zheng, The development of binary Mg-Ca alloys for use as biodegradable materials within bone, Biomaterials, 29 (**2008**), 1329–44

[12] E. Zhang, L. Yang, J. Xu, H. Chen, Microstructure, mechanical properties and bio-corrosion properties of Mg-Si(-Ca, Zn) alloy for biomedical application, Acta Biomater, 6 (**2010**), 1756–62

[13] E. Zhang, L. Yang, Microstructure, mechanical properties and bio-corrosion properties of Mg–Zn–Mn–Ca alloy for biomedical application, Materials Science and Engineering A, 497 (**2008**), 111–8

[14] X. N. Gu, W. Zheng, Y. Cheng, Y. F. Zheng, A study on alkaline heat treated Mg-Ca alloy for the control of the biocorrosion rate, Acta Biomater, 5 (**2009**), 2790–9

[15] Z. G. Huan, M. A. Leeflang, J. Zhou, L. E. Fratila-Apachitei, J. Duszczyk, In vitro degradation behavior and cytocompatibility of Mg-Zn-Zr alloys, Journal of materials science, Materials in medicine, 21 (**2010**), 2623–35

[16] F. Witte, N. Hort, C. Vogt, S. Cohen, K. U. Kainer, R. Willumeit et al., Degradable biomaterials based on magnesium corrosion, Current Opinion in Solid State and Materials Science, 12 (**2008**), 63–72

[17] G. J. Fosmire, Zinc toxicity, Am J Clin Nutr, 51 (**1990**), 225–7

[18] W. F. Gale, T. C. Totemeier, Smithells Metals Reference Book, 8th Edition, Elsevier Publishers, 2004

[19] X. Gu, Y. Zheng, S. Zhong, T. Xi, J. Wang, W. Wang, Corrosion of, and cellular responses to Mg-Zn-Ca bulk metallic glasses, Biomaterials, 31 (**2010**), 1093–103

[20] Q. F. Li, H. R. Weng, Z. Y. Suo, Y. L. Ren, X. G. Yuan, K. Q. Qiu, Microstructure and mechanical properties of bulk Mg–Zn–Ca amorphous alloys and amorphous matrix composites, Materials Science and Engineering A, 487 (**2008**), 301–8

[21] B. Zberg, P. J. Uggowitzer, J. F. Löffler, MgZnCa glasses without clinically observable hydrogen evolution for biodegradable implants, Nat Mater, 8 (**2009**), 887–91

[22] D. Vojtech, J. Kubasek, J. Serak, P. Novak, Mechanical and corrosion properties of newly developed biodegradable Zn-based alloys for bone fixatio, Acta Biomater, 7 (**2011**), 3515–22

[23] J. R. Davis (ed.), ASM Handbook: Volume 2, Properties and Selection: Nonferrous Alloys and Special-Purpose Materials, Handbook A, ASM International, Materials Park 1990

[24] G. E. J. Poinern, S. Brundavanam, D. Fawcett, Biomedical Magnesium Alloys: A Review of Material Properties, Surface Modifications and Potential as a Biodegradable Orthopaedic Implant, American Journal of Biomedical Engineering, 2 (**2013**), 218–40

[25] D. K. Pattanayak, P. Divya, S. Upadhyay, R. C. Prasad, B. T. Rao, T. R. Rama Mohan, Synthesis and Evaluation of Hydroxyapatite Ceramics, Trends Biomater Artif Organs, 18 (**2005**), 87–92

[26] N. Monmaturapoj, C. Yatongcha, Effect of Sintering on Microstructure and Properties of Hydroxyapatite Produced by Different Synthesizing Methods, Journal of Metals, Materials and Minerals, 20 (**2010**), 53–61

[27] S. Pramanik, A. K. Agarwal, K. N. Rai, Development of High Strength Hydroxyapatite for Hard Tissue Replacement, Trends Biomater Artif Organs, 19 (**2005**), 46–51

[28] A. J. Ruys, M. Wei, C. C. Sorrell, M. R. Dickson, A. Brandwood, B. K. Milthorpe, Sintering effects on the strength of hydroxyapatite, Biomaterials, 16 (**1995**), 409–15

UDK 669.715:532.6:669.058
Original scientific article/Izvirni znanstveni članek

ISSN 1580-2949
MTAEC9, 48(5)631(2014)

STRUCTURAL CHARACTERIZATION OF A BULK AND NANOSTRUCTURED Al-Fe SYSTEM

KARAKTERIZACIJA STRUKTURE OSNOVE IN NANOSTRUKTURE SISTEMA Al-Fe

Abdelhak Fekrache, Mohamed Yacine Debili, Saliha Lallouche
LM2S, Physics department, Faculty of Science, Badji Mokhtar-Annaba University, 23200 Annaba, Algeria
mydebili@yahoo.fr

Prejem rokopisa – received: 2013-08-06; sprejem za objavo – accepted for publication: 2013-11-12

The main purpose of the present paper is a study of the properties of stable and metastable structures of several binary $Al_{1-x}Fe_x$ alloys ($0 = x = 0.92$) made with high-frequency induction fusion and radiofrequency (13.56 MHz) cathodic sputtering from composite Al-Fe targets, resulting in homogeneous thin films. The study of the lattice parameters and mechanical behaviour was followed by X-ray diffraction and Vickers microhardness measurements of bulk and sputtered Al-Fe thin films. The phenomenon of a significant mechanical strengthening of the aluminium by means of iron is essentially due to a combination of the solid-solution effects and the grain-size refinement. A further decrease in the thin-film grain size can cause a softening of the solid and then the Hall-Petch relation slope turns from positive to negative at a critical size called the strongest size, which is coherent with the thin-film dislocation density.

Keywords: aluminium alloys, sputtering, microhardness, thin films, grain size, Hall-Petch

Glavni namen te predstavitve je študij lastnosti stabilnih in metastabilnih struktur v več binarnih zlitinah $Al_{1-x}Fe_x$ (x-vrednosti so v molskih deležih $0 = x = 0{,}92$), izdelanih z visokofrekvenčnim zlivanjem in radiofrekvenčnim (13,56 MHz) katodnim naprševanjem iz kompozitnih tarč Al-Fe, ki omogočajo homogene tanke plasti. Po študiju mrežnih parametrov in mehanskih lastnosti je bila izvršena rentgenska difrakcija in določena mikrotrdota po Vickersu osnove in napršene tanke plasti Al-Fe. Pojav občutnega povečanja mehanske trdnosti aluminija z železom je zaradi kombinacije med vplivi trdne raztopine in zmanjšanja velikosti zrn. Nadaljnje zmanjšanje zrn v tanki plasti lahko povzroči mehčanje in potem se smer razmerja Hall-Petch obrne od pozitivnega k negativnemu pri kritični velikosti, za katero je značilna največja koherenca z gostoto dislokacij v tanki plasti.

Ključne besede: aluminijeve zlitine, naprševanje, mikrotrdota, tanke plasti, velikost zrn, Hall-Petch

1 INTRODUCTION

The characterization of solidification microstructures is essential in many applications. However, the composition complexity of most technical alloys makes such an analysis quite difficult. Microcrystalline and nanocrystalline materials can currently be produced with several methods, like the rapid solidification (RS) or physical vapor deposition (PVD), and the resulting metal has a polycrystalline structure without any preferential crystallographic grain orientation. Aluminium and its alloys with their low densities and easy working have a significant place in the car industry, aeronautics and food conditioning. The on-glass-slides, sputter-deposited, aluminium-based, alloy thin films such as Al-Mg,[1] Al-Ti,[2,3] Al-Cr[4] and Al-Fe[5–7] exhibit a notable solid solution of aluminium in the films and microhardness values higher than those of the corresponding traditional alloys.

The inverse Hall–Petch effect (IHPE) has been observed for nanocrystalline materials by a large number of researchers.[8,9] This effect implies that nanocrystalline materials get softer as the grain size is reduced below its critical value. In this paper, we report on a study of the inverse Hall–Petch effect with respect to a practical question as to whether ductility is increased in high-strength metals.

The goal of this paper is to highlight the particular structural behaviours of different Al-Fe alloys prepared by RF magnetron sputtering on glass substrates in terms of structure, lattice parameter, grain size, dislocation density and deviation from the normal Hall-Petch relation.

2 EXPERIMENTAL DETAILS

The eight bulk samples used in the present work, shown in **Table 1**, were quenched from the liquid state after high-frequency induction fusion. Powder aluminium and iron (99.999 %) were used in the proportions defined according to the required compositions. The total mass of the samples to be elaborated was between 8 g and 10 g. A cold compaction of the mixed powder (Al-Fe) was achieved to obtain a dense product (60 %), intended for a high fusion frequency (HF). A sample densified in this way was then placed in a cylindrical alumina crucible (height of 3 cm and diameter of 16 mm), introduced into a quartz tube and placed in the coil prior to the high-frequency fusion. After the primary vacuum, the heating of the sample was carried out in steps, with a ten-minute maintenance stage towards 600 °C until the complete fusion of the alloys at a temperature of about 1140 K, as determined with a pyrometer.

Table 1: Chemical compositions of the bulk and the sputtered Al-Fe alloys (amount fractions, *x*/%)
Tabela 1: Kemijska sestava osnove in napršene zlitine Al-Fe (množinski deleži, *x*/%)

	x(Fe)/%											
Bulk	5.09	10.78	17.16	30	40	60	74	85				
Sputtered	5.6	7.8	18	23	27	29	36	39	47	70	71.9	71.9

Light microscopy (using a Philips microscope) was used for the polished surface observations. The microstructure of the alloys was examined on metallographic microsections. The mechanical polishing technique involved 600–4000 SiC grinding paper. The samples were etched for 15 s with Keller's reagent (5 mL HF + 9 mL HCl + 22 mL HNO_3 + 74 mL H_2O). X-ray diffraction analyses were performed using a Philips X-ray diffractometer working with a copper anticathode (λ = 0.154 nm) and covering 180° in 2θ. The samples were subjected to heat treatments in primary vacuum media at 500 °C for a period of 1 h.

The twelve targets used in the elaboration of the aluminium-iron thin films were made from a bulk aluminium crown of 70 mm of diameter in which is inserted a bulk copper or iron disc. Using bulk material minimizes the oxygen in the films. This target shape enables the easy control of an additional element composition in the films (**Table 1**).

The films were on 75 mm × 25 mm × 1 mm glass slides that were radiofrequency (13.56 MHz) sputter-deposited under low pressure of 0.7 Pa and a substrate temperature that does not exceed 400 K. The substrate–target distance was 80 mm. The sputtering is carried out with a constant power of 200 W, an auto-polarization voltage of –400 V, that acquired by the plasma is –30 V, a regulation intensity of 0.5 A and a argon flow of 30 cm³/min. After 1 h and 30 min, the deposition velocity is 2.5 µm/h and films of about 3 µm to 4 µm thickness were obtained.

The chemical analysis of atomic Fe in Al-Fe was made by X-ray dispersion spectroscopy. The microstructure of the films was studied by X-ray diffraction (XRD) using a Philips X-ray diffractometer working with a cobalt Kα anticathode (λ = 0.179 nm) and covering 120° in 2θ, and transmission electronic microscopy (Philips CM12) operating under an accelerating voltage of 120 kV. The Vickers indentation under low load allows us to specify by means of the microhardness the mechanical strengthening of the aluminium by iron addition. The measures were realized by means of a Matsuzawa MTX microdurometre. To reach the intrinsic hardness of the deposit and free itself from the influence of the substrate, the Bückle law[10] must be taken into account. This law imposes a depth of penetration h that does not exceed a tenth of the thickness e of the deposit. So, to have $h < 0.1$ e, it is necessary to respect the condition $D < 0.7$ e, where D is the diagonal of the square impression left by the Vickers indenter (pyramid of angle in the summit equal to 136 °). We chose to work with a normal load of 0.1 N (10 g). In addition, the deposit had to have a thickness of at least 10 µm so that the previous condition was satisfied.

Thin film specimens were sealed in silica ampoules in an argon atmosphere, after a previous evacuation to a pressure of 1.33 × 10^{-6} mbar, and then heat treated at 500 °C for a period of 1 h.

3 RESULTS AND DISCUSSION

The liquid-quenched Al-60 % Fe alloy is characterized by an ordered B_2 (FeAl) CsCl-type structure, as revealed by the X-ray diffraction pattern (**Figure 1a**), and described in **Table 2**. For 74 % Fe we observe a structural change leading to a DO_3-ordered structure (**Figure 1b**), while when the iron content reaches 85 % and as showed by X-ray diffraction pattern of **Figure 1c**, the structure changes completely, giving rise a disordered α-Fe solid solution (**Figure 2** and **Table 2**).

Table 2: Phase limits in bulk Al-Fe produced by high-frequency induction fusion
Tabela 2: Fazne meje v osnovi iz Al-Fe, izdelani z visokofrekvenčnim indukcijskim zlivanjem

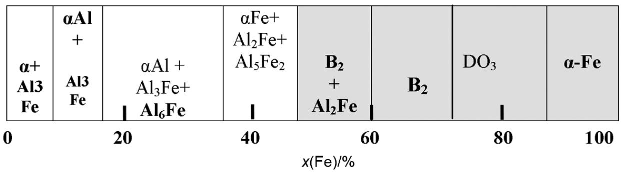

α+ Al3 Fe	**αAl + Al3 Fe**	αAl + Al_3Fe+ **Al_6Fe**	αFe+ Al_2Fe+ Al_5Fe_2	**B_2 + Al_2Fe**	**B_2**	DO_3	**α-Fe**

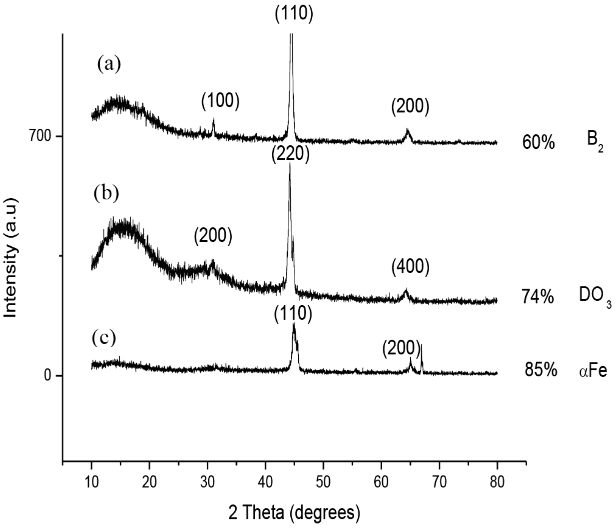

Figure 1: X-ray diffraction patterns of various as-solidified Fe-rich alloys: a) B_2, b) DO_3 and c) α-Fe
Slika 1: Posnetki rentgenske difrakcije različnih strjenih z Fe bogatih zlitin: a) B_2, b) DO_3, c) α-Fe

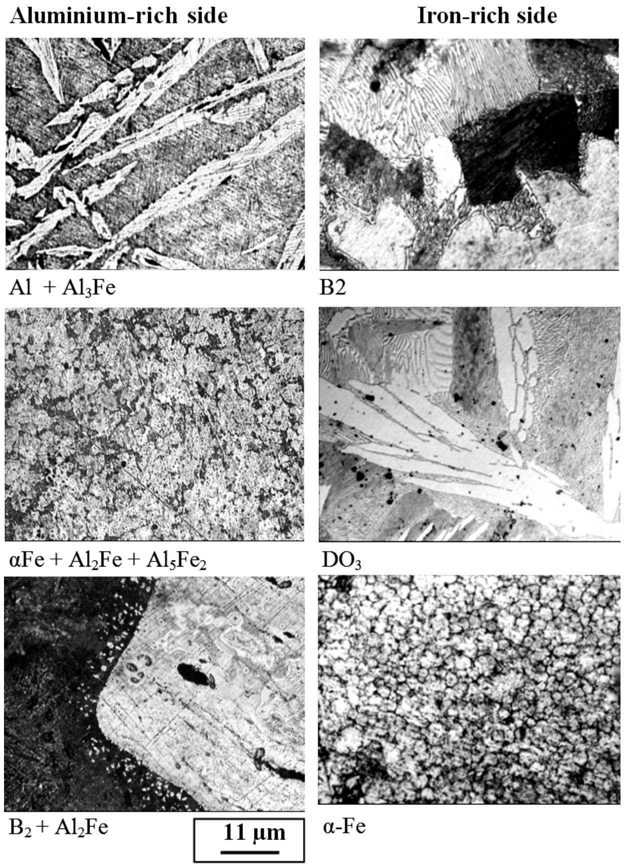

Figure 2: As-quenched microstructures from bulk Al-Fe
Slika 2: Kaljena mikrostruktura osnove iz Al-Fe

For sputtered Al-Fe, the lattice parameter of the α-Al phase decreases from 0.405 nm (pulverized pure aluminium deposit) to 0.403 nm (pulverized deposit containing x(Fe) = 5 %). This decrease in the parameter is not surprising since the radius of the iron atom (R_{Fe} = 0.124 nm) is lower than that of the aluminium atom (R_{Al} = 0.143 nm).

The lattice parameter of the body-centred-cubic phase or the B_2 phase (in the composition field x(Fe) = 45–55 %) decreases in an appreciably linear way between x(Fe) = 38 % (x(Al) = 62 %) (a = 0.295 nm) and pure iron (a = 0.287 nm) while passing the value a = 0.291 nm for the pulverized deposit containing x(Fe) = 70 % (x(Al) = 30 %) (**Figure 3**). This decrease is again explained by the difference in size between the aluminium and iron atoms.

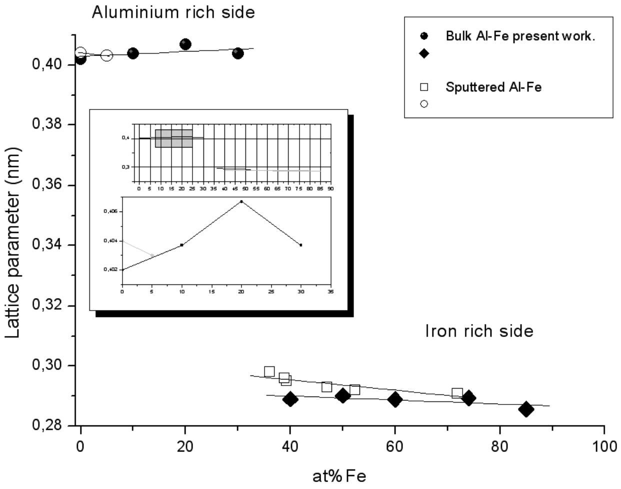

Figure 3: Lattice-parameter variation with iron composition on the aluminium-rich side and iron-rich side. Inset shows a change of the slope for 20 % iron.
Slika 3: Spreminjanje mrežnih parametrov s količino železa na z aluminijem bogati strani in z železom bogati strani. Vloženi diagram prikazuje spremembo naklona pri x(Fe) = 20 %

With the fraction of Al increasing, the bulk Al-Fe lattice parameter increases linearly, which indicates that the Al simply substitutes for Fe on the Fe sublattice. There is a change of slope that occurs at 20 % Fe, but when the percentage of Fe is larger than 20 %, the lattice parameter decreases, which may indicate that these compositions are in a two-phase field, where the BCC-to-FCC transition may occur between 30 % and 40 % Fe, see the inset in **Figure 3**. Similar results were obtained by Pike et al.[11] The results clearly indicate that the larger Fe atom preferentially occupies the anti-structure sites on the Al sublattice, and only when these are filled do the Fe atoms begin to occupy the vacancy sublattice.

Between amount fractions 10 % and 20 % Fe, the bulk alloy microhardness remains almost constant. Beyond 20 % Fe it will begin increasing until a maximum at 40 % Fe (**Figure 4**). We observed a Gaussian-shaped curve for the as-solidified alloys. The effect of iron on the mechanical properties of aluminium alloys has been reviewed extensively.[12,13] The detrimental effect of iron on the ductility is due to two main reasons: 1) the size and number density of iron-containing intermetallics like Al_3Fe and Al_2Fe increases with iron content, and the more intermetallics there are, the lower the ductility; 2) as the iron-level increases, the porosity increases, and this defect also has an impact on the ductility (**Table 2**).

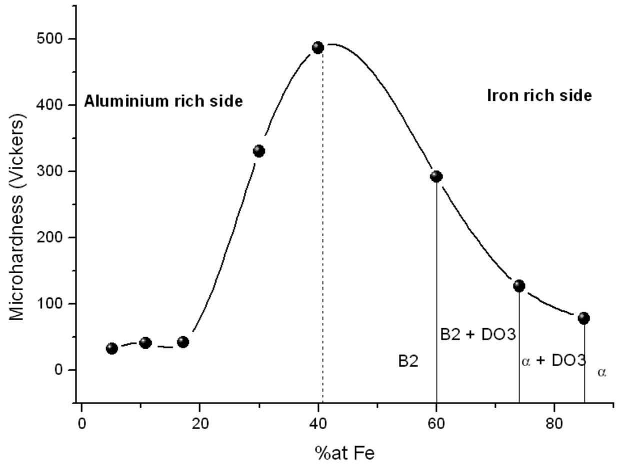

Figure 4: Microhardness evolution with iron content for bulk Al-Fe
Slika 4: Spreminjanje mikrotrdote z vsebnostjo železa v osnovi iz Al-Fe

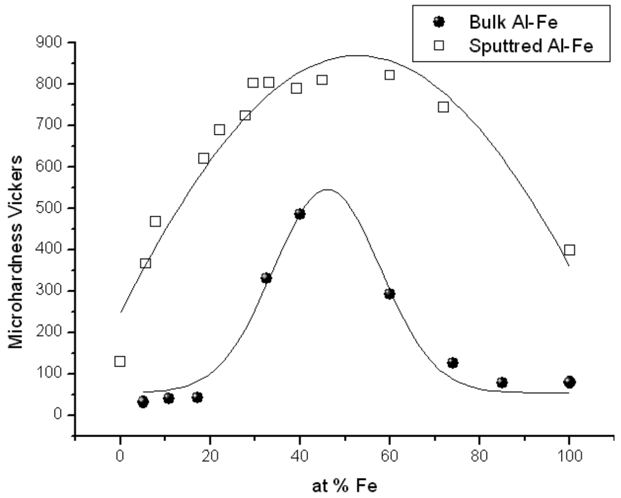

Figure 5: Comparative microhardness variations with iron content for bulk and sputtered Al-Fe

Slika 5: Primerjava spremembe mikrotrdote z vsebnostjo železa v osnovi in v napršenem Al-Fe

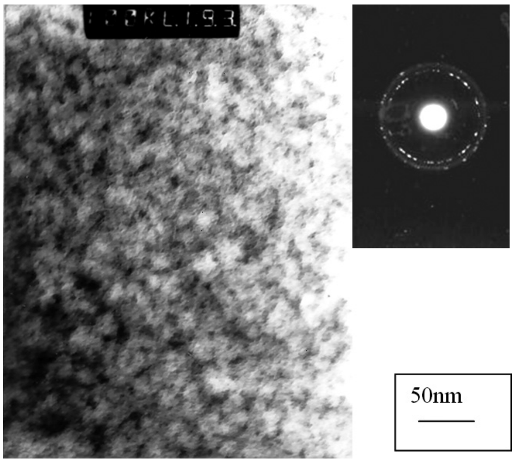

Figure 6: Bright-field transmission electron micrographs and associated selected-area diffraction ring pattern showing a mixture of nanocrystalline and amorphous phases from an Al-7.5 % Fe deposit

Slika 6: Posnetek mikrostrukture s presevnim elektronskim mikroskopom in izbrano področje difrakcije, ki prikazuje mešanico nanokristaliničnih in amorfnih faz v nanosu iz Al-7,5 % Fe

For the Al-Fe deposits the intrinsic microhardness of the thin films increases according to the content of iron from 130 HV (pure aluminium) up to a maximum in the form of plate of 800 HV, located between 45 % and 70 % Fe, and then follows a decrease to reach that of iron towards 400 HV (**Figure 5**).

We have shown in previous work[6,14] that in aluminium-based thin films the microhardness is always related to the structural and sub-structural features via the influence of the technological physical conditions of vapour condensation and film growth.

3.1 Grain size

Two methods were used for the quantitative approach of the grain size. The first is the application of the Scherer formula.[15] This is based on a measure of the width of the X-ray diffraction field via a measurement of the angular width $\Delta(2\theta)$. The crystallites average dimension being given by $\langle D \rangle = 0.\ 9\lambda/\Delta(2\theta(\cos\theta))$, where λ is the wavelength of the radiation used, θ is the angular position of the diffraction line and $\Delta\ (2\theta)$ is the width with half intensity expressed in radians. This method assumes the exploitation of diagrams obtained in $\theta/2\theta$ focusing mode with a low divergence of the incidental beam. In order to limit the errors, diagrams on aluminium and iron with coarse grains (several micrometres) allowed a free from the instrumental widths of the lines (111) αAl and (110) bcc (body centred cubic) which was used. The results that come from this method provide a good estimate of the grain size when the grain is smaller than 1 μm.

The second method consists of evaluating the grain size starting from images obtained using transmission electron microscopy (**Figure 6**). The evolution of the α-Al grain size in the presence of iron is similar to that already observed in the presence of chromium or titanium.[3,4] Whereas the grain of a pulverized pure aluminium deposit has a size of about 1 μm, this falls to approximately 500 nm for x(Fe) = 5 %. Beyond this composition, the microstructure in the two-phase field (α-Al + amorphous) becomes increasingly fine with grains whose dimensions do not exceed 30 nm to 40 nm (**Figure 7**). The refinement of the microstructure, in cathodic sputtering, at the time of the addition of an alloy element in aluminium, is constant, because this element is substituting in the solid solution[5,14] or inserting in the aluminium.[16]

Concerning the body-centred-cubic phase and the ordered B_2 simple cubic phase observed for iron concentrations higher than x = 38 %,[17] the grain size varies slightly with iron content in the range of the composition

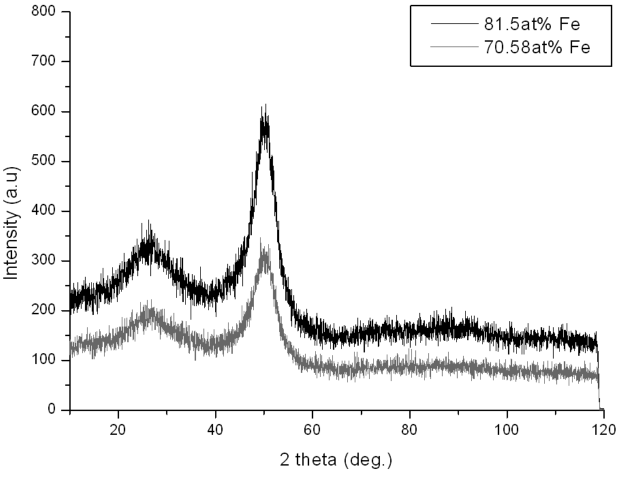

Figure 7: X-ray diffraction pattern of wholly amorphous Al-81.5 % Fe deposit and quasi-amorphous Fe-70.5 % Al deposit

Slika 7: Posnetek rentgenske difrakcije popolnoma amorfnega nanosa Al-81,5 % Fe in kvazi amorfnega nanosa iz Al-70,5 % Fe

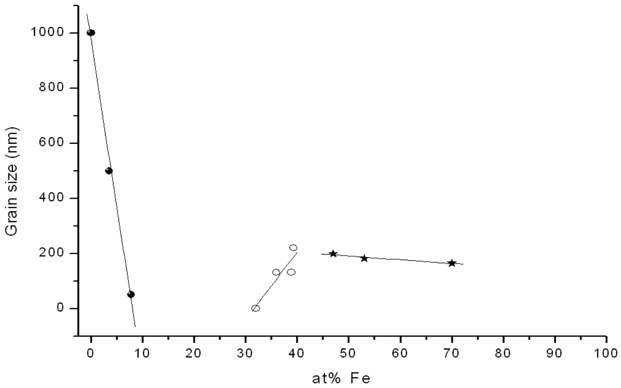

Figure 8: Grain size evolution with iron content
Slika 8: Spreminjanje velikosti zrn od vsebnosti železa

studied (38 % to 72 % Fe) and lies between 200 nm and 250 nm (**Figure 8** and **Table 3**).

Table 3: Phase limit in deposits
Tabela 3: Meje faz v nanosih

αAl	αAl + Am	Amorphous	αFe +Al	αFe	B_2	α-Fe

0 20 40 60 80
x(Fe)/%

For Al-Fe films containing between amount fractions 30 % and 40 % iron we observe an inverse evolution of the Hall-Petch relationship (IHPR) (**Figure 9**).

However, as the crystal is refined from the micrometre regime into the nanometre scale, this mechanism will break down because the grains are unable to support dislocation pile-ups. Typically, this is expected to occur for grain sizes below 10 nm for most metals.[18]

There is a growing body of experimental evidence for such unusual deformations in the nanometre regime; however, the underlying atomistic mechanisms for the IHPR remain poorly understood. The physical origin of the IHPR transition and the factors dominating the strongest size are a long-standing puzzle.[19]

Two main plausible hypotheses have been advanced to explain the deviation from the Hall-Petch relation. First in the HPR regime, crystallographic slips in the grain interiors govern the plastic behaviour of the polycrystallite; while in the IHPR regime, grain boundaries dominate the plastic behaviour. This hypothesis is supported by recent computer simulations of deformation in ultrafine-grained material.[20] However, it is not clear from these simulations that grain-boundary sliding could become dominant at grain sizes as large as 20 nm; a recent simulation for Cu suggests a transition at 6–7 nm.[9] Second, very small grains cannot support distributions of dislocations, so the pile-up and dislocation-density mechanisms for Hall-Petch behaviour cease to apply. Relevant experimental work has recently been published by Misra et al.[21]

3.2 Dislocation density

The finer the grains, the larger the area of the grain boundaries that impedes the dislocation motion. Furthermore, grain-size reduction usually improves toughness as well. The dislocation density for Al-Fe thin films has been determined by using the Williamson and Smallman method.[22] Between amount fractions 7.8 % Fe and 36 % Fe, the dislocation density of heat-treated thin films is more sensitive to iron than in the as-deposited specimen (**Figure 10**). This phenomenon may be explained by the relatively small grain size of the as-prepared coatings. From 36 % Fe the dislocation density drops drastically, probably due to the structural change of the coatings from a mixture αAl (fcc) or αFe (bcc) with an amorphous phase to crystalline (bcc) phase. This behaviour is coherent with the inverse Hall-Petch effect (IHPE)

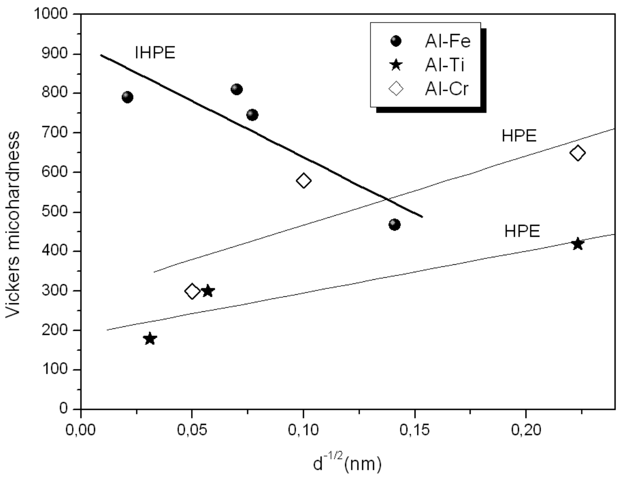

Figure 9: Variation of microhardness with the inverse square root of the grain size
Slika 9: Spreminjanje mikrotrdote z inverzno vrednostjo kvadratnega korena velikosti zrn

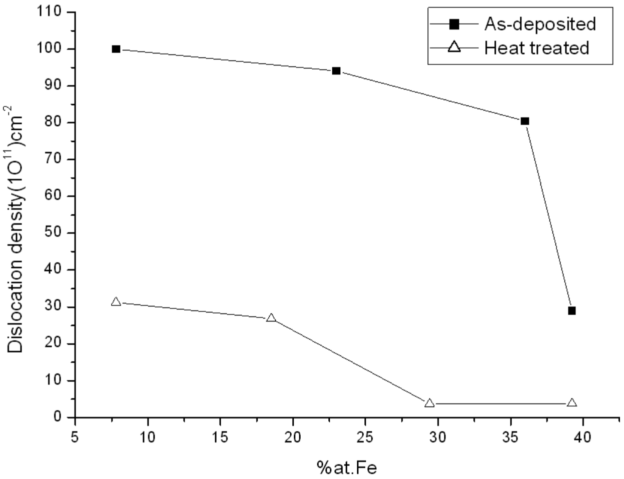

Figure 10: Dislocation density versus iron content for as-deposited and annealed Al-Fe thin films
Slika 10: Gostota dislokacij v odvisnosti od vsebnosti železa za nanesene in žarjene tanke plasti Al-Fe

observed in the same iron concentration range. However, as the crystal is refined from the micrometre scale into the nanometre scale, this mechanism will break down because the grains are unable to support dislocation pile-ups.

The dislocation density after a subsequent heat treatment of the coatings decreases in nearly the same manner as in the as-deposited state until 36 % Fe. Beyond this composition the variation become very slight, because the grain has reached its micrometre size

3.3 Micro deformation

There are several methods (we chose that of Williamson and Hall[23]) that can determine the average grain size (D) and the average microstrain rate (ε).

For aluminium compositions between amount fractions 30 % and 70 %, the microstrain coming from the tension stress varies smoothly. Beyond 70 % Al the variation become more pronounced, until 90 % Al, and corresponds to the amorphous domain phase. For aluminium compositions higher than 90 %, the microstrain falls again in the domain of α-Al solid solution (**Figure 11**).

A transition of the microstrain from tensile to compressive can be seen after the subsequent heat treatment at 500 °C for a period of 1h, for amorphous films with an aluminium content between mole fractions 68 % and 90 %.

It is well known that the atomic peening of the growing film by energetic particles is currently believed to favor both a dense morphology and grain size refinement. The energetic particles are not only the sputtered metal atoms, but also the high-energy neutral reflected gas atoms.[24,25] Both the flux and the energy of the high-energy neutral reflected gas atoms are proportional to the Mt : Mg ratio, where Mt is the atomic mass of the target material and Mg is that of the gas. As the transient metal (TM) is always heavier than Al, increasing the TM insert size on the target is equivalent to increasing the Mt : Mg ratio, and this leads to an enhancement of the in-situ bombardment of the growing film.

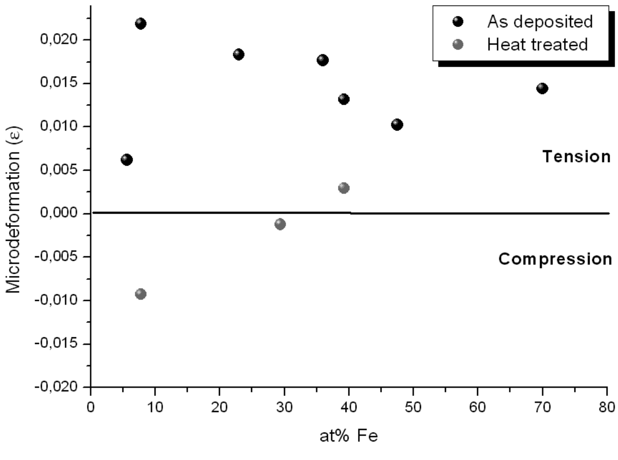

Figure 11: Micro-deformation evolution of as-deposited and heat-treated films with aluminium content

Slika 11: Odvisnost mikrodeformacije nanesenih in toplotno obdelanih plasti od vsebnosti aluminija

4 CONCLUSION

The analysis of the main experimental results issued from the present study leads to an extended solid solution in sputtered films versus liquid quenched alloys and significant mechanical strengthening of the aluminium by means of iron, essentially due to a combination of solid-solution effects and grain-size refinement. The lattice-parameter change of slope that occurs at 20 % Fe in a bulk alloy may indicate that the BCC-to-FCC transition may occur between amount fractions 30 % and 40 % Fe.

The bulk alloy microhardness is related to the detrimental effect of iron on the ductility. The Gaussian increase in the hardness of the alloys as the Fe content increases is explained by the intermetallic Al_3Fe and Al_2Fe phase formation. These phases are found in an eutectic-like structure over a wide composition range, while for Al-Fe deposits, the intrinsic microhardness of the thin films increases in a parabolic way according to the content of iron.

A transition of the microstrain from tensile to compressive can be seen after the heat treatment at 500 °C for a period of 1 h, for amorphous films with aluminium contents between mole fractions 68 % and 90 %.

On an other hand, the dislocation density is observed to exhibit a decreasing trend in both the as-deposited and heat-treated specimens. From 36 % Fe the dislocation density drops sharply, probably due to the structural change of the coatings from a mixture αAl (fcc) or αFe (bcc) with an amorphous phase to a crystalline (bcc) phase. This behaviour is in line with the inverse Hall-Petch effect (IHPE) observed for the same concentration range of iron.

5 REFERENCES

[1] R. D. Arnell, R. I. Bates,Vacuum, 43 (**1992**), 105

[2] T. Uesugi, Y. Takigawa, K. Higashi, Mat. Sci. Forum., 561–565 (**2007**), 997

[3] F. Sanchette, T. H. Loï, A. Billard, C. Frantz, Surf. Coat. Technol., 57 (**1993**), 179

[4] S. Lallouche, M. Y. Debili, Proceedings of the 14th European Microscopy Congress, Aachen, Germany, 2008, 183–184

[5] M. Y. Debili, T. H. Loi, C. Frantz, Rev. Metall., 29 (**1998**), 1501–1509

[6] M. Y. Debili, Proc. of the 10th Inter. coll. of frensh microscopy society, Grenoble, 2007, 627–641

[7] D. Wu, J. Zhang, J. C. Huang, H. Bei, T. G. Nieh, Scripta Mater., 68 (**2013**), 118–121

[8] S. Yip, Nature, 391 (**1998**), 532

[9] J. Schiotz, F. D. Di Tolla, K. W. Jacobsen, Nature, 391 (**1998**), 561

[10] H. Bückle, Met. Rev., 4 (**1959**), 49

[11] L. M. Pike, I. M. Anderson, C. T. Liu, Y. A. Chang, Acta Mater., 50 (**2002**), 3859

[12] L. A. Narayanan, F. H. Samuel, J. E. Gruzeleski, Metallurgical and Materials Transactions A, 26 (**1995**), 2161–2173

[13] L. A. Narayanan, F. H. Samuel, J. E. Gruzeleski, Metallurgical and Materials Transactions A, 25 (**1994**), 1761–1773

[14] N. Boukhris, S. Lallouche, M. Y. Debili, M. Draissia, The European Physical Journal Applied Physics, 3 (**2009**), 30501

[15] A. Guinier, Théorie et Technique de la radiocristallographie, 3rd ed., Dunod, Paris 1964, 461

[16] M. Draissia, M. Y. Debili, CEJP, 3 (**2005**), 395–408

[17] P. Visuttipitukul, T. Aizawa, H. Kuwahara, Materials Transactions, 44 (**2003**), 2695–2700

[18] H. Yoshioka, Q. Yan, K. Asami, K. Hashimoto, Mat. Sci. Eng., 134 (**1991**), 1054–1057

[19] D. Jang, M. J. Atzmon, Appl. Phys., 93 (**2003**), 9282

[20] Y. M. Wang, M. W. Chen. F. H. Zhou, E. Ma, Nature, 419 (**2002**), 912

[21] A. Misra, M. Verdier, H. Kung, M. Nastasi, J. D. Embury, J. P. Hirth, Ultrafine Grained Materials, R. S. Mishra, et al., eds., TMS, Warrendale, PA (2000), 299

[22] G. K. Williamson, R. Smallman, Phil. Mag., 1 (**1956**), 34

[23] G. K. Williamson, W. H. Hall, Acta Metall., 1 (**1953**), 22

[24] H. Windischmann, Crit. Rev. Solid State Mater. Sci., 17 (**1992**), 547

[25] M. Draissia, M. Y. Debili, Journal of Metastable and Nanocrystalline Materials, 22 (**2004**), 121

UDK 621.762:669.018.9
Original scientific article/Izvirni znanstveni članek

ISSN 1580-2949
MTAEC9, 48(5)639(2014)

WEAR BEHAVIOR OF Al/SiC/GRAPHITE AND Al/FeB/GRAPHITE HYBRID COMPOSITES

VEDENJE HIBRIDNIH KOMPOZITOV Al/SiC/GRAFIT IN Al/FeB/GRAFIT PRI OBRABI

Salim Şahın, Nilay Yüksel, Hülya Durmuş, Simge Gençalp İrızalp
Celal Bayar University, Faculty of Engineering, Materials Engineering Department, Manisa, Turkey
nilay.yuksel@cbu.edu.tr

Prejem rokopisa – received: 2013-08-12; sprejem za objavo – accepted for publication: 2013-11-26

Silicon carbide is often the preferred reinforcement in the production of aluminium-powder composites. In this study, aluminium composites were produced with 10 % and 20 % silicon-carbide and ferroboron reinforcements and (0, 0.5, 1 and 1.5) % graphite additions using powder metallurgy. The effects of the reinforcement type, the amount and the graphite content on the wear resistance were investigated. When compared with the unreinforced aluminium sample, it was clear that the increasing reinforcement increased the wear resistance. It was determined that the increasing graphite content negatively affects the wear resistance. The sample including 20 % ferroboron and 0 % graphite showed the minimum wear rate.

Keywords: aluminum hybrid composite, ferroboron, silicon carbide, wear

Silicijev karbid se pogosto uporablja za ojačanje pri proizvodnji aluminijevih kompozitov iz prahov. V tej študiji so bili aluminijevi kompoziti izdelani po metalurgiji prahov, utrjeni z 10 %, 20 % silicijevega karbida, fero-bora in dodatkom (0, 0,5, 1 in 1,5) % grafita. Raziskani so bili vplivi vrste ojačitve, količine ojačitve in količine grafita na odpornost proti obrabi. V primerjavi z neutrjenimi vzorci aluminija je razvidno, da se odpornost proti obrabi povečuje z večanjem utrjevanja. Ugotovljeno je, da povečanje količine grafita negativno vpliva na odpornost proti obrabi. Najmanjšo stopnjo obrabe je pokazal vzorec, ki je vseboval 20 % fero-bora in bil brez grafita.

Ključne besede: aluminijev hibridni kompozit, fero-bor, silicijev karbid, obraba

1 INTRODUCTION

Powder metallurgy is considered as a good technique for producing metal-matrix composites[1] and has a wide range of applications ranging from automotive to advanced aerospace components[2]. P/M components are an established economic alternative to the components made with other manufacturing processes as well as the only means to produce those components that cannot be made with other methods[2]. One of the best properties of the composites fabricated with powder metallurgy is obtained when the reinforcement is homogeneously dispersed in the matrix, as proven with both experimental and theoretical studies[3]. Another advantage of the powder-metallurgy technique is the fact that it allows us to manufacture near-net-shape products at low costs[1].

Al-based particulate-reinforced metal-matrix composites have attracted much interest due to their potential use and desirable properties[4]. Aluminum is one of the best materials for the matrix because of its low density, high conductivity and high toughness. The other advantage of using Al for the matrices of MMCs is its corrosion resistance which is very important when using composites in different environments[3,5]. Aluminum P/M alloys are used in the automobile industry for cylinder liners, cylinder blocks and drive shafts, replacing more traditional ferrous alloys[6,7]. Moreover, Al composites are used for helicopter parts in aeronautics, such as the parts of the body, the support for rotor plates and rotor vanes in compressors[7]. Their use is a part of the trend toward the materials that can reduce the weight of a vehicle[6]. However, a low wear resistance of pure aluminum is a serious drawback in using it in many applications[1]. An addition of a non-metallic second phase such as oxides, carbides, nitrides and borides to aluminum alloys can dramatically improve the mechanical properties and wear resistance of the materials[8]. Particle reinforcements are more favorable than the fiber type as they allow a better control of the microstructure and mechanical properties obtained by varying the size and the volume fraction of the reinforcement[1].

Aluminium-matrix composites (AMCs) reinforced with SiC_P are recognized as important advanced structural materials due to their desirable properties, including a high specific stiffness, a high specific strength, a high temperature resistance and an improved wear resistance[9]. So, many studies were carried out on the preparation and wear properties of the Al-matrix composites with the SiC-particle reinforcements[10–13]. However, there are not many works on the wear behavior of the Al-matrix composites with the FeB-particle reinforcements. Generally, the effect of the FeB reinforcement on the wear properties was investigated for iron-based P/M alloys[14–17].

In addition to the contact configuration for different types of the wear tester, the wear behavior of materials is related to several factors such as the properties of the materials sliding against each other and experimental conditions including environmental conditions, load, speed, etc.[8] The wear rate and friction coefficient of an Al-matrix composite strongly depends on the reinforcement particles, the amounts of the reinforcement and graphite[12,13,18,19]. It was found that the wear rate of a hard-particle composite is substantially lower than that of the base material[7,20]. The reinforcement of an aluminum matrix with SiC or FeB was generally found to improve the wear resistance[7,14,21].

In this study, an aluminum-matrix composite with the reinforcement of SiC or FeB and an addition of graphite (Gr) particulates was explored for tribological properties. In many works, it was reported that graphite particulates form a solid lubricant on a tribosurface[19,22,23]. Generally, an addition of graphite to aluminum alloys is known to decrease the strength, fracture energy, ductility and hardness of the materials. A graphite particulate has a brittle structure; therefore, the tendency of crack initiation and propagation increases at the graphite-metal interface[19,22]. Also, the final properties of the metal-matrix composites depend on the matrix and ceramic reinforcements, the bonding of the ceramic reinforcements, the size and distribution of ceramic reinforcements and the graphite particulates in an aluminum matrix. According to the literature studies, little information about the effect of the FeB reinforcement and graphite particulates on the wear properties is available. In this work, the effect of the FeB reinforcement, the SiC reinforcement and graphite on the wear properties of P/M composites was investigated.

2 MATERIALS AND METHODS

2.1 Production of the composites

In this study Al/SiC/Gr hybrid composites with the size of Ø 20 mm × 10 mm were produced using the powder-metallurgy method. The chemical composition of the aluminium powder was 98.23 % Al–0.0056 % Fe–1.52 % MgO. The sizes of aluminium, FeB and SiC powders were below 53 µm.

Al/Gr composites were reinforced with SiC and FeB particles. The composites were produced with the additions of $w = (0, 0.5, 1, 1.5)$ % graphite and $w = (10, 20)$ % FeB or SiC (**Table 1**). The powder mixtures were pressed under a 400 MPa load, with the size of Ø 20 mm × 10 mm. The green samples were sintered at 620 °C for 1 h.

Table 1: Powder compositions of composite samples (mass fractions, w/%)

Tabela 1: Sestava prahov kompozitnih vzorcev (masni deleži, w/%)

Sample	Al	SiC	Gr	Sample	Al	FeB	Gr
1	90	10	0	9	90	10	0
2	89.5	10	0.5	10	89.5	10	0.5
3	89	10	1	11	89	10	1
4	88.5	10	1.5	12	88.5	10	1.5
5	80	20	0	13	80	20	0
6	79.5	20	0.5	14	79.5	20	0.5
7	79	20	1	15	79	20	1
8	78.5	20	1.5	16	78.5	20	1.5

2.2 Microstructural investigation

Microstructural examinations were carried out with SEM to investigate the porosities and particle clusters.

2.3 Density

The densities of the composite samples were measured according to Archimedes' principle and their porosity ratios were calculated.

2.4 Wear tests

A CSM instruments ball-on-disc wear-test unit was employed in the present work for a tribological analysis under dry-sliding conditions with the Al-SiC$_p$ + Al-FeB$_p$ composites against a 100 Cr6 stainless-steel ball. The stainless-steel counter-face material had a diameter of 6 mm. All the experiments were carried out at a load of 3 N at room temperature. Each test was performed with a sliding speed of 20 cm/s and the track diameter was 8 mm. The speed, temperature and sliding-distance conditions were all kept constant in each test. This procedure was executed for each sample along the total sliding distance of 250 m. The coefficient of friction was recorded during the wear testing by a transducer on the load arm of the tribometer. The quantitative value of the wear was obtained by measuring the cross-sectional area of the wear track and then the wear rate was calculated by the TRIBOX 2.10.C program.

3 RESULTS AND DISCUSSION

3.1 Microstructural investigation

It can be seen that SiC particles dispersed uniformly in the aluminium matrix (**Figure 1**). But in the FeB-reinforced samples, some clusters of FeB particles

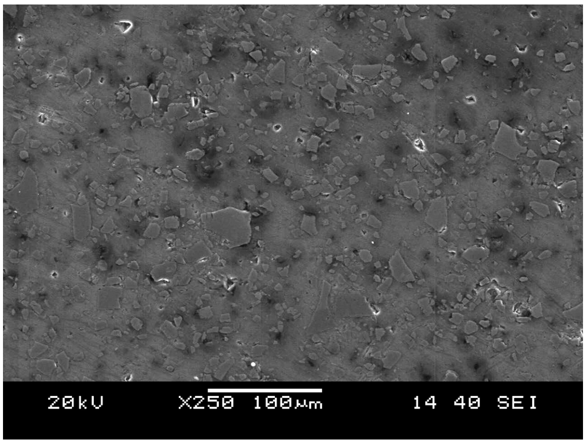

Figure 1: Microstructure of 10 % SiC + 1.5 % Gr reinforced composite

Slika 1: Mikrostruktura kompozita, ojačanega z 10 % SiC + 1,5 % grafita

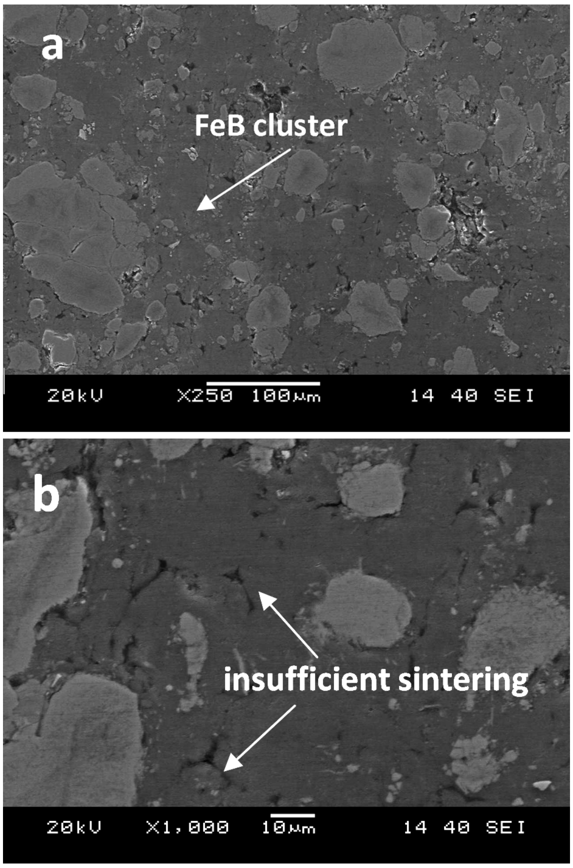

Figure 2: Microstructure of 20 % FeB + 1.5 % Gr reinforced composite: a) FeB cluster in the structure, b) porosities due to insufficient sintering
Slika 2: Mikrostruktura kompozita, ojačanega z 20 % FeB + 1,5 % grafita: a) skupek FeB v strukturi, b) poroznosti zaradi nezadostnega sintranja

were noticed (**Figure 2a**). The sample including 20 % FeB + 1.5 % Gr, exhibiting the maximum porosity, had pores around the reinforcements and also between the grain boundaries due to insufficient sintering (**Figure 2b**). In contrast, there were no pores around the reinforcement particles of the sample including 10 % SiC + 1.5 Gr which exhibited the minimum porosity (**Figure 1**); moreover, no insufficient sintering was confirmed. The maximum porosity was revealed in the sample with the maximum reinforcement. It is thought that the pores originating from insufficient sintering can result from the cold-pressing pressure. Due to the negative influence of an increase in the reinforcement on the compressibility, the sintering process for the sample reinforced with 20 % FeB + 1.5 % Gr was not adequately maintained. Moreover, the pores arising from the clusters must be considered.

3.2 Density

The compressibility of composite powders is noticeably lower than that of the unreinforced matrix, often producing a low green density and an insufficient strength to support secondary processing like sintering, machining or extrusion[4]. Reinforcement particles have a tendency to associate themselves with porosity and give rise to particle-porosity clusters[24]. The presence of non-metallics such as unreduced oxides reduces the compressibility because of their hardness and low specific gravity[2]. Rahimian et al.[25] reported that as the amount of alumina increases, the relative density declines. The reason for this, in comparison with pure aluminum, is the decline in the pressing capacity of the samples with the increase in the amount of alumina. This is due to a higher hardness of alumina. Therefore, these composites have a lower compressibility resulting in a lower relative density[25]. In **Figure 3** it can be seen that the increasing amount of reinforcement has increased the porosity. SEM images of the microstructures show the increase in the porosity with the increasing reinforcement (**Figures 1** and **2**). Also, Tekmen et al.[24] found that the increasing reinforcement volume fraction increases the porosity content. In the present study the porosity ratio of the unreinforced aluminium composite was calculated as 3.77 %. So, the minimum porosity ratio compared to the reinforced samples was shown. It was observed that the composites with an addition of FeB have a higher porosity compared to the SiC samples. During the microstructural investigation, agglomerations of FeB particles were noticed particularly in larger reinforcement amounts (**Figure 2a**). The SiC-reinforced composites showed a more homogeneous distribution in the aluminium matrix. So, it was concluded that a particle agglomeration causes an increase in the porosity.

In general, the porosity due to the increasing graphite amount exhibited a downward trend except for the composites reinforced with 20 % FeB (**Figure 3**). Due to the FeB clusters (**Figure 2a**), the graphite could not properly show its lubricant effect during cold pressing.

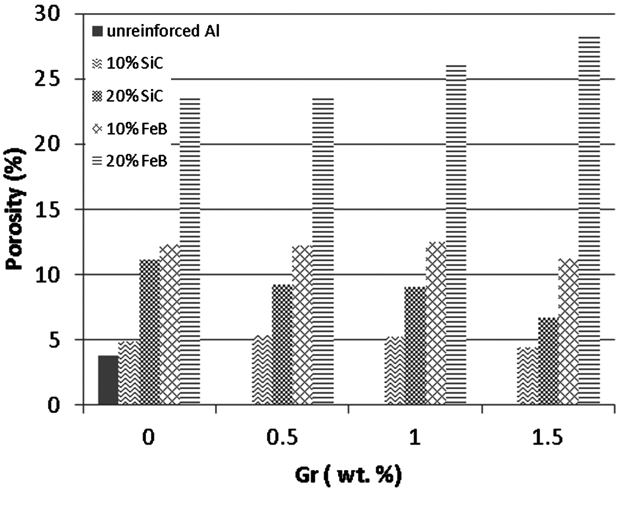

Figure 3: Porosity values of the composites (*w*/%)
Slika 3: Delež poroznosti kompozitov (*w*/%)

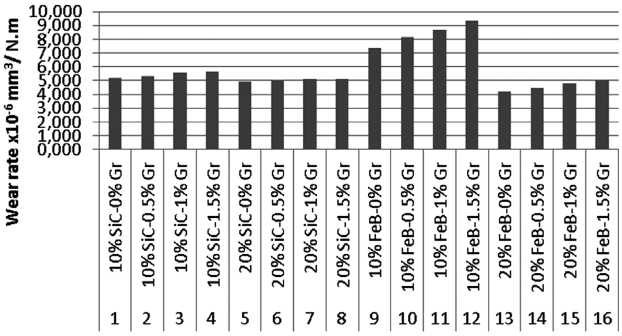

Figure 4: Wear rate
Slika 4: Hitrost obrabe

3.3 Wear tests

From **Figure 4**, it can be concluded that the maximum wear rate was obtained for the sample consisting of 10 % FeB + 1.5 % Gr and the minimum wear rate was obtained for the sample without graphite and reinforced with 20 % FeB. The wear-test parameters generated a very large wear scar on the unreinforced aluminium, so that the profilometer could not scan the whole section of the wear scar. For this reason, the wear rate of the unreinforced aluminium composite could not be calculated; however, it can be said that the unreinforced aluminium shows a higher wear rate than the reinforced ones.

The wear resistance increased as the reinforcement proportion increased from 10 % to 20 % since the hard SiC and FeB particles in the matrix resisted the counterpart. The increased reinforcement reduced the contact area between the counterpart and the relatively soft matrix, thus the abrasion (wear) was reduced. **Figure 5** explains this phenomenon. Here, the hard SiC particles outcropped and formed an impediment for the contact between the composite surface and the counterpart (**Figure 5a**). The outcropped particles abraded the counterpart. **Figure 6** also shows the abraded areas of the counterparts of the 10 % FeB + 1.5 % Gr and 20 % SiC + 0 % Gr composites. The counterpart of the 20 % SiC + 0 % Gr composite exhibited a larger abrasion area in comparison with the counterpart of 10 % FeB + 1.5 % Gr due to the increased reinforcement amount. Ravindran et al.[26] reported that the dispersion of silicon carbide, the hard phase in the soft aluminium matrix, tends to reduce the wear loss of hybrid composites.

In the literature some researchers maintain that the graphite amount in aluminium composites enhances the tribological properties and wear resistance[13,27,28]. However, Vencl et al.[29] reported that an addition of graphite particles (w = 1 %) to a composite with SiC parti-

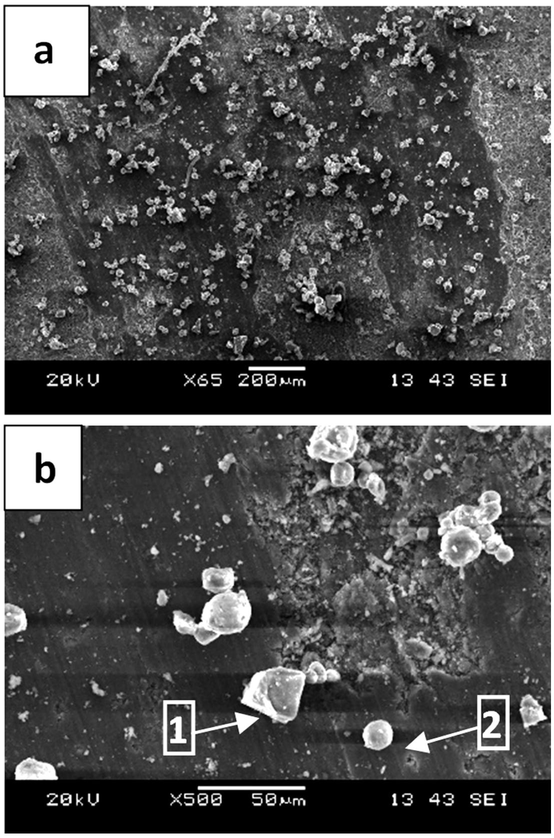

Figure 5: Wear surface of 20 % SiC + 0 % Gr reinforced composite: a) wear tracks, b) EDX analysis
Slika 5: Obrabljena površina kompozita, ojačanega z 20 % SiC + 0 % grafita: a) sledi obrabe, b) EDX-analiza

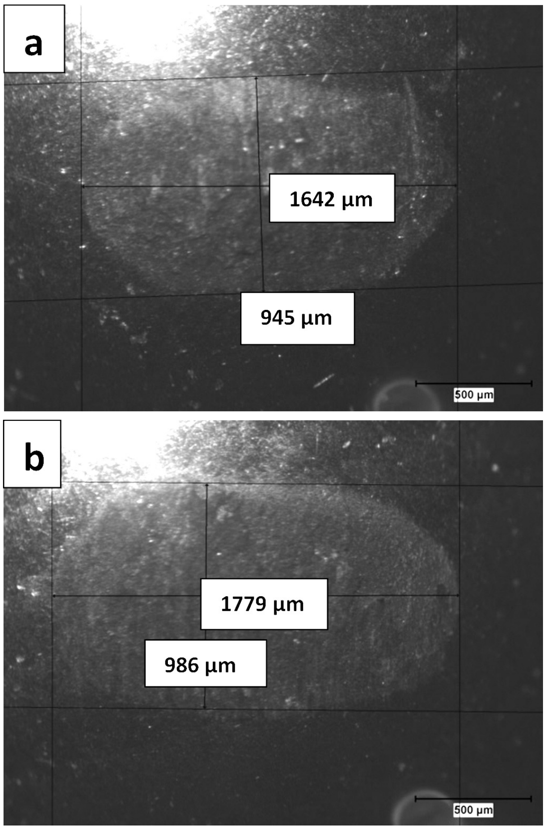

Figure 6: Counter parts of the composites: a) 10 % FeB + 1.5 % Gr, b) 20 % SiC + 0 % Gr
Slika 6: Stična površina kompozitov: a) 10 % FeB + 1,5 % grafita, b) 20 % SiC + 0 % grafita

cles further reduced the wear rate and the coefficient of friction, but this influence of such a relatively small amount of graphite was not clear enough and should be considered only as a trend of behavior. According to the results of the present study, the increased Gr amount increased the wear rate. Actually, this was an expected result because the main reason for the graphite addition to aluminium composites reinforced with hard particles was to simplify the machining. The presence of the hard, brittle and abrasive SiC reinforcement makes the material difficult to form or machine using traditional manufacturing processes. In order to improve the machinability of the SiC_p/Al composites, graphite was added to the composites[30].

As an alternative approach, an explanation for the decreasing wear rate with the increasing reinforcement might be the pores filled up with the wear debris. A high reinforcement amount causes high porosity, so the wear debris could easily fill these numerous pores instead of being pushed out of the tribological system. Actually, a negative effect of the increasing pores on the wear resistance was expected. In this case, the pores presumably filled with the wear debris gave rise to a decrease in the wear rate calculated as the volumetric wear loss. As can be seen from **Figure 7**, a pore on the worn surface of the 20 % FeB + 0 % Gr hybrid composite was filled with the wear debris. According to the results of the EDX analysis it can be concluded that wear debris is composed of the aluminium matrix, the stainless-steel counterpart and FeB-reinforcement particles (**Table 2**).

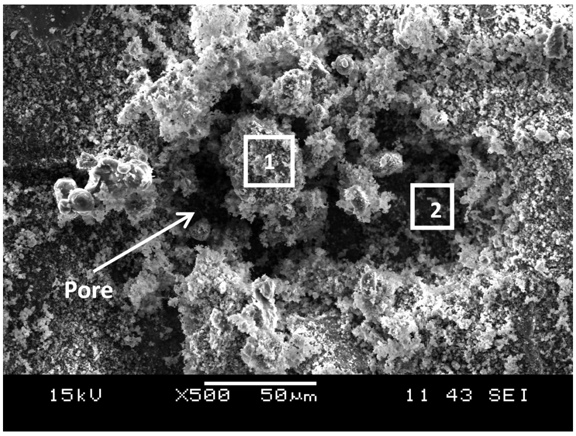

Figure 7: Pore and wear debris on the worn surface of 20 % FeB + 0 % Gr hybrid composite

Slika 7: Praznine in delci obrabe na obrabljeni površini hibridnega kompozita z 20 % FeB + 0 % grafita

Table 2: EDX analysis of the pore on the worn surface of 20 % FeB + 0 % Gr hybrid composite (*w*/%)

Tabela 2: EDX-analiza površine pore na obrabljeni površini hibridnega kompozita z 20 % FeB + 0 % grafita (*w*/%)

Element	Al	Fe	Cr	Si	Mn
1	81.799	13.687	3.542	0.203	0.769
2	76.015	18.834	4.319	0.172	0.661

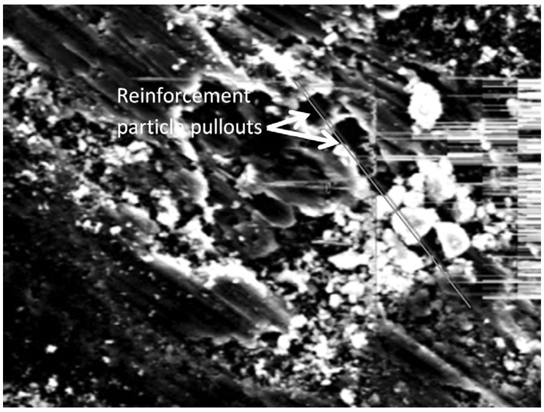

Figure 8: EDX analysis of 10 % SiC + 1.5 % Gr hybrid composite along the line; left: Si, right: C (graphite)

Slika 8: Linijska EDX-analiza hibridnega kompozita z 10 % SiC + 1,5 % grafita; levo: Si, desno: C (grafit)

The pores could have been formed due to the insufficient sintering (**Figure 2**) and they could have also been created by the mechanical force during the wear test. **Figure 8** shows the pores caused by the wear test, as the reinforcement particles were pulled out. These kinds of pores could be large and easily filled with the wear debris. The reason for the particle pullout was found with the EDX analysis carried out along a line. The EDX graph of graphite shows a significant increase of the pores arrowed as "reinforcement particle pullouts" in **Figure 8**. By means of the EDX analysis (in **Figure 8**, the EDX graph on the right-hand side shows graphite) it was realized that the wall of pores was smeared by graphite, so the wettability between the matrix and the reinforcement was reduced. In this case, the particle pullout occurred easily and due to the low bonding of the aluminium matrix and the reinforcement. Thus, a detrimental effect of graphite on the wear resistance was confirmed.

The samples that exhibit the maximum wear rate in both groups, the SiC- and FeB-reinforced composites, exhibit both abrasive and adhesive wear tracks. For both reinforcement groups, if the wear surfaces of the most and the least wear-resistant samples were compared, adhesion wear was observed to be more intense on the least wear-resistant samples.

The wear surface of the sample reinforced with 10 % SiC + 1.5 % Gr exhibited both large craters arising from adhesion and abrasion scratches (**Figure 9a**). Similarly, the wear surface of the sample including 10 % FeB + 1.5 % Gr shows adhesion craters and also flaky wear debris subjected to delamination (**Figure 10**). According to the EDX analysis (**Table 3**) the aluminium amount of the delaminated area was larger than the other analyzed area; consequently, it is maintained that the delaminated part had a smaller reinforcement amount and was subjected to a large plastic deformation. The plastically deformed part became strain hardened and brittle. Ravindran et al.[26]

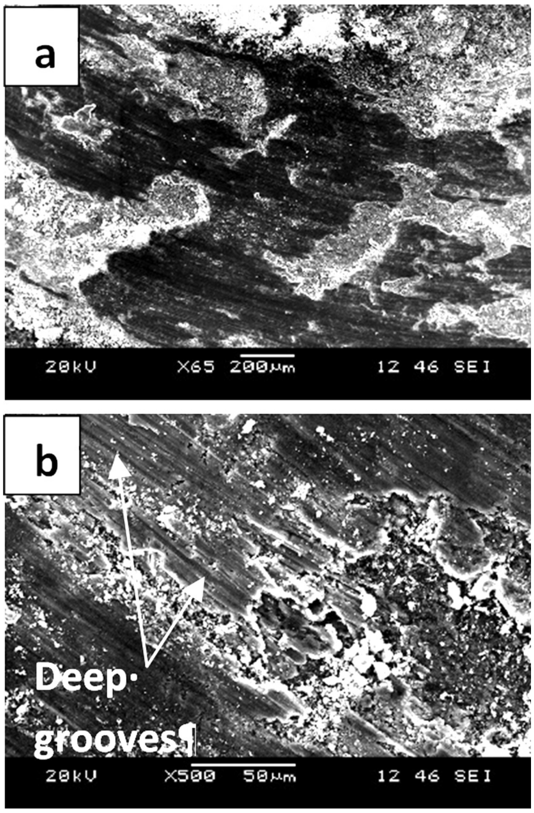

Figure 9: Wear surface of 10 % SiC + 1.5 % Gr reinforced composite: a) abrasion and adhesion marks, b) deep abrasion grooves

Slika 9: Obrabljena površina kompozita, ojačanega z 10 % SiC + 1,5 % grafita: a) obraba in lepljenje, b) globoki abrazijski utori

also observed severe plastic deformation of the Al 2024 matrix and a brittle fracture on the wear surface.

Table 3: EDX analysis of 10 % FeB + 1.5 % Gr reinforced composite (*w*/%)

Tabela 3: EDX-analiza kompozitov, ojačanih z 10 % FeB + 1,5 % grafita (*w*/%)

Element	Al	Fe	Cr	C	Si	Mn
1	93.197	4.631	1.259	0.352	0.188	0.374
2	88.810	6.680	1.628	1.184	1.069	0.630

If the wear surfaces in **Figures 9** and **11** are compared, it can be observed that the adhesive-wear tracks reduced and the abrasive scratches became shallower with the increase in the reinforcement proportion from 10 % to 20 %. Similar observations were made for the wear surfaces of the FeB-reinforced samples (**Figures 10** and **12**).

On the wear surfaces of the most wear-resistant samples including a 20 % reinforcement of (FeB or SiC) + 0 % Gr, it was observed that the reinforcement particles were pulled out but not taken away from the tribological system (**Figure 9**). It is maintained that the detached hard reinforcement particles might have become embedded a little into the soft matrix due to the applied load during the wear test and decreased the wear rate by reducing the real contact area between the surface and the counterpart. As can be seen from the EDX analysis (**Table 4**), the particle marked as "1" is the FeB reinforcement covered with some of the Al matrix (**Figure 12**). Similarly, the pulled-out SiC particle marked as "1" and the presumably oxidized aluminium particle marked as "2" were detected with EDX as presented in **Table 5** and **Figure 9**.

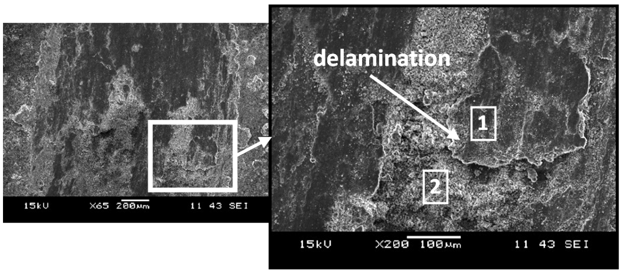

Figure 10: Wear surface of 10 % FeB + 1.5 % Gr reinforced composite

Slika 10: Obrabljena površina kompozita, ojačanega z 10 % FeB + 1,5 % grafita

The shape of the reinforcement particles caused a difference in the abrasive-wear tracks, particularly for the 10 % reinforced samples. The sharp and angularly shaped SiC particles caused narrow but deep grooves (**Figure 9**), while the relatively round-shaped FeB particles formed shallower and wider grooves (**Figure 11**).

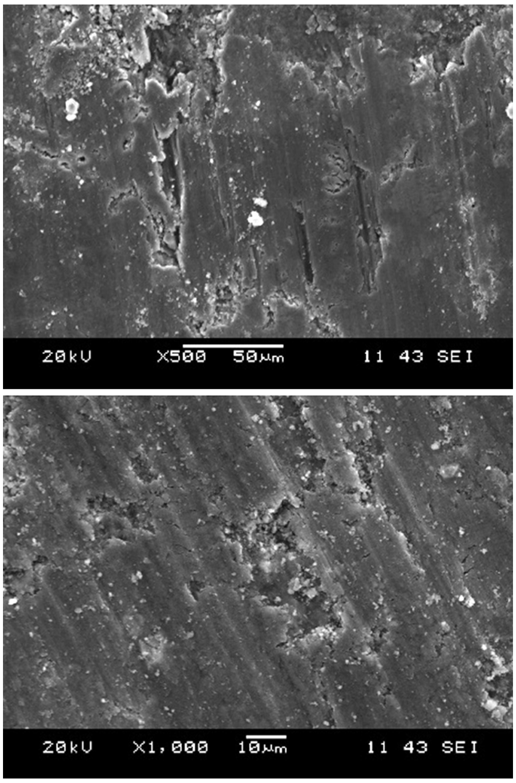

Figure 11: Wide and shallow wear tracks of 10 % FeB + 1.5 % Gr reinforced composite

Slika 11: Široke in plitve sledi obrabe na kompozitu, ojačanem z 10 % FeB + 1,5 % grafita

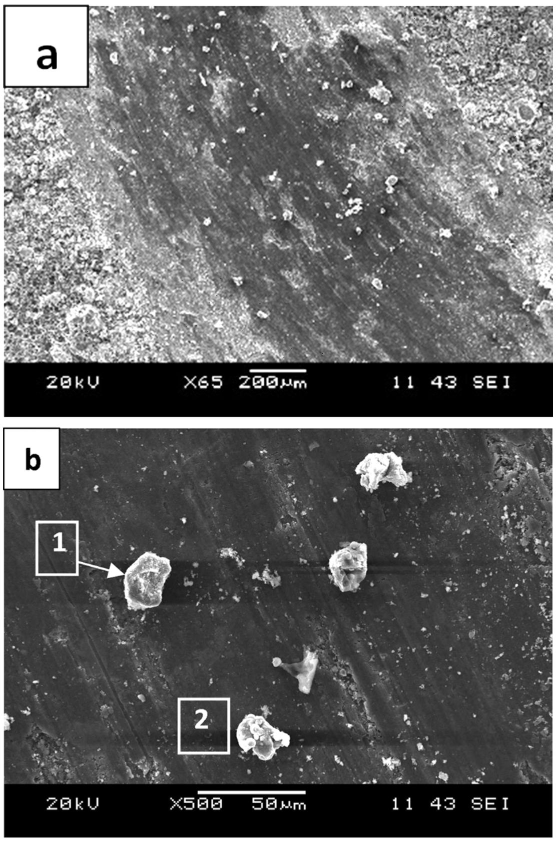

Figure 12: Wear surface of 20 % FeB + 0 % Gr reinforced composite: a) wear tracks, b) EDX analysis

Slika 12: Obraba na površini kompozita, ojačanega z 20 % FeB + 0% grafita: a) sledi obrabe, b) EDX- analiza

Table 4: EDX analysis of 20 % FeB + 0 % Gr reinforced composite (*w*/%)

Tabela 4: EDX-analiza kompozitov, ojačanih z 20 % FeB + 0 % grafita (*w*/%)

Element	Al	Fe	Cr	C	Si	Mn
1	67.211	29.460	1.326	0.030	0.945	1.027
2	79.865	17.242	1.994	-	0.459	0.441

Table 5: EDX analysis of 20 % SiC + 0 % Gr reinforced composite (*w*/%)

Tabela 5: EDX-analiza kompozitov, ojačanih z 20 % SiC + 0 % grafita (*w*/%)

Element	Al	Fe	C	Si	O
1	0.860	0.220	26.665	71.914	0.341
2	91.952	0.202	3.615	1.020	3.210

As the two surfaces are brought in contact, the nanoscale asperities are the first to come into contact, instantly plastically deforming and merging to form micro- or macro-contacts, which, upon further application of the load, may deform due to elastic or elastic-plastic deformation[31]. A further plastic deformation leads to a brittle fracture. In this study, the sample including only 20 % SiC exhibited brittle flakes during the wear test. Here, the plastically deformed aluminium matrix underwent strain hardening. The brittle layer consisted of the strain-hardened aluminium and the hard SiC particles were smeared on its surface. In **Figure 13**, the cracks and debris separated from the brittle layer can be seen. It is assumed that the existence of SiC particles contributes to the strain-hardened aluminium and so the hardness of the strain-hardened matrix increases further.

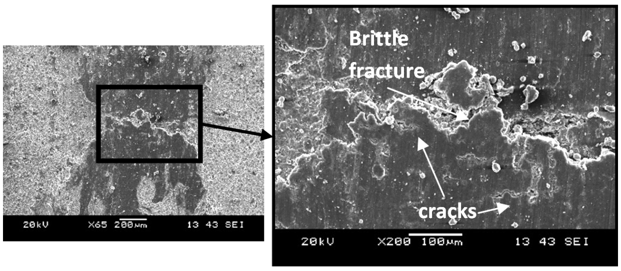

Figure 13: Brittle wear-debris structure on the wear surface of 20 % SiC + 0 % Gr reinforced composite

Slika 13: Krhki odkruški na obrabljeni površini kompozita, ojačanega z 20 % SiC + 0 % grafita

Analyzing the EDX results of the 10 % FeB + 1.5 % Gr and 20 % FeB + 0 % Gr reinforced samples (**Tables 3** and **4**), some elements such as Cr and Mn belonging to the stainless-steel counterpart were observed. In contrast, the EDX result for the 20 % SiC + 0 % Gr reinforced composite did not show any element of the stainless-steel counterpart (**Table 5**).

4 CONCLUSIONS

- The minimum wear rate was obtained for the sample without graphite and reinforced with 20 % FeB.
- The 20 % FeB-reinforced samples showed the maximum porosity and insufficient sintering due to the increased reinforcement. In a further study, pressure can be raised during cold pressing.
- The maximum wear rate was obtained for the sample consisting of 10 % FeB + 1.5 % Gr.
- The increased graphite amount increased the wear rate of all the Al-powder composites.
- The increased reinforcement increased the porosity.
- The wear rate decreased with the increasing reinforcement.

5 REFERENCES

[1] M. Rahimian, N. Parvin, N. Ehsani, The effect of production parameters on microstructure and wear resistance of powder metallurgy Al–Al_2O_3 composite, Mater. Design, 32 (**2011**), 1031–1038

[2] P. C. Angelo, R. Subramanian, Powder Metallurgy: Science, Technology and Applications, Prentice-Hall of India Pvt. Ltd., 2008

[3] H. Abdizadeh, M. Ashuri, P. T. Moghadam, A. Nouribahadory, H. R. Baharvandi, Improvement in physical and mechanical properties of aluminum/zircon composites fabricated by powder metallurgy method, Mater. Design, 32 (**2011**), 4417–4423

[4] H. R. Hafizpour, M. Sanjari, A. Simchi, Analysis of the effect of reinforcement particles on the compressibility of Al–SiC composite powders using a neural network model, Mater. Design, 30 (**2009**), 1518–1523

[5] G. Özer, K. A. Güler, H. M. Lus, Effects of Squeeze Pressure on Microstructure, Porosity and Hardness of an In-Situ Mg_2Si/Al–Si–Cu Composite, MP Materials Testing, 1 (**2012**), 26–29

[6] G. Steedman, D. P. Bishop, W. F. Caley, G. J. Kipouros, Surface porosity investigation of aluminum–silicon PM alloys, Powder Technol., 226 (**2012**), 225–230

[7] A. M. Hassan, A. Alrashdan, M. T. Hayajneh, A. T. Mayyas, Wear behavior of Al–Mg–Cu–based composites containing SiC particles, Tribol. Int., 42 (**2009**), 1230–1238

[8] A. A. Hamid, P. K. Ghosh, S. C. Jain, S. Ray, The influence of porosity and particles content on dry sliding wear of cast in situ Al(Ti)–Al_2O_3(TiO_2) composite, Wear, 265 (**2008**), 14–26

[9] J. C. Shao, B. L. Xiao, Q. Z. Wang, Z. Y. Ma, Y. Liu, K. Yang, Constitutive flow behavior and hot workability of powder metallurgy processed 20 vol. % SiC_P/2024Al composite, Mat. Sci. Eng. A-Struct., 527 (**2010**), 7865–7872

[10] N. P. Cheng, C. M. Li, Q. Hui, Z. Q. Chen, Effect of particle surface treatment on the microstructure and property of SiC_p/AA6066 composite produced by powder metallurgy, Mat. Sci. Eng. A-Struct., 517 (**2009**), 249–256

[11] K. S. Al-Rubaie, H. N. Yoshimura, J. D. Biasoli de Mello, Two-body abrasive wear of Al–SiC composites, Wear, 233–235 (**1999**), 444–454

[12] R. Ipek, Adhesive wear behaviour of B_4C and SiC reinforced 4147 Al matrix composites (Al/B_4C–Al/SiC), J. Mater. Process. Tech., 162–163 (**2005**), 71–75

[13] P. Ravindran, K. Manisekar, P. Narayanasamy, N. Selvakumar, R. Narayanasamy, Application of factorial techniques to study the wear of Al hybrid composites with graphite addition, Mater. Design, 39 (**2012**), 42–54

[14] H. Ö. Gülsoy, M. K. Bilici, Y. Bozkurt, S. Salman, Enhancing the wear properties of iron based powder metallurgy alloys by boron additions, Mater. Design, 28 (**2007**), 2255–2259

[15] H. Ö. Gülsoy, Influence of nickel boride additions on sintering behaviors of injection moulded 17-4 PH stainless steel powder, Scripta Mater., 52 (**2005**), 187–192

[16] H. Ö. Gülsoy, S. Salman, S. Özbek, Effect of FeB additions on sintering characteristics of injection moulded 17-4PH stainless steel powder, J. Mater. Sci., 39 (**2004**), 4835–4840

[17] R. Tandon, R. M. German, Sintering and mechanical properties of a boron-doped austenitic stainless steel, Int. J. Powder Metall., 34 (**1998**), 40–49

[18] L. E. G. Cambronero, E. Sánchez, J. M. Ruiz-Roman, J. M. Ruiz-Prieto, Mechanical characterisation of AA7015 aluminium alloy reinforced with ceramics, J. Mater. Process. Tech., 143–144 (**2003**), 378–383

[19] F. Akhlaghi, A. Zare-Bidaki, Influence of graphite content on the dry sliding and oil impregnated sliding wear behavior of Al 2024–graphite composites produced by in situ powder metallurgy method, Wear, 266 (**2009**), 37–45

[20] S. Das, S. Das, K. Das, Abrasive wear of zircon sand and alumina reinforced Al–4.5 wt% Cu alloy matrix composites—a comparative study, Compos. Sci. Technol., 67 (**2007**), 746–751

[21] M. Acilar, F. Gul, Effect of the applied load, sliding distance and oxidation on the dry sliding wear behaviour of Al–10Si/SiC composites produced by vacuum infiltration technique, Mater. Design, 25 (**2004**), 209–217

[22] M. L. Ted Guo, C. Y. A. Tsao, Tribological behavior of aluminum/SiC/nickel-coated graphite hybrid composites, Mat. Sci. Eng. A, 333 (**2002**), 134–145

[23] A. R. Riahi, A. T. Alpas, The role of tribo-layers on the sliding wear behavior of graphite aluminum matrix composites, Wear, 251 (**2001**), 1396–1407

[24] C. Tekmen, I. Ozdemir, U. Cocen, K. Onel, The mechanical response of Al-Si-Mg/SiCp composite: influence of porosity, Mat. Sci. Eng. A-Struct., 360 (**2003**), 365–371

[25] M. Rahimian, N. Parvin, N. Ehsani, Investigation of particle size and amount of alumina on microstructure and mechanical properties of Al matrix composite made by powder metallurgy, Mat. Sci. Eng. A-Struct., 527 (**2010**), 1031–1038

[26] P. Ravindran, K. Manisekar, P. Rathika, P. Narayanasamy, Tribological properties of powder metallurgy – Processed aluminium self lubricating hybrid composites with SiC additions, Mater. Design, 45 (**2013**), 561–570

[27] C. B. Lin, R. J. Chang, W. P. Weng, A study on process and tribological behaviour of Al alloy/Gr (p) composite, Wear, 217 (**1998**), 167–174

[28] J. Leng, L. Jiang, G. Wu, S. Tian, G. Chen, Effect of Graphite Particle Reinforcement on Dry Sliding Wear of SiC/Gr/Al Composites, Rare Metal Mat. Eng., 38 (**2009**), 1894–1898

[29] A. Vencl, I. Bobic, S. Arostegui, B. Bobic, A. Marinković, M. Babić, Structural, mechanical and tribological properties of A356 aluminium alloy reinforced with Al_2O_3, SiC and SiC + graphite particles, J. Alloy Compd., 506 (**2010**), 631–639

[30] J. Leng, G. Wu, Q. Zhou, Z. Dou, X. L. Huang, Mechanical properties of SiC/Gr/Al composites fabricated by squeeze casting technology, Scripta Mater., 59 (**2008**), 619–622

[31] B. Bhushan, Contact mechanics of rough surfaces in tribology: multiple asperity contact, Tribol. Lett., 4 (**1998**), 1–35

UDK 519.61/.64
Original scientific article/Izvirni znanstveni članek

ISSN 1580-2949
MTAEC9, 48(5)647(2014)

MATHEMATICAL MODEL FOR AN Al-COIL TEMPERATURE CALCULATION DURING HEAT TREATMENT

MATEMATIČNI MODEL ZA IZRAČUN TEMPERATURE V Al-KOLOBARJU MED TOPLOTNO OBDELAVO

Franci Vode[1], Franc Tehovnik[1], Jaka Burja[1], Boštjan Arh[1], Bojan Podgornik[1], Darja Steiner Petrovič[1], Matjaž Malenšek[2], Leonida Kočevar[2], Marjana Lažeta[2]

[1]Institute of Metals and Technology, Lepi pot 11, 1000 Ljubljana, Slovenia
[2]IMPOL d.d., Partizanska cesta 38, 2310 Slovenska Bistrica, Slovenia
franci.vode@imt.si

Prejem rokopisa – received: 2013-09-09; sprejem za objavo – accepted for publication: 2014-05-28

This paper presents the implementation of a mathematical model for an Al-coil's temperature evolution during heat treatment in a forced-circulation furnace. The coil's spatial-temperature evolution is calculated using the finite-difference method in the axial and radial directions, i.e., 2 dimensional. The model is verified by measuring the coil's temperature during reheating using 10 pre-installed thermocouples arranged in two lines of 5 thermocouples, each at a different coil radius. The sensitivities of the furnace-air temperature and the initial-coil temperature on the time to switch are determined, i.e., –52.5 s/°C and –55.5 s/°C, respectively. The mathematical model proved to be a multipurpose tool for different simulation-based reheating studies, while its industrial real-time application offers an even wider range of uses and capabilities: automatic coil-temperature control and observing reheating conditions on an industrial level.

Keywords: Al-coil, temperature, finite difference, mathematical model

Članek obravnava uporabo matematičnega modela razvoja temperature v Al-kolobarju med toplotno obdelavo v peči s prisiljeno cirkulacijo. Razvoj prostorske temperature v kolobarju je izračunan z uporabo metode končnih diferenc v osni in radialni smeri. Model je bil preizkušen z merjenjem temperature v kolobarju med ogrevanjem s predhodno vgrajenimi 10 termoelementi, razporejenimi v dveh vrstah po 5 na dveh različnih premerih kolobarja. Ugotovljena je bila občutljivost temperature atmosfere v peči in začetne temperature v kolobarju v odvisnosti od peči: –52,5 s/°C oziroma –55,5 s/°C. Matematični model se je izkazal kot večnamensko orodje za različne simulacije ogrevanja, medtem ko industrijska uporaba v realnem času ponuja še širše področje uporabe in zmogljivosti: avtomatsko kontrolo temperature kolobarja, opazovanje razmer pri ogrevanju na industrijskem nivoju.

Ključne besede: Al-kolobar, temperatura, končne diference, matematični model

1 INTRODUCTION

The description of physical processes using appropriate mathematical models is nowadays achieving practical usefulness in different fields.[1,2] One of these fields are certainly models for describing heat transfer, especially in metallic materials, where the metal's temperature drives, determines or triggers most material-transformation processes. Coil temperature is one of the most important reheating parameters for Al-coils. The precision of the reheating process is therefore limited by the precision of the coil's temperature data. The coil's temperature data can be obtained by measuring or from a calculation using mathematical models. Nowadays, furnace control systems optionally provide a control method known as the 'air-to-work ratio control system'.[3] This method uses two pairs of thermocouples to measure the 'work–coil' and 'air' temperatures and calculates the furnace-temperature set-point as a scaled difference of both. The method is efficient, but requires a proper measuring coil temperature. For this method, a hole is drilled into the coil and a thermocouple is mounted into it. If the location of the hole is correct and representative for the whole-coil temperature, the method is accurate. But the drilled hole represents a potential defect in the final strip. In any case, measuring the temperature of every coil in industry is not practical. A much more practical and non-destructive technique is to employ a mathematical model (MM) for the calculation and prediction of coil temperatures. For accurate MM coil-temperature predictions, (1) the measured air temperature in the furnace (which all furnaces already measure and use), (2) the coil-alloy and (3) the coil-dimension data are required. The rest of the required information is integrated into the MM during the development and calibration procedure. Thus the MM can be used instead of the measuring coil's temperature, but it should be capable of running in real-time. Another advantage of the MM for the coil's temperature is that the model can be used for optimizations and various other services, which are impossible without a MM. The fastest reheating of Al coils in reheating furnaces is achieved by an overshoot of the furnace-air temperature above the coil temperature.[3] The time from beginning of the reheating process until the time of decreasing the furnace temperature from T_{ot} is denoted as the time to switch, i.e., t_s (**Figure 1**).

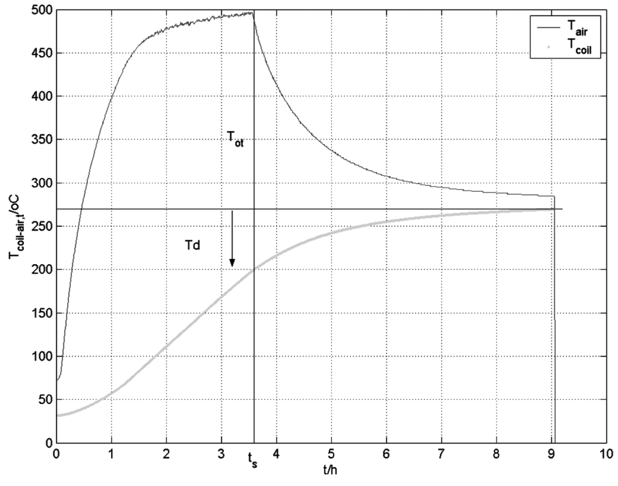

Figure 1: Furnace over-temperature; time to switch t_s
Slika 1: Višja temperatura zraka v peči; čas preklopa t_s

The aim of the work was to quantify the influence of the furnace over-temperature and the initial temperature of the coil on the time to switch (t_s) using a mathematical model.

2 MATHEMATICAL MODEL OF THE COIL TEMPERATURE

2.1 2D model of the Al-coil temperature using the finite-difference method

Heat transfer in solid state is mathematically expressed using the diffusion equation:

$$\frac{\partial T}{\partial t} = a\nabla^2 T;\ a = \frac{\lambda}{c_p \rho} \tag{1}$$

where T is the temperature, t is the time, λ is the thermal conductivity, c_p is the specific heat and ρ is the density. The temperature field is calculated in two dimensions, i.e., the radial r and the axial x directions.

Equation 1 for the selected r and x coordinate directions in a cylindrical coordinate system can be written as:

$$\rho c_p(T)\frac{\partial T}{\partial t} = \\ = \frac{\partial}{\partial x}\left(\lambda(T)\frac{\partial T}{\partial x}\right) + \frac{\partial}{\partial r}\left(\lambda(T)\frac{\partial T}{\partial r}\right) + \lambda(T)\frac{1}{r}\frac{\partial T}{\partial r} \tag{2}$$

where the heating conditions in the angle ϕ direction are assumed to be symmetric and thus the second derivative $\partial^2 T/\partial\phi^2 = 0$ is zero. In equation 2, λ is a function of temperature, while the temperature field as well as the convective boundary conditions are not constant. In fact, the boundary conditions for equation (2) are a function of the measured values of the furnace-atmosphere-gas temperature and the equation is thus analytically unsolvable. A handy way for numerically solving eq. 2, bearing in mind that the boundary conditions (furnace temperatures) for real-time operation will be available (measured) one per calculation period, is the explicit method of finite difference.

For the used finite-difference method the calculation space is discretized in both time and space:

$$\{\Delta t(\mathrm{sec}), \Delta x(\mathrm{m}), \Delta r(\mathrm{m})\} = \left\{1, \frac{21}{x}, \frac{21}{r_z - r_n}\right\},$$

so that the stability condition is satisfied[1] within the proposed coil dimensions and sample time. For each point on the grid, eq. 2 is rewritten as

$$\rho c_p \frac{\Delta x \Delta r}{\Delta t}\left(T^{t+\Delta t}_{i,j} - T^t_{i,j}\right) = \frac{\lambda_x \Delta r}{\Delta x}\left(T^t_{i-1,j} - T^t_{i,j}\right) + \\ + \frac{\lambda_x \Delta r}{\Delta x}\left(T^t_{i+1,j} - T^t_{i,j}\right) + \frac{\lambda_r \Delta x}{\Delta r}\left(T^t_{i,j-1} - T^t_{i,j}\right) + \\ + \frac{\lambda_r \Delta x}{\Delta r}\left(T^t_{i,j+1} - T^t_{i,j}\right) + \frac{\lambda_r \Delta x}{\Delta r}\frac{1}{r}\left(T^t_{i,j+1} - T^t_{i,j}\right) \tag{3}$$

According to the literature data,[4] the thermal conductivity of the Al-coils differs in the r and x directions due to the air-gap between the strip wraps and the thin oxide-layer of the strip surface. Thus, the thermal conductivities λ_r and λ_x are considered different, where λ_x equals the alloy data, while λ_r is lower then λ_x due to the air gap and the oil films between the coil wraps, which decreases the thermal conductivity in the radial direction. From eq. 3, the temperature at time $t + 1$ for each element on the grid (i, j) is expressed as:

$$T^{t+\Delta t}_{i,j} = \frac{\lambda_x \Delta t}{c_p \rho}\left(\frac{T^t_{i-1,j} + T^t_{i+1,j} - 2T^t_{i,j}}{\Delta x^2}\right) + \\ + \frac{\lambda_r \Delta t}{c_p \rho}\left(\frac{T^t_{i,j-1} + T^t_{i,j+1} - 2T^t_{i,j}}{\Delta r^2}\right) + \\ + \frac{\lambda_r \Delta t}{c_p \rho}\frac{1}{r}\left(\frac{T^t_{i,j+1} - T^t_{i,j}}{\Delta r}\right) + T^t_{i,j} \tag{4}$$

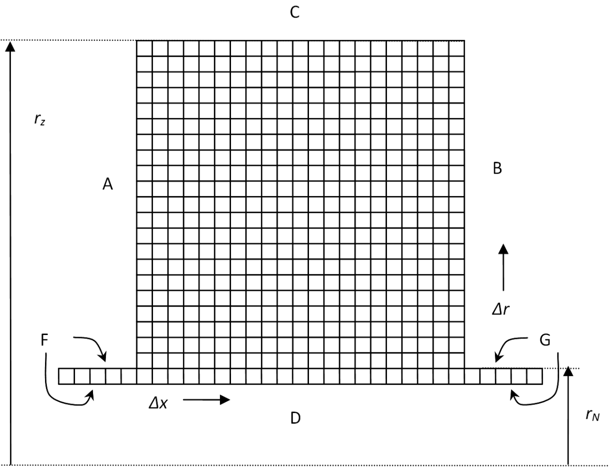

Figure 2: Coil dimensions, discretization grid, boundary lines and indexation of x–r cross-section
Slika 2: Dimenzije kolobarja, diskretizacijska mreža, robne ploskve in indeksiranje x–r prereza

Eq. 4 is recursive and is used for inner points of the calculation grid, while for the boundary points the equation is modified to consider the convective boundary conditions.[3]

2.2 Model calibration

The thermo-physical data of around 40 alloys were obtained using JMatPro software ver.4.0: ρ, c_p and λ in the desired temperature range. The MM was calibrated to the measured temperature values in 10 points, i.e., 5 points close to the outer radius r_z and the remaining 5 on the radius, which is in the middle of the coil's length. The air temperature in the furnace (boundary condition) was measured above the measured coil. The temperature of the heat treatment for Al-alloys rarely exceeds 550 °C, and thus convective heat transfer dominates the heat-transfer mode. The conductive heat-transfer mode is not present due to the stage design, while the radiative heat-transfer thermal mode is estimated to be sufficiently low compared to the conductive mode. The maximum ratio of the radiative-to-convective heat flux $\dot{q}_r/\dot{q}_c = A\varepsilon F\sigma(T_{\text{air}}^4 - T_{\text{coil}}^4)/Ah_c(T_{\text{air}} - T_{\text{coil}})$ is estimated to be ≈ 0.031. For a furnace air temperature that is 5 K above the coil temperature of 550 K (close to the end of the reheating) this ratio is estimated to be ≈ 0.025. For the estimation, the following assumptions are considered: $\varepsilon = 0.09$, $F = 1$, $h_c = 150$, $T_{\text{air}} = 823$ K, $T_{\text{coil}} = 293$ K. The radiation heat transfer is thus neglected. Note that a forced-air-circulation furnace is studied. The calibration is made by changing the convective heat-transfer coefficient h_c on the boundary surfaces of the calculated cross-section area – see the lines of A, B, C, D, F and G in **Figure 2**, until a calculated and measured temperature match is achieved. When the calculated and measured temperature profiles match at this point, it can be concluded that the model is capable of describing the heat transfer for the considered conditions ($T_{\text{air}} = f(t)$, $h_c = f(T)$). To check the possible variability of the process, additional coil-temperature measurements were performed at the same position in the furnace and with the same coil, but with a modified $T_{\text{air}} = f(t)$ profile. Unfortunately, the reheating conditions for the measured coil were slightly modified (closed steel-coil on both sides) due to studies for improving the homogeneity conditions. The boundary conditions on the inner coil surface –D were therefore modified: h_c drops from 22 to 5. The model's validation is therefore performed with a modified h_c on boundary D and this is compared to the temperature measurement obtained with the closed steel-coil. A comparison is shown in **Figure 3** and it can be seen that the maximum absolute difference in the coil temperature is around ± 10 °C. However, for a strictly correct model validation, the process condition should remain intact, so that h_c would remain intact during the validation as well.

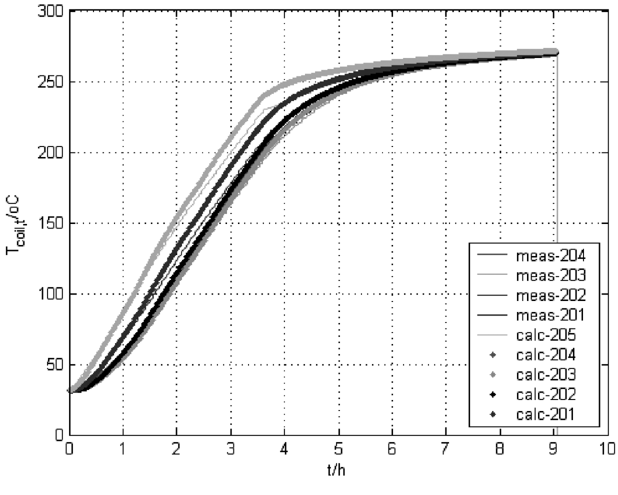

Figure 3: Comparison of measured and calculated coil temperatures. Note that the validation temperature measurements were obtained for slightly modified conditions on surface D.

Slika 3: Primerjava merjenih in izračunanih temperatur kolobarjev. Validacijske meritve temperature so bile merjene pri spremenjenih robnih pogojih na površini D.

3 USE OF THE MATHEMATICAL MODEL

3.1 Off-line calculations of the re-heating procedures

The MM was firstly applied for the prediction of the Al coil's temperature evolution for modified reheating conditions, e.g., modification of the desired end-temperature of the Al coil and the task was to modify the furnace time and temperature in such a way as to obtain a specific temperature homogeneity of the coil at the end of the treatment. To perform such a task, the boundary conditions – furnace air temperatures – need to be predicted (**Figure 4**).

This is achieved by employing another model, which predicted the furnace-air-temperature, closed-loop response, where the inputs are the furnace-temperature set-points. A first-order system[5] with a different time constant for increasing/decreasing the furnace temperatures is used to mathematically express the relation. The furnace temperature model is verified on 10 furnace-temperature profiles for various charging data (coil total mass from 22–78 t, 9 alloy grades, etc.). Due to the uncertainty of the model-obtained furnace air temperature (boundary conditions), the calculated coil tempera-

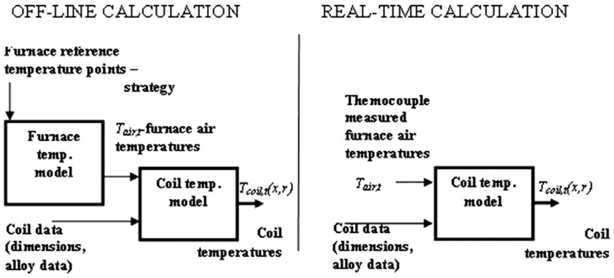

Figure 4: Furnace air temperature predictions for off-line calculations substitute measured temperatures, available in real-time calculations

Slika 4: Izračunane temperature zraka v peči v "off-line"-načinu nadomeščajo merjene temperature zraka, ki so v "real-time" načinu na voljo

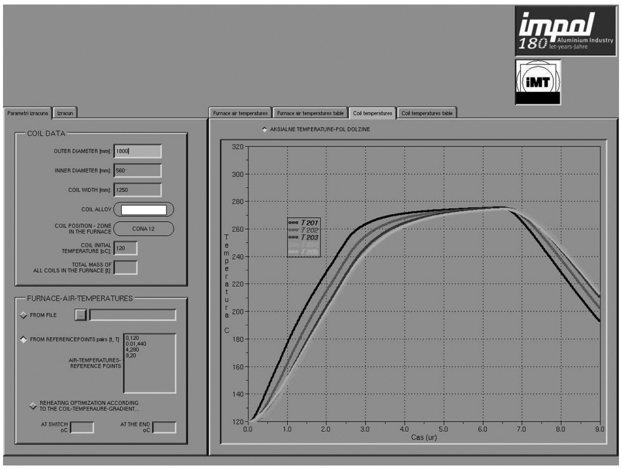

OUTER DIAMETER [mm]: 1800
INNER DIAMETER [mm]: 560
COIL WIDTH [mm]: 1250
COIL POSITION - ZONE IN THE FURNACE: CONA 12
COIL INITIAL TEMPERATURE [oC]: 120
TOTAL MASS OF ALL COILS IN THE FURNACE [t]:
FROM REFERENCEPOINTS pairs [t, T] / AIR-TEMPERATURES-REFERENCE POINTS:
0,120
0.01,440
4,280
9,20

Figure 5: GUI for offline calculations of reheating procedures
Slika 5: Grafični uporabniški vmesnik za izračune ogrevanja kolobarjev v peči

ture for these boundary conditions decreases the accuracy of the coil temperatures compared to the measured boundary conditions. Note that the prediction-accuracy of the furnace-air temperature is ± 10 °C. The crucial benefit of the model-obtained furnace-temperatures (boundary condition) combined with the coil-temperature model is the capability for off-line simulations involving various conditions and parameter sets (coil dimensions, alloy data, coil initial temperature, furnace temperature profile during reheating, etc.), but at the cost of a slightly decreased coil-temperature accuracy. For the off-line calculations a Graphical User Interface (GUI) is provided (**Figure 5**).

3.2 Quantification of the furnace-air temperature and the initial coil temperature for the coil-temperature evolution

A frequent task in the Al-coil reheating process is the modification of the reheating parameters (furnace time and temperature) according to a specific variation of the parameters, e.g., variation of the initial coil temperature of the Al coils or a higher furnace over-temperature T_{ot}. The coil with an increased initial temperature reaches the desired temperature faster. A straightforward solution to such a problem is to employ the developed mathematical model, including a furnace-temperature model (**Figure 4**) and change the reheating parameters until the conditions are met (trial-and-error method). Another way is to quantify in advance the response of a certain parameter change on the reheating parameters. For industrial production, the quantification of such reheating shortening is beneficial. For each furnace over-temperature T_{ot} = (400, 420, 440, 460, 480) °C in set and independently for each initial coil temperature $T_{coil,0}$ = (0, 20, 40, 60, 80, 100, 120, 140, 160) °C, a simulation is performed and the resulting time to switch t_s is determined from the model results (**Figure 6**).

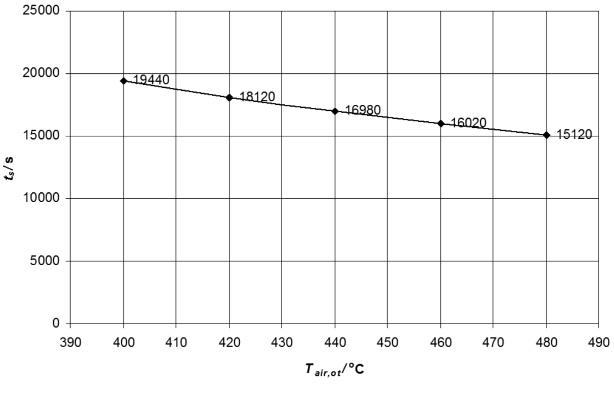

Figure 6: Influence of furnace over-temperature on the time to switch t_s
Slika 6: Vpliv višje temperature v peči na čas preklopa t_s

The t_s is actually determined by the model during the simulation, since the model also calculates the $T_{air,t}$ curve (**Figure 3**). The criterion to start decreasing the air temperature in the simulation model is when the Al-coil temperature in the node $T_{coil,t}$ (10, 10) is T_d = 30 °C under the desired final temperature of the coil, in this case (280–30) °C = 250 °C. Note that, different T_d values lead to different reheating profiles. Therefore, T_d is adjustable through the GUI. The node (10, 10) is in the middle of the coil (**Figure 2**). The other simulation parameters are constant: $T_{coil,0}$ = 20 °C, $T_{air,0}$ = 20 °C, coil dimensions r_z = 900 mm, r_N = 280 mm, x = 1250 mm, alloy EN 8079 AlFe1Si. The simulation is repeated for each T_{ot}. The obtained values are presented in **Figure 6**. The relation between T_{ot} and t_s is almost linear with a coefficient of –52.5 s/°C around the working point T_{ot} = 440 °C. The result shows that the increment of the furnace over-temperature for a single °C means t_s is shorter by 52.5 s. And conversely, the reduction of the furnace temperature by a single °C means a longer t_s for 52.5 s.

In the same way we estimated the influence of the initial coil temperature $T_{coil,0}$ on t_s. The relation between the initial coil temperature $T_{coil,0}$ and t_s is presented in **Figure 7**. The time to switch t_s is fairly linear, with a

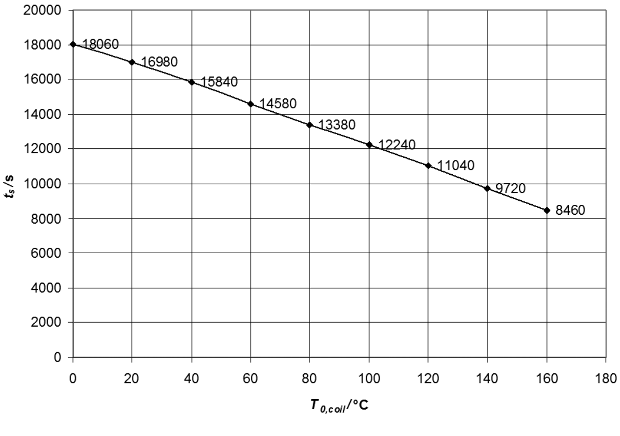

Figure 7: Influence of initial coil temperature $T_{coil,0}$ = (0 : 20 : 160) °C on the time to switch t_s
Slika 7: Vpliv začetne temperature kolobarja $T_{coil,0}$ = (0 : 20 : 160) °C na čas preklopa t_s

coefficient of –55.5 s/°C of the initial coil temperature. The simulation results show that an increment of +1 °C for the initial coil temperature means a shorter time 55.5 s to switch and, conversely, a reduction of –1 °C of the initial coil temperature means a longer time 55.5 s to switch.

3.3 Potential use of the model modified for a real-time calculation of the coil temperature

To run the developed model in real-time, accurate coil charging data, accurate air temperature in the furnace combined with the presented mathematical model are needed and thus provide the coil-temperature data without measuring the temperature in the coil. Note that the used explicit finite-difference method for the conduction calculation in the coil (eq. 4) is suitable for a real-time calculation, the only modification of the method is that the real-time simulation is interrupted after every iteration until the next measured furnace-air temperature is delivered to the model.

Unequal coil alloys, dimensions, initial temperature, malfunctions in the furnace and burners all lead to more or less unknown coil temperatures in the situation without either the coil temperature measurements or the real-time coil-temperature calculation. The MM obtained coil temperatures in such a situation are crucial for proper operator decisions and can be upgraded in the automatic coil-temperature control system. Furthermore, the stored real-time-calculated coil-temperatures can be used as documentation for coil-customer claims, research and development purposes. Real-time operation of the model is underway.

4 CONCLUSION

A mathematical model for an Al-coil temperature evolution during heat treatment proved to be an efficient and multi-purpose backbone tool for advanced planning, control and documentation of the Al-coil heat-treatment process. Employing the mathematical model, which provides coil-temperature knowledge, offers a simple, cost-effective and punctual tool for the determination of the proper furnace-temperature time settings during modified Al-coil reheating conditions.

5 REFERENCES

[1] A. Jaklič, T. Kolenko, B. Glogovac, B. Keček, J. Jamer, Simulacijski model ogrevanja gredic v peči allino, Mater. Tehnol., 38 (**2004**) 1–2, 33–38

[2] F. Vode, A. Jaklič, R. Robič, A. Košir, F. Perko, J. Novak, Determination of the deformational energy during slab-width rolling on an edger mill, Mater. Tehnol., 40 (**2006**) 2, 61–64

[3] www.secowarwick.com/assets/Documents/Brochures/AP-Aluminium-Annealing-Furnaces2.pdf

[4] A. von Starck, A. Mühlbauer, C. Kramer (eds.), Handbook of thermoprocessing technologies: Fundamentals, Processes, Components, Safety, Vulkan Verlag GmbH, Essen 2005, 557

[5] R. Burns, Advanced Control Engineering, 1st ed., Butterworth-Heinemann, 2001, 145

UDK 621.95:669.295
Original scientific article/Izvirni znanstveni članek

ISSN 1580-2949
MTAEC9, 48(5)653(2014)

INVESTIGATING THE EFFECTS OF CUTTING PARAMETERS ON THE HOLE QUALITY IN DRILLING THE Ti-6Al-4V ALLOY

PREISKAVA VPLIVA PARAMETROV REZANJA NA KVALITETO IZVRTINE, IZVRTANE V ZLITINO Ti-6Al-4V

Yahya Hışman Çelik

Mechanical Engineering Department, Faculty of Engineering-Architecture, Batman University, Batman, Turkey
yahyahisman.celik@batman.edu.tr, yahyahisman@gmail.com

Prejem rokopisa – received: 2013-09-20; sprejem za objavo – accepted for publication: 2013-11-19

In this study, the effects of cutting parameters on the surface roughness, burr height, hole-diameter deviation, cutting temperature and structure of a chip formation were investigated during the drilling of the Ti-6Al-4V alloy. For this purpose, the Ti-6Al-4V alloy was drilled at different cutting parameters, longitudinally in the 10 mm depth with Ø = 10 mm high-speed-steel (HSS) drills, having 90°, 118°, 130° and 140° point angles on the CNC vertical machining centre. Experiments were carried out at the (12.5, 18.75 and 25) m/min cutting speeds and the (0.05, 0.1 and 0.15) mm/r feed rates without using the cutting fluid. As a result, as the feed rate and the drill-point angle were increased, the surface roughness increased as well; however, as the cutting speed increased, the surface roughness decreased. When the feed rate and drill-point angle increased, the burr height decreased. On the other hand, an increase in the cutting speed increased the burr height. In general, an increase in the feed rate and drill-point angle increased the hole diameters, and the hole diameters obtained were close to the nominal size when the cutting speed was increased.

Keywords: Ti-6Al-4V, surface roughness, chip, drilling, burr height, hole diameter

V tej študiji so bili preiskovani vplivi parametrov rezanja na hrapavost površine, višino zarobka, odmike premera izvrtine, temperaturo rezanja in strukturo nastalega izvrtka pri vrtanju zlitine Ti-6Al-4V. V ta namen je bila zlitina Ti-6Al-4V vrtana na vertikalnem CNC obdelovalnem stroju pri različnih parametrih rezanja vzdolžno v globino 10 mm s svedri iz hitroreznega jekla (HSS) premera 10 mm, ki so imeli vršni kot 90°, 118°, 130° in 140°. Preizkusi so bili izvršeni pri hitrostih rezanja (12,5, 18,75 in 25) m/min in podajanju (0,05, 0,1 in 0,15) mm/r, brez uporabe hladilne tekočine. Rezultati so pokazali, da pri povečevanju podajanja in večanju vršnega kota svedra narašča tudi hrapavost površine, vendar pa se pri povečevanju hitrosti rezanja zmanjšuje hrapavost površine. Če se povečujeta podajanje in velikost vršnega kota, se zmanjšuje višina zarobka. Po drugi strani povečanje hitrosti rezanja poveča višino zarobka. Na splošno velja, da povečanje podajanja in povečanje vršnega kota svedra povečujeta premer izvrtine. Premeri izvrtin so bili blizu nazivni velikosti, če se je povečala hitrost rezanja.

Ključne besede: Ti-6Al-4V, hrapavost površine, izvrtek, vrtanje, višina zarobka, premer izvrtine

1 INTRODUCTION

Titanium and its alloys are widely used in many fields, especially in aircraft engines and automotive parts because they are light, exhibiting quite a good performance, high resistance to corrosion and high strength and being appropriate for high-temperature applications.[1,2] To give the final shape to these materials produced by casting, forging and powder metallurgy, various manufacturing methods are utilized.[3] The drilling process is one of the main manufacturing methods for obtaining the final shape of a material.[4] Nowadays, the drilling of Ti and its alloys within the desired tolerance is required. However, the drilling of these materials is very difficult because of their superior features.[5] During drilling, the chip welds to the cutting tools. In addition, the temperature of the tools and materials increase due to a low thermal conductivity of the HSS versus the Ti-Al-V alloys.[6] These factors negatively affect the tool wear, chip type, burr formation, surface roughness and geometric quality.[7] A correct selection of the cutting parameters and cutting conditions is important to minimize these problems and determine the ideal cutting conditions.[8,9] When literature studies are examined, it can be seen that there are not many studies related to this topic. Some studies performed on titanium alloys are given below.

Rahim and Sasahara[10] measured the tool wear, the temperature of the workpiece and the cutting forces occurring at various cutting parameters and different cooling types at high-speed drilling of Ti-6Al-4V. They found that the maximum temperature of the workpiece occurred when it was cooled with an air blower, being lower when using minimum quantity lubrication palm oil (MQLPO) and minimum quantity lubrication synthetic ester (MQLSE) and the lowest when using water. However, they reported that MQLSE led to a higher thrust force than MQLPO affecting the material during the cutting process. Park et al.[11] measured the thrust force and investigated the wear of tungsten carbide (WC) and polycrystalline diamond (PCD) during the drilling of titanium- and carbon-fibre-reinforced plastics. They determined that PCD drills showed a lower titanium adhesion when compared to WC drills. They also observed a higher spindle speed, causing a significant increase in the tool wear due to a higher temperature. Pujana et al.[12] applied ultrasonic vibrations on workpiece samples while drilling the Ti-6Al-4V alloy. They investigated the temperature, the chip formation and the feed force on the drill tip by means of an infrared radiation thermometer. They observed that a higher force was required for cutting because of a high-temperature occurrence when the vibration amplitude was increased. Shyha et al.[13] drilled titanium/carbon-fiber-reinforced plastic (CFRP)/aluminum stacks at different cutting parameters with a coated (a CVD diamond and a hard metal) tungsten-carbide drill. Due to out of roundness, they measured the hole size, cylindricity, burr height, hole-edge quality, average surface roughness (R_a), microhardness (of the metallic elements) and swarf morphology. The burr height was observed to be larger at the hole exit (Al 7050) compared to hole entry (Ti 6–4), while the delamination was significantly reduced by wen machining the CFRP in the stack configuration as opposed to the stand-alone configuration. However, the chip formation occurring while drilling Al 7050 was obtained using a similar cutting fluid and low cutting parameters of the titanium alloy. Isbilir and Ghassemieh[14] investigated the drilling of the Ti-6Al-4V alloy using the 3D Lagrange finite-element software. By analysing the materials, they reported that the thrust force, stresses and burr height of the drilled materials increased when the feed rate was increased. Guu et al.[15] analyzed the stresses in the micro-drilling of Ti and its alloy using finite-element methods. Kıvak and Şeker[16] investigated the effect of the cutting parameters on the cutting forces in drilling the Ti-6Al-4V alloy with coated and uncoated drills under dry and wet cutting conditions. At the end of the experimental study, they found that the coating materials provided about a 17 % decrease in the cutting forces. It was seen that the feed rate had a bigger effect than the cutting speed on the change in the cutting forces.

The main objective of metal cutting is to provide the surface quality and the burr height along with the geometric and dimensional completeness of the workpiece to be produced economically and within the desired limits. Nowadays, drilling the Ti-6Al-4V alloys that are used widely is very difficult because of their excellent properties such as high resistance to corrosion, high strength and high-temperature resistance. Therefore, in this study, the effects of the cutting parameters, together with different point angles of HSS drills, on the surface roughness, hole-diameter deviation, burr height, cutting temperature and structure of the chip formation were investigated during drilling a Ti-6Al-4V alloy at various combinations of the feed rates and cutting speeds.

Table 1: Chemical composition of the Ti-6Al-4V alloy (*w*/%)
Tabela 1: Kemijska sestava zlitine Ti-6Al-4V (*w*/%)

Ti	Al	V	Fe	C	N	H	O
89.52	6.1	4.1	0.056	0.019	0.025	0.08	0.1

Table 2: Cutting parameters and their values
Tabela 2: Parametri rezanja in njihove vrednosti

Parameters	Values
Cutting speed (m/min)	12.5, 18.75 and 25
Feed rate (mm/r)	0.05, 0.10 and 0.15

2 MATERIALS AND METHODS

2.1 Experimental study

For the experimental study, the Ti-6Al-4V alloy was provided by Sincemat Co. Ltd. The nominal chemical composition of the Ti-6Al-4V alloy with the size of 100 mm × 150 mm × 10 mm is given in **Table 1**.

In the experiments, a HUMMER VMC-1000 CNC vertical machining centre with the maximum speed of 8000 r/min and the spindle power of 15 kW was used.

The experiments were performed using 10 mm diameter HSS drills with the helix angle of 35°, with the point angles of 90°, 118°, 130° and 140°. For the experiments where no cutting fluids were used, the cutting parameters are given in **Table 2**.

2.2 Measurement of the surface roughness

A measurement of the surface roughness is quite important to see the effects of the cutting parameters on the material of a machined surface. With this regard, the surface-roughness measurements of the drilled alloy were performed for different cutting parameters using Taylor-Hobson's Surtonic 3 and a surface-roughness measuring device in accordance with ISO standards. The measurement sampling length was chosen as 5.6 mm. The measurement process was carried out parallel to the axis hole. Four surface roughness values (R_a) for the machined surfaces were obtained and then averaged.

2.3 Determining the burr height and the hole-diameter deviation

To determine the burr height and the hole-diameter deviation, a three-dimensional coordinate measuring device of the SIDIO XR brand, with a 1.4 megapixel IDIO Neo sensor, 340 mm scan area and Manfrotto Studio Tripod was used. Before scanning with this device, a non-destructive testing spray (BT 70) was sprayed on the surface of the Ti-6Al-4V alloy, where the drilling process would be applied, in order to make a better measurement and determine the reference points that were affixed to certain portions of the alloy to be drilled. For the determination of the burr height and the hole-diameter deviation, the Ti-6Al-4V alloy was scanned with a 3-D optical scanning system. For the determination of the effects of different cutting parameters and point angles of the drills on the burr height, the Ti-6Al-4V alloy scanned with the three-dimensional coordinate measuring device was transferred to the PolyWorks program. This program automatically gives minimum, mid and maximum values of the burr height at a hole exit. The burr height was determined by taking the arithmetic means of these values.

3 RESULTS AND DISCUSSION

3.1 Surface roughness

The surface roughness of the holes occurring as a result of drilling the Ti-6Al-4V alloy is given in **Figures 1** and **2**. As seen in these figures, the surface roughness increased when the feed rate was increased and it decreased when the cutting speed was increased. In addition, it was observed that the surface roughness increased with an increase in the point angle. While the lowest surface roughness was obtained with the 90° point-angle drills, 0.05 mm/r feed rate and 25 m/min cutting speed, the largest surface roughness was obtained with the 140° point-angle drills, 0.15 mm/r feed rate and 12.5 m/min cutting speed. Similar results were found by Kim et al.[17] and Sharif and Rahim.[18]

During the machining at a high cutting speed, the cutting temperature increases due a small contact length between the tool and the workpiece. This could be due to a decrease in the value of the coefficient of friction, resulting in a low friction at the tool-workpiece interface. These factors could contribute to an improvement in the surface-roughness values.[19] In addition, as the cutting speed increases, more heat is generated, thus softening the workpiece material, which, in turn, improves the surface roughness. However, a low cutting speed may lead to the formation of a built-up edge and, hence, deteriorates the machined surface. The investigation revealed that at a high feed rate the surface roughness is poor, probably due to distinct feed marks produced at the high feed rate.[10]

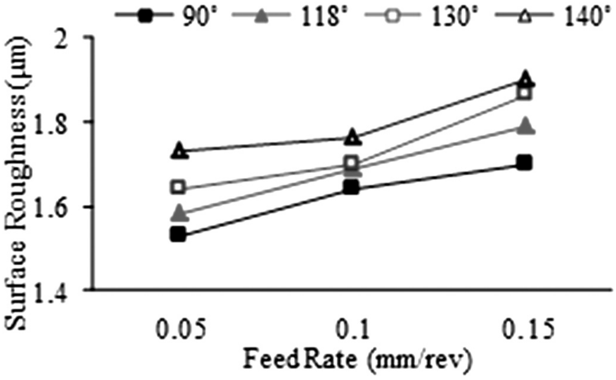

Figure 1: Effect of the feed rate on the surface roughness
Slika 1: Vpliv hitrosti podajanja na hrapavost površine

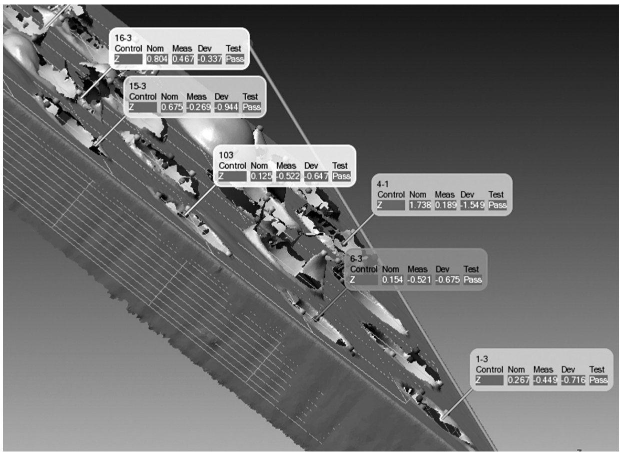

16-3

Control	Nom	Meas	Dev	Test
Z	0.804	0.467	-0.337	Pass

15-3

Control	Nom	Meas	Dev	Test
Z	0.675	-0.269	-0.944	Pass

103

Control	Nom	Meas	Dev	Test
Z	0.125	-0.522	-0.647	Pass

4-1

Control	Nom	Meas	Dev	Test
Z	1.738	0.189	-1.549	Pass

6-3

Control	Nom	Meas	Dev	Test
Z	0.154	-0.521	-0.675	Pass

1-3

Control	Nom	Meas	Dev	Test
Z	0.267	-0.449	-0.716	Pass

Figure 3: PolyWork burr measurement
Slika 3: Merjenje zarobka s PolyWork-om

3.2 Burr height

In **Figure 3**, the burr heights obtained with the PolyWork program for the alloy scanned with the three-dimensional coordinate measuring device are shown. In addition, the burr heights obtained depending on feed rates, cutting speeds and point angles are given in **Figures 4** and **5**.

The burr height occurring at the hole exit at the low feed rate was found to be larger than the burr height occurring at the hole exit at the high feed rate. However, when the cutting speed was increased, the burr height at the hole exit also increased. For this reason, the biggest burr height was obtained at the high cutting speed and low feed rate. The burr that occurred in the drilling process carried out with large point-angle drills was found to be smaller. Similar results were found by Kim et al.[20] and Dornfeld et al.[21]

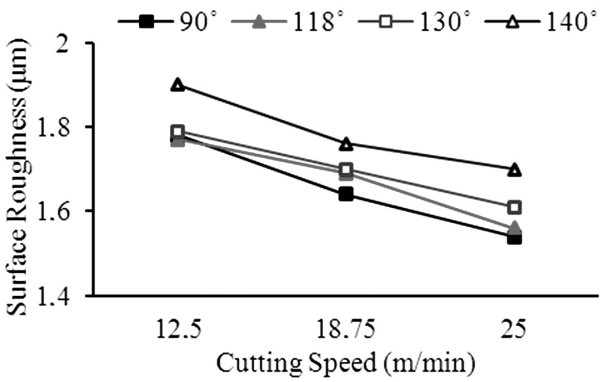

Figure 2: Effect of the cutting speed on the surface roughness
Slika 2: Vpliv hitrosti rezanja na hrapavost površine

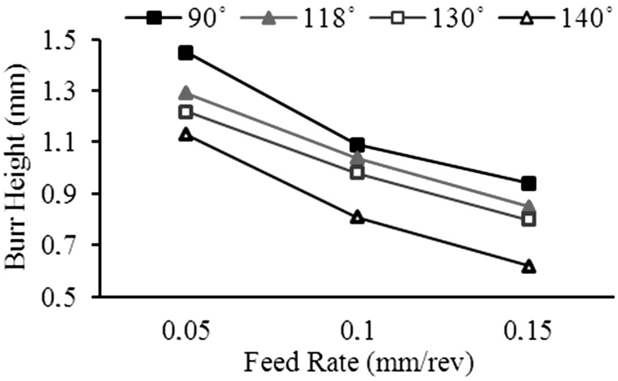

Figure 4: Effect of the feed rate on the burr height
Slika 4: Vpliv hitrosti podajanja na višino zarobka

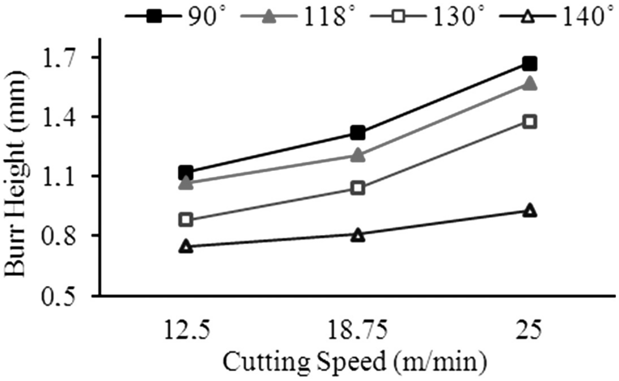

Figure 5: Effect of the cutting speed on the burr height
Slika 5: Vpliv hitrosti rezanja na višino zarobka

The cutting tool, processed materials, cutting parameters and the cooling fluid affect the burr formation.[22,23] Especially the drilling of metal materials causes the formation of burrs, resulting from the plastic deformation of workpiece materials both at the entrance and the exit of a hole.[7] ISO 13715 standards define the burr dimensions that deviate from the ideal geometry. However, the measurement of chip characteristics is rather difficult and takes time.[24] Therefore, the easiest way of charactersing chips is to measure their height and thickness.[25] The burr height and thickness are very important for deburring an unwanted formation off the workpiece. These unwanted burrs are harder than the workpiece. Therefore, deburring is quite costly forcing us to use extra tools. This causes the costs to rise by up to 30 %, especially for aircraft engines. For automobiles, on the other hand, the cost rise varies between 15 % and 20 %.[26]

3.3 Hole-diameter deviation

A hole-diameter deviation is usually a result of the effects such as deflection, vibration, wear and lack of lubrication. On the other hand, a deviation from the circularity represents the fluctuations on the surface, and it is defined as the difference between the largest and the smallest radius measured from the center point. However, there are various ways of determining the center of a hole. In this study, the hole diameter and the circularity were determined with the coordinates taken at different points. These measurements used in the evaluation of the hole diameter and circularity were transferred directly to the PolyWorks program (**Figure 6**). Thus, the hole-dia-

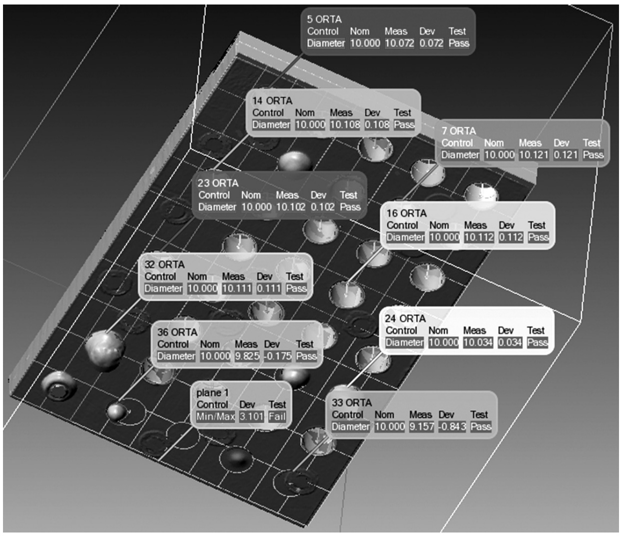
```
5 ORTA
Control   Nom     Meas    Dev    Test
Diameter  10.000  10.072  0.072  Pass

14 ORTA
Control   Nom     Meas    Dev    Test
Diameter  10.000  10.108  0.108  Pass

7 ORTA
Control   Nom     Meas    Dev    Test
Diameter  10.000  10.121  0.121  Pass

23 ORTA
Control   Nom     Meas    Dev    Test
Diameter  10.000  10.102  0.102  Pass

16 ORTA
Control   Nom     Meas    Dev    Test
Diameter  10.000  10.112  0.112  Pass

32 ORTA
Control   Nom     Meas    Dev    Test
Diameter  10.000  10.111  0.111  Pass

24 ORTA
Control   Nom     Meas    Dev    Test
Diameter  10.000  10.034  0.034  Pass

36 ORTA
Control   Nom     Meas    Dev     Test
Diameter  10.000  9.825   -0.175  Pass

plane 1
Control   Dev    Test
Min/Max   3.101  Fail

33 ORTA
Control   Nom     Meas    Dev     Test
Diameter  10.000  9.157   -0.843  Pass
```

Figure 6: PolyWork hole-diameter deviation
Slika 6: Merjenje odmika premera izvrtine s PolyWork-om

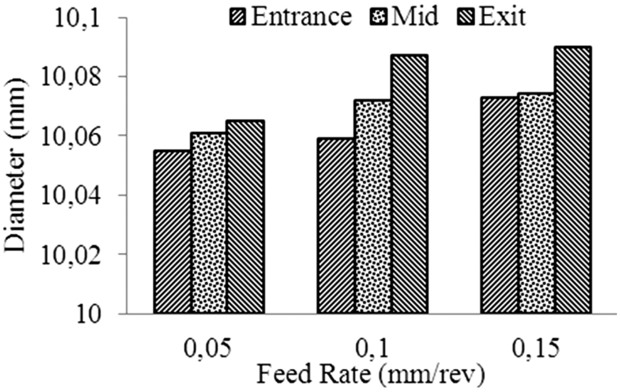

Figure 7: Effect of the feed rate on the hole diameter
Slika 7: Vpliv hitrosti podajanja na premer izvrtine

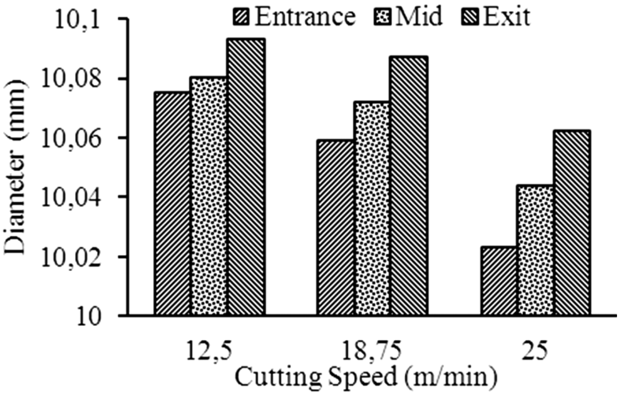

Figure 8: Effect of the cutting speed on the hole diameter
Slika 8: Vpliv hitrosti rezanja na premer izvrtine

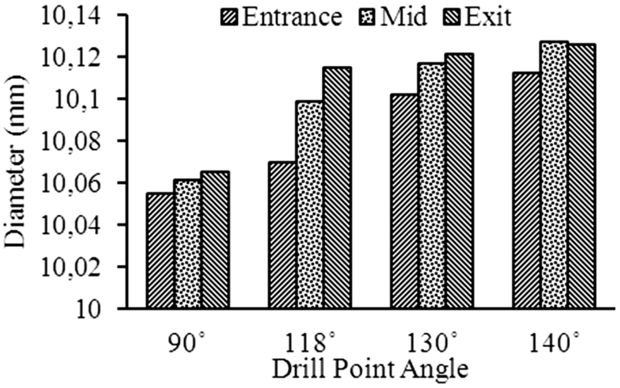

Figure 9: Effect of the drill-point angle on the hole diameter
Slika 9: Vpliv vršnega kota svedra na premer izvrtine

meter deviation was detected at the entrance, the middle and the exit of a hole.

The evaluation of the hole diameter was performed by comparing the values obtained with the cutting tool depending on different cutting parameters. The diameters affected by the feed rate, the cutting speed and the point angle are given in **Figures 7** to **9**. With an increase in the feed rate and drill-point angle, the diameter also increased significantly at the entrance, middle and exit of a hole. On the other hand, the diameter deviation decreased with an increase in the cutting speed. In addition, it was found that the deviation at the entrance of a hole was smaller than that at the exit.

3.4 Cutting temperature

During the drilling process, 90 % of work is converted to heat as a result of the plastic deformation.[27] Therefore, a very high temperature occurs in the drilling zone. This temperature affects a specific region of the chip, tools and workpiece.[28] In connection with the thermal properties of the workpiece and cutting, either the cutting tool or the workpiece is affected by this. Since Ti and its alloys, which are about 1/6 of steels,[29] have low thermal properties, a great deal of heat, as much as 80 %, is absorbed by the tool.[30] 50 % to 60 % of the heat generated during the drilling of steel is absorbed by the tool.[31] When machining Ti and its alloys, the tool reaching a high temperature wears quickly because of the high cutting temperature and a strong adhesion between the tool and the workpiece; and the high stresses developed at the cutting edge of the tool may cause a plastic deformation and accelerate the tool wear.[32]

The images of the Ti-6Al-4V alloy taken by a thermal camera at various cutting parameters are given in **Figure 10**. As seen in this figure, a low cutting speed leads to a low temperature because of the interaction between the material and the tool.

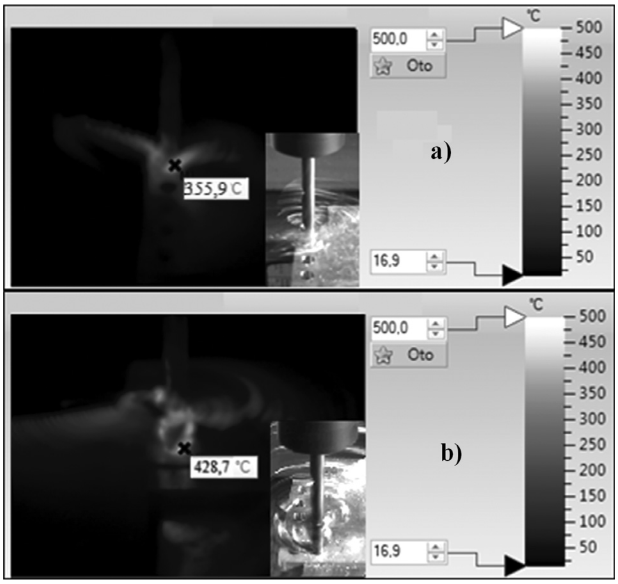

Figure 10: Temperature measurements with thermal cameras: a) low cutting speed, b) high cutting speed
Slika 10: Merjenje temperature s toplotno kamero: a) majhna hitrost rezanja, b) velika hitrost rezanja

3.5 Chip types

A chip formation of titanium alloys during the drilling process is quite difficult when compared with the other metals. There are three types of chip. These are the continuous chip, the continuous chip with a build-up edge, and the discontinuous chip.[33] When the feed rate was low, the Ti chip was long and continuous, and when the feed rate was increased, it became shorter and stiffer.[17] However, as the cutting speed was raised, the chip-serration frequency was enhanced.[34]

A few chip samples were taken from each drilling process to detect the effects of the cutting parameters and drill-point angle on them. From these chips, it was observed that the chips were formed under difficult conditions and that high cutting force and temperature took place; depending on these factors, the shapes of the

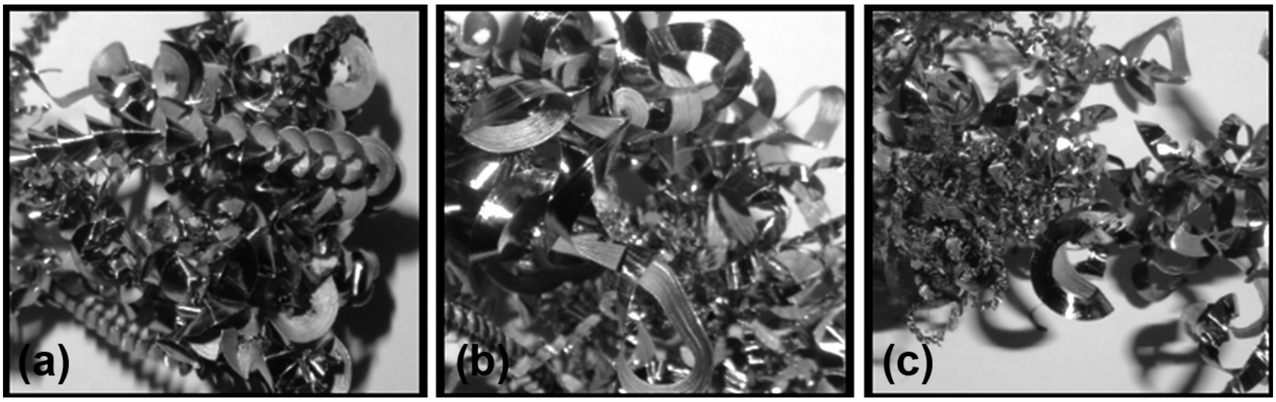

Figure 11: Some chip shapes: a) continuous chip, b) continuous chip with a build-up edge, c) discontinuous chip
Slika 11: Nekaj oblik izvrtkov: a) kontinuirni izvrtek, b) kontinuirni izvrtek s poudarjenim robom, c) razlomljeni izvrtek

chips were irregular. At a low cutting speed, feed rate and drill-point angle, the chip was observed to be ductile and continuous (**Figure 11a**). The chip was hardened and it became fragile with an increase in the cutting speed, feed rate and drill-point angle (**Figure 11b**). However, with an increase in the cutting speed, ridges appeared on the chip surface (**Figure 11c**).

The effect of the temperature on the chip hardening is very important due to the friction. Due to the temperature effect, the chip had a dark colour.

Acknowledgement

The author would like to thank İhsan Pilatin, an experienced lecturer at Batman University for his contributions and corrections to the paper.

4 CONCLUSION

In this study, the parameters such as surface roughness, burr height, hole-diameter deviation, cutting temperature and structure of a chip formation were investigated during the drilling of the Ti-6Al-4V alloy under different feed rates, cutting speeds and drill-point angles using HSS drills with 90°, 118°, 130 ° and 140° point angles and the following conclusions were reached:

- When the feed rate and drill-point angle were increased, the surface roughness increased as well; when the cutting speed increased, the surface roughness decreased.
- When the feed rate and drill-point angle were increased, the burr height decreased, but an increase in the cutting speed increased the burr height.
- Generally, when the feed rate and drill-point angle were increased, the hole diameter increased; when the cutting speed was increased, the diameter was close to the nominal value.
- For all the drill-point angles, the cutting speed and feed rate combinations, the diameters obtained were larger than the nominal values.
- For the low cutting speed and feed rate, the chip form was found to be more regular and ductile.
- With an increase in the cutting speed and feed rate, the chip formation displayed a shift from a ductile structure towards a more rigid and fragile form.
- An increase in the cutting speed caused the material to overheat due to the friction and the thermal properties of Ti-6Al-4V.

5 REFERENCES

[1] A. Hasçalık, U. Çaydaş, Electrical discharge machining of titanium alloy (Ti-6Al-4V), App. Surf. Sci., 253 (**2007**), 9007–9016

[2] Z. G. Wang, Y. S. Wong, M. Rahman, High-speed milling of titanium alloys using binderless CBN tools, Int. J. Mach. Tools & Manuf., 45 (**2005**), 105–114

[3] E. A. Loria, Recent development in the progress of super alloy 718, JOM, 44 (**1992**) 6, 33–36

[4] W. C. Chen, C. C. Tsao, Cutting performance of different coated twist drills, J. Mater. Proc. Tech., 88 (**1999**), 203–207

[5] M. Rahman, W. K. H. Seah, T. T. Teo, The machinability of Inconel 718, J. Mater. Proc. Tech., 63 (**1997**), 199–204

[6] A. R. Machado, J. Wallbank, Machining of titanium and its alloys – a review, Proceedings of the Institution of Mechanical Engineers, Part B: Journal of Engineering Manufacture, 204 (**1990**), 53–60

[7] P. P. Zhang, N. J. Churi, Z. J. Pei, C. Treadwell, Mechanical drilling processes for titanium alloys: A literature review, Mach. Sci. Tech., 12 (**2008**), 417–444

[8] S. S. Gill, J. Singh, Effect of deep cryogenic treatment on machinability of titanium alloy (Ti–6246) in electric discharge drilling, Mater. Manuf. Proc., 25 (**2010**), 378–385

[9] M. T. Hayajneh, Hole quality in deep hole drilling, Mater. Manuf. Proc., 16 (**2001**) 2, 147–164

[10] E. A. Rahim, H. Sasahara, A study of the effect of palm oil as MQL lubricant on high speed drilling of titanium alloys, Trib. Int., 44 (**2011**), 309–317

[11] K. H. Park, A. Beal, D. Kim, P. Kwon, J. Lantrip, Tool wear in drilling of composite/titanium stack using carbide and polycrystalline diamond tools, Wear, 271 (**2011**), 2826–2835

[12] J. Pujana, A. Rivero, A. Celaya, L. N. López de Lacalle, Analysis of ultrasonic-assisted drilling of Ti-6Al-4V, Int. J. Mach. Tools & Manuf., 49 (**2009**), 500–508

[13] I. S. Shyha, S. L. Soo, D. K. Aspinwall, S. Bradley, R. Perry, P. Harden, S. Dawson, Hole quality assessment following drilling of metallic-composite stacks, Int. J. Mach. Tools & Manuf., 51 (**2011**), 569–578

[14] Ö. Isbilir, E. Ghassemieh, Finite element analysis of drilling of titanium alloy, ICM11, Procedia Eng., 10 (**2011**), 1877–1882

[15] Y. H. Guu, S. Deng, M. T. K. Hou, C. H. Hsu, K. S. Tseng, Optimization of machining parameters for stress concentration in microdrilling of titanium alloy, Mater. Manuf. Proc., 27 (**2012**), 207–213

[16] T. Kıvak, U. Şeker, The effect of coating materials and cutting conditions on the cutting forces in the drilling of Ti-6Al-4V alloy, International Iron & Steel Symposium, Karabük-Turkey, 2012, 855–860

[17] D. Kim, M. Ramulu, W. Pedersen, Machinability of titanium/graphite hybrid composites in drilling, Transactions of NARMI/SME, 33 (**2005**), 445–452

[18] S. Sharif, E. A. Rahim, Performance of coated and uncoated carbide tools when drilling titanium alloy Ti-6Al-4V, J. Mater. Proc. Tech., 185 (**2007**) 1–3, 72–76

[19] E. A. Rahim, H. Sasahara, The effect of MQL fluids on the drilling performance of Nickel-Based super alloy, 4th International conference on high performance cutting, Gifu, Japan, 2010

[20] D. Kim, M. Ramulu, J. Garbini, Hole quality in drilling of graphite/biamalemide-titanium stacks, Proceedings of the 33rd International SAMPE Technical Conference, 2001, 1315–1326

[21] D. A. Dornfeld, J. S. Kim, H. Dechow, L. J. Chen, Drilling burr formation in titanium alloy, Ti-6Al-4V, CIRP Annals, 48 (**1999**) 1, 73–76

[22] U. Çaydaş, A. Hasçalık, Ö. Buytoz, A. Meyveci, Performance evaluation of drilling twist drills in dry drilling of AISI 304 austenitic stainless steel, Mater. Manuf. Proc., 26 (**2011**), 951–960

[23] E. Kılıçkap, H. Mesut, Selection of optimum parameters on burr height using response surface methodology and genetic algorithm in drilling of AISI 304 stainless steel, Mater. Manuf. Proc., 25 (**2010**), 1068–1076

[24] ISO 13715: 2000 Geometrical product specifications (GPS) – Technical drawings – Edges of undefined shape, vocabulary and indications, International Organization for Standarization, Geneve, Switzerland, 2000

[25] J. Leopold, G. Schmidt, Methods of burr measurement and burr detection, VDI-Berichte, 1860 (**2004**), 223–229

[26] D. A. Dornfeld, Strategies for preventing and minimizing burr formation, Laboratory for Manufacturing Automation, Consortium on Deburring and Edge Finishing, University of California at Berkeley, 2004

[27] E. Q. Ezugwu, Titanium alloys and their machinability – a review, Journal of Materials Proc. Tech., 068 (**1997**) 3, 262–274

[28] R. Li, Experimental and numerical analysis of high-throughput drilling of titanium alloys, Ph. D. Dissertation, University of Michigan, Ann Arbor, MI, 2007

[29] Anonymous, Tips for aerospace machining manufacturing, Manuf. Eng., 110 (**1993**) 3, 67–69

[30] W. Koning, Applied research on the machinability of titanium and its alloy, Proceeding of the Forty-Seventh Meeting of AGARD, CP256, AGARD Structural and Materials Panel, 1975, 1–10

[31] H. C. Child, A. L. Dalton, Machining of titanium alloys-metallurgical factors affecting machinability, Proceeding of Conference on Machinability, 1965, 139–142

[32] D. A. Dearnley, A. N. Grearson, Evaluation of principal wear mechanisms of cemented carbides and ceramics used for machining titanium alloy IMI 318, Mater. Sci. and Tech., 2 (**1986**) 1, 47–58

[33] D. Kim, M. Ramulu, Cutting and drilling characteristics of hybrid titanium composite laminate (HTCL), Proceedings of Materials and Processing Technologies for Revolutionary Applications Fall Technical Conference, Washington, 2005, 1–8

[34] C. J. Brown, B. K. Hinds, Force and temperature effect when machining titanium, Manufacturing Engineering Transactions, (**1985**), 238–244

UDK 66.017:620.178.1:539.92
Original scientific article/Izvirni znanstveni članek

ISSN 1580-2949
MTAEC9, 48(5)661(2014)

INFLUENCE OF GRAPHITE ON THE HARDNESS AND WEAR BEHAVIOR OF AA6061–B$_4$C COMPOSITE

VPLIV GRAFITA NA TRDOTO IN VEDENJE KOMPOZITA AA6061–B$_4$C PRI OBRABI

Subramaniam Prabagaran[1], Govindarajulu Chandramohan[2], Palanisamy Shanmughasundaram[3]
[1]Karpagam University, Department of Mechanical Engineering, Coimbatore-641021, India
[2]P.S.G. Institute of Technology and Applied Research, Coimbatore-641042, India
[3]Karpagam University, Department of Automobile Engineering, Coimbatore-641032, India
prabagaran.s@karpagam.com

Prejem rokopisa – received: 2013-09-21; sprejem za objavo – accepted for publication: 2013-12-10

Dry-sliding-wear behavior of AA6061, AA6061-B$_4$C composite and AA6061-B$_4$C-Gr hybrid composite was investigated by employing a pin-on-disc wear-test rig. Hardness tests were also carried out. Graphite was used as a solid lubricant since it is a soft, slippery and greyish-black substance. Because of the cleavage (crystal) loose interlamellar coupling, graphite has good lubricating properties. A comparative analysis was made on the hardness and wear behavior of AA6061, AA6061-B$_4$C composite and AA6061-B$_4$C-Gr hybrid composite. Boron carbide is known as a robust material having a high hardness. Worn-out surfaces of the wear specimens after the wear tests were examined with a scanning electron microscope to study the morphology of the worn surfaces. Energy dispersive spectroscopy (EDS) was employed to identify the oxides formed on the worn surfaces of the AA6061-B$_4$C and AA6061-B$_4$C-Gr composites after the wear test. It was found that a mutual transfer of the material between the wearing Al-alloy and the steel counterface occurred as the load increased. Oxidative wear occurred at low applied loads and a high velocity, whereas delamination and adhesive wear occurred at a high load and high sliding velocity.

Keywords: boron carbide, dry sliding, graphite particles, pin-on-disc, wear resistance

Preiskovano je bilo vedenje AA6061, AA6061-B$_4$C-kompozita in hibridnega kompozita AA6061-B$_4$C-Gr pri suhem drsenju z uporabo naprave “pin on disc”. Kot trdno mazivo je bil uporabljen grafit, ki je mehka, spolzka in sivo-črna snov. Zaradi cepljive šibke medlamelarne povezave (v kristalu) ima grafit dobre mazalne lastnosti. Izvršene so bile analize primerjave trdote in vedenja pri obrabi AA6061, AA6061-B$_4$C-kompozita in hibridnega kompozita AA6061-B$_4$C-Gr. Borov karbid je poznan kot zdržljiv material z veliko trdoto. Po preizkusu obrabe je bila z elektronskim vrstičnim mikroskopom izvršena preiskava morfologije obrabljene površine vzorcev, da bi ugotovili nastale okside na obrabljeni površini kompozitov AA6061-B$_4$C in AA6061-B$_4$C-Gr. Ugotovljeno je bilo, da se pri naraščanju obremenitve pojavi vzajemen prenos materiala med Al-zlitino, ki se obrablja, in jeklom. Oksidativna obraba se je pojavila pri majhnih obremenitvah in velikih hitrostih, medtem ko se je obraba zaradi delaminacije in adhezije pojavila pri velikih obremenitvah in veliki hitrosti drsenja.

Ključne besede: borov karbid, suho drsenje, grafitni delci, "pin-on-disc", odpornost proti obrabi

1 INTRODUCTION

Metal-matrix composites have received a lot of commercial attention due to their enhanced mechanical properties, wear resistance and low coefficient of thermal expansion.[1] Metal-matrix composites have many application areas such as automotive and ballistic industries, infrastructure, space and air vehicles, under-water vehicles and deep-ocean equipment. In addition, metal-matrix composites have other advantageous characteristics such as good strength-to-weight ratio, high specific stiffness, high hardness, high plastic-flow strength, good thermal expansion, thermal stability, creep resistance, and good oxidation and corrosion resistance.[2]

Boron carbide exhibits excellent physical and mechanical properties. Boron carbide is a low-density ceramic with a high hardness and Young’s modulus which make it a valuable candidate for engineering applications. Rama Rao and Padmanabhan[3] reported that an addition of boron carbide decreases the density of composites and increases the hardness. Gómez et al.[4] reported that the hardness and strength of composites increased together with the volume fraction of reinforcement, reaching its maximum value of 10 % B$_4$C. Wear is a removal of a material from one or both of the two solid surfaces in a solid-state contact. An addition of hard ceramic particles improves the wear resistance of a matrix material. The wear rate is associated with the sliding velocity, normal load, particle size, hardness, particle volume fraction and particle homogeneity.[5] Jinfeng et al.[6] observed that with an addition of graphite, the friction coefficient of Al-SiC composites decreases and the wear resistance is significantly increased. Ames and Alpas[7] reported that Al-Gr composites had a higher wear resistance than Al-SiC composites.

A solid lubricant provides protection from damage during relative movement between the sliding elements and reduces the wear. Miyazaki et al.[8] analyzed the mechanical behavior of graphite-and-boron-carbide composites made with the hot-pressing method. They reported that the strength of a composite increased with an increase in the boron-carbide content. Many research works were carried out to investigate the sliding-wear behavior of aluminum MMCs reinforced with different types of reinforcements such as SiC, Al_2O_3 and B_4C. But limited studies have been carried out on hybrid metal-matrix composites.

Shorowordi et al.[9] studied three aluminium metal-matrix composites containing the reinforcing particles of B_4C, SiC and Al_2O_3 (volume fractions, φ = 0–20 %) that were manufactured with the stir-casting method followed by hot extrusion. They reported that the B_4C-reinforced Al-composite seemed to exhibit a better interfacial bonding compared to the other two composites.

Stir casting appears to be the best method for the production of metal-matrix composites compared to the other processing techniques because of its simplicity, allowing an economical large-scale production. The aim of this study is to analyze the influence of graphite particles on the hardness and wear behavior of AA6061-B_4C composites fabricated using a two-stage stir-casting method. The wear tests were carried out by employing a pin-on-disc wear-testing rig. Scanning Electron Microscopy (SEM) was employed to study the microstructures of the composites and the morphologies of the worn surfaces of the composites. Energy Dispersive Spectroscopy (EDS) was used to characterize the Mechanically Mixed Layer (MML) formed on a worn surface during the sliding wear and to elucidate its influences on the wear behavior of the composites.

2 EXPERIMENTATION

2.1 Experimental description

In this study, a two-stage stir-casting method was employed to fabricate AA6061-B_4C and AA6061-B_4C-Gr composites. Brinell hardness testing equipment was employed to measure the hardness of the AA6061 alloy and the composites. The dry-sliding wear behavior of AA6061 and the composites was tested with a pin-on-disc wear-testing rig. Scanning Electron Microscopy (SEM) was employed to study the microstructures and morphologies of the worn surfaces of AA6061, AA6061-B_4C and AA6061-B_4C-Gr composites.

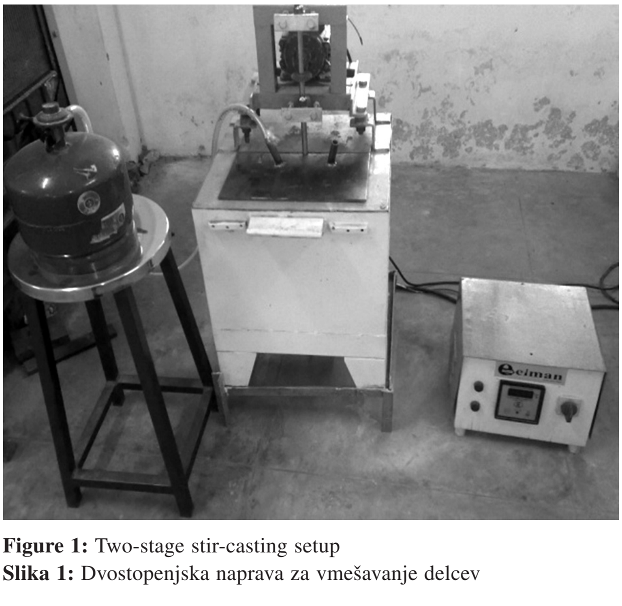

Figure 1: Two-stage stir-casting setup
Slika 1: Dvostopenjska naprava za vmešavanje delcev

2.2 Specimen preparation

In this study, we used AA6061 as the matrix material, B_4C particles with the average size of 20–50 μm as the reinforcement and graphite particles of 20 μm as the solid lubricant. The composition of AA6061 is presented in **Table 1**. The stir-casting setup is shown in **Figure 1**.

Table 1: Composition of AA6061 (mass fractions, *w*/%)
Tabela 1: Sestava AA6061 (masni deleži, *w*/%)

Element	Si	Fe	Cu	Mn	Mg	Cr	Ti	Ca	Al
%	0.359	0.221	0.219	0.032	0.901	0.053	0.141	0.013	Bal

A two-stage stir-casting route was adopted to fabricate the composites. Both B_4C and graphite particulates were preheated at 300 °C in a separate muffle furnace. AA6061 was charged into the crucible and heated up to 650 °C in order to completely melt the aluminium and then the stirring was done at 300 r/min. During the stirring, degassing tablets were added to drive away the entrapped gases from the melt. The stirring was carried out for 3 min. During the stirring, preheated w = 10 % B_4C and 3 % graphite particulates were added. The melt temperature was brought down to 575 °C to reach a semi-solid state. At this stage the stirring was done for 3 min. The composite slurry was again reheated to the temperature of 650 °C and stirred at 300 r/min for 3 min. Finally, the composite slurry was poured into a steel die cavity of 90 mm × 90 mm × 7 mm to solidify. The melting was done in an electric resistance furnace (2 kW – 1 kg capacity). The temperatures were measured with a thermocouple with an accuracy of ± 3 K.

2.2.1 Hardness-test specimens

The poured samples of 1) the AA6061 alloy, 2) composite AA6061-B_4C and 3) AA6061-B_4C-Gr were machined on their four sides to obtain 50 mm squares. All the edges and corners were made blunt/rounded to ensure safety while handling.

2.2.2 SEM analysis (microstructure)

With electric discharge machining, three different samples were machined to rectangular pieces of 10 mm × 20 mm with a thickness of 6 mm. Then these samples were mounted using a heat-conducting, quick-setting epoxy resin. After the mounting each sample was manually polished with a 1200-grade silicon-carbide emery sheet with the help of a diamond paste of 7 μm until achieving a mirror-like finish. The polished surfaces were then etched with a 2 % nitric acid and 98 % alcohol etching solution for 10 s.

2.2.3 Wear-analysis specimens

Pin specimens with a width of 6 mm and a height of 30 mm were prepared with EDM (Electric Discharge Machining). The two ends were cut with high flatness accuracy so that the pin face was thoroughly in line with the disc, held perpendicular to the disc surface during the wear test. Moreover, the wear testing equipment had a split-type holder to ensure a proper alignment throughout the test run. Prior to the wear testing, the specimens were polished with an abrasive paper of silicon carbide of grade 600 followed by grade 1000, then cleaned with ethanol and dried.

2.2.4 EDS analysis specimens

The samples prepared for the SEM analysis were also used for the EDS analysis without any modifications.

2.3 Hardness test

The hardness test was performed on AA6061 and the composite specimens of AA6061-B_4C and AA6061-B_4C-Gr using the Brinell hardness testing equipment with a 2.5 mm steel-ball diameter at a load of 1839.4 N. The loading time was 30 s. Three readings were taken for each specimen to eliminate the possibility of segregation and the mean value was considered.

2.4 Microstructure analysis

A scanning electron microscope was employed to study the distribution of boron-carbide and graphite particles in the Al-matrix. The bonding quality between the particulates and the matrix was also studied.

2.5 Dry-sliding wear test

The wear tests were carried out under varying loads of (5, 10, 15 and 20) N at the sliding velocities of 1 m/s and 3 m/s by employing a pin-on-disc wear-testing rig (DUCOM, TR-20LE) with a data-acquisition system shown in **Figure 2**. Each test was conducted for at least 30 min.

The main parts of the apparatus are a variable-speed electric motor with a steel disc attached to it and a lever arm to which the weight is added. The wear loss of the sample pins was measured in terms of the height loss in microns with the accuracy of 1.0 µm. A track diameter of 100 mm was selected for the analysis. The rotating disc was made of the EN 31 steel having the hardness of 62 HRC. The wear tests were carried out at a room temperature of 30 °C and a relative humidity of 60 % for 30 min, the contact pressure on the disc being 0.14 N/mm^2 (at 5 N load), 0.28 N/mm^2 (at 10 N load), 0.42 N/mm^2 (at 15 N load) and 0.56 N/mm^2 (at 20 N load). Two samples were tested for each condition. A SEM examination was carried out on the worn surfaces of the specimens in order to understand the wear mechanism under various test conditions.

2.6 Energy Dispersive Spectroscopy (EDS) analysis

An EDS analysis was done on the worn surfaces of the AA6061 alloy and AA6061-B_4C-Gr composite (Jeol) primarily to verify the presence of oxides on the worn surfaces. The data output plots the original spectrum showing the number of X-rays collected at each energy level and mapping the element distributions over the areas of interest.

3 RESULTS AND DISCUSSION

3.1 Microstructural analysis

The microstructure of the AA6061-B_4C-Gr hybrid composite (**Figure 3**) was fabricated with the stir-casting method. It can be seen that the boron-carbide and graphite particles are distributed uniformly, bonding well with the aluminum matrix. The interface between the Al-matrix, boron-carbide and graphite particles is clean allowing a strong interfacial bonding. No agglomeration of the particles was observed in the composite.

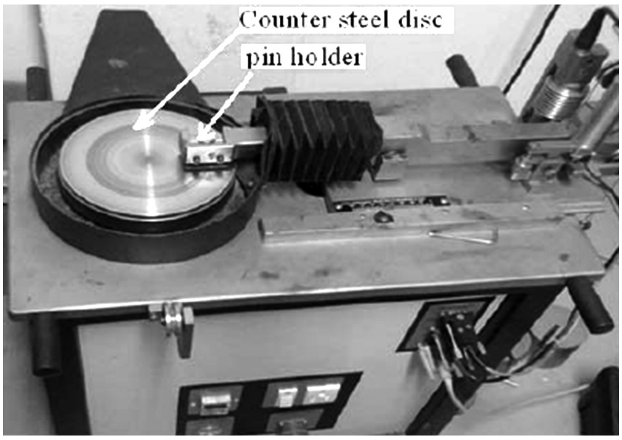

Figure 2: Pin-on-disc wear-testing rig
Slika 2: Naprava "pin on disc" za preizkušanje obrabe

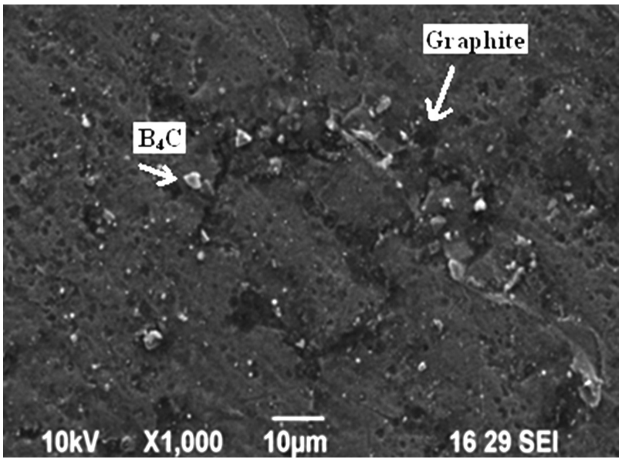

Figure 3: Microstructure of AA6061-B_4C-Gr hybrid composite
Slika 3: Mikrostruktura hibridnega kompozita AA6061-B_4C-Gr

3.2 Hardness analysis

It can be observed from **Figure 4** that the hardness of the Al-matrix increased from 50 BHN to 83 BHN due to the addition of $w = 10$ % of boron-carbide particles. This reveals an increase in the hardness due to the addition of boron carbide. On the other hand, the hardness of AA6061-B_4C composites decreased from 83 BHN to 66 BHN when graphite particles were incorporated. This can be elucidated with the fact that graphite has a lower hardness than B_4C particles. The hardness of Al–10 % B_4C–3 % graphite was by about 21 % lower than the hardness of the Al–10 % B_4C composite. A similar observation was made by Hassan et al.[10]

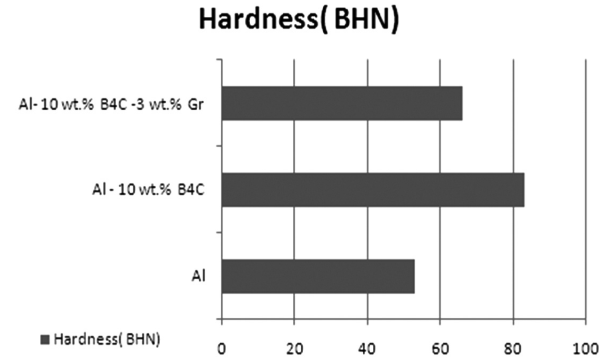

Figure 4: Hardness of AA6061, Al–10 % B_4C and Al–10 % B_4C–3 % Gr (mass fractions, *w*/%)

Slika 4: Trdota AA6061, Al–10 % B_4C in Al–10 % B_4C–3 % Gr (masni deleži, *w*/%)

3.3 Dry-sliding wear test

Typical curves of the wear loss of matrix AA6061 at the 3 m/s sliding velocity and of hybrid composite AA6061-B_4C-Gr at the sliding velocity of 3 m/s and the constant load of 20 N are presented in **Figures 5** and **6**, respectively. It can be observed that the wear of hybrid composite AA6061-B_4C-Gr is lower by 28 % when compared with matrix AA6061. This is due to the presence of the B_4C and graphite particles. This can also be attributed to a better interfacial bonding between Al and the B_4C particles. The volume of the wear debris increases with the increasing load, resulting in a greater loss of the material. The wear resistance of the Al-B_4C composites tends to decrease when the sliding velocity is increased from 1 m/s to 3 m/s at the load of 20 N. In general, a higher sliding velocity generates a higher frictional heat which increases the wear.

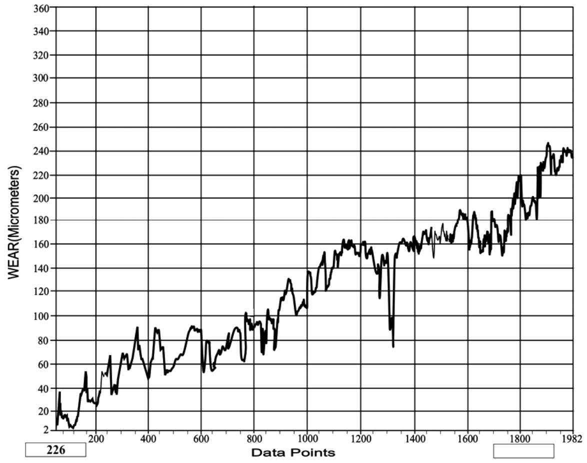

Figure 6: Typical curve of the wear-loss pattern of AA6061-B_4C-Gr at 20 N and 3 m/s sliding velocity for a duration 30 min

Slika 6: Značilna krivulja obrabe AA6061-B_4C-Gr pri obremenitvi 20 N, hitrosti drsenja 3 m/s in trajanju 30 min

It can be observed from **Figures 7** and **8** that the wear loss increased with the increasing load. The volume of the wear debris increases with the increasing load, resulting in a greater loss of the material. The wear resistance of the AA6061-B_4C composites tended to decrease when the sliding velocity was increased from 1 m/s to 3 m/s at the load of 20 N. In general, a higher

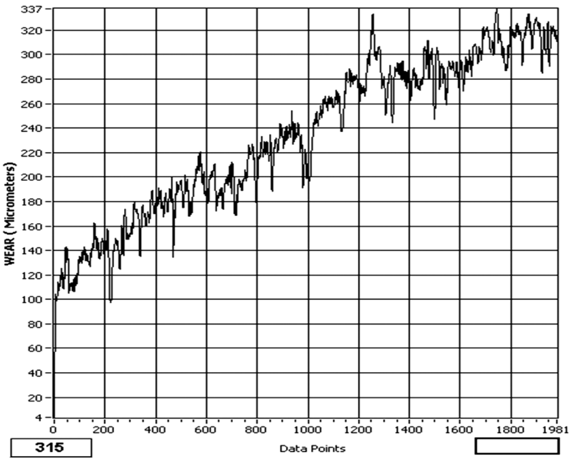

Figure 5: Typical curve of the wear-loss pattern of AA6061 at a load 20 N and 3 m/s sliding velocity for a duration 30 min

Slika 5: Značilna krivulja obrabe AA6061 pri obremenitvi 20 N, hitrosti drsenja 3 m/s in trajanju 30 min

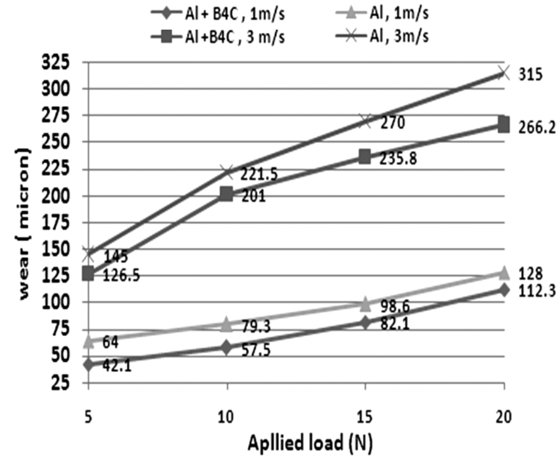

Figure 7: Variation of the wear as a function of normal loads and sliding velocities for AA6061 and AA6061-B_4C composite

Slika 7: Spreminjanje obrabe v odvisnosti od obremenitve in hitrosti drsenja za kompozita AA6061 in AA6061-B_4C

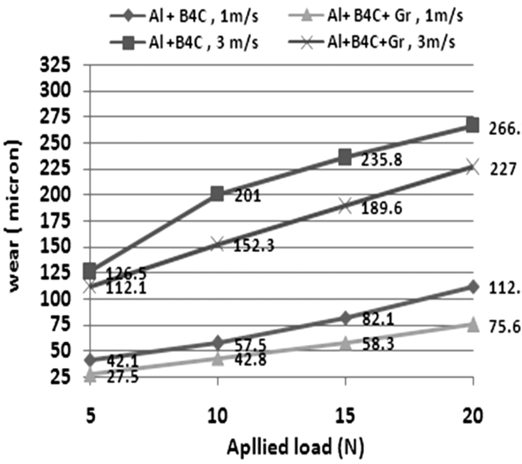

Figure 8: Variation of the wear as a function of normal loads and sliding velocities for the AA6061-B$_4$C and AA6061-B$_4$C-Gr composites

Slika 8: Spreminjanje obrabe v odvisnosti od obremenitve in hitrosti drsenja za kompozita AA6061-B$_4$C in AA6061-B$_4$C-Gr

sliding velocity generates a higher frictional heat which increases the wear.

Figure 8 shows that the wear loss of AA6061-B$_4$C is higher than that of the AA6061-B$_4$C-Gr composite irrespective of the load and speed. This could be due to the soft nature of graphite particles acting as solid lubricants with a layer lattice lamella crystal structure consisting of hexagonal rings forming thin parallel planes (graphenes). Graphenes are bonded to each other with weak van der Waals forces. The layered structure allows a sliding movement of the parallel planes, hence, reducing the frictional forces between the pin and the counter disc. This results in a reduction of the wear of the AA6061-B$_4$C-Gr composite which is 15 % lower than that of the AA6061-B$_4$C composite at the 3 m/s sliding velocity and the 20 N load. A similar observation was noticed by Shanmughasundaram et al.[11] for AA6061-Gr (w = 0–7.5 %) composites.

3.4 Morphology of worn surfaces

Figures 9 and **10** show the wear-track morphology of AA6061 and the AA6061-B$_4$C composite, respectively, at the normal load of 20 N and the 3 m/s sliding velocity. The worn surface of aluminium with large ploughing grooves is shown. The AA6061 material is much softer than the carbon-steel disc; the asperities on the steel counter face pierce to a larger depth. A larger plastic deformation is seen on the worn surface. The worn surface of the AA6061-B$_4$C composite (**Figure 10**) shows that the extent of the material removal is not as large as in the case of the AA6061 matrix (**Figure 9**). The wear grooves are smaller along the sliding direction due to the incorporation of boron carbide.

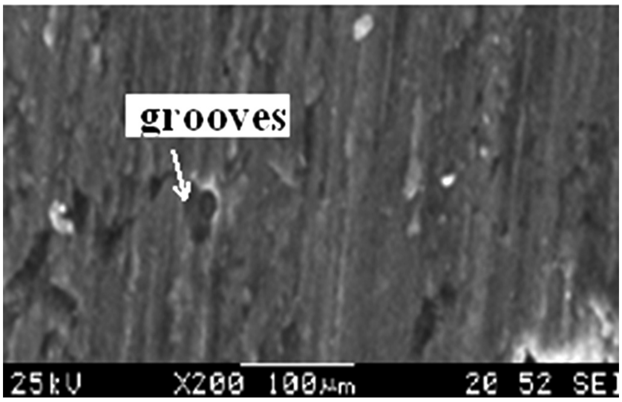

Figure 9: SEM micrograph of the worn surface of AA6061 at the normal load of 20 N and 3 m/s sliding velocity

Slika 9: SEM-posnetek obrabljene površine AA6061 pri obremenitvi 20 N in hitrosti drsenja 3 m/s

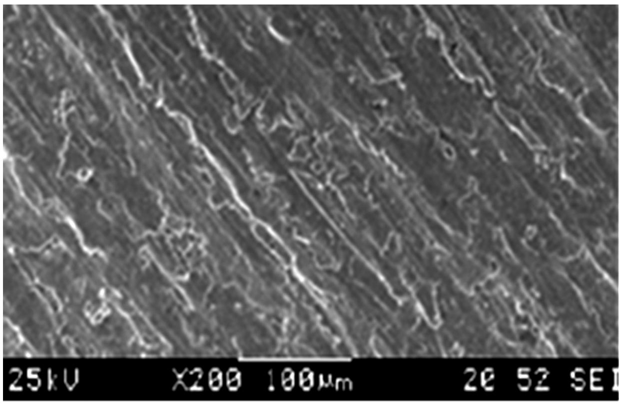

Figure 10: SEM micrograph of the worn surface of the AA6061-B$_4$C composite at the normal load of 20 N and 3 m/s sliding velocity

Slika 10: SEM-posnetek obrabljene površine AA6061-B$_4$C kompozita pri obremenitvi 20 N in hitrosti drsenja 3 m/s

The worn surface of the AA6061-B$_4$C-Gr composite subjected to the 20 N load at the 1 m/s sliding velocity is shown in **Figure 11**. It shows that the extent of the material removal is not as large as in the case of the AA6061-B$_4$C composite. Graphite is a solid lubricant and its particles are soft, slippery, greyish-black, having a layer lattice lamella crystal structure. Its layered structure allows a sliding movement of the parallel

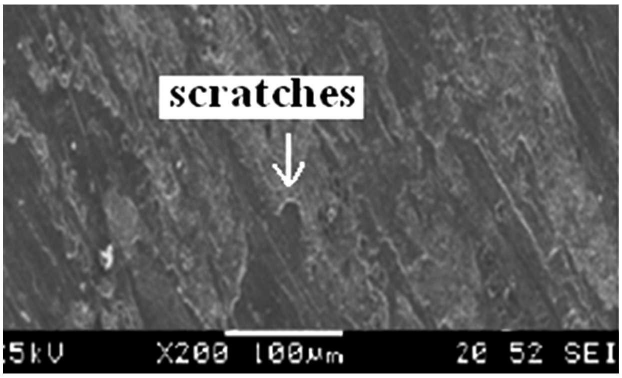

Figure 11: SEM micrograph of the worn surface of the AA6061-B$_4$C-Gr composite at the normal load of 20 N and 1 m/s sliding velocity

Slika 11: SEM-posnetek obrabljene površine kompozita AA6061-B$_4$C-Gr pri obremenitvi 20 N in hitrosti drsenja 1 m/s

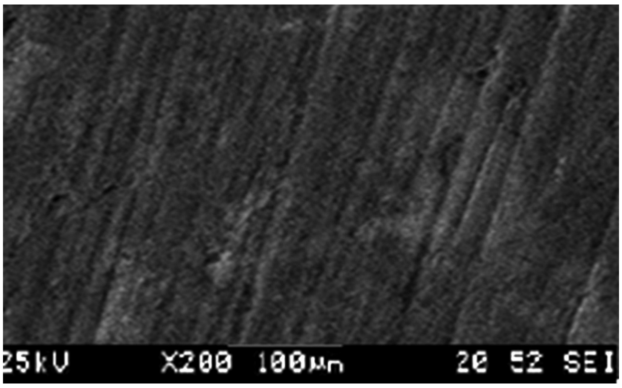

Figure 12: SEM micrograph of the worn surface of the AA6061-B_4C-Gr composite at the normal load of 20 N and 3 m/s sliding velocity

Slika 12: SEM-posnetek obrabljene površine kompozita AA6061-B_4C-Gr pri obremenitvi 20 N in hitrosti drsenja 3 m/s

planes. Hence, it reduces the friction between the pin and the disc, thus, reducing the wear. This observation proves that the wear loss of the hybrid composite of AA6061-B_4C-Gr is lower compared to the AA6061-B_4C composite. The SEM micrograph does not indicate any delamination. The sliding marks (**Figure 12**) obtained at the 3 m/s velocity are relatively higher compared with the low velocity (1 m/s) when viewed at the same magnification. This can be noticed when the sliding velocity increases from 1 m/s to 3 m/s. The morphologies of the worn surfaces gradually change from fine scratches to grooves. This shows that the transition from mild wear to severe wear takes place with an increase in the sliding velocity at a higher load. Generally, aluminium and reinforcement particles react with the oxygen in the air, forming iron oxides during the wear and a Mechanically Mixed Layer (MML) on the worn surface. This oxide film tends to deteriorate at the higher sliding velocity due to a higher frictional heat and increases the wear. It can be concluded that the SEM observation of the worn surfaces of AA6061 and the composites validate the results of the wear loss.

3.5 Energy Dispersive Spectroscopy (EDS) analysis

When the sliding velocity is increased to 3 m/s at the low load (5 N), the surface of the composite pin reacts with the oxygen and forms an oxide layer due to a higher frictional heat. It reduces the direct metallic contact between the sliding surfaces resulting in a lower wear rate of the composite. As can be seen from **Figure 13**, the peak of the oxide which is the main constituent of MML is clearly detected on the worn surface of the composite. It indicates that the oxidative wear is predominant at the low load (5N) and high sliding velocity (3 m/s). Moreover, a negligible amount of oxides was observed on the worn surface of AA6061.

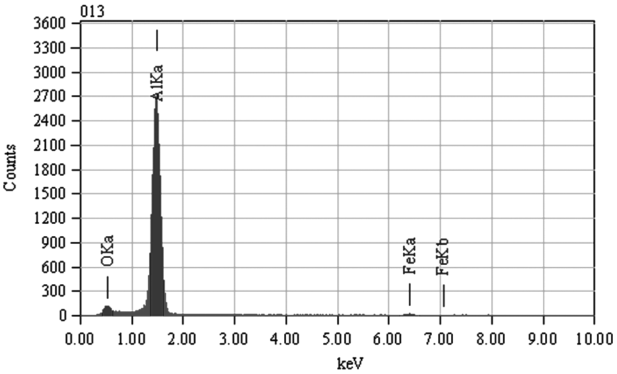

Figure 13: EDAX spectrum of MML for the Al–10 % B_4C–3 % Gr composite tested at 5 N, 3 m/s

Slika 13: EDAX-spekter MML za kompozit z Al–10 % B_4C–3 % Gr, preizkušen pri 5 N in 3 m/s

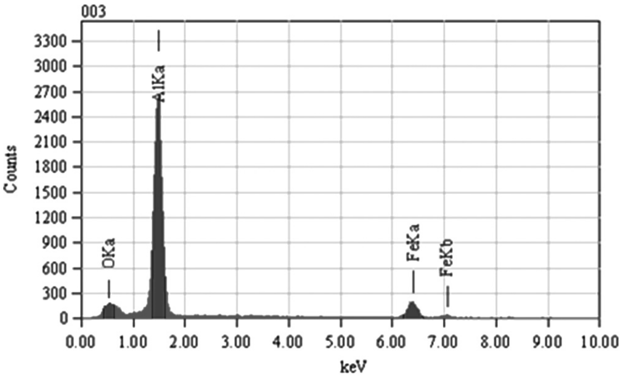

Figure 14: EDAX spectrum of MML for the Al–10 % B_4C–3 % Gr composite tested at 20 N, 3 m/s

Slika 14: EDAX-spekter MML za kompozit z Al–10 % B_4C–3 % Gr, preizkušen pri 20 N in 3 m/s

Figure 14 shows the EDAX spectrum of MML for the Al–10 % B_4C–3 % Gr composite when tested at 20 N, 3 m/s. It can be observed that the amount of the oxides present on the worn surface tends to decrease. It can also be noted from **Figure 15** that a considerable amount of iron is transferred from the counter steel disc to the composite pin. However, broken and uneven oxide segments increase the wear. Hence, MML failed to sustain

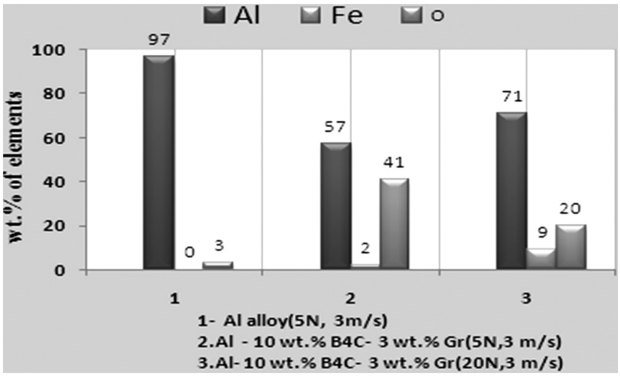

Figure 15: Weight percentage of Al, Fe and oxides as a function of the load and sliding velocity on the worn surface of the Al–10 % B_4C–3 % Gr composite against the counter steel obtained with EDS

Slika 15: Masni deleži Al, Fe in oksidov, ugotovljeni z EDS, v odvisnosti od obremenitve in hitrosti drsenja na obrabljeni površini Al-kompozita z 10 % B_4C in 3 % Gr v paru z jeklom under the high load and velocity during the sliding. A higher sliding velocity increases the interface temperature and causes a local yielding, thereby the wear mechanism changes into the delamination wear. This behavior is termed as severe wear behavior, in which the material removal occurs at a higher rate. The transition from mild to severe wear is associated with the existence of delamination and adhesion, which are the primary wear mechanisms at the higher load and sliding velocity.

4 CONCLUSIONS

AA6061-B_4C and AA6061-B_4C-Gr composites were successfully fabricated by employing the stir-casting method. A SEM analysis revealed that boron-carbide and graphite particles are distributed uniformly in the aluminium matrix. The AA6061-B_4C composite had a higher hardness compared to AA6061. The wear resistance of the AA6061-B_4C-Gr hybrid composite and Al-B_4C composite increase steadily with the sliding load and velocity. The wear resistance of the AA6061-B_4C-Gr hybrid composite is higher than that of the AA6061-B_4C composite and much higher than that of the AA6061 matrix. The formation of the oxides at the interface plays a significant role in reducing the wear rate. The oxides and reinforcing particles form a mechanically mixed layer (MML) appearing on the worn surface of the composite pin and enhancing the wear resistance. Hence, it can be concluded that graphite particles reduce the wear when included in an aluminium alloy or in an AA6061-B_4C composite.

Acknowledgement

I am grateful to the Faculty of Engineering, Department of Automobile Engineering, Karpagam University, Coimbatore, for providing the facilities for a successful completion of this project.

5 REFERENCES

[1] S. Balasivanandha Prabu, L. Karunamoorthy, S. Kathiresan, B. Mohan, Journal of Materials Processing Technology, 171 (**2006**), 268–273

[2] A. A. Cerit, M. B. Karamiş, F. Nair, K. Yildizli, Tribology in industry, 30 (**2008**), 3–4

[3] S. Rama Rao, G. Padmanabhan, International Journal of Materials and Biomaterials Applications, 2 (**2012**) 3, 15–18

[4] L. Gómez, D. Busquets-Mataix, V. Amigó, M. D. Salvador, Journal of Composite Materials, 43 (**2009**) 9, 987–995

[5] F. Toptan, I. Kerti, L. A. Rocha, Wear, 290–291 (**2012**), 74–85

[6] L. Jinfeng, J. Longtao, W. Gaohui, T. Shoufu, C. Guoqin, Rare Metal Materials and Engineering, 38 (**2009**) 11, 1894–1898

[7] W. Ames, A. T. Alpas, Metall Mater Trans, 26A (**1995**), 85

[8] K. Miyazaki, T. Hagio, K. Kobayashi, Journal of Materials Science, 16 (**1981**) 3, 752–762

[9] K. M. Shorowordi, T. Laoui, A. S. M. A. Haseeb, J. P. Celis, L. Froyen, Technology, 10 (**2003**), 738–743

[10] A. M. Hassan, G. M. Tashtoush, J. A. Al-Khalil, Journal of Composite Materials, 41 (**2007**) 4, 453–465

[11] P. Shanmughasundaram, R. Subramanian, Advances in Materials Science and Engineering, (2013), article ID 216536

UDK 539.92:621.793
Original scientific article/Izvirni znanstveni članek

ISSN 1580-2949
MTAEC9, 48(5)669(2014)

TRIBOLOGY OF CrAg7N COATINGS DEPOSITED ON VANADIS 6 LEDEBURITIC TOOL STEEL

TRIBOLOGIJA PREVLEK CrAg7N NA LEDEBURITNEM ORODNEM JEKLU VANADIS 6

Pavel Bílek, Peter Jurči, Mária Hudáková, Ľubomír Čaplovič, Michal Novák
Institute of Materials Science, Faculty of Materials Science and Technology in Trnava, Slovak University of Technology in Bratislava,
Paulínská 16, 917 24 Trnava, Slovak Republic
pavel-bilek@email.cz

Prejem rokopisa – received: 2013-09-25; sprejem za objavo – accepted for publication: 2013-11-19

Samples made from Vanadis 6 PM ledeburitic tool steel were surface machined, ground and mirror polished. Prior to the deposition, they were heat treated to a hardness of 60 HRC. The CrAg7N coating was deposited with the magnetron-sputtering technique, using pure-Cr and Ag targets in a composite low-pressure nitrogen/argon atmosphere and at a temperature of 500 °C in the Hauzer Flexicoat 850 device. Tribological testing using a pin-on-disc apparatus was carried out at ambient and elevated temperatures: (300, 400 and 500) °C, respectively. Al_2O_3, 100Cr6 and CuZn balls were used as the counterparts. The wear tracks after the pin-on-disc testing were analyzed with scanning electron microscopy and a microanalysis. The experiments have shown a strong dependence of tribological parameters on the temperature. The friction coefficient of CrN-Ag against the 100Cr6 ball at ambient temperature was $\mu = 0.56$. Tribological sliding tests of this coating system against the alumina balls indicate a decrease in the friction coefficient due to the increasing temperature. At ambient temperature $\mu = 0.68$ and its minimum occurred at the temperature of 400 °C, $\mu = 0.24$. This is attributed to the diffusion of Ag particles to the sliding top surface at elevated temperature. The testing against the CuZn brass ball generally gave a lower friction coefficient at ambient temperature, $\mu = 0.39$. In contrast, the friction coefficient slightly increased with the increasing temperature and was practically constant at elevated temperatures, ranging between $\mu = 0.43–0.48$.

Keywords: Cr-V ledeburitic steels Vanadis 6, PVD, chromium nitride with silver, pin-on-disc, friction coefficient

Vzorci, izdelani iz ledeburitnega orodnega jekla Vanadis 6 PM, so bili površinsko obdelani, brušeni in zrcalno polirani. Pred nanosom so bili toplotno obdelani na trdoto 60 HRC. S tehniko magnetronskega naprševanja in z uporabo tarč iz čistega Cr in Ag je bila nanesena CrAg7N-nanoprevleka v sestavljeni nizkotlačni atmosferi iz dušika in argona pri temperaturi 500 °C v napravi Hauzer Flexicoat 850. Tribološki preizkusi s preizkuševalnikom "pin-on-disc" so bili izvršeni pri sobni temperaturi in pri povišanih temperaturah (300, 400 in 500) °C. Krogle Al_2O_3, 100Cr6 in CuZn so bile uporabljene kot par. Sledi obrabe po preizkusu "pin-on-disc" so bile analizirane z vrstično elektronsko mikroskopijo in z mikroanalizo. Eksperimenti so pokazali močno odvisnost triboloških parametrov od temperature. Koeficient trenja CrN-Ag proti krogli 100Cr6 pri sobni temperaturi je bil $\mu = 0,56$. Tribološki drsni preizkusi te prevleke proti kroglam Al_2O_3 kažejo zmanjšanje koeficienta trenja z naraščajočo temperaturo. Pri sobni temperaturi je bil $\mu = 0,68$, minimum pa se je pojavil pri temperaturi 400 °C, $\mu = 0,24$. To se pripisuje difuziji delcev Ag na drsno površino pri povišanih temperaturah. Preizkušanje v paru s CuZn in medeninasto kroglo je dalo na splošno nižje koeficiente trenja pri sobni temperaturi, $\mu = 0,39$. Nasprotno pa je koeficient trenja malo narasel pri povišanju temperature in je bil pri povišanih temperaturah praktično konstanten v območju $\mu = 0,43–0,48$.

Ključne besede: ledeburitno jeklo Cr-V Vanadis 6, PVD, krom nitrid s srebrom, "pin-on-disk", koeficient trenja

1 INTRODUCTION

Chromium nitrides (CrN) have been extensively investigated in the applications of protective coatings due to their high hardness, good wear resistance as well as excellent corrosion and high-temperature-oxidation resistance.[1–5] They gained great scientific interest and industrial popularity due to these properties in copper machining, aluminium die casting and forming, and wood processing.[6] However, in many applications, the requirements on the coated-material surface cannot be met by such a single coating. A further development to adapt some of their properties to the levels required for specific applications leads to the production of composite coatings, combining different material properties so that certain new desired properties can be created.[7–9]

The effect of self-lubrication has gained a great scientific importance in the last few years. The main idea to develop self-lubricating and multi-purpose coatings is based upon the fact that commercially available lubricants (sulfides, oxides, graphite) exhibit considerable shortcomings and cannot be used effectively in tooling applications over a sufficiently wide temperature range.[10–12] Soft noble metals, on the other hand, show a stable chemical behavior and can exhibit self-lubricating properties due to their low shear strength. Noble-metal particles bring several benefits to the layer properties compared to metal oxides or graphite. They are stable up to relatively high temperatures, have a low hardness and do not behave as abrasive particles. A common disadvantage of noble metals is their high cost, but this can be optimized to an acceptable level. The self-lubricating effect is based on an incorporation of a small amount of noble metals, mostly silver, into the basic CrN film. Silver is completely insoluble in CrN and forms nanoparticles in the basic CrN compound. Silver-containing transition-metal-nitride films have been extensively studied in recent years.[13]

The current paper deals with the development of adaptive nanocomposite CrAgN coatings on the Vanadis 6 Cr-V ledeburitic tool steel. It describes and discusses the tribological properties, such as the friction coefficient and wear rate during the pin-on-disk testing, of the coating with the mass fraction $w = 7\ \%$ content of silver.

2 EXPERIMENTAL WORK

The substrate material was PM ledeburitic steel Vanadis 6 with nominally 2.1 % C, 1.0 % Si, 0.4 % Mn, 6.8 % Cr, 1.5 % Mo, 5.4 % V and Fe as the balance that was soft annealed to a hardness of 21 HRC.[14,15]

The samples used for the investigation were plates with the dimensions of 50 mm × 10 mm × 10 mm, heat treated (austenitized at a temperature of 1050 °C, quenched in a flow of nitrogen gas and double tempered for 2 h at a temperature of 530 °C) to the final hardness of 60 HRC and then finely ground and polished with a diamond suspension up to a mirror finish.

The conditions for depositing CrN/Ag coatings were reported elsewhere.[16] The output power on the Cr cathode was 5.8 kW and on the Ag cathode it was 0.21 kW.

Tribological properties of the coating were measured using a CSM pin-on-disc tribometer at ambient and at elevated temperatures, up to 500 °C. Balls, 6 mm in diameter, made from sintered alumina, 100Cr6 steel and CuZn brass (55 % Cu, 45 % Zn) were used for the tests. The testing against the 100Cr6 counterpart was carried out only at ambient temperature due to a low thermal stability of the 100Cr6 steel. No external lubricant was added during the measurements. The normal loading used for the investigation was 1 N. For each measurement, the total sliding distance was 100 m. The volume loss of the coated samples was calculated from the width of the track using the following formula:[17]

$$s = 2\pi R\ [r^2 \sin^{-1}(d/2r) - (d/4)\mathrm{v}(4r^2 - d^2)]$$

where R is the wear-track radius, d is the wear-track width and r is the radius of the ball.

To relate the volume loss to normal load F and sliding distance l wear rates W[17] were calculated.

After the testing, the wear tracks were examined with a scanning electron microscope (SEM) JEOL JSM-7600F and an energy-dispersive X-ray analysis (EDX).

3 RESULTS AND DISCUSSIONS

Table 1 summarizes the results of the tribological investigations. In the case of the alumina counterpart, the friction coefficient at ambient temperature was $\mu = 0.68$. Therefore, no positive effect of the Ag addition was found at the low temperature, which is in line with the previous investigation.[18]

Table 1: Results of tribological investigation of the CrAg7N coating
Tabela 1: Rezultati triboloških preiskav nanosa CrAg7N

μ	Counterpart		
Temperature	Al_2O_3	CuZn	100Cr6
20 °C	0.68	0.39	0.56
300 °C	0.40	0.43	
400 °C	0.24	0.48	
500 °C	0.29	0.46	

Basnyat et al.[19] and Yao et al.[20] established a beneficial effect of Ag on the friction coefficient at room temperature. However, the loading applied in their investigation was much higher, which makes the results incomparable with our measured data.

At a higher testing temperature, the friction coefficient of the CrN coating with $w = 7\ \%$ of silver became much lower. The minimum value, $\mu = 0.24$, was found at the temperature of 400 °C. This phenomenon is attributed to various factors. Firstly, there is an increasing mobility of silver at elevated temperature that has been reported.[21] These atoms can diffuse to the surface at elevated temperatures and effectively work as a solid lubricant due to the low shear strength of silver. The second possible contribution of the friction coefficient decreased with the increased testing temperature can be indentified on the basis of the assumption that an increased temperature makes the coating softer.[18]

Figure 1 shows the dependence of the friction coefficient on the sliding distance. At ambient temperature, the friction coefficient increased at the beginning of the test and after that it slightly decreased to a stable state of $\mu = 0.68$, typical for a steady state of sliding. At elevated temperatures, the friction coefficient was first between $\mu = 0.55–0.65$ and then it immediately decreased to the values of the steady state.

Figure 2 demonstrates the wear tracks obtained by testing the CrAg7N coating against alumina at ambient and elevated temperatures. At ambient temperature, the testing gave a smooth surface without any failure of integrity. The testing at elevated temperatures led to a creation of parallel grooves oriented along the sliding direction on the coated material and to a much wider wear track and a high volume loss of the coating and the wear rate, respectively, as documented in **Table 2**. The

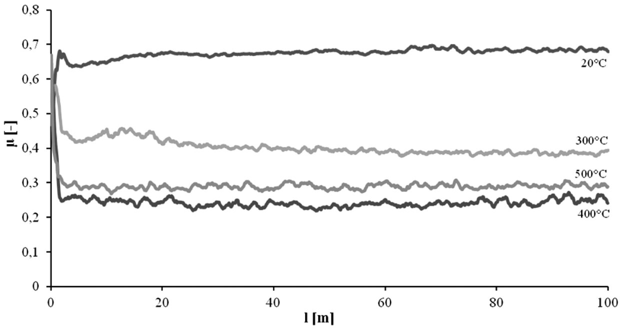

Figure 1: Dependence of friction coefficient on sliding distance for alumina counterpart
Slika 1: Odvisnost koeficienta trenja od poti drsenja za Al_2O_3 v paru

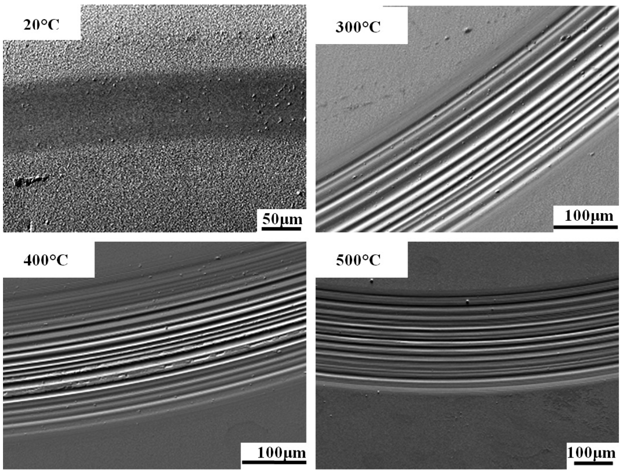

Figure 2: Wear tracks after pin-on-disc testing against alumina at ambient and elevated temperature

Slika 2: Sledi obrabe po preizkusu "pin-on-disc" v paru z Al_2O_3 pri sobni in povišani temperaturi

Table 2: Width of tracks, volume loss and wear rate after pin-on-disc testing against alumina

Tabela 2: Širina sledi, volumenska izguba in obraba pri preizkusu "pin-on-disc" v paru z Al_2O_3

Heat (°C)	d/µm	V/m^3	W/(m^3/(N m))
20	85	$2.72 \cdot 10^{-13}$	$2.72 \cdot 10^{-15}$
300	228	$5.17 \cdot 10^{-12}$	$5.17 \cdot 10^{-14}$
400	250	$6.85 \cdot 10^{-12}$	$6.85 \cdot 10^{-14}$
500	276	$9.24 \cdot 10^{-12}$	$9.24 \cdot 10^{-14}$

wider tracks can be attributed to the softening of the coating at elevated temperatures.

At the temperature of 400 °C a partial failure of the coating was observed. The EDX analysis showed the presence of iron (the base element of steel) on the surface of the track in some sites, while the contents of chromium and silver were found in the other sites (**Figure 3**). This result confirms a partial removal of the coating from the substrate.

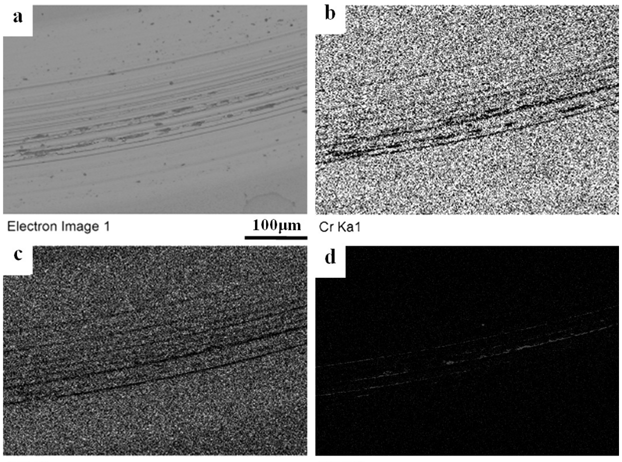

Figure 3: Partial failure of coating CrAg7N after pin-on-disc testing against alumina at the temperature of 400 °C: a) overview, b) EDX of chromium, c) EDX of silver, d) EDX of iron

Slika 3: Parcialne poškodbe nanosa CrAg7N po preizkusu "pin-on-disc" v paru z Al_2O_3 pri temperaturi 400 °C: a) videz, b) EDX kroma, c) EDX srebra, d) EDX železa

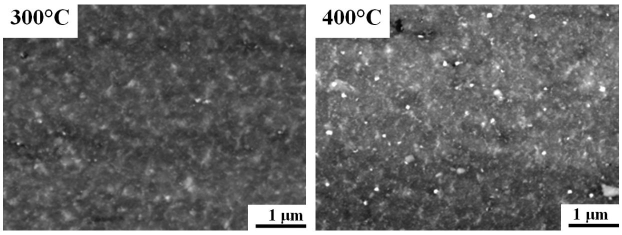

Figure 4: Nanoparticles of silver on the surface of track after pin-on-disc testing

Slika 4: Nanodelci srebra na površini sledi po preizkusu "pin-on-disc"

Our previous investigation of the CrN coating with *w* = 3 % of silver gave similar results.[22] The lowest value of the friction coefficient was also found at the temperature of 400 °C. However, the CrAg3N coating showed a much higher failure, and even at the temperature of 500 °C it was completely removed from the surface of the substrate after the test.

Figure 4 shows the surface of a track after the pin-on-disc testing at the temperatures of 300 °C and 400 °C. In both cases, Ag particles are well visible and these particles are responsible for a better friction and could act as a solid lubricant. In the wear track formed during the testing at 500 °C Ag particles were also identified, but their population density was reduced in comparison with the samples tested at lower temperatures.

Figure 5 shows the wear tracks formed by the sliding of the coating against CuZn brass. Compared to the tracks caused by the sliding of sintered alumina these tracks are wider, but no damage of the coating is observed.

On the other hand, a considerable amount of the material transferred from the counterpart to the surface of the coating was detected **(Figure 6**).

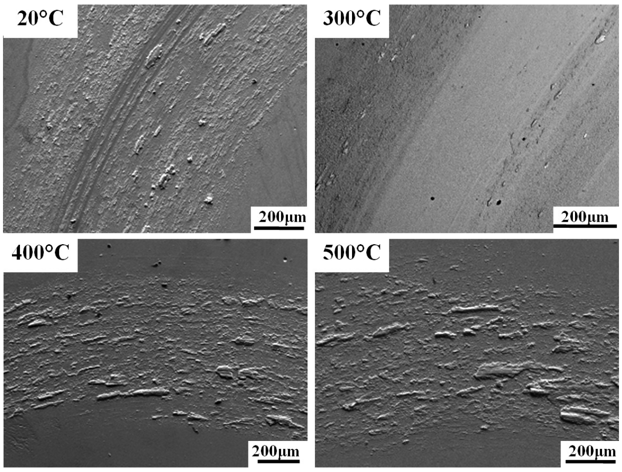

Figure 5: Wear tracks after pin-on-disc testing against CuZn at ambient and elevated temperature

Slika 5: Sledi obrabe po preizkusu "pin-on-disc" v paru s CuZn pri sobni in povišani temperaturi

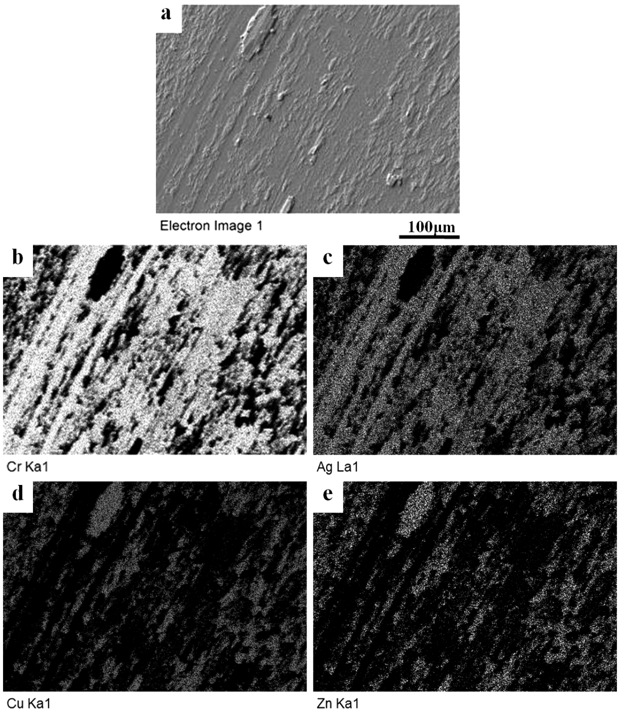

Figure 6: Material transferred from counterpart CuZn to the surface of coating CrAg7N after pin-on-disc, at the temperature of 20 °C: a) overview, b) EDX of chromium, c) EDX of silver, d) EDX of copper, e) EDX of zinc

Slika 6: Prenesen material s para CuZn na površino nanosa CrAg7N po preizkusu "pin-on-disc" pri temperaturi 20 °C; a) videz, b) EDX kroma, c) EDX srebra, d) EDX bakra, e) EDX cinka

This is due to the very low shear strength of CuZn, especially at a higher temperature. It should be noted that such a material transfer was detected irrespective of the testing temperature. These results are in good agreement with the previous work.[22]

The measurement results for the friction coefficient of the CuZn counterpart are shown in **Table 1**. The minimum friction coefficient of $\mu = 0.39$ was found at ambient temperature. With the increasing temperature, the friction coefficient becomes higher, ranging between $\mu = 0.43–0.48$. No effect of silver on the tribological performance was found here – the material transfer can be considered as a plausible explanation (**Figure 6**).

The friction coefficient against the 100Cr6 counterpart was found to be $\mu = 0.56$ (**Table 1**). The material of steel transferred to the surface of the coating is documented in **Figure 7**. The surface of the coating stayed smooth, without any damage.

4 CONCLUSIONS

The friction and wear characteristics of the CrAg7N coatings prepared with the magnetron-sputter-deposition method were examined at different temperatures and with different counterpart materials. The results can be summarized as follows:

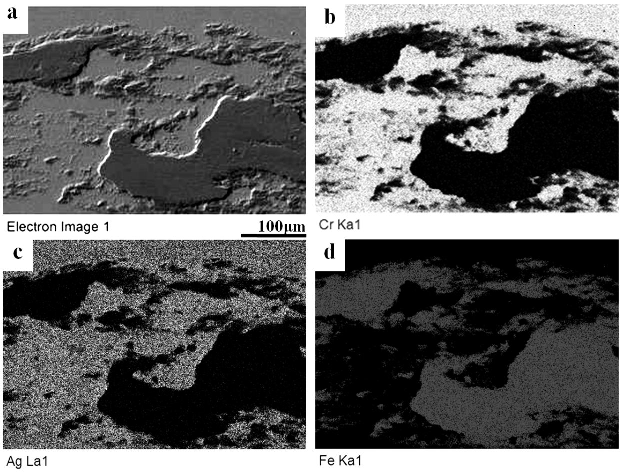

Figure 7: Material transferred from counterpart 100Cr6 to the surface of coating CrAg7N after pin-on-disc, at the temperature 20 °C: a) overview, b) EDX of chromium, c) EDX of silver, d) EDX of iron

Slika 7: Prenesen material iz para 100Cr6 na površino nanosa CrAg7N po preizkusu "pin-on-disc" pri temperaturi 20 °C: a) videz, b) EDX kroma, c) EDX srebra, d) EDX železa

- The friction coefficient rapidly decreased with the increasing testing temperature when an alumina ball was used as the counterpart, with its minimum at the temperature of 400 °C. The coating showed partial damage at elevated temperatures, but it was not removed from the substrate.
- The friction coefficient was not positively influenced when tested against the CuZn counterpart.
- No removal or other coating damage was established after the sliding against the CuZn ball and 100Cr6 ball, but a considerable material transfer from the ball to the sample was detected.
- The presence of silver in the CrN coating results in improved tribological properties at moderate temperatures. Under these conditions, the CrN coating with $w = 7\ \%$ of Ag could find its application in industry.

Acknowledgements

This publication is the result of implementing project CE for development and application of advanced diagnostic methods in processing of metallic and non-metallic materials, ITMS:26220120048, supported by the Research & Development Operational Programme funded by the ERDF. The research was supported by grant project VEGA 1/1035/12.

5 REFERENCES

[1] G. Bertrand, C. Savall, C. Meunier, Surface and Coatings Technology, 96 (**1997**), 323–329

[2] J. Xu, H. Umehara, I. Kojima, Applications of Surface Science, 201 (**2001**), 208–218

[3] S. K. Pradhan, C. Nouveau, A. Vasin, M. A. Djouadi, Surface and Coatings Technology, 200 (**2005**), 141–145

[4] S. Han, J. H. Lin, S. H. Tsai, S. C. Chung, D. Y. Wang, F. H. Lu, H. C. Shin, Surface and Coatings Technology, 133–134 (**2000**), 460–465

[5] D. Mercs, N. Bonasso, S. Naamane, J. M. Bordes, C. Codget, Surface and Coatings Technology, 200 (**2005**), 403–407

[6] R. Gahlin, M. Bronmark, P. Hedenqvist, S. Hogmark, G. Hakansson, Surface and Coatings Technology, 76/77 (**1995**), 174–180

[7] R. Hauert, J. Patscheider, Advanced Engineering Materials, 2 (**2000**), 247–259

[8] S. Zhang, D. Sun, Y. Fu, H. Du, Surface and Coatings Technology, 167 (**2003**), 113–119

[9] P. E. Hovsepian, W. D. Munz, Vacuum, 69 (**2003**), 27–36

[10] C. P. Mulligan, T. A. Blanchet, D. Gall, Wear, 269 (**2010**), 125–131

[11] S. M. Aouadi, Y. Paudel, W. J. Simonson, Q. Ge, P. Kohli, C. Muratore, A. A. Voevodin, Surface and Coatings Technology, 203 (**2009**), 1304–1309

[12] A. Erdemir, Surface and Coatings Technology, 200 (**2005**), 1792–1796

[13] S. M. Aouadi, A. Bohnhoff, M. Sodergren, D. Mihut, S. L. Rohde, J. Xu, S. R. Mishra, Surface and Coatings Technology, 201 (**2006**), 418–422

[14] Bohler-Uddelholm U.S.A. [online], Vanadis 6.: <http://www.bucorp.com/files/van_6_ds.pdf>

[15] P. Bílek, J. Sobotová, P. Jurči, Mater. Tehnol., 45 (**2011**) 5, 489–493

[16] P. Bílek, P. Jurči, M. Hudaková, J. Bohovičová, J. Sobotová, Proceedings of the 22nd Int. Conference METAL 2013, Brno, 2013

[17] Standard Test Method for Wear Testing with a Pin-On-Disk Apparatus, G 99–95a, ASTM International, 2000

[18] P. Jurči, I. Dlouhý, Applied Surface Science, 257 (**2011**), 10581–10589

[19] P. Basnyat, B. Luster, Z. Kertzman, S. Stadler, P. Kohli, S. Aouadi, J. Xu, S. R. Mishra, O. L. Eryilmaz, A. Erdemir, Surface and Coatings Technology, 202 (**2007**), 1011–1016

[20] S. H. Yao, Y. L. Su, W. H. Kao, K. W. Cheng, Surface and Coatings Technology, 201 (**2006**), 2520–2526

[21] C. P. Mulligan, T. A. Blanchet, D. Gall, Surface and Coatings Technology, 204 (**2010**), 1388–1394

[22] J. Bohovičová, P. Jurči, M. Hudáková, L. Čaplovič, M. Sahul, P. Bílek, Proceedings of the 22nd Int. Conference METAL 2013, Brno, 2013

UDK 620.3:66.017:621.318
Original scientific article/Izvirni znanstveni članek

ISSN 1580-2949
MTAEC9, 48(5)675(2014)

MORPHOLOGY AND MAGNETIC PROPERTIES OF Fe_3O_4-ALGINIC ACID NANOCOMPOSITES

MORFOLOGIJA IN MAGNETNE LASTNOSTI NANOKOMPOZITOV Fe_3O_4-ALGINSKA KISLINA

Małgorzata Kaźmierczak[1,2], Katarzyna Pogorzelec-Glaser[1], Andrzej Hilczer[1],
Stefan Jurga[2], Łukasz Majchrzycki[3], Marek Nowicki[3], Ryszard Czajka[3],
Filip Matelski[3], Radosław Pankiewicz[4], Bogusława Łęska[4], Leszek Kępiński[5],
Bartłomiej Andrzejewski[1]
[1]Institute of Molecular Physics, Polish Academy of Sciences, M. Smoluchowskiego 17, 60179 Poznan, Poland
[2]NanoBioMedical Centre, Adam Mickiewicz University, Umultowska 85, 61614 Poznan, Poland
[3]Poznan University of Technology, Nieszawska 13A, 60965 Poznan, Poland
[4]Faculty of Chemistry, Adam Mickiewicz University, Umultowska 89b, 61614 Poznan, Poland
[5]Institute of Low Temperature and Structure Research, Polish Academy of Sciences, Okolna 2, 50422 Wroclaw, Poland
malgorzata.kazmierczak@ifmpan.poznan.pl

Prejem rokopisa – received: 2013-09-27; sprejem za objavo – accepted for publication: 2013-11-19

The morphology, structure and magnetic properties of the nanocomposites of magnetite (Fe_3O_4) nanoparticles and alginic acid (AA) are studied. Magnetite Fe_3O_4 nanoparticles and the nanoparticles capped with alginic acid exhibit very distinct properties. The chemical bonding between alginic acid and the surface of magnetite nanoparticles results in the recovery of surface magnetization. On the other hand, it also leads to the enhanced surface spin disorder and unconventional behavior of the magnetization observed in Fe_3O_4-AA nanocomposites at low temperatures.

Keywords: nanocomposite, magnetite nanoparticles, alginic acid, enhanced magnetization

Preučevali smo morfologijo, strukturo in magnetne lastnosti nanokompozitov na osnovi nanodelcev magnetita (Fe_3O_4) in alginske kisline (AA). V primerjavi z magnetitnimi nanodelci izkazujejo nanokompoziti Fe_3O_4-alginska kislina precej drugačne lastnosti. Molekule alginske kisline se kemijsko vežejo na površino magnetitnih nanodelcev in s tem povzročijo vrnitev površinske magnetizacije. Hkrati pa se s tem v nanokompozitih Fe_3O_4-AA pri nižjih temperaturah poveča površinska neurejenost spinov in nekonvencionalno vedenje magnetizacije.

Ključne besede: nanokompozit, nanodelci magnetita, alginska kislina, povečana magnetizacija

1 INTRODUCTION

The interest in the composites of polymers with magnetic nanoparticles stems from their unique physical properties and potential future applications for magnetic-data storage,[1] electronic devices and sensors,[2] biomedical applications in magnetic resonance imaging,[3] drug delivery[4] and hyperthermia agents.[5] From this point of view, one of the most preferred magnetic materials is magnetite Fe_3O_4 because it is a biocompatible mineral with a low toxicity (for example, the crystals of magnetite are magnetoreceptors in the brains of some animals[6]). It also exhibits a large magnetic moment and a spin-polarized electric current – the features highly desired for the applications in spintronics.

In bulk, magnetite crystallizes in the inverse spinel AB_2O_4 structure with two nonequivalent Fe sites placed in the *fcc* lattice of O^{2-} ions. Tetrahedral A sites contain Fe^{2+} ions, whereas octahedral B sites are occupied by Fe^{2+} and Fe^{3+} ions. The magnetic sublattices located on A and B sites are ferrimagnetically coupled. The mixed valence of Fe ions and fast electron hopping between B sites are responsible for a relatively high electric conductivity of Fe_3O_4 above the Verwey transition, $T_v \approx 125$ K.[7]

Nanostructured magnetite exhibits different magnetic, electronic and optical properties than the bulk material. Particularly, a significant reduction in the magnetization at the surface of Fe_3O_4 nanoparticles makes them useless for many applications. This obstacle can be overcome by capping the magnetic nanoparticles with polymers[8] or organic acids, which allows a restoration of the surface magnetism.[9]

One of the best capping material is alginic acid, which is a cheap, common and nontoxic natural biopolymer.[10,11] The aim of this work is to study the effect of the alginic-acid capping on the surface magnetization recovery in Fe_3O_4 nanoparticles.

2 EXPERIMENTAL WORK

2.1 Sample synthesis

All the chemicals used in the experiments were purchased from SIGMA ALDRICH. To obtain the disaggregated nanoparticles of magnetite Fe_3O_4, a portion of 9.0 mmol of $FeCl_3 \cdot 6H_2O$ was dissolved in 200 mL of ethylene glycol. The solution was vigorously stirred. After 15 min 131.7 mmol of CH_3COONa and 1.575 mmol of polyethylene glycol PEG 400 were added and the stirring was continued until they completely dissolved. Then, the solution was transferred into 50 mL teflon reactors and heated using microwave radiation (MARS 5, CEM Corporation) at 160 °C for 25 min. The black suspension of the nanoparticles obtained as a result of the reaction was first cooled, isolated by centrifugation and washed with absolute ethanol. The final product was dried in a vacuum oven at 40 °C. A nanocomposite was prepared from the aqueous dispersion of the magnetite nanopowder and alginic acid (AA) that was then air-dried at room temperature. The nanocomposite had the form of flakes with flat surfaces.

2.2 Sample characterization

The crystallographic structures of the samples were studied by means of X-ray powder diffraction (XRD) using an ISO DEBYE FLEX 3000 instrument with a Co lamp (λ = 0.17928 nm). The morphology of Fe_3O_4 nanoparticles was observed using a Philips CM20 SuperTwin transmission electron microscope (TEM). The structures of nanocomposites were studied by means of an atomic force microscope (Dimension Icon®, Bruker) using the magnetic-force-microscope (MFM) mode and NANO-SENSORS™ PPP-MFMR probes. The magnetic measurements were performed using a Quantum Design physical property measurement system (PPMS) fitted with a vibrating-sample-magnetometer (VSM) probe.

3 RESULTS AND DISCUSSION

Figure 1 shows the X-ray powder diffraction patterns of the as-obtained Fe_3O_4 nanoparticles (panel a) and of the Fe_3O_4-AA nanocomposite with the magnetite content equal to the mass fraction w = 10 % (panel b).

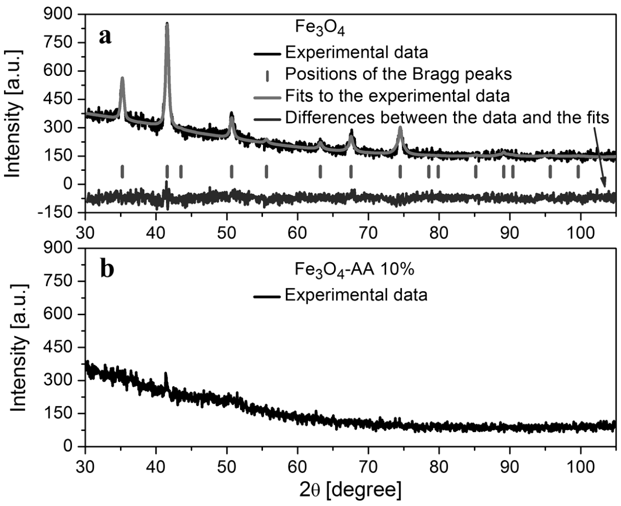

Figure 1: XRD powder pattern and line profile fitting of: a) Fe_3O_4 nanoparticles and b) Fe_3O_4-AA nanocomposite

Slika 1: XRD-difraktogrami in ujemanje linij za: a) nanodelce Fe_3O_4 in b) nanokompozit Fe_3O_4-AA

The solid line corresponds to the best Rietveld profile fit calculated by means of the FULLPROF software for the cubic crystal structure with the Fd-3m space group and X-ray radiation with the wavelength of 0.17928 nm, as used in the experiment. The vertical bars correspond to the Bragg peaks and the line below them is the difference between the experimental data and the fit. XRD studies verified the Fd-3m point group of the Fe_3O_4 nanopowder with the lattice parameters of a = 0.83641 nm and the mean crystallite size of 20 nm determined with the Scherrer method. For the composite, the intensity of diffraction peaks is too low to perform an analysis, even if the content of magnetite is high and equal to w = 10 %.

A TEM image of magnetite nanoparticles is presented in the inset to **Figure 2**. The magnetic nanoparticles are almost monodisperse and spherical. A histogram of the particle-size distribution of Fe_3O_4 nanoparticles is presented in **Figure 2**. The distribution can be fitted with a log-normal function:

$$f(x)=\frac{1}{x\sqrt{2\pi\sigma^2}}\exp\left[-\frac{1}{2\sigma^2}\ln^2\left(\frac{x}{\langle x\rangle}\right)\right] \qquad (1)$$

where $\langle x\rangle$ is the mean size of the nanoparticles and σ is the distribution width. The values characterizing the distribution are: $\langle x\rangle$ = 20.5 nm and σ = 0.11, with $\langle x\rangle$ corresponding well to the XRD data.

Figure 3 shows the topography (panel a), elastic properties (panel b) and magnetic domains (panels c and d) of the Fe_3O_4-AA composite surface with the Fe_3O_4 content of 10 %, studied with MFM. The roughness of the surface is below 10 nm for the scanned area of 500 nm × 500 nm. The knobs on the topography image (the white spots) indicate the presence of small agglomerates of Fe_3O_4 nanoparticles that are also seen as white areas on the phase-contrast image (panel b). The amplitude and phase contrast of the magnetic signal (panels c and d) indicate the presence of magnetic domains with the size close to 100 nm. The actual size of these domains

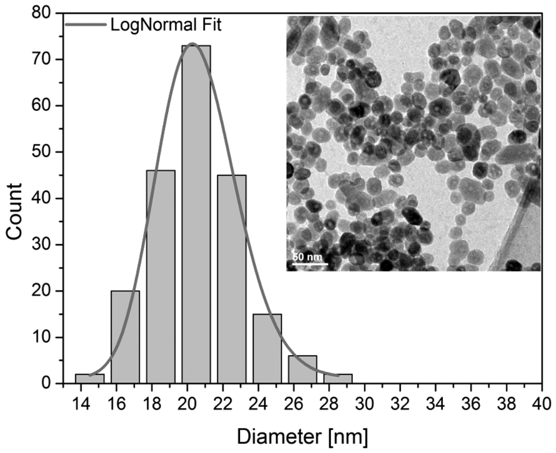

Figure 2: Histogram for Fe_3O_4 nanoparticles with a log-normal fitting. A TEM image is shown in the inset.

Slika 2: Histogram nanodelcev Fe_3O_4. TEM-posnetek je prikazan v vstavku.

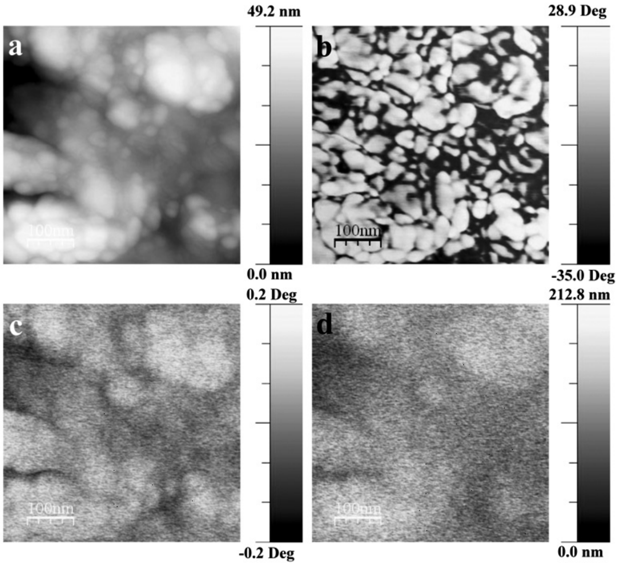

Figure 3: a) Surface topography, b) phase contrast, c) magnetic phase and d) magnetic amplitude images for the Fe_3O_4-AA composite with the Fe_3O_4 mass fraction of 10 %

Slika 3: a) Površinska topografija, b) fazni kontrast, c) magnetna faza in d) magnetna amplituda kompozitov Fe_3O_4-AA z masnim deležem Fe_3O_4 10 %

can be smaller than that presented in the figures because of the insufficient spatial resolution of the MFM method (about 50 nm) which causes a smearing of the images.

The results of the magnetic study are presented in **Figures 4** and **5**. The magnetization is normalized with respect to the content of magnetite in the samples. For the nanoparticles of Fe_3O_4, the temperature dependence of magnetization $M \approx T^{1.9}$ deviates from the Bloch law $M \approx T^{1.5}$ valid for the capped nanoparticles of magnetite (**Figure 4**). The deviation from the Bloch law for the uncapped Fe_3O_4 nanoparticles can be related to a degraded magnetic ordering at the surface. Moreover, the magnetization of the Fe_3O_4 nanoparticles at room temperature is only 51 A m^2/kg, i.e., much below the saturation value for the bulk magnetite ($\approx$ *90 A m*^{2}/kg), and also lower than the magnetization of the capped particles, equal to 60 A m^2/kg. The enhancement of the magnetization and the Bloch-like behavior of the capped nanoparticles can be explained in terms of the recovery of surface magnetism due to the chemical bonding between the AA and Fe_3O_4 nanoparticles. This bonding between the O atoms in the carboxylic groups and two of the four Fe atoms in the Fe-O surface unit cell makes the coordinations and distances close to those in the bulk.[9] The remaining two Fe atoms still exhibit a reduced magnetization because they are closer to the in-plane oxygens, which results in partially empty $d_{x^2-y^2}$ orbitals. The inhomogeneity with respect to the Fe coordination can be responsible for the increased spin disorder or unconventional magnetism at the Fe_3O_4 surface. This unconventional behavior is manifested as a rapid increase in the magnetization at a low temperature observed for Fe_3O_4-AA composites (**Figure 4**). The alternative explanation of this magnetization upturn assumes a quantization of the spin-wave spectrum due to the finite size of the particles that occurs at low temperatures and is responsible for the deviation from the Bloch law.[12]

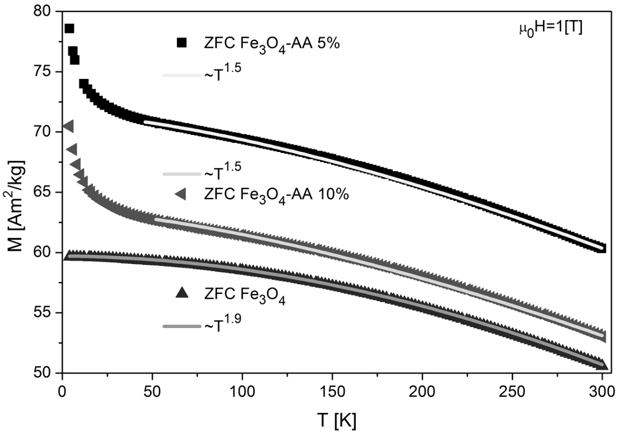

Figure 4: Magnetization $M(T)$ of the Fe_3O_4 nanoparticles and Fe_3O_4-AA composites containing mass fractions 5 % and 10 % of magnetite

Slika 4: Magnetizacija $M(T)$ nanodelcev Fe_3O_4 in kompozitov Fe_3O_4-AA z masnim deležem magnetita 5 % in 10 %

The magnetization loops $M(H)$ for the Fe_3O_4 nanoparticles and Fe_3O_4-AA composites are shown in **Figure 5**.

Both the nanoparticles and composites exhibit ferromagnetic (ferrimagnetic) hysteresis loops, which saturate above about 0.3 T. The magnetization of the composites is enhanced as compared to that of the uncapped Fe_3O_4 nanoparticles. At low temperatures the magnetization loops for the composites are the superpositions of the ferromagnetic and linear contribution from an unconventional magnetism. This unconventional behavior cannot be simply related to the paramagnetism at the degraded

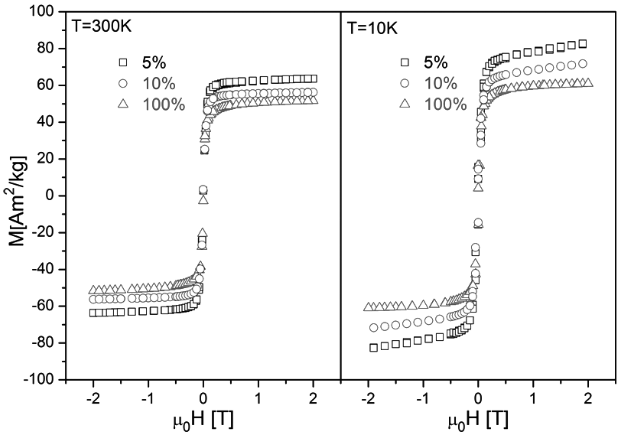

Figure 5: Magnetization loops $M(H)$ for the Fe_3O_4 nanoparticles and Fe_3O_4-AA composites with mass fractions 5 % and 10 % of the magnetite content

Slika 5: Histerezna zanka $M(H)$ nanodelcev Fe_3O_4 in kompozitov Fe_3O_4-AA z masnim deležem magnetita 5 % in 10 %

Fe_3O_4 surface because it is absent in the uncapped nanoparticles of magnetite.

4 CONCLUSIONS

The capping of Fe_3O_4 nanoparticles with alginic acid leads to a partial recovery of the surface magnetization. On the other hand, the bonding between alginic acid and Fe_3O_4 nanoparticles by means of O atoms results in an unconventional magnetism observed at low temperatures.

Acknowledgments

This project was supported by the National Science Centre through project No. N N507 229040. M.K. was supported through the European Union – European Social Fund and Human Capital – National Cohesion Strategy. We thank dr. Alja Kupec and dr. Brigita Rožič for the Slovenian translation.

5 REFERENCES

[1] D. Weller, A. Moser, IEEE Trans. Magn., 35 (**1999**), 4423

[2] I. Koh, L. Josephson, Sensors, 9 (**2009**), 8130

[3] C. W. Jung, P. Jacobs, Mag. Reson. Imaging, 13 (**1995**), 661

[4] S. Bucak, B. Yavuztürk, A. D. Sezer, Magnetic Nanoparticles: Synthesis, Surface Modifications and Application in Drug Delivery, In: A. D. Sezer (ed.), Recent Advances in Novel Drug Carrier Systems, InTech Publisher, 2012

[5] P. Wunderbaldinger, L. Josephson, R. Weissleder, Bioconjugate Chem., 13 (**2002**), 264

[6] R. R. Baker, J. G. Mather, J. H. Kennaugh, Nature, 301 (**1983**), 79

[7] F. Walz, J. Phys.: Condens. Matter, 14 (**2002**), R285

[8] E. Sówka, M. Leonowicz, B. Andrzejewski, A. D. Pomogailo, G. I. Dzhardimalieva, J. Alloys Comp., 423 (**2006**), 123

[9] J. Salafranca, J. Gazquez, N. Pérez, A. Labarta, S. T. Pantelides, S. J. Pennycook, X. Batlle, M. Varela, Nano Letters, 12 (**2012**), 2499

[10] Z. Durmus, H. Sözeri, B. Unal, A. Baykal, R. Topkaya, S. Kazan, M. S. Toprak, Polyhedron, 30 (**2011**), 322

[11] B. Unal, M. S. Toprak, Z. Durmus, H. Sözeri, A. Baykal, J. Nanopart. Res., 12 (**2010**), 3039

[12] K. Mandal, S. Mitra, P. A. Kumar, Europhys. Lett., 75 (**2006**), 618

UDK 620.186:621.78
Original scientific article/Izvirni znanstveni članek

ISSN 1580-2949
MTAEC9, 48(5)679(2014)

MICROSTRUCTURAL COMPARISON OF THE THERMOMECHANICALLY TREATED AND COLD DEFORMED Nb-MICROALLOYED TRIP STEEL

PRIMERJAVA MIKROSTRUKTUR TERMOMEHANSKO OBDELANEGA IN HLADNO DEFORMIRANEGA, Z Nb-MIKROLEGIRANEGA TRIP-JEKLA

Adam Grajcar[1], **Krzysztof Radwański**[2]
[1]Silesian University of Technology, Institute of Engineering Materials and Biomaterials, 18a Konarskiego Street, 44-100 Gliwice, Poland
[2]Institute for Ferrous Metallurgy, 12-14 K. Miarki Street, 44-100 Gliwice, Poland
adam.grajcar@polsl.pl

Prejem rokopisa – received: 2013-09-30; sprejem za objavo – accepted for publication: 2013-11-04

The work deals with a microstructural comparison of the thermomechanically processed and subsequently cold deformed Nb-microalloyed Si-Al-type multiphase steel, showing a TRIP effect. The newly developed steel was subjected to the thermomechanical rolling and controlled cooling under the conditions allowing us to obtain a fine-grained ferritic-bainitic microstructure with a large fraction of the retained austenite. Subsequently, the thermomechanically rolled sheet samples were subjected to a 10 % elongation in uniaxial tension. The comparison of the multiphase microstructures and, especially, the identification of the strain-induced martensite were carried out using light microscopy, electron transmission microscopy and electron scanning microscopy equipped with EBSD (electron backscatter diffraction). Morphological details influencing the mechanical stability of the retained austenite were indicated.

Keywords: thermomechanical treatment, TRIP effect, multiphase steel, retained austenite, strain-induced martensite, EBSD technique

Delo obravnava primerjavo mikrostruktur termomehansko obdelanega in nato hladno deformiranega, z Nb-mikrolegiranega večfaznega jekla Al-Si, ki izkazuje vedenje TRIP. Novo razvito jeklo je bilo termomehansko valjano in kontrolirano ohlajeno v razmerah, ki omogočajo doseganje drobnozrnate feritno-bainitne mikrostrukture z velikim deležem zaostalega avstenita. Termomehansko izvaljani vzorci pločevine so bili nato izpostavljeni 10-odstotnemu raztezku pri enoosni natezni obremenitvi. Primerjava multifaznih mikrostruktur in posebno določanje napetostno induciranega martenzita je bila izvršena s svetlobno mikroskopijo, elektronsko presevno mikroskopijo in elektronsko vrstično mikroskopijo, opremljeno z EBSD (Electron Backscatter Diffraction). Prikazane so morfološke podrobnosti, ki vplivajo na mehansko stabilnost zaostalega avstenita.

Ključne besede: termomehanska obdelava, učinek TRIP, večfazno jeklo, zaostali avstenit, napetostno inducirani martenzit, EBSD-tehnika

1 INTRODUCTION

The mechanical properties and technological formability of advanced high-strength steels (AHSS) for the automotive industry depend on the relative proportions and mechanical properties of individual microstructural constituents. Ferrite forms a matrix of AHSS whereas the strengthening phases consist of martensite and/or bainite. A very attractive combination of high strength and ductility can be obtained in dual-phase (DP) steels consisting of a ferrite matrix and uniformly distributed martensitic or martensitic-bainitic islands.[1–4] A further growth of the strength-ductility balance can be obtained for the steels with a ferritic matrix containing bainitic-austenitic islands, where the final mechanical properties are formed during cold working under the conditions of the strain-induced martensitic transformation of the metastable retained austenite.[5–8] Multiphase steel sheets are produced with the continuous annealing of cold-rolled sheets[3,7] or they are thermomechanically hot rolled and controlled cooled.[8,9] A further increase in the strength properties of multiphase steels requires modified chemical-composition concepts. Recently, Nb, Ti and V microalloying has been used to enhance the strength of multiphase steels[8–10], well known for its beneficial effect in HSLA steels.[11–15]

Thermomechanically processed multiphase steels are characterized by a high-grain refinement. Therefore, the qualitative and quantitative identifications of individual structural constituents are especially important. A determination of the γ-phase volume fraction is achieved using a computer-image analysis after the colour etching, X-ray or neutron diffraction and magnetic methods.[5,6,8,16] Recently, the EBSD technique of a scanning electron microscope (SEM) has had an essential significance in determining the fractions and morphological features of various microstructural constituents.[17–19] Microstructural details of cold-rolled multiphase steels have been characterized to a sufficient extent.[7,17–19] However, there are very few reports concerning morphological details of thermomechanically rolled TRIP steels.[9] Hence, the present study addresses the microstructure evolution of a hot-rolled Nb-microalloyed Si-Al multiphase steel.

2 EXPERIMENTAL PROCEDURE

The chemical composition of the newly developed steel was designed with the focus on maximizing the retained-austenite fraction and obtaining the carbide-free bainite. The steel contains: 0.24 % C, 1.55 % Mn, 0.87 % Si, 0.40 % Al, 0.034 % Nb, 0.023 % Ti, 0.004 % S and 0.010 % P. Nb and Ti were used to increase the strength and to achieve the grain refinement during hot rolling. The ingot was produced with vacuum induction melting and then it was hot forged to a thickness of 22 mm. Subsequently, the flat samples were roughly rolled to a thickness of 4.5 mm within the temperature range between 1200 °C and 900 °C. The thermomechanical rolling was conducted in 3 passes between 1100 °C and 850 °C to the final sheet thickness of about 2 mm. After the final deformation at 850 °C the specimens were air cooled to 700 °C and then slowly to the temperature of 650 °C for 50 s using furnace cooling. The next step included immerse cooling of the sheets at a rate of about 50 °C/s, using a water-polymer medium, to the isothermal holding temperature (450 °C) at the bainitic transformation range. The specimens were held at 450 °C for 600 s and finally cooled at a rate of about 0.5 °C/s to room temperature. Then, standard-sized, A50 tensile-test samples with a gauge length of 50 mm and a width of 12.5 mm were cut parallel to the rolling direction of the sheets and deformed to 10 % of the plastic strain at a strain rate of 5×10^{-3} s^{-1}. Metallographic specimens were taken at different points along the rolling direction for both thermomechanically processed samples and those subjected to cold deformation.

For the purpose of a detailed analysis of all the microstructural constituents and, especially, to identify the strain-induced martensitic transformation, light microscopy (LM), scanning electron microscopy (SEM) and transmission electron microscopy (TEM) were used. Additionally, orientation imaging microscopy (OIM) using SEM was applied. Etching in a 10 % aqueous solution of sodium metabisulfite was used. Metallographic observations at the magnification of 1000-times were carried out with a Leica MEF 4A light microscope. Morphological details of microstructural constituents of the steel were revealed with SUPRA 25 SEM using back-scattered electrons (BSE). Observations were performed on nital-etched samples at the accelerating voltage of 20 kV. The EBSD technique was performed using Inspect F SEM equipped with Shottky field emission. After the classical grinding and polishing, the specimens were polished with Al_2O_3 with a granularity of 0.1 µm. The final stage of the sample preparation was the ion polishing using the GATAN 682 PECS system. A fraction of the retained austenite in both the initial state and after cold deformation, assessed with EBSD (the average value of five measurements) was determined at a magnification lower than 3000-times to obtain reliable quantitative results.

The thin-foil investigations were carried out using a JEOL JEM 3010 at the accelerating voltage of 200 kV. Mechanically grinded disk specimens were polished at the voltage of 17 V and current density of 0.2 A/cm². The mixture of 490 mL H_3PO_4 + 7 mL H_2SO_4 + 50 g CrO_3 was used as the electrolyte.

3 RESULTS AND DISCUSSION

Applying the thermomechanical rolling and controlled cooling results in a fine-grained ferritic matrix with a volume fraction of about 60 % containing uniformly distributed bainitic-austenitic and austenitic islands (**Figure 1a**). The amount of the retained austenite determined by EBSD is about 13.8 %. The carbon content (C_γ) of the γ phase determined earlier[8] using the

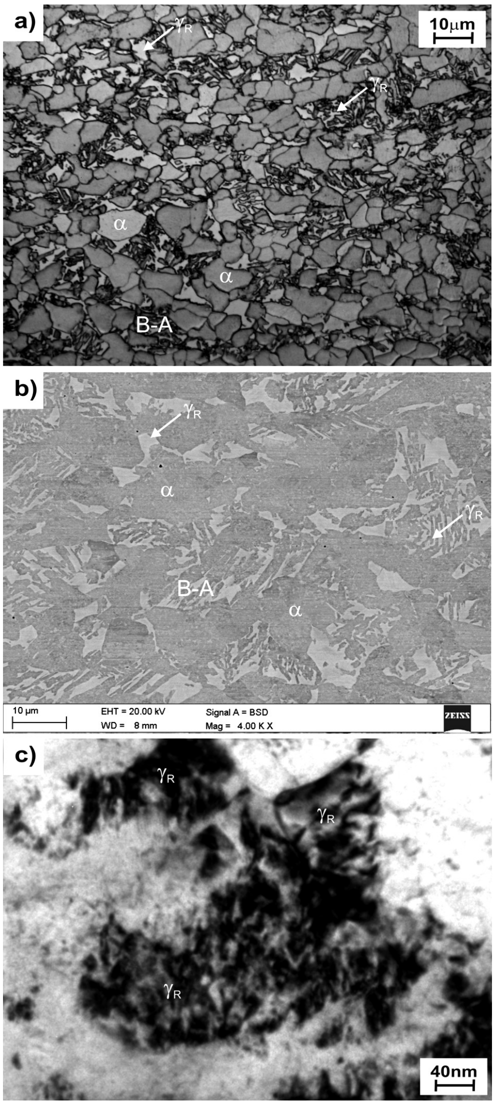

Figure 1: a), b) Fine-grained ferritic matrix containing bainitic-austenitic and austenitic islands after the thermomechanical processing and c) the finest regions of the retained austenite; α – ferrite, B-A – bainitic-austenitic islands, γ_R – retained austenite

Slika 1: a), b) Drobnozrnata feritna osnova vsebuje po termomehanski obdelavi bainitno-avstenitne in avstenitne otočke in c) najdrobnejša področja zaostalega avstenita; α – ferit, B-A – bainitnoavstenitni otočki, γ_R – zaostali avstenit

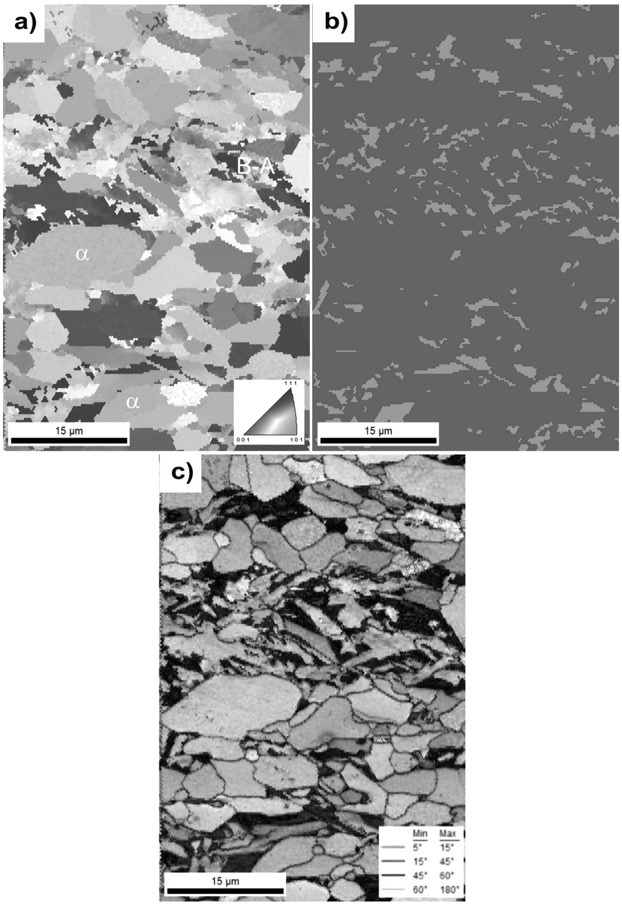

Figure 2: Microstructure images of the thermomechanically processed steel obtained with EBSD: a) inverse pole-figure map showing the grains with different crystallographic orientations, b) marked regions of the retained austenite, c) image-quality map with crystallographic misorientation angles

Slika 2: EBSD-posnetki mikrostrukture termomehansko predelanega jekla: a) zemljevid inverznih polovih figur, ki prikazuje zrna z različno kristalografsko orientacijo, b) označena področja zaostalega avstenita, c) zemljevid kvalitete zrn s kristalografsko različnimi koti

X-ray analysis equals mass fraction 1.14 %, which corresponds to lowering the martensite start temperature of the γ phase to about 10 °C. The mean ferrite grain size is equal to 6 μm and the retained austenite is located along the ferrite boundaries as blocky grains with the size up to 5 μm. Some retained austenite forms a halo around the α-phase grains whereas another part is located at the ferrite-bainite interfaces. A large fraction of the retained austenite, formed as thin layers or small blocky grains with the size of between 1 μm and 3 μm, is a constituent of the bainitic islands (B-A) (**Figure 1b**). A utilization of TEM reveals the finest regions of the retained austenite with the sizes from 50 nm to 200 nm (**Figure 1c**).

Figure 2 is an EBSD map using colour coding for determining individual grains. The inverse-pole figure (**Figure 2a**) shows the crystal direction parallel to the normal direction of the specimen using the colour coding according to the unit triangle. The grains of the highest size with a random crystallographic orientation can be recognized as ferrite. In the grey-scale image-quality (IQ) map (**Figure 2c**) they correspond to the brightest regions of the best diffraction quality. The IQ factor represents a quantitative description of the sharpness of the EBSD pattern. A lattice distorted by crystalline defects such as dislocations and subgrain boundaries has a distorted Kikuchi pattern, leading to lower IQ values.[7,8] The retained austenite, bainite and grain boundaries are represented by different levels of dark grey because their pattern contrast is lower than that of the ferrite. The color-coded phase map in **Figure 2b** clearly shows the distribution of the retained austenite. The BCC constituents and the retained austenite are distinguished on the basis of the differences in their crystal structures, whereas for a discrimination of the bainite from the ferrite the differences in the IQ values have to be used.

Due to a very small size of the retained austenite, its phase map is highly fragmented. The grain area of the retained-austenite particles covers a range of up to 14 μm^2 but the majority of the grains is smaller than 6 μm^2 (**Figure 3**). Having the knowledge of the retained-austenite presence and analyzing the IQ map in **Figure 2c** as well as the misorientation-angle distribution of the retained austenite (**Figure 4**), it is possible to indicate the bainite regions. Firstly, this phase always occurs in conjunction with the retained austenite and, secondly, having high-lattice imperfections, it corresponds to the dark regions of the low IQ. High-angle boundaries (> 15°) occur between the ferrite grains, BCC constituents and the retained austenite as well as between the ferrite and the bainite (**Figure 2c**). A large fraction of the retained austenite exhibits a misorientation angle close to 45° with the neighboring BCC constituents (**Figure 4**). This is in line with the earlier results obtained by Zaefferer et al.[19] for the 0.2C-1.4Mn-0.5Si-0.7Al steel and Petrov et al.[7], Wasilkowska et al.[18] for the 0.2C-1.5Mn-1.5Si steel, according to which bainite regions require a Kurdjumov-Sachs (K-S) or Nishiyama-Wasserman

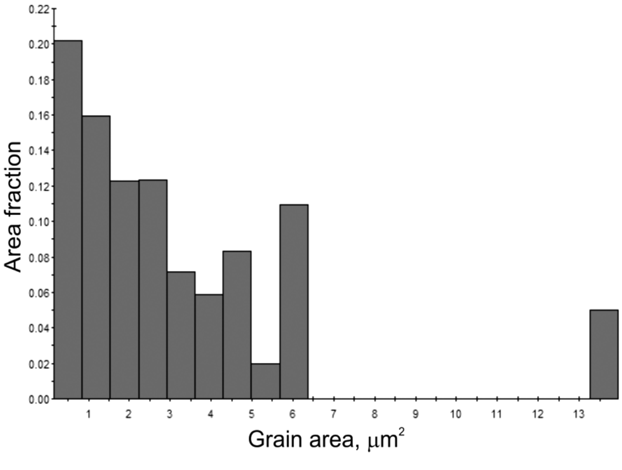

Figure 3: Distribution of the retained-austenite grain area

Slika 3: Razporeditev področij zrn zaostalega avstenita

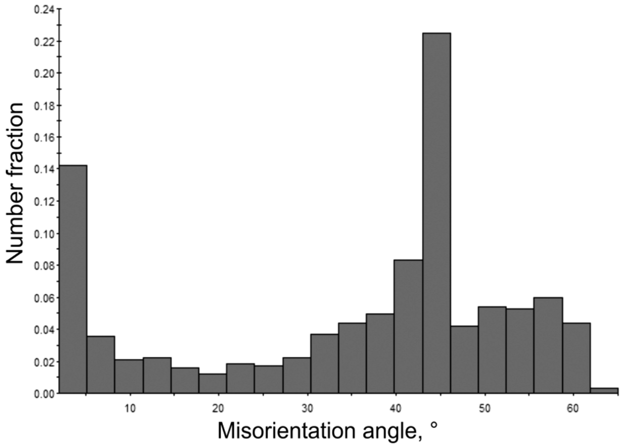

Figure 4: Distribution of the crystallographic misorientation angles of the grains

Slika 4: Razporeditev zrn z različnimi kristalografskimi koti

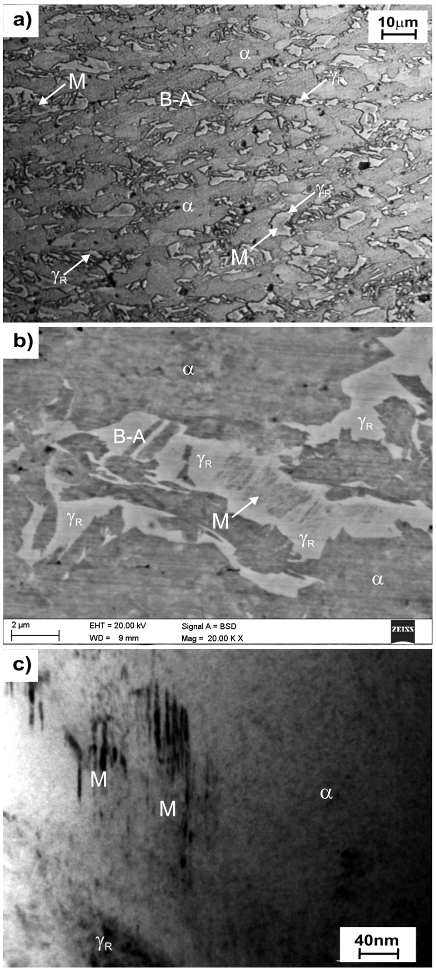

Figure 5: a), b) Ferritic-bainitic microstructures containing the retained austenite and strain-induced martensite of the steel strained to the elongation of 10 %, c) plate morphology of the strain-induced martensite; α – ferrite, B-A – bainitic-austenitic islands, γ_R – retained austenite, M – martensite

Slika 5: a), b) Feritno-bainitna mikrostruktura z zaostalim avstenitom in napetostno induciranim martenzitom v jeklu z 10-odstotno natezno deformacijo, c) ploščata morfologija napetostno induciranega martenzita; α – ferit, B-A – bainitno-avstenitni otočki, γ_R – zaostali avstenit, M – martenzit

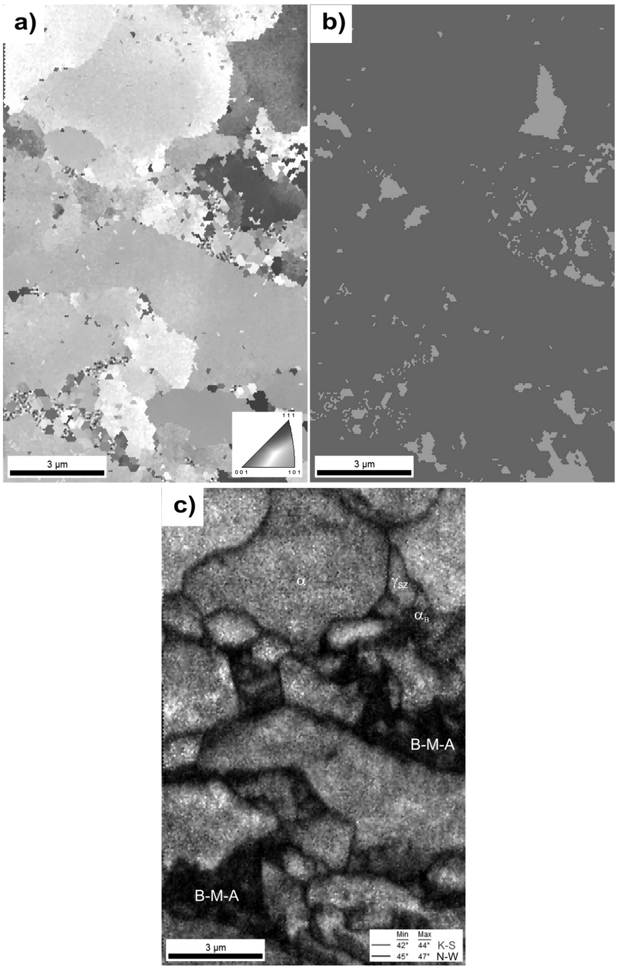

Figure 6: Microstructure images of the steel strained to the elongation of 10 %: a) inverse pole-figure map showing grains with different crystallographic orientations, b) marked regions of the retained austenite, c) image-quality map with the crystallographic misorientation angles corresponding to the K-S and N-W relationships; α – ferrite, α_B – bainitic ferrite, B-M-A – bainitic-martensitic-austenitic regions, γ_{SZ} – retained austenite

Slika 6: Posnetki mikrostrukture jekla, natezno obremenjenega do raztezka 10 %: a) zemljevid inverznih polovih figur, ki prikazujejo zrna z različno kristalografsko orientacijo, b) označena področja zaostalega avstenita, c) zemljevid kvalitete z različnimi kristalografskimi koti, ustrezno razmerjem K-S in N-W; α – ferit, α_B – bainitni ferit, B-M-A – bainitno-martenzitno-avstenitno področje, γ_{SZ} – zaostali avstenit

(N-W) orientation for their growth, confirming a displacive growth mechanism of bainite.

The γ-phase content decreases to about 7.7 % after applying a 10 % tensile strain. It corresponds to the 44 % initial austenite volume fraction transformed into martensite due to a strain-induced transformation. Generally, the strain-induced martensitic transformation initially proceeds in the largest and medium-sized austenite grains located in a ferritic matrix (**Figure 5a**). Martensite usually forms in the central zones of the grains whereas the borders remain untransformed (**Figure 5b**). This confirms a higher enrichment in carbon of the regions adjacent to the ferrite grains and a smaller enrichment of the central austenite regions as a result of a longer

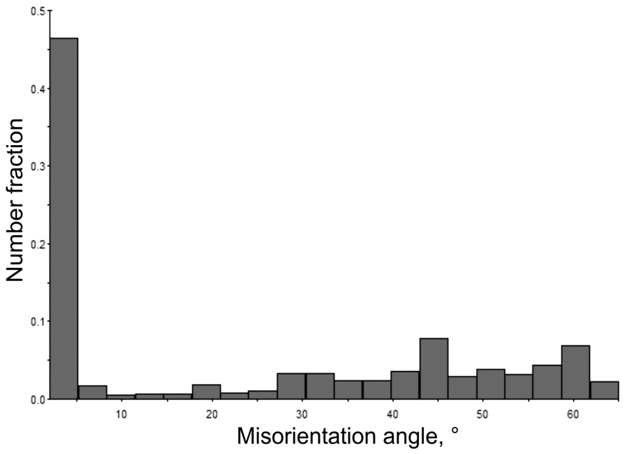

Figure 7: Distribution of crystallographic misorientation angles of the grains after cold deformation
Slika 7: Razporeditev zrn s kristalografsko različnimi koti po hladni deformaciji

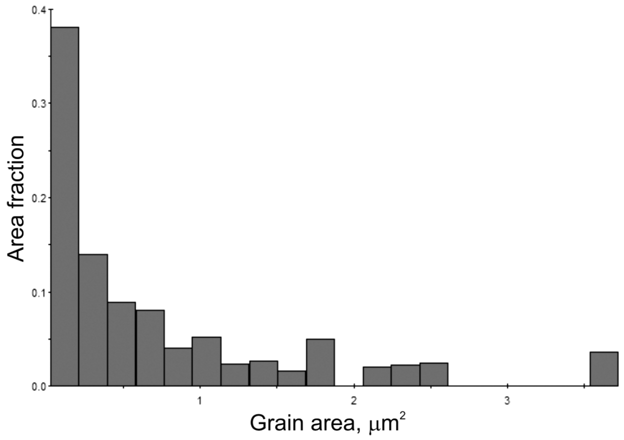

Figure 8: Distribution of the retained-austenite grain area of the cold-deformed steel
Slika 8: Razporeditev področij zrn zaostalega avstenita hladno deformiranega jekla

diffusion path of carbon. The formed martensite has a plate morphology (**Figure 5c**) and it contributes to a fragmentation of the untransformed austenite fostering its further stabilization due to a reduction in the particle size. It is clear from **Figure 6** that the strain-induced martensitic transformation is also initiated inside the largest bainitic-austenitic islands resulting in a further fragmentation of γ-phase particles. Moreover, the detailed analysis from **Figure 6c** indicates that the K-S and N-W relationships are partially kept between the austenite and the bainitic ferrite. However, the fraction fulfilling the special crystallographic orientations decreases (**Figure 7**) compared to the initial state (**Figure 4**). The fragmentation of the retained austenite is revealed through a reduction of the grain-size area below 4 μm^2 (**Figure 8**). It should be noted that the fraction of the grain area changes roughly in proportion to the inverse of the particle size.

4 CONCLUSIONS

A detailed identification of the morphological features of individual microstructural constituents of thermomechanically processed multiphase steels is a challenging problem due to a high dispersion of particular phases. The problem becomes even more complicated during cold deformation, when the highly dispersed retained austenite transforms into the strain-induced martensite. It was shown that the investigated Si-Al TRIP steel is characterized by a fine-grained ferritic matrix containing bainitic-austenitic and austenitic islands. The retained austenite occurs as small blocky grains or thin layers forming bainitic-austenitic islands. The strain-induced martensite initially forms in large and medium-sized austenite grains located along the boundaries of the α phase. The transformation is initiated in the central parts of the grains whereas the border regions of the austenite remain untransformed. The essential effect increasing the stability of the retained austenite against the strain-induced martensite is a fragmentation of the γ-phase regions. This effect is additionally enhanced by the neighboring bainitic-ferrite laths and the formed plate martensite creating a hydrostatic pressure against the deformation progress.

5 REFERENCES

[1] M. Pouranvari, E. Ranjbarnoodeh, Mater. Tehnol., 46 (**2012**) 6, 665–671
[2] M. Weglowski, K. Kwiecinski, K. Krasnowski, R. Jachym, Arch. Civ. Mech. Eng., 9 (**2009**), 85–97
[3] M. Pernach, K. Bzowski, R. Kuziak, M. Pietrzyk, Mater. Sci. Forum, 762 (**2013**), 699–704
[4] Z. Gronostajski, A. Niechajowicz, S. Polak, Arch. Metall. Mater., 55 (**2010**), 221–230
[5] S. Wiewiorowska, Steel Res. Int., 81 (**2010**), 262–265
[6] A. Kokosza, J. Pacyna, Arch. Metall. Mater., 55 (**2010**), 1001–1006
[7] R. Petrov, L. Kestens, A. Wasilkowska, Y. Houbaert, Mater. Sci. Eng. A, 447 (**2007**), 285–297
[8] A. Grajcar, K. Radwanski, H. Krzton, Solid State Phenom., 203–204 (**2013**), 34–37
[9] I. B. Timokhina, P. D. Hodgson, E. V. Pereloma, Metall. Mater. Trans. A, 35 (**2004**), 2331–2341
[10] J. Jung, S. J. Lee, S. Kim, B. C. De Cooman, Steel Res. Int., 82 (**2011**), 857–865
[11] D. A. Skobir, Mater. Tehnol., 45 (**2011**) 4, 295–301
[12] J. Majta, K. Muszka, Mater. Sci. Eng. A., 464 (**2007**), 186–191
[13] D. A. Skobir, M. Godec, M. Balcar, M. Jenko, Mater. Tehnol., 44 (**2010**) 6, 343–347
[14] A. Lisiecki, Proc. of the 10th Conf. on Laser Technology – Applications of Lasers, 8703 (**2013**), DOI: 10.1117/12.2013429
[15] M. Opiela, A. Grajcar, Arch. Civ. Mech. Eng., 12 (**2012**), 427–435
[16] C. P. Scott, J. Drillet, Scripta Mater., 56 (**2007**), 489–492
[17] J. Wu, P. J. Wray, C. I. Garcia, M. Hua, A. J. DeArdo, ISIJ Int., 45 (**2005**), 254–262
[18] A. Wasilkowska, R. Petrov, L. Kestens, E. A. Werner, C. Krempaszky, S. Traint, A. Pichler, ISIJ Int., 46 (**2006**), 302–309
[19] S. Zaefferer, J. Ohlert, W. Bleck, Acta Mater., 52 (**2004**), 2765–2778

UDK 621.74.042:54-145.55:669.787
Original scientific article/Izvirni znanstveni članek

ISSN 1580-2949
MTAEC9, 48(5)685(2014)

CONTROL OF THE METALLURGICAL PROCESSING OF ICDP CAST IRONS

KONTROLA METALURŠKE OBDELAVE LITEGA ŽELEZA ICDP

Jiří Hampl[1], Tomáš Válek[2], Petr Lichý[1], Tomáš Elbel[1]
[1]VŠB -Technical University of Ostrava, FMMI, Department of Metallurgy and Foundry, 17. listopadu 15/2172, 708 33 Ostrava, Czech Republic
[2]Vítkovické slévárny spol., s. r. o., Halasova 2904/1, Ostrava –Vítkovice, Czech Republic
jiri.hampl@vsb.cz

Prejem rokopisa – received: 2013-09-30; sprejem za objavo – accepted for publication: 2013-11-18

The article is focused on the use of the measurement of oxygen activity for the management of cast-iron metallurgical processing in the operating conditions of a centrifugal-roll casting foundry. The paper presents the results of the oxygen-activity measurement recorded during the metallurgical processing of cast iron from the beginning of the melting to the inoculation of cast iron. The measurement of oxygen activity was made with specifically developed devices and the probes with a high sensitivity designed for measuring a_O in cast iron by Heraeus Electro-Nite Celox Foundry. The oxygen activities in cast iron correlate with the properties of cast iron.

Keywords: oxygen activity, ICDP iron, inoculation

Članek je osredinjen na merjenje aktivnosti kisika za vodenje metalurške obdelave litega železa v livarni pri centrifugalnem ulivanju valjev. Članek predstavlja rezultate meritev aktivnosti kisika, spremljane med metalurško obdelavo litega železa od začetka taljenja do inokulacije litega železa. Meritev aktivnosti kisika je bila izvršena s posebno razvito napravo in sondo z veliko občutljivostjo za merjenje a_O v litem železu s Celox – Foundry Heraeus ElectroNite. Aktivnosti kisika v litem železu so odvisne od lastnosti litega železa.

Ključne besede: aktivnost kisika, ICDP-železo, inokulacija

1 INTRODUCTION

The methods for the control of the metallurgical processing of cast iron in the molten state are based on the analyses of solid samples, i.e., the thermal analysis, the chill test and the spectral analysis. For a quick interpretation of the metallurgical quality of molten cast iron, the measurement of oxygen activity can be used too. The measurements are made in the furnace after melting, in the last stage before casting, after the inoculation or modification in the ladle. It is possible to rapidly analyse the level of metallurgical processing (quality) of the melt on the basis of the measured oxygen activity in real time and, if necessary, to make its adjustment.

2 OXYGEN IN CAST IRON

The oxygen content in molten cast iron influences the mechanism of solidification in the phase of eutectic transformation and it has positive, but also negative, effects on molten cast iron. The positive role of oxygen is primarily to support the formation of stable oxides for the crystallization of graphite; it also supports the heterogeneous nucleation and stabilises the solidification of cast iron. An intense formation of graphitization nuclei occurs during the transition of a melt into the solid phase, especially during the eutectic transformation. During this solidification phase, the optimum amount of oxygen has to be available.

A higher oxygen activity is also able to support the formation of exogenous and endogenous gas bubbles and pinholes in cast iron, or an increased amount of slag and inclusions in the castings. Excessive amounts of oxides can be unstable at elevated temperatures, and under certain conditions (the temperature, time, and viscosity of the melt) they dissociate or coagulate, creating an increased amount of slag. The oxygen activity in cast irons is strongly dependent on the temperature. The oxygen activity is increased by the liquidus temperature as a consequence of a release of the crystallization heat. The heat is secreted from the austenite in the concentration melt of carbon. This creates good conditions for the graphite nuclei.

A drop in the liquidus temperature starts a decrease in the oxygen activity, taking place until the beginning of the eutectic reaction. The decline in the oxygen activity is simultaneously accompanied by a formation of oxides. An increase in the oxygen activity occurs again during the eutectic transformation, as a consequence of the crystallization-heat eutectic reaction.[1,2]

The measurement of oxygen activity is normally used to control the deoxidation process of steel during the melting and casting of steel castings.

The oxygen activities in molten steel are of a higher-order, in the range of 10×10^{-6} to 100×10^{-6}, depending on the degree of deoxidation under the temperature of molten steel. Relatively high levels of oxygen activity in steel during melting correspond to the sensitivity of the probes used for the measurement (ppm).

Table 1: Informative chemical composition of the ICDP iron (*w*/%)
Tabela 1: Okvirna kemijska sestava ICDP-železa (*w*/%)

C	Mn	Si	P_{max}	S_{max}	Cr	Ni	Mo
3.0 3.5	0.5 1.5	0.7 1.5	0.1	0.03	1.5 2.0	3.8 4.8	0.2 1.0

The oxygen activity in cast iron is by about 3–4 orders of magnitude lower than that of steel, depending on whether it is measured in the cast iron with lamellar or spheroidal graphite (**Figure 1**). The relationship between the oxygen activity and the shape of graphite in the processed FeSiMg cast irons was set with the Mampay and CELOX-Foundry equipment for measuring oxygen activity, the Heraeus Electro-Nite company[3–5].

The way of the metallurgical processing of cast iron, i.e., the management of the melt, the holding temperature and the time greatly influence the oxygen content, i.e., its activity in cast iron and the metallurgical quality of cast iron[6–8]. The default level of the oxygen activity in cast iron before an inoculation or modification consequently influences its graphitization ability, the process of crystallization, the microstructure and the resulting quality of the castings.

3 METALLURGICAL PROCESSING OF CAST IRON

The melting of the shell iron (ICDP – Indefinite Child Double Pour) of the centrifugally cast rolls was performed in 4-ton electric induction furnaces. The regulation of the chemical composition of iron (alloy) was performed in the furnaces and the subsequent inoculation was performed in the ladles. In total, 14 melts were analyzed. The microstructure of the ICDP iron is formed by the ledeburite basic metal material (BMM), in which there is extruded graphite whose surface portion is optimized in the range of 2–5 % in the evaluated area of the scratch pattern. The cast iron is controlled during its melting with a spectral analysis and cooling curves analyses[7,9].

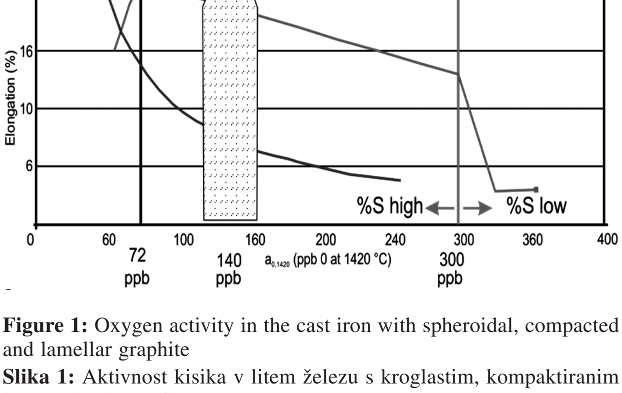

Figure 1: Oxygen activity in the cast iron with spheroidal, compacted and lamellar graphite
Slika 1: Aktivnost kisika v litem železu s kroglastim, kompaktiranim in lamelarnim grafitom

An informative chemical composition of the ICDP iron is shown in **Table 1**. The samples are sampled from the castings for metallurgical analyses, the tests of the quantity of graphite and of the hardness.

Table 2: Timeline of the melts and the measured values of oxygen activities, a_{O}
Tabela 2: Potek izdelave taline in izmerjene vrednosti aktivnosti kisika, a_0

Number of the melt	End of melting (h:min)	Dwell time of the charge (h:min)	a_{O} (10^{-9}) Furnace	a_{O} (10^{-9}) Ladle	Δa_{O} (10^{-9}) F-L
1	1:30	2:06	1159.9	699.8	460.1
2	1:40	1:40	932	721.2	210.8
3	1:40	1:30	996.1	718	278.1
4	1:40	2:00	829.3	693.5	135.8
5	1:10	3:50	877.6	766.2	111.4
6	1:40	0:45	1522.9	695.4	827.5
7	2:00	1:33	1496	708.7	787.3
8	1:20	0:55	1213.7	726.9	486.8
9	2:00	2:30	1028	700	328
10	1:20	1:20	895	518.5	376.5
11	2:25	6:20	811.4	792.63	18.77
12	1:20	0:55	1034.1	709.04	325.06
13	2:00	2:35	797.7	717.2	80.5
14	1:20	1:15	874.4	717.2	157.2

4 METHODOLOGY FOR MEASURING OXYGEN ACTIVITY

For the measurement of the oxygen activity we used Multi-Lab III by Heraeus Electro-Nite, which consists of a generator, connecting cables and a vibrating lance with a single measuring probe. The measured values are: the temperature (°C), the Emf electromotive voltage (mV), converted to a value of the oxygen activity by the melt temperature and the oxygen activity, converted to a reference temperature of 1420 °C. The reference temperatures are shown in the measurement results. The measured values are displayed on the display device in real time approximately 20–30 s after the immersion of the probe into the melt.

The aim of the measurement was to measure the oxygen activity after every metallurgical processing of the ICDP cast iron in real time in the interval of the melting of the charge, while keeping the iron at the set temperature until the inoculation in the ladle. The timeline of the melts (h) and the measured values of the oxygen activities (a_{O}) are shown in **Table 2**.

The graph in **Figure 2** presents the dependency of the oxygen activity (a_{O}) on the time (h) of melting in the furnace. The highest activity was measured in the melts with the shortest dwell time at the set temperature.

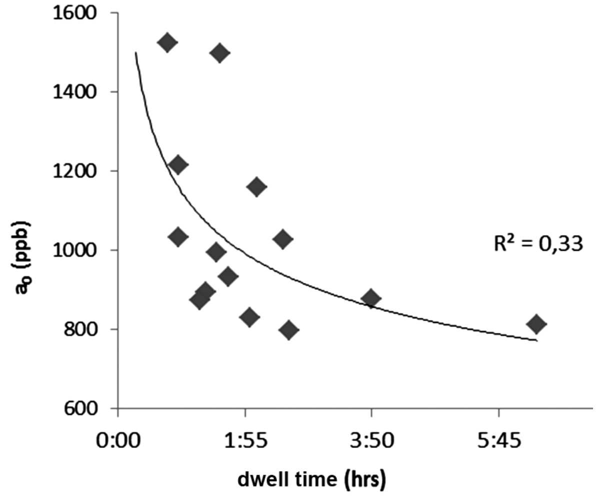

Figure 2: Oxygen activity (a_O) dependent on the dwell time (h) of the melt in the furnace

Slika 2: Odvisnost aktivnosti kisika (a_O) od časa (h) med držanjem taline v peči

With an increasing dwell time in the furnace, the oxygen activities gradually decrease from the maximum value of 1522.9×10^{-9} at the dwell time of 45 min up to the lowest value of 811.4×10^{-9} at the dwell time of 6.3 h.

Figure 3 shows the dependence of the oxygen activity (a_O) measured in the ladle after the inoculation and the dwell time of the melt in the furnace. For the melt with the shortest dwell time, the oxygen activity was measured to be $a_O = 1522.9 \times 10^{-9}$ and after the inoculation it was $a_O = 695.4 \times 10^{-9}$. In this case, the difference in the activities a_O before and after the inoculation is the largest (54 %).

In contrast, for the melt with the longest dwell time, the lowest activity, $a_O = 811.4 \times 10^{-9}$, was measured in the furnace and after the inoculation in the ladle, it was $a_O = 792.63 \times 10^{-9}$. The decrease was only 18.8×10^{-9}. In this case the difference in the oxygen activity before and after the inoculation is only 2.5 %.

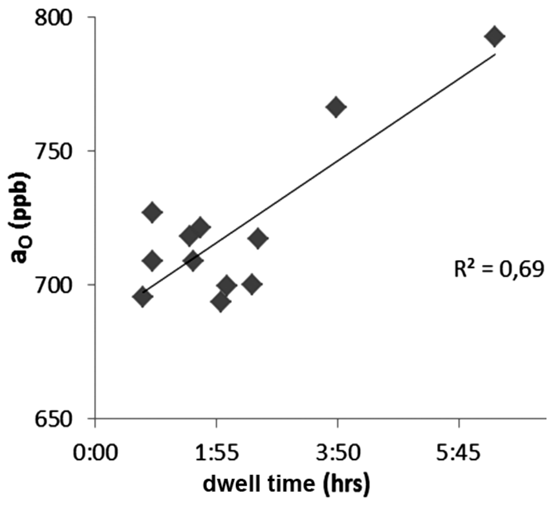

Figure 3: Oxygen activity a_O in the ladle after the inoculation and the dwell time

Slika 3: Aktivnost kisika a_O v ponvi po inokulaciji in času zadržanja

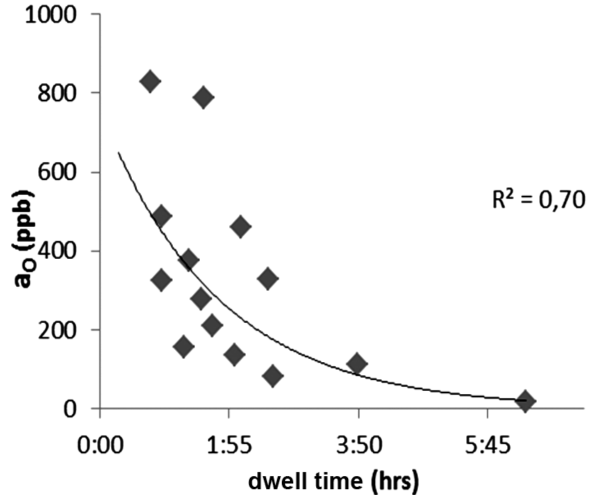

Figure 4: Difference between the initial oxygen activity a_O and the finishing a_O

Slika 4: Razlika med začetno aktivnostjo kisika a_0 in končno aktivnostjo kisika a_O

The differences between the initial oxygen activity a_O in the furnace, before pouring the melt into the ladle, and the finishing a_O, after the inoculation in the ladle (**Figure 4**) show a similarly decreasing trend as the activity a_O in the furnace depends on the dwell time of the cast iron (**Figure 2**).

5 RESULTS AND DISCUSSION

The oxygen activities were measured for the molten ICDP iron in an electric induction furnace, showing a large range of measured values (711.5×10^{-9}). The

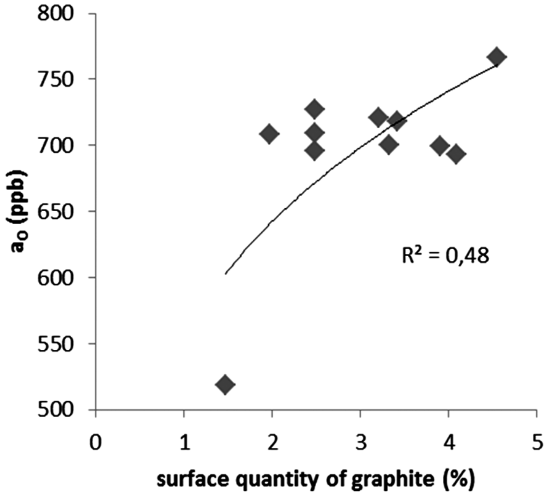

Figure 5: Dependence of the oxygen activity in the ladle and the surface quantity of graphite

Slika 5: Odvisnost med aktivnostjo kisika v ponvi in količino grafita na površini measurements were in the range of 1522.9×10^{-9} up to 811.4×10^{-9}.

The oxygen activities were measured after the inoculation in the ladle (**Figure 2**). A relatively narrow range of values (99.4×10^{-9}) from the lowest activity of $a_{\mathrm{O}} = 693.5 \times 10^{-9}$ to the highest activity of $a_{\mathrm{O}} = 792.6 \times 10^{-9}$ was measured.

The oxygen activities in the iron covered a relatively wide range after the melting and the dwell time. It was caused by different melting times. After the inoculation a narrow range of oxygen activities was measured in the ladle. This corresponds to the criterion set for the optimum quantity of graphite (2–5 %) in the ledeburite base of the metal mass of the ICDP iron (**Figure 5**). The quantity of graphite was established on the basis of an image analysis.

6 CONCLUSIONS

On the basis of an evaluation of these melts, it can be concluded that the value of about $a_{\mathrm{O}} = 700 \times 10^{-9}$, obtained after the inoculation, provides the optimum level of metallurgical quality of this iron (type ICDP).

By measuring the oxygen activity a_{O} (10^{-9}) in real time, metallurgical processing and quality can be evaluated relatively quickly so as to achieve the desired parameters of the casting.

Acknowledgements

The paper was prepared with the financial support from the Ministry of Industry and Trade of the Czech Republic within the TIP project Nr TIP: FR-TI2/188 "Research and development of working-layer materials of spun-cast multi-layered rolls focused to modern trends of rolling mills".

7 REFERENCES

[1] Z. Bůžek, Základní termodynamické výpočty, Hutnické aktuality, Informetal, 1988, VÚHŽ

[2] I. C. Kulikov, Raskislenije metalov, Metalurgia, Moskva 1975

[3] F. Mampaey, D. Habets, J. Plessers, F. Seutens, On-line oxygen activity measurements to determine optimal graphite form during compacted graphite iron production, International Journal of Metalcasting, 4 (**2010**) 2, 25–40

[4] F. Mampaey, K. Beghym, Oxygen activity in cast iron measured in induction furnace at variable temperature, AFS Transactions, 114 (**2006**), 637–656

[5] HEN, Heraeus Electro-Nite, Celox-Foundry, CP 10700692, http://heraeus-electro-nite.com/en/sensorsformoltenmetals/iron/oxygencontrol_2/oxygencontrol_3.aspx

[6] J. Hampl, T. Elbel, On modelling of the effect of oxygen on graphite morphology and properties of modified cast irons, Archives of foundry engineering, 10 (**2010**) 4, 55–60

[7] T. Válek, J. Hampl, Prediction of metallurgic quality of ICDP material before tapping, 2011 International Conference on Physics Science and Technology, Physics Procedia, 22 (**2011**), 191–196

[8] J. Hampl, T. Elbel, Effect of oxygen on graphite morphology and properties of modified cast irons, Proceedings of the 10th International Foundry Conference, Opatija, 2010

[9] T. Válek, J. Hampl, Control of microstructure of cast iron Indefinite Chill Double Pour – ICDP, Archives of Foundry Engineering, 11 (**2011**) 4, 199–203

UDK 620.3:66.017:621.318.1
Original scientific article/Izvirni znanstveni članek

ISSN 1580-2949
MTAEC9, 48(5)689(2014)

SYNTHESIS COMPARISON AND CHARACTERIZATION OF CHITOSAN-COATED MAGNETIC NANOPARTICLES PREPARED WITH DIFFERENT METHODS

PRIMERJAVA POSTOPKOV IN KARAKTERIZACIJA MAGNETNIH NANODELCEV, PREVLEČENIH S HITOZANOM

Gordana Hojnik Podrepšek, Željko Knez, Maja Leitgeb
University of Maribor, Faculty of Chemistry and Chemical Engineering, Laboratory for Separation Processes and Product Design,
Smetanova ul. 17, 2000 Maribor, Slovenia
maja.leitgeb@um.si

Prejem rokopisa – received: 2013-09-30; sprejem za objavo – accepted for publication: 2013-11-26

In this study, magnetic maghemite nanoparticles were prepared with the coprecipitation method, due to its simplicity and productivity. Thereafter, chitosan-coated magnetic nanoparticles were synthesized with three different methods, the micro-emulsion process, the suspension cross-linking technique and the covalent binding. Subsequently, a comparison of the used methods was done using various analyses such as Fourier transform infrared spectroscopy (FTIR), scanning electron microscopy (SEM), thermogravimetry (TGA), differential scanning calorimetry (DSC), vibrating-sample magnetometry (VSM) and dynamic light scattering (DLS). The characterization results from Fourier transform infrared (FTIR) spectroscopy and thermogravimetric analysis (TGA) indicated a successful binding of chitosan on the magnetic nanoparticles. SEM pictures showed that spherical structured particles with an increased particle size were obtained as the chitosan layer around the particles was increased. Considering that the magnetic-separation technique has the advantages of rapidity, high efficiency, cost-effectiveness and lack of negative effect on the biological activity, these carriers may be applied in enzyme immobilization.

Keywords: magnetic nanoparticles, chitosan, surface functionalization

V prispevku je opisana enostavna priprava magnetnih nanodelcev, prevlečenih s hitozanom. Postopek je potekal v dveh stopnjah. V prvi smo sintetizirali magnetne nanodelce s koprecipitacijo železovih ionov. V drugi smo nanodelce prevlekli s hitozanom, da bi preprečili aglomeracijo, z uporabo treh različnih postopkov: z metodo mikroemulzije, metodo zamreženja in s kovalentno vezavo. Karakterizacija tako pripravljenih nanodelcev je bila izvedena s Fourierjevo transformacijsko infrardečo spektroskopijo (FTIR), z vrstično elektronsko mikroskopijo (SEM), s termogravimetrično analizo (TGA), z diferencialno dinamično kalorimetrijo (DSC), z analizo vibracijskega magnetometra (VSM) in dinamičnim sipanjem laserske svetlobe (DLS). Rezultati analiz FTIR in TGA so potrdili vezavo hitozana na magnetne nanodelce, medtem ko je bila oblika in debelina sloja hitozana določena s SEM-analizo. Ker ima tehnika magnetnih nanodelcev veliko prednosti pri ločevanju, cenejši proizvodnji in nima negativnih učinkov na biološko aktivnost, se lahko potencialno uporablja pri encimski imobilizaciji.

Ključne besede: magnetni nanodelci, hitozan, površinska funkcionalizacija

1 INTRODUCTION

Recently, magnetic nanoparticles such as maghemite (γ-Fe_2O_3) have attracted a great deal of attention due to their unique, controllable sizes, shapes, other physical properties, compositions and also for their wide applications in biomedicine, biotechnology, engineering, material science and environmental areas[1–3]. They have a magnetic response and can be manipulated with an external magnetic-field gradient (**Figure 1**).

Chitosan, a deacetylated derivative of chitin, is a polysaccharide with both a hydroxyl and an amine group in its structure. In addition, it is non-toxic, biocompatible, biodegradable, and anti-bacterial[4]. It is insoluble in water, but becomes soluble and positively charged in acidic media. Nowadays, the preparation of chitosan-modified magnetic nanoparticles are of great interest[5,6]. In addition, this polymer has been used successfully to colloidally stabilize magnetic nanoparticles and has also been used as a matrix for enzyme immobilization since it has numerous amino groups that can interact with enzyme[7,8]. The amino groups are responsible for the distinct characteristics attributed to this basic polymer. Therefore, the characterization of chitosan is extremely important with respect to the structure-property relationship, defining a possible industrial application[9].

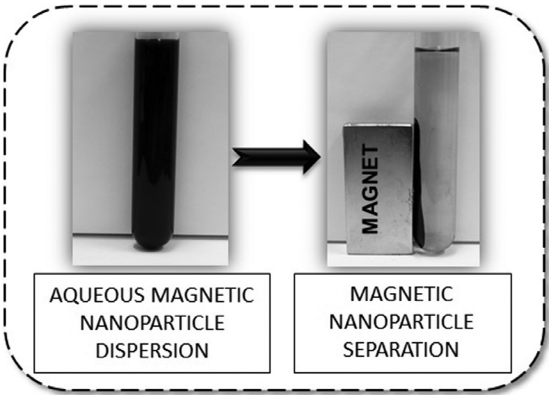

Figure 1: Magnetic-property illustration of the maghemite nanoparticles dispersed in water
Slika 1: Prikaz magnetnih lastnosti nanodelcev maghemita, dispergiranega v vodi

2 EXPERIMENTS

2.1 Materials

Iron (II) chloride tetrahydrate (FeCl2 · 4H2O), iron (III) chloride hexahydrate (FeCl3 · 6H2O) and acetic acid were supplied from Merck, (Germany). Chitosan (CTS, MMW, the degree of deacetylation was 75–85 %), glutaraldehyde (GA) and Span-80 were obtained from Sigma-Aldrich. Ammonia was purchased from Carlo Erba and paraffin from Kreiger. All the solutions were prepared with Milli-Q water.

2.2 Apparatus and procedures

Maghemite nanoparticles were synthesized by coprecipitating Fe^{2+} and Fe^{3+} ions in the presence of ammonium. A functionalization of chitosan was carried out with three different methods: the micro-emulsion process[10], the suspension cross-linking technique[11] and the covalent binding of chitosan[12]. These methods differ with respect to the chitosan concentration, the presence and concentration of the acetic acid solution, the glutaraldehyde concentration, the synthesis temperature, the pH of the medium and the time of the synthesis.

The properties and structures of non-functionalized magnetic iron-oxide nanoparticles and chitosan-functionalized magnetic maghemite nanoparticles were characterized with Fourier transform infrared spectroscopy (FTIR), scanning electron microscopy (SEM), differential scanning calorimetry (DSC), dynamic light scattering (DLS), vibrating-sample magnetometry (VSM) and potentiometric titration.

3 RESULTS

3.1 Characterization of chitosan-coated magnetic nanoparticles

The FTIR spectra of chitosan, chitosan-coated maghemite and maghemite nanoparticles are shown in **Figure 2a** to **2c**. Undoubtedly, the FTIR spectra of chitosan showed a broader band at 3410 cm^{-1}, which was attributed to the hydroxyl (OH) stretching as reported in[6]. For the IR spectra of chitosan, the characteristic absorption bands appeared at 1654 cm^{-1} which can be assigned to the N-H bending vibrations, and at 1377 cm^{-1} assigned to the C-O stretching of the primary alcohol group in chitosan. For the magnetic maghemite nanoparticles, the peaks at 570 cm^{-1} and 628 cm^{-1} were related to the Fe-O group[10]. However, the adsorption of chitosan on the surface of the magnetic iron-oxide nanoparticles was confirmed with the FTIR analysis.

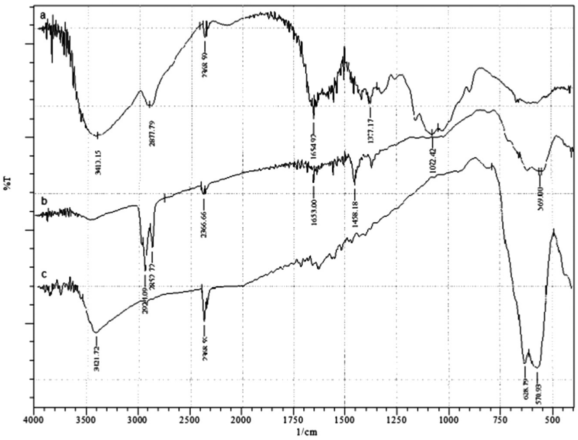

Figure 2: FTIR spectra of: a) chitosan, b) maghemite coated with chitosan and c) maghemite

Slika 2: FTIR-spektri: a) hitozan, b) maghemit z nanosom hitozana in c) maghemit

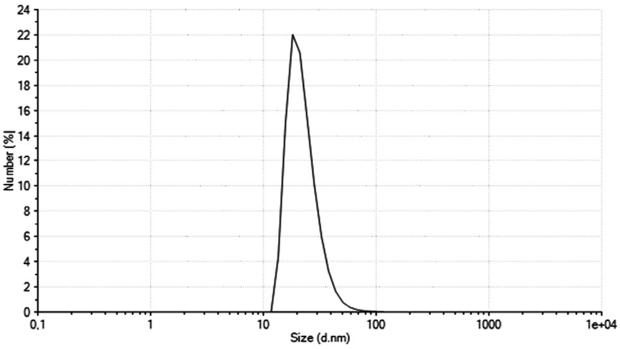

Figure 3: Particle-size distribution of non-functionalized magnetic nanoparticles

Slika 3: Razporeditev velikosti nefunkcionaliziranih magnetnih nanodelcev

Figure 3 shows the size distribution of the magnetic nanoparticles determined with DLS in an aqueous solution with the mean diameter of 22.8 nm.

The results of the TGA characterization of the maghemite nanoparticles coated with chitosan obtained with three different methods were used for an estimation of the amount of the chitosan coating on the maghemite

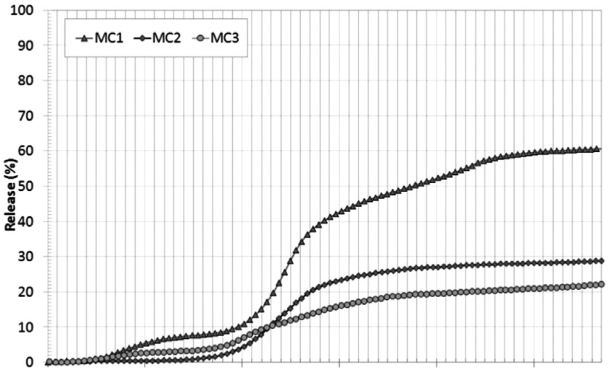

Figure 4: Weight-loss curve of chitosan by sample; (MC1) maghemite particles coated with chitosan with the micro-emulsion process, (MC2) maghemite nanoparticles coated with chitosan with the suspension cross-linking technique and (MC3) maghemite nanoparticles coated with chitosan with the covalent-binding method

Slika 4: Krivulje zmanjšanja mase hitozana v vzorcih; (MC1) delci maghemita, pokriti s hitozanom s postopkom mikroemulzije, (MC2) delci maghemita, pokriti z metodo zamreženja in (MC3) maghemitni nanodelci, pokriti s hitozanom z metodo kovalentne vezave

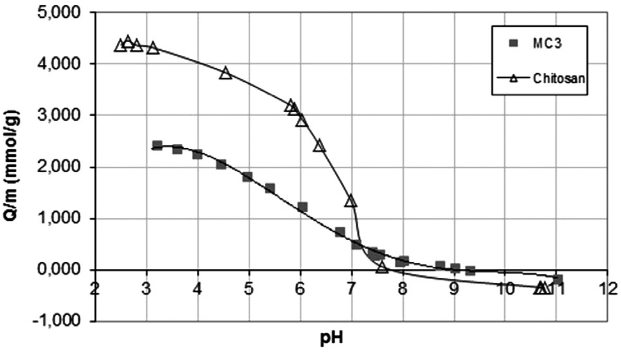

Figure 5: Charging isotherms of pure chitosan and MC3 nanoparticles
Slika 5: Izoterme naboja čistega hitozana in MC3-nanodelcev

nanoparticles. The actual weight loss of pure maghemite nanoparticles was subtracted from the actual weight loss of maghemite nanoparticles coated with chitosan to get the mass loss of chitosan in percentages for MC1, MC2 and MC3, presented in **Figure 4**. The mass loss of chitosan for MC3 (22.2 %) is lower than for MC2 (28.8 %) and MC1 (60.7 %).

The presence of the amino-group amount was studied for pure chitosan and chitosan-functionalized magnetic nanoparticles, using a potentiometric titration. The resulting charging isotherms QV_t/m_f versus pH are presented in **Figure 5**. The figure contains the titration data for pure chitosan and the MC3 sample. The amount of amino group in free chitosan was 4.22 mmol/g, while in sample MC3 it was 2.48 mmol/g.

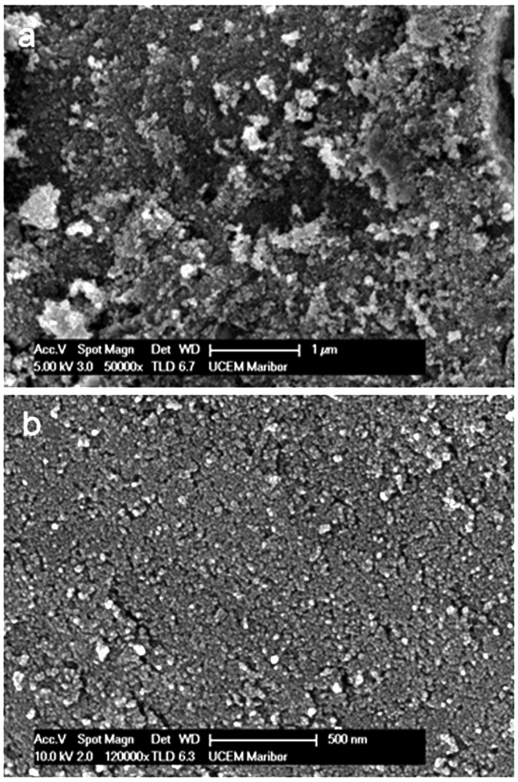

Figure 6: SEM images of: a) magnetic maghemite nanoparticles and b) maghemite nanoparticles, coated with chitosan with the covalent-binding method (MC3)
Slika 6: SEM-posnetka: a) magnetnih nanodelcev maghemita in b) nanodelcev maghemita, pokritih s hitozanom s kovalentno metodo vezanja (MC3)

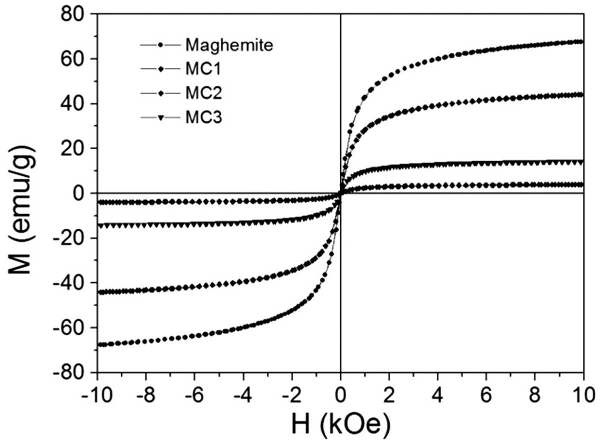

Figure 7: Hysteresis loops of the maghemite and chitosan-functionalized maghemite nanoparticles
Slika 7: Histerezna zanka maghemita in s hitozanom funkcionaliziranih nanodelcev maghemita

Typical SEM micrographs for maghemite nanoparticles and chitosan-coated maghemite nanoparticles are shown in **Figure 6**, presenting maghemite nanoparticles (a) and maghemite nanoparticles, coated with chitosan with the covalent-binding method (b). **Figure 6** reveals that the maghemite particles, coated with chitosan (MC3) have spherical shapes and a size range of 50–100 nm.

Figure 7 shows the magnetization curves for the maghemite nanoparticles, revealing superparamagnetic properties. The magnetization of the micro- and nanoparticles, coated with chitosan with the micro-emulsion process was found to be 3 emu/g, for the suspension cross-linking technique it was 40 emu/g and for the covalent-binding method it was 20 emu/g. These values were compared to the value for the uncoated maghemite nanoparticles. Therefore, it can be concluded that a chitosan-surface functionalization of the maghemite nanoparticles was achieved.

4 CONCLUSION

In this paper, chitosan-coated maghemite nanoparticles were synthesized with the micro-emulsion process, the suspension cross-linking technique and covalent binding of chitosan. The samples exhibited clear differences in the saturation magnetization, which can be ascribed mainly to different chemical compositions and magnetic moments of Fe. The chitosan-coated maghemite nanoparticles appeared in granules with the average sizes of 40–350 μm after the micro-emulsion process, 400 nm after the suspension cross-linking technique and 50–100 nm after the covalent binding of chitosan. The size of the nanoparticles was increased with an increase in the concentration of chitosan and decreased with an increase in the cross-linker concentration. We found that the magnetic nanoparticles, coated with chitosan with the covalent-binding method (MC3) are suitable for practical applications due to their sufficiently high values of amino groups and nanosized particles. The maghemite nanoparticles, functionalized with chitosan, have a potential to be used in assisted drug-delivery systems, cell/enzyme immobilization, separation processes, medical diagnosis and therapy and many other industrial applications.

Acknowledgements

This work was entirely supported by the Slovenian Research Agency (PhD researcher fellowship contract No. 1938/FKKT-2010) and financially supported through Project J2-4232.

5 REFERENCES

[1] L. Zeng, R. Hu, Z. Wu, Q. He, Preparation and characterization of amino-coated maghemite nanoparticles, Bioinformatics and Biomedical Engineering (iCBBE), (**2010**), 1–5

[2] M. Faraji, Y. Yamini, M. Rezaee, Magnetic nanoparticles: Synthesis, stabilization, functionalization, characterization, and applications, Journal of the Iranian Chemical Society, 7 (**2010**) 1, 1–37

[3] S. K. Janardhanan, Synthesis of iron oxide nanoparticles using chitosan and starch templates, Transition Metal Chemistry, 33 (**2008**), 127–131

[4] D. Kavaz, T. Cirak, E. Öztürk, C. Bayram, E. B. Denkbas, Functionalized Nanoscale Materials, Devices and Systems, Springer, Netherlands 2008, 313

[5] G. Li, Y. Jiang, K. Huang, P. Ding, J. Chen, Preparation and properties of magnetic Fe_3O_4-chitosan nanoparticles, Journal of Alloys and Compounds, 466 (**2008**), 451–456

[6] C. Yuwei, W. Jianlong, Preparation and characterization of magnetic chitosan nanoparticles and its application for Cu(II) removal, Chemical Engineering Journal, 168 (**2011**), 286–292

[7] G. Hojnik Podrepšek, Ž. Knez, M. Leitgeb, Different preparation methods and characterization of magnetic maghemite coated with chitosan, Journal of Nanoparticle Research, 15 (**2013**), 1–12

[8] S. Jenjob, P. Sunintaboon, P. Inprakhon, N. Anantachoke, V. Reutrakul, Chitosan-functionalized poly(methyl methacrylate) particles by spinning disk processing for lipase immobilization, Carbohydrate Polymers, 89 (**2012**) 3, 842–848

[9] E. S. Alvarenga, Characterization and Properties of Chitosan, In: M. Elnashar (ed.), Biotechnology of Biopolymers, InTech, 2011, 91

[10] H. Y. Zhu, R. Jiang, L. Xiao, W. Li, A novel magnetically separable γ-Fe_2O_3/crosslinked chitosan adsorbent: Preparation, characterization and adsorption application for removal of hazardous azo dye, Journal of Hazardous Materials, 179 (**2010**), 251–257

[11] G. Y. Li, Y. R. Jiang, K. L. Huang, P. Ding, J. Chen, Preparation of magnetic Fe_3O_4-chitosan nanoparticles, Journal of Alloys and Compounds, 466 (**2008**), 451–456

[12] D. Bhattacharya, S. K. Sahu, I. Banerjee, M. Das, D. Mishra, T. K. Maiti, P. Pramanik, Synthesis, characterization, and in vitro biological evaluation of highly stable diversely functionalized superparamagnetic iron oxide nanoparticles, Journal of Nanoparticle Research, 13 (**2011**), 4173–4188

UDK 669.14:669.017.3
Original scientific article/Izvirni znanstveni članek

ISSN 1580-2949
MTAEC9, 48(5)693(2014)

STUDY OF PHASE TRANSFORMATIONS IN Cr-V TOOL STEEL

ŠTUDIJ FAZNIH PREMEN V ORODNEM JEKLU Cr-V

Matej Pašák, Roman Čička, Pavel Bílek, Peter Jurči, Ľubomír Čaplovič
Institute of Materials Science, Faculty of Materials Science and Technology, Slovak University of Technology, Paulinska 16, 917 24 Trnava, Slovak Republic
matej.pasak@stuba.sk

Prejem rokopisa – received: 2013-10-01; sprejem za objavo – accepted for publication: 2013-11-12

The properties of steels are very dependent on the phases present in the microstructure. The wear resistance and thermal stability of tool steels are achieved with the presence of different types of carbides. So the chemical composition and heat treatment play crucial roles in optimizing the properties of tool steels.

The phase transformations in Cr-V tool steel were analyzed during the heating from room temperature up to 1100 °C using DTA and dilatometry. After soft annealing the microstructure of the investigated steel consists of a ferritic matrix and M_7C_3 and MC carbides, as determined with SEM, EDX and XRD techniques. The experimental results were compared to the computational results (Thermo-Calc).

Keywords: phase transformation, Cr-V tool steel, Thermo-Calc

Lastnosti jekla so močno odvisne od faz, ki so v mikrostrukturi. Odpornost proti obrabi in toplotna stabilnost orodnih jekel se dosežeta z različnimi vrstami karbidov. Kemijska sestava in toplotna obdelava imata ključno vlogo pri optimiranju lastnosti orodnih jekel.

DTA in dilatometrija sta bili uporabljeni za preučevanje faznih premen v orodnem jeklu Cr-V med ogrevanjem od sobne temperature do 1100 °C. Tehnike SEM, EDX in XRD so potrdile, da po mehkem žarjenju mikrostrukturo preiskovanega jekla sestavlja feritna osnova ter karbidi M_7C_3 in MC. Eksperimentalni rezultati so bili primerjani z izračunanimi (Thermo-Calc).

Ključne besede: fazna premena, orodno jeklo Cr-V, Thermo-Calc

1 INTRODUCTION

At present Cr-V ledeburitic steels are often used for the manufacturing of cutting, forming and other tools in the industry. To meet the industrial requirements for high stability and reliability, they have to withstand the wear and plastic deformation. They are usually produced with powder metallurgy. This technology enables us to obtain a uniform carbide size and distribution and also to produce the materials with particular compositions that cannot be prepared by conventional casting. The technology of powder metallurgy provides good results in achieving high homogeneity. The phase composition, microstructure and mechanical properties of ledeburitic tool steels are determined by the matrix and the type, quantity, size and distribution of the carbides.[1] The properties of the material thus depend on the microstructure obtained after heat treatment.

The phase transformations during heating can be described with thermodynamic modeling using the CALPHAD method.[2–4]

Thermal-analysis techniques are suitable for an experimental determination of the phase transformations in materials. For steels, the DTA and dilatometry techniques are often used.[5,6]

Carbide phases have a different thermal stability and some of them are dissolved during the austenitizing in the solid state.[7,8] Bílek et al.[9] investigated the phase composition of Cr-V tool steel after heat treatment, using SEM+EDX, a quantitative analysis of the microstructure and hardness measurements. They found two types of carbides in the microstructure of Cr-V tool steel. Carbide M_7C_3 was partially dissolved during the austenitizing at 1000 °C and it completely disappeared after the austenitizing at 1100 °C. Carbide MC is more stable and starts to dissolve only at a temperature higher than 1200 °C.

The aim of this paper is to enhance and explain the results published previously by Bílek et al.[9] using additional experimental techniques (XRD, DTA and dilatometry) and thermodynamic calculations (Thermo-Calc).

2 EXPERIMENTAL WORK

2.1 Sample material

Cr-V tool steel was used as the experimental material with the chemical composition of $w(\mathrm{C}) = 2.1\ \%$, $w(\mathrm{Si}) = 1\ \%$, $w(\mathrm{Mn}) = 0.4\ \%$, $w(\mathrm{Cr}) = 6.8\ \%$, $w(\mathrm{Mo}) = 1.5\ \%$, $w(\mathrm{V}) = 5.4\ \%$, balanced by Fe.[10]

The sample was initially annealed at the temperature of 900 °C for 1 h and then slowly cooled down to room temperature.

The X-ray diffraction (XRD) analysis was accomplished with a Panalytical Empyrean X-ray diffractometer. A cobalt anode ($U = 40$ kV and $I = 40$ mA) with a parallel-beam X-ray mirror was used. The sample was measured with a PIXcel3D detector at room temperature in the angular range of 45–110° with a step size of 0.0131°. The microstructure and chemical composition of the phases were analyzed with a JEOL JSM 7600F electron microscope equipped with a secondary and back-scattered electron detector and a MAX 50 EDX detector from Oxford Instruments. The differential thermal analysis (DTA) was done using a NETZSCH STA 409CD simultaneous thermal analyzer in an inert gas (Ar 6.0) with a magnetic frame enabling also the measurements of the magnetic transition in the temperature range of 100–1100 °C, at the heating rate of 10 K/min. The dilatometry measurements were performed using a NETZSCH DIL 402C dilatometer. The inert-gas atmosphere (Ar 6.0) in the temperature range of 100–1000 °C and different heating rates (2, 5, 8, 12, 16, 20, 25) K/min were used. The thermodynamic calculations were done using the Thermo-Calc software and TCFE6 thermodynamic database.

2.2 Results

The XRD analysis (**Figure 1**) confirms that only MC and M_7C_3 carbides are present as the secondary phases in the ferrite at room temperature.

Figure 2a illustrates the microstructure of Cr-V tool steel after annealing, with the coarse M_7C_3 particles (some of these particles are in an extraordinary fine form) and finer MC particles in the ferritic matrix.

In the EDX mapping mode the distribution of vanadium (**Figure 2b**) and chromium (**Figure 2c**) can be seen.

The phase transformations in the investigated steel during heating are shown with the DTA and thermomagnetometry curves in **Figure 3**. The magnetic transition of the ferrite from the ferromagnetic to paramagnetic state is detected at 754.0 °C from the thermomagnetometry curve and at 753.6 °C from the DTA curve. The next peak on the DTA curve with the onset at 855.3 °C corresponds to the austenitization process.

These results were verified with thermodynamic calculations using the Thermo-Calc software. **Figure 4** shows the temperature dependence of the volume fractions of individual phases. It can be seen that the amount of the M_7C_3 carbide starts to decrease already during the ferrite-to-austenite transformation, in the temperature range of 814–837 °C.

After the completion of the ferrite-to-austenite transformation, the dissolution of M_7C_3 in austenite continues until its completion at about 1200 °C.

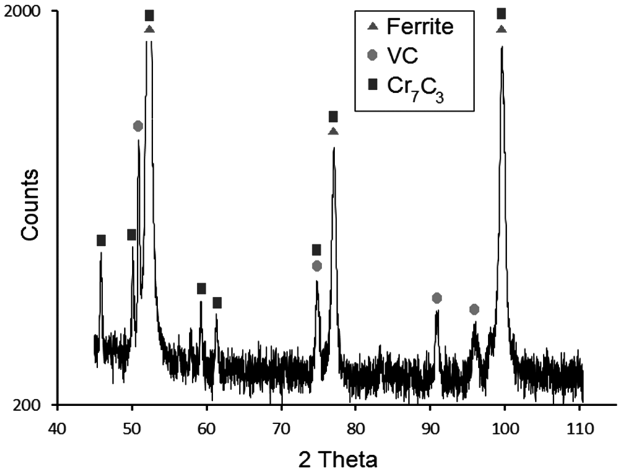

Figure 1: Diffractogram of the annealed sample measured at room temperature

Slika 1: Rentgenski difraktogram žarjenega vzorca, posnet pri sobni temperaturi

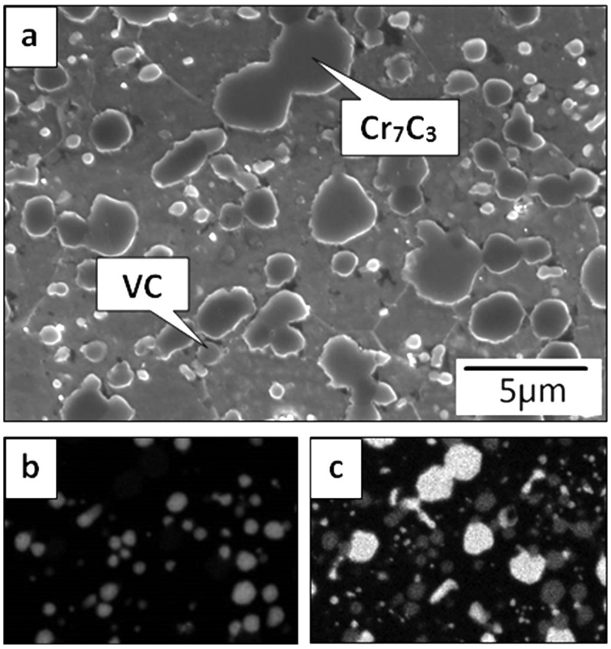

Figure 2: Microstructure of the ledeburitic Cr-V tool steel in the soft-annealing state: a) overview (SEM), b) EDX map of vanadium from **Figure 2a**, c) EDX map of chromium from **Figure 2a**

Slika 2: Mikrostruktura ledeburitnega orodnega jekla Cr-V v mehko žarjenem stanju: a) SEM, b) EDX-razporeditev vanadija s **slike 2a**, c) EDX-razporeditev kroma s **slike 2a**

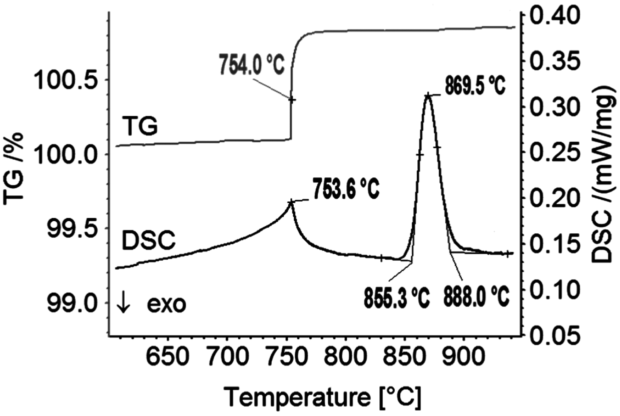

Figure 3: DTA and TG curves of the as-prepared tool-steel powder at the heating rate of 10 K/min

Slika 3: Krivulji DTA in TG prahu orodnega jekla pri hitrosti ogrevanja 10 K/min

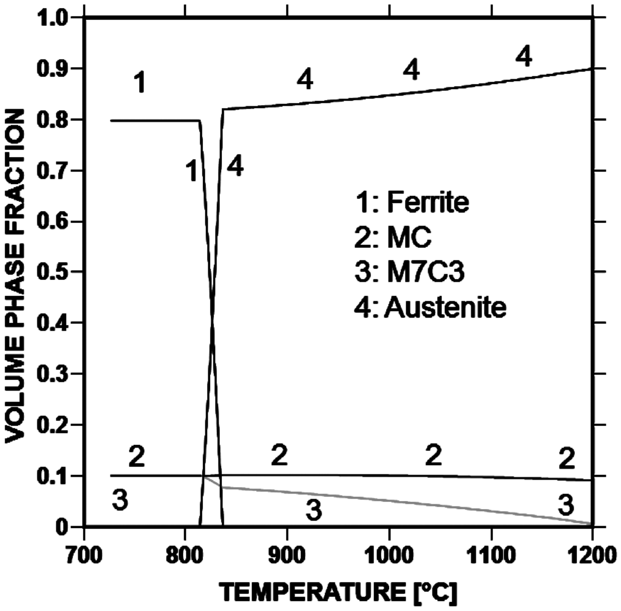

Figure 4: Volume-phase fractions in dependence on the temperature calculated with Thermo-Calc

Slika 4: Volumenski delež faz v odvisnosti od temperature, izračunane s Thermo-Calc

Figure 5 shows the dilatometry curves of Cr-V tool steel during heating (2 K/min) and cooling (3 K/min). By analyzing the curve of the thermal-expansion coefficient, the characteristic temperatures of the ferrite-to-austenite transformation were determined. The transformation start and finish temperatures during the heating are thus 843.0 °C and 872.6 °C, respectively. The transformation start and finish temperatures during the cooling were determined as 760.2 °C and 732.3 °C, respectively.

The other dilatometry measurements were performed at different heating rates and the results regarding the transformation start and finish temperatures of the ferrite-austenite transformation are summarized in **Table 1** and **Figure 6**.

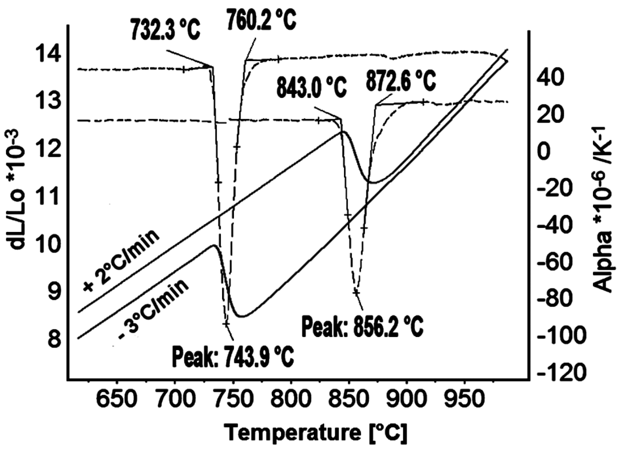

Figure 5: Dilatometric curves at the heating rate of 2 °C/min and the cooling rate of 3 °C/min

Slika 5: Dilatometrijska krivulja pri hitrosti ogrevanja 2 °C/min in pri hitrosti ohlajanja 3 °C/min

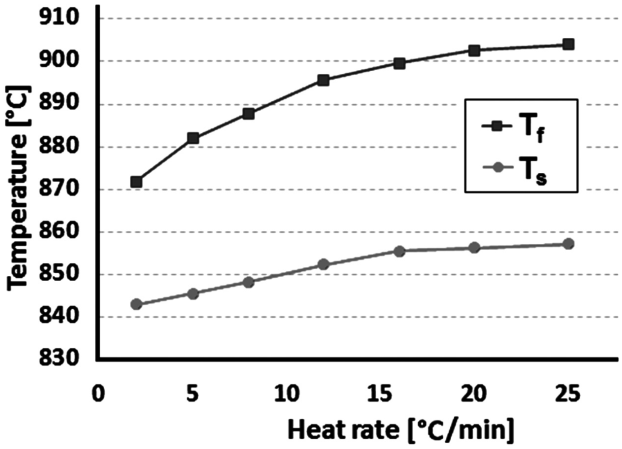

Figure 6: Transformation start and finish temperatures of the ferrite-austenite transformation in dependence on the heating rate

Slika 6: Temperature začetka in konca pretvorbe ferit-avstenit v odvisnosti od hitrosti ogrevanja

Table 1: Start/finish temperatures of the ferrite-to-austenite transformation at different heating rates, with the calculated temperature range of the transformation

Tabela 1: Temperature začetka – konca pretvorbe ferita v avstenit pri različnih hitrostih ogrevanja z izračunanimi temperaturnimi območji pretvorbe

Heating rate	2 °C/min	5 °C/min	8 °C/min	12 °C/min	16 °C/min	20 °C/min	25 °C/min
T_s/°C	843.0	845.5	848.2	852.3	855.5	856.3	857.1
T_f/°C	871.8	881.9	887.8	895.6	899.6	902.6	904.0
ΔT/°C	28.8	36.4	39.6	43.3	44.1	46.3	46.9

3 DISCUSSIONS

In this work it was confirmed that the microstructure of Cr-V tool steel after soft annealing consists of a ferritic matrix and M_7C_3 and MC carbides. M_7C_3 starts to dissolve during the ferrite-to-austenite phase transformation and a complete dissolution of M_7C_3 in the austenite occurs at the temperature of about 1200 °C. The MC carbide is more stable and its amount remains unchanged from room temperature up to 1200 °C. The temperature range of the ferrite-to-austenite phase transformation determined with dilatometry is 843.0–872.6 °C using a slow heating rate (2 °C/min) and the transformation during cooling occurs in the temperature range of 760.2–732.3 °C. The temperature range of this phase transformation calculated with Thermo-Calc is 814–837 °C. If the heating rate in dilatometry measurements increases (2–25 °C/min), the transformation start temperature also increases from 843.0 °C to 857.1 °C, while the transformation finish temperature increases from 871.8 °C to 904.0 °C and the temperature range of this transformation also increases from 28.8 °C to 46.9 °C.

The results for the thermal stability of M_7C_3 and MC carbides in Cr-V steel are in agreement with and explain the results published previously.[10] The future work will be focused on developing a kinetic model of the ferrite-austenite phase transformation in this system using the dilatometry data. The dissolution of M_7C_3 in austenite will be modeled using the Dictra software to enhance the knowledge about these kinetic processes occurring in Cr-V tool steel during heating.

4 CONCLUSIONS

The microstructure and phase transformations in Cr-V tool steel were analyzed using experimental and computational techniques. The main results are summarized as follows:

- the microstructure of Cr-V tool steel after soft annealing consists of a ferritic matrix and M_7C_3 and MC carbides
- M_7C_3 starts to dissolve during the ferrite-to-austenite phase transformation and is completely dissolved in the austenite at 1200 °C
- MC is more stable and its amount does not change from room temperature up to 1200 °C
- the phase transformation of ferrite to austenite proceeds in the temperature range of 843.0–871.8 °C, determined at the low heating rate by dilatometry by using the dilatometry data obtained at different heating rates, a kinetic model of the ferrite-to-austenite phase transformation will be proposed in the near future, and the kinetics of the dissolution of M_7C_3 in austenite will be calculated using the Dictra software.

Acknowledgements

The authors wish to thank the European Regional Development Fund (ERDF) for the financial support of projects ITMS:26220120014 and ITMS:26220120048 "Center for development and application of advanced diagnostic methods in processing of metallic and non-metallic materials" funded within the Research & Development Operational Programme.

5 REFERENCES

[1] P. Grgac, R. Moravcik, M. Kusy, J. Toth, M. Miglierini, E. Illekova, Thermal stability of metastable austenite in rapidly solidified chromium–molybdenum–vanadium tool steel powder, Materials Science and Engineering A, 375–377 (**2004**), 581–584

[2] J. Kohout, Modelling of changes in properties of alloys at elevated temperatures, Materials Science and Engineering A, 462 (**2007**) 1–2, 159–163

[3] A. Costa e Silva, J. Ågren, M. T. Clavaguera-Mora, D. Djurovic, T. Gomez-Acebo, B. J. Lee, Z. K. Liu, P. Miodownik, H. J. Seifert, Applications of computational thermodynamics – the extension from phase equilibrium to phase transformations and other properties, Calphad, 31 (**2007**) 1, 53–74

[4] P. Maugis, M. Goune, Kinetics of vanadium carbonitride precipitation in steel: A computer model, Acta Materialia, 53 (**2005**) 12, 3359–3367

[5] C. Garciá de Andrés, F. G. Caballero, C. Capdevila, L. F. Álvarez, Application of dilatometric analysis to the study of solid-solid phase transformations in steels, Materials Characterization, 48 (**2002**) 1, 101–111

[6] T. C. Tszeng, G. Shi, A global optimization technique to identify overall transformation kinetics using dilatometry data – applications to austenitization of steels, Materials Science and Engineering, 380 (**2004**) 1–2, 123–136

[7] P. Jurči, Structural changes in Cr-V ledeburitic steel during austenitizing and quenching. Materials Engineering A, 17 (**2010**) 1, 1–10

[8] P. Jurči, Nástrojové oceli ledeburitického typu, ČVUT, Praha 2009, 221

[9] P. Bílek, J. Sobotová, P. Jurči, Evaluation of the microstructural changes in Cr-V ledeburitic tool steels depending on the austenitization temperature, Mater. Tehnol., 45 (**2011**) 5, 489–493

[10] Material list of Uddeholm company, Vanadis 6 [online], 2009 [cit.2013-24-9], www: http://www.bucorp.com/files/van_6_ds.pdf

UDK 678.7
Original scientific article/Izvirni znanstveni članek

ISSN 1580-2949
MTAEC9, 48(5)697(2014)

MODEL ANTIMICROBIAL POLYMER SYSTEM BASED ON POLY(VINYL CHLORIDE) AND CRYSTAL VIOLET

MODEL PROTIMIKROBNEGA POLIMERNEGA SISTEMA NA OSNOVI POLIVINILKLORIDA IN KRISTAL VIOLETA

Jiří Klofáč[1,2], Ivo Kuřitka[1,2], Pavel Bažant[1,2], Kristýna Jedličková[1,2], Jakub Sedlák[1,2]

[1]Polymer Centre, Faculty of Technology, Tomas Bata University in Zlin, Nam. T. G. Masaryka 275, 762 72 Zlin, Czech Republic
[2]Centre of Polymer Systems, University Institute, Tomas Bata University in Zlin, Nad Ovcirnou 3685, 760 01 Zlin, Czech Republic
j_klofac@ft.utb.cz

Prejem rokopisa – received: 2013-10-03; sprejem za objavo – accepted for publication: 2013-11-11

The development of novel antimicrobial materials for biomedical application in indwelling devices such as catheters is very important as the resistance of the pathogens responsible for nosocomial infections towards recent systems has been emerging with an increasing rate. The work presented here is focused on the preparation and characterization of an antimicrobial polymeric system composed of poly(vinyl chloride) in combination with crystal violet as a model compound of organic ionic active species. The antimicrobial activity of the system against gram-negative bacteria *Escherichia coli*, gram-positive bacteria *Staphylococcus aureus* and yeasts *Candida albicans* as the representative microorganisms were evaluated with a disk-diffusion test. The release profile of the active substance was observed with UV-VIS spectrometry. The mechanical properties of the prepared material were tested to verify that they were not altered with respect to the original medical-grade polymer matrix.

Keywords: poly(vinyl chloride), crystal violet, antibacterial, antimicrobial, release

Pomemben je razvoj novega protimikrobnega materiala za biomedicinsko uporabo notranjih pripomočkov, kot so katetri, ker se vedno pogosteje pojavlja odpornost patogenov, odgovornih za bolnišnične okužbe. Predstavljeno delo je osredinjeno na pripravo in karakterizacijo protimikrobnega polimernega sistema, ki ga sestavlja polivinilklorid v kombinaciji s kristal violetom kot model za spojine organskih ionskih aktivnih vrst. S ploščinskim difuzijskim preizkusom je bila ocenjena protimikrobna dejavnost sistema proti predstavnikom mikroorganizmov: gramnegativni bakteriji *Escherichia coli*, grampozitivni bakteriji *Staphylococcus aureus* in kvasovkam *Candida albicans.* Profil sprostitve aktivnih snovi je bil opazovan z UV-VIS-spektrometrijo. Mehanske lastnosti pripravljenega materiala so bile preizkušene, da bi potrdili, da niso drugačne od navadnega medicinskega polimera.

Ključne besede: poli(vinil) klorid, kristal violet, protibakterijski, protimikrobni, sproščanje

1 INTRODUCTION

Polymers are known for their high versatility and excellent physical-chemical properties and, in some cases, they are suitable as biomaterials for the medical sector and packaging industry. As a candidate for these applications, the third most common polymer, poly(vinyl chloride) (PVC), can be considered due to its high mechanical and chemical resistance, inertness against biological fluids and a wide range of processing possibilities.[1–3]Among many products, urinal catheters, blood bags and cardiovascular implants are typical items used in the medical sector; nevertheless, they exhibit a vulnerability towards surface bacterial colonization.[2,4] Therefore, it is important to enhance their antimicrobial properties by modifying the surfaces of such materials with a plasma treatment, corona discharge and chemical grafting.[5,6] Another promising strategy of modifying PVC is to incorporate an antimicrobial substance within the polymer matrix.[4,7,8] Such modifications have long-term effects and are relatively easy to perform, showing high rates of success. The solvent-cast technique allowing a preparation of the films with extremely high quality requirements and great uniformity of the thickness is often employed due to its advantage of easy blending of the films with the active molecular compounds soluble in the used solvent system.[9,10] The effectiveness of the antimicrobial properties of such films is strongly dependent on the release profile of the antimicrobial substance from the polymer matrix.[11]

Organic substances migrate, over time, out of the polymer matrix and onto the polymer surface and are then released into the surrounding liquids. Migration occurs as the organic molecules follow down a concentration gradient and exit the plastic. The migration is driven by the inherent compatibility differences between the organic antimicrobials and the polymer substrates in which they are dispersed. The losses of the organic molecules into the environment are replenished by the additives within the substrate volume. The benefit of this mode of action is that it can have a very high activity rate, and the migratory molecules can very quickly interact with large numbers of microbes. This does, however, affect the lifespan of the activity, as the additives leach out over time, emptying the polymer's reservoir. The concentration and choice of the respective organic additive depend on the level of efficacy required and the duration of the action needed.[12]

An antimicrobial agent release that is too fast can be harmful under certain conditions and perceived as undesirable. Besides inorganic fillers, ionic organic compounds can provide a real option in the material design having long-lasting mild effects due to their relatively slow migration rates. An organic salt structure comprised of a large bulky organic cation and a small inorganic anion can be considered to have the migration rates in a polyolefinic matrix slow enough in comparison with the molecular organic antimicrobial additives. As a well-known model representative for this class of compounds crystal violet (CV) can be chosen. It is a triarylmethane dye formerly used in medicine due to its antibacterial, antifungal, anthelmintic and antiseptic properties.[13–15] CV was generally considered to be safe for a long time in the history of medicine; however, many studies have reported that CV has potentially mutagenic and carcinogenic effects on humans and animals.[16–19] In spite of this, CV is an excellent model compound for the release-profile studies. This dye can be easily mixed with polymers; it has a very good and broad antimicrobial activity, giving deep violet colour to its solutions; hence, its concentration can be easily monitored with an UV-VIS absorption spectrometer.

This study focuses on the modification of a medical-grade PVC with a crystal-violet (CV) addition, using the solvent-casting technique resulting in a model organic antimicrobial polymer system. Its composition, morphology, mechanical properties, antimicrobial tests and the kinetics of the CV release from a polymeric matrix in water and physiological solution used as model liquids, were investigated in the presented work.

2 EXPERIMENTAL WORK

2.1 Materials

Medical-grade thermoplastic plasticized poly(vinyl chloride) (PVC) compound RB3 was purchased from Modenplast Medical (Italy). This material is in compliance with the European Pharmacopeia and biocompatible according to ISO 10993, USP, Class VI. Crystal violet $C_{25}N_3H_{30}Cl$ (CV) and cyklohexanone $C_6H_{10}O$ (CYH) were purchased from PENTA (Czech Republic). All the chemicals were of the analytical grade and used as received without further purification. Demineralized water was used for all of these experiments.

2.2 Sample preparation

PVC/CYH/CV films were prepared with the solvent-casting technique. In the first step a solution of CV in CYH was prepared: 0.2522 g of CV was added to 250 mL CYH to get a concentration of 1 g/L. 20.005 raw PVC in the form of granules was dissolved in 300 mL of CYH during a period 16 h at the room temperature under continuous stirring. The amount of 250 mL of the CV solution was added and this blend was left to mix for another 8 h. Finally, the mixing was finished with a sonication of the solution for 15 min in an ultrasonic bath. The solution was then poured into glass dishes and the solvent was allowed to evaporate at the laboratory temperature for 10 d. The PVC/CYH control sample was prepared with the same procedure, but without incorporating the CV. The conditions for the film preparation were chosen on the basis of practical laboratory experience, with the aim to achieve the smoothest fine films of comparable quality. The thickness of the resultant films was about 500 μm.

2.3 Characterization

2.3.1 Infrared absorption spectroscopy

A FTIR analysis was used to compare the PVC pellets, PVC/CYH and PVC/CYH/CV films. All the measurements were performed with a Nicolet 6700 spectrophotometer (Nicolet, Czech Republic) with the ATR accessory and the Ge crystal for the attenuated-total-reflection method.

2.3.2 SEM analysis

The micrographs of the prepared materials were taken with a Vega II LMU scanning electron microscope (Tescan, Czech Republic). The freeze fracture surfaces were obtained with liquid nitrogen and observed after the coating with a thin layer of gold/palladium by an SC 7640 sputter coater (Quorum Technologies Ltd, UK).

2.3.3 Tensile tests

The effects of the CV added to the PVC matrix on the mechanical properties were studied using a tensile test. The specimens for the test were cut from the prepared film samples as rectangular stripes with the width of 5 mm and the length of 36 mm. The specimens were tested on a tensile testing machine Testometric M350-5CP (LABOR machine, Ltd.) at 25 °C according to standard ISO 37:2005. The speed of the moving clamp was 500 mm/min. The Young´s modulus, the stress at break and the strain at break were determined. All the samples were measured in 5 replicates and standard deviations were estimated.

2.3.4 Antimicrobial tests

The antimicrobial properties of the PVC/CYH/CV films were assessed using the agar-diffusion test. Round specimens (8 mm in diameter) were placed on Petri dishes with the nutrient agar inoculated with the dispersion of microorganisms (a concentration of CFU 1.0×10^7 mL^{-1}). The samples were tested against gram-negative *Escherichia coli* (EC) 4517, gram-positive *Staphylococcus aureus* (SA) 4516, and yeast *Candida albicans* (CA) CCN 8215. After a incubation 72 h at 23 °C for the yeast and a incubation 24 h at 37 °C for bacteria, the dimensions of the inhibition zones were measured in four directions, and the average values were used to calculate the diameter of the circle-zone inhibition area and its standard deviation. All the tests were done in triplicates.

2.3.5 Release of CV and plasticizers from the PVC matrix

Round specimens with a diameter of 12.7 mm were cut from the PVC/CYH/CV samples to be used in the release-profile study of CV in the water and physiological-solution environment. One specimen was always placed in a beaker with 50 mL of elution liquid and the beaker was shaken at 60 r/min to ensure a good homogenization of the liquid media. The measurement of the CV release was performed with a UV-VIS spectrophotometer Cary 300 (VARIAN, USA) equipped with a sipper (a peristaltic pump) and a flow cell (a cuvette). The whole spectral range (200–800 nm) was monitored and the spectra were recorded in the preselected time intervals covering representatively the full time range of each individual release experiment. The same procedure was used for obtaining the reference leachate for the specimens cut from the neat PVC sample with the thickness of 0.5 mm obtained by hot pressing at 170 °C for 5 min to evaluate the release of the plasticizers after three days, which was done to investigate the influence of either the CV addition or the preparation process on the release of the plasticizers from the PVC matrix. The absorbance value at the wavelength of 580 nm was chosen for a quantitative evaluation of the observed release profile of CV because this is the position of the absorption maximum of CV in the elution medium. The data were then converted to the concentration of the released CV using calibration curves. The data were fitted with a non-linear fitting procedure using the Lavenberg-Marquart algorithm incorporated in the Origin 7.0 software.

3 RESULTS AND DISCUSSION

3.1 Infrared absorption spectroscopy

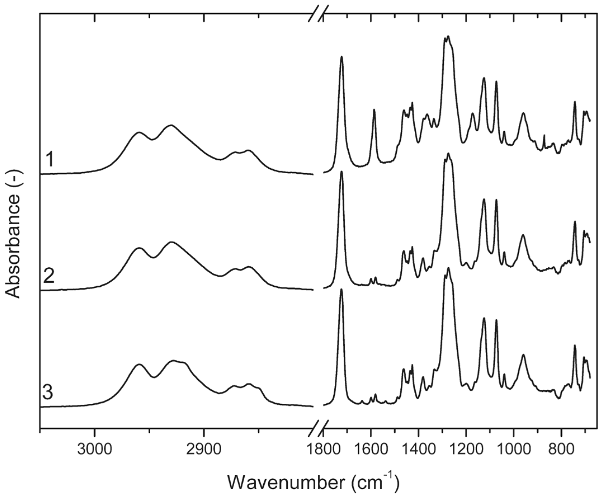

Figure 1: FTIR ATR spectra of neat PVC pellets (curve 3), PVC/CYH film (curve 2) and PVC/CYH/CV film (curve 1) samples. The region between 2800–1800 cm^{-1} is hidden in the graph as no absorption peaks were manifested.

Slika 1: FTIR ATR-spektri vzorcev gladkih PVC-pelet (krivulja 3), PVC/CYH-plast (krivulja 2) in PVC/CYH/CV-plast (krivulja 1). Področje 2800–1800 cm^{-1} je skrito v grafu, ker tam ni bilo izrazitih absorpcijskih vrhov.

The aim of the FTIR analysis was to study a possible modification of the PVC material with the preparation process and an addition of CV. In **Figure 1**, the FTIR spectra of the neat PVC (pellets), the processed PVC/CYH sample and the modified PVC/CYH/CV material are plotted. The infrared absorption spectrum of an unplasticized polyvinyl chloride contains the bands typical for the aliphatic CH groups at their most typical positions, except that, due to the CH_2 deformation vibration, a band is shifted by about 30 cm^{-1} to the lower wavenumbers, nearly to 1430 cm^{-1} as typically observed for PVC. In addition to the aliphatic CH bands, the spectra of PVC contain contributions due to the C-Cl vibrations that can be found as a weak band at 1425 cm^{-1} and as a medium-intensity band at 959 cm^{-1}. The most intense and significant band for the C-Cl vibration at 610 cm^{-1} cannot be observed due to the range of measurement. In general, the spectrum of the neat PVC material is greatly affected by the presence of plasticizers and dominated by their absorption bands. The manifestation of the polymer matrix is, therefore, quite weak. The most prominent band at 1725 cm^{-1} can be assigned to the carbonyl group (C=O) stretching mode typically observed for the plasticizers. It can be expected that the medical-grade PVC contains the additives circumventing the crucial plasticizer migration problem associated with the softened PVC. The position of this peak is too low for the aliphatic low-molecular plasticizers such as dioctyl-sebacate, citrate or adipate esters. On the other hand, a common phthalic ester plasticizer with a typical manifestation of the carbonyl group at 1720 cm^{-1} cannot be successfully used as a medical material intended for modern indwelling applications. A careful analysis of the wavenumber region between 1500 cm^{-1} and 1650 cm^{-1} revealed that there is a quadruplet of peaks at positions (1540, 1580, 1600 and 1637) cm^{-1}, while the phthalic ester plasticizers only display doublets at 1580 cm^{-1} and 1600 cm^{-1}. Alkyde (based on vegetable fatty acids) polyanhydrides were found as the highest scoring records in the available IR spectra database[20]; however, the exact identification was impossible. There is virtually no difference between the spectra recorded for the neat material and for the PVC/CYH sample, proving that the RB3 composition did not change during the solution-casting process and that no solvent residuals were manifested.

The IR absorption spectrum of the PVC/CYH/CV sample displays all the characteristic peaks of CV in addition to the aforementioned spectral features of the plasticized medical-grade PVC; namely, 1587 cm^{-1} due to the C=C stretching in phenyl rings, 1365 cm^{-1} due to the C-H deformation vibrations in methyl groups, 1174 cm^{-1} due to the C-H in-plane deformation in 1,3,5 substituted aromatic ring, and 1128 cm^{-1} due to the C-N stretching vibration in trisubstituted aromatic amines.

3.2 SEM analysis

SEM images were obtained for the freeze-fracture surfaces of the films prepared with CV. The PVC/CYH/CV film morphology before the immersion into the liquid media is shown in **Figure 2a** and the morphology of the PVC/CYH/CV film after the release-profile measurement is shown in **Figure 2b**. First, there are no observable crystals of CV in the polymer matrix, and second, there is no observable change in the material after the release test.

3.3 Tensile tests

The influence of the PVC modification with CV on the mechanical properties of the material prepared by casting from a CYH solution can be seen in **Table 1** where the measured values with their standard deviations are summarized. The mechanical properties of the PVC/CYH film and the PVC/CYH/CV film are very similar. The Young's modulus of PVC/CYH and PVC/CYH/CV is about 5 MPa and the tensile stress at break is about 11–13 MPa. The only property showing a slight difference between the samples is the strain at break. The PVC with CV shows a higher deformation (elongation) ability than the pure PVC sample, which can be considered as an advantage of the material with the additive. Moreover, the obtained result is in accordance with the microscopic observation, both testifying a good dispersion (blending) of CV in the material.

Table 1: Selected mechanical properties of the PVC/CYH and PVC/CYH/CV samples and their standard deviations

Tabela 1: Izbrane mehanske lastnosti vzorcev PVC/CYH in PVC/CYH/CV in njihov standardni odmik

Sample	Young's modulus (MPa)	Strain at break (%)	Tensile stress at break (MPa)
PVC/CYH	5.0 ± 0.6	490 ± 40	11 ± 3
PVC/CYH/CV	4.8 ± 0.4	620 ± 50	13 ± 3

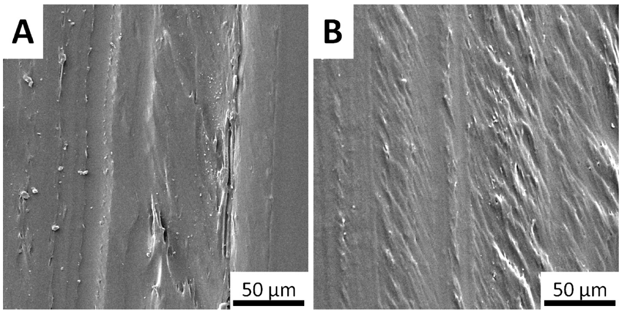

Figure 2: Microphotographs of: a) PVC/CYH/CV before immersion and b) after 3 d in the liquid

Slika 2: Posnetka: a) PVC/CYH/CV pred potopitvijo v tekočino in b) po 3 d

3.4 Antimicrobial activity

The results of the antimicrobial-activity halo-zone test against *S. aureus, E. coli* and *C. albicans*, performed with the agar-diffusion test method, are presented in **Table 2**, while **Figure 3** demonstrates the inhibition zones around the samples of the antimicrobial material (PVC/CYH/CV) studied with the agar-diffusion test. The obtained values show that the pure PVC material has no antimicrobial properties, but the PVC with CV shows an activity against all the tested microorganisms.

Table 2: Antimicrobial activity expressed as inhibition-zone diameters and their standard deviations for PVC/CYH and PVC/CYH/CV

Tabela 2: Protimikrobna aktivnost, izražena kot premer področja zaviranja in njegov standardni odmik za PVC/CYH in PVC/CYH/CV

SAMPLE	*SA*	*EC*	*CA*
PVC/CYH (mm)	0	0	0
PVC/CYH/CV (mm)	14.8 ± 0.9	10.3 ± 1.0	15 ± 3

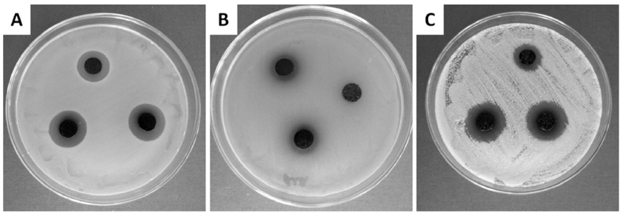

Figure 3: Photographs of Petri dishes after cultivation in the agar-test diffusion zone against: a) *S. aureus*, b) *E. coli,* c) *C. albicans*

Slika 3: Posnetki petrijevke po kultiviranju v difuzijski coni preizkusa z agarjem proti: a) S. *aureus*, b) *E. colli*, c) *C. albicans*

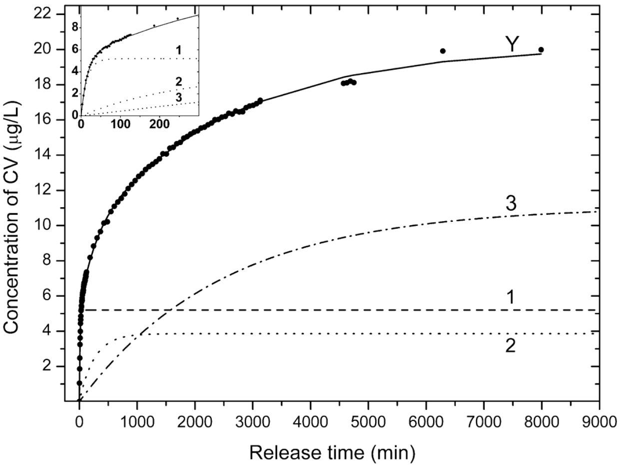

Figure 4: Release profile of CV from PVC/CYH/CV in the demineralised water. The experimental data points are represented by full-circle symbols; curve Y represents equation (3) fitted into the data; curves 1, 2 and 3 represent the single-term contributions to curve Y, respectively. The inset graph shows detailed data from the initial stage of the experiment.

Slika 4: Profil sproščanja CV iz PVC/CYH/CV v demineralizirani vodi. Eksperimentalni podatki so prikazani s polnimi krogci, krivulja Y ponazarja enačbo (3), urejeno s podatki; krivulje, označene z 1, 2 in 3 so posamezni prispevki h krivulji Y. Vstavljeni diagram prikazuje podrobne podatke iz začetka preizkusa.

3.5 Release profile of CV from PVC/CYH/CV films

The obtained release profiles are shown in **Figures 4** and **5** where the dependences of the CV concentration in the elution liquids are plotted in dependence on the release time for demineralised water and physiological solution, respectively. According to the literature, the first-order kinetic model can be a suitable formal kinetic description of the process of a water-soluble compound release from an insoluble polymer matrix to the liquid medium although it cannot be straightforwardly related to the sample geometry and it is difficult to conceptualize this mechanism on a theoretical basis.[21]

The release rate of the model compound (CV in our case) that obeys first-order kinetics can be expressed with the following equation:

$$\frac{\mathrm{d}c}{\mathrm{d}t}=-\frac{1}{\tau}c \tag{1}$$

where c is the concentration of the model compound in the elution media, the expression on the left side of the equation is the release rate defined as the concentration increase rate in the elution medium (directly obtained from absorbance, which is the observable quantity in this study), t is the release time, τ^{-1} is the first-order release-rate constant. Equation (1) can be integrated into the following form:

$$c=C_{\max}\left(1-exp\left(-\frac{t}{\tau}\right)\right) \tag{2}$$

where parameter $C_{\max}$ is the integration constant representing the maximum achievable concentration of the model compound in the elution media for the infinite time. With respect to the second boundary condition, it is assumed that the initial concentration of the model compound is zero in the liquid media at the beginning of all the experiments. The rest of the variables and constants have the same meanings as in equation (1).

It can be expected that this formal description only relates to a limited concentration range and to certain boundary conditions. According to our observations, several mechanisms can be active at different time scales during the release process and, thus, it is reasonable to extend the kinetic description by one or two more terms for the first-order processes if they differ significantly in their rate constants, i.e., by orders of magnitude. The following equation represents the extension of equation (2) for three formally independent and additive contributions to the release process:

$$c=C_{\max}-C_1\cdot exp\left(-\frac{t}{\tau_1}\right)-C_2\cdot exp\left(-\frac{t}{\tau_2}\right)-C_3\cdot exp\left(-\frac{t}{\tau_3}\right) \tag{3}$$

where C_1, C_2, C_3 represent the maximum contribution of each process to the infinite time $C_{\max}$ concentration. The rest of the variables and constants have the same meanings as in equation (2) with the indexes showing their relations to the respective process. It is obvious that:

$$C_1+C_2+C_3=C_{\max} \tag{4}$$

For the two processes involved in the release, equation (3) can be simplified by omitting the third term.

Obtained equation (3) was fitted into the experimental data as can be seen in **Figure 4** representing the water and **Figure 5** representing the physiological solution where the two-term variant was used. The contributions of each process are plotted separately with simulated curves for a better clarity. The obtained parameters are summarized in **Table 3**. This mathematical analysis was performed with a full awareness of the fact that the terms in equation (3) are not sequential but running parallel as

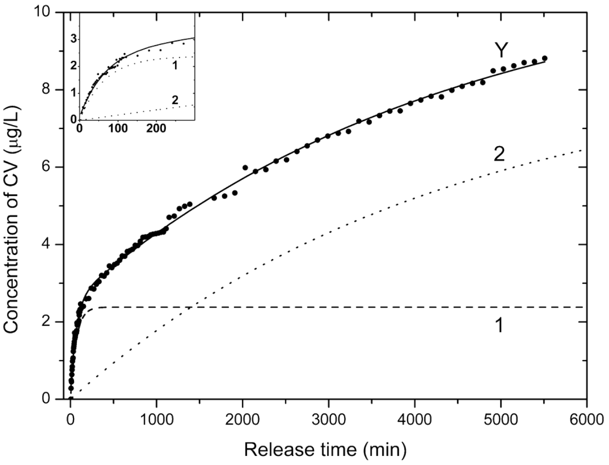

Figure 5: Release profile of CV from PVC/CYH/CV in the physiological solution. The experimental data points are represented by full-circle symbols, curve Y represents simplified equation (3) without the third term fitted into the data; curves 1 and 2 represent the single-term contributions to curve Y, respectively. The inset graph shows detailed data from the initial stage of the experiment.

Slika 5: Profil sproščanja CV iz PVC/CYH/CV v fiziološki raztopini. Eksperimentalni podatki so prikazani kot simboli polnega kroga, krivulja Y ponazarja poenostavljeno enačbo (3) brez vključitve tretjega izraza v podatke; krivulji z oznako 1 in 2 pomenita posamezen prispevek h krivulji Y. Vstavljeni diagram prikazuje podrobne podatke iz začetka preizkusa.

Table 3: Fitting-equation parameters and their standard errors describing the release profile of CV from the polymer matrix in the PVC/CYH/CV sample

Tabela 3: Parametri urejanja enačb in njihove standardne napake, ki opisujejo profil sproščanja CV iz polimerne osnove v vzorcu PVC/CYH/CV

Environment	Water	Physiological solution
$C_{\max}$ /(μg/L)	20.19 ± 0.14	11.15 ± 0.24
C_1/(μg/L)	5.20 ± 0.12	2.38 ± 0.06
T_1/min	15.2 ± 0.7	66 ± 3
C_2/(μg/L)	3.86 ± 0.16	8.63 ± 0.21
T_2/min	256 ± 24	4340 ± 220
C_3 /(μg/L)	11.09 ± 0.14	n. a.
T_3/min	2488 ± 98	n. a.

they use the common time and start at $t = 0$. However, the differences in the rate-constant magnitude separate them to an acceptable level resulting in a good approximation. Each process (term) dominates its own time-scale window and relies on its specific concentration range as it can be seen from the graphs.

The first exponential component (the term with the shortest time constant, τ_1) probably represents the release of CV from the matrix surface, because this process is the shortest and could only be limited by the CV solubility in water that is 10 g/L as indicated by the supplier. It is evident, that even the highest CV concentrations in the elution medium are far from approaching this limit. In the case of the physiological solution that shares a chloride anion with CV the solubility must be lower due to the solubility-product limitation; however, even here the solubility is more than several orders in magnitude higher than the observed concentrations. The value of the solubility product is $K_s = 6 \times 10^{-4}$ mol^2 dm^{-6} estimated roughly from the CV solubility in water. The solubility in the physiological solution can be derived by solving the following equation:

$$(x + 0.154 \text{ mol/L})x = K_s \qquad (5)$$

where x is the maximum CV concentration and 0.154 mol/L is the chloride concentration in the physiological solution. The equation gives only one positive root, $x = 0.0038$ mol/L, which corresponds to the CV concentration of 1.55 g/L. This value is about six and a half times lower than the limitation for the sample in distilled water.

The second phase of the release process is slower because the CV readily available from the matrix surface is already depleted and the CV from the subsurface layers of the film needs to cross an energetic barrier before being released into the demineralised water.

The third phase is characterized by a further significant decrease-release rate that can be ascribed to the diminishing of the gradient between the film surface and the solution layer in its proximity and to the depletion of the extractable CV in the subsurface of the film. According to the macroscopic observation, the material changed neither its colour nor any other property after its immersion into the liquid for several days. No dimension or significant mass changes were observed which confirms there was no swelling or matrix-component dissolution. Therefore, we believe that the CV located in the deeper layers of the material is not released into the solution in the relevant time horizon.

These three phases were observed for the sample immersed in the water. The sample in the demineralised water has a higher saturation value ($C_{\max}$) than the sample in the physiological solution. In general, this might be caused by the omnipresence of chloride anions with a relatively high concentration diminishing all the gradients discussed above in the case of pure water.

The first and second processes of the sample in the physiological (saline) solution were slow and the third process was not observed at all. In this case, the solubility of CV is influenced by the presence of the chloride anion, which is commonly shared between CV and the physiological solution. Moreover, the CV molecule can leave the polymer matrix as a CV$^+$ cation and a Cl$^-$ anion, always in a pair, i.e., in the ratio of 1 : 1 due to the electroneutrality condition that must always be kept. This condition is obviously satisfied in the case of water, whereas in the case of the physiological solution this pair would be released into a medium with a high concentration of chloride anions. Alternatively, a lone CV$^+$ cation can be released into the liquid with a concurrent counter transport of a Na$^+$ cation to the matrix. Both options can be considered for significantly slowing and limiting the diffusion process, so only the first two phases were observed within the time scale of several days.

3.6 Plasticizer role in the release of CV from PVC/CYH/CV films

Although the neat PVC material has been approved for medical use and can be considered as safe from the point of view of the release of the contained plasticizer or plasticizers, it must be re-evaluated after being mixed with CV as the eventual synergic effects cannot be excluded and the release of the plasticizer could be enhanced by adding other species to the compound. A simplified test was performed analysing the absorption spectra in the wavelength region where both the plasticizer and CV absorb light.

The graph in **Figure 6** shows the UV absorption spectra of the leachates obtained for the PVC/CYH/CV and neat PVC samples after a three-day elution in water. The third curve represents the absorption spectrum of CV in water with the same concentration as that in the liquid media collected for PVC/CYH/CV. It can be

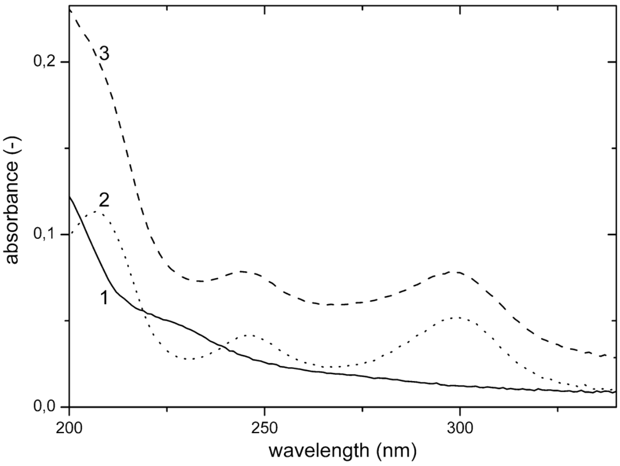

Figure 6: UV absorption spectra recorded for the CV solution in water (curve 2), leachate from the neat PVC specimen (curve 1) and leachate obtained for the PVC/CYH/CV specimen (curve 3). For details, see the text.

Slika 6: Posneta absorpcija UV-spektra za raztapljanje CV v vodi (krivulja 2), izcedna voda iz čistega PVC-vzorca (krivulja 1) in izcedna voda iz PVC/CYH/CV-vzorca (krivulja 3). Za podrobnosti glej tekst.

clearly seen, that there is no enhancement of the plasticizer release and that only a simple additivity of the signals takes place as the absorption spectrum recorded for PVC/CYH/CV is approximately the sum of the spectra of the plasticizer released from the neat PVC sample into the liquid medium and the CV solution. The test for the physiological solution showed the same result, but it is not shown here for the sake of brevity.

4 CONCLUSIONS

A model organic antimicrobial polymeric PVC/CYH/CV system based on medical-grade poly(vinyl chloride) and crystal violet was prepared with the solvent-casting technique. The work was focused on investigating the effects of the used technique for preparing and entering substances and it was shown that the CYH solvent and the model CV-active substance did not have any adverse influence on the chemical structure, morphology and mechanical properties.

The prepared solvent-cast materials can be used in the form of a film, as a volume material or as an additive for further compounding but, preferentially, we aim at various coatings and thin-film applications on the surfaces of medical devices or other plastic articles wherever this technique allows hopes for a good adhesion and compatibility with the substrate material, especially when coated on the plastic articles made of the same neat PVC resin.

The antimicrobial activity was investigated using the agar-diffusion test method and the PVC/CYH/CV material manifested a good antimicrobial activity against gram-positive *S. aureus,* gram-negative *E. coli* and yeast *C. albicans*. Although the material is an organic-doped antimicrobial polymer system, the release profile of CV, as the representative model compound with a large organic cation and halide anion, to the demineralised water and physiological solution simulating body liquids is appropriately slow allowing a long-lasting mild delivery effect of the active species on the closest proximity of the place of insertion or application. Next, no adverse effect of either the CV addition to the PVC matrix or the preparation process on the release of the plasticizers from the PVC matrix was observed.

These results suggest that the prepared model material has a potential in medical plastic industries and the obtained knowledge can be generalised to a certain degree, without losing its relevance, covering the whole class of modelled compounds and used for a further development of the materials or coatings for PVC medical devices and hygienic products.

Acknowledgment

The authors wish to thank for the internal grant of TBU in Zlin, No. IGA/FT/2013/026 funded from the resources for specific university research.

This article was written with the support of the Operational Program "Research and Development for Innovations" co-funded by the European Regional Development Fund (ERDF) and the national budget of the Czech Republic, within the "Centre of Polymer Systems" project (reg. number: CZ.1.05/2.1.00/03.0111).

This article was written with the support of the Operational Program "Education for Competitiveness" co-funded by the European Social Fund (ESF) and the national budget of the Czech Republic, within the "Advanced Theoretical and Experimental Studies of Polymer Systems" project (reg. number: CZ.1.07/2.3.00/20.0104).

5 REFERENCES

[1] R. R. Xu, L. X. Song, Y. Teng, J. Xia, Thermochimica Acta, 565 (**2013**), 205–210

[2] N. R. James, A. Jayakrishnan, Biomaterials, 24 (**2003**), 2205–2212

[3] M. Polaskova, M. Sowe, I. Kuritka, T. Sedlacek, M. Machovsky, P. Sáha, International Journal of Polymer Analysis and Characterization, 15 (**2010**), 18–26

[4] V. Sedlarik, T. Galya, J. Sedlarikova, P. Valasek, P. Saha, Polymer Degradation and Stability, 95 (**2010**), 399–404

[5] M. Herrero, P. Tiemblo, J. Reyes-Labarta, C. Mijangos, H. Reinecke, Polymer, 43 (**2002**), 2631–2636

[6] M. Herrero, R. Navarro, Y. Grohens, H. Reinecke, C. Mijangos, Polymer Degradation and Stability, 91 (**2006**), 1915–1918

[7] W. Zhang, P. K. Chu, J. Ji, Y. Zhang, X. Liu, R. K. Y. Fu, P. C. T. Ha, Q. Yan, Biomaterials, 27 (**2006**), 44–51

[8] M. Sowe, M. Polaskova, I. Kuritka, T. Sedlacek, M. Merchan, International Journal of Polymer Analysis and Characterization, 14 (**2009**), 678–685

[9] M. Merchan, J. Sedlarikova, A. Vesel, M. Machovsky, V. Sedlarik, P. Saha, International Journal of Polymeric Materials, 62 (**2013**), 101–108

[10] M. Merchan, J. Sedlarikova, V. Sedlarik, M. Machovsky, J. Svobodova, P. Saha, Journal of Applied Polymer Science, 118 (**2010**), 2369–2378

[11] J. M. Schierholz, H. Steinhauser, A. F. E. Rumps, R. Berkels, G. Pulverer, Biomaterials, 18 (**1997**), 839–844

[12] A. Jones, Plastics Engineering, 64 (**2008**), 34–40

[13] S. Budavari, The Merck Index: An Encyclopedia of Chemicals, Drugs, and Biologicals, 11th ed., Merck, Rahway, NJ, USA 1989

[14] R. Docampo, S. N. Moreno, Drug Metabolism Reviews, 22 (**1990**), 161–178

[15] M. J. Harris, Medical Journal of Australia, 154 (**1991**), 782

[16] W. Au, S. Pathak, C. J. Collie, T. C. Hsu, Mutation Research, 58 (**1978**), 269–276

[17] N. A. Littlefield, B. N. Blackwell, C. C. Hewitt, D. W. Gaylor, Fundamental and Applied Toxicology, 5 (**1985**), 902–912

[18] H. S. Rosenkra, H. S. Carr, British Medical Journal, 3 (**1971**), 702–703

[19] Y. Liu, J. J. Lin, M. M. Chen, L. Song, Food and Chemical Toxicology, 58 (**2013**), 264–272

[20] D. O. Hummel, Polymers and Additives FTIR Spectral Library, Software OMNIC, Nicolet Instrument Corp, 2011

[21] D. Suvakanta, M. N. Padala, N. Lilakanta, Ch. Prasanta, Acta Poloniae Pharmaceutica Drug Research, 67 (**2010**), 217–223

UDK 678.7:621.791
Original scientific article/Izvirni znanstveni članek

ISSN 1580-2949
MTAEC9, 48(5)705(2014)

EFFECT OF THE TOOL GEOMETRY AND WELDING PARAMETERS ON THE MACROSTRUCTURE, FRACTURE MODE AND WELD STRENGTH OF FRICTION-STIR SPOT-WELDED POLYPROPYLENE SHEETS

VPLIV GEOMETRIJE ORODJA IN PARAMETROV VARJENJA NA MAKROSTRUKTURO, VRSTO PRELOMA IN TRDNOST ZVARA PRI TORNO-VRTILNEM TOČKASTEM VARJENJU POLIPROPILENSKIH PLOŠČ

Mustafa Kemal Bilici[1], **Ahmet İrfan Yükler**[1], **Alim Kastan**[2]
[1]Department of Materials Technology, Marmara University, 34722 Istanbul, Turkey
[2]Department of Materials Technology, Afyon Kocatepe University, 03200 Afyon, Turkey
mkbilici@marmara.edu.tr

Prejem rokopisa – received: 2013-10-05; sprejem za objavo – accepted for publication: 2013-11-19

The effect of the tool geometry and welding parameters on the macrostructure, fracture mode and weld strength of the friction-stir spot welds of polypropylene sheets was studied. Three fracture modes were observed: the nugget pull-out failure, the cross-nugget failure and the mixed nugget failure under a lap-shear tensile test and nugget debonding and a pull out under a cross-tension loading, while the lap-shear tensile load was not affected significantly by the delay time. The lap-shear tensile load and the nugget thickness increased with the increasing tool rotation speed and dwell time. The macrostructure shows that the welding parameters have a determinant effect on the weld strength (*x*: the nugget thickness, *y*: the thickness of the upper sheet). Finally, when different welding parameters were used, different fracture modes of the joints were obtained in the friction-stir spot welding of polypropylene sheets. Based on the experimental observation of the macrostructures, the effect of the welding parameters and tool geometry on the lap-shear tensile load and the fracture mode were discussed.

Keywords: polymers (thermoplastics), polypropylene, friction-stir spot welding, polymer welding, welding parameters

Preučevan je bil vpliv geometrije orodja in parametrov varjenja na makrostrukturo, vrsto preloma in trdnost zvara pri torno-vrtilnem točkastem zvaru polipropilenskih plošč. Opaženi so trije načini preloma: porušitev z izpuljenjem jedra, porušitev s pretrgom jedra in mešan prelom jedra pri prekrivnem strižnem preizkusu ter prekinitve v jedru in izpuljenje jedra pri prečni natezni obremenitvi, medtem ko na prekrivno natezno obremenitev ni bilo velikega vpliva. Prekrivna strižna napetost in debelina jedra sta naraščali z naraščanjem rotacijske hitrosti orodja in časa zadržanja. Makrostruktura kaže, da parametri varjenja igrajo pomembno vlogo pri trdnosti zvara (*x*: debelina jedra, *y*: debelina zgornje plošče). Končno, če so bili uporabljeni različni parametri varjenja, so bili različni tudi načini porušitve pri torno-vrtilnem točkastem varjenju polipropilenskih plošč. Na osnovi eksperimentalnih opažanj makrostrukture je prikazan vpliv parametrov varjenja in geometrije orodja na prekrivno strižno natezno obremenitev in vrsto preloma.

Ključne besede: polimeri (termoplasti), polipropilen, torno-vrtilno točkasto varjenje, varjenje polimera, parametri varjenja

1 INTRODUCTION

Recently, a new joining technique called friction-stir spot welding (FSSW) or friction spot joining (FSJ) has been developed[1]. This technique has the same advantages as friction-stir welding (FSW) such as the solid-state process, ease of handling, joining of dissimilar materials and the materials that are difficult to fusion weld, a low distortion, excellent mechanical properties and little waste or pollution. Hence, it is expected to be used for joining lightweight materials in order to achieve a high performance and save the energy and costs of the machines.

The FSSW process consists of three phases: plunging, stirring and retracting[2]. The process starts with the spinning of a tool at a high rotation speed. Then the tool is forced into the workpiece until the shoulder of the tool plunges into the upper workpiece. The plunge movement of the tool causes the material to be expelled. When the tool reaches the predetermined depth, the plunge motion ends and the stirring phase starts. In this phase, the tool rotates in the workpieces without plunging. Frictional heat is generated in the plunging and stirring phases and, thus, the material adjacent to the tool is heated and softened. The softened upper and lower workpiece materials mix together in the stirring phase. The shoulder of the tool creates a compressional stress on the softened material. A solid-state joint is formed in the stirring phase. When a predetermined bonding is obtained, the process stops and the tool is retracted from the workpieces. The resulting weld has a characteristic keyhole in the middle of the joint created during the friction-stir spot welding. Different welding-parameter configurations and their consequences on the weld strength and fracture mode can be identified. FSSW has been successfully applied to aluminium[3], magnesium[4] and steel sheets[5], but there are very few publications on its applications to polymer[6–9].

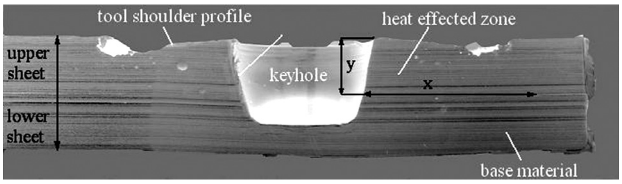

Figure 1: Schematic illustration of the cross-section of a friction-stir spot weld (*x*: nugget thickness, *y*: the thickness of the upper sheet and *t*: the total material thickness)

Slika 1: Shematski prikaz prereza torno-vrtilnega točkastega zvara (*x*: debelina jedra, *y*: debelina vrhnje plošče in *t*: skupna debelina materiala)

Based on the observations of the FSSW macrostructures, the weld zone of a FSSW joint is schematically illustrated in **Figure 1**. From the appearance of the weld cross-section, two particular points can be identified[10]. The first point is the thickness of the weld nugget (*x*) which is an indicator of the weld-bond area (**Figure 1**). The weld-bond area increases with the nugget thickness. The second point is the thickness of the upper sheet under the shoulder indentation (*y*). The sizes of these points determine the strength of a FSSW joint.

In this study, FSSW was performed to join PP sheets in order to understand the influence of the welding parameters and tool geometry on welds. The modifications of the macrostructural features (the fracture mode, the nugget thickness and the thickness of the upper sheet) induced by these different processing configurations are identified and their consequences on the weld strength and fracture mode during the lap-shear tensile tests are discussed. The purpose of this investigation was to improve the strength of the spot welds. Both the nugget thickness and the upper-sheet thickness have significant effects on the fracture modes under tensile loading.

2 EXPERIMENTS

In this investigation 4-mm-thick polypropylene sheets were used. The polypropylene sheets were purchased from SIMONA AG, Germany (the tensile yield stress of 34 MPa or lap-shear fracture load of 4500 N). Specimens were made by using 60 mm by 150 mm sheets with a 60 mm by 60 mm overlap area. In order to carry out the FSSW tests, a properly designed clamping feature was utilized to fix the specimens to be welded on an NC milling machine. The tool was made of the SAE 1040 steel and heat-treated to a hardness of 35 HRC. Four different tool-pin profiles (straight cylindrical, tapered cylindrical, threaded cylindrical and triangular) were used to fabricate the joints (**Figure 2**).

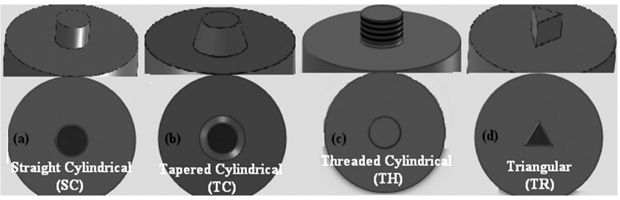

Figure 2: FSSW tool profiles: a) straight cylindrical, b) tapered cylindrical, c) threaded cylindrical, d) triangular

Slika 2: Profil FSSW-orodja: a) raven valjast, b) stožčast valjast, c) valjast z navojem, d) trikoten

Each tool had a pin length 5.5 mm and pin size 7.5 mm. The tapered pin had a 15° pin angle. For the straight cylindrical, tapered cylindrical and threaded cylindrical pins, the pin size was determined by measuring the bottom diameter of the pin. For the triangular pins, the pin size was determined by calculating the diameter of the cross-section area formed by the turning pin.

In all the cases, the constant tool-plunge rate of 0.26 mm/s and the shoulder-plunge depth of 0.2 mm below the upper-plate surface were applied. The tool rotation speeds and the tool dwell times also varied, being between 560 r/min and 1400 r/min, and between 20 s and 200 s, respectively.

The welded lap-shear specimens were tested on a ZWICK machine at the constant cross-head speed of 5 mm/s. The load and displacement were simultaneously recorded during the test. The fracture mode of each specimen was then determined. The fracture-mode-appearance observations of the joints were done with a camera. For the weld-macrostructure studies, thin slices (of 20 μm) were cut from the welded specimens using a Leica R 6125 rotary microtome. These thin slices were investigated using a video spectral comparator. The photographs of the cross-sections were obtained.

3 EXPERIMENTAL RESULTS

During the FSSW of polyetprophlene, three types of fracture mode were observed as shown in **Figure 3**: (a) the nugget pull-out failure, *P*; (b) the cross-nugget failure, *C*; and (c) the mixed nugget failure, *M*. By changing the welding parameters, these three types of fracture mode were changed. These three types of fracture mode are affected by the heat amount: insufficient heat, ideal heat and excessive heat. Consequently, the orientation of the fracture mode changes the weld strength. While the highest lap-shear fracture load causes a nugget pull-out

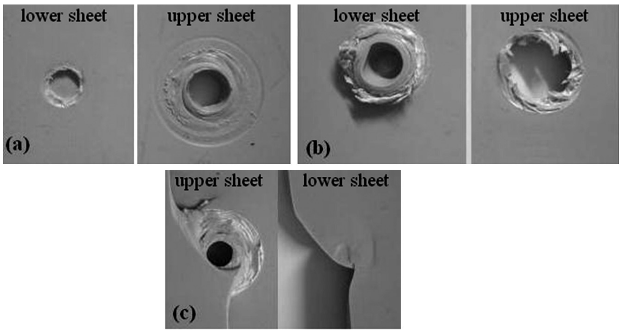

Figure 3: Three types of fracture mode: a) nugget pull-out failure, b) cross-nugget failure and c) mixed nugget failure

Slika 3: Tri vrste preloma: a) izvlečenje jedra, b) prečna porušitev jedra in c) mešana porušitev jedra

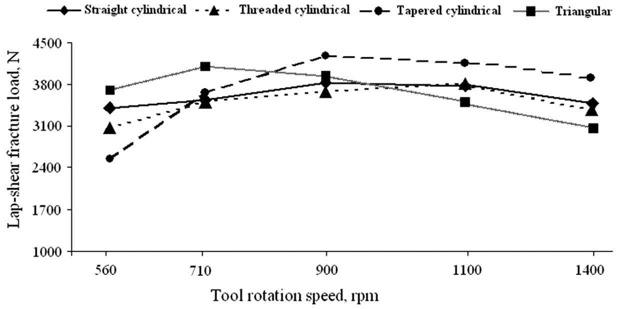

Figure 4: Effect of tool profile and tool rotation speed on weld strength

Slika 4: Vpliv profila orodja in hitrosti vrtenja orodja na trdnost zvara

failure, the lowest lap-shear load causes a cross-nugget failure.

The effect of the tool-pin geometry on the lap-shear fracture load is shown in **Figure 4**. In these tests the welding parameters were kept constant: the tool rotation speed ranged from 360 r/min to 1400 r/min, the tool-plunge rate was 0.26 mm/s, the dwell time was 120 s and the tool-plunge depth was 5.7 mm. The maximum fracture load (900 r/min) was obtained with the tapered cylindrical pin (4280 N) and the threaded cylindrical pin resulted in the lowest fracture load (3305 N). Due to the maximum fracture load obtained with the tapered cylindrical pin, all the experiments were made with the tapered cylindrical pin. The effect of the tool profile on the welding zone is shown in **Figure 5**. The three photographs illustrate that the size of the keyhole formed in the welding zone depend directly on the pin profile. The wall slope of the keyhole changed with the pin-angle of the tool. The nugget thickness was 8.4 mm for the straight cylindrical pin, 9.9 mm for the 15° angled tapered pin and 7.8 mm for the threaded cylindrical pin. The tapered pin created a thicker nugget and a bigger weld-bond area than the straight cylindrical pin. The nugget thickness increased with the pin profile changes, as shown in **Figure 5**. Also, the nugget thickness exhi-

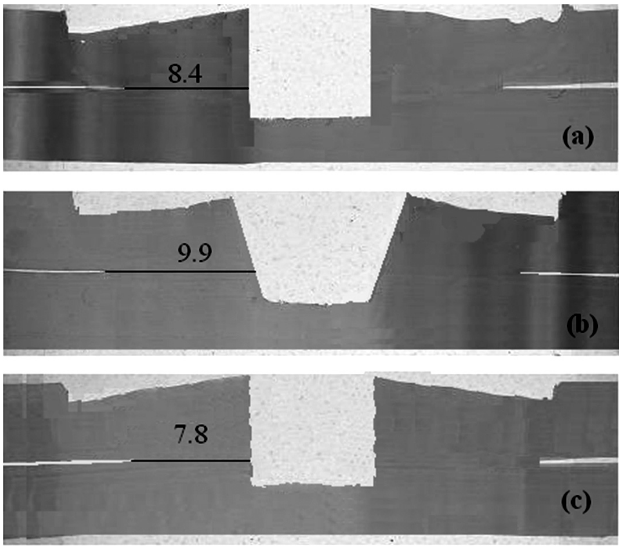

Figure 5: Effect of tool geometry on weld-nugget formation: a) straight cylindrical pin, b) 15° angled tapered cylindrical pin and c) threaded cylindrical pin

Slika 5: Vpliv geometrije orodja na nastanek jedra: a) cilindrična konica, b) stožčasta valjasta konica s kotom 15° in c) valjasta konica z navoji

Table 1: Effect of tapered cylindrical pin on the fracture mode and nugget thickness

Tabela 1: Vpliv valjaste konice na način preloma in debelino jedra

Tool rotation speed (r/min)	Fracture mode	Macrostructure	Quality of weld-metal consolidation	Probable reason for the formation
360	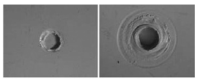		very poor	Insufficient flow of the joining materials due to low heat
560		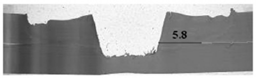	poor	Although there was insufficient heat, a weld was formed
710	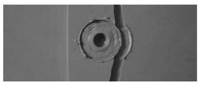		better than in the previous case	Heat input is sufficient for a good-quality weld
900	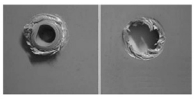	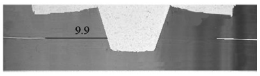	very good	Heat input is sufficient for a good-quality weld
1120	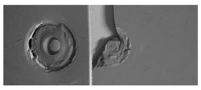	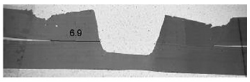	good	Heat input is sufficient for a good-quality weld
1400	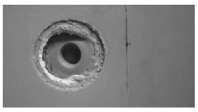	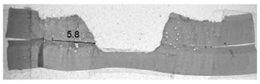	worse than in the previous case	Poor weld quality occurred due to excessive heat

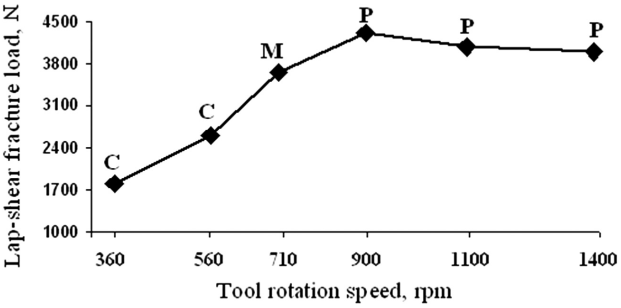

Figure 6: Effect of tapered cylindrical pin on lap-shear fracture load
Slika 6: Vpliv stožčasto valjaste konice na prekrivno strižno obremenitev

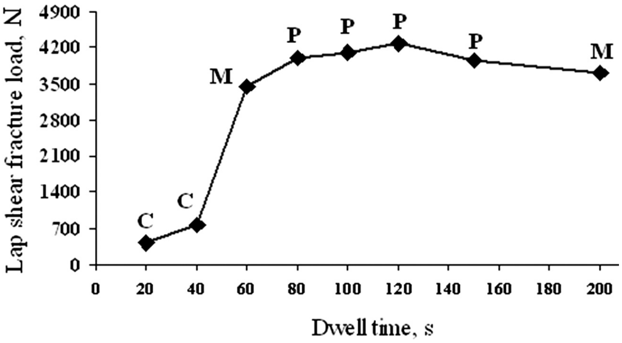

Figure 7: Effect of dwell time on lap-shear fracture load
Slika 7: Vpliv časa zadržanja na prekrivno strižno obremenitev

bited a very large decrease with the threaded cylindrical pin, as shown in **Figure 5**.

The best results were obtained in the experiments involving the tapered cylindrical pin. For this reason, for the following experiments, investigating the effect of the welding parameters the tapered pin was used. In order to determine the effect of the tool rotation speed on the FSSW of polypropylene, seven different speeds were used. For all the welds, the plunge rate was 0.26 mm/s, the dwell time was 120 s and the tool-plunge depth was 5.7 mm. These three parameters were kept constant and only the dwell time was allowed to vary in the welding operations. Increasing the tool rotation speed from 360 r/min to 1400 r/min resulted in a linear progress in the strength of the welds. The effects of these speeds are shown in **Figure 6**. While the lap-shear fracture load dramatically increased up to the rotation speed of 900 r/min, it decreased after 900 r/min. The maximum fracture load obtained at 900 r/min was 4280 N. The fracture modes obtained were the cross-nugget failure at the speeds of 360 r/min and 560 r/min, the nugget pull-out failure at 710 r/min, and the mixed nugget failure at (900, 1120 and 1400) r/min. The fracture mode and the macrostructure are shown in **Table 1**.

The largest nugget thickness was 9.9 mm obtained at the tool rotation speed of 900 r/min. The lowest nugget thickness was 4.5 mm obtained at the tool rotation speed of 360 r/min. This nugget thickness is very important for the lap-shear fracture load. At the tool rotation speed of 900 r/min, a thicker nugget and a larger weld-bond area than at the other tool rotation speeds were obtained. The nugget thickness and the fracture load increased with the tool rotation speed as shown in **Table 1** and **Figure 6**.

Figure 7 shows the effect of the dwell time on the lap-shear tensile strength of FSSW joints. For all the welds, the plunge rate was 0.26 mm/s, the tool rotation speed was 900 r/min and the plunge depth was 5.7 mm. These three parameters were kept constant and only the dwell time was allowed to vary during the welding operations. The dwell-time experiments used the tapered pin. Increasing the dwell time from 20 s to 180 s resulted in a linear progress in the strength of the welds. The transition time for the failure modes of the PP sheets 4 mm under the above-mentioned welding parameters was found to be 45 s. In the period between the dwell times of 20 s and 120 s, there was a slight increase in the weld strength. For the dwell times of more than 120 s, the lap-shear fracture load showed a linear decrease after 120 s. A longer tool stirring time did not affect the weld strength. Only the fracture mode was changed during the lap-shear tests. The effect of the dwell time on the weld cross-sections is shown in **Table 2**. A thin nugget of the weld developed over the dwell time of 20 s (**Table 2**). The nugget thickness increased with the dwell time

Table 2: Influence of dwell time on the fracture mode and nugget thickness
Tabela 2: Vpliv časa zadržanja na vrsto preloma in debelino jedra

Dwell time (s)	Fracture mode	Macrostructure	Quality of weld-metal consolidation	Probable reason for the formation
20	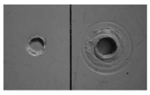	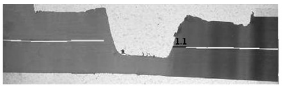	very poor	Insufficient flow of the joining materials due to low heat
120	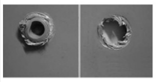	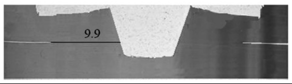	very good	Heat input is sufficient for a good-quality weld
200	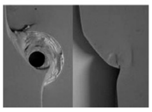		worse than in the previous case	Poor weld quality due to excessive heat

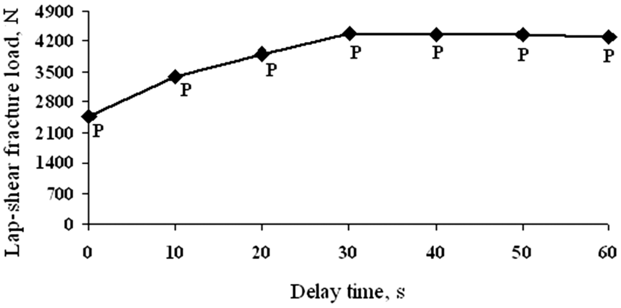

Figure 8: Effect of delay time on lap-shear fracture load
Slika 8: Vpliv časa zakasnitve na prekrivno strižno obremenitev

(**Table 2**). The maximum fracture load was obtained at the dwell time of 120 s. Different fracture modes were obtained during the dwell-time tests: the cross-nugget failure at the dwell times of 20 s and 45 s; the pull-nugget failure at the dwell times of (80, 100, 120 and 150) s; and the mixed nugget failure at the dwell times of 60 s and 200 s. The fracture mode and the macrostructure are shown in **Table 2**. The largest nugget thickness was 9.9 mm obtained at the dwell time of 120 s. The smallest nugget thickness was 1.1 mm obtained at the dwell time of 20 s. The dwell time is very important for the nugget thickness. At the dwell time 120 s, a thicker nugget and a bigger weld-bond area were produced than at the dwell times 20 s and 200 s, as shown in **Table 2**.

In order to determine the effect of the delay time on the FSSW of polypropylene, seven different delay times were used. **Figure 8** shows the effect of the delay time on the weld strength. In all the welds, the plunge rate was 0.26 mm/s, the dwell time was 120 s and the plunge depth was 5.7 mm. These three parameters were kept constant and only the dwell time was allowed to vary during the welding operations. The lap-shear fracture load was on an increase up to the dwell time of 30 s. After this dwell time, the lap-shear fracture load decreased very little. Although the delay time increased up to seven fold, the weld strength changed only within the experimental scatter limits (delay times of (0, 10, 20) s). The highest lap-shear fracture load was obtained after 30 s. For all the delay times the fracture mode was observed to be the nugget pull-out failure. The largest nugget thickness was 9.9 mm obtained with the delay time of 45 s. The delay time is very important for the nugget thickness. The delay time 45 s led to a thicker nugget and a bigger weld-bond area than the delay times of 0 s to 30 s, as shown in **Table 3**.

4 DISCUSSION

The importance of the tool pin profile is shown in **Figure 4**. The tapered cylindrical pin resulted in the biggest and the threaded cylindrical pin resulted in the lowest lap-shear fracture load. The reason for this difference can be easily explained with the weld-nugget thicknesses that are shown in **Figure 5**. The straight cylindrical pin and tapered cylindrical pin have the same pin size (7.5 mm), but the weld-nugget thicknesses obtained with these pins are different. The nugget thickness obtained with the straight cylindrical pin was 8.4 mm as shown in **Figure 5a**. The tapered cylindrical pin provided the weld-nugget thickness of 9.9 mm (**Figure 5b**). The threaded cylindrical pin provided the weld-nugget thickness of 7.8 mm (**Figure 5c**). The tapered pin created a thicker nugget and a bigger weld-bond area than the other tools. With the straight cylindrical pin a small amount of frictional heat was produced in the weld; therefore, a small weld-bond area and a very low strength were obtained. The stirring of the pin increased with the tool rotation speed[11]. The frictional heat also increased with the rotation speed. The maximum strength was obtained with the speed 900 r/min. The welding residual stresses of the upper sheet increased with the tool rotation speed[12]. When the rotation speed exceeded 900 r/min, the strength decreased because of the increased residual stresses. The lap-shear fracture load of a FSSW joint is directly proportional to the nugget thickness and the weld-bond area[10]. The tapered pin produced more frictional heat and a larger weld thickness, as shown in **Figure 5**. The heat produced in the weld area is directly proportional to the welding parameters and the tool geometry[13]. Suitable welding parameters produce more heat and a large weld area, causing a high weld strength[14]. Therefore, the tapered pin produces a higher lap-shear fracture load than the other pins. As seen in **Figure 4**, the strength varies significantly with the tool pin profile. **Figure 5** shows that the maximum nugget thickness (9.9 mm) changes with the pin profile. In fact, a change in the pin profile results in a more extensive stirring and a higher heat input during the

Table 3: Influence of delay time on the fracture mode and nugget thickness
Tabela 3: Vpliv časa zakasnitve na vrsto preloma in debelino jedra

Delay time (s)	Fracture mode	Macrostructure	Quality of weld-metal consolidation	Probable reason for the formation
0	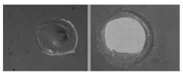	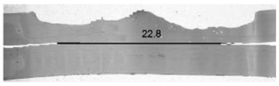	very poor	Insufficient flow of the joining materials due to low heat
45	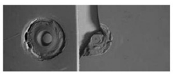	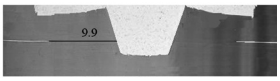	very good	Heat input is sufficient for a good-quality weld

FSSW, causing the nugget thickness to develop. The shear fracture of the nugget takes place easily when the nugget thickness is small, having a low tensile-shear strength. The results presented in **Figure 5** are in agreement with the work up to a certain tool profile (tapered pin). Different tool profiles resulted in three types of fracture in the FSSW of PP. These three types of fracture mode are affected by the heat amount: insufficient heat, ideal heat and excessive heat. Consequently, frictional heat occurred with different tool profiles. The fracture-mode changes associated with the nugget thickness and weld strength are shown in **Figure 5**. As a result, the reason for this strength difference is the chain scission[15]. The chain scission lowers the strength of a thermoplastic material[16]. If a molten thermoplastic material is heated to a high temperature and then a high pressure is applied to it, a decrease in the molecular weight of the material occurs[15]. The mechanical properties of thermoplastics decrease with lowering the molecular weight[17]. In FSSW the welding tool produces a compressive pressure in the weld zone[18]. In the FSSW of thermoplastics, the material in the weld area melts[7].

Figure 6 shows the effect of the tool rotation speed of the tapered pin on the weld strength. The lowest strength was obtained at the tool rotation speed of 360 r/min. In this weld, a small amount of frictional heat was produced; therefore, a small weld-bond area, a very low strength and the cross-nugget failure were obtained. The stirring of the pin increased with the tool rotation speed[13]. The frictional heat increased with the rotation speed. The maximum strength (4280 N) was obtained with the speed 900 r/min. The welding residual stresses of the upper sheet increased with the tool rotation speed[12]. When the rotation speed exceeded 900 r/min, the strength decreased because of the increased residual stresses. The fracture mode changed with the increasing tool rotation speed. The fracture mode changed due to the frictional heat. The lowest frictional heat led to the cross-nugget failure, while the excessive frictional heat led to the mixed nugget failure (**Table 1**). A high frictional heat causes a high material temperature in the welding zone[7] and a thicker nugget, as shown in **Table 1**. The fracture also occurs due to the high frictional heat in the welding zone. The tapered pin forms a thicker nugget and a bigger weld-bond area than the other pins. In the FSSW fracture experiments, the ideal fracture type is the nugget pull-out failure due to the high weld strength.

Figure 7 shows the effect of the dwell time of the tapered pin on the weld strength. The effects of the dwell time on the weld strength and fracture mode are shown in **Table 2**. Short dwell times cause a thin nugget thickness and the cross-nugget failure, as shown in **Table 2**. The nugget thickness, bond area and fracture mode have a direct effect on the weld strength. Increasing the dwell time from 20 s to 40 s resulted in a linear progress in the strength of the welds. All these welds were fractured under small tensile loads because of the small weld-bond areas. As the dwell time increased, the frictional heat increased as well. Larger weld nuggets were obtained with longer dwell times, increasing the joint strength (**Table 2**). An increase in the dwell time changed the fracture mode. The maximum weld strength was obtained with the nugget pull-out failure, as shown in **Figure 7** (dwell time 120 s). The shape of the weld-bond area in FSSW is found to be of high importance. The weld nugget represents the weld bond in FSSW. The cross-section area of a weld nugget determines the strength of a weld[19]. Very high temperatures were recorded in the FSW of plastics[8,12]. High melt temperatures and high welding forces cause chain scission in the welding zones of the plastics, decreasing the weld strength[20]. The physical properties of a polymer are strongly dependent on the size or length of the polymer chain. For example, if a chain length is increased, the melting and boiling temperatures increase quickly as well. The weld strength also tends to increase with the chain length, as does the viscosity, or the resistance to flow, of the polymer in its melt state. The FSSW process produces high temperature and pressure. But the excessive heat and pressure cause the chain structure to break. Most of the molten material is expelled, so a very small weld stir zone is formed, resulting in a very small fracture load. Thus, a reduction in the weld strength occurs. In friction-stir welding it is very important to check the excessive heat and pressure. Furthermore, the tool geometry is very important in the production of heat and pressure.

In this study each mechanical-test diagram shows an extremum. The lap-shear fracture load increases with the tool rotation speed (**Figure 6**), the dwell time (**Figure 7**) and the delay time (**Figure 8**). All these diagrams indicate that there is an optimum value for each welding parameter. When a variable value exceeds the critical value, the weld strength starts to decrease. The size of the weld increases continuously with the welding-parameter variables (**Figures 6**, **7** and **8**). For example, the weld-nugget thickness increases with the tool rotation speed (**Figure 6**). The lap-shear fracture load reaches its highest value with the tapered pin (**Figure 6**). The reason for this strength difference is the mechanical scission[15]. Mechanical scission lowers the strength of a thermoplastic material[16]. If a liquid thermoplastic material is heated to a high temperature and then a high pressure is applied to it, a decrease in the molecular weight of the material occurs[15]. The mechanical properties of thermoplastics decrease with lowering the molecular weight[17]. In FSSW the welding tool produces a compressive pressure in the weld zone[18]. In the FSSW of thermoplastics, the material in the weld area melts[21]. High liquid temperatures and high welding forces cause mechanical scission in the welding zones of the plastics, which lowers the weld strength[20].

The frictional heat produced in the vicinity of the tool increased with the dwell time[11,22], so the temperature of the material increased as well. The temperature of the material reached the melting temperature (131 °C) in the dwell time 45 s. The temperature rose up to 142 °C within the dwell time 50 s and it did not change with the extended dwell time. Similar temperatures were calculated for the friction-stir welding of PP sheets[12,22]. If the tool was retracted at the end of the predetermined dwell time, the liquid filled the space of the pin, as shown in **Table 3**. This weld does not have a characteristic keyhole in the nugget. If the pin was retracted with the delay time 45 s, the liquid in the vicinity of the pin cooled down and solidified. Such a weld has a keyhole as shown in **Table 3**. During all the experiments, the nugget pull-out failure occurred at the end of the delay time. Also, an increase in the delay time increases the weld strength. The dwell times from 30 s to 60 s resulted in a linear progress in the strength of the welds. All these welds were fractured with small tensile loads because of the small weld-bond areas. Larger weld nuggets were obtained with longer delay times, which increased the joint strength (**Figure 8**). The shape of a weld-bond area in FSSW is found to be of high importance. The cross-section area of a weld nugget determines the strength of a weld[23]. A weld with a small bond area fractures under a low tensile force in the zero delay time. In the FSSW of PP sheets 4 mm, the ideal delay time was found to be 45 s.

Fracture modes were changed in accordance with the welding parameters and tool geometry. This change in the welds causes the melting and boiling temperatures to increase quickly. For example, as a chain length is increased, the melting and boiling temperatures increase quickly. The weld strength also tends to increase with the chain length, as does the viscosity, or resistance to flow, of the polymer in its melt state. Due to these properties of polypropylene, the weld strength and fracture mode can be changed. Therefore, in the FSSW of polypropylene, both the fracture mode and the weld strength were very important.

5 CONCLUSIONS

The macrostructures, the weld strength and the fracture mode of friction-stir spot welds of polypropylene sheets were investigated.

- In the FSSW of polypropylene, three types fracture mode were observed: the nugget pull-out failure, the cross-nugget failure and the mixed nugget failure.
- The weld strength during FSSW was found to mainly depend on two macrostructural features: the weld-nugget thickness (*X*) and the thickness of the upper sheet under the shoulder indentation (*Y*).
- With the increasing rotation speed (up to 900 r/min), the lap-shear fracture load decreased because of the increased amount of the heat generated by the mechanical scission in the stir zone.
- The tool rotation speed and dwell time must be sufficient to allow a high weld strength and the appropriate fracture mode.
- During the FSSW of polypropylene, the pin geometry affects the nugget formation and lap-shear fracture load.
- The optimum tool for sheets 4 mm was found to be the tapered cylindrical pin.
- Mechanical scission can occur during the FSSW of polypropylene, if excessive frictional heating is created in the weld zone, so the optimum welding parameters should be chosen (the tool rotation speed of 900 r/min, the dwell time of 120 s and the delay time of 45 s).

6 REFERENCES

[1] Y. Tozaki, Y. Uematsu, K. Tokaji, Fatigue Fracture Materials Structure, 30 (**2007**), 143–148

[2] P. C. Lin, J. Pan, T. Pan, Journal Fatigue, 30 (**2008**), 90–105

[3] M. Merzoug, M. Mazari, L. Berrahal, A. Imad, Materials Design, 31 (**2010**), 3023–3028

[4] Y. C. Chen, K. Nakata, Materials Design, 30 (**2009**), 3913–3919

[5] M. I. Khan, M. L. Kuntz, P. Su, A. Gerlich, T. North, Y. Zhou, Technology Welding Joining, 12 (**2007**), 175–182

[6] M. K. Bilici, A. I. Yukler, M. Kurtulmus, Materials Design, 32 (**2011**), 4074–4079

[7] A. Arıcı, S. Mert, Journal of Reinforce Plastics and Composite, 1 (**2008**), 1–4

[8] P. F. H. Oliveria, S. T. A. Filho, J. F. Santos, E. Hage, Materials Letters, 64 (**2010**), 2098–2101

[9] M. K. Bilici, A. I. Yukler, Materials Design, 33 (**2012**), 145–152

[10] Y. Tozaki, Y. Uematsu, K. Tokaji, International Journal of Machine Tools and Manufacture, 47 (**2010**), 2230–2236

[11] N. Ma, A. Kunugi, T. Hirashima, K. Okubo, M. Kamioka, Welding International, 23 (**2009**), 9–14

[12] M. Aydin, Polymer Plastics Technology Engineering, 49 (**2010**), 595–601

[13] M. Awang, V. H. Mucino, Z. Feng, S. A. David, SAE International, 1 (**2005**), 1251–1256

[14] S. J. Vijay, N. Murugan, Materials Design, 31 (**2010**), 3585–3589

[15] H. M. Costa, V. D. Ramos, M. C. G. Rocha, Polymer Testing, 24 (**2005**), 86–93

[16] C. Capone, L. D. Landro, F. Inzoli, M. Penco, L. Sartore, Polymer Engineering Science, 47 (**2007**), 1813–1819

[17] S. T. Lim, C. A. Kim, H. Chung, H. J. Choi, J. H. Sung, Korea-Australia Rheology Journal, 2 (**2004**), 57–62

[18] A. Gerlich, T. H. North, M. Yamamoto, Science and Technology of Welding and Joining, 12 (**2007**), 472–480

[19] R. S. Mishra, Z. Y. Ma, Materials Science Engineering, 50 (**2005**), 1–78

[20] Y. X. Gan, S. Daniel, Materials, 3 (**2010**), 329–350

[21] W. Yuan, R. S. Mishra, S. Web, Y. L. Chen, B. Carlson, D. R. Herling, G. J. Grant, Journal of Materials Processing Technology, 211 (**2011**), 972–977

[22] J. E. Mark, Polymer Data Handbook, Oxford University Press, New York 1999

[23] S. M. Chowdhury, D. L. Chen, S. D. Bhole, X. Cao, Materials Science Engineering A, 527 (**2010**), 6064–6075

UDK 669.35:620.17
Original scientific article/Izvirni znanstveni članek

ISSN 1580-2949
MTAEC9, 48(5)713(2014)

MICROSTRUCTURAL ANALYSIS OF CuAlNiMn SHAPE-MEMORY ALLOY BEFORE AND AFTER THE TENSILE TESTING

ANALIZA MIKROSTRUKTURE ZLITINE CuAlNiMn Z OBLIKOVNIM SPOMINOM PRED NATEZNIM PREIZKUSOM IN PO NJEM

Ivana Ivanić[1], Mirko Gojić[1], Stjepan Kožuh[1], Borut Kosec[2]
[1]University of Zagreb, Faculty of Metallurgy, Aleja narodnih heroja 3, 44103 Sisak, Croatia
[2]University of Ljubljana, Faculty of Natural Sciences and Engineering, Aškerčeva cesta 12, 1000 Ljubljana, Slovenia
iivanic@simet.hr

Prejem rokopisa – received: 2013-10-07; sprejem za objavo – accepted for publication: 2013-11-18

In this paper the results of a microstructural analysis before and after fracture along with the mechanical properties and hardness of the CuAlNiMn shape-memory alloy are presented. The melting of the alloy was carried out in a vacuum-induction furnace in a protective atmosphere of argon. The alloy was cast into an ingot of 15 kg. After casting the alloy was forged and rolled into rods with a diameter of approximately 10 mm. A microstructural characterization was performed with light microscopy (LM) and scanning electron microscopy (SEM) equipped with energy-dispersive spectrometry (EDS). Martensitic microstructure was observed in the rods after the deformation. The fractographic analysis of the samples after the tensile testing revealed some areas with intergranular fracture. However, the greater part of the fracture surface indicated the pattern of transgranular brittle fracture. The results of the tensile tests showed the tensile strength of 401.39 MPa and elongation of 1.64 %. The hardness of the CuAlNiMn alloy is 290.7 HV0.5.

Keywords: shape-memory alloy, CuAlNiMn, fracture analysis, microstructure, hardness

V prispevku so predstavljeni rezultati analize mikrostrukture pred prelomom in po njem skupaj z mehanskimi lastnostmi in trdoto zlitine CuAlNiMn z oblikovnim spominom. Taljenje zlitine je bilo izvedeno v vakuumski peči v zaščitni atmosferi argona. Zlitina je bila ulita v ingot mase 15 kg. Po litju je bila zlitina kovana in zvaljana na premer približno 10 mm. Karakterizacija mikrostrukture je bila izvedena s svetlobno mikroskopijo (SM) in vrstično elektronsko mikroskopijo (SEM), opremljeno z energijskim disperzijskim spektrometrom (EDS). Analizirana je bila martenzitna mikrostruktura zlitine CuAlNiMn pred izvedenim nateznim preizkusom. Izvedena sta bila natezni preizkus in meritve trdot. Fraktografska analiza je pokazala več področij z interkristalnim in pogosto transkristalnim krhkim prelomom. Rezultati nateznega preizkusa so pokazali, da je natezna trdnost 401,39 MPa in raztezek 1,64 %. Trdota zlitine CuAlNiMn je 290,7 HV0,5.

Ključne besede: zlitina z oblikovnim spominom, CuAlNiMn, analiza preloma, mikrostruktura, trdota

1 INTRODUCTION

Shape-memory alloys (SMAs) based on copper such as CuZnAl and CuAlNi are attractive for practical applications because of their special properties (shape-memory effect and pseudoelasticity) which are based on the crystallographic reversible thermoelastic martensitic transformation. They are also suitable due to lower costs (compared to NiTi) and the advantages with regard to electrical and thermal conductivities.[1–5]

However, the polycrystalline copper-based shape-memory alloys with coarse grains are very brittle and they are prone to intergranural fracture because of the high elastic anisotropy of the parent β phase, the existence of the brittle γ_2 (Cu_9Al_4) phase and the formation of the stress-induced martensites along the grain boundaries upon quenching.[6–10] The usual way to improve the disadvantages mentioned above is to alloy them with the elements that are grain refiners like Ti, B and Zr, which create the precipitates limiting the grain size and grain growth. Also, the production of the alloy with the rapid-solidification technique or powder metallurgy is very effective in obtaining a fine-grain microstructure.[2,11] The mechanical properties of the polycrystalline CuAlNi alloy can be improved effectively with grain refinement and texture control. Both of them play important roles in relaxing the stress concentration at grain boundaries, which prevents intergranular fracture and improves the plasticity of the alloy. The fatigue and memory properties of the CuAlNi alloy with fine grains are considerably limited because the fine grains inevitably tend to grow during hot-working or heat treatment, leading to a degradation of mechanical properties.[6,12]

Manganese is added as an alloying element to improve the ductility of the CuAlNi alloy by replacing the partially aluminum content. It also increases the stability domain of the β phase and allows the betatising process to be performed at lower temperatures.[8,12] Also, manganese was provided to enhance the thermoelastic and pseudoelastic behavior.[11,13]

The aim of this paper was to carry out the strength testing, hardness measurements, microstructural characterization and a fractographic analysis of the CuAlNiMn alloy.

2 EXPERIMENTAL WORK

The CuAlNiMn shape-memory alloy was produced by melting in a vacuum-induction furnace in a protective atmosphere of argon and cast into a classical iron mould with the dimensions of 100 mm × 100 mm × 200 mm. The heating temperature was 1330 °C. After casting the alloy was forged and rolled with step heating at 900 °C after every reduction into the bars with a diameter of approximately 10 mm. From the bars the samples were prepared as standard round tensile-test probes with the dimensions of ϕ 6 mm × 100 mm. The tensile test was made with a Zwick/Roell Z050 universal tensile-testing machine at room temperature. Light microscopy (LM) and scanning electron microscopy (SEM) equipped with energy-dispersive spectroscopy (EDS) were applied for the microstructural characterization of the alloy. For the microstructural analysis, the samples were grinded (120–800 grade paper) and polished (0.3 µm Al_2O_3). After polishing, the samples were etched in a solution composed of 2.5 g $FeCl_3$ and 48 mL methanol in 10 mL HCl for 15 s. A fractographic analysis using a JOEL JSM5610 scanning electron microscope was carried out to observe the surfaces of the samples after the tensile testing. The hardness of the alloy was carried out with the Vickers method with the applied force of 5 N.

3 RESULTS AND DISCUSSION

The average chemical composition of the alloy measured with EDS was Cu-8.05 % Al-3.51 % Ni-2.44 % Mn (*w*/%).

3.1 Microstructural characterization before fracture

The obtained microstructures are presented on **Figures 1** to **3**. It can be observed that the microstructure of the alloy after the deformation (forging and rolling) is martensitic. Because of the plastic deformation after the casting, it can be assumed that most of the martensite in

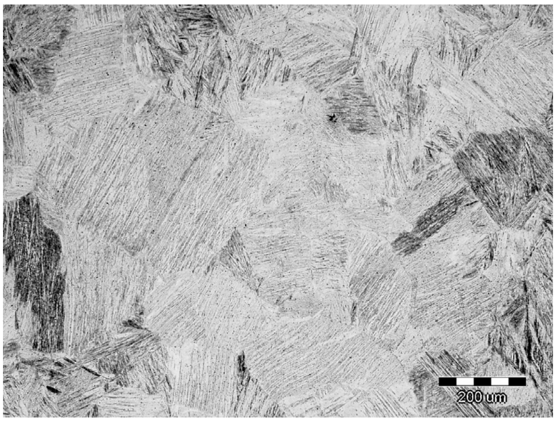

Figure 1: LM micrograph of the CuAlNiMn shape-memory alloy, magnificaton 100-times

Slika 1: Mikrostruktura zlitine CuAlNiMn z oblikovnim spominom, povečava 100-kratna

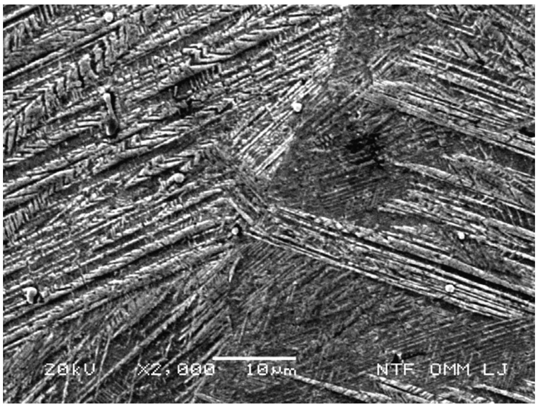

Figure 2: SEM micrograph of the CuAlNiMn shape-memory alloy

Slika 2: SEM-posnetek mikrostrukture zlitine CuAlNiMn z oblikovnim spominom

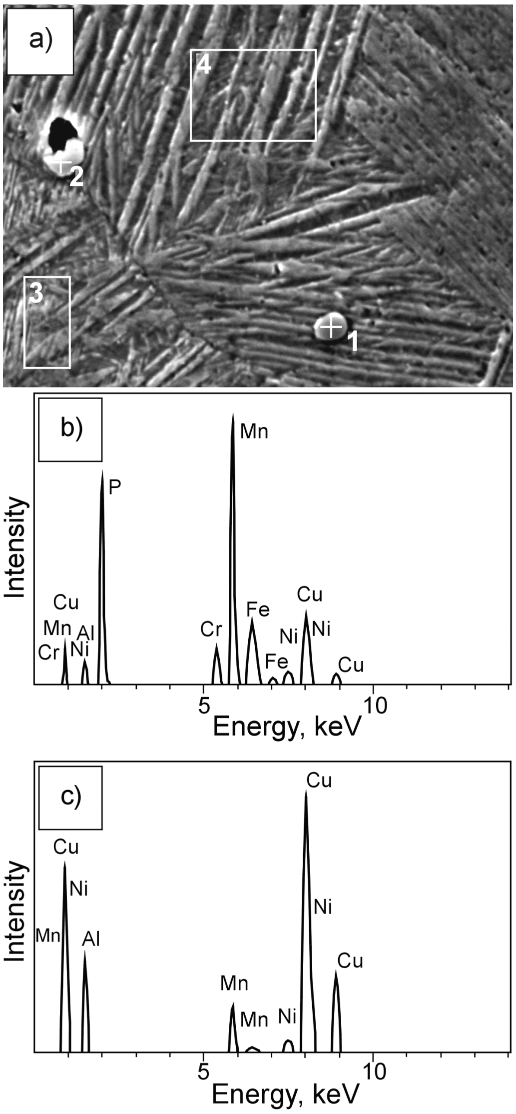

Figure 3: a) SEM micrograph of the CuAlNiMn shape-memory alloy with the positions marked for EDS analysis, b) EDS spectrum for position 1 and c) EDS spectrum for position 3

Slika 3: a) SEM-posnetek mikrostrukture zlitine CuAlNiMn z oblikovnim spominom z označenimi mesti za EDS-analizo, b) EDS-spekter na mestu 1 in c) EDS-spekter na mestu 3

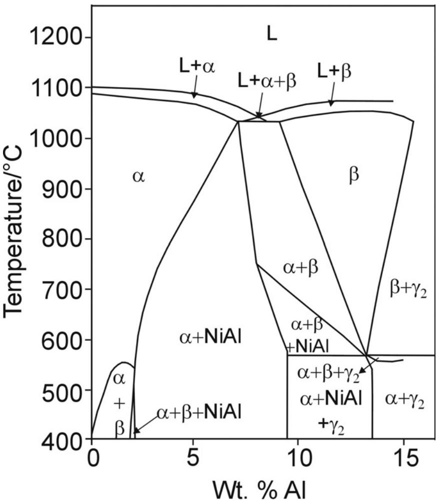

Figure 4: Ternary phase diagram of the CuAlNi alloy; a vertical cross-section at the mass fraction of Ni $w = 3$ % [9]

Slika 4: Ternarni fazni diagram zlitine CuAlNi; vertikalni prerez pri masnem deležu Ni $w = 3$ % [9]

the structure is the stress-induced martensite. The grains appear clearly and the martensite plates have different orientations in individual grains. We also noticed a large grain size which commonly appears in Cu-based alloys.[12]

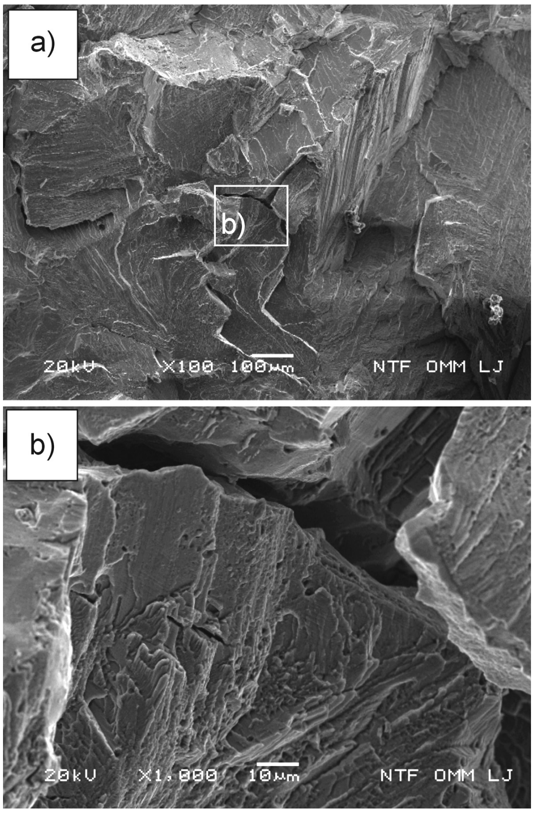

Figure 5: SEM microfractographs of the CuAlNiMn shape-memory alloy after tensile testing: a) magnification 100-times and b) the magnified section

Slika 5: SEM-posnetek preloma zlitine CuAlNiMn z oblikovnim spominom po izvedenem nateznem preizkusu: a) povečava 100-kratna in b) povečano območje

In our previous paper[14] it was observed that the CuAlNiMn SMA in the as-cast state has a martensitic microstructure with some areas of the γ_2 phase.

The CuAlNi ternary phase diagram, **Figure 4**, shows the main phases that appear in the CuAlNi shape-memory alloy. The β phase, which is essential for the shape-memory effect, can exist independently and stably above 565 °C. The eutectoid reaction ($\beta \rightarrow \alpha + \gamma_2$) occurs in the alloy at 565 °C. Meanwhile, the adequate cooling rate can suppress the eutectoid reaction, and the β phase can be totally transformed into martensites when the temperature decreases to M_s (the martensite start temperature).[2,6]

On the SEM micrographs (**Figures 2** and **3**), martensitic microstructure is confirmed. Several inclusions can be noticed and their chemical compositions (positions 1 and 2 on **Figure 3a**) are presented in **Table 1**. It can be seen that the inclusions contain the highest amount of Mn, along with Cu, Al and Ni (which are the main constituents of the alloy), and there are also other elements – "impurities" (Fe, Cr, P) (**Figure 3b**).

Table 1: Results of the EDS analysis before tensile testing for the positions marked on **Figure 3a**, (w/%)

Tabela 1: Rezultati EDS-analize, izvedene pred nateznim preizkusom na mestih označenih na **sliki 3a**, (w/%)

Position	Cu	Al	Ni	Fe	Mn	Cr	P
1	25.20	1.73	3.58	8.59	40.65	4.75	15.50
2	17.28	1.86	3.82	9.63	46.18	5.23	15.99
3	86.07	8.04	3.53	–	2.36	–	–
4	85.95	8.06	3.48	–	2.51	–	–

The usual chemical composition of the CuAlNi SMA is Cu-(11–14) % Al-(3–4.5) % Ni (w/%). According to the literature[12] an addition of manganese replacing the aluminum content is effective as it can improve the ductility. The EDS analysis of positions 3 and 4 (**Figure 3a**) and the EDS spectrum on **Figure 3c** confirm such a replacement.

U. Sari[13] investigated the influence of the mass fraction $w = 2.5$ % of manganese on the CuAlNi SMA, and he concluded that, due to a manganese addition, the grain size, which is over 1 mm for CuAlNi, is reduced by 75 %, to the average value of 350 μm.

3.2 Fracture analysis of the CuAlNiMn shape-memory alloy

The results of the SEM microfractography analysis after the tensile testing of the CuAlNiMn shape-memory alloy are presented on **Figures 5** to **8**.

It can be seen that a crack often occurs at a three-fold node of grain boundaries, **Figure 5**. It is known that the brittleness of copper-based alloys arises from the high degree of order in the parent phase with B2, DO_3 and $L2_1$ structures; the brittleness was also attributed to their high elastic anisotropy ($A \cong 13$) which is a reason for the brittle-grain-boundary cracking.[15–17] The second cause is

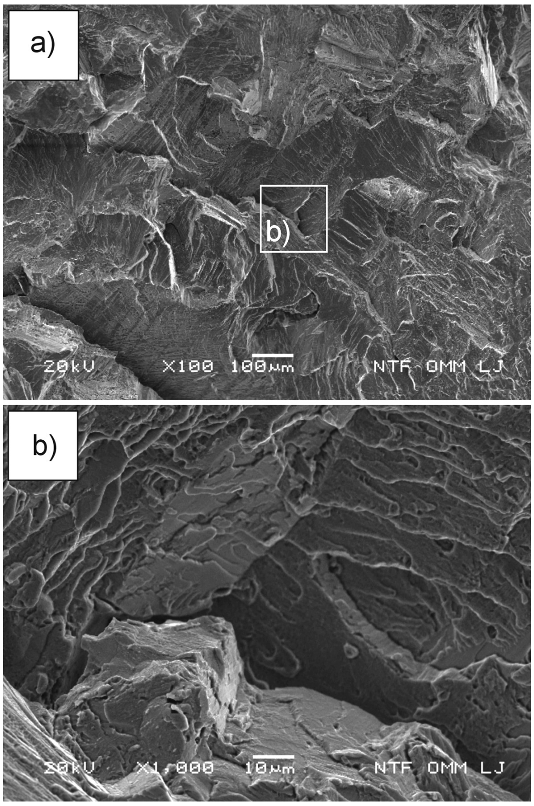

Figure 6: SEM microfractographs of the CuAlNiMn shape-memory alloy: a) magnification 100-times and b) the magnified section
Slika 6: SEM-posnetka preloma zlitine CuAlNiMn z oblikovnim spominom: a) povečava 100-kratna in b) povečano območje

the grain size of β-phase alloys which is usually in order of 1 mm.[12,13] The causes mentioned above probably constitute the essential differences between NiTi alloys and Cu-based alloys, influencing the fracture behavior. A large stress concentration occurs at the grain boundaries due to a large elastic anisotropy under loading. The result is that very brittle intergranular cracking occurs even during elastic deformation.[16]

It may be assumed that the cracks nucleate at the grain-boundary nodes where the stress concentrations develop.[15] This assumption is confirmable with the cracks visible on **Figures 5** to **7**. Grain boundaries provide the easiest crack-propagation path. The cracks nucleate at the grain boundaries where the stress-level concentration is high and the intergranular fracture is obtained. It is mostly a transgranular type of fracture with the characteristic river pattern that can be observed (**Figures 5** and **6**) but sporadic intergranular fracture can also be noticed. At a higher magnification it is visible that the plane of fracture displays the river patterns typical of a cleavage – like a rupture (**Figures 5b** and **6b**).[18] On **Figures 7a** and **7b** there are parallel lines near the grain-boundary plane that probably represent the stress-induced martensite. There are some small and shallow dimples on the fracture surface of the investigated alloy, indicating that the alloy underwent a certain plastic deformation during the fracture (**Figure 7c**).

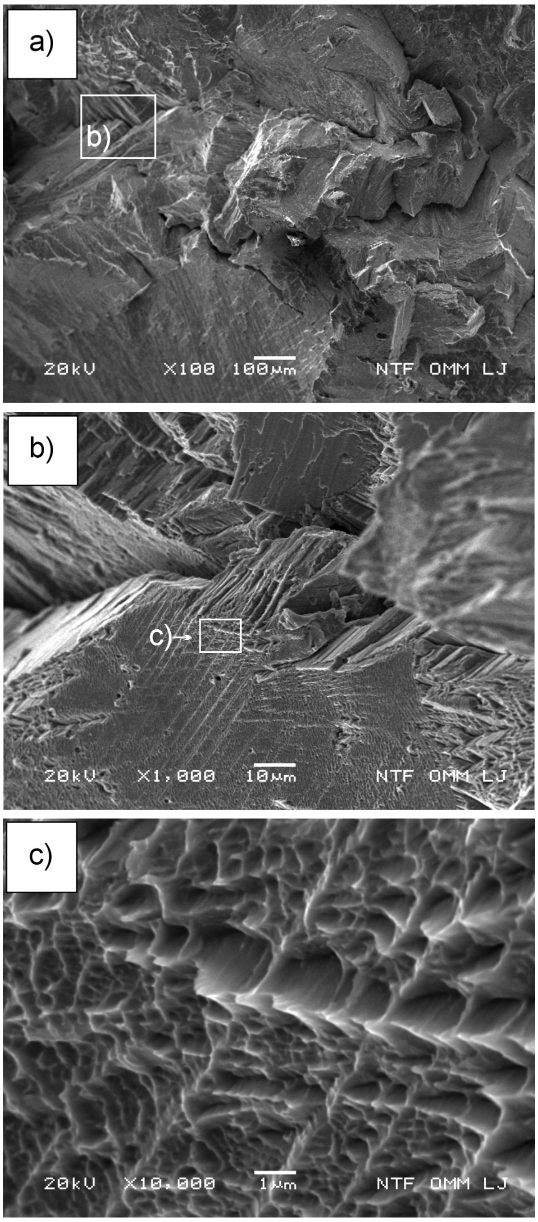

Figure 7: SEM microfractographs of the CuAlNiMn shape-memory alloy: a) magnification 100-times, b) the magnified section and c) the area with transgranular brittle fracture – the magnified section
Slika 7: SEM-posnetek preloma zlitine CuAlNiMn z oblikovnim spominom: a) povečava 100-kratna in b) povečano območje ter c) področje z transkristalnim krhkim prelomom – povečano območje

The fracture surface was examined with an EDS analysis (**Figure 8**), and the chemical composition of the fracture surface is presented in **Table 2**. It can be noticed that the amount of Cu was from 88.15–93.55 %, Al was from 1.78–5.81 %, Ni was from 3.19– 3.46 % and Mn was from 1.25–2.60 % (*w*/%). Lower concentrations of alloying elements probably influence the fracture mechanism and properties of the alloy by decreasing the strength in the region of grain boundaries. Reduced concentrations of the alloying elements at the grain boundaries are probably due to slow cooling rates and

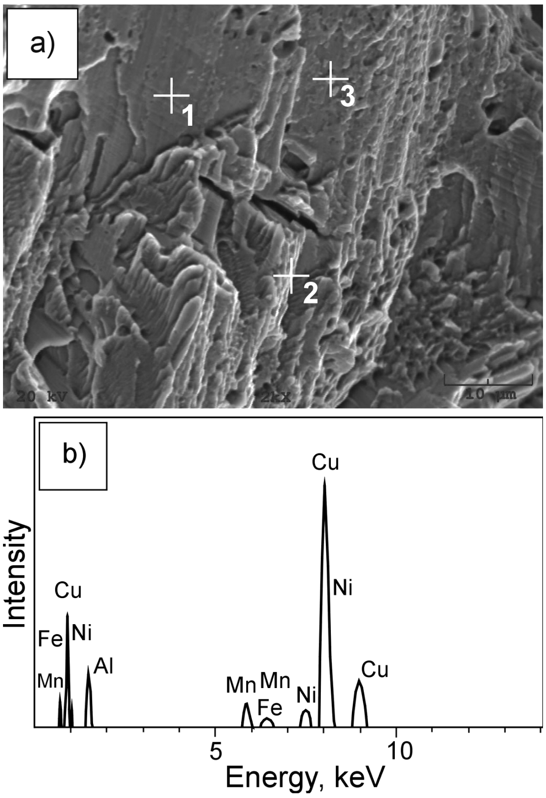

Figure 8: a) SEM microfractograph of the CuAlNiMn shape-memory alloy with the positions marked for EDS analysis and b) EDS spectrum of position 1

Slika 8: a) SEM-posnetek preloma zlitine CuAlNiMn z oblikovnim spominom z označenimi mesti za EDS-analizo in b) EDS-spekter na mestu 1

low solidification velocities that are the consequences of the alloy-casting procedure.

Table 2: Results of the EDS analysis after tensile testing for the positions marked on **Figure 7a**, (*w*/%)

Tabela 2: Rezultati EDS-analize po izvedenem nateznem preizkusu na mestih označenih na **sliki 7a**, (*w*/%)

Position	Cu	Al	Ni	Fe	Mn
1	88.96	4.89	3.46	0.22	2.47
2	93.55	1.78	3.19	0.23	1.25
3	88.15	5.81	3.44	0.00	2.60

3.3 Mechanical properties of the CuAlNiMn shape-memory alloy

The results obtained after the tensile testing are given in **Table 3**. The tensile strength/elongation curves are presented in **Figure 9**. The tensile strength was 401.39 MPa, calculated as the average value of three measurements. The Young's modulus and yield strength were 67.72 GPa and 242.81 MPa, respectively. According to the literature,[19] this value of the tensile strength is satisfactory for a Cu-based alloy. The elongation (*A*) after fracture was very low (1.64 %) and without a measurable contraction. In the literature[19] the maximum elongation after tensile testing for a continuously cast Cu-13 % Al-4 % Ni (*w*/%) SMA was 1.45 % and this is below the limit of the typical recoverable strain of 4–6 %. U. Sari[13] found that the compression strength for Cu-11.6 % Al-3.9 % Ni-2.5 % Mn (*w*/%) amounts to 952 MPa and the ductility is 15 %.

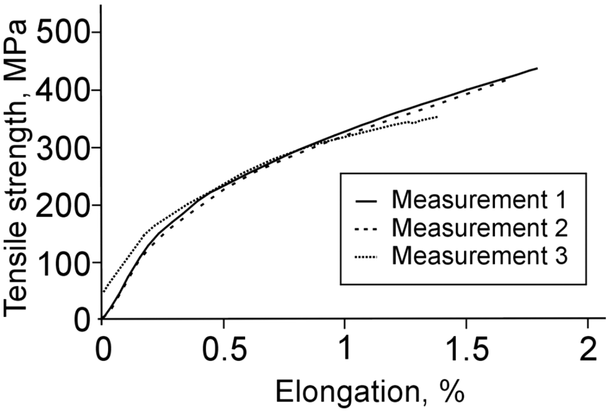

Figure 9: Tensile stress – elongation curves of the CuAlNiMn SMA

Slika 9: Krivulje natezna napetost – raztezek zlitine CuAlNiMn SMA

The hardness of the CuAlNiMn shape-memory alloy was 290.7 HV0.5. As manganese favorably influences the alloy plasticity, it is fair to assume that the hardness of the CuAlNiMn alloy should be lower than that of the alloy without manganese.[13,14]

4 CONCLUSIONS

The microstructure analysis of CuAlNiMn before the tensile testing shows the presence of a martensitic microstructure. According to the plastic deformation carried out after the casting, it is fair to assume that the martensite existing in the microstructure is stress induced. The fracture surface indicates intergranular fracture and mainly transgranular brittle fracture with the characteristic river pattern. There are also some parts with shallow dimples indicating that the alloy was plastically deformed. The cracks nucleate at the grain boundaries where the stress-level concentration is high. Mechanical properties of CuAlNiMn show satisfactory results for the

Table 3: Tensile-test results for the CuAlNiMn shape-memory alloy

Tabela 3: Rezultati nateznega preizkusa zlitine CuAlNiMn z oblikovnim spominom

Mechanical properties	Young's modulus / GPa		Yield strength / MPa		Tensile strength / MPa		Elongation / %	
Measurement results with mean value	60.76	**67.72**	244.04	**242.81**	350.78	**401.39**	1.41	**1.64**
	66.94		245.99		416.10		1.74	
	75.45		238.39		437.30		1.79	

tensile strength (401.39 MPa) and a very low value for the elongation (1.64 %). The hardness of the alloy is 290.7 HV0.5.

Acknowledgement

The authors want to thank professor Franc Kosel and Brane Struna (University of Ljubljana) for the tensile testing and technical information.

5 REFERENCES

[1] M. Gojić, L. Vrsalović, S. Kožuh, A. Kneissl, I. Anžel, S. Gudić, B. Kosec, M. Kliškić, Journal of Alloys and Compounds, 509 (**2011**), 9782–9790

[2] G. Lojen, I. Anžel, A .C. Kneissl, A. Križman, E. Unterweger, B. Kosec, M. Bizjak, Journal of Materials Processing Technology, 162–163 (**2005**), 220–229

[3] M. Čolić, R. Rudolf, D. Stamenković, I. Anžel, D. Vučević, M. Jenko, V. Lazić, G. Lojen, Acta Biomaterialia, 6 (**2010**), 308–317

[4] Y. Sutou, T. Omori, K. Yamauchi, N. Ono, R. Kainuma, K. Ishida, Acta Materialia, 53 (**2005**), 4121–4133

[5] Y. Sutou, R. Kainuma, K. Ishida, Materials Science and Engineering A, 273–275 (**1999**), 375–379

[6] Z. Wang, X. F. Liu, J. X. Xie, Progress in Natural Science, Materials International, 21 (**2011**), 368–374

[7] A. C. Kneissl, E. Unterweger, M. Bruncko, G. Lojen, K. Mehrabi, H. Scherngell, Metalurgija, 14 (**2008**) 2, 89–100

[8] C. Segui, E. Cesari, Journal de Physique IV, Colloque C2, supplement au Journal de Physique III, 5 (**1995**), 187–191

[9] K. Otsuka, C. M. Wayman, Shape memory alloys, Cambridge University Press, Cambridge 1998, 97–116

[10] Z. G. Wei, H. Y. Peng, W. H. Zou, D. Z. Yang, Metallurgical and Materials Transactions A, 28 (**1997**), 955–967

[11] Z. Li, Z. Y. Pan, N. Tang, Y. B. Jiang, N. Liu, M. Fang, F. Zheng, Materials Science and Engineering A, 417 (**2006**), 225–229

[12] J. Van Humbeck, L. Delaney, A comparative review of the (Potential) Shape Memory Alloys, ESOMAT 1989 – Ist European Symposium on Martensitic Transformations in Science and Technology, Germany, 1989, 15–26

[13] U. Sari, International Journal of Minerals, Metallurgy and Materials, 17 (**2010**) 2, 192–198

[14] I. Ivanić, M. Gojić, I. Anžel, S. Kožuh, M. Rimac, O. Beganović, K. Begović, B. Kosec, Microstructure and properties of casted CuAlNi and CuAlNiMn shape memory alloys, Proceedings of the 13th International Foundrymen Conference, Opatija, 2013, 153–162

[15] G. N. Sure, L. C. Brown, Metallurgical Transactions, 15A (**1984**), 1613–1621

[16] H. Sakamoto, Y. Kijima, K. Shimizu, Transactions of the Japan Institute of Metals, 23 (**1982**) 10, 585–594

[17] Y. Sutou, T. Omori, R. Kainuma, N. Ono, K. Ishida, Metallurgical and Materials Transactions A, 33 (**2002**), 2817–2824

[18] L. A. Matlakhova, E. C. Pereira, A. N. Matlakhov, S. N. Monteiro, R. Toledo, Materials Characterization, 59 (**2008**), 1630–1637

[19] G. Lojen, M. Gojić, I. Anžel, Journal of Alloys and Compounds, 580 (**2013**), 497–505

UDK 669.018.258:539.374 ISSN 1580-2949
Original scientific article/Izvirni znanstveni članek MTAEC9, 48(5)719(2014)

EFFECT OF THE INITIAL MICROSTRUCTURE ON THE PROPERTIES OF LOW-ALLOYED STEEL UPON MINI-THIXOFORMING

VPLIV ZAČETNE MIKROSTRUKTURE NA LASTNOSTI MALOLEGIRANEGA JEKLA PO PREDELAVI MINI-THIXOFORMING

Bohuslav Mašek, David Aišman, Hana Jirková
University of West Bohemia in Pilsen, Research Centre of Forming Technology – FORTECH, Univerzitní 22, 30614 Pilsen, Czech Republic
daisman@vctt.zcu.cz

Prejem rokopisa – received: 2013-10-19; sprejem za objavo – accepted for publication: 2013-12-06

Thixoforming is an unconventional forming process based on semi-solid processing. Semi-solid processing involves heating the feedstock to a temperature at which it becomes partly liquid and partly solid. Thanks to partial melting and rapid solidification, unconventional microstructures can be obtained even in conventional materials. Today's research efforts mainly involve high-alloyed steels with a wide freezing range at lower temperatures. By contrast, low-alloyed steels with the solidification temperatures above 1400 °C are not under extensive investigation.

The main objective of the study was to find whether and how the attributes of the feedstock microstructure can be transmitted to the final semi-solid processed microstructure of the 30MnVS6 microalloyed steel. The first stage of the experiment involved mini-thixoforming of the as-received specimens of the steel. In order to assess the effects of the initial microstructure, specimens with three types of microstructure were prepared with high-pressure torsion (HPT), a severe-plastic-deformation (SPD) technique. Initial and final microstructures were examined using light and electron microscopes and image-analysis techniques.

The phase composition was determined with the aid of the X-ray diffraction analysis. The mechanical properties were determined with tensile and hardness testing. Information on the local properties and the properties of microstructure constituents was obtained with microhardness measurement.

Keywords: minithixoforming, 30MnVS6, severe plastic deformation, high pressure torsion

Thixoforming je neobičajen postopek preoblikovanja, ki temelji na preoblikovanju v testastem stanju. Preoblikovanje v testastem stanju vključuje ogrevanje preoblikovanca do temperature, pri kateri postane material delno v staljenem in delno v strjenem stanju. Po zaslugi delnega taljenja in hitrega strjevanja se lahko doseže neobičajne mikrostrukture celo pri navadnih materialih. Sedanje raziskave se izvajajo večinoma na močno legiranih jeklih s širokim intervalom strjevanja pri nižjih temperaturah. Nasprotno se malolegirana jekla s temperature strjevanja nad 1400 °C ne preiskuje intenzivno.

Glavni cilj te študije je ugotoviti, ali in kako atribute mikrostrukture surovca prenesti po preoblikovanju v testastem stanju pri mikrolegiranem jeklu 30MnVS6. Prva stopnja eksperimentov je vključevala minithixoforming preoblikovanje dobavljenih vzorcev jekla. Za oceno vpliva začetne mikrostrukture so bili pripravljeni vzorci s tremi vrstami mikrostrukture s torzijo pri visokem tlaku (HPT), to je s tehniko velike plastične deformacije (SPD). Začetne in končne mikrostrukture so bile preiskane s svetlobno mikroskopijo, z elektronsko mikroskopijo in s tehnikami analize slik.

Sestava faz je bila določena z rentgensko difrakcijsko analizo. Mehanske lastnosti so bile določene z nateznim preizkusom in z merjenjem trdote. Informacija o lokalnih lastnostih in lastnostih posameznih mikrostrukturnih faz je bila dobljena z meritvami mikrotrdote.

Ključne besede: minithixoforming, 30MnVS6, plastična deformacija, torzija pri visokem tlaku

1 INTRODUCTION

Mini-thixoforming was developed for processing small volumes of a material using highly dynamic heating and cooling processes.[1,2] Thanks to these characteristics, the processing induces transformations that are not commonly encountered in the conventional processes. As a consequence, various types of microstructure are obtained which contain metastable constituents, such as austenite in ferritic-pearlitic steel.[3] Owing to the highly dynamic nature of the phenomena involved, the initial condition of a material cannot be neglected because the material's history is often reflected in its final microstructure. This fact frequently fails to be acknowledged and has not been explored adequately. The objective of the present experiment was to compare the character of the resulting microstructure with the initial condition. The method used to modify the microstructures was a severe-plastic-deformation technique known as high-pressure torsion (HPT)[4] and it involved various amounts of the applied strain.

2 EXPERIMENTAL PROGRAMME

The experimental programme was conducted with the 30MnVS6 microalloyed steel (**Table 1**). This steel, alloyed predominantly with manganese and silicon, is typically used for making forged parts. The as-received material was in the form of rolled and peeled normalized bars. The as-received microstructure consisted of ferrite and pearlite (**Figure 1**). The ultimate and yield strengths in the as-received condition were 770 MPa and 570 MPa, respectively, and the hardness was 237 HV10.

Table 1: Chemical composition of 30MnVS6 steel in mass fractions (*w*/%)
Tabela 1: Kemijska sestava jekla 30MnVS6 v masnih deležih (*w*/%)

C	Mn	Si	P	S	Cu	Cr	Ni	Al	N	Mo	V	Ti
0.31	1.50	0.62	0.018	0.024	0.03	0.20	0.02	0.02	0.0122	0.007	0.098	0.0261

With regard to the low content of alloying elements, a tentative simulation using the JMatPro program was used to ascertain that the freezing range of the material was relatively narrow and lying at high temperatures.[5] The temperature interval was 1425–1490 °C. The temperature to be used for achieving the semi-solid state region was set at 1455 °C.

2.1 Refinement of the initial microstructure using HPT

The structure of the material was refined using the HPT method, one of the severe-plastic-deformation techniques. Its principle is a torsional deformation between stationary and rotating dies that compress the material (**Figure 2**).[6] The magnitude of the strain introduced depends on the number of revolutions. The feedstock was a disc with a 35 mm diameter. The forming process reduced its height to 7.5 mm and expanded its diameter to 38 mm (**Figure 3**). The forming was performed at ambient temperature. The material did not undergo any recrystallization. The effect of the initial microstructure was explored using three specimens upon various numbers of revolutions: 3.5, 4.25 and 7.

Figure 3: Final products of the HPT process
Slika 3: Končni proizvod HPT-postopka

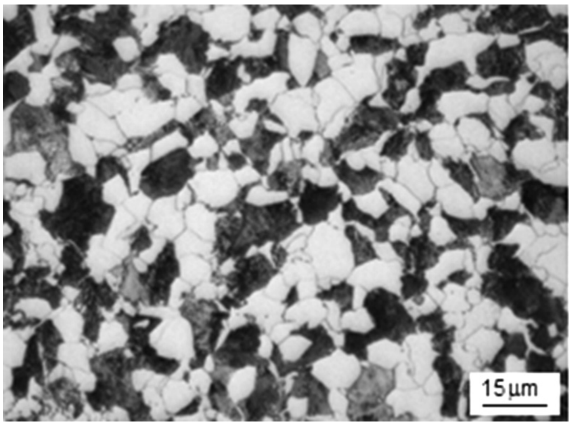

Figure 1: As-received microstructure of 30MnVS6 steel
Slika 1: Mikrostruktura jekla 30MnVS6 v dobavljenem stanju

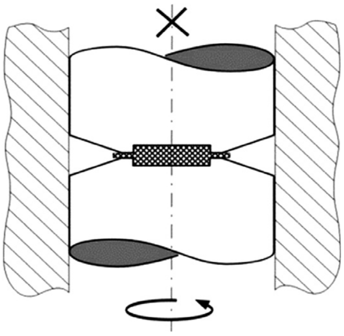

Figure 2: Schematic of the HPT process[6]
Slika 2: Shematski prikaz HPT-postopka[6]

2.2 Microstructure after HPT

As the amounts of the strain in the centre and by the edge of the formed disc differ, the metallographic section was prepared on the disc face. The observations with both the light and electron microscopes confirmed that the resulting microstructure was heavily distorted, in contrast to the as-received material. The most severe distortion was found in the specimen upon the highest number of revolutions, which was seven (**Figure 4a**). Its microstructure still contained the ferrite and pearlite mixture but both phases were heavily deformed (**Figure 4b**). Its hardness, up to 502 HV10, was higher than that of the as-received material. The surprising finding was that the pearlite lamellae underwent a heavy deformation without any fracturing. Another interesting feature was

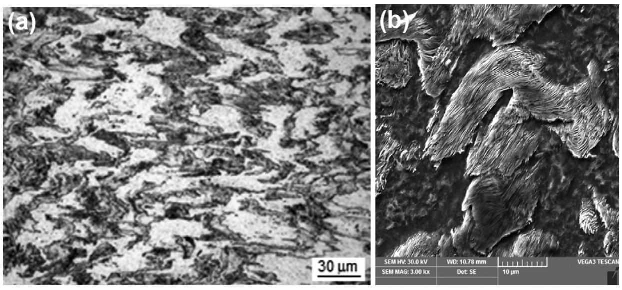

Figure 4: a) Microstructure of 30MnVS6 steel upon HPT processing, 7 revolutions,;) detail of distorted pearlite lamellae
Slika 4: a) Mikrostruktura jekla 30MnVS6 po HPT-predelavi, 7 vrtljajev, b) detajl izkrivljene lamele perlita

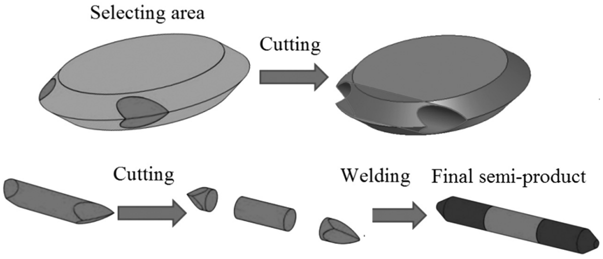

Figure 5: Schematic of the workpiece manufacturing sequence
Slika 5: Shematski prikaz korakov priprave obdelovanca

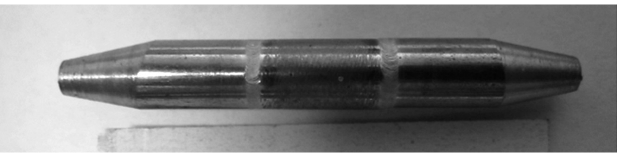

Figure 6: Final workpiece welded together with an electron beam
Slika 6: Končna oblika obdelovanca, zvarjenega z elektronskim curkom

that upon three or even four revolutions, the microstructures in the centre of a disc and by its edge showed little difference. This was evidenced by similar hardness levels for all the areas of the deformed disc. Upon 3.5 revolutions, the hardness was 421 HV10. Upon 4.25 revolutions, it rose to 465 HV10.

2.3 Preparation of the workpieces for semi-solid processing

The non-uniform strain intensity was reflected in the not quite uniform microstructures of the discs upon HPT. The difference was most notable between the outermost edge and the centre of a disc. For this reason, the edge and the centre of a disc were not used for further experiments. Cylinders of a 15 mm height were cut from the discs. This dimension is consistent with the length of the active part of the workpiece for mini-thixoforming. The remaining conical parts of the workpiece were made for low-carbon steel with a high melting temperature. The entire workpiece for semi-solid processing was thus assembled from three parts and electron-welded in a vacuum (**Figure 5**). This low-energy welding method left the special microstructure in the active part of the workpiece unaffected. The workpieces from the as-received material were made in one piece. Their length was 48 mm and their diameter was 6 mm (**Figure 6**). The purpose of their conical ends is to carry the electric current for heating and to centre the workpieces inside the die.

3 SEMI-SOLID PROCESSING

All the workpieces were formed in a titanium die with a groove-shaped cavity with a 20 mm length and a 5 mm × 1.9 mm cross-section. This die was specially

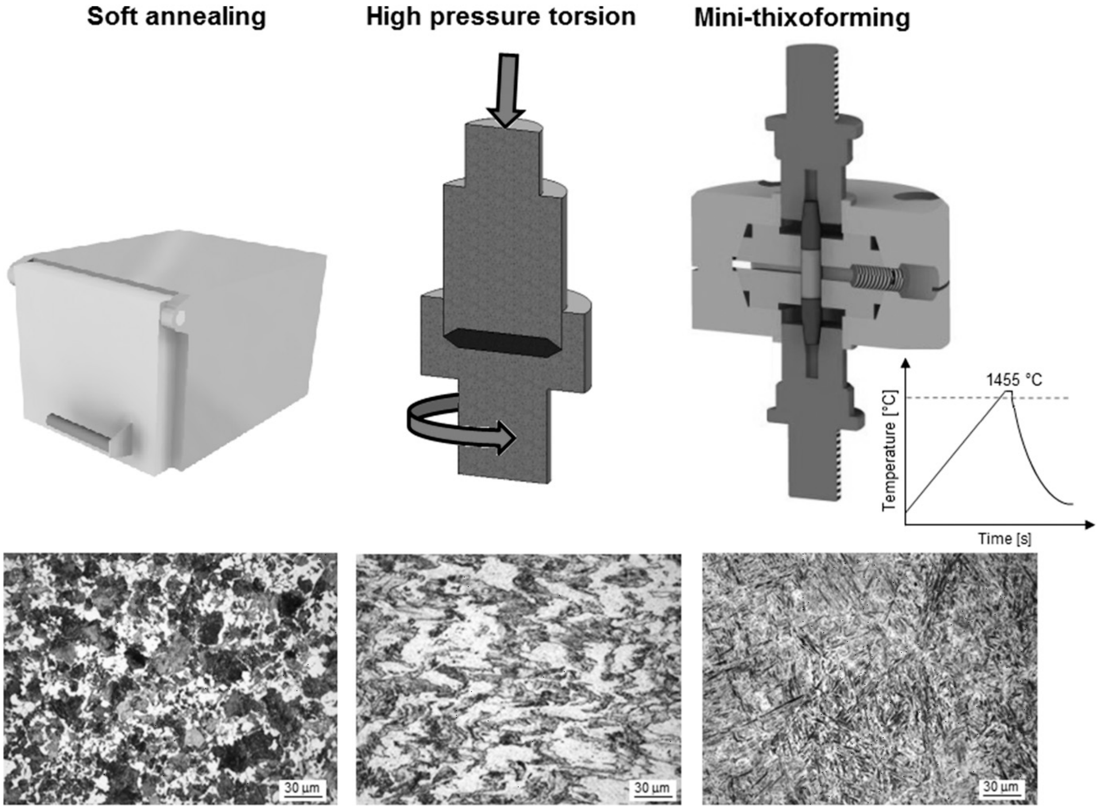

Figure 7: Schematic illustration of the whole process with the microstructure development after individual steps
Slika 7: Shematski prikaz celotnega postopka z razvojem mikrostrukture po vsakem koraku

developed for the mini-thixoforming process.[7] With respect to the high heating temperature, an R-type thermocouple (rhodium-platinum) was used. The heating temperature was found using stepwise optimization. Despite the temperature being high, it was maintained accurately, as was the heating rate (**Figure 7**).

The initial experiments were conducted with the as-received specimens. Only after all the mini-thixoforming parameters were determined, the HPT-processed specimens were employed. First, a suitable heating temperature was sought. A total of three temperatures were tried: (1450, 1455 and 1460) °C. The heating time was 61 s. The deformation applied within 0.3 s was followed by rapid solidification enhanced by the contact with the metal cavity surface. The initial cooling rate reached 300 °C/s.

4 DISCUSSION OF RESULTS

At the first stage, the semi-solid processing parameters were optimized for the 30MnVS6 steel employed outside its typical domain. Mini-thixoforming of the as-received non-refined material produced a martensitic microstructure with some amount of bainite. This is unusual, considering the typical thixo-formed microstructure, which consists of polyhedral austenite grains embedded in a ledeburite network. In the specimen heated to 1460 °C, the etchant used for outlining prior austenite grains (the picric acid) revealed that the majority of the product and the interior of the workpiece had a dendritic morphology. In response to this finding, the heating temperature was reduced. However, with the temperature reduced by 10 °C, the cavity was not filled completely because the liquid fraction was inadequate.

The most suitable heating temperature proved to be 1455 °C. Once the processing parameters were optimized, the product filled the die cavity completely. The microstructure in the centre of the product contained mostly martensite and some bainite (**Figures 8a** and **8b**). Its hardness was approximately 767 HV10. The etchant for the prior austenite grain boundaries revealed that the proportion of the dendrites in the product decreased. Besides the dendrites, there were polygonal shapes of the prior austenite grains in the microstructure. These shapes were found predominantly in the product formed by forcing the semi-liquid material into the groove in the titanium die. A higher proportion of bainite was found in the workpiece interior, whose cooling rate was lower than that of the product.

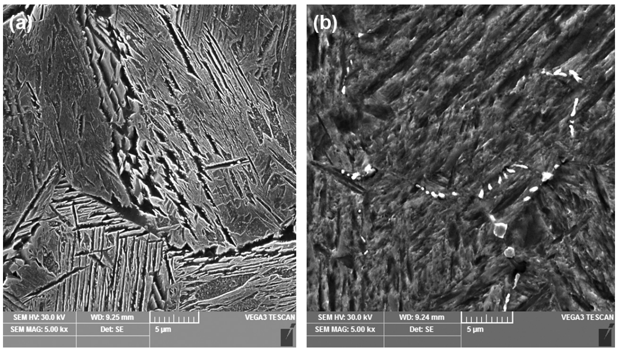

Figure 8: Micrographs of the as-received material upon semi-solid processing: a) workpiece centre, b) centre of the extruded product

Slika 8: Mikrostruktura dobavljenega materiala po predelavi v testastem stanju: a) sredina obdelovanca, b) sredina vzorca po ekstruziji

Processing the workpieces made from the discs upon 3.5 revolutions led to a similar character of the microstructure. It consisted of a mixture of martensite and bainite. The hardness in the centre of the product reached no more than 500 HV10. The variation in the microstructure was only found after outlining the prior austenite grain boundaries by etching, whereas the normally etched martensitic-bainitic microstructure appeared uniform. The morphology of the prior austenite grains in the mini-thixoformed HPT-refined material was polygonal. In contrast to the as-received material, no large dendritic areas were found upon mini-thixoforming (**Figures 9a** and **9b**). Etching the material processed with HPT with 4.25 revolutions and picric acid revealed areas with very fine globular particles with the size of approximately 20 µm (**Figure 9c**). The matrix consisted of martensite and bainite, as in the previous cases. The hardness in the centre of the product was 713 HV10. No effects of a further refinement were found in the specimens upon 7 revolutions.

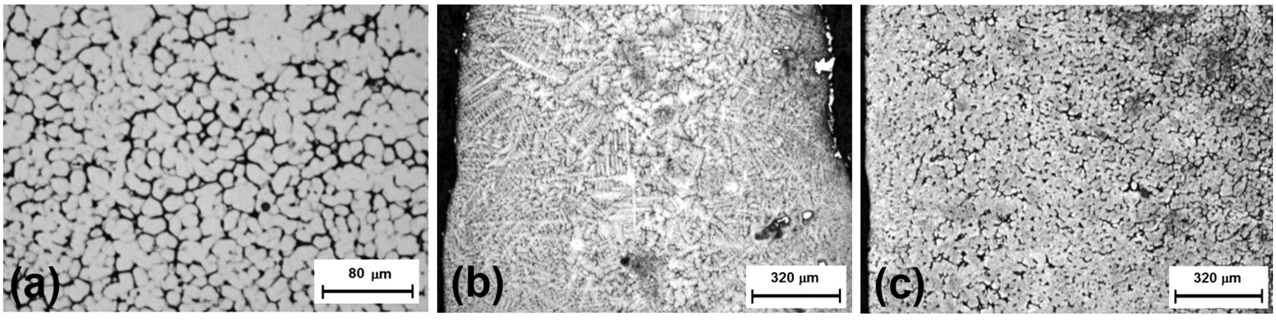

Figure 9: Comparison between the morphologies of prior austenite grains upon semi-solid processing of the material with two different initial microstructures: a) micrograph of as-received material, b) micrograph of HPT-refined material, c) detail of fine globular grains

Slika 9: Primerjava videza prvotnih avstenitnih zrn po predelavi v testastem stanju materiala z dvema različnima začetnima mikrostrukturama: a) mikrostruktura dobavljenega materiala, b) mikrostruktura materiala po HPT-postopku, c) detajl drobnih globulitnih zrn

5 CONCLUSION

The effect of the initial microstructure of the microalloyed 30MnVS6 steel on its final microstructure upon semi-solid processing was explored. The material in the two initial states was mini-thixoformed under identical conditions. The first state was characterized by a ferrite-pearlite microstructure with the hardness of 237 HV10 and the other was a plastically deformed microstructure caused by high-pressure torsion. The hardness level was between 421 and 502 HV10, depending on the strain intensity.

All the products made with mini-thixoforming contained martensite with a small fraction of bainite. The final hardness was high, reaching 713 HV10 in some cases. The refinement of the initial microstructure was not reflected substantially in the semi-solid processed microstructure. After the heaviest deformation, the workpiece material had a very fine morphology of the prior austenite grains. In order to characterize them, additional microscopic techniques will have to be used such as EBSD to find their size or X-ray diffraction analysis to describe their texture.

Acknowledgement

The authors gratefully acknowledge the funding by the German Research Foundation (Deutsche Forschungsgemeinschaft, DFG) and the Czech Science Foundation (Grantové agentura České republiky, GAČR) through joint, binational projects WA 2602/2-1 and GA ČR P107/11/J083.

6 REFERENCES

[1] H. Mišterová, A. Ronešová, Š. Jeníček, Mini-thixoformnig of tool steel X210Cr12, 22nd International Conference on Metallurgy and Materials, Metal 2013, Brno, 2013

[2] I. Sen, H. Jirkova, B. Masek, M. Böhme, M. F. X. Wagner, Microstructure and Mechanical Behavior of a Mini-Thixoformed Tool Steel, Metallurgical and Materials Transactions A, 43 (**2012**) 9, 3034–3038

[3] M. N. Mohammed, M. Z. Omar, J. Syarif, Z. Sajuri, M. S. Salleh, K. S. Alhawari, Microstructural Evolution during DPRM Process of Semisolid Ledeburitic D2 Tool Steel, The Scientific World Journal, (2013), article ID 828926

[4] T. C. Lowe, R. Z. Valiev (eds.), Investigations and Applications of Severe Plastic Deformation, Kluwer Academic Publishers, Dordrecht 2000

[5] JMatPro, The Java-based Materials Property Simulation Package, Version 6.1, Sente Software Ltd., Surrey Technology Center, UK

[6] T. Hebesberger, H. P. Stüwea, A. Vorhauer, F. Wetscher, R. Pippan, Structure of Cu deformed by high pressure torsion, Acta Materialia, 53 (**2005**) 2, 393–402

[7] B. Mašek et al., Minithixoforming of high chromium tool steel X210Cr12 with various initial states, Annals of DAAAM for 2011 & Proceedings of the 22nd International DAAAM Symposium, Vienna, Austria, 2011

UDK 621.96:691.73:620.179.11
Original scientific article/Izvirni znanstveni članek

ISSN 1580-2949
MTAEC9, 48(5)725(2014)

EXPERIMENTAL INVESTIGATION OF THE SURFACE PROPERTIES OBTAINED BY CUTTING BRASS-353 (α+β) WITH AN ABRASIVE WATER JET AND OTHER CUTTING METHODS

PREISKAVA LASTNOSTI POVRŠINE MEDENINE 353 (α+β) PO REZANJU Z ABRAZIJSKIM VODNIM CURKOM IN DRUGIMI METODAMI REZANJA

Adnan Akkurt
Gazi University, Faculty of Technology, Department of Industrial Design Engineering, Ankara, Turkey
aakkurt@gazi.edu.tr

Prejem rokopisa – received: 2013-10-26; sprejem za objavo – accepted for publication: 2013-11-18

In the manufacturing industry different methods are used to provide the fastest, cheapest and the most cost-effective way of facilitating the process of cutting with the minimum surface deformation. Apart from the conventional methods, non-traditional methods such as abrasive water jet (AWJ), laser, plasma, underwater plasma and wire erosion are used intensely for the cutting of hard-to-cut materials and products. Research has been conducted on the AWJ method. Brass materials are widely used in industry. In this study the results of the cutting process for brass material with AWJ were investigated. Based on the results the ideal cutting method for the investigated material was found to be AWJ.

Keywords: cutting methods, unconventional cutting, surface properties

V industriji se uporabljajo različne metode za hitro, cenejše in stroškovno bolj ugodne metode rezanja z minimalno deformacijo površine. Poleg navadnih metod za rezanje trdih materialov in proizvodov se uporabljajo tudi netradicionalne, kot je abrazijsko rezanje z vodnim curkom (AWJ), laser, plazma, podvodna plazma in žična erozija. Izvršene so bile raziskave AWJ. Medenina se pogosto uporablja v industriji. V tej študiji je bil preiskan postopek rezanja medenine z AWJ. Glede na dobljene rezultate je ugotovljeno, da je za preiskovani material najboljša metoda abrazijsko rezanje z vodnim curkom.

Ključne besede: metode rezanja, neobičajno rezanje, lastnosti površine

1 INTRODUCTION

Cutting quality can be determined by measuring the surface roughness, dimensional tolerances, etc. In the cutting processes for different materials, there are no significant differences in general macro-morphological surface properties. For example, the surface obtained on cut glass is the same as on metal, ceramic and composites. However, when examined at the micro-level, micro-qualities of surfaces vary depending on the differences between the cutting mechanisms of different methods. The properties of the surfaces obtained with an abrasive water jet are listed below:

- The surface is not affected by thermal impacts or heat.
- No crusting is found on brittle materials. Surface is almost free of refractions.
- An insignificant hardness alteration may occur on the surface.
- The width of the cut may be narrowed depending on the diameter of the jet.
- Abrasive fragment sedimentation may occur in the material.
- Small chamfers may occur in the holes to the surface.

The quality of the obtained surface could be improved by increasing the power spent for each unit of the cutting length. A better surface quality is obtained by increasing the water pressure, decreasing the jet speed, increasing the abrasive magnitude rate in the jet and selecting a larger nozzle. Abrasive-surface properties as well as abrasive-particle shape and dimension are important factors. The width of the cutting channel is controlled with the mixture tube nozzle and the jet speed[1].

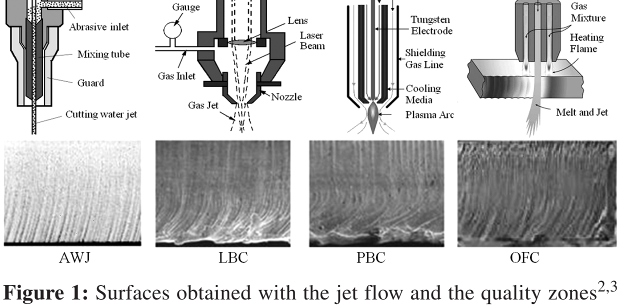

Figure 1: Surfaces obtained with the jet flow and the quality zones[2,3]
Slika 1: Površine, dobljene s curkom, in njihova kvaliteta [2,3]

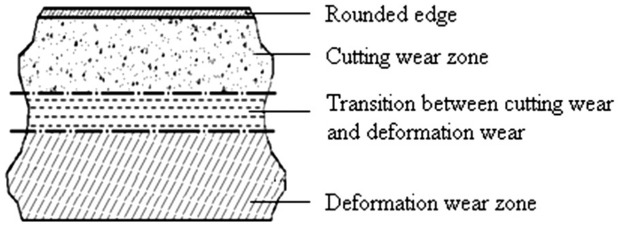

Figure 2: Surface sections cut by the abrasive water jet[4]
Slika 2: Področja površine reza pri abrazijskem vodnem curku[4]

Characteristics of the cut surface: When examined in order to determine the surface quality, the surfaces cut with different methods are similar. Surface roughness is defined with the waves on the surface and the size of the wave is proportional to the jet diameter (**Figure 1**)[2,3].

While the wave size depends on the jet diameter and the penetration of the abrasive water jet, the surface roughness is related to the micro-interaction between each abrasive and the workpiece. The cutting quality depends on the inner physical effects caused by the jet and the external factors such as various cutting parameters, nozzle vibration and job fragment. When a surface cut with abrasive water is examined, three different sections can be seen as shown in **Figure 2**[2,4].

1. In the upper corner of the cut surface there is a small curve caused by the hitting articles departing from the jet. This section is usually accepted as an ignorable edge impact.

2. This is a smoother surface section located under the first section. This section is formed by the particle erosion caused by the abrasive particles hitting the surface at a low impact angle. Experimental studies performed recently have proven the fact that a 1.3 μm surface-roughness quality can be obtained on this section.

3. The cutting capability is reduced as the kinetic energy of the abrasives decreases and the jet looses it regularity. This is a transition section where the second cutting mechanism prevails and the surface is formed by faults due to parallel jet deviations. In this second cutting mechanism, the impulse angle of the hitting particles against the surface is bigger and defined as "the deformation erosion". The deformation abrasive mechanism is realized by the particles hitting the surface at a bigger angle. When the travelling speed of the jet is reduced, the transition area between the second and third sections is smaller[4].

If a quality cutting process is required, the parameters must be adjusted and the cutting process must be completed before entering the deformation abrasion section. By adjusting the parameters, the flaking will also be avoided. By selecting a sufficiently low lateral speed level, a considerably smooth surface without any flaking will be obtained on the first section. Smaller abrasive particles and a bigger abrasive mass of the jet flow will reduce the surface-roughness value. A particle with bigger dimensions will consequently cause a larger cut area and the surface will be rougher (it will have a larger roughness value)[3–5].

Increasing the abrasive mass of the jet or reducing the jet speed will improve the quality by increasing the number of the particles hitting against the surface being cut. When greater cutting speeds are used in a rough cutting operation, each of the three sections can be seen on the surface. A deviation of the jet on the third section and a formation of parallel lines appear as a function of the parameters of lateral speed alterations, abrasive feeding-flow rate, liquid pressure and nozzle geometry. Abrasive substances form holes and pockets at the lower parts, where they are accumulated and embedded during the rough cutting operations. Such residual particles may damage the nozzle during the operations. These negative effects must be taken into consideration. When the surface quality and energy of the particle are considered, we find that as the cutting depth gets bigger the deviation of the jet increases causing an increase in the energy of the particle.[6,7] Thus, a greater energy applied on the surface show that the surface roughness and surface waviness are more robust and there are more deviations of the jet (**Figure 3**)[1,4].

Comparison of the abrasive water jet with the alternative methods: In **Figure 4**, the inverse relationship between the thickness and lateral feed rate is shown, considering the surface quality of the cutting surface. The AWJ method has the lowest lateral feed rate, while the plasma method has the highest feed rate. An overall comparison of the abrasive water jet and the alternative cutting methods in **Table 1** shows that the most efficient cutting method is the cutting with AWJ, being independent of the material thickness and its characteristics. However, there are some disadvantages of this method. The most important one is the dependency of the system and the cutting parameters on several variables. Because of this dependency, it is hard to provide a continuous

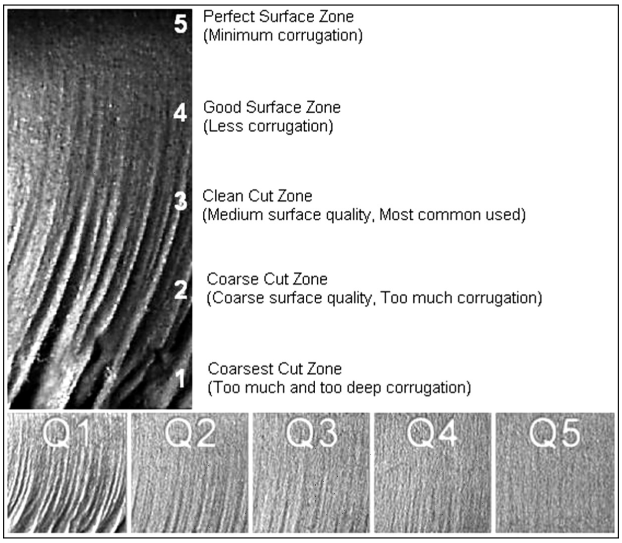

Figure 3: Cut-face quality zones based on jet flow[143]
Slika 3: Področja na površini, rezani s curkom[1,4]

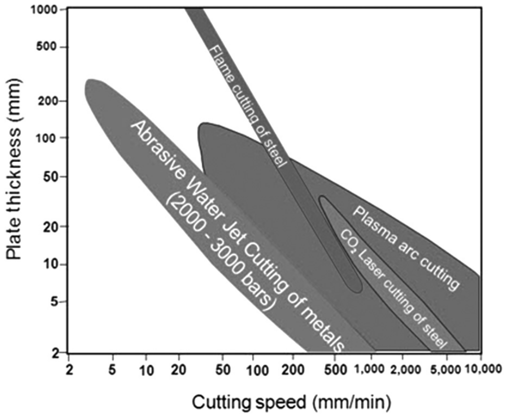

Figure 4: Comparison of the cutting abilities of different cutting methods using single-orifice jet beams[8]

Slika 4: Primerjava zmogljivosti različnih metod rezanja pri uporabi curka z eno šobo[8]

surface quality on the cutting surface. An increasing surface roughness is inevitable, as in the cases of laser, plasma, underwater plasma and oxygen-flame cutting methods[4,8–12].

There are several studies that compare the AWJ method with the other methods. The studies give different results due to different materials used. The techniques of AWJ and the other methods are compared by Hashish[2] as shown in **Figures 5a** and **5b**. This comparison is based on an evaluation of different processing methods in terms of their power levels and typical machining removal rates. There are various techniques for cutting materials (**Figure 6**)[2,9,13].

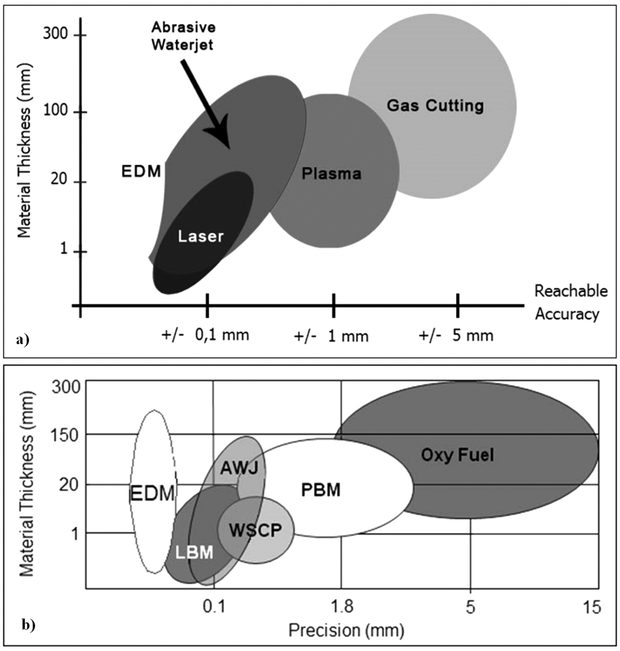

Figure 5: Comparison of the abrasive water jet with the other cutting methods[4,8]

Slika 5: Primerjava rezanja z abrazivnim vodnim curkom z drugimi metodami rezanja[4,8]

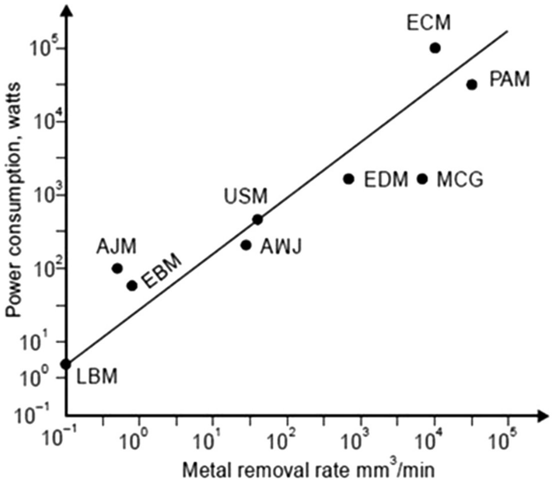

Figure 6: Comparison of the abrasive water jet with the other cutting methods[2,9,13]

Slika 6: Primerjava rezanja z abrazivnim vodnim curkom z drugimi metodami rezanja[2,9,13]

According to Hashish,[4] when compared with the traditional methods, AWJ forms a jet that is able to perform a cutting process with a very low energy and an intense energy distribution where most of the energy is lost due to friction. Just as in the other unipolar, ductile cutting operations, AWJ can be given directions perfectly well with a low energy applied, and it can perform cutting in all directions and can form considerably narrow cuts. Particularly due to no thermal effects on the cut materials, AWJ is more effective than the other competitive methods. However, in spite of the many advantages of the WJ and AWJ processing technologies, there are still certain disadvantages[2,14].

There are many studies comparing AWJ and the other methods. When these are examined different results are set forth depending on the material. Powell et al.[10] performed a study comparing the economical aspect of AWJ and laser. In their analysis they discussed the technical and commercial advantages and disadvantages of both methods and focused on the relative productivity of both processes. Ohlsson et al.[11] studied the pressure, abrasive flow and lateral-speed impacts on the steel cut with AWJ, the grey-cast-iron cutting depth and surface properties. Zheng et al.[14] made comparisons based on the quality and process costs, aiming at helping the users decide which methods would be more convenient for various applications. They made their comparison by using stainless steel with different thicknesses, soft steel and aluminum[12–14]. In the studies by Hashish and Ramulu,[13] focusing on the mechanical properties of laser and AWJ, they discussed the unique cutting abilities and characteristics of both methods. The researchers drew the attention of the users not only on the technical performance of the methods but also on how they affect the completed products; they evaluated the mechanical impacts of both methods on the titanium-alloy (Ti6Al4V) and steel (A286) materials[12]. As the optimum parameters have not been completely determined yet for the vast majority of these methods, there are plenty of other studies still being currently performed. The best data to set forth the superiority of AWJ is probably the figure given below. Furthermore, a graph is given indicating the capability of the method with respect to material thickness and a general comparison is given in **Tables 1** and **2**[1,9,15–17].

Applications of various machining methods are summarised in **Tables 2** and **3**. The machining characteristics of different non-conventional processes can be analyzed with respect to metal-removal rate, tolerance maintained, surface obtained, depth of surface damage and power required for machining. The physical parameters of the non-conventional machining processes have direct impacts on the metal removal as well as on the energy consumed for different processes. These

Table 1: Overall comparison of abrasive water jet and the alternative cutting methods [1,9,16]
Tabela 1: Primerjava abrazijskega vodnega curka z drugimi metodami rezanja[1,9,16]

Comparison of Disconnections by Water Jet and the Other Machining Methods								
Comparison Factor	Abrasive Water Jet	Laser Cutting	Plasma Cutting	Underwater Plasma	Wire EDM	Milling Cutting	Band Saw	Oxygen Cutting
Material Thickness	A	C	B	B	A	B	B	A
Cutting Quality	A	A	C	B	A	B	B	C
Lateral Speed	B	A	B	B	B	B	A	B
Multi-Purpose Use	A	D	B	B	B	B	B	C
Heat Affected Zone (HAZ)	A	D	D	C	C	B	B	D
Sensitive Cutting	A	A	B	B	A	A	C	D
Secondary Process Requirement	A	B	B	B	B	B	C	C
Chip Formation	B	C	C	C	A	B	D	B
Production Flexibility	A	B	C	C	B	A	C	D
Overall Process Time	B	B	D	D	B	B	A	C
A: Excellent B: Good C: Acceptable D: Unacceptable								

Table 2: Material applications of some machining methods[1,9]
Tabela 2: Uporabnost obdelovalnih metod glede na material[1,9]

Materials Applications								
Process	Aluminium	Steel	Super Alloys	Titanium	Refectories	Plastics	Ceramics	Glass
Ultrasonic Machining	C	B	C	B	A	B	A	A
Abrasive Jet Machining	B	B	A	B	A	B	A	A
Electrochemical Machining	B	A	A	B	B	D	D	D
Chemical Machining	A	A	B	B	C	C	C	B
Electric Discharge Machining	B	A	A	A	A	D	D	D
Electron Beam Machining	B	B	B	B	A	B	A	B
Laser Beam Machining	B	B	B	B	C	B	A	B
Plasma Arc Machining	A	A	A	B	C	C	D	D
Abrasive Water Jet Machining	A	A	A	A	A	B	A	A
A: Good Application B: Fair C: Poor D: Not Applicable								

Table 3: Process capabilities of non-conventional cutting processes[9,12]
Tabela 3: Zmogljivosti nekonvencionalnih postopkov rezanja[9,12]

Process Capability						
Process	Metal Removal Rate (mm/min)	Tolerance (μm)	Surface (μm) CAL	Depth of Surface Damage (μm)	Corner	Power (W)
Ultrasonic Machining	300	75	0.2–0.5	25	0.025	2 400
Abrasive Jet Machining	0.8	50	0.5–1.25	2.5	0.100	250
Electrochemical Machining	0.15	15	0.1–2.5	50	0.025	100000
Chemical Machining	150	50	0.4–2.5	50	0.125	–
Electric Discharge Machining	800	15	0.2–1.25	125	0.025	2 700
Electron Beam Machining	16	25	0.4–2.5	250	250	150 (average), 200 (peak)
Laser Beam Machining	0.1	25	0.4–1.25	125	250	2 (average)
Plasma Arc Machining	75000	125	Rough	500	–	50000
Abrasive Water Jet Machining	1.3	25	0.4–2.5	125	0.025	220
Conventional Milling of Steel	50000	50	0.4–5.0	25	0.050	3000

Table 4: Effects of different machining methods on equipment and tooling[9]
Tabela 4: Vpliv različnih metod obdelovanja na opremo in orodje[9]

Effects on Equipment and Tooling				
Process	Tool Wear Ratio	Machining Medium Contamination	Safety	Toxicity
Ultrasonic Machining	10	B	A	A
Abrasive Jet Machining	–	B	B	A
Electrochemical Machining	0	C	B	A
Chemical Machining	0	C	B	A
Electric Discharge Machining	6.6	B	B	B
Electron Beam Machining	–	B	B	A
Laser Beam Machining	–	A	B	A
Plasma Arc Machining	–	A	A	A
Abrasive Water Jet Machining	–	B	B	A
Tool Wear Ratio = Volume of work material removed / Volume of tool electrode removed A: No Problem B: Normal Problem C: Critical Problem				

Table 5: Economic performance of different machining methods[9]
Tabela 5: Ekonomičnost posameznih metod rezanja[9]

Process Economy					
Process	Capital Investment	Tooling and Fixtures	Power Requirement	Efficiency	Tool Consumption
Ultrasonic Machining	B	B	B	D	C
Abrasive Jet Machining	A	B	B	D	B
Electrochemical Machining	E	C	C	B	A
Chemical Machining	C	B	D*	C	A
Electric Discharge Machining	C	D	B	D	D
Electron Beam Machining	D	B	B	E	A
Laser Beam Machining	C	B	A	E	A
Plasma Arc Machining	A	B	A	A	A
Abrasive Water Jet Machining	B	B	B	C	C
Conventional Milling of Steel	B	B	B	A	B
A: Very Low Cost B: Low C: Medium D: High E: Very High *Indicates cost of chemicals.					

characteristics of different methods are given in **Tables 4** and **5**[9,17–19].

2 EXPERIMENTAL STUDIES

In this study the samples of (**Figure 7**) brass-353 (α+β) material 20 mm were cut with conventional (oxygen flame, hydraulic saw and freeze) and eight unconventional methods (abrasive water jet, laser-plasma arc, underwater plasma, wire erosion). The cutting edges obtained with these methods were examined in terms of their hardness and their effect on the microstructures. A comparison was made between the initial microstructures and the microstructures of the materials after cutting them with different methods; the effectiveness of the methods was evaluated. Water-jet-cutting parameters are shown in **Table 6**. Other cutting-process parameters were selected according to the parameters recommended by the lathe-manufacturing companies.

Chemical composition of the material: w/% (S 0.831, Pb 2.21, Zn 36.37, P 0.216, Mn 0.0778, Fe 0.293, Si 0.0829, Al 0.442, Cu < 59.23, Ni 0.237)

The average hardness level was calculated by taking the arithmetic average of the measured values at five different points at a given height on the surface. The value of HV 30 was calculated with an INSTRON WOLPERT TESTER hardness-measurement device. Additionally, hardness was measured in intervals 1 mm from the edge

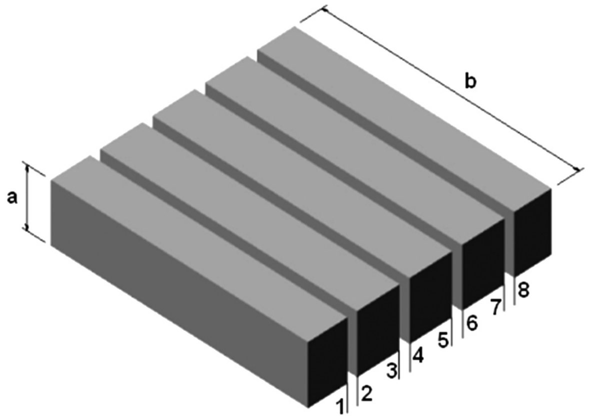

Figure 7: Samples after cutting
Slika 7: Vzorci po rezanju

Table 6: Cutting systems and cutting parameters
Tabela 6: Sistemi rezanja in parametri rezanja

<table>
<tr><td colspan="11">Abrasive Water Jet Cutting</td></tr>
<tr><td colspan="2">Water consumption</td><td>≈ 3.5 L/min</td><td colspan="5">Pump piston diameter</td><td colspan="3">20 mm</td></tr>
<tr><td colspan="2">System temperature of water</td><td>48 °C</td><td colspan="5">Inlet pressure of water into the pressure booster</td><td colspan="3">6 bar</td></tr>
<tr><td colspan="2">Working pressure of the booster</td><td>200 bar</td><td colspan="5">Inlet diameter of water into the nozzle</td><td colspan="3">0.25 mm</td></tr>
<tr><td colspan="2">Outlet pressure of water from the pressure booster</td><td>20 bar</td><td colspan="5">Abrasive nozzle inlet diameter into the nozzle</td><td colspan="3">0.75 mm</td></tr>
<tr><td colspan="2">Water flow rate</td><td>3 L/min</td><td colspan="5">Stand-off distance</td><td colspan="3">4 mm</td></tr>
<tr><td colspan="2">Outlet velocity of water from the nozzle</td><td>800 m/s</td><td colspan="5">Water pressure at the instance of discharge</td><td colspan="3">400 MPa</td></tr>
<tr><td colspan="2">Temperature at the instance of cutting</td><td>≈ 55 °C</td><td colspan="5">Jet angle at the nozzle</td><td colspan="3">90°</td></tr>
<tr><td colspan="2">Current consumption during work</td><td>380 V</td><td colspan="5">Energy consumption</td><td colspan="3">58 kW h</td></tr>
<tr><td colspan="2">Amount of abrasive consumed</td><td>250 g/min</td><td colspan="5">Material used in the nozzle orifice</td><td colspan="3">Sapphire</td></tr>
<tr><td colspan="2">Abrasive used</td><td>GMA Garnet</td><td colspan="5">Chemical composition</td><td colspan="3">$Fe_2O_3Al_2\ (SIO_4)_3$</td></tr>
<tr><td colspan="2">Abrasive hardness (Mohs)</td><td>7.5–8</td><td colspan="5">Abrasive particle size</td><td colspan="3">300 µm</td></tr>
<tr><td colspan="2">Abrasive water outlet diameter from the nozzle</td><td>0.75 mm</td><td colspan="5">Nozzle length</td><td colspan="3">76.2 mm</td></tr>
<tr><td colspan="2">Slurry content</td><td>18 %</td><td colspan="5">Mixing tube length</td><td colspan="3">88.9 mm</td></tr>
<tr><td colspan="2">Mixing tube diameter</td><td>1.27 mm</td><td colspan="5">Nozzle orifice life</td><td colspan="3">40–50 h</td></tr>
<tr><td colspan="3">Laser Beam Cutting</td><td colspan="8">Plasma Beam and Water Shield Plasma Cutting</td></tr>
<tr><td colspan="2">Cutting rate (Lateral feed rate)</td><td>20 m/min</td><td colspan="5">Cutting rate (Lateral feed rate)</td><td colspan="3">20 m/min</td></tr>
<tr><td colspan="2">Position rate</td><td>140 m/min</td><td colspan="5">Plate positioning</td><td colspan="3">By Laser</td></tr>
<tr><td colspan="2">Laser power</td><td>1550 W</td><td colspan="5">Current for maximum cutting</td><td colspan="3">760 A</td></tr>
<tr><td colspan="2">Main power supply</td><td>GW 0–100 %</td><td colspan="5">Nozzle pressure</td><td colspan="3">12 bar</td></tr>
<tr><td colspan="2">Pulse type</td><td>Mega pulse</td><td colspan="5">Operating pressure</td><td colspan="3">24 bar</td></tr>
<tr><td colspan="2">Pulse change frequency</td><td>2000 Hz</td><td colspan="5">Operating frequency</td><td colspan="3">50 Hz</td></tr>
<tr><td rowspan="2">Pulse time</td><td>NP(T)</td><td>1500 µs</td><td colspan="5" rowspan="2">Cooling capacity</td><td colspan="3" rowspan="2">16747 kJ/h</td></tr>
<tr><td>SP(t)</td><td>120 µs</td></tr>
<tr><td colspan="2">Mod type</td><td>Sürekli mod (CW)</td><td colspan="5">Nominal voltage</td><td colspan="3">400 V</td></tr>
<tr><td colspan="2">Focus distance</td><td>7.5 mm</td><td colspan="5">Average sound level (A)</td><td colspan="3">68 dB</td></tr>
<tr><td colspan="2">Cutting gas</td><td>Nitrogen</td><td colspan="5">Cutting gas</td><td colspan="3">Oxygen + Nitrogen</td></tr>
<tr><td colspan="2">Cutting gas pressure</td><td>1.2 bar</td><td colspan="5">Maximum cutting thickness</td><td colspan="3">35 mm</td></tr>
<tr><td colspan="2">Cooling temperature</td><td>$TA = 25$ °C</td><td colspan="5">Cutting capacity</td><td colspan="3">4000 mm × 7000 mm</td></tr>
<tr><td colspan="3">Oxygen Flame Cutting</td><td colspan="8">Wire Electrical Discharge Cutting</td></tr>
<tr><td>Cutting rate (Lateral feed rate)</td><td>20 m/min</td><td colspan="6">Processing condition</td><td colspan="3">C521</td></tr>
<tr><td>Current for maximum cutting</td><td>760 A</td><td colspan="6">Feed rate</td><td colspan="3">3 m/min</td></tr>
<tr><td>Nozzle pressure</td><td>10 bar</td><td colspan="9">Processing conditions and parameters</td></tr>
<tr><td>Operating pressure</td><td>20 bar</td><td>ON</td><td>OFF</td><td>IP</td><td>HP</td><td>MA</td><td>SV</td><td>V</td><td>SF</td><td>C</td></tr>
<tr><td>Operating frequency</td><td>50 Hz</td><td>006</td><td>15</td><td>17</td><td>2</td><td>15</td><td>0.3</td><td>0.3</td><td>005</td><td>0</td></tr>
<tr><td>Cooling capacity</td><td>16747 kJ/h</td><td>Voltage</td><td colspan="8">32 V</td></tr>
<tr><td>Receiver tank capacity</td><td>30 l</td><td>Current</td><td colspan="8">5.6 A</td></tr>
<tr><td>Nominal voltage</td><td>400 V</td><td>Wire tension</td><td colspan="8">Level 8</td></tr>
<tr><td>Average sound level (A)</td><td>68 dB</td><td>Wire feed rate</td><td colspan="8">7 m/min</td></tr>
<tr><td>Cutting gas</td><td>Oxygen+Propane</td><td>Control system</td><td colspan="8">Fine APT</td></tr>
<tr><td colspan="11">Parameters for each cutting methods are selected in accordance with the machine manufacturers' recommendations.</td></tr>
</table>

of the material towards the inner part along a linear line, so that the hardness changes depending on the heat distribution were observed. The microstructures of the main material and the cut edges were viewed with a PANASONIC WV-CP410 Model, Type N334, light microscope, with a magnification of 280-times. Alumina and diamond paste were used to examine the microstructure of the material in the polishing operation followed by the etching process when dipped in the mixture of 2 mL of HNO3 and 98 mL of methane alcohol for 20 s.

Examination of different cutting methods in terms of the structural variations created on the materials: In order to perform metallographic examinations and find structural deterioration on the cut section of the material, a microstructure photo of the section resistant to the cutting process was taken as shown in **Figure 8**. For an accurate assessment, plenty of photos were taken from every cutting edge, and the deformations due to the cutting method formed on the material structure as well

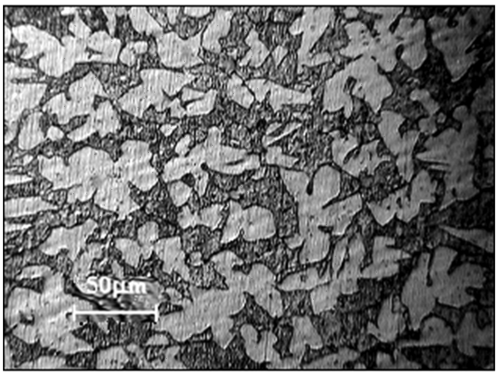

Figure 8: Microstructure of brass-353 ($\alpha+\beta$)
Slika 8: Mikrostruktura medenine 353 ($\alpha+\beta$)

as their changes were evaluated at the end of examining these photos.

Stripe (hydraulic) saw cutting: A considerably rough surface profile was obtained on the cut section. This cut profile was similar to the gear shape and it had a rather rough surface. Again, in the distance of approximately 25 µm a hard rough surface was observed due to the effect of cool deformation. No remarkable morphological change is seen, but there is a structural change caused by the deformation (**Figure 9a**).

Cutting with a milling cutter: A very flat profile was gained on the cut section. In the distance of nearly 10 µm, there is a remarkable, strong surface affected by the impact of cool deformation. Also, no strong structural change due to heat is noticed, but there is a change due to deformation (**Figure 9b**).

Cutting with underwater plasma: In the distances of approximately 75 µm the grain size of α and β phases got smaller and thinner but on the remaining section the grain size remained same. Also, structural deformations exist on the cut section due to excessive warming and fast cooling in the water (**Figure 9c**).

Laser cutting: On the cut section a rough cut profile is visible and due to a high temperature and cooling in air, the geometries of α and β phases turned into acicular forms. At the same time, the structure of the cut section was entirely deformed and α grains became different from their original forms. On the cut section and around it, a new rigid and fragile form emerged (**Figure 9d**).

Cutting with plasma: Owing to the heat effect, in the distances of approximately 75 µm, the grain size of α and β phases got smaller and over the main metal section the size of these grains got infinitesimally small as well. Moreover, due to excessive heat and fast cooling, the grains forming the structure got thinner. This trend continues towards the inner sections. A new hard and fragile structure was formed (**Figure 9e**).

Cutting with abrasive water jet: A very flat cut surface was obtained and in the distance of approximately 10 µm, a layer affected by cool deformation was observed. Apart from that, no structural alteration was observed on the cut section (**Figure 9f**).

Cutting with wire erosion: In the distance of approximately 20 µm the particle size of α and β phases got smaller and over the remaining part the particle size remained the same. Also, on the cut section, the particles forming the structure got thinner, more rigid and fragile due to excessive heat and rapid cooling (**Figure 9g**).

Cutting with oxygen flame: Over the cut section, the structure was entirely deformed and there was a new form, different from the original one. Due to an excessive heat input and rapid cooling in air, the geometries of α and β phases changed and α particles, apparently acicular, were also formed around the cutting section (**Figure 9h**).

In **Figure 10**, the surface-roughness values obtained by cutting thick brass-353 20 mm with different methods are compared. If this graph is carefully analyzed, it is clear that the roughest surface is obtained by cutting the material with the oxygen-flame method and the smooth-

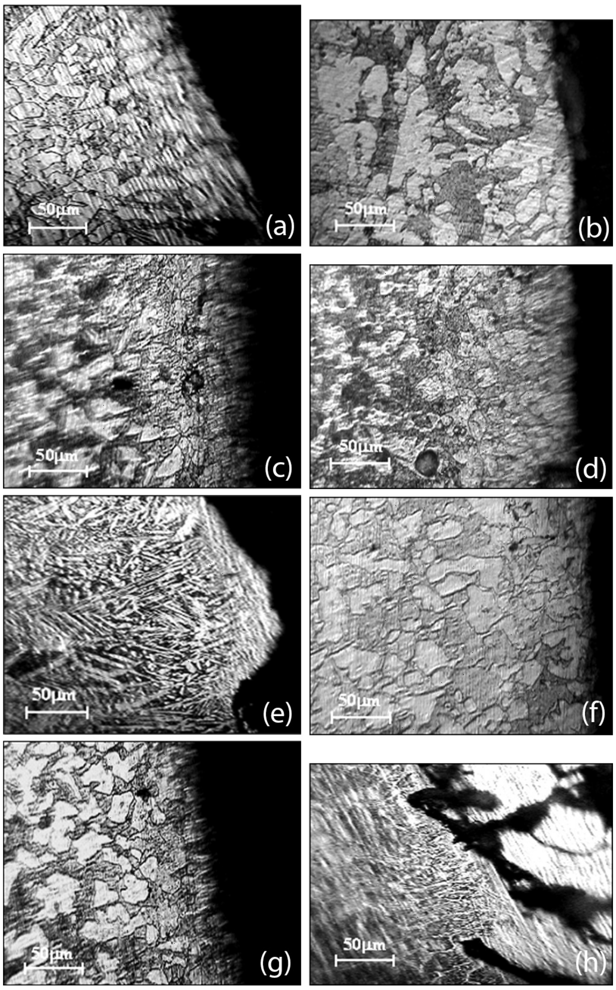

Figure 9: a) Stripe-saw cutting, b) milling cutting, c) underwater plasma cutting, d) laser cutting, e) plasma cutting, f) abrasive water jet cutting, g) wire-erosion cutting, h) oxygen-flame cutting
Slika 9: a) Rezanje s tračno žago, b) rezanje z rezkanjem, c) podvodno rezanje s plazmo, d) rezanje z laserjem, e) rezanje s plazmo, f) abrazijsko rezanje z vodnim curkom, g) rezanje z žično erozijo, h) plamensko rezanje s kisikom

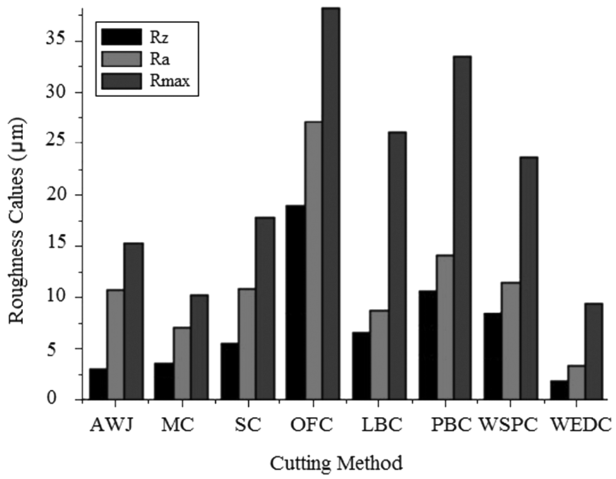

Figure 10: Comparison of the roughness values of cut faces obtained by cutting brass-353 with different methods

Slika 10: Primerjava hrapavosti površine reza pri rezanju medenine 353 z različnimi metodami

est surface is obtained by cutting it with the wire-erosion method.

The obtained outcomes of the study were evaluated using the unprocessed surface-microstructure photographs of the material shown in **Figure 11** and the surface microstructures of different methods shown in **Figure 12**. With the conventional cutting methods (in this study they include the milling cutter and the band saw) nearly the entire energy used for the machining was liberated as heat and a very small percentage of the energy turned into lost energy in the form of an elastic loss[14,15,19].

If the heat liberated in this way is not controlled, it will lead to a change in the metallurgical properties of the material. When the temperature is higher than the recrystallization heat of the material, it will lead to significant changes in the metallurgical properties of the material. The cooling conditions applied during machining will also affect the metallurgical forms of the material. Transformation of the energy into heat and the cooling conditions can be interpreted as the underlying reasons of the main metallurgical and mechanical changes such as the hardness of the material. The fundamental principle of the oxygen-flame cutting operation relies on rising the temperature of the material to the melting point. Rising the heat to the melting temperature and the successive cooling conditions will lead to significant changes in the mechanical and metallurgical formation of the material. This study also gave the expected result, according to which both metallurgical and hardness properties revealed the most significant changes to the material cut with this method.

The causes for the metallurgical changes and hardness variations in the materials are based on the frameworks of the methods applied. The laser, plasma and wire-erosion methods are based on the principle of cutting the material at the melting heat level. Different energy inputs and cooling conditions are the main causes for different metallurgical and hardness formations. Among the traditional methods, the hardness values obtained with the underwater-plasma (focusing) and wire-erosion methods were a little better than those obtained with the laser and plasma methods, because they were implemented in a preserving liquid and, thus, the temperature level was controlled. If a comparison is to be made between the executed cutting methods in terms of metallurgical properties and hardness factors on the basis of the original material structure and the hardness alteration, the best outcome is obtained for the AWJ cutting method. The hardness values for the surfaces cut with AWJ are fairly close to the original hardness ratios (for all the materials). This can be explained in terms of abrasion mechanisms. When cutting with AWJ, the heat variation remains very low (around Δt = 75 °C)[1,4,7]. This shows that no section (HAZ) is affected by the heat factor when using the AWJ cutting method. Taking this feature into account, it is clear that the AWJ cutting method is outstanding, not causing any form of metallurgical and mechanical alteration of the original material.

For the bras-353 materials used in this study, the hardness differences caused by different methods on the cut surfaces are shown in **Figure 11** and the impact rates of these effects are shown in **Table 7**. Following the AWJ cutting method, the second lowest change in the

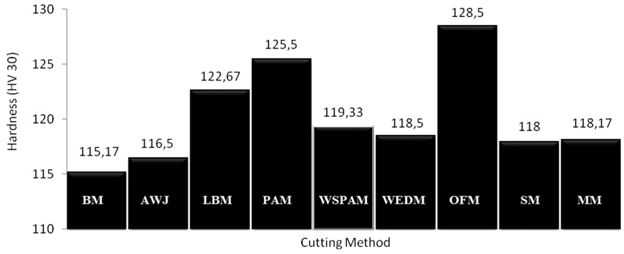

Figure 11: Comparison of the hardness values for the brass-353 (α+β) samples cut with different methods in comparison with the original hardness of the material core

Slika 11: Primerjava trdot medenine 353 (α+β), odrezane z različnimi metodami, v primerjavi s trdoto jedra materiala

Table 7: Hardness variations for brass-353 (α+β) cut with different methods

Tabela 7: Spreminjanje trdote medenine 353 (α+β)

Cutting Method	Brass-353	
	Hardness (HV_{30})	Change (%)
Base material	115.17	-
Cutting by Abrasive Water Jet	116.50	1.15
Cutting by Milling Cutter	118.17	2.60
Stripe (Hydraulic) Saw Disconnection	118.00	2.46
Cutting by Oxygen Flame	128.50	11.57
Cutting by Laser	122.67	6.51
Cutting by Plasma	125.50	8.97
Cutting by Underwater Plasma	119.33	3.61
Wire EDM Cutting	118.50	2.89

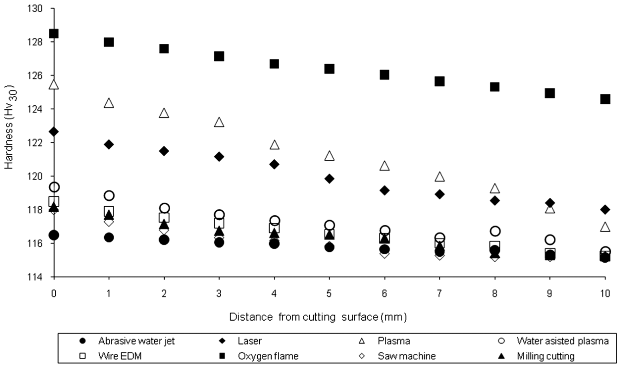

Figure 12: Hardness variations for brass-353(α+β) from the cutting edge to the center due to various cutting methods

Slika 12: Spreminjanje trdote medenine 353 (α+β) od roba rezanja proti sredini pri različnih metodah rezanja

hardness is observed for the conventional methods such as the milling cutter and the band saw. This finding may be attributed to the fact that for the classical methods the cutting parameters are selected so as to avoid excessive recrystallization heat levels.

The depth of the section exposed to the heat also changes depending on the properties of the cutting method. Due to the changes in the metallurgical structures caused by the method, the measurement of the hardness, in the distance 1 mm starting from the cut surface towards the inner part, provides the information on the width of the section affected by the heat factor. The results of these measurements for brass-353 are shown in **Figure 12**. The most outstanding result observed from the graphs is the fact that there is a linear slope for the AWJ cutting method and, thus, no section on the brass material is affected by heat. The AWJ cutting method appears to be a process causing almost no change in the material hardness and metallurgical properties. On the other hand, the oxygen-flame cutting causes the highest level of change to the metallurgical and hardness properties. With this method, the hardness varies significantly from the surface to the core, and the whole material is affected by the heat factor. With the laser and plasma-cutting methods known as the biggest rivals to the AWJ cutting method, the hardness changes from the surface to the core, indicating that a large percentage of the surface of the material is affected by the heat factor. With respect to the metallurgical properties of the material, these methods cannot compete with AWJ.

When all the methods are taken into consideration, the hardness of brass changes constantly. This tendency, which is higher up to some point in steel materials, is reduced after a certain point[18,19]. This circumstance may be explained as a dependency on the heat conductivity of the material. For brass-353, the heat conductivity is higher than that of steel and, thus, the section affected by the heat factor is larger.

3 CONCLUSION

When the effects of different cutting methods on the metallurgical properties of the surface are taken into consideration, the AWJ cutting prevails outstandingly over the other cutting methods.

While different cooling and heat impacts caused by different cutting methods have important effects on the metallurgical properties of the material, in the AWJ cutting method, no section is affected by the heat as the temperature on the surface (HAZ) is not very high and there is no destruction of the original properties of the material. This finding shows that the mechanical properties of the material will remain unchanged as well.

Depending on the changes in the microstructure properties of the material, the section affected by the heat factor and the width of this section are subjected to structural change because of the high heat and cooling of some methods. Depending on the features of the cutting methods, some methods cause a rough particle formation and others cause a thin particle formation, due to instant cooling. Again, due to the effects of the methods, gas holes in the structure and microcracks are likely to emerge. In the AWJ cutting method, a high heat and instant cooling are the fundamental reasons for the microstructures not being destroyed.

When evaluating the eight different methods examined in this study on the basis of the changes in the microstructure properties of the section affected by the heat factor, it is clear that the least effective method is the oxygen-flame cutting and the most effective one is the AWJ cutting. Among the applied methods, the oxygen-flame cutting is viewed as the poorest method because of the variation in the hardness of the material it creates.

Depending on the effects of different methods on the metallurgical forms of the material, the mechanical properties of the material also change. In the experimental studies, the hardness values of the material, after using different methods, are different from the original values. This finding proves that the other cutting methods change the mechanical properties of the materials.

All the cutting methods tested in this study change the hardness of the material. This variation is changeable depending on the heat, temperature and cooling conditions occurring during the cutting operation.

When comparing different cutting methods with respect to the metallurgical properties and the hardness of the material, the best method is the AWJ cutting. This finding proves that during the AWJ cutting no section is affected by the heat factor (HAZ).

When the hardness changes caused by the heat factor are examined from the surface to the centre of the material cut with different methods, the AWJ cutting stands out as the most effective cutting method because with AWJ no section is affected by the heat factor and the cutting operation does not cause any metallurgical and mechanical changes to the material.

In the laser and plasma methods, considered as the most important alternatives to the AWJ cutting, the changes in the hardness from the surface to the center of the material show that, with these methods, the section affected by the heat is much larger than in the case of AWJ.

When compared with the other methods, AWJ is an effective and contemporary alternative cutting method in terms of the surface properties of the materials processed.

4 REFERENCES

[1] A. Akkurt, Surface Properties of Various Materials in Abrasive Water Jet, Comparative Examination of Hardness and Micro Structure Changes in Different Methods, Doctoral Thesis, G. U. Science Department Institution, Ankara, 2002 (In Turkish)

[2] M. Hashish, Application of Abrasive-Waterjets to Metal Cutting, Proceedings of The Nontraditional Machining Conference, ASM, Cincinnati, OH, 1985, 1–11

[3] N. S. Guo, H. Louis, G. Meier, A Surface structure and kerf geometry in abrasive water jet cutting: formation and optimization, Proc. 7th American Water Jet Conf., 1 (1993), 1–25

[4] M. Hashish, On the Modeling of Surface Waviness Produced by Abrasive-Waterjets, Proceedings of the 11th International Conference on Jet Cutting Technology, St. Andrews, Scotland, 1992, 17–34

[5] N. S. Guo, H. Louis, G. Meier, Surface structure and kerf geometry in abrasive water jet cutting: formation and optimization, Proceedings of the 7th American Waterjet Conf., Seattle WA, USA, 1993, 1–26

[6] A.W. Momber, R. Kovacevic, Principles of AWJ Machining, Springer-Verlag, London Limited 1988, 284–324

[7] A. W. Momber, H. Kwak, R. Kovacevic, An alternative method for the evalution of the abrasive water jet cutting process in gray cast iron, J. of Mater. Process. Technol., (**1997**), 65–72

[8] http://www.aliko.fi/english/watercut.htm

[9] M. K. Singh, Unconventional Manufacturing Process, http://www.newagepublishers.com/samplechapter/001566.pdf

[10] J. Powell, L. Ohlsson, E. M. Olofsson, An Economic Comparison of Laser and Abrasive Water Jet Cutting, Lulea University of Technology, Division of Materials Processing, Sweden, 1995

[11] L. Ohlsson, J. Poweell, A. Ivarson, C. Magnusson, Comparison between abrasive water jet cutting and laser cutting, J. Laser Appl., 3 (**1991**) 3, 46–50

[12] S. A. Brown, J. E. Lemons (Eds.), Medical Applications of Titanium and its alloys, ASTM STP 1272, ASTM, Coshohochen, PA 1996

[13] M. Ramulu, M. Hashish (Eds.), Machining Characteristics of Advanced Engineering Materials, MD-Vol.16, ASME Publ, New York NY 1989

[14] H. Y. Zheng, Z. Z. Han, Z. D. Chen, W. L. Chen, S. Yeo, Quality and Cost Comparisons between Laser and Waterjet Cutting, Journal of Materials Processing Technology, 62 (**1996**) 4, 294–298

[15] Y. W. Seo, M. Ramulu, D. Kim, Machinability of Titanium Alloy (Ti-6Al-4V) by Abrasive Waterjets, Proc. Instn Mech. Engrs, Part B: Journal of Engineering Manufacture, 217 (**2003**), 1709–1721

[16] A. Akkurt, M. K. Külekçi, U. Şeker, F. Ercan, Effect of feed rate on surface roughness in abrasive waterjet cutting applications, Journal of Materials Processing Technology, 147 (**2004**), 389–396

[17] J. A. McGeough, Advanced Methods of Machining, Chapman and Hall Ltd, London UK 1988

[18] A. Akkurt, Surface properties of the cut face obtained by different cutting methods from AISI 304 stainless steel materials, Indian Journal of Engineering and Materials Sciences, 16 (**2009**), 373–384

[19] D. Arola, M. L. McCain, M. Ramulu, S. Kunaporn, Waterjet and abrasive waterjet surface treatment of titanium: a comparison of surface texture and residual stress, Wear, 249 (**2001**) 10–11, 943–950

UDK 621.74.043:669.018.258
Original scientific article/Izvirni znanstveni članek

ISSN 1580-2949
MTAEC9, 48(5)735(2014)

INFLUENCE OF THE WORKING TECHNOLOGY ON THE DEVELOPMENT OF ALLOYS H13-w(Cu) 87.5 %

VPLIV TEHNOLOGIJE IZDELAVE NA RAZVOJ ZLITINE H13-w(Cu) 87,5 %

Uroš Artiček[1], Marko Bojinovič[2], Mihael Brunčko[3], Ivan Anžel[3]
[1]EMO – Orodjarna, d. o. o., Bežigrajska cesta 10, 3000 Celje, Slovenia
[2]TIC-LENS, d. o. o., Bežigrajska cesta 10, 3000 Celje, Slovenia
[3]Faculty of Mechanical Engineering, University of Maribor, Smetanova 17, 2000 Maribor, Slovenia
uros.articek@gmail.com

Prejem rokopisa – received: 2013-11-04; sprejem za objavo – accepted for publication: 2013-11-22

Most dies in the casting industry for injection moulding are machined from the premium-grade H13 tool steel. They provide excellent performance in terms of mechanical properties and service life; however, these dies are characterised by a relatively low thermal conductivity. The tool-and-die industry is interested in depositing a material of a high thermal conductivity onto steel in order to improve the thermal management and productivity. We have explored the possibility of using copper with a new technology. In this study, the microstructure evolution and mechanical properties are discussed using the Laser Engineered Net Shaping^{TM} (LENS^{TM}) technology. For a better understanding of the solidification, the microstructure of a LENS sample was compared with the microstructure of a reference alloy produced with the ingot-casting technology having the same chemical composition of H13-w(Cu) 87.5 %. We carried out light microscopy, scanning electron microscopy, an EDS microchemical analysis, the tensile test and microhardness testing. The results show a successful fabrication of LENS samples; their microstructure is more homogeneous compared to the castings; they show better mechanical properties and represent a good potential for further development and use.

Keywords: LENS, casting, microstructure evolution, mechanical properties

V industriji tlačnega litja se za izdelavo matric orodij pogosto uporablja visokokakovostno orodno jeklo H13, ki ima odlične mehanske lastnosti in dolgo trajnostno dobo, vendar je zanj značilna relativno nizka toplotna prevodnost. Orodjarska industrija želi dodati jeklu material z visoko toplotno prevodnostjo za dosego boljše porazdelitve toplote in večje produktivnosti. Z novo tehnologijo, imenovano Laser Engineered Net Shaping^{TM} (LENS^{TM}), smo raziskali možnost uporabe bakra, spremljali razvoj mikrostrukture ter ugotovili mehanske lastnosti. Za boljše razumevanje strjevanja smo primerjali mikrostrukturo vzorca LENS z mikrostrukturo referenčne zlitine z enako kemijsko sestavo H13-w(Cu) 87,5 %, izdelano s tehnologijo litja. Karakterizacija zlitin je potekala s svetlobno mikroskopijo, vrstično elektronsko mikroskopijo, mikrokemično EDS-analizo, z nateznim preizkusom in merjenjem mikrotrdote. Rezultati kažejo uspešno izdelavo vzorcev LENS, katerih mikrostruktura je bolj homogena in ima boljše mehanske lastnosti v primerjavi z odlitki. Tehnologija LENS je dober potencial za nadaljnji razvoj in uporabo v praksi.

Ključne besede: LENS, litje, razvoj mikrostrukture, mehanske lastnosti

1 INTRODUCTION

In the injection-moulding industry, new materials and technologies are required for mould dies in order to optimize the production and keep the costs as low as possible. Despite their excellent mechanical properties, tool steels that are nowadays used as the materials for moulds limit the productivity due to their low thermal conductivity. To solve this problem, designers have been focusing on how to design the tool geometry and construction to achieve higher cooling rates. Complex cooling channels are being designed to enable the cooling liquid to extract the heat from a mould. Ejector pins, slides and air-stream gates are used to eject a part from a mould cavity so the space left in it is small. An alternative way to solve this problem is the use of copper-beryllium inserts[1], which have a higher thermal conductivity. However, they can leave marks on the part and are not environmentally friendly.

Therefore, new technologies and materials, like a Cu-deposition on tool steel, or functionally graded materials (FGM) with a combination of high strength, wear resistance and thermal conductivity are explored as potential candidates for a more efficient injection-moulding tool. The use of a direct-metal-deposition (DMD) fabrication process makes it possible to create an optimum configuration of fin trees and cooling channels as well as to use FGM without being concerned with the limitations of the traditional manufacturing method[2,3]. The laser-engineered-net-shaping™ (LENS) process is seen as one of the most promising DMD technologies for the production of such materials[4–6]. LENS is a relatively new technology capable of rapidly producing complex, fully dense parts directly from a computer-aided design (CAD). A high-power Nd-YAG laser is used to heat and melt a metal powder, thereby producing a melt pool on a substrate attached to an X-Y table. The metal powder from coaxial powder-feed nozzles is injected into the melt pool as the table is moved along pre-designed 2-D tool paths generated using the sliced CAD models. The additions of multiple layers produce a 3-D net or a near-net shape. The fabrication takes place under a controlled,

Table 1: Chemical composition of tool steel H13 in mass fractions, *w*/%
Tabela 1: Kemijska sestava orodnega jekla H13 v masnih deležih, *w*/%

Element	C	Si	Mn	Cr	Ni	Mo	V	Fe
Composition (*w*/%)	0.32 - 0.45	0.8 - 1.2	0.2 - 0.5	4.75 - 5.5	0.3 max	1.1 - 1.75	0.8 - 1.2	bal.

inert atmosphere of argon. Some of the important process parameters are laser power, powder flow rate, layer thickness, hatch width, deposition speed and oxygen level.

The iron-copper (Fe-Cu) alloying system[7] is one of the most suitable systems to produce an efficient FGM mould material. The thermal conductivity of copper is approximately 13 times higher than that of the H13 tool steel at the operating temperatures between 220–600 °C. Unfortunately, a large solidification temperature range and a high amount of the Cu-rich terminal liquid over a wide range of Cu concentration promote solidification cracking in Fe-Cu alloys[8,9]. Additionally, a Fe-Cu phase diagram contains two peritectics and a nearly flat liquidus; they exhibit a high tendency for non-equilibrium solidification that probably has a significant influence on the susceptibility to cracking[7,8]. At the same time, LENS is considered to be a technology that involves a high velocity of solidification with the possibilities of specific reactions, new phases and a metastable microstructure formation. While the properties of materials mainly depend on the microstructures, it is important to know the microstructure development during the LENS process as well as the final microstructure of the layers, depending on the thermal influence of the additional layers.

Our main objective is to explore the microstructure development with the LENS technology. As it is evident from the previous research[8], some chemical compositions are more susceptible to the formation of cracks when using DMD in a Fe-Cu system. Based on the current data, it is not yet possible to conclude how the LENS technology will influence the formation of cracks. In the first part of our research, the composition of H13-*w*(Cu) 87.5 % was selected. Despite the fact that this composition belongs to the crack-free composition range, the question of how the LENS technology influences the microstructure evolution is still open. Namely, the thermal impact of the solidifying layers on the microstructure of the previously solidified layers and the irregularities of the previous layers is not yet known. In our research, the resulting microstructures and mechanical properties of the samples produced in this way were compared with the conventional-casting samples with the same composition, which enabled us to evaluate the effect and the rationality of the technology.

2 EXPERIMENTAL WORK

The conventional solidification of the alloying system consisting of the H13 tool steel and the mass fraction of Cu *w* = 87.5 % was studied using the mould casting. For the preparation of the alloy, oxygen-free high-conductivity copper (*w* (Cu) = 99.99 %) and the H13 tool steel with the chemical composition presented in **Table 1** were used. The material system was vacuum-induction heated at 10^{-2} mbar. Before melting, the chamber was backfilled with the high-purity Ar gas up to 1150 mbar. The melt was homogenized at 1450 °C and then cast at 1400 °C into, cylindrically shaped, grey-cast-iron moulds 50 mm. The inner walls of the moulds were protected with a thin layer of ZrO_2. Before casting, the moulds were preheated to 400 °C to decrease the cooling rate and lower the melt undercooling prior to the primary solid nucleation.

For the layered manufacturing experiments a LENS 850-R machine made by Optomec Inc. with a high-power Nd:YAG laser with a capacity of 1000 W was used. The machine consists of a dual-powder feeder system that allows a simultaneous delivery of two different material mixtures. Several cylindrically shaped samples (*D* = 10 mm, *L* = 100 mm) were successfully produced using the following parameters: the laser power of 530 W, the traverse speed of 5.3 mm/s, the layer thickness of 0.35 mm, the hatch spacing of 0.46 mm, the hatch angle of 60° and the powder-flow rate of 2.75 g/min. In our experiments, we used the powders produced using gas atomisation with the particle sizes ranging from 45 μm to 160 μm (**Figure 1**). The greater

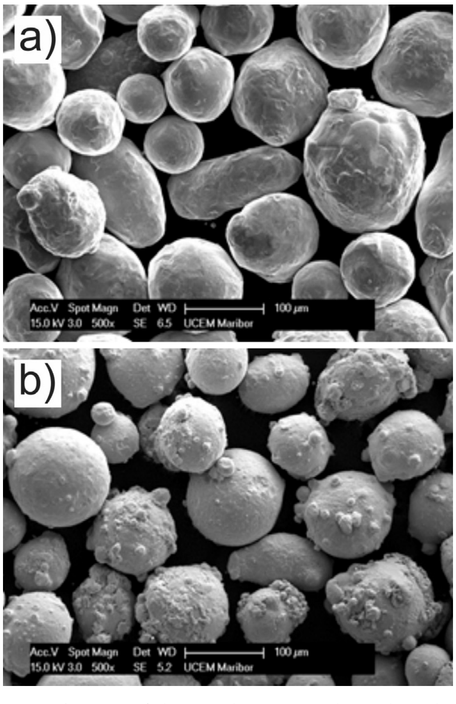

Figure 1: SEM images of the powders: a) Cu, b) tool steel H13
Slika 1: SEM-posnetka prahov: a) Cu, b) orodno jeklo H13

parts of the powders of both materials were spherical, providing the solution to the porosity problem[10,11]. The powders were delivered by the argon carrier gas (2 L/min) to the focus of the laser beam. The oxygen level during all the experiments was maintained below $10 \cdot 10^{-6}$.

The influence of the microstructure on the mechanical properties was evaluated using uniaxial tensile testing and microhardness measurements. The static tensile tests were performed on a Zwick/Roell ZO 10 tensile-testing machine with a load cell capacity of 10 kN at a constant position and a controlled speed of the crosshead of $v = 1.5$ mm/min at ambient temperature. The shapes and dimensions of the tensile-test samples complied with the SIST EN 10002-1 standard. The mechanical properties of several testing samples cut out from the cylinder-shaped casting produced with the conventional casting technology were compared with the tensile bars obtained with the LENS technology, machined in the longitudinal orientation so that the axis of the tensile bars was parallel to the cladding direction. The hardness measurements were carried out according to the 6507-1:1998 standard by means of the Vickers test on a Zwick 3212 microhardness-measurement device.

A microstructural characterisation of the conventionally cast and LENS materials was carried out with light microscopy, LM (Nikon Epiphot 300) and scanning electron microscopy, SEM (FEG Sirion 400 NC) as well as the energy dispersive X-ray analysis, EDX (INCA 6650). The samples for light and electron microscopies were grinded, polished and etched according to the standard metallographic procedures. The etching in a solution consisting of 5 g $FeCl_3$, 10 mL HCl and 100 mL ethanol for about 20 s was used to reveal the microstructure.

3 RESULTS AND DISCUSSION

The microstructure evolution during solidification depends on the alloy characteristics, its chemical composition and it is primarily a function of the solidification condition. For a better understanding of the solidification process under the LENS conditions, the microstructure obtained with conventional solidification in the mould casting of an alloying system with the same composition was studied first.

3.1 Microstructure of conventional-casting samples

The typical microstructure of the conventionally cast material composed of the H13 tool steel and w(Cu) = 87.5 % is shown in **Figure 2**. The microstructure consists of the Fe-rich dendritic-like primary phase (P1) and Cu-rich matrix (M1). However, the size, morphology and distribution of the primary-phase particles are very different throughout the volume of the casting, indicating a high inhomogeneity of the microstructure.

A detailed microstructural analysis of the samples at a higher magnification revealed very fine dendrites (P2) in the Cu-rich matrix and the Cu-rich zone (M2) around the Fe-rich particles (**Figure 3**). An elemental EDX analysis performed within the FE SEM indicates that the Fe-rich primary phase and the surrounding zone contain the alloying elements of the H13 tool steel, while the Cu-rich matrix and fine dendrites consist only of copper and iron (**Table 2**). Because of the inaccuracy of the EDX method used for a quantitative analysis of light

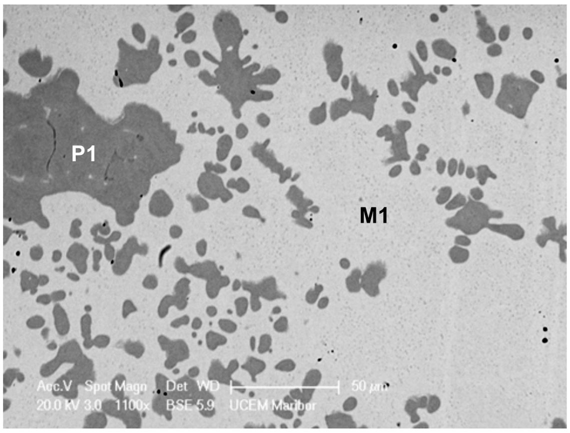

Figure 2: Microstructure of the as-cast sample (SEM back-scattered electron image – BEI)

Slika 2: Mikrostruktura litega vzorca (SEM-posnetek povratno sipanih elektronov – BEI)

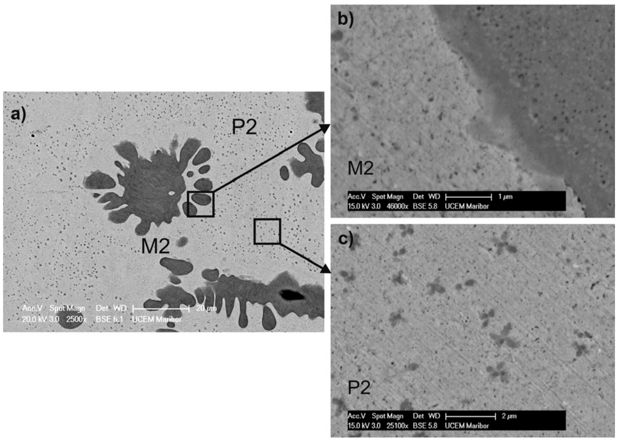

Figure 3: SEM BEI of the: a) as-cast sample, b) showing the Cu-rich zone around the Fe-rich particle and c) fine dendrites in the Cu-rich matrix

Slika 3: SEM BEI: a) litega vzorca, b) področje, bogato z bakrom, okrog delca, bogatega z železom, in c) fini dendriti v matrici, bogati z bakrom (c)

Table 2: Chemical compositions of different microstructural regions in mass fractions, $w/\%$

Tabela 2: Kemijska sestava različnih področij mikrostrukture v masnih deležih, $w/\%$

Microstructural region	Chemical composition ($w/\%$)						
	Fe	Cu	Cr	Mo	Si	V	Mn
P1	78.9	14.5	3.8	1.2	0.6	0.9	0.1
M1	3.6	96.4					
M2	4.5	95.0	0.3		0.1		0.1

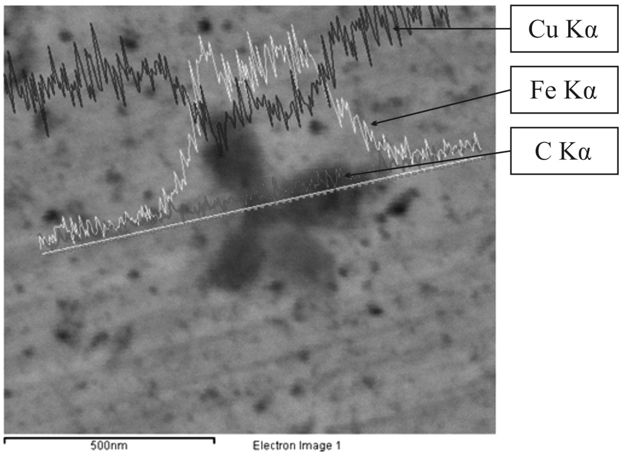

Figure 4: Line microanalysis across a fine dendrite in the Cu-rich matrix

Slika 4: Linijska mikroanaliza preko finega dendrita v matrici, bogati z bakrom

elements, the detected carbon concentration was not taken into consideration in these results. Also, in the microchemical analysis of fine dendrites, the size of the interaction volume was too large for a correct quantitative evaluation of the elements. Therefore, a line analysis is presented in **Figure 4** to show the detected chemical elements in the region of fine dendrites.

It is well known that the alloys from the ternary Cu-Fe-Cr system[12,13] indicate a high tendency for non-equilibrium solidification with metastable transformations. The phase diagrams of the constituent binary Cu-Fe and Cu-Cr systems have flat parts of the liquidus lines, and a metastable liquid-phase separation has been established for these systems[13,14]. The Cu-Fe system displays a large solidification-temperature range and a peritectic reaction at both ends of the phase diagram. Under the near-equilibrium condition, the solidification of the hypo-peritectic composition with $w(\mathrm{Cu}) = 87.5$ % starts with the γ-Fe dendrite nucleation. A further cooling leads to the growth of the primary phase, and the solidification ends with a peritectic reaction, where the rest of the remaining liquid reacts with an equivalent part of the primary solid, i. e., $\gamma\text{-Fe} + \mathrm{L} \rightarrow \varepsilon\text{-Cu}$. On the other hand, if the melt is undercooled below the metastable miscibility gap, the metastable liquid-phase separation takes place, i. e., $\mathrm{L} \rightarrow \mathrm{L1}$ (Fe-rich) + L2 (Cu-rich). In this case, the L1 phase solidifies as the leading phase under the non-equilibrium conditions and the solidification of the L2 phase proceeds under the near-equilibrium condition.

According to the Cu-Fe binary-phase diagram with metastable miscibility lines, the minimum undercooling which is required for the liquid-phase separation depends on the chemical composition[15]. For the alloy with $w(\mathrm{Cu}) = 87.5$ %, the estimated critical value of ΔT based on the metastable miscibility line in the phase diagram is about 70 K. An addition of Cr increases the critical temperature of the miscibility gap of the Cu-Fe binary system[15,16] and decreases the necessary undercooling for the metastable liquid separation.

The results of our microstructural analysis indicate that the obtained undercooling in the mould casting of the material composed of the H13 tool steel and $w(\mathrm{Cu}) = 87.5$ % exceeded the critical value for the melt separation into two liquids: Fe-rich and Cu-rich. After the separation, both liquid phases were undercooled. In accordance with different copper concentrations, the Fe-rich liquid was more undercooled, having a larger driving force for nucleation. Consequently, the solidification started with the Fe-rich primary-phase nucleation in the Fe-rich liquid. The lower undercooling as well as the recalescence event during the Fe-rich liquid solidification enabled the Cu-rich liquid to solidify at a much smaller deviation from equilibrium. The composition and fraction of each liquid changed as the sample was being continuously cooled and probably followed the metastable miscibility-gap phase boundary as the time was allowed for the transfer of the atoms between the two liquids. The solidification of both liquids was terminated by a peritectic reaction, which resulted in the formation of a Cu-rich zone around the Fe-rich primary phase.

3.2 Microstructure of LENS samples

The LENS process can be analysed as a sequence of discrete events, given that it is a layer-by-layer process. Each layer of the melted powders composed of H13-$w(\mathrm{Cu})$ 87.5 % was highly supercooled below the liquidus temperature; the liquid entered an immiscibility gap and separated into two liquids[17]. The phase separation generally appeared as dispersed Fe-rich liquid spheres (L1) in the Cu-rich liquid matrix (L2). **Figure 5** shows a typical microstructure of a LENS sample in the longitudinal direction. The microstructure is not fully homogeneous, but still much more homogeneous than in the cast samples. It consists of dark and bright areas

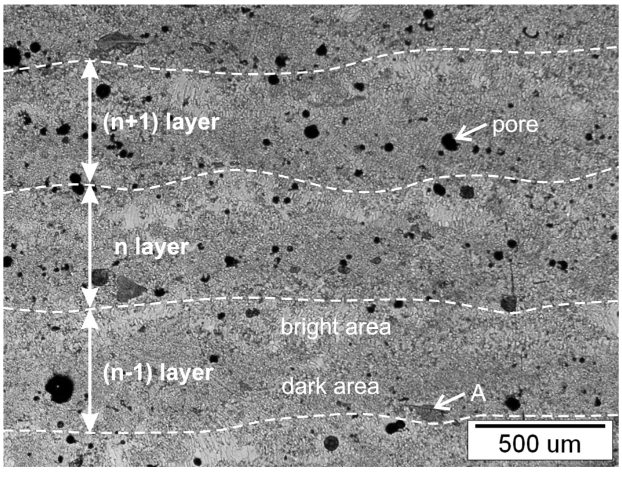

Figure 5: Typical microstructure of a LENS sample layer deposition in the longitudinal direction

Slika 5: Tipična mikrostruktura vzdolžnega prereza vzorca plastne gradnje procesa LENS depending on the distribution and size of the Fe-rich phase, which are a consequence of the heat-affected zone (HAZ) and re-melting zone (RMZ). The dark (wide) area consists of fine copper grains, dispersed fine spherical particles of the Fe-rich phase and some individual coarse Fe-rich particles. In the bright (tight) area – the interlayer zone – the copper grain sizes are bigger, and the area includes a considerably lower amount of Fe-rich spherical particles that are also of a smaller size. There are no individual coarse Fe-rich particles.

If we compare the average size of the dendritic-like primary phase in the as-cast microstructure, being in the range of 100 µm, with small Fe-rich spherical-type particles of the LENS samples, we can see that they are much smaller (2–8 µm) and also more uniformly distributed. The size of these Fe-rich particles depends on the dark/bright area of the microstructure. Some individual coarse Fe-rich particles (A) can also be observed, but they occur less often, normally in the dark area of the microstructure, and belong to the size range of 100 µm (**Figure 5**).

In the microstructure, a uniformly distributed micro-spherical-type gas porosity is present. The gas dissolved or entrapped in the melt did not have sufficient time to escape to the top of the melt pool due to a rapid solidification. However, the concentration of porosity is much smaller than it can often be because of the spherical morphology of atomized powders[10,11]. An light micrograph (**Figure 5**) clearly shows the presence of porosity, indicated by small dark spots, having a diameter smaller than 50 µm.

For a better understanding of the microstructure evolution, we clad one single layer on the substrate. In this case, the primary microstructure was preserved because there was no HAZ or RMZ caused by additional layers. The temperature distribution was different. The absence of HAZ and RMZ, and significantly higher cooling rates because of the cold-plate substrate prevented the Fe-rich liquid spheres (L1) from coarsening. There were no individual coarse Fe-rich particles. The results show that the resultant microstructure with a very fine grain size of approximately 1 µm is homogeneous, and the minority Fe-rich phase spheres are homogenously dispersed in the Cu-rich matrix so that there are no dark or bright areas (**Figure 6**).

A further deposition of layers led to the changes in the primary single-layer microstructure. As the previous layer was re-melted, some of the Fe-rich particles lifted up into the new layer due to the lower density of iron compared to copper. RMZ provides a directional solidification and a grain growth of Cu-crystals in the bright area. Ahead of the solid-liquid interface, liquid L1 becomes highly undercooled and begins to solidify forming a solid and dark area. The latent heat is released to the previous layer slowing down the growth of Cu in RMZ (**Figure 7a**). The figure shows the distribution and size of the Fe-rich particles in the Cu-rich matrix in the dark and bright areas of an individual clad layer, in which the bright area is in the upper part and the dark area in the lower part of **Figure 7b**.

The theoretical layer thickness is 355 µm. For the cyclical layer deposition technique, an interlayer zone – the bright area between two deposition layers – is characteristic, being a consequence of re-melting. The bright and dark areas depend on the local heat input and

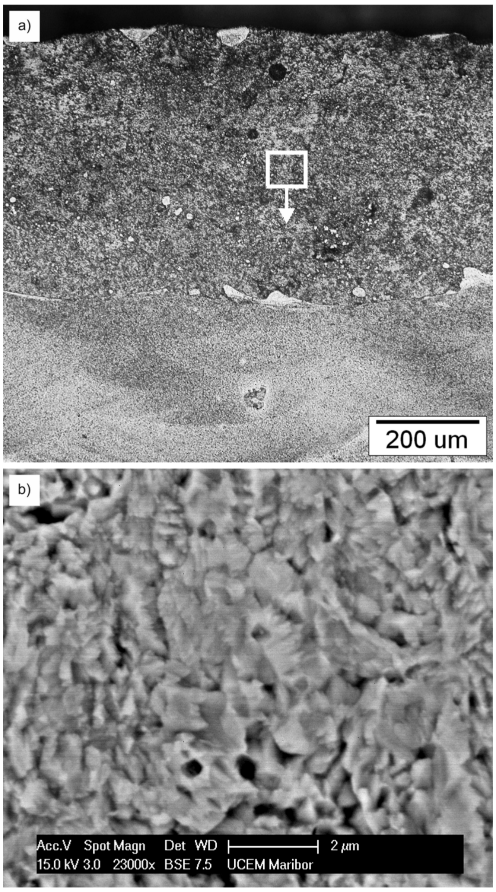

Figure 6: Single-layer weld build-up shows a very fine-grained microstructure: a) LM micrograph, b) SEM BEI micrograph

Slika 6: Ena sama navarjena plast izkazuje zelo finozrnato mikrostrukturo: a) LM-posnetek, b) SEM BEI-posnetek

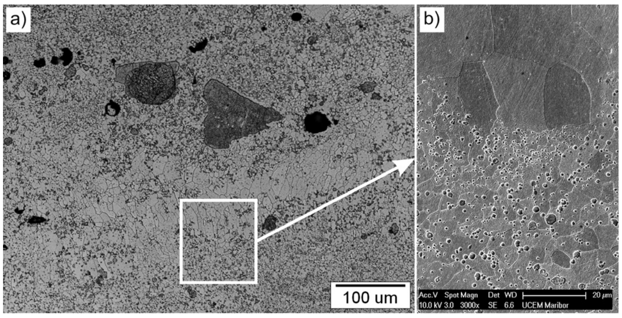

Figure 7: Border area of an individual layer recorded with: a) LM, and b) SEM micrograph of the transitional zone between a dark and a bright area

Slika 7: Mejno področje posamezne plasti, posneto z: a) LM in b) SEM-posnetek prehoda iz temnega v svetlo področje the mechanism of the turbulence in the melt due to cladding the next layer (**Figure 5**).

After the liquid-phase separation, Fe-rich droplets grow and coagulate in order to reduce the interface area with the Cu-rich phase. Since the system still remained a complete liquid during the period between the separation and solidification, the liquid Fe-rich spheres can grow and move relative to the Cu-rich matrix and to each other.

Several mechanisms have been proposed to explain the evolution of size distribution of the dispersion phase, including the wetting behaviour, Ostwald ripening and coarsening of droplets due to collisions, whereby the size of the dispersed L1 spheres increases with the increasing undercooling. Generally, as the cooling rates become higher, the solidification time becomes shorter and the microstructure becomes finer[18]. The area with a higher amount of dispersed Fe-rich particles exhibits very fine grains of the Cu-rich matrix (**Figure 7**).

High undercooling favours a long interval between the separation and nucleation temperatures. As shown in the upper part of **Figure 8**, there was enough time for the spheres to grow through coagulation or coalescence. With the coalescence, some droplets collided with each other so that they may have mutually lost surface energy by joining to form a larger single one. Coagulation, on the other hand (a lower temperature, a higher viscosity) is a process when particles come together irreversibly, i.e., they get stuck together and cannot be separated. Coagulation and coalescence constitute a process, in which fine, dispersed, primary spherical Fe-rich particles (2–8 μm) aggregate together to form individual coarse Fe-rich particles that belong to the size range of 100 μm.

Furthermore, low undercooling provides a short coarsening time, in which a free movement and coagulation cannot occur. Therefore, the coarsening of the L1 spheres in this undercooling range should be attributed to Ostwald ripening[19]. This is a mechanism, allowing the droplets to coalesce due to the solute diffusion between them. The solute solubility depends on the curvature of a droplet; the smaller the curvature, the larger is the radius and the lower is the solubility. This diffusion-dependent coarsening mechanism plays a dominant role when the dispersion phase has a small diameter. With an increase in the droplet radius and a decrease in the temperature, the solid-liquid interface tension increases, whereas the solubility decreases, resulting in the weakening of Ostwald ripening. This mechanism can be observed in the lower part of **Figure 8**, in the bright area.

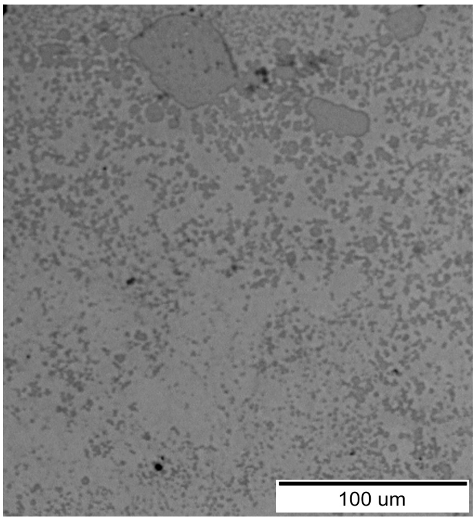

Figure 8: Coagulation and coalescence mechanisms in liquid-liquid mixtures and the Ostwald ripening mechanism in solid-liquid mixtures
Slika 8: Mehanizem koagulacije in koalescence v zmesi tekoče-tekoče in mehanizem Ostwaldovega zorenja v zmesi trdo-tekoče

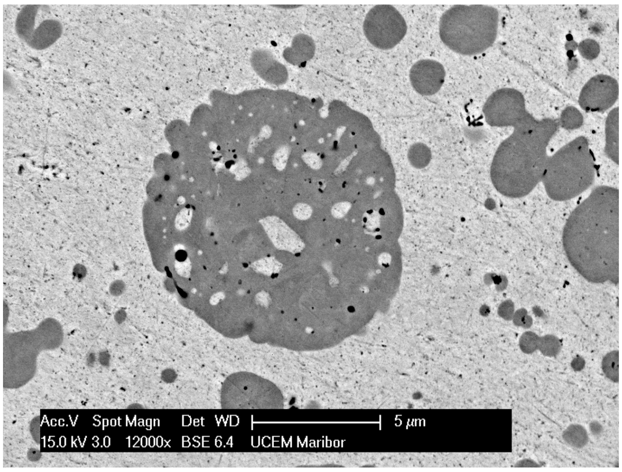

Figure 9: SEM BEI micrograph of a secondary phase separation inside an Fe-rich particle
Slika 9: SEM BEI-posnetek prikazuje sekundarno ločitev faze v delcu, bogatem z železom

It should also be noted that the secondary phase separation was observed in the highly undercooled areas of the H13-w(Cu) 87.5 % alloy, i.e., inside the L1 phase, and some Cu-rich spheres occurred due to the secondary phase separation (**Figure 9**), which is a monotonic increasing function of undercooling. Multi-phase separation has been rarely observed in stable metallic immiscibles. Since liquid metals exhibit a low viscosity and high diffusion coefficient, less time is needed to adjust the composition of the primary phases[20]. However, as undercooling increases, the viscosity rises and diffusion coefficient declines. In this case, a complete diffusion is absent and a multi-phase separation in the liquid becomes more likely to occur.

3.3 Mechanical properties

The solidification parameters of the alloys directly affect the microstructures of the alloy systems, and also significantly influence their mechanical behaviours. The LENS samples have higher tensile-strength values and the cast samples are more ductile (**Figure 10**). This is due to their microstructures, which are finer and more homogenous in the LENS samples that solidified at much higher rates. The uniformly distributed particles of

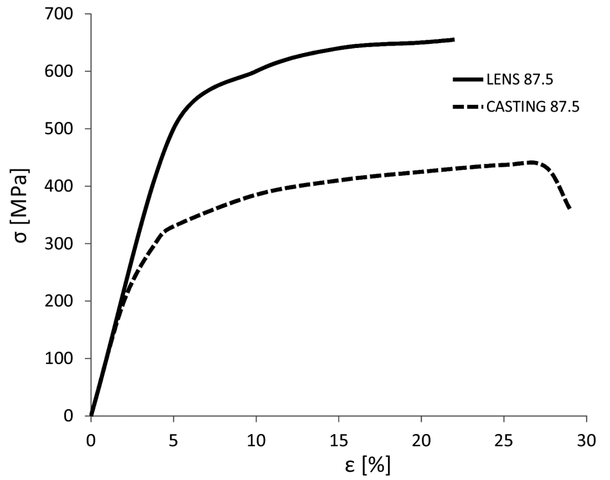

Figure 10: Stress-strain curves of the cast and LENS alloys at room temperature

Slika 10: Krivulja napetost – raztezek lite in LENS-zlitine pri sobni temperaturi

Table 3: Results of the average microhardness-measurement values according to Vickers

Tabela 3: Rezultati povprečnih vrednosti merjenja mikrotrdote po Vickersu

CASTING	of dendrites	near the dendrites	without dendrites
	194 HV 0.01	67 HV 0.01	49 HV 0.01
LENS	α_{Fe}	α_{Cu}	α_{Cu} (HAZ)
	734 HV 0.01	102 HV 0.01	81 HV 0.01

the Fe-rich phase, which are of a smaller size and in a larger quantity, represent the regions that require an increased amount of energy for the dislocations to pass through.

The elongation (ε) of cast samples is greater than the elongation of LENS samples. This is due to different solidification rates of the alloys. A LENS microstructure is the result of faster cooling and solidification – a metastable solidification where the Cu-rich matrix with a higher strength is formed (containing more alloying elements and precipitates due to which ε is smaller). In the case of cast samples where the solidification is slower, the matrix – practically pure copper – has a lower strength, resulting in a larger ε.

There is a trend of the LENS samples to have a slightly higher value of elastic modulus E than the cast samples because they are more metastable due to a greater number of the alloying elements in the Cu-rich matrix, affecting the bond strength.

These characteristics of the microstructure are reflected on the results of the microhardness measurements. A very fine-grained microstructure, a smaller size, a larger quantity of the uniformly distributed Fe-rich spherical phase and the amounts of the alloying elements in the Cu-rich matrix result in significantly higher average microhardness values of the LENS samples. **Table 3** shows the average measures of the microhardness values of the cast samples in the areas of dendrites, near dendrites and without dendrites and the microhardness of the LENS samples in Fe-rich phases, Cu-rich phases and the re-melted HAZ.

4 CONCLUSIONS

In this research, two different technologies were compared, i.e., the LENS technology and the conventional mould casting to produce an alloy with the same chemical composition, H13- w(Cu) 87.5 %. The obtained results can be summarized as follows:

- During the solidification of the conventional castings, the melt is undercooled and separated into two phases. The Fe-rich phase solidifies as the leading phase under the non-equilibrium condition and the solidification of the Cu-rich phase proceeds under the near-equilibrium condition according to the phase diagram.
- Large local variations in the temperature gradient of the castings cause a very inhomogeneous microstructure.
- The microstructure of the LENS samples is much more homogeneous than that of the cast samples. During the LENS process, where a much higher undercooling takes place, the undesired dendritic morphology of primary Fe-rich crystals becomes spherical.
- There is a significant change in the microstructure of a LENS sample between the first layer and the following layers that are re-melted and heat affected, resulting in dark and bright areas of the microstructure. The largest differences are due to HAZ, where a bright area occurs, containing a very small amount of Fe-rich spherical particles. The bright area represents the weaker part of the material, which should be minimized as much as possible by optimizing the energy intake. However, the microstructure is sufficiently homogeneous to allow homogeneous mechanical properties of the bulk samples.
- The porosity found in the LENS samples was considered low and uniformly distributed due to the spherical morphology of the atomized powders.
- The tensile data show that the as-deposited yield strength of the LENS fabricated materials is substantially higher than that of the cast materials; better properties are obtained as a result of a rapid solidification and grain refinement. The tensile data and microstructure characterisation indicate a good metallurgical bonding of individual layers of LENS deposits.
- It has been shown that the H13-w(Cu) 87.5 % alloy fabricated with the LENS technology can perform well in real-life applications. A good thermal conductivity of copper and a high wear resistance of steel can be achieved without any cracks as well as better

mechanical properties compared to conventional mould casting.

Acknowledgments

The research is partially funded by the European Social Fund. Invitations to tenders for the selection of the operations are carried out under the Operational Programme for Human Resources Development for 2007–2013, 1. development priority: Promoting entrepreneurship and adaptability, the priority guidelines, 1.1: Experts and researchers for enterprises to remain competitive.

5 REFERENCES

[1] J. C. Rebelo, A. M. Dias, R. Mesquita, P. Vassalo, M. Santos, An experimental study on electro-discharge machining and polishing of high strength copper–beryllium alloys, Journal of Materials Processing Technology, 103 (**2000**) 3, 389–397

[2] V. E. Beal, P. Erasenthiran, N. Hopkinson, P. Dickens, C. H. Aharens, Fabrication of x-graded H13 and Cu powder mix using high power pulsed Nd:YAG laser, Proc. of SolidFreeform Fabrication Symposium, Austin, Texas, 2004, 187–197

[3] W. Jiang, R. Nair, P. Molian, Functionally graded mold inserts by laser-based flexible fabrication: processing modeling, structural analysis, and performance evaluation, Journal of Materials Processing Technology, 166 (**2005**) 2, 286–293

[4] Optomec, Additive manufacturing system, Laser Engineered Net ShapingTM [online], 2006 [25. 8. 2013], available from the World Wide Web: http://www.optomec.com/Additive-Manufacturing-Technology/Laser-Additive-Manufacturing

[5] F. F. Noecker II, J. N. DuPont, Functionally Graded Copper – Steel Using Laser Engineered Net ShapingTM Process, Department of Materials Science and Engineering, Lehigh University, Bethlehem, PA 2002, 231–238

[6] G. N. Levy, R. Schindel, J. P. Kruth, Rapid manufacturing and rapid tooling with layer manufacturing (LM) technologies, state of the art and future perspectives, CIRP Annals - Manufacturing Technology, 52 (**2003**) 2, 589–609

[7] L. J. Swartzendruber, Binary Alloy Phase Diagrams, T. B. Massalski (ed.), 2nd ed., vol. 1, ASM, New York 1990, 1408–1409

[8] F. F. Noecker II, J. N. DuPont, Microstructural development and solidification cracking susceptibility of Cu deposits on steel: Part I, Journal of Materials Science, 42 (**2007**) 2, 495–509

[9] F. F. Noecker II, Cracking susceptibility of steel - copper alloys, Advanced Materials & Processes, 161 (**2003**) 2, 22–25

[10] D. F. Susan, J. D. Puskar, J. A. Brooks, C. V. Robino, Quantitative characterization of porosity in stainless steel LENS powders and deposits, Materials Characterization, 57 (**2006**), 36–43

[11] A. J. Pinkerton, L. Li, Direct additive laser manufacturing using gas- and water-atomised H13 tool steel powders, The International Journal of Advanced Manufacturing Technology, 25 (**2005**) 5–6, 471–479

[12] L. A. Dreval, M. A. Turchanin, A. R. Abdulov, A. A. Bondar, Thermodynamic assessment of the Cu–Fe–Cr phase diagram, Chem. Met. Alloys, 3 (**2010**), 132–139

[13] C. P. Wang, X. J. Liu, I. Ohnuma, R. Kainuma, K. Ishida, Thermodynamic database of the phase diagrams in Cu-Fe base ternary systems, Journal of Phase Equilibria and Diffusion, 25 (**2004**) 4, 320–328

[14] M. A. Turchanin, P. G. Agraval, Thermodynamics of Liquid Alloys, and Stable and Metastable Phase Equilibria in the Copper – Iron System, Powder Metallurgy and Metal Ceramics, 40 (**2001**) 7–8, 337–353

[15] C. D. Cao, Z. Sun, X. Bai, L. B. Duan, J. B. Zheng, F. Wang, Metastable phase diagrams of Cu-based alloy systems with a miscibility gap in undercooled state, Journal of Materials Science, 46 (**2011**) 19, 6203–6212

[16] C. P. Wang, X. J. Liu, I. Ohnuma, R. Kainuma, K. Ishida, Phase equilibria in Fe-Cu-X (X: Co, Cr, Si, V) ternary systems, Journal of Phase Equilibria, 23 (**2002**) 3, 236–245

[17] A. Munitz, Liquid separation effects in Fe-Cu alloys solidified under different cooling rates, Metallurgical Transactions B, 18 (**1987**) 3, 565–575

[18] Y. Z. Chen, F. Liu, G. C. Yang, X. Q. Xu, Y. H. Zhou, Rapid solidification of bulk undercooled hypoperitectic Fe–Cu alloy, Journal of Alloys and Compounds, 427 (**2007**) 1–2, L1–L5

[19] R. Monzen, T. Tada, T. Seo, K. Higashimine, Ostwald ripening of rod-shaped α-Fe particles in a Cu matrix, Materials Letters, 58 (**2004**) 14, 2007–2011

[20] M. B. Robinson, D. Li, T. J. Rathz, G. Williams, Undercooling, liquid separation and solidification of Cu-Co alloys, Journal of Materials Science, 34 (**1999**) 15, 3747–3753

UDK 669.715'3:620.187:536.7
Original scientific article/Izvirni znanstveni članek

ISSN 1580-2949
MTAEC9, 48(5)743(2014)

MICROSTRUCTURE CHARACTERISTICS OF THE Al-*w*(Cu) 4.5 % MODEL ALLOY

MIKROSTRUKTURNE ZNAČILNOSTI MODELNE ZLITINE Al-*w*(Cu) 4,5 %

Borivoj Šuštaršič[1], Monika Jenko[1], Božidar Šarler[1,2]
[1]Institute of Metals and Technology, Lepi pot 11, 1000 Ljubljana, Slovenia
[2]Laboratory for Multiphase Processes, University of Nova Gorica, Vipavska 13, 5000 Nova Gorica, Slovenia
borivoj.sustarsic@imt.si

Prejem rokopisa – received: 2014-04-14; sprejem za objavo – accepted for publication: 2014-05-12

Samples of the model alloy Al-*w*(Cu) 4.5 % with a controlled microstructure obtained at different cooling rates were synthesized. We investigated the microstructure and the microchemistry using light and scanning electron microscopy in order to determine the segregation on the macro and micro scales, depending on the cooling rate of the synthesized model alloy. Theoretical thermodynamic and kinetic analyses of the model alloy were also performed.

Keywords: model alloy Al-*w*(Cu) 4.5 %, thermodynamics, kinetics, microstructure, microchemistry, segregation

Pripravili smo vzorce modelne zlitine Al-*w*(Cu) 4,5 % s kontrolirano mikrostrukturo, doseženo pri različnih hitrostih ohlajanja. Študirali smo mikrostrukturo in mikrokemijo s svetlobnim (LM) in vrstičnim elektronskim mikroskopom (FE SEM) ter uporabili analizni metodi EDS in AES za določitev obsega izcejanja na makro- in mikronivoju v odvisnosti od hitrosti ohlajanja. Naredili smo tudi teoretične termodinamske in kinetične preiskave modelne zlitine.

Ključne besede: zlitina Al-*w*(Cu) 4,5 %, termodinamika, kinetika, mikrostruktura, mikrokemija

1 INTRODUCTION

The selected alloy is of the eutectic type (**Figure 1**) and is positioned mainly in the region of the homogeneous solid solution of α-Al and the secondary θ-phase (Al_2Cu). This type of alloy can be heat treated by the so-called precipitation hardening (combination of homogenisation annealing, fast cooling and natural/artificial ageing) due to the improvement in the mechanical properties. CALPHAD-based (Calculation of Phase Diagrams)[1,2] software based on theoretical thermodynamic and kinetics also enable a determination of the equilibrium and metastable phases in more complex systems. The theoretical binary phase diagram (**Figure 2**) calculated by ThermoCalc[1] is in a good agreement with the experimental diagram,[3,4] shown in **Figure 1**. A theoretical calculation (at standard pressure 1 bar) for the pure binary alloy predicts the existence of only three phases in the whole (20 °C to 700 °C) temperature region. Between 20 °C and 521 °C two phases coexist: crystals of the α-Al solid solution and the eutectic θ-phase (Al_2Cu). Between 521 °C and 564 °C only the α-Al phase is present (complete solid solubility of Cu in Al) and then between 564 °C and 648 °C exists the two-phase α-Al + L region. Above 648 °C only the liquid L is still present. A theoretical calculation shows that the Cu content in the Al_2Cu phase increases with temperature from mass fractions (*w*) 46 % to 47.7 %. The solubility of Cu in the α-Al solid solution is minimal at 20 °C (only approx. 5.3×10^{-4}) and then increases up to approximately $w = 5$ % at 560 °C. Theory also predicts the existence of the θ’ (theta prime) phase up to 339 °C, containing approximately 54 % Cu and 46 % Al in metastable equilibrium.

The selected alloy is a simple binary alloy (nominal $w(Cu) = 4.5$ %); however, bulk and microchemical analyses by SEM/EDS have shown that the synthesised alloy also contains some impurities and trace elements because of the use of impure raw materials (technical purity $w_p > 99.7$ %). Therefore, in the alloy, besides Cu some Si is also present (approx. $w(Si) = 0.14$ %), Fe (approx. $w(Fe) = 0.09$ %) and traces of Ni and Mg. The

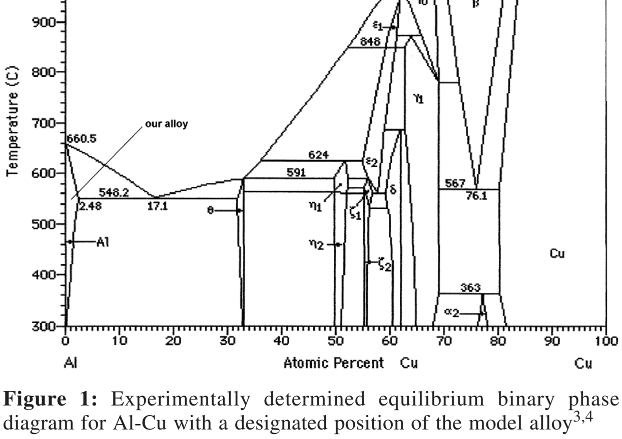

Figure 1: Experimentally determined equilibrium binary phase diagram for Al-Cu with a designated position of the model alloy[3,4]

Slika 1: Eksperimentalno določen ravnotežni binarni fazni diagram Al-Cu z označenim mestom, kjer se nahaja modelna zlitina[3,4]

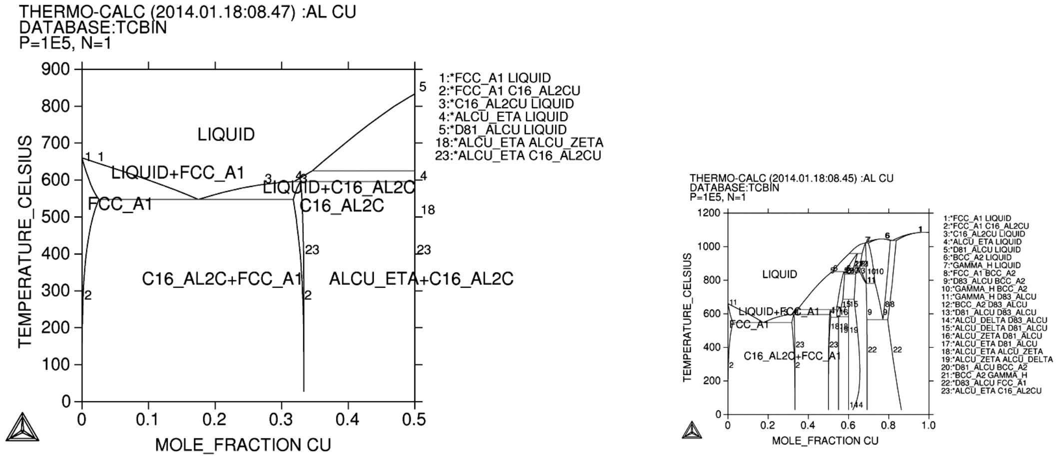

Figure 2: Theoretical equilibrium binary phase diagram Al-Cu, calculated by ThermoCalc[1] (TCBin database)
Slika 2: Teoretični ravnotežni binarni fazni diagram Al-Cu, izdelan s ThermoCalc-om[1] (podatkovna baza TCBin)

Al, Mg and Si have a large affinity for oxygen (ΔG_f = –277.8 kJ/mol at the melting point of Al). Therefore, some surface oxidation and a thin Al_2O_3 film is formed during the alloy synthesis if a very pure protective atmosphere (Ar or N_2) is not used. Some complex inclusions containing Al_2O_3, MgO and SiO_2 can also be formed.

For this type of alloy there is a typical dendrite morphology of solidification during the cooling and casting into a sand, metal or graphite model at normal cooling rates (0.1 K/s to 100 K/s). The measure for cooling rate and segregation is the so-called Secondary Dendrite Arm Spacing (*SDAS*). It generally follows exponent law, $\lambda = k \cdot v^{-n}$; i.e., the larger is the cooling rate v, the finer are the dendrites and the smaller is the space between the secondary dendrite arms λ, as well as the alloy being more micro homogeneous over its volume. Some theoretical models exists[5,6] for a determination of λ, and recently some researchers have also tried to predict λ with ANNs (Artificial Neuron Networks)[7]. For Al alloys different values for the alloy-dependent parameter k (approx. 110) and exponent n (approx. 0.30) are reported. Generally, the parameter k depends on the chemical composition; i.e., decreasing with an increasing concentration of alloying elements.

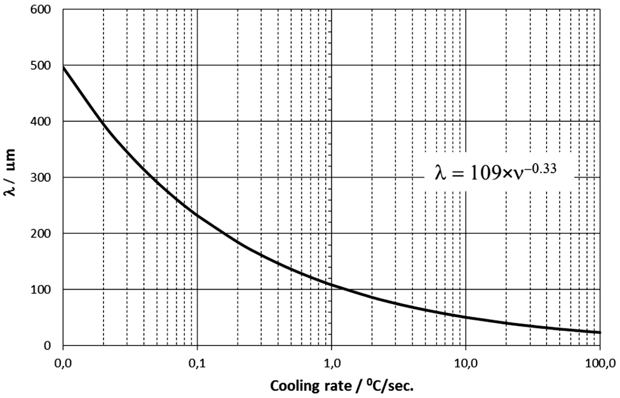

Figure 3: Prediction of the secondary dendrite arms space vs. cooling rate for the Al-based alloy and selected values of the alloy-dependent parameters
Slika 3: Napoved razdalje med sekundarnimi dendritnimi vejami v odvisnosti od hitrosti ohlajanja za zlitino na osnovi Al in izbrane zlitinske parametre

Figure 3 shows an example of the secondary dendrite arm spacing λ vs. cooling rate v diagram for the selected values of $k \approx 109$ and $n \approx 0.33$. One can clearly see that for the selected parameters λ decreases from approximately 500 μm at cooling rate v = 0.01 °C/s, over 110 μm at v = 1 °C/s, and finally at v = 100 °C/s it is only approximately 24 μm.

The physical and mechanical properties of metal-based alloys are dependent on the chemical composition (alloying and trace elements) and the microstructure controlled by the solidification rate connected with the type and geometry of the model and product, respectively. A higher initial solidification rate (cooling rate in the mushy zone) produces a finer dendrite morphology of solidification, a smaller segregation of alloying elements, as well as better are mechanical properties (higher yield/tensile strength and hardness). The refinement of the microstructure also improves the ductility and toughness for a given strength level. Recently, new software[6] has been developed for the relatively accurate prediction of the mechanical properties of Al alloys over a wide range of chemical compositions and solidification conditions.

Figure 4 shows the theoretical equilibrium thermodynamic phase stability of the model alloy with actual chemical composition determined at the Institute of Metals and Technology (IMT), Ljubljana Slovenia (**Table 1**). It is clear that in this case seven phases are stable in the temperature region between 20 °C and 700 °C. However, also in this system the main phases remain α-Al (fcc-A1 solid solution), Al_2Cu and liquid L. The theoretical calculation predicts the existence of the pro-eutectic θ-phase (Al_2Cu) between 20 °C and 514 °C. The solid solution α-Al is stable up to 646.4 °C. In this case the autonomous one-phase region of the α-Al solid

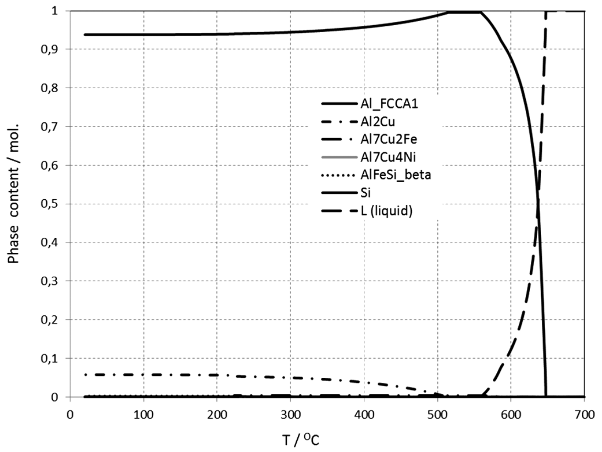

Figure 4: Theoretical equilibrium thermodynamic stability of the phases in the alloying system with the real chemical composition of the model alloy, calculated by ThermoCalc[1].

Slika 4: Teoretična ravnotežna termodinamska stabilnost faz v sistemu z dejansko kemijsko sestavo modelne zlitine, izračunana s ThermoCalc-om[1]

solution does not exist, because the Fe-based intermetallic phase Al_7Cu_2Fe is stable up to 579 °C. The optimal temperature interval for homogenization annealing is between 547 °C and 559 °C. But in this temperature region there is also a small content of Al_7Cu_2Fe. Only liquid is present above 646.4 °C. Silicon has a low solubility in the present alloy. Therefore, it appears in the temperature region between 20 °C and 223 °C as β-phase (AlFeSi) and between 223 °C and 340 °C as elementary crystals of Si, respectively. As already mentioned, in the temperature region between 223 °C and 579 °C, the intermetallic phase Al_7Cu_2Fe is also stable, because of the presence of iron in the model alloy. Besides this, the presence of traces of Ni can stabilize the Al_7Cu_4Ni phase in the temperature region between 20 °C and 548 °C. Some traces of Mg are also detected in the model alloy. In this case we can also expect the presence of the $Al_5Cu_2Mg_8Si_6$ intermetallic phase. However, it should be noted that the content of Ni and Mg in the model alloy is very low and these phases could be neglected.

2 EXPERIMENTAL

The model alloy Al-*w*(Cu) 4.5 %, was prepared in the frame of the project entitled *"Advanced modelling and simulation of liquid-solid state processes"*[8]. In the frame of this project the development of the microstructure during solidification in the mushy zone are studied on the macro and micro levels for the selected Al- and Fe-based complex alloys. The microscopic model is to be solved by the cellular automata concept.

2.1 Synthesis of the model alloy

The model alloy was synthesised in a graphite pot of a laboratory melting furnace 10 kW under an Ar protective atmosphere. The furnace is one of the basic components of the Melt-Spinner M-10 Marco Materials Inc. (**Figure 5a**) which serves primarily for the preparation of rapidly solidified ribbons with the casting of the melt on a rotating Cu-wheel.

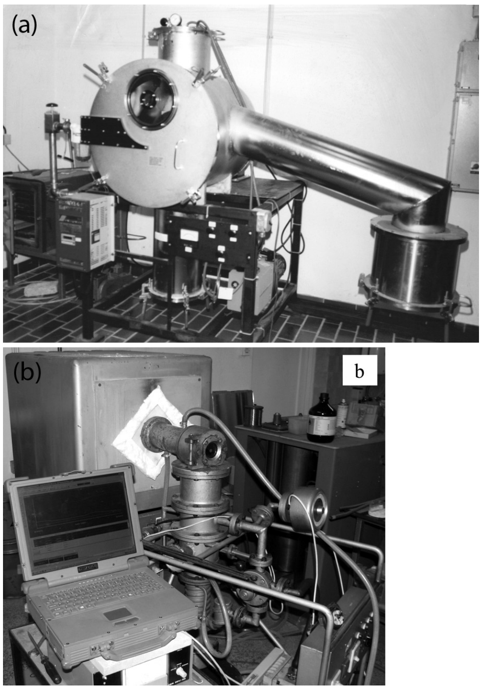

Figure 5: a) Chamber of melt-spinner with inductive melting furnace and b) laboratory tube furnace for heat treatment of the model alloy

Slika 5: a) Laboratorijska naprava Melt-Spinner z induktivno talilno pečico in b) laboratorijska cevna peč za toplotno obdelavo modelne zlitine

As the basic raw materials for the preparation of the model alloy, commercially available materials of technical purity (Al 99.7 % of manufacturer Impol Slovenska Bistrica and commercial Cu 99.9 %) were used. Four batches of 200 g were prepared. Each weight was melted and then cooled under natural cooling conditions down to the room temperature. The chamber of the melt-spinner was evacuated with a rotary vacuum pump (absolute pressure approx. 10 Pa) and then filled with Ar (over pressure 60 kPa abs.) before melting. Individual weights were heated up in the inductive melting furnace to 800 °C in 20 min, homogenized for 10 min and then cooled down. The temperature was followed with a DataLogger and measured with a Pt-PtRh10 thermocouple, located in the middle of the graphite melting pot. It was protected against the melt by a ceramic (alumina) protective tube. The final bulk chemical composition of the prepared alloys was checked using a fast portable XRF (X-Ray Fluorescence) analyser XL3Thermo Fischer Scientific Niton and a more accurate classical ICP OES (Ion Coupled Plasma – Optical Emission Spectroscopy) Agilent 720 instrument with a lower limit of detection (w < 0.001 % of individual element). **Table 1** shows the results of both chemical analyses. Some impurities are detected because of the use of technically pure raw materials. Besides Al and Cu, some Fe and Si, as well as traces of Ni, Zn and Mg, were detected.

Table 1: Average bulk chemical composition of prepared batches of model alloy in mass fractions, *w*/%

Tabela 1: Povprečna kemijska sestava izdelanih šarž modelnih zlitin v masnih deležih, *w*/%

Chemical composition	Cu	Si	Zn	Fe	Mg	Ni	Al
XRF	4.30	0.14	0.010	0.12	–	–	balance
ICP OES	4.45	0.14	0.002	0.09	$< 10^{-3}$	0.006	balance

Five cylinders of diameter 45 mm and height 40 mm weighing approximately 200 g were prepared in this way (**Figure 6**) for further experiments and microstructure investigations. The cylinders were cleaned of surface oxidation by smooth drilling. Further heat treatments of the cylinder were performed due to the formation of an appropriate microstructure at different cooling rates. It is very difficult to obtain the required cooling rate because the real cooling conditions vary over the cross-sections (volume) of relatively large samples, and they are not constant in different temperature regions. The laboratory equipment also does not enable the use of a larger number of thermocouples at different locations of the samples. It can be considered that below 200 °C significant microstructure changes do not happen in a relatively short period of time. Therefore, we can assess the average cooling rate above this temperature. However, in the literature[6] one can find different approaches to cooling-rate definition (initial, average, for a given temperature interval etc.) depending on how it can influence the microstructure formation. During the planning of the present project we did not have in mind that for the formation of a selected Al-4.5 Cu binary alloy that the initial cooling rate and cooling rate in the mushy zone are important. Therefore, it was planned that three different characteristic average cooling rates will be obtained; i.e., very slow (< 0.1 °C/min or 0.0017 °C/s), natural cooling rate (30 °C/min to 40 °C/min or 0.5 °C/s to 0.7 °C/s) and very fast quenching (300–400 °C/min or 5.0 °C/s to 6.7 °C/s). Actually, the following experimental cooling rates are obtained:

Sample 0 to 4 – reference materials – only synthesised alloy (melted in graphite pot of inductive furnace and cooled down). **Figure 7** shows the temperature profile of the alloy synthesis, i.e., heating and cooling in a graphite melting pot. During cooling there is a clearly visible solidification interval between approximately 645 °C and 550 °C. This is in relatively good agreement with the theoretical prediction, which predicts that the solidification starts at 648 °C and ends at 564 °C (**Figure 4**). The obtained cooling rate between 645 °C and 100 °C is approximately 10 °C/min and approximately 0.17 °C/s, respectively. For the formation of the dendrite morphology of solidification the cooling rate in the mushy zone is important. This was assessed at approximately 30 °C/min and 0.5 °C/s, respectively. In this case, one can estimate from **Figure 3** the *SDAS* on 130 µm.

Samples 0 and 1 were retained in the original state for metallographic investigations. However, the samples 2, 3 and 4 were additionally heat treated in order to obtain the planned cooling rates. The samples were heated up to 610 °C into the mushy zone (semi-solid state) and then cooled down.

With sample 2 we tried to simulate natural cooling conditions in the tube furnace (**Figure 5b**). A half part of the cylinder was heated up to 610 °C for 10 min and then a ceramic tube was pulled from the heating chamber of the furnace. The obtained cooling rate in the temperature interval between 610 °C and 200 °C was approximately 12 °C/min (0.2 °C/s) and below 200 °C it was approximately 0.7 °C/min (0.012 °C/s) (**Figure 8**). The maximum cooling rate in the mushy zone was estimated to be approximately 0.4 °C/s (*SDAS* ≈ 138 µm). But it has to be noted that the prepared alloy was not completely melted. As one can see the average cooling rate of the material is rather lower than planned 30–40 °C/min (0.5–0.7 °C/s) and similar to that obtained during the alloy synthesis.

Sample 3 was heated to 610 °C for 10 min and then fast cooled, i.e., quenched in water. The estimated aver-

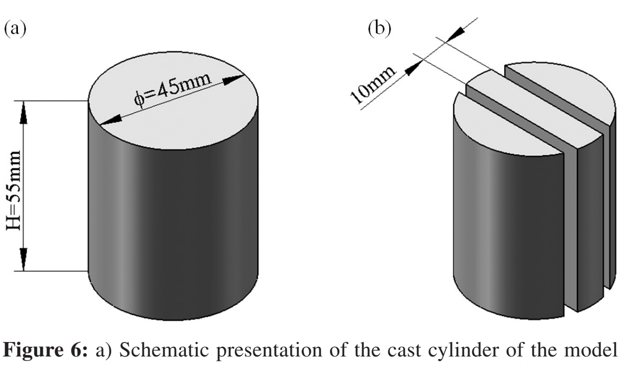

Figure 6: a) Schematic presentation of the cast cylinder of the model Al-*w*(Cu) 4.5 % alloy and a) its cutting into specimens for the preparation of metallographic samples

Slika 6: a) Shematični prikaz ulitka modelne zlitine Al-*w*(Cu) 4,5 % in b) njegov razrez za pripravo metalografskih vzorcev

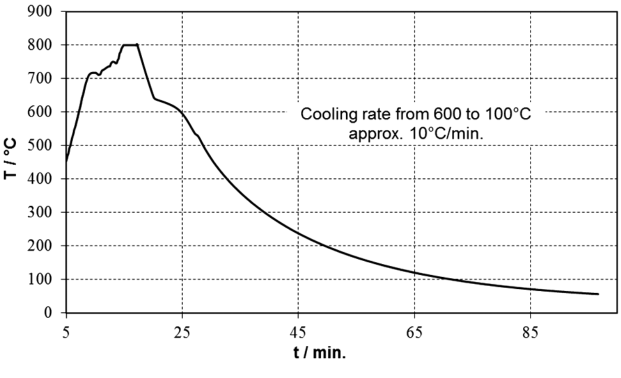

Figure 7: Temperature profile obtained during the synthesis of the model alloy Al-*w*(Cu) 4.5 %

Slika 7: Temperaturni profil sinteze vzorca modelne zlitine Al-*w*(Cu) 4,5 %

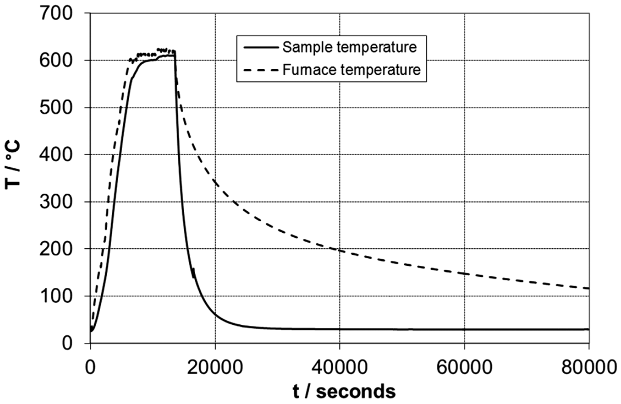

Figure 8: Heating/cooling diagram for model alloy Al-*w*(Cu) 4.5 % in the ceramic tube of the furnace, sample 2, ceramic tube with sample pulled from the furnace chamber

Slika 8: Diagram segrevanja in ohlajanja modelne zlitine Al-*w*(Cu) 4,5 % v cevi cevne peči (po segrevanju je cev potegnjena iz peči), vzorec 2

age cooling rate of this sample was 1220 °C/min (20.3 °C/s), which is rather faster than planned.

Sample 4 – with this sample we tried to simulate very slow cooling. The cylinder was cooled down from 610 °C over approximately 4 d with an approximate cooling rate of 0.1 °C/min, (0.002 °C/s) (**Figure 9**). In this case the maximum cooling rate was 0.7 °C/min and 0.01 °C/s, respectively (*SDAS* ≈ 500 μm).

From the above-described experiments we can conclude that the experimental work was not completely successful, as planned in the frame of the project. In spite of this the obtained results are very interesting and are published as follows.

2.2 Microstructure investigations of the model alloy

Cast and heat-treated cylinders of the model alloy Al-*w*(Cu) 4.5 % were cut up into slices and prepared for microstructure investigations (**Figure 10**). The metallographic specimens were prepared with Struers equipment (electron saw Accutom 50, automatic press Pronto-Press-20 and grinding/polishing apparatus Abramin with MD-system). The microstructure characterization with a light (LM, Nikon Microphot FXA with 3CCD video camera Hitachi HV-C20AMP and software AnalySIS PRO 3.1) and a scanning electron microscope (SEM; JEOL FE HR JSM-6500F) combined with micro-chemical analysis based on a measurement of the dispersed kinetic energy of X-rays (EDS – Energy Dispersive X-ray Spectrometer) on polished and etched metallographic plates 20 mm × 20 mm (specimens) were performed. A systematic non-continuous point profile (10-points per 20 μm) and surface (mapping) EDS analyses at different locations (**Figure 11**) of the samples were then performed.

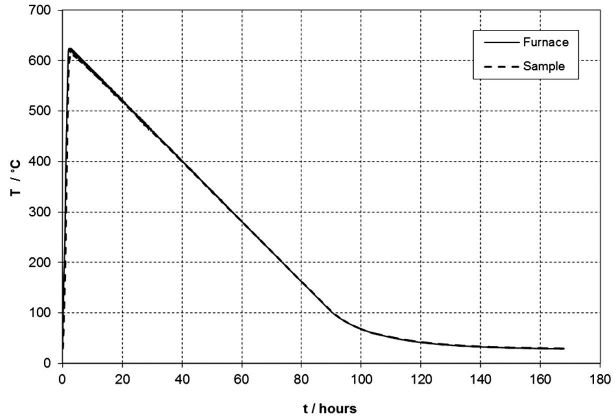

Figure 9: Diagram of heating and very slow cooling of sample 4 of model alloy Al-*w*(Cu) 4.5 % in tube furnace

Slika 9: Diagram segrevanja in zelo počasnega ohlajanja vzorca 4 modelne zlitine Al-*w*(Cu) 4,5 % v cevni peči

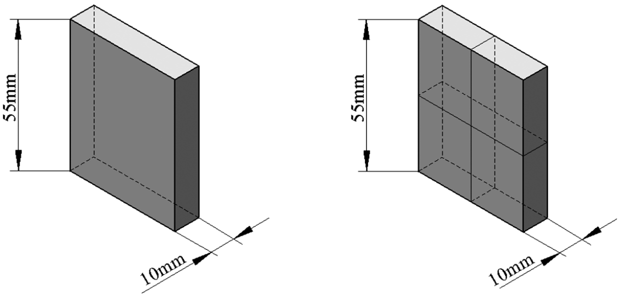

Figure 10: Schematic presentation of ingot cutting of the model alloy for the preparation of metallographic samples

Slika 10: Shematični prikaz razreza ingota modelne zlitine Al-*w*(Cu) 4,5 % za pripravo metalografskih obruskov

3 RESULTS AND DISCUSSION

The prepared model alloys were cooled down with cooling rates between 0.002 °C/s and 20.3 °C/s. In all these cases one can expect a dendrite morphology of

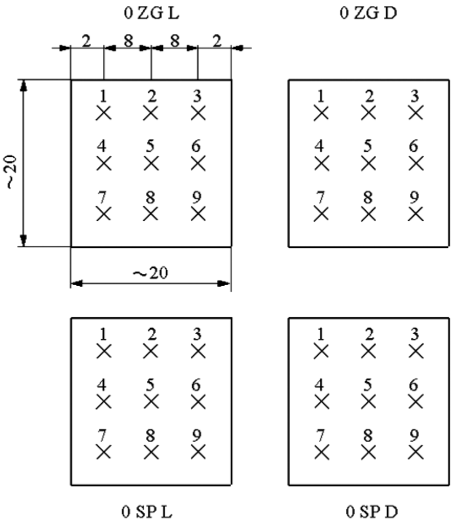

Figure 11: Schematic presentation of EDS analyses' locations on metallographic samples of the model alloy Al-*w*(Cu) 4.5 %

Slika 11: Shematični prikaz analiznih mest SEM/EDS na metalografskih obruskih modelne zlitine Al-*w*(Cu) 4,5 %

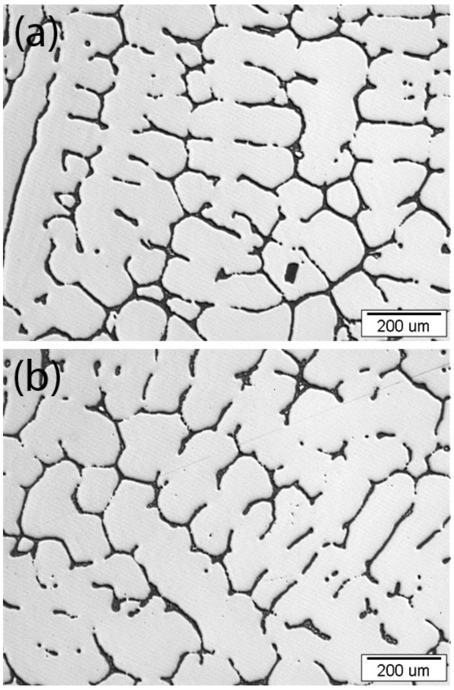

Figure 12: Microstructure of model alloy Al-*w*(Cu) 4.5 % visible under LM: a) sample 1, *SDAS* = 83 µm and b) sample 2, *SDAS* = 100 µm, magnification 50-times

Slika 12: Mikrostruktura modelne zlitine Al-*w*(Cu) 4.5 %, vidna pod LM: a) vzorec 1, *SDAS* = 83 µm in b) vzorec 2, *SDAS* = 100 µm, povečava 50-kratna

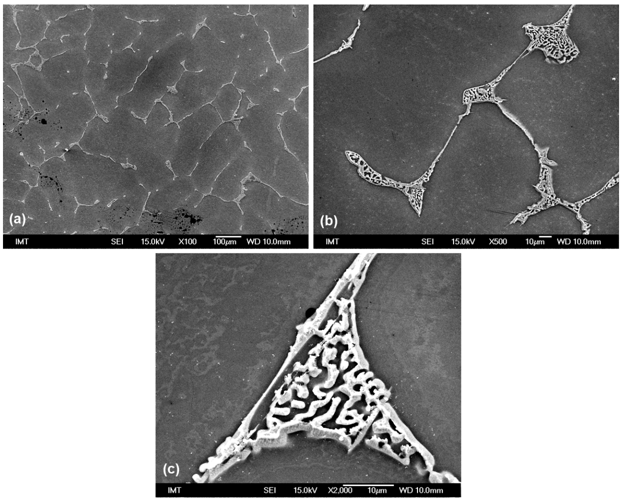

Figure 13: SE images of microstructure of model alloy Al-*w*(Cu) 4.5 % at different magnifications; sample 1: a) magnification 100-times, b) magnification 500-times and c) magnification 2000-times

Slika 13: SE-posnetki mikrostrukture modelne zlitine Al-*w*(Cu) 4,5 %, vzorec 1: a) povečava 100-kratna, b) povečava 500-kratna in c) 2000-kratna

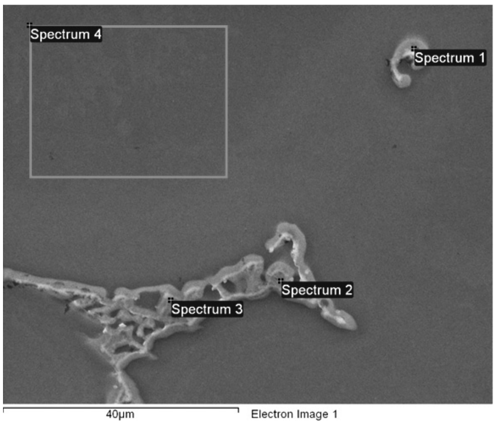

Spectrum	O	Al	Ni	Cu
Spectrum 1	4.37	67.29		28.34
Spectrum 2	4.01	68.25		27.74
Spectrum 3	5.23	65.72	0.58	28.47
Spectrum 4		99.03		0.97

Figure 14: Area (metal matrix of α-Al solid solution) and point SEM/EDS analyses (secondary phase) of model alloy Al-*w*(Cu) 4.5 %

Slika 14: Ploskovna (kovinska matrica α-Al) in točkovna (sekundarna faza) SEM/EDS modelne zlitine Al-*w*(Cu) 4,5 %

solidification with different *SDAS* in the range between 500 µm and 35 µm, and, actually this was obtained. **Figure 12** shows a typical dendrite morphology of the solidification formed during the alloy synthesis. **Figure 13** shows this microstructure visible under the SEM at different magnifications. At the highest magnification one can clearly see the micro-chemical segregation due to non-equilibrium solidification.

Microchemical point, profile and EDS mapping were performed at different locations on the samples in order to obtain information about the local microchemical composition and the alloy segregation. **Figure 14** shows an example of point (Spectrums 1, 2 and 3) and mapping (Spectrum 4) EDS analyses. One can clearly see that in the interdendritic regions a secondary Al_2Cu phase, as well as Al_2O_3 oxide based is formed. It could be anticipated that the oxide inclusions are the nuclei for a secondary phase precipitation. **Figure 15** shows an example of profile analyses across the dendrite region. It is clear that the Cu-rich secondary phase has approximately

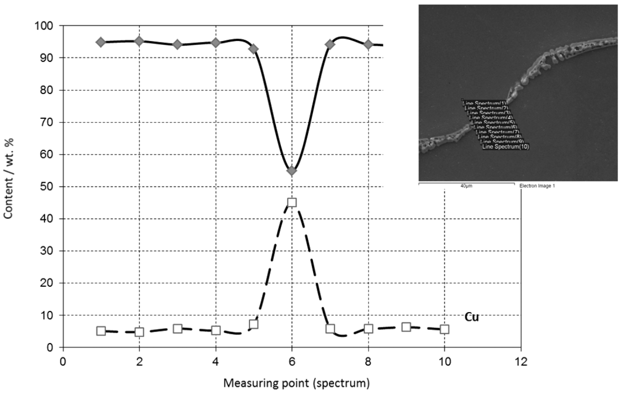

Figure 15: EDS profile analysis from Al metal matrix across secondary phase back to the metal matrix; Al and Cu concentration distribution

Slika 15: EDS profilna analiza iz kovinske α-Al osnove preko sekundarne faze in nazaj v kovinsko osnovo; porazdelitev koncentracije Al in Cu

w(Cu) = 44 %, but the metal matrix, i.e., the α-Al solid solution, has approximately w(Cu) = 5 %.

Non-continuous profile (10-points per 20 µm) SEM/EDS analyses of metallographic samples cooled down with an average cooling rate of 10–12 °C/min have shown that four typical concentration profiles exist:

Generally, the concentration of Al continuously falls to a minimum crossing the secondary phase in the interdendritic regions (dendrite pockets) and then again the Al concentration increases back to the Al-based metal matrix. Simultaneously, the concentration of Cu changes in the opposite direction (**Figure 15**). The average local microchemical composition of the Al matrix is approximately w = 95 % Al and w = 5 % of Cu (amount fractions φ = 97.7 % Al and 2.3 % of Cu) and the average local microchemical composition of the secondary phase is approximately w = 56 % of Al and 44 % Cu (φ = 75 % Al and 25 % of Cu). Theoretically, the metal matrix α-Al solid solution contains w = 100 % of Al at room temperature and approximately φ = 98 % Al and 2 % Cu at 550 °C. The secondary phase Al_2Cu contains theoretically at room temperature φ = 66.7 % of Al and 33.3 % of Cu up to 68 % of Al and 32 % of Cu at 550 °C. The experimentally determined composition is close to the equilibrium composition theoretically predicted at approximately 550 °C. This is a consequence of the non-equilibrium solidification and the metastable condition of the model alloy at room temperature. It also has to be noted that the EDS information comes from a depth of about 1 µm to 3 µm. The size and shape of this interaction volume is dependent on the primary beam energy and the sample material (**Figure 16**). For the surface analysis EDS is not the proper analytical method. In the case of very thin secondary phases, inclusions and surface analyses one must use a surface-sensitive analytical method such as Auger Electron Spectroscopy (AES).

Theoretical thermodynamic analyses predict the existence of some intermetallic phases (Al_7Cu_2Fe, Al_7Cu_4Ni, AlFeSi and crystals of Si) because of the presence of Fe, Si and Ni in the investigated model alloy. Actually, at some places inside the secondary Al_2Cu phase we detected the presence of these elements. In the middle of the secondary phase, where the concentration of Cu is the highest, the EDS analyser detected small concentrations of Ni (**Figure 17**). The intermetallic phase

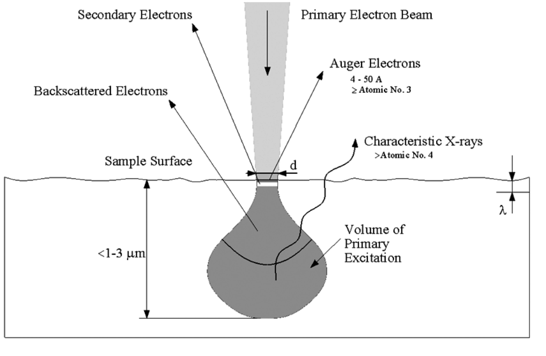

Figure 16: The interaction between an incident electron beam and the solid sample, showing the analysis volumes for Auger, secondary electrons, back scattered electrons and X-ray fluorescence

Slika 16: Interakcija vpadnega elektronskega curka s površino trdnega vzorca prikazuje analizni volumen za Augerjeve elektrone, sekundarne elektrone, povratno sipane elektrone in rentgensko fluorescenco

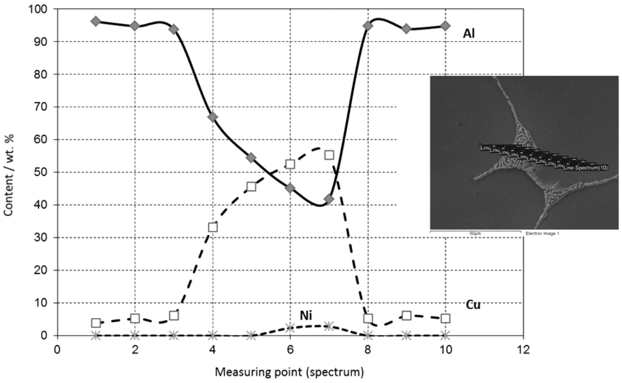

Figure 17: EDS profile analysis across α-Al dendrite region into the inter-dendritic region and back into the metal matrix; concentration distribution of Al, Cu and Ni

Slika 17: EDS profilna analiza iz kovinske α-Al osnove preko sekundarne faze in nazaj v kovinsko osnovo; porazdelitev koncentracije Al, Cu in Ni

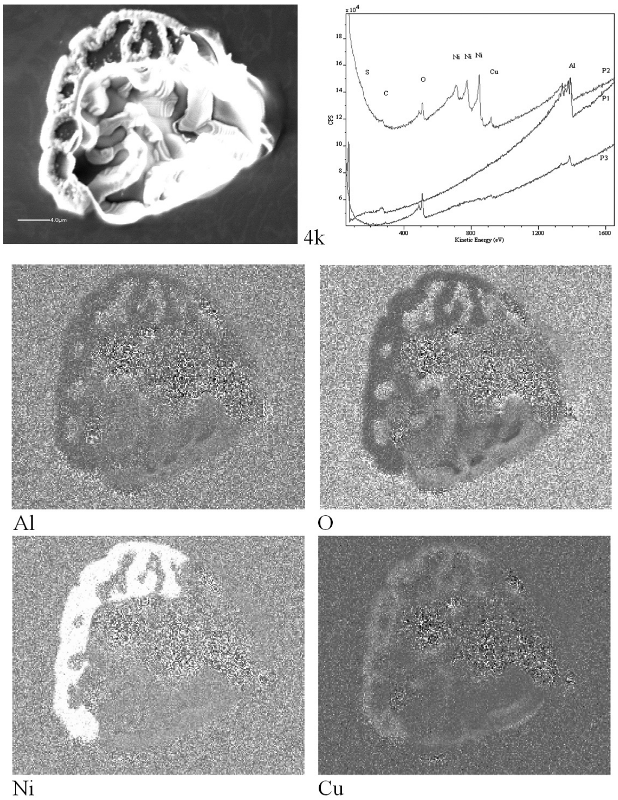

Figure 18: AES mapping of a precipitate of secondary phase in the model alloy Al-w(Cu) 4.5 % (sample 2) showing the distribution of selected elements Al, O, Ni and Cu and a clearly visible increased concentration of Ni

Slika 18: AES-mikroskopija porazdelitve izbranih elementov Al, O, Ni in Cu v izločku sekundarne faze v modelni zlitini Al-w(Cu) 4,5 % (vzorec 2) z dobro vidnim področjem povečane koncentracijo Ni

Al_7Cu_4Ni is stable from room temperature up to 550 °C and theoretically contains mass fractions w = 51 % Cu, 38 % Al and 11 % of Ni. The EDS analyses give a lower Ni concentration (w = 1.5 % to 3.5 %). However, the ratio Cu : Al (58 % Cu : 40 % Al) perhaps confirms that at these places the Al_7Cu_4Ni phase or its non-equilibrium approximate is present. Therefore, we also performed SEM/AES analyses which suggest that at some places there is a higher local concentration of Ni (**Figure 18**). GIXRD (Grazing incidence X-Ray Diffraction) can help in the exact identification of the presence of this phase. However, this investigation was not planned in the frame of the project. It will be performed later and published elsewhere.

Aluminium has a high affinity for oxygen; therefore, it was expected that a slight oxidation of the alloy could happen during its synthesis. The SEM/EDS microanalyses have shown the presence of oxygen at some locations at the interdendritic locations. **Figure 19** shows the profile EDS analysis across the secondary phase. The presence of a $x\mathrm{SiO_2}\ y\mathrm{Al_2O_3}$-based inclusion is clearly visible at the edge of it.

At some locations only Al_2O_3 is present. A proof of this is the simultaneous increased concentration of Al at these locations (**Figure 20**).

Finally, EDS analyses have also shown that practically all the elements of impurities are present at some locations in the interdendritic regions (**Figure 21**). This is important from the mechanical properties point of view because hard intermetallic phases in the interdendritic locations worsen the cohesive strength between the metal matrix and the interdendritic phase. Additionally, segregations are more extensive and the *SDAS* is larger, respectively, if the cooling rate is lower.

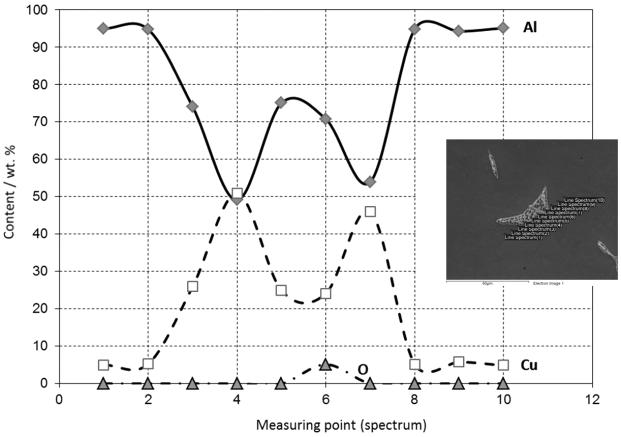

Figure 20: EDS profile analysis across α-Al dendrite region into the inter-dendritic region and back into the metal matrix; concentration distribution of Al, Cu and O

Slika 20: EDS profilna analiza iz kovinske α-Al osnove preko sekundarne faze in nazaj v kovinsko osnovo; porazdelitev koncentracije Al, Cu in O

Figure 22 shows the average *SDAS* measured on samples 0, 1 and 2. The performed *SDAS* measurements show a relatively larger scatter of measured values from location to location. No evident law or regular change in *SDAS* as expected; for example, from the surface to the middle of the sample. The average measured values are between 79 μm and 110 μm, which corresponds to the theoretical initial cooling rate between 1.0 °C/s and approximately 2.5 °C/s (from 60 °C/min to 150 °C/min.). These cooling rates are higher than determined during the experiment (20–30 °C/min) at the thermocouple location. Besides, the thermocouple was isolated with an alumina tube against the effects of the melt. Therefore, further experimental work has to be considerably improved. In particular, the techniques of cooling-rate detection during solidification (smaller sample, larger number of thermocouples at different locations,

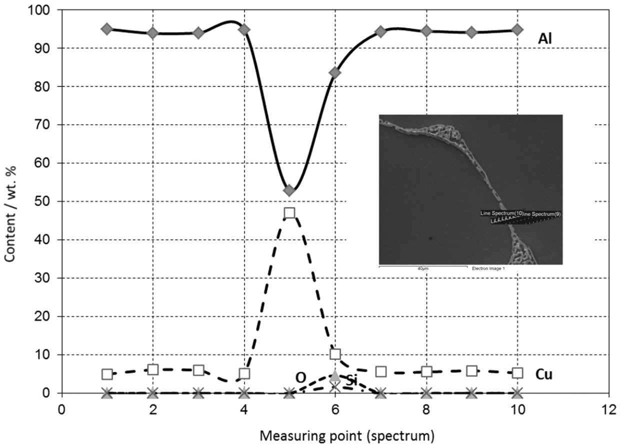

Figure 19: EDS profile analysis across α-Al dendrite region into the inter-dendritic region and back into the metal matrix; concentration distribution of Al, Cu, Si and O

Slika 19: EDS profilna analiza iz kovinske α-Al osnove preko sekundarne faze in nazaj v kovinsko osnovo; porazdelitev koncentracije Al, Cu, Si in O

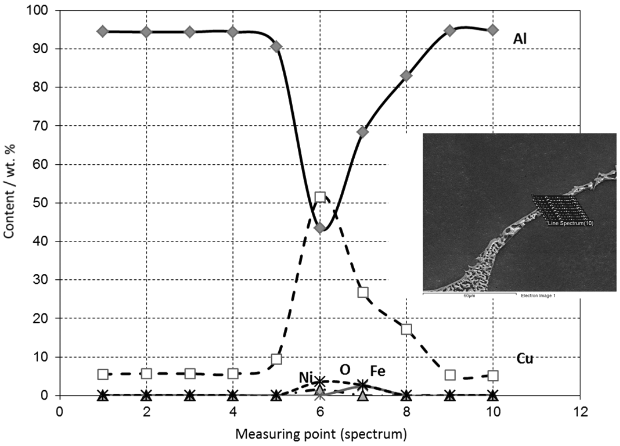

Figure 21: EDS profile analysis across α-Al dendrite region into the inter-dendritic region and back into the metal matrix; concentration distribution of Al, Cu, Fe, Ni and O

Slika 21: EDS profilna analiza iz kovinske α-Al osnove preko sekundarne faze in nazaj v kovinsko osnovo; porazdelitev koncentracije Al, Cu, Fe, Ni in O

Sample 0:

0_zg_L				0_zg_D		
79.1	94.4	90.6		81.8	98.6	107.9
87.8	89.2	79.0		89.4	91.3	84.0
67.0	90.5	97.8		92.8	90.1	93.3
83.8	82.3	103.9		95.2	81.6	76.3
83.1	87.5	88.6		88.5	79.0	76.4
100.4	102.6	94.5		102.1	108.2	87.7
0_sp_L				0_sp_D		

Sample 1:

1_zg_L				1_zg_D		
96.8	79.2	98.8		86.9	98.7	84.0
104.7	114.2	85.9		69.4	84.1	94.7
90.5	83.9	72.2		90.8	84.9	95.4
87.6	126.0	79.5		87.3	107.2	76.3
71.8	100.4	87.1		96.1	119.0	98.0
87.1	95.2	105.5		83.5	92.2	97.7
1_sp_L				1_sp_D		

Sample 3:

3_zg_L				3_zg_D		
106.9	99.7	100.2		89.9	77.5	92.3
98.8	97.7	112.6		94.5	69.9	99.4
92.2	77.1	99.3		84.5	91.4	97.3
94.3	104.7	86.4		90.8	86.5	106.4
109.8	90.3	95.4		104.4	100.8	89.0
100.5	93.2	99.2		110.0	91.0	94.4
3_sp_L				3_sp_D		

Figure 22: Average *SDAS* measured in micrometers, measured on metallographic LM snapshots on individual samples cooled with different average cooling rates, in accordance with **Figure 11**

Slika 22: Povprečna velikost *SDAS* v mikrometrih, izmerjena na metalografskih LM-posnetkih na posameznih vzorcih, ohlajanih z različno povprečno hitrostjo; vezano na **sliko 11**

appropriate melting furnace etc.) must be additionally improved.

The most important for the formation of the solidification microstructure is the initial cooling rate and the cooling rate in the mushy zone, respectively. In the case of our model alloy the solidification interval is rather narrow and it is very difficult to control the solidification process on the relatively large samples that were initially selected. At the beginning of our experimental work we did not have enough experiences in the field. However, we became acquainted with the problems and gained a lot of experience in the field during the execution of the present project. In the late phase of the project we performed much more controlled cooling experiments in the DSC/TG apparatus (Netzsch STA 449C Jupiter) with smaller samples (ϕ 4.5 mm × 5 mm, $m \approx 0.2$ g) and much more controlled cooling rates in the mushy zone. However, this equipment does not allow us to perform the experiments with very high cooling rates. Therefore, the selected cooling rates were (0.1, 0.5, 1.0, 10 and 25) °C/min. The DSC cooling curves show a big difference in solidification and phase precipitation, respectively, if the cooling rate is changed. A very clear and sharp phase formation is noticed at the lowest cooling rate (**Figure 23**). Details of these experiments will be published elsewhere separately, because of the limited space here.

4 CONCLUSIONS

Samples of the model alloy Al-*w*(Cu) 4.5 % with a controlled microstructure obtained at different cooling rates were synthesized in the frame of the present investigation. The obtained average cooling rates on larger samples (**Figure 6**) in the temperature interval from 600 °C to 200 °C are estimated to be 0.1 °C/min,

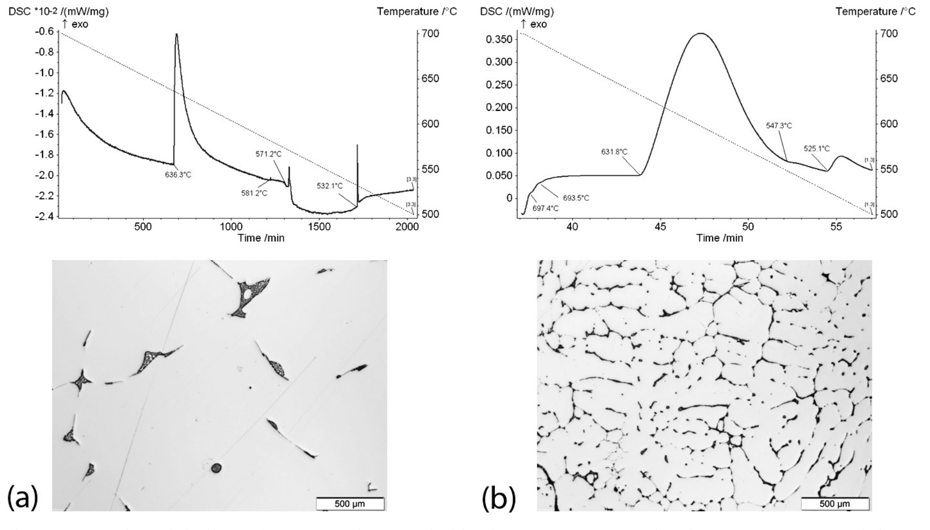

Figure 23: DSC cooling curves of model alloy Al-*w*(Cu) 4.5 %, cooled in the temperature region between 700 °C and 500 °C with two different cooling rates: a) 0.1 °C/min (*SDAS* > 700 μm) and b) 10 °C/min (*SDAS* ≈ 100 μm), with appertain microstructural characteristics visible by LM.

Slika 23: DSC ohlajevalna krivulja modelne zlitine Al-*w*(Cu) 4,5 %, ohlajane v temperaturnem območju med 700 °C in 500 °C s hitrostjo: a) 0,1 °C/min (*SDAS* > 700 μm) in b) 10 °C/min (*SDAS* ≈ 100 μm), s pripadajočimi mikrostrukturnimi značilnostmi, vidnimi s svetlobnim mikroskopom

12 °C/min. and 1 220 °C/min. The size of the *SDAS* is controlled by the initial cooling rate and the cooling rate in the mushy zone, respectively. This cooling rate was estimated to be approximately 0.7 °C to 30 °C/min in the case of natural cooling and very slow cooling in the furnace. It is a rather larger cooling rate than the average measured cooling rate in the middle of the samples. The average measured *SDAS* on all the samples are between approximately 79 µm and 110 µm. This corresponds to the theoretical initial cooling rate of approximately between 1.0 °C/s and 2.5 °C/s. The only exception is the sample with the lowest selected average cooling rate (approx. 0.002 °C/s). In this case the *SDAS* was assessed to be more than 700 µm. But it was difficult to measure because even the lowest magnification (50-times) of the LM does not enable exact measurements. For this case much lower magnifications (10- to 25-times) are necessary. The performed investigations showed that more exact measurements of the cooling/solidification rate, especially in the mushy zone, are necessary. The experiments performed on smaller samples in the DSC/TG apparatus enabled better control of the solidification, but in a limited range (from 0.1 °C/min to 25 °C/min) of cooling rates. Therefore, new lab equipment (furnace) with a controllable atmosphere and accurate temperature control over a wider range of cooling rates (0.1–100 °C/s) for relatively small samples must be developed or purchased, respectively.

The next step of the performed investigations was the preparation of metallographic samples, as well as microstructural and microchemical investigations under the LM and SEM combined with EDS and AES microanalyses. The aim of these investigations was a determination of the segregation at the macro and micro levels, depending on the cooling rate of the synthesized model alloy. The microstructural composition of the naturally cooled model alloy is markedly in the non-equilibrium state, and similar to those predicted theoretically at 550 °C. Four characteristic states of chemical composition are detected in the interdendritic regions because of the presence of impurities (Fe, Si, Ni) in the model alloy, as well as its slight oxidation during synthesis. For the synthesis and study of the pure binary Al-*w*(Cu) 4.5 %, model alloy it is necessary to select completely pure raw materials. Impurities can disturb some of the investigations to a certain extent. However, on the other hand, it can also help in understanding the complexity of multicomponent alloying systems.

Acknowledgement

The authors wish to thank the Slovenian Research Agency for financial support in the frame of project no.: J2-4120 and P2-0132, and to Professor Jožef Medved, Department for Metallurgy and Materials, University of Ljubljana, for assistance with the DSC/TG experiments.

5 REFERENCES

[1] Software package for thermodynamic calculations: Thermocalc; internet address: http://www.thermo-calc.com/start/

[2] U. R. Kattner: Thermodynamic Modelling of Multicomponent Phase Equilibria, JOM, 49 (**1997**) 12, 14–19

[3] TAPP – Thermochemical and Physical Properties, A computer database, 1994

[4] E. A. Brandes, G. B. Brook, Smithells Metals Reference Book, 7-th Edition, Butterworth Heinemann Ltd., Oxford UK 199

[5] J. F. Chinella, Z. Guo, Computational Thermodynamics Characterization of 7075, 7039, and 7020 Aluminum Alloys Using JMatPro, ARL, MD, USA, 2011

[6] Z. Guo, N. Saunders, A. P. Miodownik, J. P. Schillé, Prediction of room temperature mechanical properties in aluminium castings, Proceedings of the 7-th Pacific Rim International Conference on Modeling of Casting and Solidification Processes, Dalian, China, 2007

[7] D. Hanumantha Rao, G. R. N. Tagore, G. Ranga Janardhana, Evolution of Artificial Neural Network (ANN) model for predicting secondary dendrite arm spacing in aluminium alloy casting, J. Braz. Soc. Mech. Sci. & Eng., 32 (**2010**) 3, 276–281

[8] B. Šarler et al., Advanced modelling and simulation of liquid-solid state processes, small basic project J2-4120, Slovenian Research Agency, internal reports, 2010–2013

UDK 669.187:669.015.8 ISSN 1580-2949
Original scientific article/Izvirni znanstveni članek MTAEC9, 48(5)753(2014)

CHROMITE SPINEL FORMATION IN STEELMAKING SLAGS

NASTANEK KROMITNIH SPINELOV V JEKLARSKIH ŽLINDRAH

Jaka Burja[1], Franc Tehovnik[1], Jožef Medved[2], Matjaž Godec[1], Matjaž Knap[2]
[1]Institute of Metals and Technology, Lepi pot 11, 1000 Ljubljana, Slovenia
[2]University of Ljubljana, Faculty of Natural Sciences and Engineering, Department of Materials and Metallurgy, Aškerčeva 12,1000 Ljubljana, Slovenia
jaka.burja@imt.si

Prejem rokopisa – received: 2014-05-13; sprejem za objavo – accepted for publication: 2014-05-21

During the processing of stainless-steel grades in an electric arc furnace (EAF) a considerable amount of chromium can be lost due to oxidation. These chromium oxides form different phases in the slag, the most stable being the spinel phase. The basicity of the slag has a major impact on the composition of the chromium oxide phase. A phase analysis revealed two types of chromium oxide phases, calcium chromites and chromite spinels, which are dependent on the chemistry and the basicity of the slag. The calcium chromites only form at a high slag basicity, while the chromite spinels form at both high and low basicity. The effects of ferrosilicon additions were observed as they have a profound effect on both the slag and the chromite spinel chemical composition.

Keywords: chromite spinel, calcium chromite, stainless steel slag, chromium loss

Med izdelavo nerjavnih jekel v EOP lahko pride do znatnih izgub kroma zaradi oksidacije. Kromovi oksidi v žlindri tvorijo različne faze, najstabilnejša je spinelna faza. Bazičnost žlindre ima velik vpliv na fazno sestavo kromitnih oksidov. Fazna analiza je pokazala prisotnost dveh vrst kromovih oksidov, odvisnih od kemijske sestave žlindre in bazičnosti, to sta kalcijev kromit in kromitni spinel. Kalcijevi kromiti so prisotni ob visoki bazičnosti, medtem ko so spineli prisotni tako ob visoki kot nizki bazičnosti. Opazovani so bili učinki dodatkov ferosilicija, ki odločilno vplivajo na kemijsko sestavo žlindre in kromitnih spinelov.

Ključne besede: kromitni spinel, kalcijev kromit, nerjavna žlindra, izguba kroma

1 INTRODUCTION

Chromium promotes ferrite[1] and is an important alloying element in steels, especially stainless steels. Stainless steels contain chromium in excess of the mass fraction $w = 10$ %;[2] higher amounts of chromium in steel leads to a higher corrosion resistance.[3] Chromium is added through the melting of stainless-steel scrap and ferrochromium additions. Ferrochromium is available in different grades that contain different amounts of chromium and other alloying elements. Carbon plays the most important role as an alloying element in ferrochromium besides chromium, because oxygen blowing is needed to remove the carbon from the melt, which can cause chromium losses.

Chromium-rich slags typically form during the melting of stainless-steel grades. Studies show that 97 % of the chromium losses are attributed to the electric arc furnace (EAF),[2] during melting and to a large extent during the blowing of oxygen into the melt in order to remove the carbon.[4,5] The oxidation of chromium takes place alongside that of other alloying elements in the steel, such as aluminum, carbon, silicon, manganese and a certain amount of iron itself. The reaction of chromium and oxygen dissolved in steel can be described as:[6]

$$\begin{gathered} 2\mathrm{Cr}_{(s)} + 3[\mathrm{O}] = \mathrm{Cr}_2\mathrm{O}_{3(s)} \\ \Delta G_1^0 = -1\ 127\ 100 + 250.80T\ (\mathrm{J}) \end{gathered} \tag{1}$$

The dominant chromium oxide in the slag at the melting temperature, without a protective atmosphere, is Cr_2O_3.[7] Oxides of alloying elements, among them chromium oxides, along with slag-forming oxide additions, form different phases in the slag. There are two types of chromium-oxide-based phases that are generally found in a chromium slag, i.e., chromium-oxide-based spinels, which are solid solutions, and calcium chromites, which are stoichiometric compounds.[8] Chromium-oxide-based spinels contain Cr_2O_3, Al_2O_3, FeO, MgO and MnO, while calcium chromites contain only CaO and Cr_2O_3. Chromium oxide spinels precipitate in the liquid slag[9] and affect the slag's properties. The slag stiffens and becomes inactive, thus preventing the reduction of oxides and attributing to the loss of alloying elements. When spinels are formed, the activity of the chromium decreases because of the strong bonding in the spinel, especially in the $MgCr_2O_4$.[10]

Reductive agents such as aluminum, carbon, ferrosilicon and even calcium carbide are introduced into the slag in order to minimize the chromium losses.[4,5,9,11–15] In the case of the decarburization of the melt a typical stainless-steel slag can contain from $w = 30$ % to 40 % Cr_2O_3.[15] The aim of this work is to study the phase composition of chromium-rich slags and the composition of chromium-oxide-based phases in order to establish the basic conditions for further studies of the thermodynamic equilibrium mechanism of the chromium distribution between the steel and the slag.

2 EXPERIMENTAL

Slag samples were taken with a special spoon during the steel processing in the EAF. One sample was taken after the ferrochrome addition and the oxygen blowing and another after the ferrosilicon addition. The samples were left to cool; smaller pieces were cut away and put into the mass for metallographic investigation. They were grinded and polished and then carbon was evaporated onto the surface to provide electrical conductivity for the electron microscope. Other pieces of the same slag samples were crushed in a steel mortar, then in a steel ball mill, and finally in an agate mortar to achieve the final fine powder that is needed for the X-ray diffraction. The slag samples underwent light microscopy (LM), (Microphot FXA, Nikon), electron microscopy and electron-dispersive spectroscopy (EDS) analysis (SEM-EDS, JEOL – JSM6500F) and X-ray diffractometry (XRD, Panalytical XPert Pro PW3040/60).

3 RESULTS AND DISCUSSION

Slag samples, before and after the ferrosilicon addition, were taken from high and low basicity slag.

The basicity is defined as:

$$B = \frac{\%\text{CaO}}{\%\text{SiO}_2} \tag{2}$$

The samples with high basicity before the ferrosilicon addition contain both calcium chromites and spinels, whereas the low-basicity samples after ferrosilicon contain only spinels. The formation of spinels is preferred over the formation of calcium chromites.[16] The spinels are particles that precipitate at processing temperatures from liquid slag, and the equations for precipitation are:[17,18]

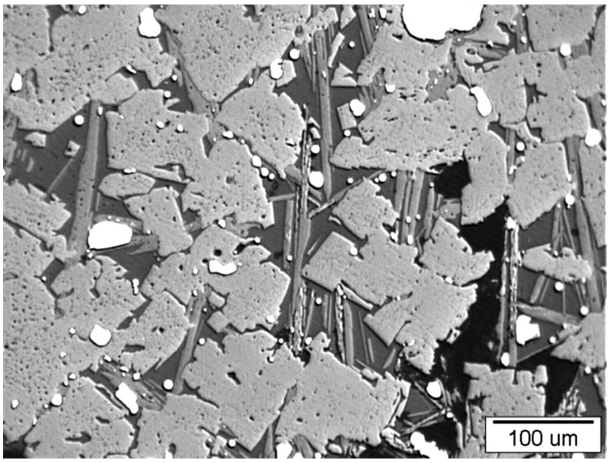

Figure 2: Microstructure of slag with chromites, and calcium chromites (*B* = 2, before FeSi addition)

Slika 2: Mikrostruktura žlindre s kromitnimi spineli in kalcijevimi kromiti (*B* = 2, pred dodatkom FeSi)

$$\text{MgO}_{(S)} + \text{Cr}_2\text{O}_{3(S)} = \text{MgO}\cdot\text{Cr}_2\text{O}_{3(S)}$$
$$\Delta G_3^0 = -30\ 221 - 19.945T\ (\text{J}) \tag{3}$$

$$\text{FeO}_{(S)} + \text{Cr}_2\text{O}_{3(S)} = \text{FeO}\cdot\text{Cr}_2\text{O}_{3(S)}$$
$$\Delta G_4^0 = -37\ 706 + 3.846T\ (\text{J}) \tag{4}$$

$$\text{MgO}_{(S)} + \text{Al}_2\text{O}_{3(S)} = \text{MgO}\cdot\text{Al}_2\text{O}_{3(S)}$$
$$\Delta G_5^0 = -20\ 740 - 11.57T\ (\text{J}) \tag{5}$$

The precipitated spinels are solid solution of all the oxides mentioned above. The analyzed samples can be divided into two groups, i.e., those with high basicity and those with low basicity. The low-basicity samples contain only chromites and no calcium chromites. The spinels are of various sizes, from 10 µm to 100 µm, as shown in **Figure 1**. The high-basicity slags (**Figure 2**), on the other hand, contain large spinels that can reach

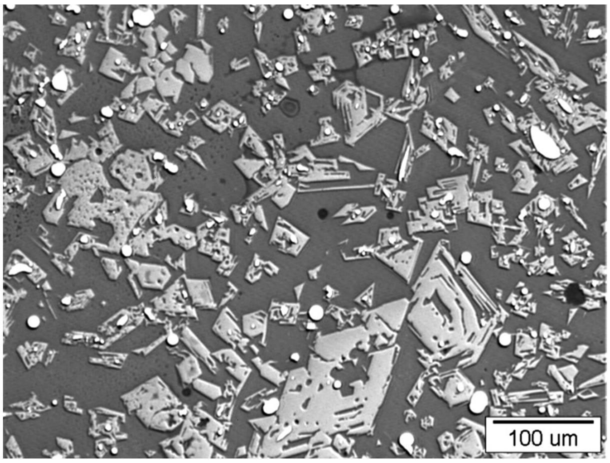

Figure 1: Microstructure of slag with chromite spinels (*B* = 0.8, after FeSi addition)

Slika 1: Mikrostruktura žlindre s kromitnimi spineli (*B* = 0,8, po dodatku FeSi)

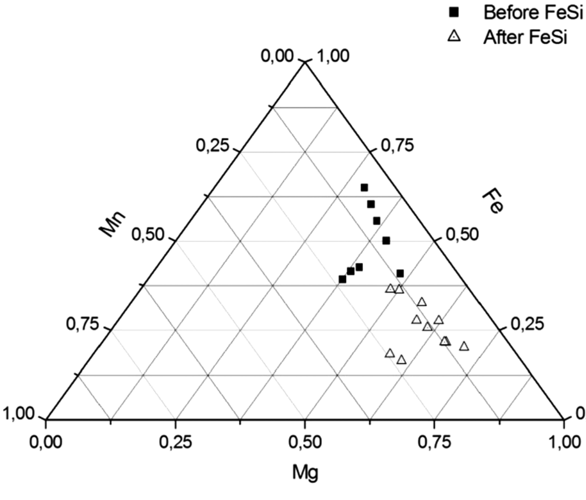

Figure 3: Ternary diagram of Mn-Fe-Mg in spinels (mole fraction) before and after FeSi addition

Slika 3: Ternarni diagram Mn-Fe-Mg v spinelih (molski delež) pred dodatkom FeSi in po njem

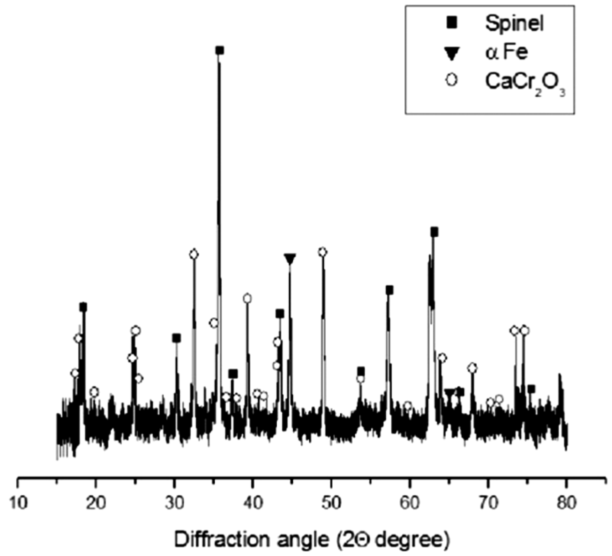

Figure 4: XRD spectrum of a slag sample before the FeSi addition
Slika 4: XRD-spekter vzorca žlindre pred dodatkom FeSi

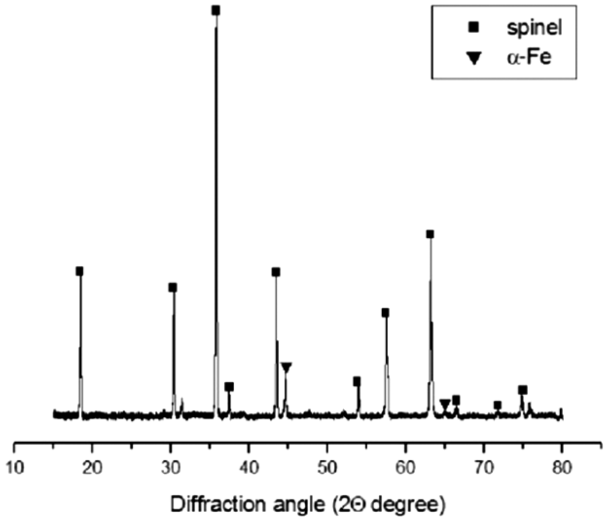

Figure 5: XRD spectrum of a slag sample after FeSi addition
Slika 5: XRD-spekter vzorca žlindre po dodatku FeSi

sizes above 100 μm in diameter. The main difference, however, is the presence of needle-shaped calcium chromites. The EDS analysis of the slag samples showed that the chemical composition of the spinels changes during the processing. After the ferrosilicon addition, the content of FeO in the spinels is lowered, as can be seen in **Figure 3**.

Iron oxide is the most easily reduced of all the oxides in the spinels and is therefore the most impacted by the addition of FeSi. Magnesium oxide, on the other hand, is very stable in the spinel phase and is not reduced, its content is also increased by refractory degradation.[19,20] FeSi is mainly added in order to reduce the chromium content in the slag, but a significant part is used to reduce the iron oxides. The diagram in **Figure 3** shows that FeSi does not reduce the manganese from the spinels very effectively. The composition of spinels follows the parallel Mn concentration lines in the ternary diagrams, showing only slight deviations.

The XRD spectrum of the slag before the FeSi addition at high basicity (**Figure 4**) shows the presence of spinels, calcium chromites and alpha iron.

After the FeSi addition at low basicites there are no calcium chromites present, only spinels and alpha iron, as can be seen in **Figure 5**. There are no more calcium chromites present.

Alpha iron is the presence of metal droplets that form due to the entrapment of the melt during the steelmaking process, either because of mixing during the arc melting and oxygen blowing or during the reduction of the oxides to the metal state. The XRD spectra confirm the observations under both SEM and LM. In fact, the SEM EDS analysis of the metal droplets revealed that they contained mostly iron and chromium, hence the ferrite phase, the composition spanning from $w(\mathrm{Cr}) = 10$ % up to 20 %.

The examinations of the slags revealed that although all of the slags contained calcium chromites before the FeSi additions, none of the samples after the FeSi additions did. The tendency of calcium oxide to form phases with silicon oxides is clearly greater than that of forming them with chromium oxides.

4 CONCLUSION

Chromium slags contain two types of chromium-based oxides: calcium chromites and chromite spinels.

The composition of the chromites changes during the processing; the addition of ferrosilicon (FeSi) significantly decreases the Fe content in the spinels.

The magnesium contents in spinels increases during the steelmaking process, both due to the relative increase of the content (FeO and Cr_2O_3 reduction) during ferrosilicon injection and due to MgO dissolution from the refractory.

Calcium chromites form only in slags with high basicity, when the silicon content in the slag is low; the slag is saturated with CaO.

Acknowledgment

The authors would like to thank mag. Alojz Rozman and Metal Ravne d.o.o. for financing this research project.

5 REFERENCES

[1] F. Tehovnik, B. Arzenšek, B. Arh, D. Skobir, B. Pirnar, B. Žužek, Microstructure Evolution in SAF 2507 Super Duplex Stainless Steel, Mater. Tehnol., 45 (**2011**) 4, 339–345

[2] S. Sun, P. Uguccioni, M. Bryant, M. Ackroyd, Chromium control in the EAF during stainless steelmaking, Proc. of the 55th Electric Furnace Chicago, 1997, 297–302

[3] F. Tehovnik, B. Žužek, B. Arh, J. Burja, B. Podgornik, Hot Rolling Of The Superaustenitic Stainless Steel AISI 904L, Mater. Tehnol., 48 (**2014**) 1, 137–140

[4] B. Arh, F. Tehovnik, The Oxidation and Reduction of Chromium, Metalurgija, 50 (**2011**), 179–182

[5] B. Arh, F. Tehovnik, The Oxidation And Reduction of Chromium During the Elaboration of Stainless Steels in an Electric Arc Furnace, Mater. Tehnol., 41 (**2007**) 5, 203–211

[6] Y. Xiao, L. Holappa, M. A. Reuter, Oxidation State and Activities of Chromium Oxides in CaO-SiO_2-CrO_x Slag System, Met. and Mater. Trans. B, 33 (**2002**), 595–603

[7] K. Morita, N. Sano, Activity Of Chromium Oxide in CaO-SiO_2 Based Slags At 1873 K, Proc. of the VII International Conference on Molten Slags Fluxes and Salts, Johannesbourg, 2004, 113–118)

[8] J. H. Park, I. H. Jung, S. B. Lee, Phase Diagram Study for the CaO-SiO2-Cr2O3-5 mass.%MgO-10 mass.%MnO System, Met. Mater. Int., 15 (**2009**), 677–681

[9] S. Mostafaee, A Study of EAF High-Chromium Stainless Steelmaking Slags Characteristics and Foamability, PhD. Thesis, Stockholm, 2011

[10] G. J. Albertsson, Investigations of Stabilization of Cr in Spinel Phase in Chromium-Containing Slags, Licentiate Thesis, Stockholm, 2011

[11] N. Sano, Reduction Of Chromium Oxide In Stainless Steel Slags, Proc. of 10th Int. Ferroalloys Congr. INFACON X Transformation through Technol., Cape Town, 2004, 670–677

[12] E. Shibata, S. Egawa, T. Nakamura, Reduction Behavior of Chromium Oxide in Molten Slag Using Aluminum, Ferrosilicon and Graphite, SIJ Int., 42 (**2002**), 609–613

[13] J. Björkvall, S. Ångström, L. Kallin, Reduction Of Chromium Oxide Containing Slags Using CaC_2, Proc. of the VII Int. Conf. Molten Slags Fluxes Salts, Johannesbourg, 2004, 663–670

[14] X. Hu, H. Wang, L. Teng, S. Seetharaman, Direct Chromium Alloying by Chromite Ore with the Presence of Metallic Iron, J. Min. Metall. Sect. B Metall., 49 (**2013**), 207–215

[15] R. I. L. Guthrie, M. Isac, Z. Lin, A Fluid Dynamics Simulation Of Chromium Recovery From Aod Slags During Reduction With Ferrosilicon Additions, Proc. of the VII Int. Conf. Molten Slags Fluxes Salts, Johannesbourg, 2004, 465–472

[16] H. Cabrera-Real et al., Effect of MgO and CaO/SiO_2 on the Immobilization of Chromium in Synthetic Slags, J. Mater. Cycles Waste Manag., 14 (**2012**), 317–324

[17] M. Hino, K. Higuchi, T. Nagasaka, S. Ban-Ya, Phase Equilibria and Activities of the Constituents in FeO·Cr2O3- MgO·Cr2O3 Spinel Solid Solution Saturated with Cr203, ISIJ Int., 34 (**1994**), 739–745

[18] S. Jo, B. O. Song, S. Kim, Thermodynamics on the Formation of Spinel ($MgO \cdot Al_2O_3$) Inclusion in Liquid Iron Containing Chromium, Met. and Mater. Trans. B, 33 (**2002**), 703–709

[19] M. Guo, S. Parada, S. Smets, P. T. Jones, J. Van Dyck, B. Blanpain, P. Wollants, Laboratory Study of the Interaction Mechanisms Between Magnesia-Chromite Refractories and Al_2O_3-rich VOD slags, Proc. of the VII Int. Conf. Molten Slags Fluxes Salts, Johannesbourg, 2004, 327–336

[20] M. Guo, P. T. Jones, S. Parada, E. Boydens, J. Van Dyck, B. Blanpain, P. Wollants, Degradation Mechanisms of Magnesia-Chromite Refractories by High-Alumina Stainless Steel Slags under Vacuum Conditions, J. Eur. Ceram. Soc., 26 (**2006**), 3831–3843

UDK 658.567.3: 677.13.004.8
Professional article/Strokovni članek

ISSN 1580-2949
MTAEC9, 48(5)757(2014)

RECYCLING OF JUTE WASTES USING PULPZYME ENZYME

RECIKLIRANJE ODPADKOV JUTE Z UPORABO ENCIMA PULPZIMA

Khashayar Mohajershojaei[1], Fatemeh Dadashian[2]
[1]Department of Polymer Engineering and Color Technology, Amirkabir University of Technology, Tehran, Iran
[2]Department of Textile Engineering, Amirkabir University of Technology, Tehran, Iran
khashayar045@yahoo.com, dadashia@aut.ac.ir

Prejem rokopisa – received: 2012-12-22; sprejem za objavo – accepted for publication: 2013-11-06

In this paper, enzymatic treatment of jute wastes using pulpzyme was studied. The jute wastes from the machine-made carpet-production factories were used as a model. The effects of several parameters such as enzyme concentration, pH and time on the recycling process were evaluated. The optimum enzyme concentration, reaction time and pH for the recycling of jute wastes were 1.5 %, 2 h and 8, respectively.
The results showed that the enzymatic process using pulpzyme was an effective method to hydrolyse cellulosic chains, shorten cellulosic fibers such as jute and decrease its moisture regain (%). The products obtained from the enzymatic process using pulpzyme are suitable raw materials for paper-making processes due to their length range between 0 mm to 4 mm.

Keywords: recycling process, jute wastes, pulpzyme enzyme, mass loss, length reduction, fiber shortening

V članku je prikazana encimska obdelava odpadkov jute z uporabo pulpzima. Kot model so bili uporabljeni odpadki jute pri strojni izdelavi preprog. Ocenjen je bil učinek več parametrov, kot so koncentracija encima, pH in čas za postopek recikliranja. Optimalna koncentracija encima, čas reakcije in pH pri recikliranju odpadkov jute so bili 1,5 %, 2 h in 8.
Rezultati so pokazali, da je encimski postopek z uporabo pulpzima učinkovita metoda za hidrolizo celuloznih verig, skrajšanje celuloznih vlaken jute in zmanjšanje njene ponovne navlaženosti. Dobljeni produkti iz encimskega postopka z uporabo pulpzima so zaradi njihove dolžine od 0 mm do 4 mm primerni za izdelavo papirja.

Ključne besede: postopek recikliranja, odpadki jute, encim pulpzim, zmanjšanje mase, zmanjšanje dolžine, skrajšanje vlaken

1 INTRODUCTION

Waste management is an important issue in various industries. Nowadays, environmental concerns, ecological and economic considerations constitute the driving force for the waste management in the textile industry. In these cases, managing wastes involves modifying the old systems, developing new processes to limit, optimize and process waste materials and finding usage for post-consumer textile wastes.[1] Managing wastes in a correct way will lead to saving the energy and cost, reducing the landfill usage and solving the present environmental and ecological problems.[2]

According to the importance of the recycling processes in developed countries, different physical, chemical or biological methods are used to recycle various wastes from different industries. Cellulosic wastes such as cotton, viscose, lyocell and jute constitute a major part of the textile industries such as the machine-made carpet production. Nowadays, different methods such as chemical and biological ones are used to recycle these wastes. Some of the chemical processes proceed slowly; therefore, catalysts (especially enzymes) are needed to enhance the rate of chemical reactions. In these cases, a small quantity of an enzyme is able to react with a large amount of a substrate in a mild condition.[3]

Hemmpel[4] used cellulase enzyme in different pH conditions to modify woven and knitted cellulose fabrics. The results showed that cellulose enzyme has a significant effect on cellulose fabrics when pH is lower than 5, by hydrolyzing the cellulose bonds.

Cellulase enzyme was used for bio-polishing of cotton, viscose and lyocell fabrics by Garret.[5] He concluded that cotton, viscose and lyocell fabrics could be modified using cellulase enzyme due to the surface-fiber removal.

The effect of an enzymatic treatment on the fine structure of cellulosic fibers and the properties of cellulose dissolved in aqueous 7.6 % NaOH and ionic liquid were analyzed by F. Dadashian[6] and P. Rosenberg et al.[7] It can be concluded from the SEM photographs that cellulase enzyme has a significant effect on modifying the fine structure of cellulosic fibers.

G. Buschle-Diller et al.[8] concluded that the cellulases from *Trichoderma viride* have a significant effect on the pore structure of different types of bead cellulose.

A literature review showed that the recycling of jute wastes using pulpzyme was not studied. In this paper, enzymatic recycling of jute wastes using pulpzyme enzyme was studied. The jute wastes from machine-made carpet-production factories were used as a model. The effects of several parameters such as enzyme concentration, pH and time on the recycling of the jute wastes were evaluated with respect to the mass- and length-loss fractions.

2 EXPERIMENTAL WORK

2.1 Materials

The jute waste and pulpzyme enzyme were obtained from the Novo Nordisk and Akij (Bangladesh) Companies, respectively. All the other chemicals were of an analytical grade and purchased from Merck (Germany).

The main constituents of the jute fiber are represented in **Table 1**.[9]

Table 1: Contents of jute fibers[9]
Tabela 1: Sestava vlaken jute[9]

Content	Fraction (%)
Ash	3.04
Benzene alcohol	2.72
Lignin	21.61
Acid soluble lignin	0.95
Alpha cellulose	42.91
Beta cellulose	20
Others	8.77

2.2 Jute recycling

Experiments were carried out in a batch-mode reactor with the total capacity of 250 ml. The recycling of jute wastes was performed using a 100 mL solution containing a specified amount of jute wastes (5 g) using pulpzyme enzyme. The solution pH was adjusted using a phosphate buffer.[8,9] The samples were withdrawn from the sample point at certain time intervals and analyzed for mass and length losses.

The mass- and length-loss fractions were checked and controlled by measuring the mass and length of the jute fiber before and after the enzymatic process.

In this study an light projection microscope (400 X) and a Philips scanning electron microscope (690 X) were used to measure the fiber length and evaluate the surface morphology of the enzyme-treated and untreated jute wastes, respectively.

The effects of the enzyme concentration (0.5–2 %) on the mass- and length-loss fractions of the samples were investigated by treating 5 g of jute wastes at the pH of 8 at 55 °C for 2 h.

The effects of the pH (3–9) on the mass- and length-loss fractions of the samples were investigated by treating 5 g of jute wastes with a 1.5 % enzyme concentration at 55 °C for 2 h.

The effect of the time of treatment (0–3 h) on the mass- and length-loss fractions of the samples were investigated by treating 5 g of jute wastes with a 0.5 % enzyme concentration at the pH of 8 at 55 °C.

The mass-loss fractions of the samples were measured by weighting jute wastes before and after the enzymatic treatments.

The mass-loss fraction was defined as follows:

$$\text{Mass-loss fraction /\%} = (A_2 - A_1)/A_1 \times 100 \qquad (1)$$

where A_1 and A_2 stand for the dry mass and conditioned mass of the samples before and after the enzymatic treatment, respectively.

The moisture regain of the samples was measured with the gravimetric method. The moisture regain was defined as follows:

$$\text{Moisture regain /\%} = (W_2 - W_1)/W_1 \times 100 \qquad (2)$$

where W_1 and W_2 stand for the dry mass and conditioned mass of the samples, respectively. The FTIR spectra were obtained using a Nicolet Magna IR spectrophotometer equipped with a microscope.

3 RESULTS AND DISCUSSION

3.1 Enzyme concentration

The mass-loss and length-reduction fractions of jute samples for different enzyme concentrations are shown in **Figure 1**. According to the data from **Figure 1**, with the increasing enzyme concentration, the mas-loss and length-reduction fractions increased gradually because of the existing excess enzyme molecules relative to the fixed amount of jute. With the 1.5 % enzyme concentration, the optimum mass-loss (almost 46 %) and length-reduction (almost 73.45 %) fractions were obtained; therefore, the optimum enzyme concentration for the recycling of jute was 1.5 %.

3.2 pH

The mass-loss and length-reduction fractions of jute samples at different pH values are shown in **Figure 2**.The results show that the pH significantly influenced the pulpzyme action during jute recycling. The mass-loss and length-reduction fractions were found to improve with an increase in the aqueous-phase pH up to the value of 8 and, thereafter, an increase in the aqueous-phase pH from 8.0 to 9.0 caused the efficacy of the enzymatic recycling process to decrease. The aqueous-phase pH of 8.0 had a significant effect on the rate of the mass-loss and length-reduction fractions compared to the other pH

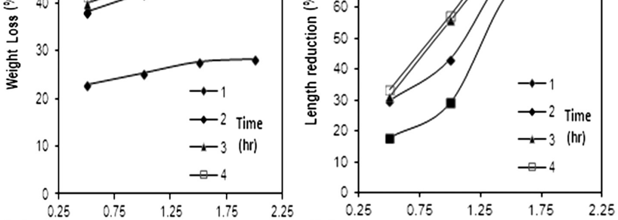

Figure 1: Effect of enzyme concentration on: a) mass-loss fraction, b) length-reduction fraction of the samples

Slika 1: Vpliv koncentracije encima na: a) delež zmanjšanja mase, b) delež zmanjšanja dolžine vzorcev

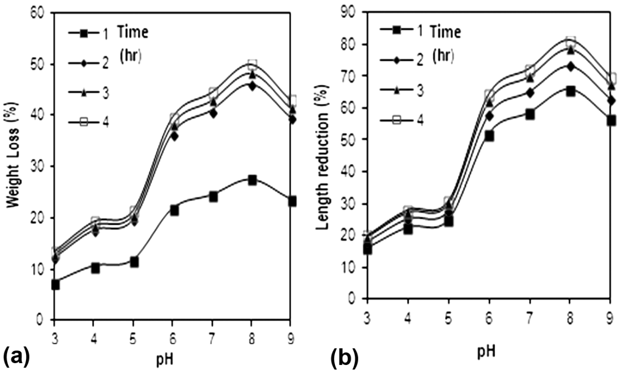

Figure 2: Effect of pH on: a) mass-loss fraction, b) length-reduction fraction of the samples

Slika 2: Vpliv pH na: a) delež zmanjšanja mase, b) delež zmanjšanja dolžine vzorcev

conditions. Thus, the aqueous-phase pH plays a significant role in enzymatic reactions. Moreover, the pH-activity relationship of any given enzyme depends on the acid-base behavior of the enzyme and the substrate (the jute waste) as well as on many other factors that are usually difficult to analyze quantitatively.[10]

3.3 Time of treatment

The mass-loss and length-reduction fractions of the jute samples at different times are given in **Table 2**. The results show that the time of treatment significantly influenced the pulpzyme action during jute recycling. The mass-loss and length-reduction fractionswere found to improve with an increase in the time up to 2 h and, thereafter, an increase in the time of the enzymatic treatment from 2 h to 4 h was without any significant changes.

After the 2 h enzyme reaction, the optimum mass-loss (almost 46 %) and length-reduction fractions (almost 73.45 %) of a jute sample were obtained; therefore, the optimum time for the enzymatic treatment was 2 h.[10]

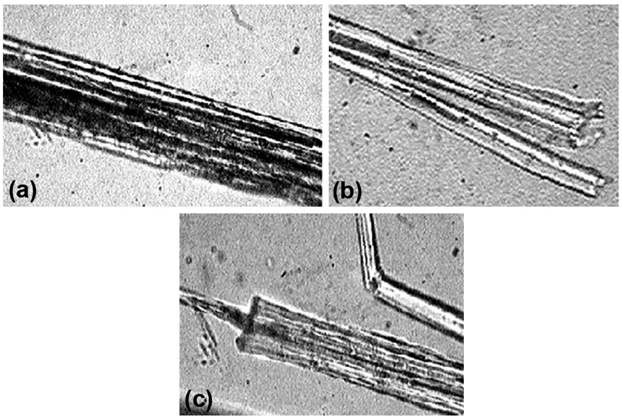

Figure 3: Light micrographs of: a) untreated jute-fibre wastes, b) jute-fibre wastes treated with enzyme in optimum concentration

Slika 3: Svetlobni posnetki a) neobdelanega vlakna odpadne jute, b) vlakna odpadne jute, obdelanega z encimom pri optimalni koncentraciji encima

Table 2: Effect of the time of treatment on mass-loss fraction and length-reduction fractions of the samples for the optimum enzyme concentration and pH

Tabela 2: Vpliv časa obdelave na delež zmanjšanja mase in delež zmanjšanja dolžine vzorcev pri optimalni koncentraciji encima in pH

Time (h)	1	2	3	4
Mass loss (%)	27.6	46	48.3	50
Length reduction (%)	65.76	73.45	78.5	81.3

3.4 Effect of the enzymatic process on the moisture regain (%)

The moisture regains of the samples before and after the enzymatic treatment were measured according to equation (2). According to the data from **Table 3**, the enzyme-treated jute has a lower (22.37 %) moisture regain than the untreated jute in the optimum condition. The results show that the enzymatic treatment of jute has a specific effect on increasing the crystallinity.[6,11]

Table 3: Moisture regain of jute-fiber wastes after and before the enzymatic treatment in the optimum conditions

Tabela 3: Ponovno navlaženje vlaken odpadne jute pred obdelavo z encimi in po njej v optimalnih razmerah

Sample	Conditioned mass (g)	Dry mass (g)	Moisture regain (%)
Raw jute	0.63	0.54	14.3
Enzyme-treated jute	0.63	0.57	11.1

3.5 Microscopic structure

The effect of pulpzyme enzyme on the macrostructures of the samples was studied using SEM and light

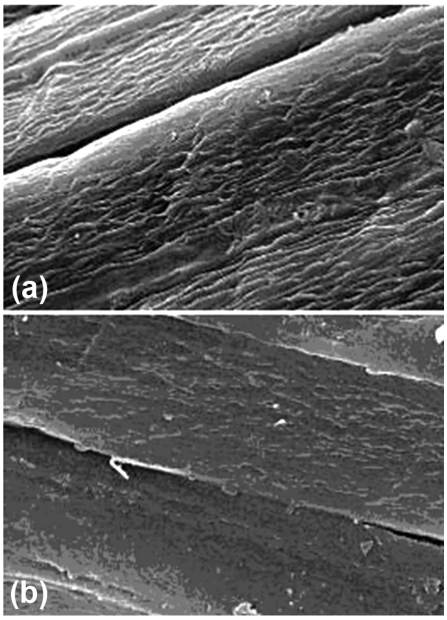

Figure 4: SEM photographs of: a) fiber wastes enzyme treated with the optimum enzyme concentration and b) untreated jute-fiber wastes

Slika 4: SEM-posnetka površine vlakna odpadne jute: a) obdelanega z encimom pri optimalni koncentraciji encima in b) neobdelanega vlakna odpadne jute microscopic photographs. The light microscopic and scanning electron microscopic (SEM) photographs of the samples before and after the enzymatic processes are shown in **Figures 3** and **4**. The results show that pulpzyme enzyme has a significant effect on the destruction of the molecular structure of jute in the longitudinal direction due to the hydrolyzing reaction. This phenomenon has a significant effect on the shortening of the jute samples.

4 CONCLUSION

In this study, enzymatic treatments were used to modify jute wastes. The effect of several parameters such as enzyme concentration, pH and time on the recycling of jute wastes was evaluated.

The results showed that the enzymatic treatment has a significant effect on the mass loss and shortening of the jute samples by hydrolyzing cellulosic chains.

Moreover, the enzymatic treatment leads to a decrease in the moisture regain of the samples due to the increasing crystallinity. It can be concluded from the SEM and light microscopic photographs that pulpzyme enzyme has a significant effect on the destruction of the molecular structure of jute in the longitudinal direction due to the hydrolyzing reaction. Finally, it leads to the shortening of the jute samples.

According to the obtained data, the optimum enzyme concentration, reaction time and pH for recycling jute wastes were 1.5 %, 2 h and 8, respectively. The obtained samples are suitable for a usage in the paper-making industries due to their longitudinal distribution.

5 REFERENCES

[1] M. J. Cornell, Getting to zero Wastes, [cited fall 2007], Available from World Wide Web: http://www.toenall.org

[2] L. Wang, Y. Z. Zhang, H. Yang, Carbohydrate Research, 339 (**2004**), 819–824

[3] Enzyme kinetics, Thomas Jefferson University, Maintained by AISR Education Services (EdServices@jeffline.tju.edu)

[4] W. H. Hemmpel, International Textile Bulletin Dyeing/ Printing/Finishing, 37 (**1992**) 3, 1–5

[5] A. S. Garret, D. M. Cedroni, In AATCC Book of Paper, AATCC International Conference & Exhibition, Atlanta, 1992

[6] F. Dadashian, Changes in the Fine Structure of Lyocell Fibers during Enzymatic Degradation, Proceedings of the World Textile Conference, 2nd Autex Conference, Bruges, Belgium, 2002, 464–473

[7] P. Rosenberg, T. Budtova, M. Rom, P. Fardim, Effect of Enzymatic Treatment on Solubility of Cellulose in 7.6 % NaOH-Water and Ionic Liquid, ACS Symposium Series, Chapter 12, 2010, 213–226

[8] G. Buschle-Diller, C. Fanter, F. Loth, Cellulose, 2 (**1996**) 3, 179–203

[9] T. C. Ranjan, Handbook of Jute, vol. 3, Oxford and IBH, New Delhi 1973

[10] K. P. Katuri, S. V. Mohen, S. Sridhar, B. R. Pati, P. N. Sarma, Water Resource, 43 (**2009**), 3647–365

[11] K. M. Shojaei, F. Dadashian, M. Montazer, Applied Biochemistry and Biotechnology, 166 (**2011**) 3, 744–52

UDK 621.791:669.14.018.8
Professional article/Strokovni članek

ISSN 1580-2949
MTAEC9, 48(5)761(2014)

INFLUENCES OF THE HEAT INPUT ON A 2205 DUPLEX STAINLESS STEEL WELD

VPLIV VNOSA TOPLOTE V ZVAR DUPLEKSNEGA NERJAVNEGA JEKLA 2205

Bansal Rajkumar Gnanasundaram[1], **Murugan Natarajan**[2]
[1]United Institute of Technology, Coimbatore, Tamilnadu, India
[2]Coimbatore Institute of Technology, Coimbatore, Tamilnadu, India
bansalgnanasundaram@gmail.com

Prejem rokopisa – received: 2013-02-05; sprejem za objavo – accepted for publication: 2013-11-19

In arc welding, the energy is transferred from the electrode to the base metal via an electric arc. The energy transferred per unit length is measured as the heat input. The heat input is an important factor that influences the cooling rate and affects the metallurgical and mechanical properties of welds. In this study, the flux-cored arc-welding process was used to join duplex stainless steel. The experiment was conducted on the basis of a three-factor, five-level central composite rotatable design using the full-replication technique. A mathematical model was developed for the heat input. The effects of the welding-process parameters on the heat input are discussed. Metallographic techniques were employed to study the microstructure produced at low, medium, high and optimum heat-input conditions.

Key words: heat input, FCAW, duplex stainless steel, microstructure

Pri obločnem varjenju se energija prenaša iz elektrode na osnovno kovino z električnim oblokom. Energija, prenesena na enoto dolžine, se meri kot vnos toplote. Vnos toplote je pomemben faktor, ki vpliva na hitrost ohlajanja, na metalurške in mehanske lastnosti zvara. V tej študiji je bilo za spajanje dupleksnega nerjavnega jekla uporabljeno varjenje pod praškom. Eksperiment je bil izvršen na osnovi treh faktorjev in petnivojske centralno vrtljive izvedbe s polno možnostjo ponovitve. Za vnos toplote je bil razvit matematični model. Obravnavan je bil vpliv parametrov varilnega procesa na vnos toplote. Za študij mikrostrukture, nastale pri nizkem, srednjem, velikem in optimalnem vnosu toplote, so bili uporabljeni metalografski postopki.

Ključne besede: vnos toplote, FCAW, dupleksno nerjavno jeklo, mikrostruktura

1 INTRODUCTION

The flux-cored arc welding (FCAW) is widely used by industries because it produces welds with better and more consistent mechanical properties and fewer weld defects, it is a high-deposition-rate process and suitable for stainless steel. Generally, FCAW produces a stronger weldment than SMAW at room temperature.[1] Duplex stainless steel (DSS) is widely used in industrial applications due to its excellent corrosion resistance and its strength that is higher compared to types 316 and 317 of austenite stainless steel.[2] It is a combination of 50 % austenitic and 50 % ferritic steels. In the present study, 2205 DSS was used as the base metal for the experiment and a diameter 1.2 mm (E2209T1-4/1) filler wire was used for depositing the metal. For the shielding purpose, a combination of 75 % argon plus 25 % CO_2 was used as the welding gas for horizontal-position welding. 2205 DSS was procured from Outokumpu Stainless AB, Sweden.

2 EXPERIMENTAL SETUP

The FCAW setup available at the Welding Research Centre of Coimbatore Institute of Technology (CIT), Coimbatore, India was used to conduct the experiments. The welding setup consists of a power source, namely, INDARC 400 MMR, a unit feeding the filler wire with the shielding-gas-flow control, a welding gun and a welding manipulator that helps to deposit the filler metal on the desired area as shown in **Figure 1**.

The selection of significant FCAW process parameters helps us to get the desired weld-bead quality.[3] In accordance with the available literature, the welding current (*I*), the welding speed (*S*) and the open-circuit voltage (*OCV*) were taken as the significant process parameters. The trial runs were conducted by varying

Figure 1: FCAW experimental setup
Slika 1: Eksperimentalni sestav FCAW

one process parameter while keeping the other two parameters constant. The working range was selected, by visual inspection, on the basis of the appearance of the weld bead with respect to how smooth and continuous it was, and with respect to the absence of defects like porosity, undercut, etc. The welding parameters and their levels are given in **Table 1**. The experiment was conducted as per the design matrix and 20 runs were made by varying the process variables as shown in **Table 2**.

Table 1: Welding parameters and their factor levels
Tabela 1: Parametri varjenja in faktorji njihovih nivojev

S. No.	Parameter/unit	Factor level				
		–1.682	–1	0	1	1.682
1	Welding current (A)	170	182	200	218	230
2	Welding speed (cm/min)	25	27	31	35	37
3	Open-circuit voltage (V)	28	30	32	34	36

Table 2: Design matrix and the observed heat-input values
Tabela 2: Postavitev matrice in opažene vrednosti vnosa toplote

Sp. No.	I/A	S/(cm/min)	OCV/V	U/V	H_I/(kJ/cm)
1	–1	–1	–1	28.7	9.87
2	1	–1	–1	24.35	10.03
3	–1	1	–1	27.75	7.36
4	1	1	–1	27.7	8.80
5	–1	–1	1	31.55	10.85
6	1	–1	1	31.35	12.91
7	–1	1	1	30.9	8.19
8	1	1	1	29.35	9.32
9	–1.682	0	0	31.25	8.74
10	1.682	0	0	31.8	12.03
11	0	–1.682	0	32	13.06
12	0	1.682	0	32.55	8.97
13	0	0	–1.682	24.7	8.13
14	0	0	1.682	34.5	11.35
15	0	0	0	32.85	10.81
16	0	0	0	32.25	10.61
17	0	0	0	31.75	10.45
18	0	0	0	29.4	9.67
19	0	0	0	30.6	10.07
20	0	0	0	27.45	9.03

3 DEVELOPMENT OF A REGRESSION MODEL FOR THE HEAT INPUT

The heat input could not be measured directly; however, with the help of the welding current, the arc voltage and the welding speed it could be calculated. The arc voltage was measured with the voltmeter of the welding transformer, the welding current was determined on the basis of the wire feed rate and the welding speed on the basis of the movement of the table. The heat input was calculated as the ratio of the power to the velocity of the heat source:

$$H_I = 60\ UI\eta\ /1000\ S \tag{1}$$

where H_I = heat input (kJ/cm), U = arc voltage (V), I = current (A), S = travel speed (cm/min) and η = arc efficiency accounting for the heat dissipation to the surrounding as a result of the convection and radiation (0.85). The observed heat-input values are shown in **Table 2**.

The response function representing the parameters is expressed with the following equation:

$$Y = f\,(X_1, X_2, X_3) \tag{2}$$

where Y = heat input, X_1 = current (I), X_2 = speed (S) and X_3 = open circuit voltage (V).

The second-order polynomial equation represents the response for K factors given in equation:[4]

$$Y = b_0 + \sum_{I=1}^{K} b_i X_i + \sum_{ij=1}^{K} b_{ij} X_i X_j + \sum_{\substack{I=1\\ i\neq j}}^{K} b_{ii} X_i^2 \tag{3}$$

For the three factors, the above polynomial equation can be expressed as:

$$Y = b_0 + b_1 I + b_2 S + b_3 V + b_{12} IS + b_{13} IV + b_{23} SV + \\ + b_{11} I^2 + b_{22} S^2 + b_{33} V^2 \tag{4}$$

where b_0 = free term, coefficients b_1, b_2, b_3 = linear terms, coefficients b_{12}, b_{13}, b_{23} = interaction terms and coefficients b_{11}, b_{22}, b_{33} = quadratic terms. The developed regression model in the coded form is given below; adequacy was checked with the ANOVA method.

Heat input:

$$H_I = 10.213 + 0.756I - 1.235S + 0.778V - \\ - 0.294V^2 - 0.314SV \tag{5}$$

4 RESULTS

Figure 2 depicts the effects of the process parameters on the heat input. The welding speed shows a significant effect on the heat input. The heat input increases up to 12.67 kJ/cm with the lower welding speed of 25 cm/min and it gradually falls down to 8.52 kJ/cm at the higher

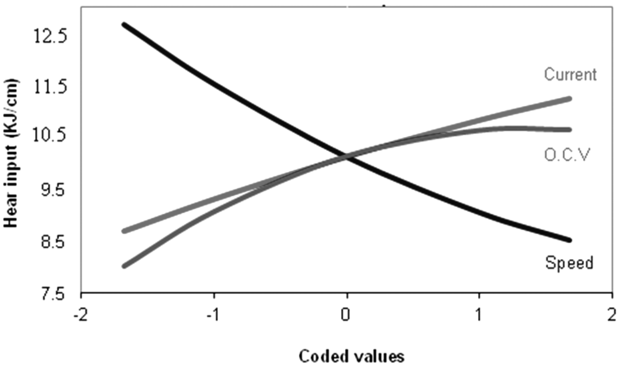

Figure 2: Effects of process parameters on the heat input
Slika 2: Vpliv parametrov procesa na vnos toplote

Figure 3: Microstructure of the weld metal zone at different conditions: a) low heat input (H_I = 7.36 kJ/cm), b) medium heat input (H_I = 10.45 kJ/cm), c) high heat input (H_I = 13.06 kJ/cm); magnification: 400-times

Slika 3: Mikrostruktura zvara v različnih razmerah: a) nizek vnos toplote (H_I = 7,36 kJ/cm), b) srednji vnos toplote (H_I = 10,45 kJ/cm), c) visok vnos toplote (H_I = 13,06 kJ/cm); povečava 400-kratna

welding speed of 37 cm/min. At the lower welding speed, the heat input per unit length of the weld is higher resulting in large heat-affected zones and causing a severe distortion. The heat input increases from 8.01 kJ/cm to 11.24 kJ/cm with the increasing welding current and open-circuit voltage. Obviously, the higher voltage and the higher current increase the discharge and elevate the heat input.

In **Figure 3a**, the ferrite phase is shown in white color. The presence of a columnar dendrite structure represents a faster cooling rate due to the low heat-input condition.[5] It is evident from **Figure 3b** that a vermicular structure is observed in the weld metal at the magnification of 400-times. The delta ferrite is pale yellow, the austenitic regions are greenish blue, and the final-solidification regions are bluish. In **Figure 3c**, the microstructure reveals the presence of ferrite (white) and austenite (dark). The coarse austenite grains found in the microstructure may be due to the higher heat input during the welding.

5 CONCLUSION

At the higher welding speed, the heat input per unit length of the weld decreases.

A higher heat input reduces the weld quality and increases the distortion.

The microstructure study reveals the morphology of 2205 DSS welds at various heat-input conditions.

6 REFERENCES

[1] Z. Zhang, A. W. Marshall, G. B. Holloway, Flux cored arc welding: the high productivity welding process for P91 steels, Proceedings of the 3rd conference on advances in materials technology for fossil power plants, The Institute of Materials, University of Wales Swansea, London, 2001, 267–282

[2] I. Alvarez-Armas, Duplex Stainless Steels: Brief History and Some Recent Alloys, Recent Patents on Mechanical Engineering, 1 (**2008**), 51–57

[3] K. Y. Benyounis, A. G. Olabi, Optimization of different welding processes using statistical and numerical approaches – A reference guide, Adva. Engg. Software, 39 (**2008**), 483–496

[4] K. M. Carley, Response surface methodology, CASOS Technical Report, Carnegie Mellon University, 2004

[5] J. Elmer, S. M. Allen, T. W. Eagar, Microstructural development during solidification of stainless steel alloys, Metallurgical Transactions A, 20A (**1989**), 2117–2131

UDK 539.92:669.14:621.793/.795
Professional article/Strokovni članek

ISSN 1580-2949
MTAEC9, 48(5)765(2014)

TRIBOLOGICAL BEHAVIOR AND CHARACTERIZATION OF BORIDED COLD-WORK TOOL STEEL

TRIBOLOŠKO VEDENJE IN KARAKTERIZACIJA BORIRANEGA ORODNEGA JEKLA ZA DELO V HLADNEM

Ibrahim Gunes

Department of Metallurgical and Materials Engineering, Faculty of Technology, Afyon Kocatepe University, 03200 Afyonkarahisar, Turkey
igunes@aku.edu.tr

Prejem rokopisa – received: 2013-08-20; sprejem za objavo – accepted for publication: 2013-11-19

In the present study, tribological and characterization properties of the borides formed on cold-work tool steel were investigated. Boriding was performed in a solid medium consisting of Ekabor-II powders at 850 °C and 950 °C for 2 h and 6 h. The boride layer was characterized with light microscopy, X-ray diffraction technique and a micro-Vickers hardness tester. An X-ray diffraction analysis of the boride layers on the surface of the steel revealed the existence of FeB, Fe_2B, CrB, Cr_2B and MoB compounds. Depending on the chemical compositions of the substrates and the boriding time, the boride-layer thickness on the surface of the steel ranged from 13.14 µm to 120.82 µm. The hardness of the boride compounds formed on the surface of the steel ranged from 1806 $HV_{0.05}$ to 2342 $HV_{0.05}$, whereas the Vickers-hardness value of the untreated steel was 428 $HV_{0.05}$. The wear tests were carried out in a ball-disc arrangement under a dry friction condition at room temperature with an applied load of 10 N and with a sliding speed of 0.25 m/s at a sliding distance of 1000 m. The wear surfaces of the steel were analyzed using SEM microscopy and X-ray energy-dispersive spectroscopy (EDS). It was observed that the wear rate of the unborided and borided cold-work tool steels ranged from 11.28 $mm^3/(N\ m)$ to 116.54 $mm^3/(N\ m)$.

Keywords: cold-work tool steel, boriding, microhardness, wear rate, friction coefficient

V tej študiji so bile preiskovane tribološke in druge značilne lastnosti boridov, nastalih na orodnem jeklu za delo v hladnem. Boriranje je bilo izvršeno v trdnem mediju, ki ga je sestavljal prah Ekabor-II pri 850 °C in 950 °C v 2 h in 6 h. Boriran sloj je bil preiskan s svetlobno mikroskopijo, rentgensko difrakcijo in izmerjena je bila Vickersova mikrotrdota. Rentgenska difrakcija boriranega sloja na površini jekla je potrdila prisotnost spojin FeB, Fe_2B, CrB, Cr_2B in MoB. Odvisno od kemijske sestave podlage in časa boriranja je bila debelina boriranega sloja na površini jekla med 13,14 µm in 120,82 µm. Trdota boridov, nastalih na površini jekla, je bila v razponu od 1806 $HV_{0,05}$ do 2342 $HV_{0,05}$, medtem ko je bila Vickersova trdota neobdelanega jekla 428 $HV_{0,05}$. Preizkusi obrabe so bili izvršeni na napravi krogla-disk pri suhem trenju pri sobni temperaturi z uporabljeno obtežbo 10 N, hitrostjo drsenja 0,25 m/s in pri razdalji drsenja 1000 m. Površina z obrabo je bila analizirana s SEM-mikroskopijo in energijsko disperzijsko spektroskopijo rentgenskih žarkov (EDS). Ugotovljeno je bilo, da je hitrost obrabe neboriranega in boriranega orodnega jekla za delo v hladnem v razponu od 11,28 $mm^3/(N\ m)$ do 116,54 $mm^3/(N\ m)$.

Ključne besede: orodno jeklo za delo v hladnem, boriranje, mikrotrdota, hitrost obrabe, koeficient trenja

1 INTRODUCTION

Industrial boriding processes can be applied to a wide range of steel alloys including carbon steel, low and high-alloy steel, tool steel and stainless steel. Cold-work tool steels have a wide range of applications. Therefore, there has been an extensive research on the development of surface-treatment processes to improve the wear resistance, corrosion and oxidation resistance of the cold-work tool steels for high-temperature and high-pressure applications in recent years.[1–7] Boriding is a thermochemical surface treatment, in which boron atoms diffuse into the surface of a workpiece to form borides with the base material.[8,9] The main advantages of this technique are a high resistance to abrasion wear and a high oxidation resistance when compared with the other conventional surface treatments. The thermal diffusion treatments of boron compounds used to form iron borides typically require the process temperatures of 700 °C and 1000 °C. The process can be carried out in a solid, liquid, gaseous or plasma medium.[10–14]

In recent years, the boriding treatment has been used for a wide range of applications in industries such as the manufacture of machine parts for plastics, food processing, packaging and tooling, as well as pumps and hydraulic machine parts, crankshafts, rolls and heavy gears, motor and car constructions, cold- and hot-working dies and cutting tools. The wear behavior of borided steels has been evaluated by a number of investigators.[15–20] However, there is no information about the friction and wear behavior of the borided cold-work tool steel. The main objective of this study was to investigate the friction and wear behavior of the borided cold-work tool steel. Structural and tribological properties were investigated using light microscopy, XRD, SEM, EDS, microhardness tests and a ball-on-disc tribotester.

2 EXPERIMENTAL METHOD

2.1 Boriding and characterization

The high-alloy cold-work tool steel essentially contained mass fractions 0.90 % C, 0.50 % Mn, 7.80 % Cr, 2.50 % Mo and 0.50 % V. The test specimens were cut into the cylinders with the dimensions of ø 25 mm × 10 mm, ground up to 1200 G and polished using a diamond solution. The boriding heat treatment was carried out in a solid medium containing an Ekabor-II powder mixture placed in an electrical-resistance furnace operated at the temperatures of 850 °C and 950 °C for 2 h and 6 h under atmospheric pressure. Following the completion of the boriding process, the test specimens were removed from the sealed stainless-steel container and allowed to cool down in still air. The microstructures of the polished and etched cross-sections of the specimens were observed with a Nikon MA100 light microscope. The presence of the borides formed in the coating layer was confirmed by means of X-ray diffraction equipment (Shimadzu XRD 6000) using Cu K_α radiation. The hardness measurements of the boride layer for each steel type and the unborided steel substrate were made on the cross-sections using a Shimadzu HMV-2 Vickers indenter with a load 50 g.

2.2 Friction and wear

To perform the friction and wear tests of the borided samples, a ball-on-disc test device was used. In the wear tests, WC-Co balls of 8 mm in diameter supplied by H. C. Starck Ceramics GmbH were used. The errors caused by a distortion of the surface were eliminated using a separate abrasion element (WC-Co ball) for each test. The wear experiments were carried out in a ball-disc arrangement under a dry friction condition at room temperature with an applied load of 10 N and with the sliding speed of 0.25 m/s at a sliding distance of 1000 m. Before and after each wear test, each sample and the abrasion element were cleaned with alcohol. After the tests, the wear volumes of the samples were quantified by multiplying the cross-sectional areas of the wear by the width of the wear track obtained from a Taylor-Hobson Rugosimeter Surtronic 25 device. The wear rate was calculated with the following formula:

$$W_k \,/(\mathrm{mm}^3/(\mathrm{N\ m})) = W_v / M \cdot S \qquad (1)$$

where W_k is the wear rate, W_v is the wear volume, M is the applied load and S is the sliding distance. The friction coefficients depending on the sliding distance were obtained through a friction-coefficient program. The surface profiles of the wear tracks on the samples and the surface roughness were measured with the Taylor-Hobson Rugosimeter Surtronic 25. The worn surfaces were investigated with scanning electron microscopy (SEM) and energy-dispersive X-ray spectroscopy (EDS).

3 RESULTS AND DISCUSSION

3.1 Characterization of boride coatings

Light micrographs of the cross-sections of the cold-work tool steel borided at the temperatures of 850 °C and 950 °C for 2 h and 6 h are shown in **Figure 1**. As can be seen, the borides formed on the cold-work tool-steel substrate have a smooth morphology due to the high-alloy content. It was found that the coating/matrix interface and the matrix could be significantly distinguished and that the boride layer had a columnar structure. Depending on the chemical compositions of the substrates and the boriding time, the boride-layer thickness on the surface of the steel ranged from 13.14 μm to 120.82 μm.

In this study, the presence of borides was identified using an XRD analysis (**Figure 2**). The XRD patterns show that the boride layer consists of the borides such as AB and A_2B (A = metal: Fe, Cr). The XRD results showed that the boride layers formed on the steel contained the FeB, Fe_2B, CrB, Cr_2B and MoB compounds (**Figure 2**). The microhardness measurements were carried out along a line between the surface and the interior in order to see the variations in the boride-layer hardness, the transition zone and the matrix, respectively. The microhardness of the boride layers was measured at 10 different locations at the same distance from the surface, and the average value was taken as the hardness result. The microhardness measurements were carried out on the cross-sections, along a line between the surface and the interior (**Figure 3**). The hardness of the boride compounds formed on the surface of the steel ranged from 1806 $HV_{0.05}$ to 2342 $HV_{0.05}$, whereas the Vickers-hardness value of the untreated steel was 428 $HV_{0.05}$. When the hardness of the boride layer is compared with the matrix, the boride-layer hardness is approximately four times greater than that of the matrix.

3.2 Friction and wear behavior

Table 1 shows the surface-roughness values of the borided and unborided cold-work tool steels. The surface-roughness values of the unborided and borided cold-work tool steels varied from 0.12 to 0.54, as can be seen in **Table 1.** It was observed for the cold-work tool

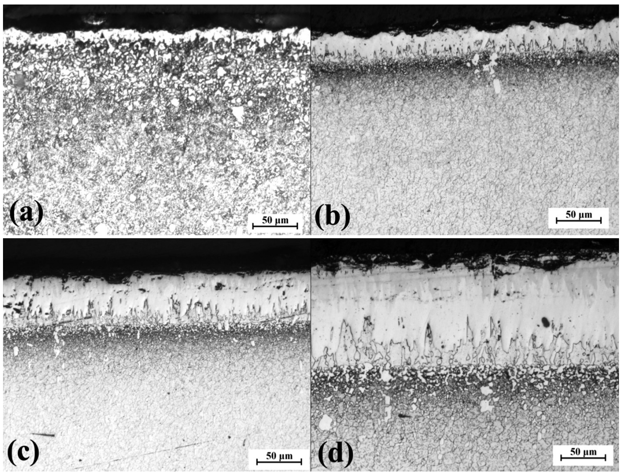

Figure 1: Cross-sections of borided cold-work tool steel: a) 850 °C, 2 h, b) 850 °C, 6 h, c) 950 °C, 2 h, d) 950 °C, 6 h

Slika 1: Prerez boriranega orodnega jekla za delo v hladnem: a) 850 °C, 2 h, b) 850 °C, 6 h, c) 950 °C, 2 h, d) 950 °C, 6 h

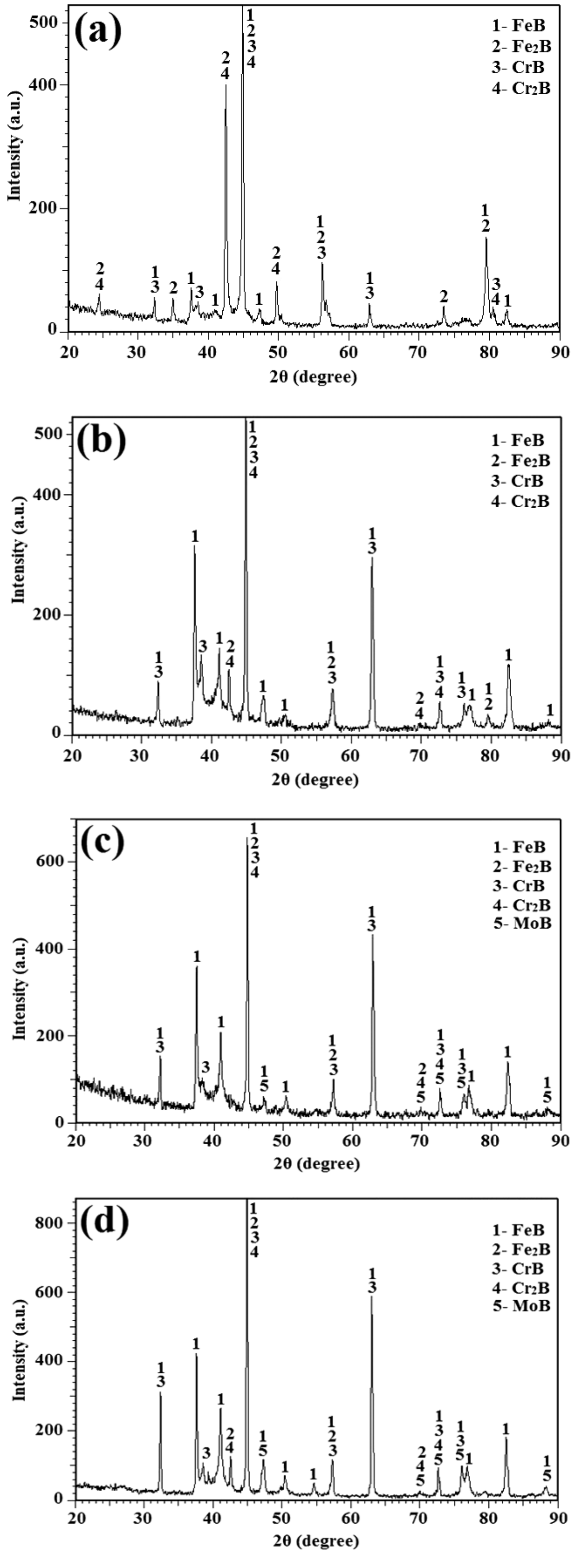

Figure 2: X-ray diffraction patterns of borided cold-work tool steel: a) 850 °C, 2 h, b) 850 °C, 6 h, c) 950 °C, 2 h, d) 950 °C, 6 h
Slika 2: Rentgenska difrakcija boriranega orodnega jekla za delo v hladnem: a) 850 °C, 2 h, b) 850 °C, 6 h, c) 950 °C, 2 h, d) 950 °C, 6 h

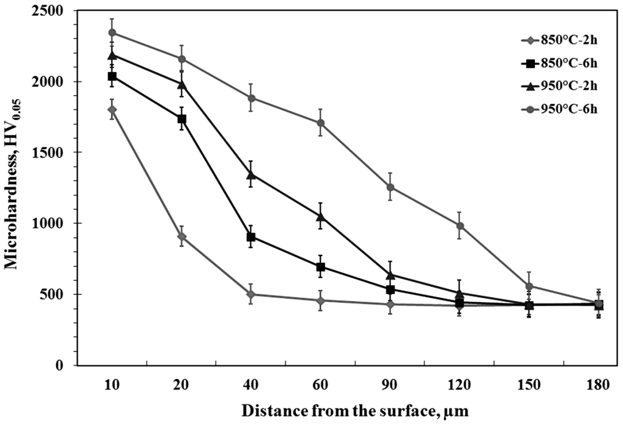

Figure 3: Variation of the hardness depth for borided steel
Slika 3: Spreminjanje trdote po globini boriranega jekla

Table 1: Surface roughness values for unborided and borided steels
Tabela 1: Vrednosti za hrapavost površine neboriranega in boriranega jekla

Unborided	Borided			
	850 °C,2 h	850 °C,6 h	950 °C,2 h	950 °C,6 h
0.12	0.32	0.37	0.43	0.54

Table 2: Friction coefficients for unborided and borided steels
Tabela 2: Koeficient trenja za neborirano in borirano jeklo

Unborided	Borided			
	850 °C,2 h	850 °C,6 h	950 °C,2 h	950 °C, 6 h
0.65	0.38	0.41	0.48	0.56

steel that the surface-roughness values increased with the boriding treatment and time. Gunes[18] studied plasma-paste-borided AISI 8620 steel and reported that the surface-roughness values increased with an increase in the boriding temperature. On the other hand, the friction coefficients of the unborided and borided cold-work tool steels varied from 0.38 to 0.65, as can be seen in **Table 2.** With the boriding treatment, a slight reduction was observed in the friction coefficients of the borided steels.

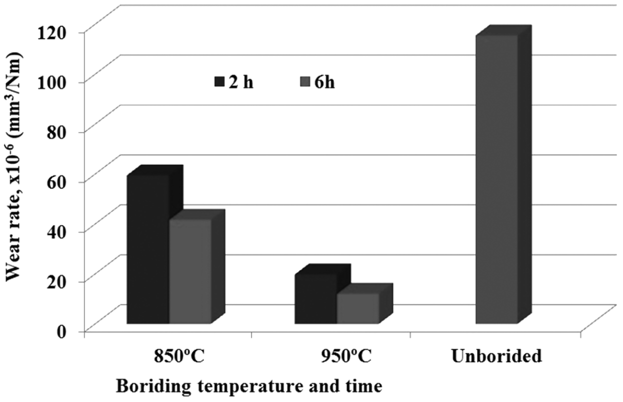

Figure 4: Wear rate of unborided and borided cold-work tool steels
Slika 4: Obraba neboriranega in boriranega orodnega jekla za delo v hladnem

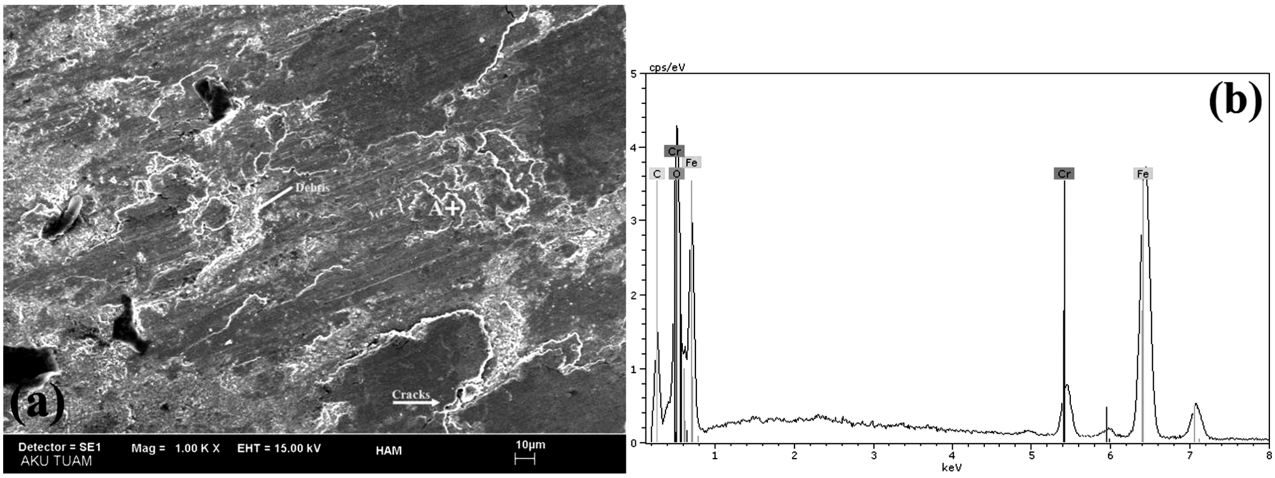

Figure 5: a) SEM micrograph and b) EDS analysis of the wear surfaces of unborided steel

Slika 5: a) SEM-posnetek in b) EDS-analiza obrabljenih površin na neboriranem jeklu

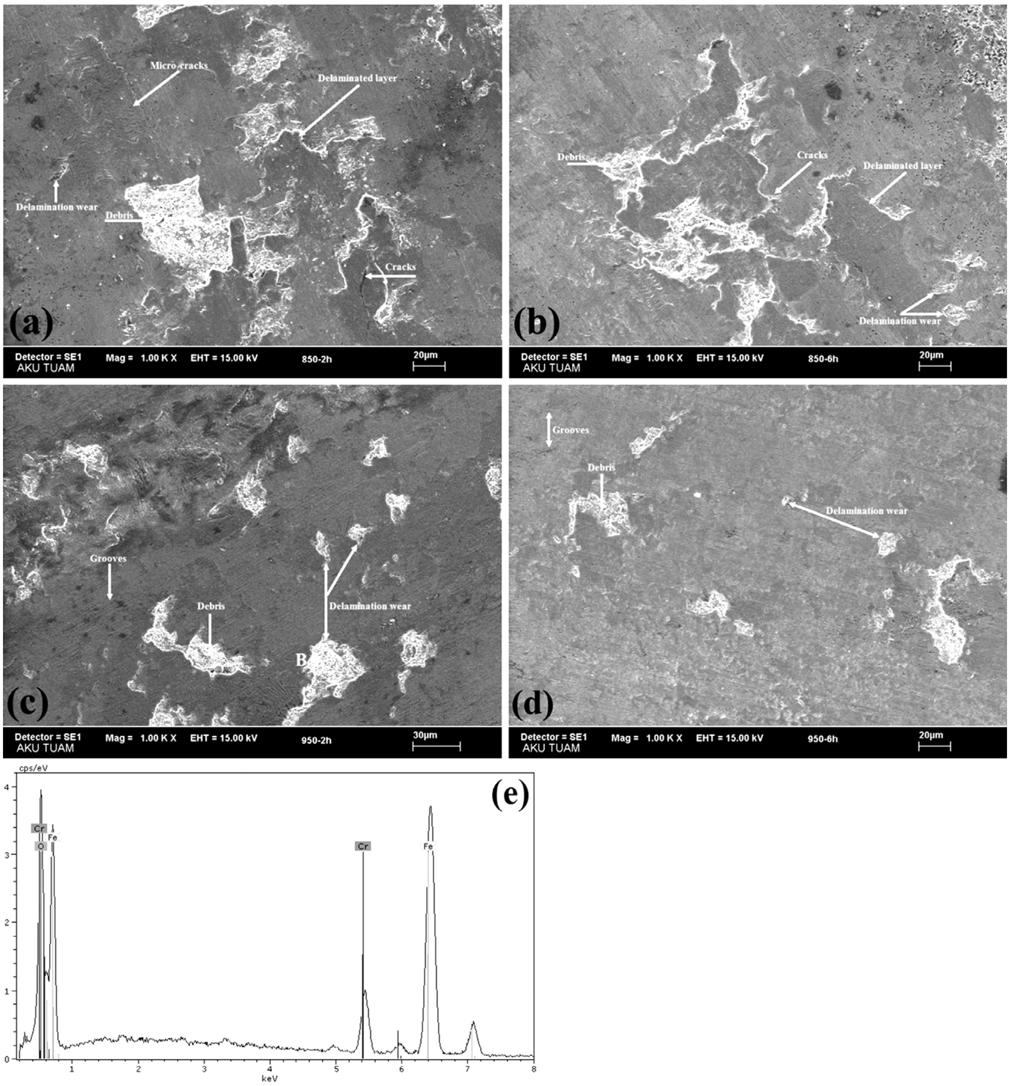

Figure 6: SEM micrographs and EDS analysis of the wear surfaces of borided steel: a) 850 °C, 2 h, b) 850 °C, 6 h, c) 950 °C, 2 h, d) 950 °C, 6 h, e) EDS

Slika 6: SEM-posnetki in EDS-analiza obrabljene površine na boriranem jeklu: a) 850 °C, 2 h, b) 850 °C, 6 h, c) 950 °C, 2 h, d) 950 °C, 6 h, e) EDS

Figure 4 shows the wear rate of the unborided and borided cold-work tool steels. The reductions in the wear rates of the borided steels were observed with respect to the unborided steels. Due to the toughness of the FeB, Fe_2B, CrB, Cr_2B and MoB phases, these steels showed a larger resistance to wear. The lowest wear rate was obtained for the steel borided at 950 °C for 6 h, while the highest wear rate was obtained for the unborided steel. The wear test results indicated that the wear resistance of borided steels increased considerably with the boriding treatment. It is well known that the hardness of the boride layer plays an important role in the improvement of the wear resistance. As shown in **Figures 3** and **4**, the relationship between the surface microhardness and the wear resistance of borided samples also confirms that the wear resistance was improved with an increased hardness. This is in agreement with the reports of the previous studies.[20–23] When the wear rate of the borided steel is compared with the unborided steel, the wear rate of the borided steel (950 °C, 6 h) is approximately nine times lower than that of the unborided steel.

SEM micrographs of the worn surfaces of the unborided and borided cold-work tool steels are in **Figures 5** and **6**. **Figure 5a** shows a SEM micrograph of the wear surface of the unborided steel. In the wear region of the unborided steel, deeper and wider wear scars, debris, surface grooves and cracks can be observed on its surface. **Figure 5b** shows an EDS analysis obtained from **Figure 5a** (point A). Fe-based oxide layers formed as a result of the wear test.

Figure 6 shows SEM micrographs of the wear surfaces of the borided cold-work tool steel. In **Figure 6a**, the worn surface of the borided steel is rougher, and coarser wear debris is present. There are microcracks, a delamination layer and wear, grooves, cracks and abrasive particles on the worn surfaces of the boride coatings (**Figures 6a** to **6d**). In the wear region of the borided cold-work tool steel there are cavities, probably formed as a result of the layer fatigue (**Figure 6**) and cracks formed due to the delamination wear. **Figure 6e** shows an EDS analysis obtained from **Figure 6c** (point B). The Fe-based oxide layers formed as a result of the wear test. The spallation of the oxide layers in the sliding direction and their orientation along the wear track were identified. When the SEM image of the worn surface of the unborided sample in **Figure 5a** is examined, it can be seen that the wear marks are larger and deeper.

4 CONCLUSIONS

In this study, the wear behavior and some of the mechanical properties of the borides on the surface of the borided cold-work tool steel were investigated. Some of the conclusions can be drawn as follows:

- Boride types formed on the surface of the cold-work tool steel have a smooth morphology.
- The boride-layer thickness on the surface of the cold-work tool steel was between 13.14–120.82 µm, depending on the chemical compositions of the substrates.
- The multiphase boride coatings that were thermochemically grown on the cold-work tool steel were constituted of the FeB, Fe_2B, CrB, Cr_2B and MoB phases.
- The surface hardness for the borided steel was in the range of 1806–2342 $HV_{0.05}$, while for the untreated steel substrate, it was 428 $HV_{0.05}$.
- The lowest wear rate was obtained for the steel borided at 950 °C for 6 h, while the highest wear rate was obtained for the unborided steel.
- The wear rate of the borided steel was found to be approximately nine times lower than the wear rate of the unborided steel.

5 REFERENCES

[1] A. K. Sinha, B. P. Division, Boriding (Boronising) of Steels, ASM Handbook, Vol. 4, J. Heat Treating, ASM International, 1991, 437–447

[2] C. Bindal, A. H. Ucisik, Surface and Coatings Technology, 122 (**1999**), 208

[3] A. G. von Matuschka, Boronizing, Heyden and Son Inc., Philadelphia, USA 1980, 11

[4] N. Ucar, O. B. Aytar, A. Calik, Mater. Tehnol., 46 (**2012**) 6, 621–625

[5] I. Ozbek, S. Sen, M. Ipek, C. Bindal, S. Zeytin, A. H. Ucisik, Vacuum, 73 (**2004**), 643

[6] I. Gunes, Sadhana, 38 (**2013**), 527

[7] S. Ulker, I. Gunes, S. Taktak, Indian Journal Eng. Mater. Sci., 18 (**2011**), 370

[8] Y. Sun, T. Bell, G. Wood, Wear, 178 (**1994**), 131

[9] K. Genel, Vacuum, 80 (**2006**), 451

[10] I. Celikyurek, B. Baksan, O. Torun, R. Gurler, Intermetallics, 14 (**2006**), 136

[11] I. Uslu, H. Comert, M. Ipek, O. Ozdemir, C. Bindal, Materials and Design, 28 (**2007**), 55

[12] J. H. Yoon, Y. K. Jee, S. Y. Lee, Surface and Coatings Technology, 112 (**1999**), 71

[13] M. Hudáková, M. Kusý, V. Sedlická, P. Grgač, Mater. Tehnol., 41 (**2007**) 2, 81–84

[14] I. Gunes, S. Ulker, S. Taktak, Materials and Design, 32 (**2011**), 2380

[15] C. Bindal, A. H. Ucisik, Vacuum, 82 (**2008**), 90

[16] O. Ozdemir, M. A. Omar, M. Usta, S. Zeytin, C. Bindal, A. H. Ucisik, Vacuum, 83 (**2009**), 175

[17] T. Eyre, Wear, 34 (**1975**), 383

[18] I. Gunes, Journal of Materials Science and Technology, 29 (**2013**), 662

[19] S. Taktak, Surface and Coatings Technology, 201 (**2006**), 2230

[20] M. Ulutan, M. M. Yildirim, O. N. Celik, S. Buytoz, Tribology Letters, 38 (**2010**), 231

[21] E. Atık, U. Yunker, C. Meric, Tribology International, 36 (**2003**), 155

[22] C. Li, B. Shen, G. Li, C. Yang, Surface and Coatings Technology, 202 (**2008**), 5882

[23] I. Ozbek, C. Bindal, Vacuum, 86 (**2011**), 391

UDK 669.715:621.74.046
Professional article/Strokovni članek

ISSN 1580-2949
MTAEC9, 48(5)771(2014)

MICROSTRUCTURES OF THE Al-Fe-Cu-X ALLOYS PREPARED AT VARIOUS SOLIDIFICATION RATES

MIKROSTRUKTURA ZLITIN Al-Fe-Cu-X PO RAZLIČNIH HITROSTIH STRJEVANJA

Milena Voděrová, Pavel Novák, Filip Průša, Dalibor Vojtěch
Institute of Chemical Technology, Department of Metals and Corrosion Engineering, Technická 5, 166 28 Prague 6, Czech Republic
voderovm@vscht.cz

Prejem rokopisa – received: 2013-08-26; sprejem za objavo – accepted for publication: 2013-11-08

Aluminium alloys are usually prepared with conventional casting, but rapid-solidification methods lead to the alloys with better mechanical properties or thermal stability. When an improved thermal stability is required, aluminium is alloyed with one or more of the elements from the group of transition metals (TM), for example, Ni, Fe, Cr or Ti. These elements are characterized by a low diffusivity and solubility in aluminium even at elevated temperatures, while Cu in an alloy forms a $CuAl_2$ phase that enables precipitation hardening. In this work, the microstructures of the Al-7Fe-4Cu, Al-4Fe-4Cu-3Ni and Al-7Fe-4Cu-3Cr (mass fraction, *w*/%) alloys prepared with various solidification processes were investigated. The aim of this work was to determine the changes in the microstructure caused by the increasing solidification rate and to determine the influence of the copper present in each alloy. All the samples were prepared with single-roll melt spinning, water quenching of the melt and conventional casting. The microstructures of the alloys were studied with light and scanning electron microscopy (SEM). The phase composition was determined with X- ray diffraction (XRD). Vickers hardness (HV 5) and microhardness (HV 0.005) were measured to compare the mechanical properties of the alloys. The microstructure and the hardness of the alloys strongly depended on the solidification rate. The fine microstructure and high microhardness values obtained with melt spinning are promising for the use of these alloys in special applications at elevated temperatures.

Keywords: aluminium alloy, rapid solidification, melt spinning, transition metals, microstructure

Zlitine aluminija se najpogosteje izdelujejo z navadnim ulivanjem, vendar pa metode hitrega strjevanja povzročijo nastanek zlitin z boljšimi mehanskimi lastnostmi ali toplotno stabilnostjo. Kadar se zahteva toplotna stabilnost, se aluminij legira z enim ali dvema elementoma iz skupine prehodnih kovin (TM), na primer: Ni, Fe, Cr ali Ti. Značilno za te elemente je majhna difuzivnost in topnost v aluminiju celo pri povišanih temperaturah, medtem ko Cu v zlitini tvori fazo $CuAl_2$, ki omogoča izločevalno utrjanje. V tem delu so preiskovane mikrostrukture zlitin Al-7Fe-4Cu, Al-4Fe-4Cu-3Ni in Al-7Fe-4Cu-3Cr (masni deleži, *w*/%), pripravljenih z različnimi postopki strjevanja. Namen tega dela je bil opredeliti razlike v mikrostrukturi, ki jih povzroči povečanje hitrosti strjevanja, in opredeliti vpliv bakra v vsaki od navedenih zlitin. Vsi vzorci so bili pripravljeni z ulivanjem tankega traku na bakren valj, z ohlajanjem v vodi in z navadnim ulivanjem. Mikrostruktura zlitin je bila pregledana s svetlobnim mikroskopom in z vrstičnim elektronskim mikroskopom (SEM). Sestava faz je bila določena z rentgensko difrakcijo (XRD). Trdota HV 5 in mikrotrdota HV 0,005 sta bili izmerjeni za primerjavo z mehanskimi lastnostmi zlitin. Mikrostruktura in trdota zlitin sta močno odvisni od hitrosti strjevanja. Drobnozrnata mikrostruktura in velika mikrotrdota, dobljeni z ulivanjem na valj iz bakra, sta obetajoči za uporabo teh zlitin v posebnih primerih pri povišanih temperaturah.

Ključne besede: zlitina aluminija, hitro strjevanje, ulivanje na bakreni valj, prehodne kovine, mikrostruktura

1 INTRODUCTION

Aluminium alloys processed with the conventional technologies, such as casting and forming, are widely used in many technical branches such as the aerospace and automotive industries. The main advantages of aluminium alloys are price, good strength-to-weight ratio, good castability, formability or the ability of precipitation hardening. However, the mechanical properties of traditional alloys made of Zn, Mg or Cu strongly degrade at elevated temperatures, which means that their application is then limited to 150–200 °C. One way of improving the thermal stability of aluminium alloys is to use the elements from the transition metals group (TM). Transition metals, such as Ni, Fe, Cr or Mo, are characterized by a low diffusivity and solubility in aluminium even at elevated temperatures and they are able to stabilize the materials properties up to relatively high temperatures (about 400 °C). Cu is used as an alloying element to increase both the strength and the hardness due to the $CuAl_2$ phase that allows precipitation hardening of the material.[1] Conventional casting processes produce the alloys containing coarse particles of hard and brittle Al-TM intermetallic phases, degrading the mechanical properties.[2] Therefore, it is desirable to keep these alloying elements dissolved in the matrix or in the finely dispersed intermetallic particles. A fine microstructure can be obtained by increasing the solidification rate, e.g., by atomisation or melt spinning.[3,4]

The alloying elements mentioned above are often the contaminants of Al scrap. In recent years, the consumption of aluminium alloys in engineering has been rising, causing the problems of recycling and waste disposal. Al scrap is never only pure aluminium, but it is mixed with steel, cast iron, copper alloys, etc. Parts of ferromagnetic iron-based alloys can be separated using magnetic separation. The other way is to dilute the melt with pure aluminium, but this technique increases the cost of recycled aluminium alloys. In general, the transition elements included, e.g., in the austenitic-stainless-steel admixtures in Al scrap are very difficult and costly to remove. We would like to develop a new way of preparing the alloys with interesting mechanical properties and a thermal stability using this contaminated Al scrap. The manufactured alloys would have better properties such as hardness, thermal stability and ductility associated with the low density. Due to the mentioned properties these alloys could be able to replace titanium alloys in some applications, while their price and density would be lower.

This work describes the microstructure and properties of the Al-Fe-Cu-X alloys prepared at various cooling rates. These alloys simulate the real alloys originating from melting the contaminated Al scrap. The alloys with the mentioned chemical composition have not been studied yet; there are only a few studies dealing with the microstructures of the rapidly solidified ternary alloys or systems of the quasicrystal chemical compositions.[1,5–8]

2 MELT-SPINNING PRINCIPLES

Atomization of a melt with an inert gas or water produces the powders that solidify with the rate ranging from 10^2–10^4 K s^{-1}. Melt spinning allows even higher cooling rates (10^4–10^6 K s^{-1}). In this process, a molten alloy is ejected on a high-speed rotating metallic wheel. The alloy solidifies rapidly in contact with the wheel. This method produces thin ribbons, whose thickness varies in the order of ten micrometres. Due to rapid-solidification processes transition metals can be added to aluminium even above their equilibrium-solubility limits. Increased solidification rates lead to the formation of supersaturated solid solutions and fine particles of metastable and stable intermetallic phases. The amounts of intermetallic phases are reduced and the shape is usually spherical. The slow decomposition of a supersaturated solution containing transition metals at higher temperatures can lead to the precipitation strengthening of the material. The layout of the melt-spinning process is shown in **Figure 1**.[3]

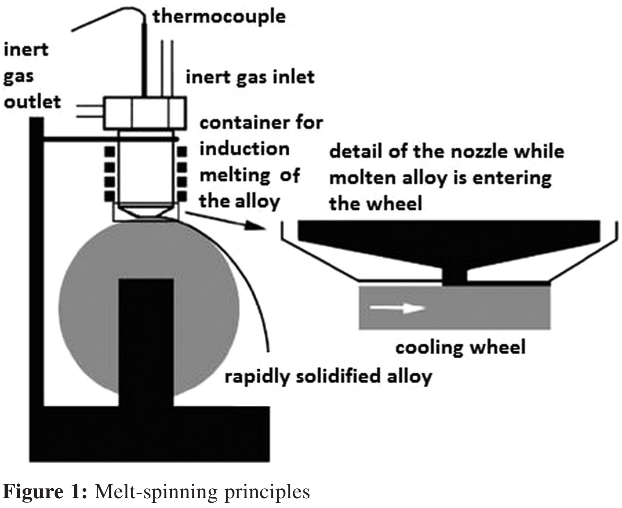

Figure 1: Melt-spinning principles
Slika 1: Shematski prikaz ulivanja na bakreni valj

To obtain a bulk material, the rapid-solidification process is associated with the compaction of the RS product. At first, the powder has to be milled, e.g., by cryogenic milling, to obtain a metallic powder with a well-preserved fine microstructure The most suitable technology is hot extrusion or e.g., hot isostatic pressing (HIP) or spark plasma sintering (SPS).[9–11]

3 EXPERIMENTAL WORK

Alloys with the chemical compositions of Al-7Fe-4Cu, Al-4Fe-4Cu-3Cr and Al-4Fe-4Cu-3Ni were prepared by melting the master alloy Al-11Fe (w/%) with the additions of pure Cu, Cr and Ni in an electric-resistance furnace in a graphite crucible and then poured into a brass mould. The second series was prepared by remelting the alloy and subsequent water quenching. The third series was prepared with single-roll melt spinning. The melting was carried out under an argon protective atmosphere and the temperature of the melt was 950 °C. The material was melted in a quartz-glass nozzle and then poured onto a copper wheel using overpressured argon. The circumferential speed of the wheel was 30 m s^{-1}. The process yielded aluminium-alloy ribbons approximately 40 µm thick. The metallographic cuts of the investigated alloys were etched in Kroll's reagent (10 mL HF, 5 mL HNO_3 and 85 mL H_2O) and investigated with an Olympus PME3 light microscope and a TESCAN VEGA 3 LMU scanning electron microscope (SEM) equipped with an Oxford Instruments INCA 350 EDS analyser. The phase composition was determined with X- ray diffraction (XRD, PANalytical X'Pert Pro). The mechanical properties of the investigated alloys were examined with Vickers-hardness measurements with the 5 kg (HV 5) and 0.005 kg (HV 0.005) loads. The microhardness was measured using a Neophot 2 light microscope equipped with a Hanemann microhardness tester.

4 RESULTS AND DISCUSSION

4.1 Microstructure

The microstructures of the aluminium alloys prepared by conventional casting into a brass mould are shown in **Figures 2** to **4**. It is obvious that the microstructure obtained after the conventional casting is composed of an inhomogeneous material with large amounts of coarse and brittle binary intermetallic phases $Al_{13}Fe_4$ and $CuAl_2$ and ternary phase $Al_{23}CuFe_4$ in the solid solution of the alloying elements in aluminium. Moreover, the nickel-alloyed material contains Al_4Ni_3, Al_7Cu_4Ni and $Al_{75}Ni_{10}Fe_{15}$ as well.

Figures 5 to **7** show the microstructures of the alloys prepared by melting at 1000 °C and then water quenched. Intermetallic phases $Al_{13}Fe_4$ and $CuAl_2$ become finer due

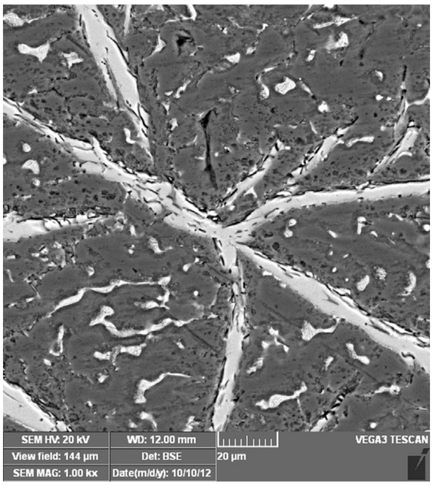

Figure 2: Microstructure of the as-cast Al-7Fe-4Cu (SEM)
Slika 2: Strjevalna struktura Al-7Fe-4Cu (SEM)

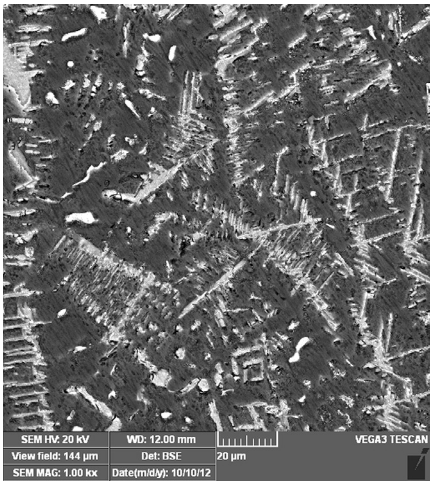

Figure 3: Microstructure of the as-cast Al-4Fe-4Cu-3Cr (SEM)
Slika 3: Strjevalna struktura Al-4Fe-4Cu-3Cr (SEM)

Figure 4: Microstructure of the as-cast Al-4Fe-4Cu-3Ni (SEM)
Slika 4: Strjevalna struktura Al-4Fe-4Cu-3Ni (SEM)

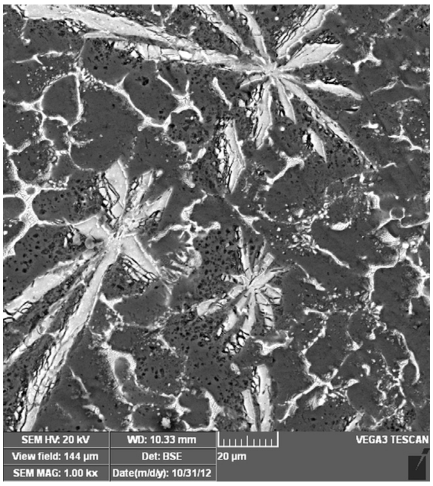

Figure 5: Microstructure of the water-quenched Al-7Fe-4Cu (SEM)
Slika 5: Mikrostruktura Al-7Fe-4Cu po ohlajanju v vodi (SEM)

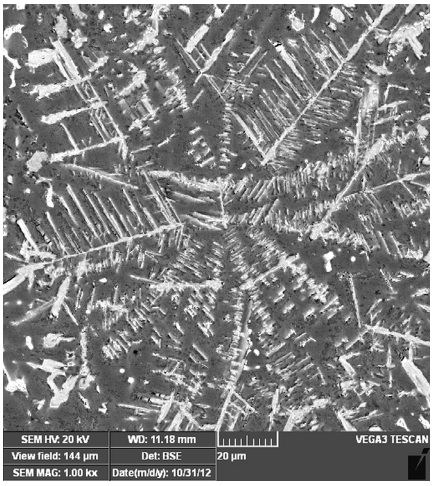

Figure 6: Microstructure of the water-quenched Al-4Fe-4Cu-3Cr (SEM)
Slika 6: Mikrostruktura Al-4Fe-4Cu-3Cr po ohlajanju v vodi (SEM)

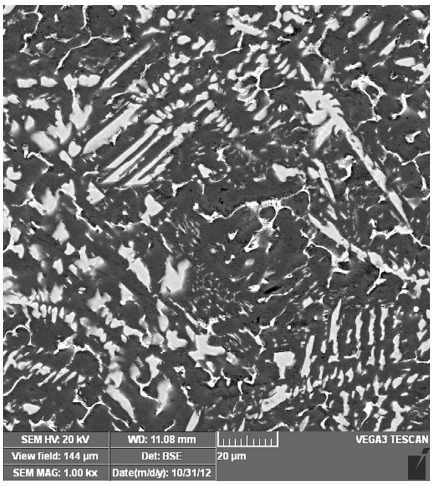

Figure 7: Microstructure of the water-quenched Al-4Fe-4Cu-3Ni (SEM)
Slika 7: Mikrostruktura Al-4Fe-4Cu-3Ni po ohlajanju v vodi (SEM)

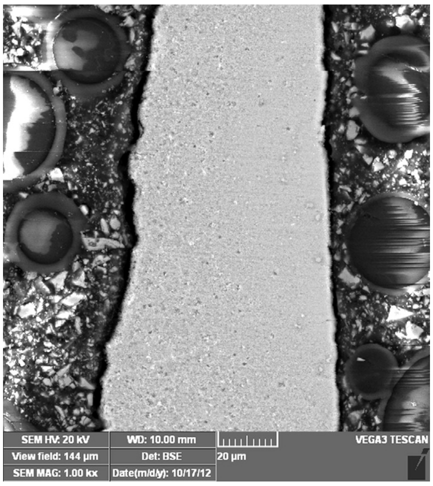

Figure 8: Microstructure of the rapidly solidified Al-7Fe-4Cu (SEM)
Slika 8: Mikrostruktura hitro strjenega traku iz Al-7Fe-4Cu (SEM)

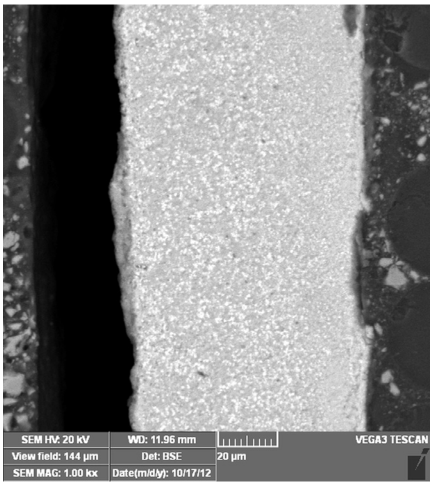

Figure 9: Microstructure of the rapidly solidified Al-4Fe-4Cu-3Cr (SEM)
Slika 9: Mikrostruktura hitro strjenega traku iz Al-4Fe-4Cu-3Cr (SEM)

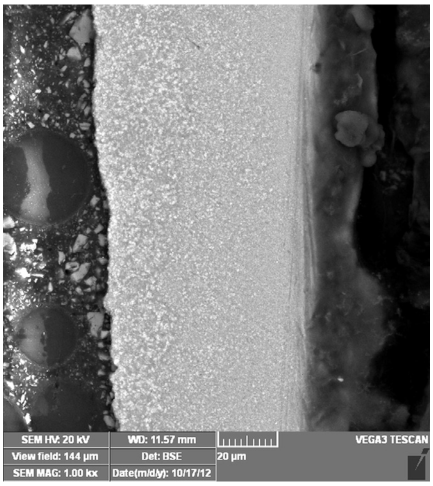

Figure 10: Microstructure of the rapidly solidified Al-4Fe-4Cu-3Ni (SEM)
Slika 10: Mikrostruktura hitro strjenega traku iz Al-4Fe-4Cu-3Ni (SEM)

to a more intensive cooling and the amount of the intermetallics in the microstructure is decreasing. In Al-7Fe-4Cu, quasicrystalline $Al_{65}Cu_{20}Fe_{15}$ is formed instead of a stable $Al_{23}CuFe_4$. On the other hand, no quasicrystalline phases were detected in the water-quenched Al-4Fe-4Cu-3Cr, but $Al_{13}Cr_2$ occurred in the microstructure. No differences in the phase composition of the alloy containing nickel in the as-cast and water-quenched states were detected.

The microstructures of the rapidly solidified alloys in the longitudinal cuts are documented in **Figures 8** to **10**. It is evident that the microstructure of a prepared ribbon is strongly dependent on the distance from the cooling wheel. On the wheel side, which is cooled more intensely, a supersaturated solid solution with nanocrystalline intermetallics is formed. On the free side, fine spherical intermetallic particles are formed. The saturation of the solution decreases when moving the ribbon from the wheel side to the free side. The amounts of the $Al_{13}Fe_4$ and $CuAl_2$ phases are negligible; instead of them, metastable phases Al_4Ni_3, $Al_{75}Ni_{10}Fe_{15}$, $Al_{23}CuFe_4$ or Al_7Cu_4Ni and quasicrystalline phase $Al_{65}Cu_{20}Fe_{15}$, are formed.[12–14] The phase compositions of all the samples

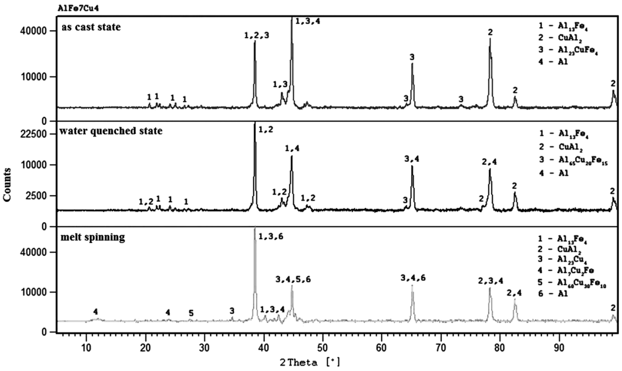

Figure 11: XRD patterns of the Al-7Fe-4Cu prepared with different methods

Slika 11: XRD-posnetki Al-7Fe-4Cu, izdelane po različnih metodah

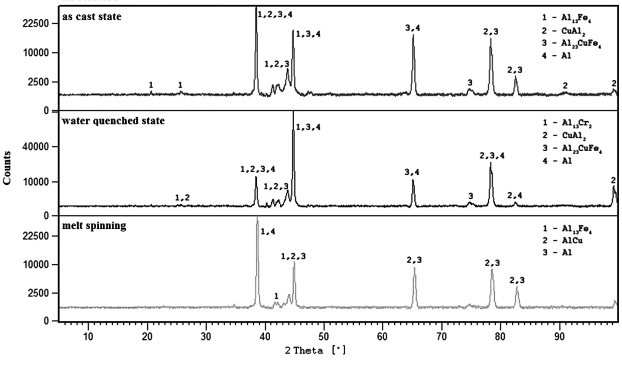

Figure 12: XRD patterns of the Al-4Fe-4Cu-3Cr prepared with different methods

Slika 12: XRD-posnetki Al-4Fe-4Cu-3Cr, izdelane po različnih metodah

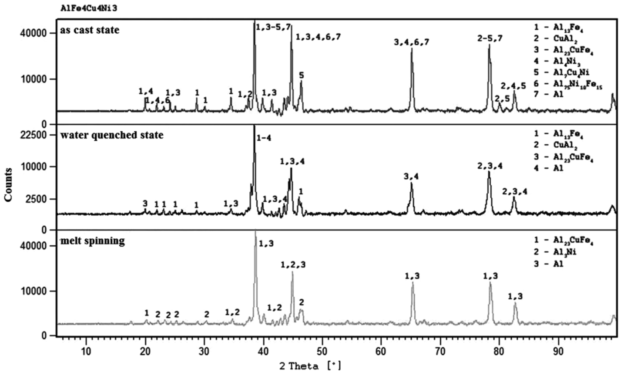

Figure 13: XRD patterns of the Al-4Fe-4Cu-3Ni prepared with different methods

Slika 13: XRD-posnetki Al-4Fe-4Cu-3Ni, izdelane po različnih metodah

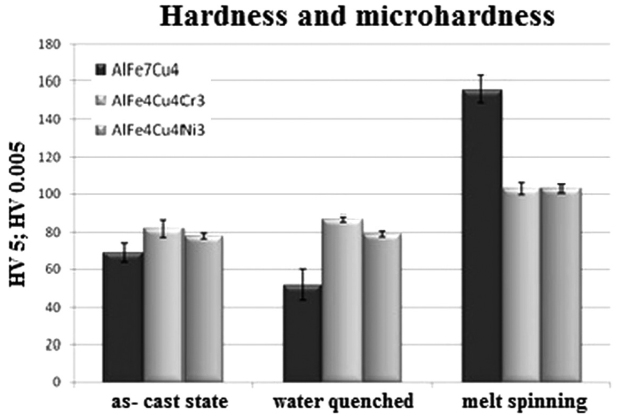

Figure 14: Hardness and microhardness measurements

Slika 14: Izmerjene trdote in mikrotrdote

are summarized in **Figures 11** to **13**. The phase composition, the amounts of intermetallics and the particle size are inevitably dependent on the solidification rate.

4.2 Hardness measurement

The Vickers hardness of the as-cast and water-quenched samples was measured with a 5 kg load. The microhardness of the rapidly solidified alloys was measured with a 5 g load because of the low thickness of the produced ribbons. The microhardness of the rapidly solidified alloys was measured in the centre of a ribbon to avoid the influence of the epoxy resin surrounding the sample. The measurement results are shown in **Figure 14**. It is obvious that the hardness increases with the increasing solidification rate. The as-cast alloys consist of large sharp-edged particles of the intermetallics that have a negative effect on the hardness. A decrease in the particle size and the strengthening caused by the presence of the supersaturated solutions are the main explanations of the increased hardness.

5 CONCLUSIONS

This work focused on a comparison of the microstructures of the Al-Cu-Fe-X alloys prepared at various solidification rates. The microstructures of the alloys prepared with traditional casting and water quenching are considerably inhomogeneous. There are large amounts of coarse $Al_{13}Fe_4$ and $CuAl_2$ intermetallic phases in the aluminium matrix. The amount of intermetallics decreases and the particles become finer, if the solidification rate increases. In the rapidly solidified alloys, the amounts of $Al_{13}Fe_4$ and $CuAl_2$ are limited because these phases are replaced by metastable and quasicrystalline intermetallics. The microstructures of RS alloys consist of aluminium supersaturated with transition metals and spherical intermetallics. The hardness of the investigated materials is hardly dependent on the cooling rate; higher values were reached for very fine materials.

Acknowledgement

This research was financially supported by the Czech Science Foundation, within project No. P108/12/G043.

6 REFERENCES

[1] S. J. Andersen, Materials Science and Engineering A, 179–180 (**1994**), 665–668

[2] P. Jurči, M. Dománková, M. Hudáková, B. Šuštaršič, Mater. Tehnol., 41 (**2007**) 6, 283–287

[3] D. Vojtěch, J. Verner, B. Bártová, K. Saksl, Metal Powder Report, 61 (**2006**), 32–35

[4] D. Vojtěch, B. Bártová, J. Verner, J. Šerák, Chemické listy, 98 (**2004**), 180–184

[5] J. Q. Guo, N. S. Kazama, Materials Science and Engineering A, 232 (**1997**) 1–2, 177–182

[6] E. Huttunen-Saarivirta, J. Vuorinen, Intermetallics, 13 (**2005**), 885–895

[7] G. Rosas, J. Reyes-Gasga, R. Pérez, Materials Characterization, 58 (**2007**), 765–770

[8] D. J. Sordelet, M. F. Besser, J. L. Logsdon, Materials Science and Engineering A, 255 (**1998**), 54–65

[9] N. L. Loh, K. Y. Sia, Journal of Materials Processing Technology, 30 (**1992**), 45–65

[10] E. Vollertsen, A. Sprenger, J. Kraus, H. Anet, Journal of Materials Processing Technology, 87 (**1999**), 1–27

[11] L. Wang, J. Zhang, W. Jiang, Int. Journal of Refractory Metals and Hard Materials, 39 (**2013**), 103–112

[12] D. Holland-Moritz, J. Schroers, B. Grushko, D. M. Herlach, K. Urban, Materials Science and Engineering A, 226–228 (**1997**), 976–980

[13] E. Huttunen-Saarivirta, Journal of Alloys and Compounds, 363 (**2004**), 150–174

[14] J. Colín, S. Serna, B. Campillo, O. Flores, J. Juárez-Islas, Intermetallics, 16 (**2008**), 847–853

UDK 677.4:66.017
Professional article/Strokovni članek

ISSN 1580-2949
MTAEC9, 48(5)777(2014)

ASSESSMENT OF THE POST-IMPACT DAMAGE PROPAGATION IN A CARBON-FIBRE COMPOSITE UNDER CYCLIC LOADING

OCENA NAPREDOVANJA POŠKODBE PO UDARCU PRI PONAVLJAJOČIH SE OBREMENITVAH KOMPOZITA Z OGLJIKOVIMI VLAKNI

Daniel Kytýř[1], Tomáš Fíla[2], Jan Šleichrt[2], Tomáš Doktor[1], Martin Šperl[1]

[1]Institute of Theoretical and Applied Mechanics, v.v.i., Academy of Sciences of the Czech Republic, Prosecká 76, 190 00 Prague 9, Czech Republic

[2]Czech Technical University in Prague, Faculty of Transportation Sciences, Department of Mechanics and Materials, Konviktská 20, 110 00 Prague 1, Czech Republic

kytyr@itam.cas.cz

Prejem rokopisa – received: 2013-09-30; sprejem za objavo – accepted for publication: 2013-11-11

Carbon fibre in polyphenylene sulfide composites (C/PPS) became a popular material in the aircraft industry but its fragility and low impact resistance limits its application in primary aircraft structures. This study is focused on damage propagation in the laminated composites reinforced with carbon fibres. The damage may be inflicted during the ground maintenance, by an inflight bird strike or during a flight in severe meteorological conditions (heavy storms). The initial damage was created by a drop-weight out-of-plane impact using a spherical indenter. The response of the material was analysed by monitoring the impacted zones and their propagation history. The influenced area and specimen thickness in the centres of indents were chosen as the degradation parameters. The post-impact damage propagation induced by cyclic loading was assessed using a custom-designed computer-controlled laser-profilometery device. Both the upper and lower profiles of the specimen were scanned during the interruptions of the fatigue test. Global deformation was described with an analytically determined centroidal-axis curve. Local topography changes were obtained with a subtraction of this curve. Surface-deformation maps were created and used for a demonstration of the damage propagation in the specimen.

Keywords: carbon-fibre composites, post-impact damage, laser profilometry

Ogljikova vlakna v kompozitih iz polifenilen sulfida (C/PPS) so postala priljubljen material v letalski industriji, toda njihova krhkost in slaba odpornost proti udarcem omejujeta njihovo uporabo v primarnih letalskih konstrukcijah. Ta raziskava se osredinja na napredovanje poškodbe na laminiranih kompozitih, ojačanih z ogljikovimi vlakni. Poškodba lahko nastane med vzdrževanjem na tleh, pri trčenju s ptico med letom ali med letom v hudih vremenskih razmerah (huda nevihta). Začetna poškodba je bila narejena z udarno pregibnim preizkusom s kroglastim vtiskovalcem. Odziv materiala je bil analiziran z opazovanjem območij udarca in potekom napredovanja. Prizadeto območje in debelina vzorca v področju vtiska sta bila izbrana kot parametra degradacije. Napredovanje poškodbe po cikličnem obremenjevanju po udarcu je bilo ocenjeno s po meri oblikovane računalniško vodene naprave za lasersko profilometrijo. Zgornji in spodnji profil vzorca sta bila skenirana med prekinitvami preizkušanja utrujenosti. Celotna deformacija je bila opisana z analitično določeno krivuljo težiščnice. Lokalne spremembe topografije so bile dobljene z odštetjem te krivulje. Ustvarjeni videzi deformacije površine so bili uporabljeni za prikaz napredovanja poškodbe na vzorcu.

Ključne besede: kompoziti z ogljikovimi vlakni, poškodba po udarcu, laserska profilometrija

1 INTRODUCTION

The design and safe operation of lightweight structures, especially in the aviation industry, is particularly important and challenging due to the inauspicious load spectra composed of a large number of low-amplitude cycles and sudden impacts[1]. Low-amplitude cycles are caused by aerodynamic loads and engine vibrations. Wayward strikes may be inflicted during the ground maintenance, by inflight collisions (bird strikes) or severe meteorological conditions (heavy storms).

The damage-tolerance approach commonly used in aerospace engineering requires a comprehensive knowledge of the material-degradation process and a reliable prediction of a structure safe life[2]. The thermoplastic composites commonly used for these purposes allow an application of an optimised manufacturing technology[3,4]. An application of a polymeric matrix lowered the tendency towards brittle behaviour (common for carbon-fibre composites) and exhibited the advantages of high chemical resistivity, insensitivity to moisture, good fatigue performance[5,6] and recyclability.

Micromechanical modelling of the composites with imperfections[7] sufficiently describes the degradation process. However, the material models based on the X-ray computed tomography of the specimen representing the material at the macroscopic level including a complex microstructure could not be evaluated using the finite-element simulations with the plasticity applied due to the computational complexity and enormous memory requirements[8]. The presented work aimed to extend the range of non-destructive testing (NDT) techniques comprising the lock-in thermography[9] or the modified-impulse excitation technique[10].

2 MATERIALS AND METHODS

2.1 Specimen description

The base material, a carbon-fibre/polyphenylene sulphide (C/PPS) composite manufactured by Letov letecká výroba, s. r. o., was delivered as plates with a thickness of (2.5 ± 0.05) mm. The material consists of quasi-isotropic 8-ply carbon fabric with its volume fraction higher than 90 %, bonded with a thermoplastic matrix. The surface is covered with a thin glass-fibre cloth protecting the core against mechanical and chemical influences. The final specimens with a rectangular shape with the dimensions of 250 mm × 25 mm were cut from the plates using a water-jet cutter.

2.2 Initial damage

The first step of the experimental procedure was to inflict the initial damage to the specimens under controlled conditions. A drop tower designed within project SGS12/163/OHK2/2T/16 with the maximum impact energy of 50 J was used. The strike was carried out using a spherical indenter with a diameter of 20 mm and the energies of (10, 20 and 15) J on (30, 50 and 70) % of the length of the samples. The imprints of the diameter in the range of millimetres and the depth in the range of tens of micrometers then occurred.

2.3 Fatigue loading

For a life-cycle assessment the specimens were cyclically loaded using a Mikrotron (Russenberger Prüfmaschinen, AG) resonant testing machine (**Figure 1**). To ensure the loading at the chosen stress level (33 % of the tensile strength) the mean loading-force value of 6 kN and the amplitude of 5 kN were set. A sinusoidal force was applied in the force-driven experiments.

Due to a relatively high testing frequency (approximately 75 Hz), the experiment was monitored with a thermal imaging camera SC7600 (FLIR Systems, Inc.). To prevent exceeding 50 % of the glass transition temperature the specimen temperature was held at maximally 60 °C. At the same time, the lower frequency limit was set in order to avoid a specimen rupture[11]. The fatigue experiment was interrupted six times at the predefined numbers of cycles to perform profile scanning.

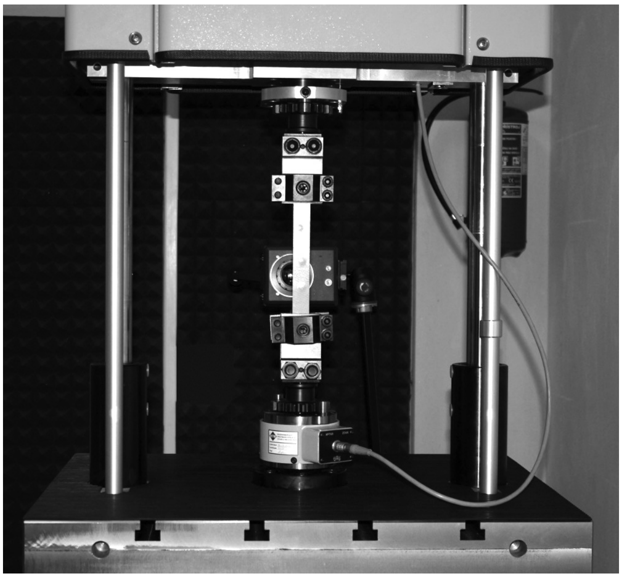

Figure 1: Experimental device for dynamic loading
Slika 1: Eksperimentalna naprava za dinamično obremenjevanje

2.4 Profile measurement

To obtain the information about damage propagation during the life cycle, a set of profilometery experiments was performed. A custom-designed scanning device equipped with laser scanner ScanControl LLT2600-25 (Micro-Epsilon Messtechnik) depicted in **Figure 2** was used for this purpose. The device allowed us to measure the line profiles with the length of 20–40 mm, defined by 1024 measured points. The altitude resolution of the scans was 4 μm. The scanner was mounted on a motorised computer-controlled single-axis linear stage with the minimum incremental motion of 10 μm and the on-axis accuracy of ± 0.5 μm. One scanning sequence took approximately 15 minutes.

2.5 Damage-propagation assessment

The changes in the impact depth, the sample thickness and the area of influenced zones were chosen as the degradation parameters. The automatic procedure for a surface reconstruction (**Figure 3**) and profile-change assessment was carried out using the tools developed in the MATLAB (Mathworks, Inc.) computational environment. The variable position of the samples in the scanning area required the use of the corner detection

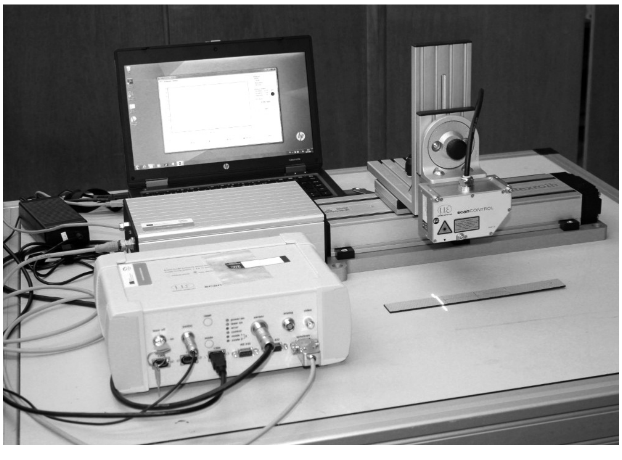

Figure 2: Custom-designed computer-controlled profilometery device equipped with a ScanControl LLT2600-25 laser scanner
Slika 2: Po meri oblikovana računalniško vodena naprava za profilometrijo, opremljena z laserskim optičnim bralnikom ScanControl LLT2600-25

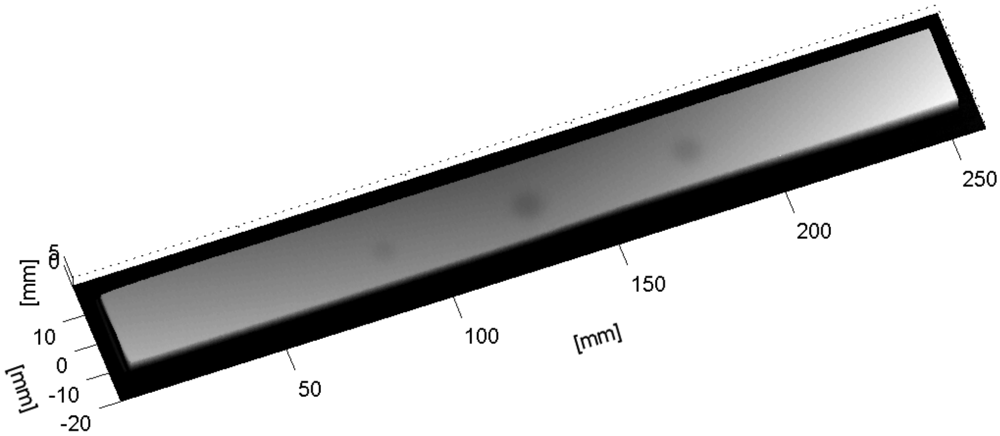

Figure 3: Reconstruction of the sample surface based on laser triangulation
Slika 3: Rekonstrukcija površine vzorca, ki temelji na laserski triangulaciji

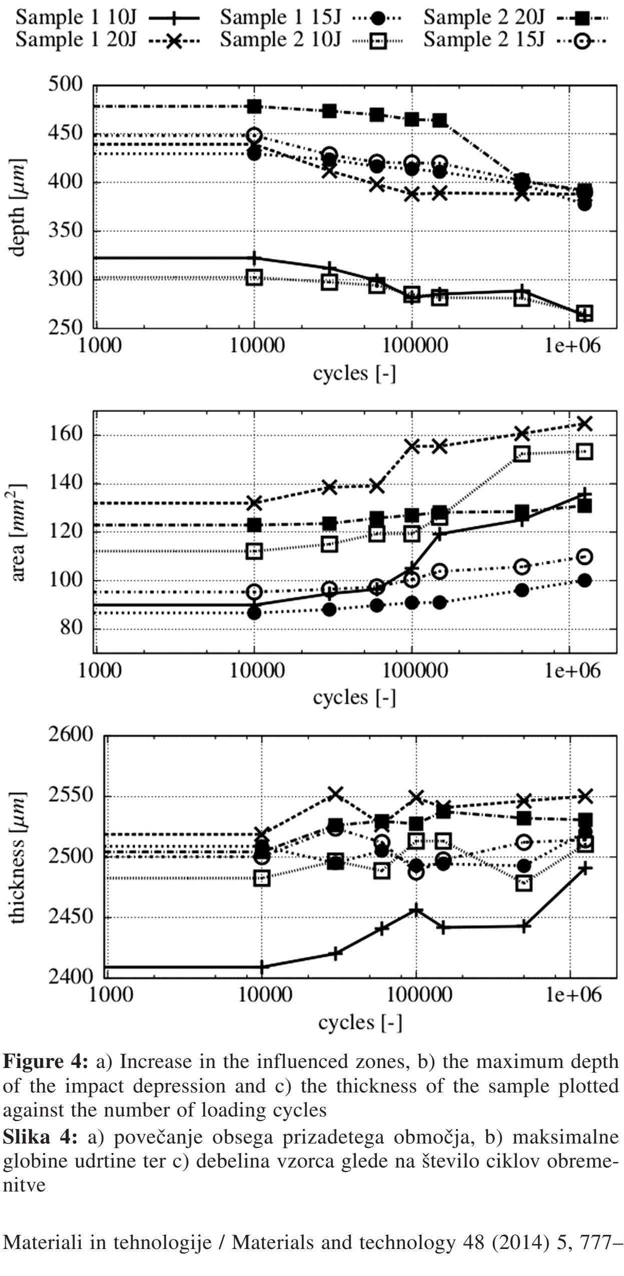

Figure 4: a) Increase in the influenced zones, b) the maximum depth of the impact depression and c) the thickness of the sample plotted against the number of loading cycles
Slika 4: a) povečanje obsega prizadetega območja, b) maksimalne globine udrtine ter c) debelina vzorca glede na število ciklov obremenitve

algorithm based on the altitude threshold to detect the specimen boundaries in the captured data. Transformation functions were obtained and the objects were transformed into a unitary coordination system.

Divergence of the laser beam was taken into account for the real-altitude matrix estimation and the blur of the edges caused by the same effect was reduced with gradient filters. The curvature of the surfaces was not caused only by the local impact zones but also by the overall bending of the samples due to a combination of the initial impact damage and cyclic loading. A piecewise continuous second-order curve (the centroidal axis) was fitted and set as a new reference level. Then the altitude matrices were updated. On the straightened surfaces, the local impacted zones were quantified (area, maximum depth) using the data-registration procedure. From the subtraction of the upper and lower profile, the change in the sample thickness was obtained.

3 RESULTS

Based on the reconstructed profiles from the laser measurements, the influenced zones were identified on the basis of thresholding. In the areas of interest, the impact depression depth and the local thickness were assessed. Propagation of the chosen degradation parameters on two selected samples for several distinct impact levels is depicted in **Figure 4**.

Damage propagation exhibits similar evolution on different tested samples. The most significant parameter was the maximum depth of the impact on the impacted side. The initial depth corresponds to the strike energy, while later the depth decreases with the increasing number of the loading cycles. The area of influenced zones grows with the number of the loading cycles but, surprisingly, the initial areas were not proportional to the strike energy. The area of damaged zones inflicted by lower energy impacts also showed a faster increase. The changes in the thickness of the samples due to the influenced zones were negligible as the differences in the thickness were only two or three times higher than the noise.

4 CONCLUSIONS

The presented study describes the possibility of a time-lapse profilometery measurement for an evaluation of the post-impact damage propagation in a C/PPS composite under cyclic loading. The chosen parameters (the area of impacted zone, the maximum depth and the sample thickness) provide the information about damage accumulation in the material. Generally, laser profilometery is a suitable method for the NDT testing and evaluation of the surface damage. The described modified method is applicable to bigger components and structures. With respect to our measured data, the reliability of the method was reduced by the resolution of the available laser scanner.

Acknowledgements

The research was supported by Technology Agency of the Czech Republic (grant No. TA03010209), Grant Agency of the Czech Technical University in Prague (grant No. SGS12/205/OHK2/3T/16), research plan of the Ministry of Education, Youth and Sports MSM6840770043 and by institutional support RVO: 68378297.

5 REFERENCES

[1] R. Aoki, J. Heyduck, An Experimental Study of Impact-Damaged Panels under Compression Fatigue Loading, In: J. Füller et al. (eds.), Developments in the Science and Technology of Composite Materials, Elsevier Science Publishers Ltd., 1990, 633–642 1990, 633–642

[2] J. P. Gallagher, USAF damage tolerant design handbook, Flight Dynamics Laboratory, Air Force Wright Aeronautical Laboratories, 1984

[3] Z. Padovec, M. Růžička, Mechanics of Composite Materials, 49 (**2013**) 2, 221–230

[4] I. C. Finegan, R. F. Gibson, Composite Structures, 44 (**1999**) 2–3, 89–98

[5] J. Minster, O. Bláhová, J. Hristova, J. Lukeš, J. Němeček, M. Šperl, Journal of Applied Polymer Science, 123 (**2012**) 4, 2090–2094

[6] J. Minster, O. Blahová, J. Lukeš, J. Němeček, Mechanics of Time-Dependent Materials, 14 (**2010**) 3, 243–251

[7] M. Šejnoha, J. Zeman, International Journal of Engineering Science, 46 (**2008**) 6, 513–526

[8] J. Vorel, J. Zeman, M Šejnoha, International Journal for Multiscale Computational, 11 (**2013**) 5, 443–462

[9] R. Montanini, Infrared Physics & Technology, 53 (**2010**) 5, 363–371

[10] D. Kytyr, T. Fila, J. Valach, M. Šperl, UPB Scientific Bulletin, Series D: Mechanical, 75 (**2013**) 2, 157–164

[11] M. Pirner, S. Urushadze, International Applied Mechanics, 40 (**2004**) 5, 487–505

UDK 669.18:620.187:548.4
Professional article/Strokovni članek

ISSN 1580-2949
MTAEC9, 48(5)781(2014)

POSSIBILITIES FOR INCREASING THE PURITY OF STEEL IN PRODUCTION USING SECONDARY-METALLURGY EQUIPMENT

MOŽNOSTI POVEČANJA ČISTOSTI JEKLA PRI PROIZVODNJI Z UPORABO OPREME ZA SEKUNDARNO METALURGIJO

Martin Korbáš[1], Libor Čamek[2], Milan Raclavský[3]
[1]Vítkovice Heavy Machinery a.s., Ruská 2887/101, Vítkovice, Ostrava, Czech Republic
[2]VŠB-Technical University of Ostrava, Faculty of Metallurgy and Material Engineering, Department of Metallurgy and Foundry, 17. listopadu 15/2172, Ostrava – Poruba, Czech Republic
[3]ECOFER s.r.o., Kaštanová 182, 739 61 Třinec, Dolní Líštná, Czech Republic
martin.kor@centrum.cz

Prejem rokopisa – received: 2013-09-30; sprejem za objavo – accepted for publication: 2013-12-09

The possibilities for increasing the purity of steel during the production of the liquid phase using secondary metallurgy mainly relate to affecting the number of emerging occlusions, their size, morphology and chemical composition. The metallographic purity of steel during production in an electric-arc furnace (EAF), in a ladle furnace (LF) and during processing with VD caisson technology was assessed. The steel samples were processed by means of an electron microscope and were simultaneously tested using the single-spark-evaluation (SSE) method.
The aim of this investigation was to find the possibility for an operative steel-quality control and to obtain the desired mechanical properties already while processing the liquid phase.

Keywords: steel purity, secondary metallurgy, occlusions, electron microscope, single-spark evaluation

Možnosti povečanja čistosti staljenega jekla med proizvodnjo z uporabo sekundarne metalurgije so predvsem glede na količino vključkov, njihove velikosti, vrsto morfologije in kemijsko sestavo. Metalografsko je bila ugotavljana čistost jekla med proizvodnjo v elektroobločni peči (EAF), nato v ponovčni peči (LF) in po obdelavi v VD. Vzorci so bili pregledani z elektronskim mikroskopom in so bili preizkušeni z metodo plamenskega odžiganja (SSE).
Namen je bil poiskati učinkovito kontrolo jekla in vplive na želene mehanske lastnosti že med obdelavo taline.

Ključne besede: čistost jekla, sekundarna metalurgija, zapore, elektronska mikroskopija, ocena s plamenskim odžiganjem

1 INTRODUCTION

The continuously increasing requirements for achieved levels of mechanical values like ductility, toughness and fatigue properties for steel are increasing the demands put on manufacturers when it comes to searching for new technological processes. One of the main possibilities for achieving higher levels of mechanical properties for steel increases with its metallurgical purity. This can be achieved with the technological processes utilised in secondary metallurgy that can affect the size, the quantity of inclusions and their morphology.[1] Within the conditions existing at the steelworks of Vítkovice Heavy Machinery a.s. (VHM), there are facilities for processing steel in a ladle furnace (LF) and for vacuum steel processing in a caisson (VD).

The objective of the study was to assess the continuous metallographic purity in the course of steel production in an electric-arc furnace (EAF), in a ladle furnace (LF) and during vacuum processing in a caisson using the VD technology. The study was based on the idea that the implemented technological processes (TS No. 1 and TS No. 2) can assist in obtaining metallographic purity.

Metallic disk-pin samples were collected during the steel's production from secondary-metallurgical aggregates of LF and VD. Consequently, they were processed with an optical emission spectrometer, which assesses the analytical signal, while differentiating each individual spark with the single-spark-evaluation (SSE) method. A part of the analytical signal corresponds with the average content of an element in the collected sample (classically in the course of the steel's production process), while the second signal part corresponds with the elemental concentration in the inclusion. The single-spark-evaluation (SSE) method helps us assess information about the amount, the type and the composition of the inclusion. A big advantage of the SSE method is the fact that the sample preparation for the analysis with a spectrometer is identical to the disk-pin sample preparation. Analyses of the standard control sample of the steel's chemical composition were extended by only 20 s. The method took place online. The software for the optical emission spectrometer was set up for an elemental analysis in relation to the chemical composition of the produced steel.[2]

In order to express certain opinions about the values measured with the SSE method, identical samples, collected in the course of the steel's production, were consequently also processed with a roentgen spectral analysis (using an electron microscope) and subjected to a metallographic assessment, which was generally recognised within the metallurgical practice. The analyses of the inclusions with the assistance of the roentgen spectral analysis were performed on the basis of the Pirelli Norm No. 18. V. 008 rev. 7 metallographic test of the microstructure and of the defects of the rod wires. The test was slightly modified for the disk-pin measurements. The device scans the image in the BSE mode (reflected electrons); the image size is 1024 × 1024 pixels at a magnification of 500-times; the field of vision has a size of 0.25 mm × 0.25 mm; and the scanning time for a single pixel is 2800 ns. It looks for inclusions based on the set brightness threshold and then it analyses them. The threshold is set in such a way that all the oxides are recorded, while in the case of sulphides only the partly complex ones (with an oxidative core) are recorded. The analysis is performed for 5 s at about 25 % of the detector's dead time. This corresponds to an intensity of about 4500 impulses per second. The electron beam focuses on the particle's centre of gravity during the analysis. The set of results from the analysed particles passes through a filter that ensures the exclusion of the non-oxidative included particles and, as a result, records them in a ternary diagram with the silicates in one corner, aluminates in the second corner and the remaining oxides (Mn, Ca, and Mg) in the third corner. Particles larger than 1 µm are measured. The total assessed area of a sample consisted of 80 fields, i.e., 5 mm^2, which corresponded to the size of the metallic-sample areas analysed with the SSE method. The measured areas were fully comparable for both measurement techniques.

2 EXPERIMENTAL

The samples were manually collected from the furnace with the assistance of submersible disk-pin samplers and they were identical for both methods of steel purity assessment. The first sample, marked as LF1, represented the beginning of the steel-processing technology in the ladle furnace and, at the same time, the result of the preliminary steel de-oxygenation in the ladle furnace (LP) after the completed tapping, without slag, of the electric-arc furnace. In order to ensure standardisation, a temperature of 1580 °C was selected for the LF at the beginning of the collection of each LF1 sample. Considering a certain time delay, related to the necessary heating of the tapped and de-oxygenated melt to that temperature, we assumed a good melt-concentration homogeneity was achieved, including a good liquid, and mixed the newly occurring basic slag. The sample LF2 represents the melt situation at the end of the melt processing in the ladle furnace, where the main stress was put on the creation of the melt slag mode. The LP with the melt was prepared for the subsequent steel vacuuming in the caisson furnace using the VD process. A detailed technological prescription TS 1, prepared by VHM, established the steel temperature before the vacuuming, the steel's chemical composition, the slag parameters, and the oxygen activity. The samples VD1 and VD2 were collected at the beginning and at the end of the steel's vacuum processing in the furnace. The 15 min of homogenisation using porous argon followed after the sample's VD2 collection. The samples were collected from melts processed by following two technological processes. The sample collections from melts No. K58494, K58500, K58507, K58508, K58509, K58555 were performed following the technological process TS No. 1, while the sample collections from melts No. K58489 and No. K58495 followed the technological process TS No. 2 prepared at VHM.

The technological instructions differ, especially in terms of the method of the preliminary steel de-oxygenation in the ladle furnace after the tapping of the electric arc furnace. Other principles of the melt management in the ladle furnace or in the caisson are almost identical.[2]

TS No. 1

- 2 kg/t of CaC_2 into the ladle furnace (LP) before the tapping,
- FeSi to 0.15 % (steel in the furnace without Si after the oxygenation),
- Calcinated anthracite in the course of carbonaceous steels, e.g., C45,
- Al 0.3–0.6 kg/t into the flow in the course of the first tapping third, depending on the produced steel and according to the melted C content
- Pieces of CaO + synthetic slag + FeMn follow (up to 2/3 of the production composition),
- Possibly FeCr (none in the case of melts monitored by us)
- 0.3–0.6 kg/t of Al, again in the course of the last tapping third

TS No. 2

- 3.0 kg/t CaC_2 + min. of 3.0 kg/t of the calcinated anthracite into the ladle furnace (LP)
- FeMn (up to 2/3 of the production composition) + CaO + synthetic slag during the tapping, before the end of the tapping
- 0.5–0.7 kg/t of Al, according to the melted C

3 DISCUSSION

When assessing the research results, we must consider that the performed analysis could not be identical to the resulting composition of inclusions in the final product. The difference is given especially by the different speeds of cooling for the relatively small metallic sample, when compared with, for example, an ingot of many tons. The analysis does not present the inclusion composition and their quantity in the final product, but the actual inclusion types and the purity of the steel, which are analysed in the course of the technological steps LF and VD.

The following set of figures (**Figures 1** to **6**) summarises the results of the analysis of the number of inclusions performed with a microprobe.

The above-presented figures clearly show that the inclusion density in the individual melts progressively decreased in the course of the technological process. The fundamental decrease in the inclusion density took place in the course of the melt processing in the ladle furnace. This trend is clear for inclusions up to 4 µm in size. The density of the smallest inclusions then changed only a little, or not at all, in the subsequent vacuum steel processing because of their low concentration. In the case of some melts, even a small increase was noticed. Inclusions larger than 4 µm occur rarely in the samples and their occurrence is thus accidental. No clear trend was noticed. However, we can assume that their occurrence at the end of the technological process in VD is close to zero. The melts 58489, 58495 and 58527, which went through a different de-oxygenation process, differ to some extent from the set. The density of inclusions is lower at the beginning. These melts were produced by TS No. 2.

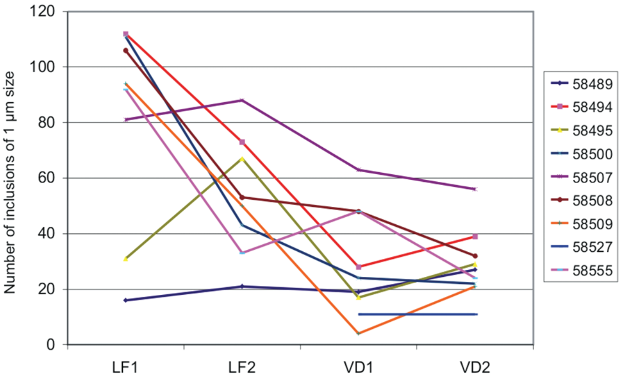

Figure 1: Summary of 1-µm inclusions' density during individual technological operations, in all the monitored melts
Slika 1: Seštevek vključkov velikih 1 µm med posameznimi tehnološkimi operacijami v vseh preiskovanih talinah

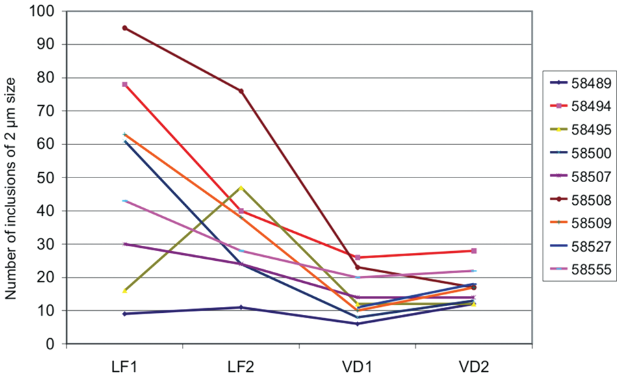

Figure 2: Summary of 2-µm inclusions' density during individual technological operations, in all the monitored melts
Slika 2: Seštevek vključkov velikih 2 µm med posameznimi tehnološkimi operacijami v vseh preiskovanih talinah

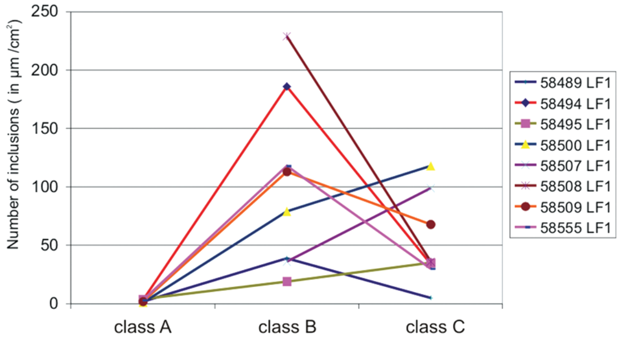

Figure 3: Numbers of inclusions in individual areas of the ternary diagram for the sample LF1 collection
Slika 3: Število vključkov v posameznih področjih ternarnega diagrama za vzorce iz LF1

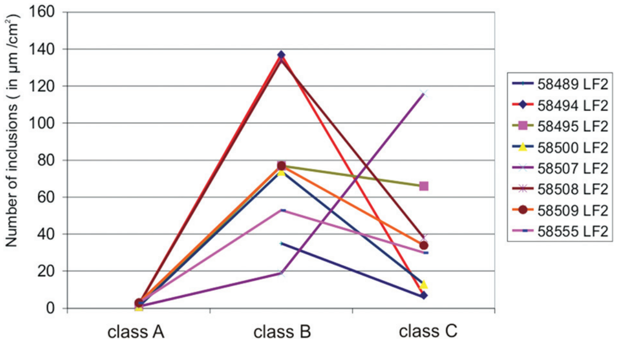

Figure 4: Numbers of inclusions in individual areas of the ternary diagram for the sample LF2 collection
Slika 4: Število vključkov v posameznih področjih ternarnega diagrama za vzorce iz LF2

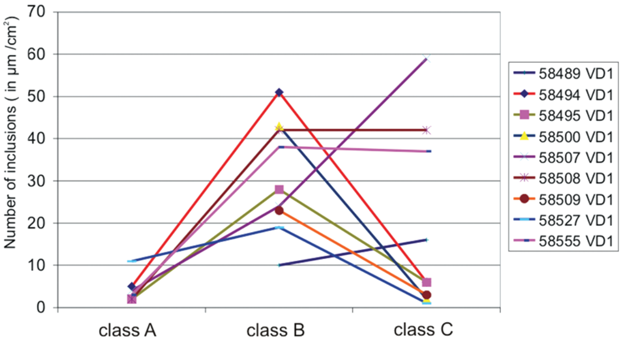

Figure 5: Numbers of inclusions in individual areas of the ternary diagram for the sample VD1 collection
Slika 5: Število vključkov v posameznih področjih ternarnega diagrama za vzorce iz VD1

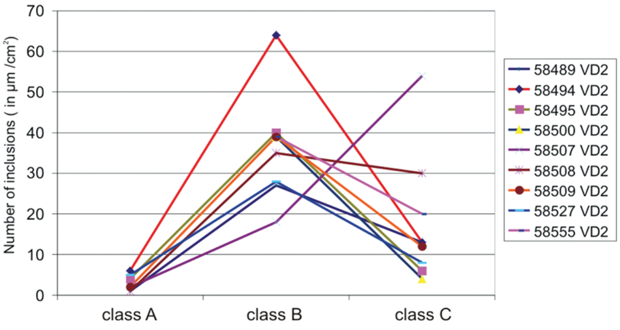

Figure 6: Numbers of inclusions in individual areas of the ternary diagram for the sample VD2 collection
Slika 6: Število vključkov v posameznih področjih ternarnega diagrama za vzorce iz VD2

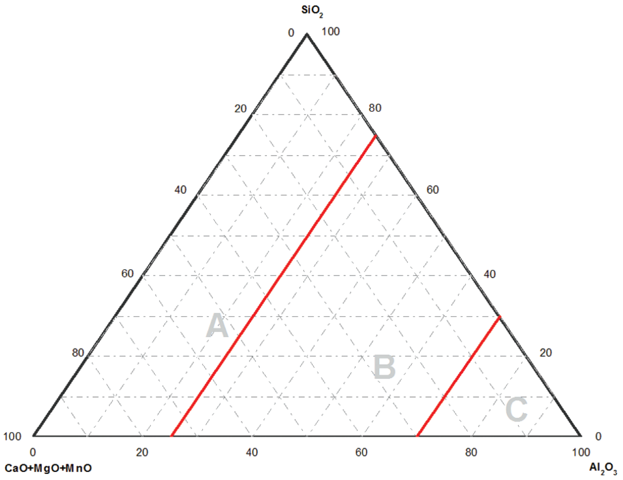

Figure 7: Scheme of the inclusions' division into individual classes
Slika 7: Shematičen prikaz razporeditve vključkov v posamezne razrede

The inclusions were divided into three groups using the following scheme (**Figure 7**) to monitor their chemical composition.

The inclusion compositions in individual melts and stages were similar. We can claim that:

- Inclusions from Zone A in the ternary diagram are practically absent in LF
- A small number of inclusions from Zone A occur in VD
- The dominant inclusion group consists of the inclusions from Zone B
- The main parts of the individual inclusions are Al, Ca, and O

The measured and presented results suggest that their effects, from the point of view of the number of inclusions in both technologies, TS No. 01 and TS No. 02, are similar. The result of the use of TS No. 02 is only the smaller number of inclusions at the beginning of the technological process in LF. When using TS No. 01

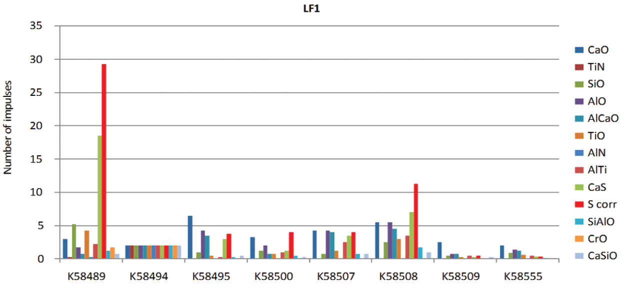

Figure 8: The average number of impulses for the individual elements and melts LF1
Slika 8: Povprečno število impulzov za posamezne elemente iz taline LF1

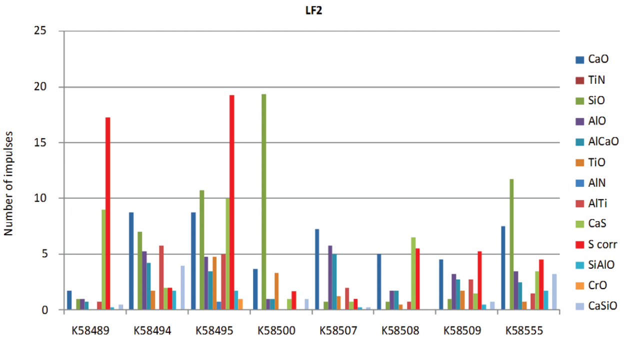

Figure 9: The average number of impulses for the individual elements and melts LF2
Slika 9: Povprečno število impulzov za posamezne elemente iz taline LF2

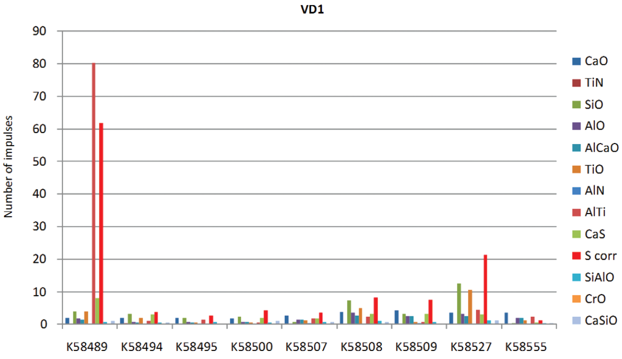

Figure 10: The average number of impulses for the individual elements and melts VD1
Slika 10: Povprečno število impulzov za posamezne elemente iz taline VD1

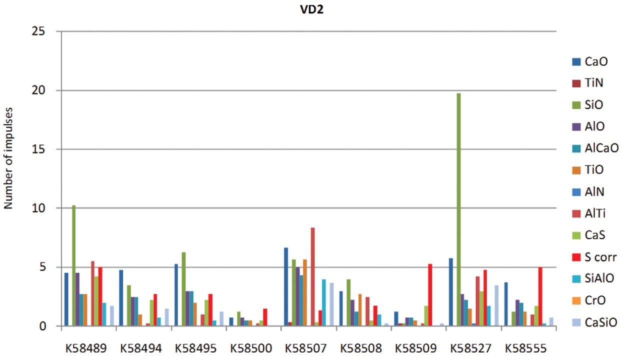

Figure 11: The average number of impulses for the individual elements and melts VD2
Slika 11: Povprečno število impulzov za posamezne elemente iz taline VD2

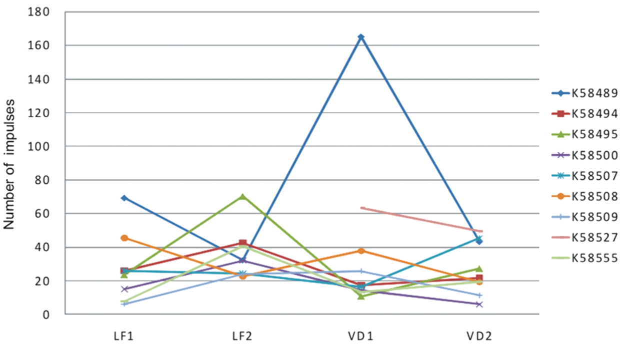

Figure 12: The number of impulses in the course of the steel processing LF1-VD2
Slika 12: Število impulzov med izdelavo jekla (LF1-VD2)

and TS No. 02, the inclusion number and their size become almost equal at the end of the processing in LF. Inclusions larger than 4 μm occur very rarely and accidentally.

The fundamental decrease in the number of inclusions occurs only by 3/4 in the course of steel processing in the LF. The processing in VD does not present a more pronounced change in the number of smaller inclusions, up to 2 μm. The occurrence of inclusions larger than 3 μm is negligible.

From the chemical inclusion composition in the LF point of view, the inclusions from Zone A are not present in any of the tested melts. A slight increase occurs only in the course of the VD technology. The inclusions from Zone B are the dominant ones. Their number from LF1 to VD 2 decreases in accordance with the above-presented conclusions. The Zone C is basically a half of Zone B, where the inclusions of the type $CaO.Al_2O_3$ prevail. Only very fine inclusions of the $CaO.Al_2O_3$ type and pure Al_2O_3, but also CaO, remain at the end of the VD technology.

The results obtained with the SSE method were based on an analysis of 2000 sparks. If any particles of a different composition than those in the basic metallic matrix, occurred in a given place, they are in the peaks of the present elements and, then, their bonds could be analysed. Each analysis of the relevant sample (disk-pin) was performed in three places, always in such a way that the relevant axis part of the sample was not affected and the measurements were averaged.

The measured values of the analysed samples are summarised graphically in **Figures 8** to **11**. The number of sparks for the melt and the technological step are on the *x*-axis (2000 for each measurement). The individual colours mark inclusions based on the mentioned elements. The number of impulses is on the *y* axis.[3]

The individual analyses and melt graphics, inclusion types and technological steps of the production material flow suggest that the mutual connections in the inclusion volume and number, between individual samples for melting or for individual technological steps LF1, LF2, VD1 and VD2, seem difficult to define. Inclusions based on elements like aluminium and oxygen (AlO) occur more frequently than those based on aluminium, calcium and oxygen (AlCaO). Inclusions based on manganese and oxygen (MnO) or on manganese and sulphur (MnS) were not detected because the optical spectrometer Spectro Lab M10 was not equipped with a photomultiplier for manganese. MnS inclusions were thus derived by calculation from the value S corr. There is a relation MnS = S corr – CaS, where (S corr) is the total content of inclusions incorporating sulphur and (CaS) are the inclusions based on calcium and sulphur. The analysis suggests that the number of inclusions (CaS) means a significant amount. We assume that the remaining number of inclusions based on sulphur has got the form of MnS inclusions. The occurrence and the number of inclusions based on aluminium and nitrogen (AlN) and those based on titanium and nitrogen (TiN) is not important. The occurrence of inclusions based on aluminium and oxygen (CaO) and the sulphur content show mostly the decreasing character. The relatively high and unbalanced contents of inclusions based on silicon and oxygen (SiO) are an oddity.

The graphical presentation of the development in the total number of recorded impulses, in the course of individual technological operations, in all the assessed melts is in **Figure 12**. These data, in the sum of recorded impulses, correspond to the number or, possibly, to the volumes of steel inclusions. The assumption that the curve of recorded impulses would decrease in correspondence to the inclusion analysis made with the assistance of roentgen spectral analysis and the process of steel processing LF1-VD2 has not been quite proved.

Thanks to the graphic assessment in **Figures 8** to **12**, which describe the number of impulses or the relative frequency of the individual elements and melts, we can say in summary that:

- It is very difficult to find any similarity in the number of inclusions in individual samples in a melt and, also, in the technological step
- The similarities of the trends' decreases or increases in individual inclusion types could be followed to a melt or to a technological step
- The occurrence of AlCaO inclusions is not the dominant detected bond
- The occurrence of AlO inclusions is more frequent, when compared with AlCaO inclusions, but the trend after VD2 is relatively balanced in most melts
- The number of AlO and AlCaO inclusions is lower, when compared with VD1<VD2
- The occurrence of CaO inclusions is a dominant part in all the technological steps and it is lower in VD1<VD2
- The number of SiO inclusions is a dominant part in all the technological steps
- When the occurrence of AlO inclusions exceeds the value 0.1, the number of SiO inclusions is lower than AlO
- The number of SiO inclusions shows a lower value in VD1<VD2
- The analysis of the occurrence of the inclusions with the bond MnS or MnO has not been performed because the item for manganese was not purchased for the device and we could not thus analyse it by the SSE method
- The number of S corr inclusions mostly decreases in VD1>VD2; the number of CaS inclusions logically decreases
- The AlN and TiN inclusions do not practically occur and are not created in the liquid stage
- The CaS inclusions make the dominant sulphur bond, while the remaining sulphur amount was not identified and it will possibly be connected with inclusions of the MnS type

- The number of CaO inclusions occurs in a relatively large number
- The number of TiO inclusions is not negligible and it is lower in VD1<VD2
- Some inclusions show in a relatively larger number after vacuuming

The comparison of the two methods assessing some steel purity factors with the assistance of roentgen spectral analysis and the SSE method is suggested in **Table 1**. In spite of the fact that the testing performance identity of both methods was made as much as possible for individual melts and samples, we have not achieved comparable results. It is probable that the volume of the analysed sample part makes an important difference because the roentgen spectral analysis provides for the relative point character of the detection in an area, while the SSE method examines a larger volume of metal. The comparison of the two methods shows that the difference in the number of Al_2O_3-CaO inclusions, which prevail, and the minimum number of CaO inclusions, detected by the roentgen spectral analysis, is the most important. The occurrence of these inclusions is more probable in every technological step, when compared with the smaller number of AlCaO inclusions and the large number of occurring CaO inclusions detected by the SSE method.

Table 1: Comparison of some results measured by the Roentgen spectral analysis and the SSE method

Tabela 1: Primerjava med rezultati, izmerjenimi z rentgensko spektralno analizo in SSE-metodo

	Roentgen spectral analysis-	SSE method
Number of inclusions	It decreases in the course of processing in the order LF1-LF2-VD1-VD2	The number of impulses does not depend on the technological step; usually VD1<VD2
Mn	Assessed	Not assessed
MnS	The assessed Mn and S, they occur at the same time	The calculated MnS = S corr – CaS
AlN, TiN	Not assessed	Assessed
AlCaO	The dominant occurrence of Al_2O_3 and CaO at the same time	Not the dominant detected bond
CaO	It does not practically occur	Relatively frequent
Ti	Titanium oxide makes the dominant element in some inclusions	TiO occur practically in all samples

4 CONCLUSIONS

The new method Single Spark Evaluation, or its variant Spark – Data, which are available for modern optical emission spectrometers, performs an analysis of the chemical composition of steel. At the same time, they may identify the inclusion compositions within conditions of the steel production at Vítkovice Heavy Machinery a.s. The advantage of this method is operability, because the inclusion analysis takes place at the same time as the analysis of the steel's chemical composition. The method has already been implemented in the steelworks of VHM, but the correct interpretation of the measured values and their utilisation within the operative influencing of technological process of melts' processing is still discussed. The conclusions of the performed study partly suggested a further verification process and the practice, which might be utilised when interpreting the measured values.

We recommend not comparing the SSE method with the method of the roentgen spectral analysis. The research of the utilisation of the SSE method should continue in various technological production processes, for example, in the condensing or diffusing de-oxygenation technologies. The used de-oxygenation determines the type of an inclusion and its majority share in steel. Similarly, the same should be applied in various technological production processes. For example, in an EAF and in the technology processing melts by facilities of secondary metallurgy with the assistance of the chemical heating by aluminium (VOD), or in production processes in an EAF and when processing in a LF with the shortened heating and in VD, possibly within other tested combinations.

The current idea considers the fact that in such a way the prepared technological processes would require the creation of etalons - the steel status for the specific kind of inclusions and the technological indicator of contaminated steel or pure steel. The number and the probable size of inclusions will be determined by 3 Sigma, 7 Sigma and 9 Sigma. For example, the differential way for the likely occurrence of fine inclusions, classified for an assessment in accordance with the given technological process, should be tested in a similar way and there should be kinds of inclusions specified and determined for the assessment in accordance with the given technological process.

The study results suggest a chance for the Single Spark Evaluation method's utilisation in the steel working practice when determining the inclusions in an online steel production process with secondary metallurgical facilities LF or VD at Vítkovice Heavy Machinery a.s.

5 REFERENCES

[1] G. Stolte, Secondary Metallurgy, Verlag Stahleisen GmbH, 2002, p. 216

[2] M. Korbáš, M. Raclavský, L. Čamek, Change of quantity, sizes and chemical composition of inclusions during treatment of steel in EAF-LF-VD equipment, METAL 2012, Brno, 2012

[3] M. Korbáš, L. Čamek, Evaluation of the results of steel purity achieved in steel production using SSE method, In 22nd International Conference on Metallurgy and Materials, METAL 2013, Brno, 2013

UDK 621.78:620.178
Professional article/Strokovni članek

ISSN 1580-2949
MTAEC9, 48(5)787(2014)

EFFECT OF DIFFERENT SURFACE-HEAT-TREATMENT METHODS ON THE SURFACE PROPERTIES OF AISI 4140 STEEL

VPLIV RAZLIČNIH TOPLOTNIH OBDELAV POVRŠINE NA LASTNOSTI POVRŠINE JEKLA AISI 4140

Aysun Ayday, Mehmet Durman
Sakarya University, Faculty of Engineering, Department of Metallurgical and Materials Engineering, Sakarya 54187, Turkey
aayday@sakarya.edu.tr

Prejem rokopisa – received: 2013-10-01; sprejem za objavo – accepted for publication: 2013-11-19

In this study, the effect of different heat treatments on the hardness and wear properties of AISI 4140 steel was investigated. Sample surfaces of AISI 4140 steel were modified with traditional induction heat treatment and the new treatment of electrolytic-plasma hardening. The microstructural characteristics of surface-treated steel samples were examined with scanning electron microscopy (SEM). The mechanical properties of the samples including the surface microhardness and modified-layer thickness were also evaluated. The test results indicate that the wear resistance increases with the increasing modified-layer hardness, due to the transformation of the martensitic structure. The electrolytic-plasma hardening is as suitable a technique for improving the mechanical properties of AISI 4140 steel as the traditional hardening method.

Keywords: electrolytic-plasma treatment (EPT), induction, hardness, wear

V tej študiji je bil preiskovan vpliv različnih toplotnih obdelav na trdoto in obrabne lastnosti jekla AISI 4140. Površina vzorcev jekla AISI 4140 je bila obdelana z navadnim indukcijskim kaljenjem in z novim postopkom elektrolitskega utrjevanja s plazmo. Značilnosti mikrostrukture površinsko obdelanih vzorcev jekla so bile preiskane z vrstičnim elektronskim mikroskopom (SEM). Ovrednotene so bile mehanske lastnosti vzorcev, vključno z mikrotrdoto površine in debelino spremenjenega sloja. Rezultati preizkusov kažejo, da se povečuje odpornost proti obrabi s povečanjem trdote modificiranega sloja zaradi pretvorbe v martenzitno mikrostrukturo. Elektrolitsko utrjevanje s plazmo je enako primerna tehnika za izboljšanje mehanskih lastnosti jekla AISI 4140, kot običajna metoda utrjevanja površine.

Ključne besede: elektrolitska obdelava s plazmo (EPT), indukcija, trdota, obraba

1 INTRODUCTION

AISI 4140 steel (DIN 42CrMo4) is a widely used material in industrial applications, such as automotive, aerospace and manufacturing industries. However, the parts required for mechanical working must have not only high strength but also toughness, abrasion resistance and corrosion resistance. AISI 4140 steel includes Cr and Mo alloying elements that provide high hardenability and toughness after the surface treatments.[1,2]

Induction hardening (IH) is one of the most widely employed treatments to improve component durability. It determines, in a workpiece, a tough core with tensile residual stresses and a hard surface layer with compressive stresses, which have proved to be very effective in extending a component's fatigue life and wear resistance.[3,4] On the other hand, the conventional induction-hardening treatment has some disadvantages: distortion, change of coil, surface deformation, etc.[5–7]

Nowadays, the novel electrolytic-plasma treatment (EPT) is one of the most promising surface-hardening methods as an alternative to the induction hardening. EPT has been successfully used to improve the hardness, the wear resistance and the corrosion resistance of materials.[8] When hardening is not necessary for the whole surface or bulk of a material, EPT is a suitable method for treating a specific location on the surface, like the induction hardening.[9] The standard mechanisms of the two hardening treatments include two main steps: the austenitization, during which the material is heated above the critical temperature (but below the melting point) to achieve the austenite formation and the quenching or cooling down, when austenite is transformed into martensite.[10,11] Also, with EPT, the surface-treated zones have an average depth of 0.1–10 mm, exhibiting an increased hardness, improved resistance to wear, better corrosion resistance and higher fatigue strength (e.g., piston ring groove, valve seat, compressor screws, diesel-engine cylinder liners, gears, etc.).[8,12]

The present study aims at determining the wear resistance of AISI 4140 steel treated with different surface-hardening procedures: the induction hardening and the electrolytic-plasma hardening. The modified samples were characterized before and after the wear tests with metallographic, SEM microscopy and microhardness techniques.

2 EXPERIMENTAL PROCEDURE

AISI 4140 steel was selected for the present study and **Table 1** shows its chemical composition. The diameter of cylindrical samples was 20 mm and the height was 10 mm. All the samples were modified with EPT and induction hardening. The EPT voltage, heating and cooling times were 310–260 V, 3 s and 3 s, respectively, and a constant thermal cycle was selected. The specimens were induction hardened with 30 kW and 300 kHz for 6 s and quenched in water. The sample codes and EPT parameters are listed in **Table 2**.

The morphology of the modified layers was investigated with a scanning electron microscope (SEM Jeol, JSM 6060-LU). The hardness measurements were conducted on the cross-sections of the samples with a Vickers microhardness tester. The test load was 100 g for the hardness measurements at the cross-sections. The hardness value was obtained by averaging the results of three measurements. The temperature distribution of the samples from the plasma-treated side to the internal side was investigated via thermocouples during the process. The surface temperature data were collected from the system with the aid of a computer-data-acquisition system. The volume fractions of different phases were measured with an image analyzer on the metallographic sections.

Table 1: Chemical composition (*w*/%) of AISI 4140 steel
Tabela 1: Kemijska sestava (*w*/%) jekla AISI 4140

C	Si	Mn	Cr	Mo	P	S	Fe
0.41	0.21	0.8	0.95	0.18	0.025	0.027	Balance

Table 2: Treatment parameters
Tabela 2: Parametri obdelave

Parameter code	Electrolytic solution	Heating (V)	Cooling (V)	Total time	Thermal cycle
Untreated	Original AISI 4140				
EPT–6	Na_2CO_3; 12 %	310	260	(3 s and 3 s) × 6 = 36 s	6
IH	30 kW, 300 kHz, 6 s				

The wear tests were performed on the original AISI 4140 and on the modified specimens to determine the best process and parameters. All the wear tests were carried out under dry sliding conditions at room temperature using a ball-on-disc (CSM tribometer), friction- and wear-test machine. The counterpart was an Al_2O_3 ball (Ø = 6 mm) used in accordance with DIN 50 324 and ASTM G 99-95a. The tests were performed with a nominal load of 3 N and a sliding speed of 0.10 m/s for the total sliding distance of 200 m.

3 RESULTS AND DISCUSSION

Figure 1 shows the features of the modified layers, observed on the cross-sections of the EPT and induction materials. During both modification treatments, austenite transforms completely or partially into martensite on the surface called the hardened zone (HZ). An amount of the retained austenite may be present in this region.[13] In the neighborhood of the HZ with the base material, a narrow heat-affected zone was observed, consisting of martensite, bainite and some traces of the initial pearlitic structure. These are the most probable structures according to[13,14]. The base-material microstructure is composed of ferrite and pearlite. All the experimental data showing the results of the mechanical tests are given in **Table 3**. The maximum layer thicknesses of the modified surfaces were 5.2 mm for the EPT and 2.1 mm for the IH (**Table 3**). An effective increase in the hardness was observed after the surface heat treatments. The EPT-sample hardness was higher than that of the induction-hardened samples, as shown in **Table 3**. The hardness of the modified layers depends on the martensitic transformation, and its high hardness is usually explained with the martensite volume fraction (MVF).[15,16] The volume fractions of martensite are given in **Table 3**. The martensite volume fraction of the EPT and induction hardening

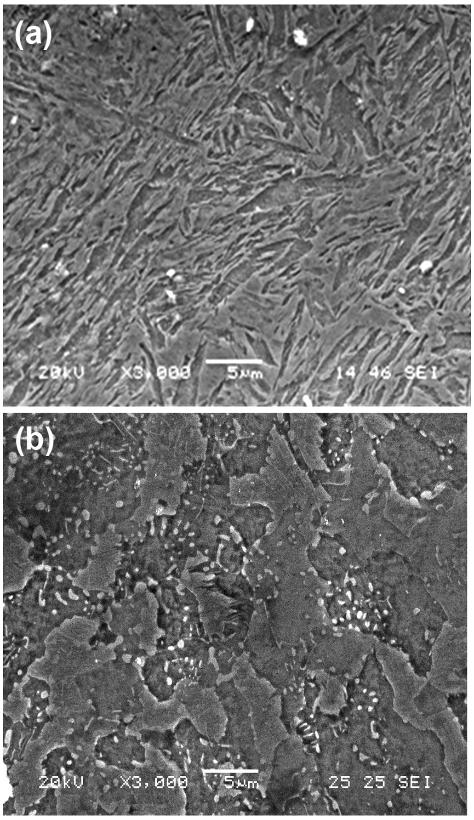

Figure 1: Cross-sectional appearance of modified samples: a) EPT, b) IH
Slika 1: Prerez modificiranega vzorca: a) z EPT, b) z IH

Table 3: General results for modified samples
Tabela 3: Rezultati na modificiranih vzorcih

	Thickness (mm)	Hardness ($HV_{0.1}$)	Surface temperature (°C)	MVF (%)	Friction coefficient	Wear rate (mm^3/(N m))
Untreated	–	200	–	–	0.2	9.06 E–05
EPT	5.2	930	835	47.4	0.203	4.66 E–05
IH	2.1	810	800	39.4	0.377	4.96 E–05

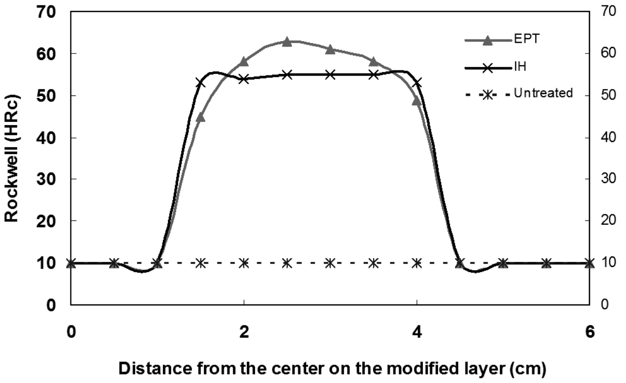

Figure 2: Surface-hardness profiles of untreated AISI 4140, EPT and IH samples
Slika 2: Profil trdote neobdelanega AISI 4140, EPT in IH vzorca

were 47.4 % and 39.4 %, respectively. As shown in **Table 3**, the EPT volume fraction of martensite is higher than in the case of induction because of the surface temperature.

Figure 2 shows the longitudinal hardness profiles for both specimen types. A significant surface hardening was observed on all the modified samples. The hardness of the AISI 4140 steel was 10 HRC. The surface hardness of the specimens increased considerably after the surface-hardening treatments. The surface-hardening behavior of the steel depended on its microstructure constituents, i.e., the martensite (or bainite) morphology and volume fraction with reference to[12,15,17]. The EPT-modified sample shows the maximum hardness in the center, corresponding to the martensitic structure. The hardness along the EPT track decreases rapidly for about 20 mm from its center, while the induction-hardened sample has a single hardness value. This fact can be explained by examining the shape and the intensity profile of the EPT. In addition, the exposure (heating) time is lower at the border of the EPT tracks due to the elliptical nozzle shape. The combination of these two effects results in significantly lower temperatures reached at the external limits of the modified zone, at which the austenization does not take place, so no hard-quenched martensite can be achieved.

Figure 3 shows the wear surfaces of the original AISI 4140, EPT and induction-modified samples, tested at a load of 3 N. The modified samples have quite smooth surfaces with shallow abrasive-wear scars due to the high hardness of the samples. The original AISI 4140 steel was tested under a similar wear-test condition. In this case, the plastic deformation caused due to a low surface hardness is obvious, as shown in **Figure 3**. The lowest wear rate was obtained for the EPT-modified sample followed by the induction-hardened and untreated AISI 4140 samples (**Table 3**). This is due to the microstructure of the sample, consisting of martensite (47.4 % MVF) and having the highest hardness among the tested samples.

4 CONCLUSIONS

In this study, the following results were observed:

AISI 4140 steel surfaces were successfully hardened with the electrolytic-plasma technique and the traditional induction-hardening method. The maximum surface hardness was obtained with the EPT. The maximum microhardness value increased from 200 $HV_{0.1}$ to 930 $HV_{0.1}$ during the experiments. After the wear experiments, the EPT-modified samples had the lowest wear rate, showing almost the same wear resistance as observed for the induction-hardened samples. The untreated samples, as expected, had the highest wear rate. The hardness of the surface is a very important factor with respect to the wear rate. It is a result of the microstructure of the modified samples, which consisted of martensite.

5 REFERENCES

[1] S. Choo, S. Lee, M. G. Golkovski, Materials Science and Engineering A, 293 (**2000**), 56–70

[2] T. Miokovic, V. Schulze, O. Vohringer, D. Lohe, Acta Materialia, 55 (**2007**), 589–599

[3] Y. Totik, R. Sadeler, H. Altun, M. Gavgali, Materials and Design, 24 (**2003**), 25–30

[4] J. Yi, M. Gharghouri, P. Bocher, M. Medraj, Chemistry and Physics, 142 (**2013**), 248–258

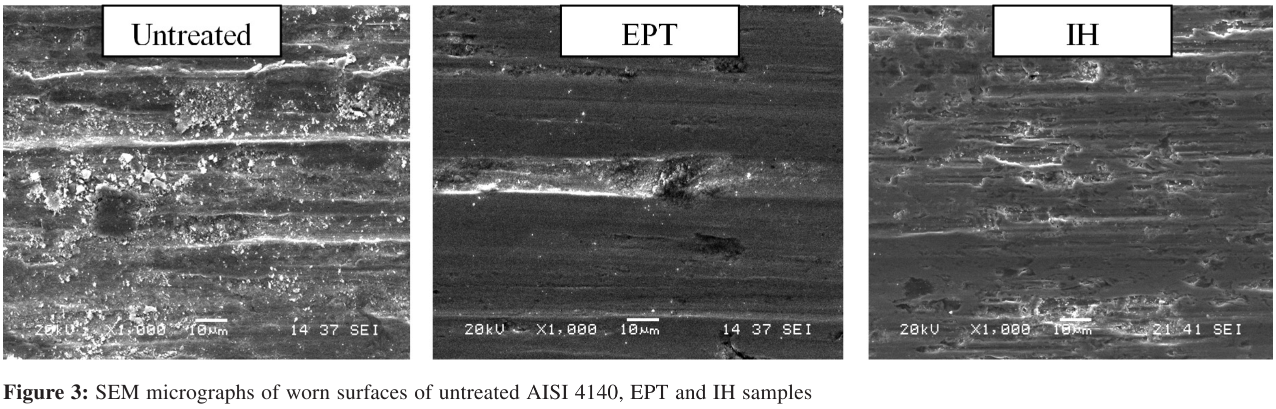

Figure 3: SEM micrographs of worn surfaces of untreated AISI 4140, EPT and IH samples
Slika 3: SEM-posnetki obrabljene površine neobdelanega AISI 4140, EPT in IH vzorca

[5] W. M. Sten, J. Mazumder, Laser Material Processing, 4th ed., Springer, Berlin, 2010, 297

[6] ASM Handbook, Surface Engineering, vol. 5, 10th ed., ASM International, 1994

[7] A. K. Sinha, Physical Metallurgy Handbook, vol. 16-2, McGraw-Hill, 2003

[8] Yu. N. Tyurin, A. D. Pogrebnyak, Surface and Coatings Technology, 142–144 (**2001**), 293–299

[9] C. Ye, S. Suslov, B. J. Kim, E. A. Stach, G. J. Cheng, Acta Materialia, 59 (**2011**), 1014–1025

[10] S. A. Jenabali Jahromi, A. Khajeh, B. Mahmoudi, Materials and Design, 34 (**2012**), 857–862

[11] N. S. Bailey, W. Tan, Y. C. Shin, Surface & Coatings Technology, 203 (**2009**), 2003–2012

[12] A. Ayday, Surface Properties Improvement of Nodular Cast Iron Modified by Electrolytic Plasma Technology, PhD thesis, Sakarya University, 2013

[13] C. Soriano, J. Leunda, J. Lambarri, V. G. Navas, C. Sanz, Applied Surface Science, 257 (**2011**), 7101–7106

[14] C. T. Kwok, K. I. Leong, F. T. Cheng, H. C. Man, Materials Science and Engineering A, 357 (**2003**), 94–103

[15] Y. Sahin, M. Erdogan, M. Cerah, Wear, 265 (**2008**), 196–202

[16] A. Ayday, M. Durman, Mater. Tehnol., 47 (**2013**) 2, 177–180

[17] A. Zare, A. Ekrami, Materials Science and Engineering A, 530 (**2011**), 440–445

UDK 678.7
Professional article/Strokovni članek

ISSN 1580-2949
MTAEC9, 48(5)791(2014)

PREPARATION AND APPLICATION OF POLYMER INCLUSION MEMBRANES (PIMs) INCLUDING ALAMINE 336 FOR THE EXTRACTION OF METALS FROM AN AQUEOUS SOLUTION

PRIPRAVA IN UPORABA MEMBRANE IZ POLIMERA (PIM) IN ALAMINA 336 ZA LOČENJE KOVIN IZ VODNIH RAZTOPIN

Yasemin Yildiz[1], Aynur Manzak[1], Büşra Aydın[1], Osman Tutkun[2]
[1]Department of Chemistry, Sakarya University, Sakarya, Turkey
[2]Beykent University, Department of Chemical Engineering, Engineering and Architecture Faculty, Istanbul, Turkey
manzak@sakarya.edu.tr

Prejem rokopisa – received: 2013-10-12; sprejem za objavo – accepted for publication: 2013-11-12

Polymer inclusion membranes (PIMs) present an attractive approach for the separation of metals from an aqueous solution. The present study is about the application of Alamine 336 as an ion carrier in PIMs. The separation of copper (II), cobalt (II), nickel (II) and cadmium (II) from aqueous solutions with polymer inclusion membranes was investigated. PIMs are formed by casting a solution containing a carrier (extractant), a plasticizer and a base polymer, such as cellulose tri-acetate (CTA) or poly(vinyl chloride) (PVC), to form a thin, flexible and stable film. Several important transport parameters such as the type and amount of the plasticizer, the type of the stripping solution, the thickness of the membrane, the pH of the acid in the donor phase and the concentration of the base in the acceptor phase are discussed. The membrane was characterized to obtain information regarding its composition using AFM, FT-IR and SEM.

Keywords: polymer inclusion membranes, plasticizer, extractant, thickness of membrane

Membrane, ki vsebujejo polimere (PIM), so zanimive za ločenje kovin iz vodnih raztopin. Prikazana je študija uporabe Alamina 336 kot nosilca ionov v PIM. Preiskovano je bilo ločenje bakra (II), kobalta (II), niklja (II) in kadmija (II) iz vodnih raztopin z membrano s polimeri. PIM je bila izdelana z ulivanjem raztopine z nosilcem (ekstraktantom), z mehčalcem in osnovo iz polimera, kot je celuloza-tri-acetat (CTA) ali polivinil klorid (PVC), da je nastala tanka, gibljiva plast. Razloženih je več pomembnih transportnih parametrov, kot so delež mehčalca, vrsta raztopine za snemanje, debelina membrane, pH kisline v donorski fazi in koncentracija baze v aceptorski fazi. Izvršene so bile preiskave z AFM, FT-IR in SEM, da bi dobili podatke o sestavi membrane.

Ključne besede: membrane s polimerom, mehčalec, ekstraktant, debelina membrane

1 INTRODUCTION

The separation of metals from sulphate and chloride media has been of practical interest to the researchers. Solvent extraction is a well-established technology used for the production of metals from a relatively concentrated feed. However, industrial diluent effluents pose an important challenge as the solvent-extraction technique is not cost effective for the separation of metals from a dilute solution[1].

Recently, the supported liquid membrane (SLM) extraction has been emerging as an alternative to the conventional solvent extraction due to its advantages such as high selectivity, operational simplicity, low solvent inventory, low energy consumption, zero effluent discharge, and a combination of extraction and stripping in a single unit[2,3]. Currently, considerable attention is focused upon polymer inclusion membranes (PIMs)[4]. Their specific advantages are an effective carrier immobilization, easy preparation, versatility, stability, good chemical resistance and better mechanical properties than in the case of SLM[5]. The large surface-area-to-volume ratio exhibited by PIMs gives them the potential to be used in nuclear and harmful-metal waste remediation on an industrial scale. They consist of a polymer providing the mechanical strength, a carrier molecule that effectively binds and transports the ions across the membrane, and a plasticizer that provides elasticity and acts as the solvent, in which the carrier molecule can diffuse. PIMs are formed by casting a solution containing a carrier (extractant), a plasticizer and a base polymer, such as cellulose tri-acetate (CTA) or poly(vinyl chloride) (PVC), to form a thin, flexible and stable film[6].

The choice of different constituents of the membrane is crucial to ensure its separation efficiency, so it is important to investigate the effect of different components on the extraction and transport of the target species. Among the polymers used to form a gel-like network that entraps the carrier and plasticizer/modifier, poly(vinyl chloride) (PVC) and cellulose triacetate (CTA) are most frequently encountered[7].

Examples of such membranes are those containing only PVC and Aliquate 336 that have been used successfully for the transport of both metallic (e.g., Cd (II) and Cu (II)[8] and non-metallic (e.g., thiocyanate)[9] ionic species. Moreover, Konczyk et al.[10] have used Aliquate 336 as a plasticizer in a PIM system containing D2EHPA as the carrier for the removal of Cr (III).

The present study focuses on the application of Alamine 336 as an ion carrier in PIMs and deals with the selective separation of Co, Cd, Ni and Cu ions from an acidic media into an NH_4SCN aqueous solution. Amines were used to extract the metal ions. The amine extraction chemistry of thiocyanate complexes was investigated by Sanuki et al.[11]

2 EXPERIMENTAL WORK

2.1 Materials

All the reagents used were of analytical grade. Cellulose triacetate (CTA), 2-nitrophenyl pentyl ether (NPPE) and 2-nitrophenyl octyl ether (NPOE) were obtained from Fluka. Tributyl phosphate (TBP), dichloromethane, $CoCl_2 \cdot 6H_2O$, $NiSO_4 \cdot 6H_2O$, $3CdSO_4 \cdot 8H_2O$, $CuSO_4 \cdot 5H_2O$, acetic acid, NaOH, ammonium, triethanolamine, NH_4SCN and Alamine 336 were of analytical grade (Merck) and all the stock solutions were prepared by dissolving the salts in distilled water.

2.2 Preparation of PIMs

PIMs were prepared in accordance with the casting solution. CTA (480 mg) was dissolved in 70 mL of dichloromethane at room temperature. In the following step 0.1–0.5 mL of 2-NPPE was added into the solution. After stirring, the carrier (Alamine 336 and TBP) was added and the solution was stirred for 6 h to obtain a homogenous solution. The solvent of this mixed solution was allowed to slowly evaporate in a square glass container (24 cm × 24 cm). The organic solvent was allowed to evaporate overnight at room temperature. After the evaporation of the solvent, a few drops of cold and distilled water swirled on the top of the polymer film. Afterwards, the membrane was peeled out of the container. The average thickness of the membrane was determined as 25 µm with a digital micrometer (Salu Tron Combi-D3).

2.3 PIM transport experiment

The prepared polymeric film was sandwiched between two glass cells. The transport of metal ions across the PIM from the aqueous solutions was studied by using a two-compartment permeation cell made from Pyrex glass, having flat-sheet membranes with the 12.56 cm^2 area (*A*), as shown schematically in **Figure 1**.

The volumes of both the aqueous feed and the strip phases were 250 mL. The feed solutions were prepared by adding cobalt, nickel, cadmium and copper salts to study the effect of the feed composition. Ammonium thiocyanate (NH_4SCN) was added into the feed mixture to increase the selectivity of cobalt against nickel. 1 M acetic acid/1 M sodium acetate buffer was used to maintain the desired feed pH. A stripping solution containing 1 M NH_3 + 1 M TEA was selected as the stripping-phase mixture. The feed and stripping phases were mechanically stirred at the desired mixing speed of (20 ± 1) °C to avoid the concentration polarization conditions at the membrane interfaces and in the bulk of the solutions. During the PIM-transport experiments, the samples of the feed and strip phases (about 1 mL) were periodically removed for a determination of the metal concentration with ICP-OES.

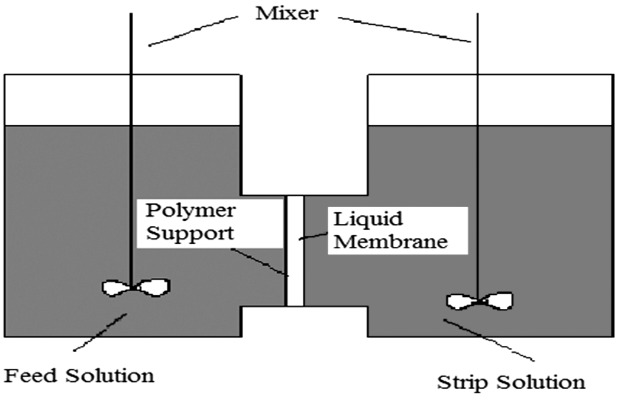

Figure 1: Schematic diagram of the experimental apparatus
Slika 1: Shema naprave za preizkuse

3 RESULTS AND DISCUSSION

3.1 Plasticizer type and concentration

The nature of the plasticizer used to form the membrane is also a key parameter to consider. Plasticizers are organic compounds incorporating a hydrophobic alkyl backbone and one or several highly solvating polar groups. They are added to hard, stiff plastics to make them softer and more flexible. The softening action of the plasticizers, plasticization, is usually attributed to their ability to reduce the intermolecular attractive forces between the polymer chains. For this reason, it is anticipated that in PIMs the presence of these compounds may also influence the mobility of membrane components, the degree of interaction between different constituents of the membrane and the characteristics of the polymeric medium[7]. A low plasticizer concentration may cause more rigid and brittle membranes. So, it is not preferred[4]. The minimum plasticizer concentration varies widely depending on both the plasticizer and the base polymer. The influence of the plasticizer nature on the Cd^{2+}, Co^{2+}, Ni^{2+}, and Cu^{2+} transport through PIMs with different plasticizers, i.e., 2-Nitrophenyl octyl ether (NPOE) and 2-nitrophenyl pentyl ether (NPPE) was tested. Copper was precipitated in the feed phase. Nickel was not transferred to the stripping solution. The cobalt and cadmium ions in the acidic feed solutions reacted with the excess NH_4SCN, whereas in the case of nickel ions, they hardly formed a thiocyanate complex[12,13].

The results obtained for the Cd^{2+} and Co^{2+} ion transport with different concentrations of the plasticizers

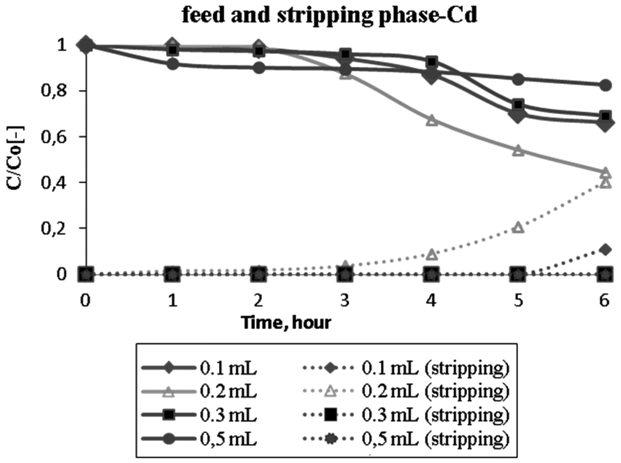

Figure 2: Effect of the NPPE concentration on the cadmium extraction (feed phase: 100 mg/L Co^{2+}, 100 mg/L Ni^{2+}, 100 mg/L Cd^{2+}, 100 mg/L Cu^{2+}; feed stirring speed: 1200 r/min; strip-phase stirring speed: 1200 r/min; strip solution: 1 M NH_3 + 1 M TEA; complex reagent (NH_4SCN): 0.5 mol/l; temp.: 20 °C; feed solution pH: 4)

Slika 2: Vpliv koncentracije NPPE na ekstrakcijo kadmija (iz raztopine: 100 mg/L Co^{2+}, 100 mg/L Ni^{2+}, 100 mg/L Cd^{2+}, 100 mg/L Cu^{2+}; hitrost mešanja raztopine: 1200 r/min; hitrost mešanja v fazi traku: 1200 r/min; raztopina traku: 1 M NH_3 + 1 M TEA; kompleksni reagent (NH_4SCN): 0.5 mol/l; Temp.: 20 °C; raztopina pH: 4)

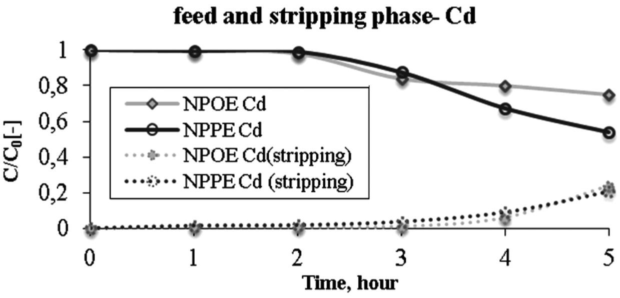

Figure 4: Effect of the plasticizer type on the cadmium transport (feed phase: 100 mg/L Co^{2+}, 100 mg/L Ni^{2+}, 100 mg/L Cd^{2+}, 100 mg/L Cu^{2+}; feed stirring speed: 1200 r/min; strip-phase stirring speed: 1200 r/min; strip solution: 1 M NH_3 + 1 M TEA; complex reagent (NH_4SCN): 0.5 mol/l; temp.: 20 °C; feed solution pH: 4)

Slika 4: Vpliv vrste mehčalca na prenos kadmija (raztopina: 100 mg/L Co^{2+}, 100 mg/L Ni^{2+}, 100 mg/L Cd^{2+}, 100 mg/L Cu^{2+}; hitrost mešanja raztopine: 1200 r/min; hitrost mešanja v fazi traku: 1200 r/min; raztopina traku: 1 M NH_3 + 1 M TEA; kompleksni reagent (NH_4SCN): 0.5 mol/l; Temp.: 20 °C; raztopina pH: 4)

in the PIMs are shown in **Figures 2** and **3**. For NPPE, this concentration can be in the range of up to 0.2 mL (*w* = 27 %) (**Figure 2**). Above this upper limit the mass transport diminishes.

The results obtained for the Cd^{2+} and Co^{2+} ion transport with different types of plasticizers in the PIMs are shown in **Figures 4** and **5**. 2-Nitrophenyl pentyl ether (NPPE) is the most frequently used plasticizer in PIMs due to its high dielectric constant that enhances the membrane permeability. A decrease in the permeability, together with an increase in the plasticizer content, is probably related to a reduction in the viscosity of the medium[4].

The recovery factor (*RF*) of the metal ions from the feed phase into the stripping phase is given by:

$$RF=\frac{C_I - C}{C_I}\cdot 100\% \tag{1}$$

where *C* is the metal-ion concentration in the feed phase at some given time and C_i is the initial metal-ion concentration in the feed phase. Recovery factors (*RF*) for different plasticizers are shown in **Table 1**.

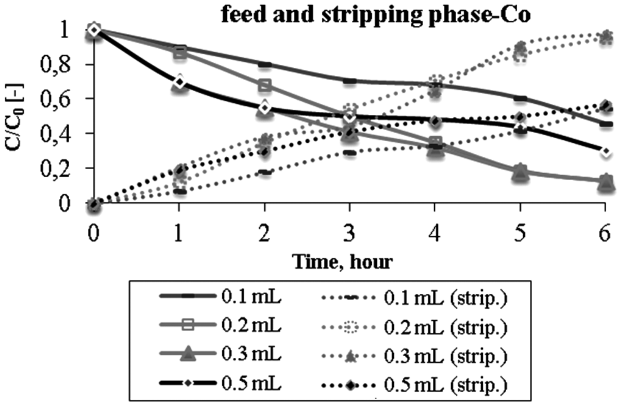

Figure 3: Effect of the NPPE concentration on the cobalt extraction (feed phase: 100 mg/L Co^{2+}, 100 mg/L Ni^{2+}, 100 mg/L Cd^{2+}, 100 mg/L Cu^{2+}; feed stirring speed: 1200 r/min; strip-phase stirring speed: 1200 r/min; strip solution: 1 M NH_3 + 1 M TEA; complex reagent (NH_4SCN): 0.5 mol/l; temp.: 20 °C; feed solution pH: 4)

Slika 3: Vpliv koncentracije NPPE na ekstrakcijo kobalta (raztopina: 100 mg/L Co^{2+}, 100 mg/L Ni^{2+}, 100 mg/L Cd^{2+}, 100 mg/L Cu^{2+}; hitrost mešanja raztopine: 1200 r/min; hitrost mešanja v fazi traku: 1200 r/min; raztopina traku: 1 M NH_3 + 1 M TEA; kompleksni reagent (NH_4SCN): 0.5 mol/l; temp.: 20 °C; raztopina pH: 4)

Table 1: Effect of the plasticizer type on the cobalt and cadmium transport

Tabela 1: Vpliv vrste mehčalca na prenos kobalta in kadmija

Plasticizer type	*RF* (Co)	*RF* (Cd)

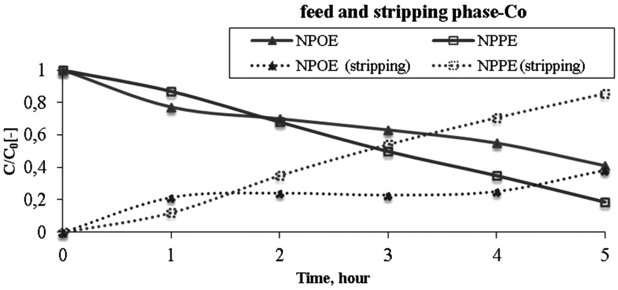

Figure 5: Effect of the plasticizer type on the cobalt transport (feed phase: 100 mg/L Co^{2+}, 100 mg/L Ni^{2+}, 100 mg/L Cd^{2+}, 100 mg/L Cu^{2+}; feed stirring speed: 1200 r/min; strip-phase stirring speed: 1200 r/min; strip solution: 1 M NH_3 + 1 M TEA; complex reagent (NH_4SCN): 0.5 mol/l; temp.: 20 °C; feed solution pH: 4)

Slika 5: Vpliv vrste mehčalca na prenos kobalta (raztopina: 100 mg/L Co^{2+}, 100 mg/L Ni^{2+}, 100 mg/L Cd^{2+}, 100 mg/L Cu^{2+}; hitrost mešanja raztopine: 1200 r/min; hitrost mešanja v fazi traku: 1200 r/min; raztopina traku: 1 M NH_3 + 1 M TEA; kompleksni reagent (NH_4SCN): 0.5 mol/l; temp.: 20 °C; raztopina pH: 4)

NPOE	59	25
NPPE	81	46

3.2 Effect of the stripping-solution type

In general, metallic ions extracted by amines can be stripped from the protonated amine with the removal of a proton using neutral or alkaline solutions. 1 M ammonia and 1 M triethanol amine solution mixtures were used as the reagents to strip and separate the cobalt and cadmium from the membrane phase to the aqueous phase.

3.3 Membrane characteristics

One important aspect of PIMs is the microstructure of the membrane materials, which determines the distribution of the carriers in the polymer matrix and ultimately affects the membrane transport efficiency. Consequently, a considerable research effort was devoted to clarifying this issue. While a variety of surface-characterization techniques were employed in these studies, scanning electron microscopy (SEM) and atomic force microscopy (AFM) were most frequently used. The results obtained from the SEM and AFM studies consistently indicate a remarkable influence of the polymeric composition on the membrane morphology.

The membrane was characterized to obtain information regarding its composition using AFM (**Figure 6**), SEM (**Figure 7**) and FT-IR (**Figure 8**).

The AFM technique was used to characterize the surface morphology of the prepared membranes. The AFM picture of the PIM formed with CTA + NPPE + TBP + Alamine 336 is shown in **Figure 6**. The surface morphology of the membrane shows a rough surface. These regions may have occurred because of either a different speed of the solvent vaporization[14, 15] or the membrane having a porous structure where the pores were filled by NPPE or NPPE + Alamine 336 + TBP[16,17].

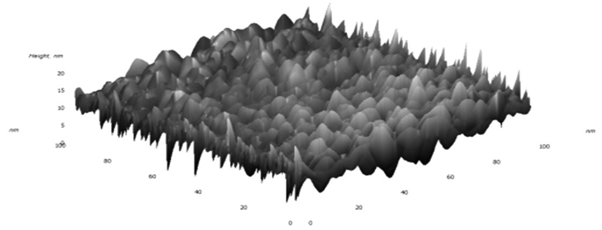

Figure 6: CTA + NPPE + Alamine 336 + TBP, AFM image
Slika 6: AFM-posnetek CTA + NPPE + Alamin 336 + TBP

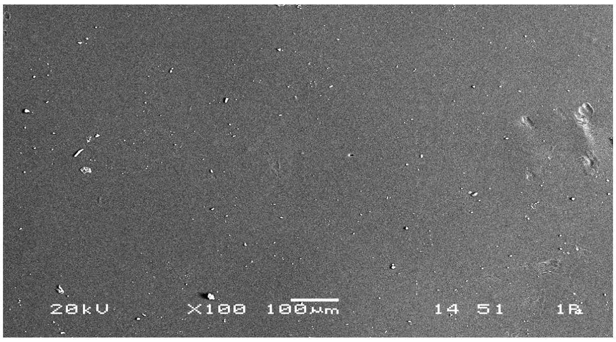

Figure 7: CTA + NPPE + Alamine 336 + TBP, SEM image
Slika 7: SEM-posnetek CTA + NPPE + Alamin 336 + TBP

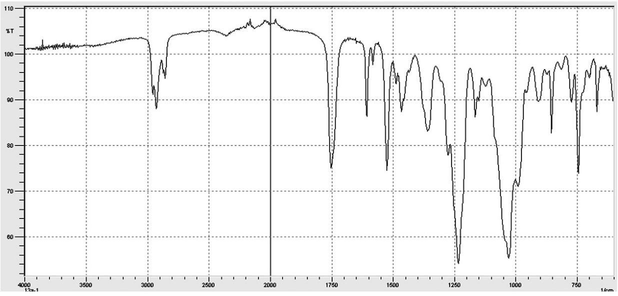

Figure 8: CTA + NPPE + Alamine 336 + TBP, FT-IR
Slika 8: FT-IR-posnetek CTA + NPPE + Alamin 336 + TBP

Although both SEM and AFM techniques are versatile and can provide a good image of the membrane surface and, to some degree, of the membrane interior structure, to date, the studies employing these techniques have not been able to clearly elucidate the distribution of the carrier and the plasticizer within the membrane. Consequently, more advanced material-characterization techniques have been attempted.[4]

In order to investigate the absorption bands of the constituents of the membranes containing CTA + NPPE+ Alamine 336 + TBP, FTIR was performed as shown in **Figure 8**. The bands at 2986 cm^{-1} and 2936 cm^{-1} were attributed to the stretching vibration of C–H in $-CH_2$ and $-CH_3$. The absorption at 1750 cm^{-1} was assigned to the stretching vibration of C=O in CTA.

The fingerprint region of the spectra becomes complicated because of the P–O, C–O and C–N vibrations. These three vibrations are absorbed in the same region. For example, the peaks in the 1250 cm^{-1} and 1100 cm^{-1} region appear in both CTA and TBP and they overlap completely. The expected peaks in the spectra appear in almost the same region as in the case of pure components like CTA, Alamine 336 and TBP. This indicates that these four compounds do not form any new covalent interactions, but only secondary interactions like hydrogen bonding or electrostatic interactions[18].

Consequently, the analysis and comparison of the obtained spectra revealed that all the membrane constituents remained as pure components inside the membrane[17,18]. The surface of the films shows a good uniformity and the absence of cracks indicates a good regularity of the membranes as shown in **Figure 7**.

3.4 Membrane thickness

The investigated membrane thickness was 20 µm to 45 µm, shown in **Figures 9** and **10**. The best recovery factor (*RF*) was obtained with a thickness of 25 µm, with 81 % in the feed phase over 5 h as shown in **Table 2**. The

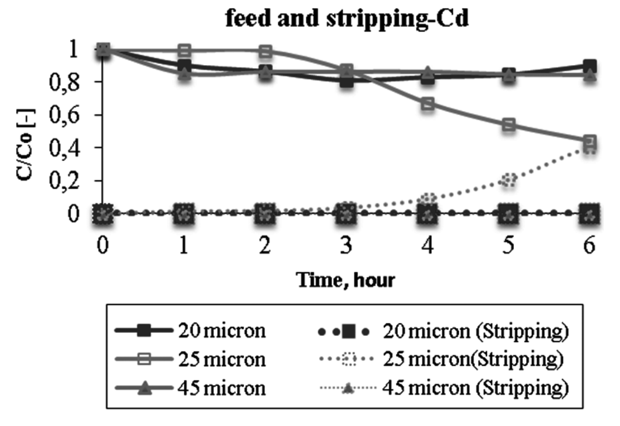

Figure 9: Effect of the membrane thickness on the cadmium transport (feed phase: 100 mg/L Co^{2+}, 100 mg/L Ni^{2+}, 100 mg/L Cd^{2+}, 100 mg/L Cu^{2+}; feed stirring speed: 1200 r/min; strip-phase stirring speed: 1200 r/min; strip solution: 1 M NH_3 + 1 M TEA; complex reagent (NH_4SCN): 0.5 mol/l; temp.: 20 °C; feed-solution pH: 4)

Slika 9: Vpliv debeline membrane na prenos kadmija (raztopina: 100 mg/L Co^{2+}, 100 mg/L Ni^{2+}, 100 mg/L Cd^{2+}, 100 mg/L Cu^{2+}; hitrost mešanja raztopine: 1200 r/min; hitrost mešanja v fazi traku: 1200 r/min; raztopina traku: 1 M NH_3 + 1 M TEA; kompleksni reagent (NH_4SCN): 0.5 mol/l; temp.: 20 °C; raztopina pH: 4)

Table 2: Effect of the membrane thickness on the cobalt and cadmium transport

Tabela 2: Vpliv debeline membrane na prenos kobalta in kadmija

Membrane thickness (μm)	*RF* (Co)	*RF* (Cd)
20	39	15
25	81	46
45	54	15

optimum membrane thickness was 25 μm. As the membrane thickness increased, the extraction would decrease.

As shown in[19] thinner membranes exhibiting high permeability are formed. However, the thinnest membranes only partly allow high permeability due to a decrease in the extractant content limiting the transport efficiency.

As shown in reference[20] the flux decreased linearly with the membrane thickness. This is unambiguous evidence that the slow step in the transport process represents the migration through the membrane and not a decomplexation from the carrier.

4 CONCLUSIONS

With the use of Alamine 336 and TBP as the carriers, the competitive transport of metal ions shows the preferential selectivity order: Co (II) > Cd (II). The transport facilitated through the polymer inclusion membranes containing Alamine 336 and TBP was found to be an effective method for separation and recovery of cobalt (II) and cadmium (II) from aqueous solutions. Copper was precipitated in the feed phase. Nickel was not transferred to the stripping solution. The recovery factor for the cobalt ions was over 87 % over a period 6 h.

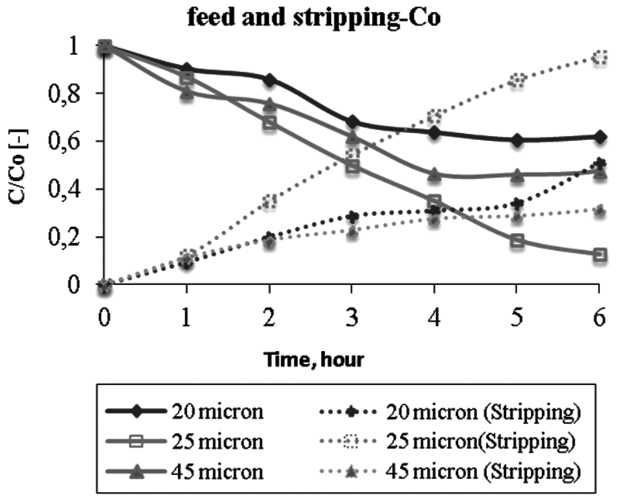

Figure 10: Effect of the membrane thickness on the cobalt transport (feed phase: 100 mg/L Co^{2+}, 100 mg/L Ni^{2+}, 100 mg/L Cd^{2+}, 100 mg/l Cu^{2+}; feed stirring speed: 1 200 r/min; strip-phase stirring speed: 1200 r/min; strip solution: 1 M NH_3 + 1 M TEA; complex reagent (NH_4SCN): 0.5 mol/l; temp.: 20 °C; feed solution pH: 4)

Slika 10: Vpliv debeline membrane na prenos kobalta (raztopina: 100 mg/l Co^{2+}, 100 mg/l Ni^{2+}, 100 mg/l Cd^{2+}, 100 mg/l Cu^{2+}; hitrost mešanja raztopine: 1 200 r/min; hitrost mešanja v fazi traku: 1 200 r/min; raztopina traku: 1 M NH_3 + 1 M TEA; kompleksni reagent (NH_4SCN): 0.5 mol/l; temp.: 20 °C; raztopina pH: 4)

Acknowledgement

The financial support of this work, provided by the scientific research commission of Sakarya University (BAPK), Project No: 2010-02-04-025, is gratefully acknowledged.

5 REFERENCES

[1] G. M. Ritcey, A. W. Ashbrook, Solvent Extraction Principles and Applications to Process Metallurgy, volume 2, Elsevier, Amsterdam 1979, 279–361

[2] B. Swain, K. Sarangi, R. P. Das, Separation of cadmium and zinc by supported liquid membrane using TOPS-99 as mobile carrier, Sep. Sci. Technol., 39 (**2004**) 9, 2171–2188

[3] B. Swain, K. Sarangi, R. P. Das, Effect of different anions on separation of cadmium and zinc by supported liquid membrane using TOPS-99 as mobile carrier, Journal of Membrane Science, 277 (**2006**) 1–2, 240–248

[4] L. D. Nghiem, P. Mornane, I. D. Potter, J. M. Perera, R. W. Cattrall, S. D. Kolev, Extraction and transport of metal ions and small organic compounds using polymer inclusion membranes (PIMs), Journal of Membrane Science, 281 (**2006**), 7–41

[5] A. O. Saf, S. Alpaydin, A. Coskun, M. Ersoz, Selective transport and removal of Cr(VI) through polymer inclusion membrane containing 5-(4-phenoxyphenyl)-6H-1,3,4-thiadiazin-2-amine as a carrier, Journal of Membrane Science, 377 (**2011**), 241–248

[6] C. Sgarlata, G. Arena, E. Longo, D. Zhang, Y. Yang, R. A. Bartsch, Heavy metal separation with polymer inclusion membranes, Journal of Membrane Science, 323 (**2008**), 444–451

[7] O. Kebiche-Senhadji, S. Tingry, P. Seta, M. Benamor, Selective extraction of Cr(VI) over metallic species by polymer inclusion membrane (PIM) using anion (Aliquat 336) as carrier, Desalination, 258 (**2010**), 59–65

[8] L. Wang, R. Paimin, R. W. Cattrall, W. Shen, S. D. Kolev, The extraction of cadmium (II) and copper (II) from hydrochloric acid solutions using an Aliquat 336/PVC membrane, Journal of Membrane Science, 176 (**2000**), 105–111

[9] Y. Cho, C. Xu, R. W. Cattrall, S. D. Kolev, A polymer inclusion membrane for extracting thiocyanate from weakly alkali solutions, Journal of Membrane Science, 367 (**2011**), 85–90

[10] J. Konczyk, C. Kozlowski, W. Walkowiak, Removal of chromium (III) from acidic aqueous solution by polymer inclusion membranes with D2EHPA and Aliquat 336, Desalination, 263 (**2010**), 211–216

[11] S. Sanuki, M. Yata, H. Majima, Stripping of silver from Primene JMT loaded with silver thiocyanate complexes, Hydrometallurgy, 52 (**1999**), 123–135

[12] M. S. Uddin, M. Kathiresan, Extraction of metal ions by emulsion liquid membrane using bi-functional surfactant: equilibrium and kinetic studies, Sep. Pur. Technol., 19 (**2000**) 1–2, 3–9

[13] R. R. Amirov, Influence of cations on the formation of cobalt (II) complexes with thiocyanate ions in solutions of nonionic micelles, Russ. J. Coord. Chem., 29 (**2003**), 559–563

[14] C. A. Kozlowski, W. Walkowiak, Applicability of liquid membranes in chromium (VI) transport with amines as ion carriers, Journal of Membrane Science, 266 (**2005**), 143–150

[15] A. Tor, G. Arslan, H. Muslu, A. Celiktas, Y. Cengeloglu, M. Ersoz, Facilitated transport of Cr(III) through polymer inclusion membrane with di(2-ethylhexyl)phosphoric acid (DEHPA), Journal of Membrane Science, 329 (**2009**), 169–174

[16] M. Ulewicz, U. Lesinska, M. Bochenska, Transport of lead across polymer inclusion membrane with p-tert-butylcalix [4] arene derivative, Physicochem. Probl. Miner. Process., 44 (**2010**), 245–256

[17] N. Bayou, O. Arous, M. Amara, H. Kerdjoudj, Elaboration and characterization of a plasticized cellulose triacetate membrane containing trioctylphosphine oxyde (TOPO): Application to the transport of uranium and molybdenum ions, C. R. Chim., 13 (**2010**), 1370–1376

[18] O. Kebiche-Senhadji, L. Mansouri, S. Tingry, P. Seta, M. Benamor, Facilitated Cd(II) transport across CTA polymer inclusion membrane using anion (Aliquat336) and cation (D2EHPA) metal carriers, Journal of Membrane Science, 310 (**2008**), 438–445

[19] E. R. San Miguel, M. Monroy-Barreto, J. C. Aguilar, A. L. Ocampo, J. Gyves, Structural effects on metal ion migration across polymer inclusion membranes: Dependence of membrane properties and transport profiles on the weight and volume fractions of the components, Journal of Membrane Science, 379 (**2011**), 416–425

[20] A. Gherrou, H. Kerdjoudj, R. Molinari, P. Seta, Preparation and characterization of polymeric plasticized membranes (PPM) embedding a crown ether carrier application to copper ions transport, Materials Science and Engineering C, 25 (**2005**), 436–443

UDK 621.77:669.111.3
Professional article/Strokovni članek

ISSN 1580-2949
MTAEC9, 48(5)797(2014)

ACCELERATED CARBIDE SPHEROIDISATION AND REFINEMENT (ASR) OF THE C45 STEEL DURING CONTROLLED ROLLING

POSPEŠENA SFEROIDIZACIJA IN UDROBNJENJE KARBIDOV (ASR) PRI KONTROLIRANEM VALJANJU JEKLA C45

Daniela Hauserova, Jaromir Dlouhy, Zbysek Novy
COMTES FHT, Prumyslova 995, 334 41 Dobrany, Czech Republic
daniela.hauserova@comtesfht.cz

Prejem rokopisa – received: 2013-10-14; sprejem za objavo – accepted for publication: 2013-11-06

Current industry trends include the search for cost- and energy-saving procedures and technologies. A new process has been discovered recently, which allows a significant refinement of ferrite grains and a carbide spheroidisation in a shorter time than in the case of conventional heat-treatment techniques. During this newly-developed ASR-based (accelerated spheroidisation and refinement) plastic deformation an accelerated spheroidisation and a refinement due to the heat treatment in the vicinity of the A_1 temperature occur.

Controlled rolling enables a production of the materials with a fine microstructure and better mechanical properties than conventional production processes. Accelerated carbide spheroidisation and refinement (ASR) is aimed to produce steel workpieces with a microstructure consisting of a fine-grained ferrite matrix and globular carbide particles. In carbon steels, this microstructure has higher yield strength and toughness than the conventional ferritic-pearlitic microstructure.

The presented paper describes the effect of the ASR process on the C45 steel. The pearlite morphology was influenced by forming it at the temperatures around critical temperature A_1 and an accelerated carbide-particle spheroidisation was achieved. The deformation increases the dislocation density and enhances the diffusion rate. Cementite globules form rapidly, within seconds or minutes at the most.

Keywords: accelerated spheroidisation, refinement, rolling, C45 steel

Sedanje usmeritve industrije vključujejo tudi iskanje stroškovno in energijsko ugodnejših postopkov in tehnologij. Razvit je bil nov postopek, ki omogoča znatno udrobnjenje zrn ferita in sferoidizacijo karbidov v krajšem času v primerjavi s konvencionalnimi tehnikami toplotne obdelave. Pri tej novo razviti plastični deformaciji, na kateri temelji ASR (pospešena sferoidizacija in udrobnjenje), se pri plastični deformaciji pojavi pospešena sferoidizacija in udrobnjenje med toplotno obdelavo v bližini temperature A_1.

Kontrolirano valjanje omogoča izdelavo materialov z drobno mikrostrukturo in z boljšimi mehanskimi lastnostmi kot pri navadnih proizvodnih procesih. Namen pospešene sferoidizacije karbidov in udrobnjenja zrn (ASR) je izdelava jekla z mikrostrukturo iz drobnih zrn ferita in globularnih karbidnih zrn. Pri ogljikovih jeklih ima ta mikrostruktura višjo mejo tečenja in večjo žilavost kot navadna feritno-perlitna mikrostruktura.

Članek opisuje učinek ASR-procesa na jeklo C45. Na morfologijo perlita se vpliva s preoblikovanjem pri temperaturah okrog kritične temperature A_1, in s tem je dosežena sferoidizacija karbidnih delcev. Deformacija povečuje gostoto dislokacij in poveča hitrost difuzije. Globularni cementit največkrat nastane v nekaj sekundah ali minutah.

Ključne besede: pospešena sferoidizacija, udrobnjenje, valjanje, jeklo C45

1 INTRODUCTION

The current processes leading to a carbide-particle spheroidisation rely on diffusion of carbon in a workpiece heated to a temperature close to or slightly below A_{c1}.[1] Diffusion-based processes of this type are usually time-consuming and the times of up to tens of hours[2] make this type of annealing a very expensive heat-treatment process. During annealing, softening processes occur in the microstructure and, in some cases, a recovery and a recrystallization also take place.[3] The strength and hardness of the steel workpiece decline, whereas its ductility and plastic-deformation capability are increased. The newly-designed and patented thermomechanical process brings a several-fold reduction in the processing time and cost.[4,5]

The present paper describes an investigation of the influence of the plastic-deformation intensity and strain applied at various stages of transformation on the steel microstructure and mechanical properties. A significant acceleration of the process is due to the steel heating at a temperature just below transformation temperature A_{c1} and the plastic strain.[6]

2 EXPERIMENTAL WORK

2.1 Material and thermomechanical treatment

The experimental work was performed using the carbon steel C45 with the chemical composition listed in **Table 1**. The initial microstructure consisted of ferrite and lamellar pearlite with pronounced banding along the bar axis (**Figure 1**). The hardness of the as-received material was 180 HV, the 0.2 proof stress was 345 MPa, the ultimate tensile strength was 629 MPa, the elongation was A_5 = 29 % and the impact toughness was KCV = 29 J/cm^2.

Table 1: Chemical composition of the C45 steel (mass fractions, *w*/%)
Tabela 1: Kemijska sestava jekla C45 (masni deleži, *w*/%)

C	Si	Mn	S	P	Cr	Ni	Cu	Mo	W
0.42	0.24	0.69	0.019	0.016	0.12	0.16	0.12	0.02	0.01

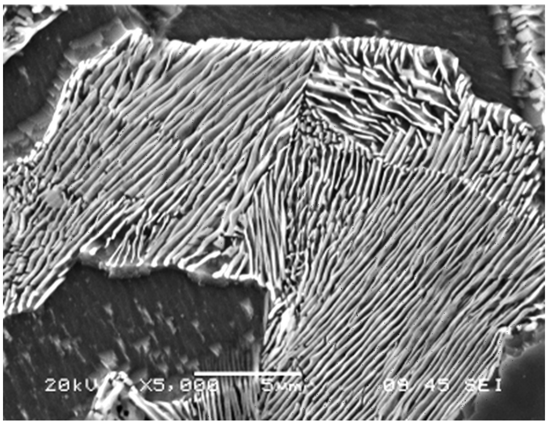

Figure 1: SEM micrograph of the initial state
Slika 1: SEM-posnetek začetne mikrostrukture

The thermomechanical treatment was carried out in a universal rolling mill that can be configured as either a four-high rolling mill or a two-high mill. The two-high configuration is used for hot rolling. The working roll diameter is 550 mm. The maximum width of the rolled plate is 400 mm and the thickness may range from 100 mm to 5 mm. The maximum rolling speed is 1.5 m/s. During rolling the induction heating system, situated on both sides of the rolling mill, can be used and a water-spray facility for quenching is provided on the mill. The rolling mill also includes hydraulic shears. The initial dimensions of the specimens for thermomechanical treatment were 330 mm × 50 mm × 30 mm.

Thermomechanical-treatment schedules (**Table 2**) were proposed for investigating the impact of the strain magnitude and the strains applied at various stages of the pearlitic transformation on the microstructure and mechanical properties. The main focus was the degree of carbide spheroidisation and ferrite-grain refinement.

Austenitizing at 850 °C was followed by a thickness reduction with the isothermal strain of $\varphi = 0.4$. Before the second and third deformations, the specimens were air cooled. The second and third deformation steps were applied at various stages of the austenite-to-pearlite transformation (I, II, III – **Figure 2**). The strain magnitudes applied at these lower temperatures and at various stages of the pearlitic transformation were 0.5 (one pass) or 1 (two passes). When two passes were used, they immediately followed each other and took place at a virtually equal temperature. The temperature at point I was approximately 675 °C. At point II, it was 685 °C and at point III it was 675 °C. In all the cases, the deformation speed was 1.5 m/s. After the last pass, the specimens were either air cooled or quenched in water. The quenching immediately followed the last pass to allow a later determination of the austenite content.

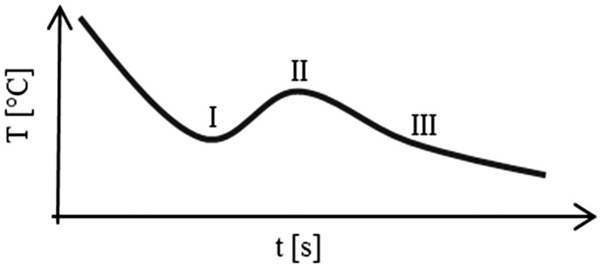

Figure 2: Transformation stages during deformation
Slika 2: Faze transformacije pri deformaciji

3 RESULTS AND DISCUSSION

3.1 Metallographic observation

Specimens 1w, 2w, 3w were processed using the schedules with a deformation at 850 °C applied at various stages of the transformation (I, II, III) and quenched in water. The metallographic examination clearly revealed varying amounts of martensite in the microstructure. In the course of the last deformation, the expected austenite amounts in the specimens in schedules 1w, 2w and 3w were approximately 50 %, 25 % and 10 % max., respectively. These fractions correspond

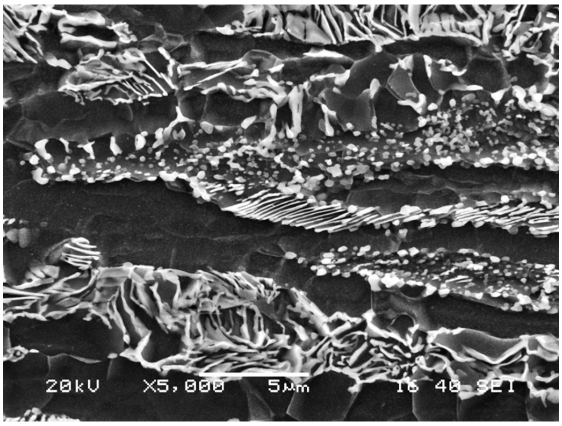

Figure 3: SEM micrograph of the 4a specimen
Slika 3: SEM-posnetek mikrostrukture vzorca 4a

Table 2: List of schedules
Tabela 2: Seznam poteka preizkusov

Schedule	Temperature of first deformation φ =0.4	Temperature of second deformation φ = 0.5	Temperature of third deformation φ = 0.5	Cooling
1a	850 °C	I	-	Air
1w	850 °C	I	-	Water
2a	850 °C	II	-	Air
2w	850 °C	II	-	Water
3a	850 °C	III	-	Air
3w	850 °C	III	-	Water
4a	850 °C	I	I	Air
4w	850 °C	I	I	Water
5a	850 °C	II	II	Air
5w	850 °C	II	II	Water
6a	850 °C	III	III	Air
6w	850 °C	III	III	Water

to the fractions of lamellar pearlite in the air-cooled specimens (1a, 2a, 3a). The lamellar pearlite exhibits no sign of spheroidisation or lamellae fragmentation and it is assumed that the pearlite formed after the deformation. However, in the pearlite already present in the microstructure during the last deformation, the lamellae were transformed into elongated particles or, less frequently, to globules and only a small fraction of the initial pearlite lamellae spheroidised completely.

The 4a, 5a and 6a schedules comprised a deformation at 850 °C, consisting of two deformation steps at various stages of transformation, and the final air cooling. The specimens contained two pearlite morphologies, as in the 1a, 2a and 3a specimens, with parts of lamellar pearlite and, by regions, with globules and rod-like cementite particles. The fraction of lamellar pearlite decreases from the 4a to the 6a schedule (**Figures 3** and **4**), i.e., with the progress of transformation of the austenite present during the plastic deformation. The amount of austenite was found by mapping the martensite fraction in water-quenched specimens 4w, 5w and 6w, with the decreasing martensite proportion in this order.

The mechanical deformation of austenite at transformation stages I or II (**Figure 2**) caused it to transform to lamellar pearlite, as in the transformation of the austenite unaffected by deformation. The deformation of lamellar pearlite with the strain magnitude $\varphi = 0.5$ at stages I, II or III led to a fragmentation of the lamellae and to a formation of predominantly elongated cementite particles. Strain magnitude 1 (i.e., two passes with the strains of 0.5) caused a partial spheroidisation of pearlite lamellae at all the stages of the pearlitic transformation, producing cementite in the form of globules and rod-like particles.

3.2 Ferrite Grains

The characteristics of the ferrite grains in the microstructure depend strongly on the transformation stage (I, II or III), at which deformation was applied (**Figure 2**).

The strain of 0.5 applied at stage I led to a 90 % recrystallization of ferrite. The resulting grain size was less than 8 μm (**Figure 5**). The strain of 0.5 applied at stages II and III caused a recrystallization of only a small fraction of ferrite grains. Approximately 80 % of the ferrite grains exhibited a deformation substructure with elongated grains and deformation-induced subgrains (**Figure 6**). The size of the elongated ferrite grains was approximately 20 μm.

In the case of the strain of magnitude 1, the differences between the ferrite grains after the schedules involving the deformation at stages I and III were smaller. The larger strain caused a recrystallization of approximately 50 % of the ferrite grains even after the deformation applied at stage III (**Figures 4** and **7**). Upon schedules 4a, 5a and 6a, the size of the recrystallized grains was 4 μm. Scarcely recrystallized grains with the size of approximately 10 μm were also observed. With an EBSD analysis the grain size and the volume fractions of deformed and recrystallized grains could be assessed.

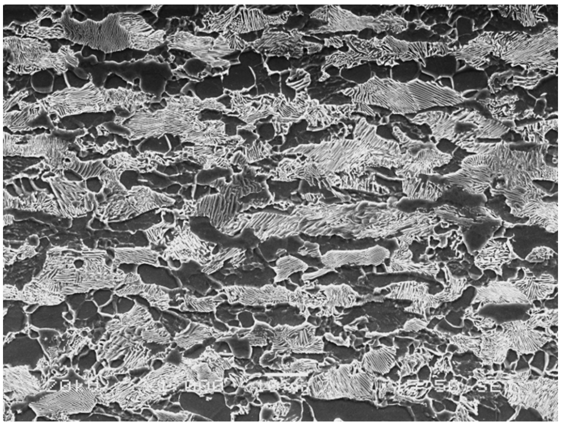

Figure 5: SEM micrograph of the 1a specimen
Slika 5: SEM-posnetek mikrostrukture vzorca 1a

3.3 Mechanical properties

Tensile tests were performed on the flat specimens with the dimensions of 35 mm × 6 mm × 4 mm. The V-notch impact-toughness test-specimen size was 3 mm × 4 mm with the notch depth of 1 mm. The HV10 hardness was measured as well.

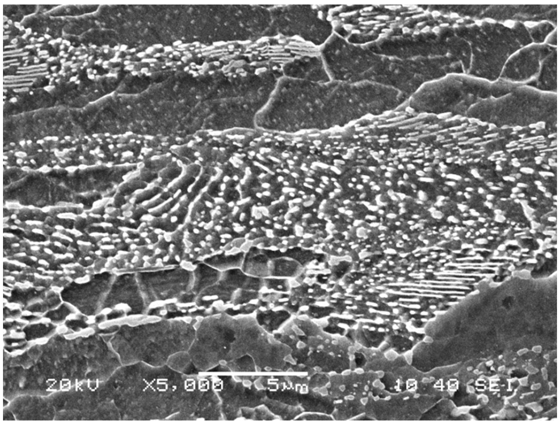

Figure 4: SEM micrograph of the 6a specimen
Slika 4: SEM-posnetek mikrostrukture vzorca 6a

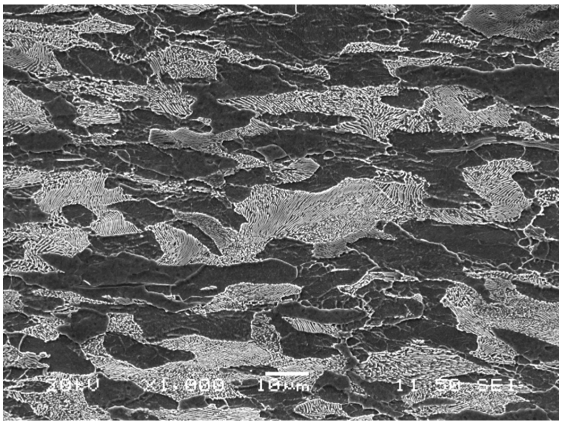

Figure 6: SEM micrograph of the 3a specimen
Slika 6: SEM-posnetek mikrostrukture vzorca 3a

Different proof stresses and ultimate strengths were measured for three specimens upon these schedules (**Table 3**). One of the three specimens showed approximately 50 MPa higher proof stress and ultimate tensile strength than the others. The figures listed in **Table 3** are the average values of three tests.

Table 3: Mechanical properties
Tabela 3: Mehanske lastnosti

Schedule	*PS*/ MPa	*UTS*/ MPa	A_5/ %	*KCV*/ (J cm^{-2})	HV 10
Initial condition	345	629	29	29	180
1a	489	702	26	38	204
2a	511	710	25	36	213
3a	542*	688*	21	35	201
4a	547	709	28	36	212
5a	550	708	27	35	210
6a	534*	668*	25	35	199

Different properties will be the subject of a further investigation. All the thermomechanical treatment schedules led to higher proof stress, ultimate tensile strength, hardness and impact toughness (**Table 3**). The final elongation was slightly lower than, or equal to, the initial elongation. Upon the schedules with smaller strain magnitudes (1a, 2a and 3a) the following trends were observed for the specimens: If deformation was applied at an early stage of the pearlitic transformation [I], the resulting proof stress was the lowest of those measured. When deformation was applied at a later stage of the transformation [III], the resulting proof stress was higher. In the specimens under the schedules with higher strains (4a, 5a, 6a), this trend was not observed and their strengths were virtually equal. The schedules with the higher strains applied at the same transformation stage as in the other schedules lead to a higher proof stress. This observation does not apply to specimen 6a, as the strength levels achieved are very similar (**Table 3**). In terms of proof stress, less strain is sufficient (φ = 0.5), provided that it is applied at the final stage of the pearlitic transformation.

Figure 7: SEM micrograph of the 6a specimen
Slika 7: SEM-posnetek mikrostrukture vzorca 6a

4 CONCLUSION

The purpose of the investigation was to improve the mechanical properties, promote the carbide spheroidisation and refine the ferrite grains in the medium-carbon C45 steel using controlled rolling. The final deformation was applied in the intercritical range at various stages of the transformation of austenite into ferrite and carbide particles. In the specimens quenched in water after the final deformation, no carbide spheroidisation or fragmentation was observed. On the contrary, in the specimens cooled in air spheroidised carbides were observed. A higher proportion of spheroidised particles was found in the specimens after a larger final deformation with φ = 1. The fraction of spheroidised carbides increased with the applied strain magnitude at the advanced stages of transformation. The microstructure showed that after the deformation applied at the final stages of transformation, recrystallisation also took place in the ferrite grains. The proof stress and ultimate tensile strength of the processed material were higher by 200 MPa and almost 100 MPa, respectively, than the corresponding characteristics of the feedstock. The elongation levels were identical, whereas the toughness of the final material was slightly higher than that of the feedstock. The experimental rolling, thus, improved the mechanical properties, facilitated a partial spheroidisation of the carbides and required less time in comparison with the conventional carbide-spheroidising methods.

Acknowledgment

The results were achieved within the project Thermo-chemical treatment of steels using fluidised bed with thermoactive micropowders no. LF13032 co-funded by the Ministry of Education, Youth and Sports of the Czech Republic.

5 REFERENCES

[1] S. Ghosh, Rate-controlling parameters in the coarsening kinetics of cementite in Fe–0.6C steels during tempering, Scripta Materialia, 63 (**2010**) 3, 273–276

[2] K. G. Ata, S. A. Meisam, Spheroidizing Kinetics and Optimization of Heat Treatment Parameters in CK60Steel Using Taguchi Robust Design, Journal of Iron and Steel Research, 17 (**2010**) 4, 45–52

[3] W. J. Nam, C. M. Bae, Coarsening Behavior of Cementite Particles at a Subcritical temperature in a medium Carbon Steel, Scripta Materialia, 41 (**1999**) 3, 313–318

[4] B. Masek, H. Jirkova, L. Kucerova, Rapid Spheroidization and Grain Refinement Caused by Thermomechanical Treatment for Plain Structural Steel, Materials Science Forum, 706–709 (**2012**), 2770–2775

[5] H. Jirkova, D. Hauserova, L. Kucerova, B. Masek, Energy and Time Saving Low Temperature Thermomechanical Treatment of Low Carbon Plain Steel, Mater. Tehnol., 47 (**2013**) 3, 335–339

[6] S. L. Zhang, X. J. Sun., H. Dong, Effect of deformation on the evolution of spheroidization for the ultra high carbon steel, Materials Science and Engineering, 432 (**2006**) 1–2, 324–332